From: McClure, Dean, EMNRD
To: Darin Savage; ripharwoodrbhpc@gmail.com
Cc: Thompson, Hailee, EMNRD; Aol.; Garcia, John, EMNRD; McClure, Dean, EMNRD
Subject: RE: [EXTERNAL] Report re Upward Vertical Growth of Fracs for Cases 22853 & 23295
Date: Monday, July 31, 2023 1:37:06 PM
Attachments: image001.png
image002.png

Thank you Mr. Savage. The report has been downloaded and will be uploaded to the case file. Due to the size of the raw data files, the link to it will be included in the case file via this email, but the files themselves will not be.

Raw Data:
https://edx.netl.doe.gov/group/gti-hfts-2

Dean McClure
Petroleum Engineer, Oil Conservation Division
New Mexico Energy, Minerals and Natural Resources Department
(505) 469-8211

From: Darin Savage <darin@abadieschill.com>
Sent: Friday, July 21, 2023 5:45 PM
To: ripharwoodrbhpc@gmail.com
Cc: McClure, Dean, EMNRD <Dean.McClure@emnrd.nm.gov>; Thompson, Hailee, EMNRD <Hailee.Thompson@emnrd.nm.gov>; Aol. <jamesbruc@aol.com>
Subject: [EXTERNAL] Report re Upward Vertical Growth of Fracs for Cases 22853 & 23295

Download full resolution images
Available until Aug 20, 2023

Good afternoon,

Attached below is the Report regarding upward vertical growth of fracs, along with links to the datasets on which the Report is based. Because the size of the datasets are so immense, we have also attached two pdf graphs that summarize the relevant data in the Report.

Included with the links are instructions on how to access the data and notes describing the pages and locations of the specific data that would be relevant to the Cases.

This Report is referenced in Cimarex's reservoir engineering exhibits submitted by Mark McCoy, and the Report and Data are provided to the Division as requested in Cases 22853 & 23295 as well as to Counsel of Pride Energy, as directed.

Please let us know if you need any additional information or have questions.

Thank you,

Darin

DARIN SAVAGE

Abadie | Schill P.C.

214 McKenzie Street, Santa Fe, New Mexico 87501

*P | **970.385.4401** :: F | **970.385.4901** :: C | **970.764.8191***

This Technical report represents the best efforts of industry leaders partnered with the DOE to understand Wolfcamp hydraulic fracturing in the Delaware Basin. There is an immense amount of analysis in here which supports our argument. I've called out the most relevant below, It is focused on pressure depletion in observation wells which is the most meaningful data from the study in my opinion.

1. **Technical Report Link**

HFTS-2 (Final Report) (Technical Report) | OSTI.GOV

Or paste this in browser **https://www.osti.gov/biblio/1907894**

- **Pg 167 of pdf labeled pg 166 shows gauge depletion on the vertical B5PH at 9 months vs tops from the grid describing the project and the laterals labeled with B#H around the well that are causing the drainage**
- **The report supports our concerns in aggregate and we focus on pressure data because it has no interpretation involved .**

2. **Here is a place to download data available to the public pressure, logs, surveys, etc. again we recommend Pressure.**

Link :GTI-HFTS-2 - Groups - EDX (doe.gov)
Paste this in browser, referenced in public technical report
https://edx.netl.doe.gov/group/gti-hfts-2

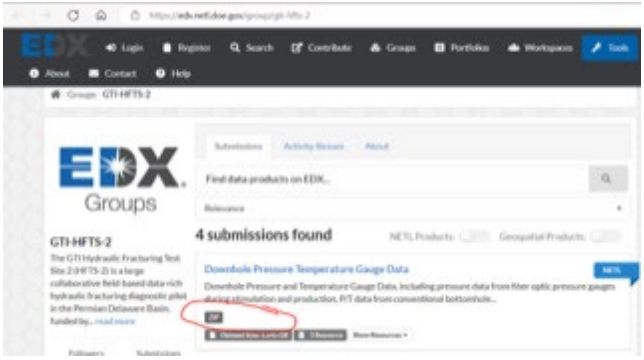

File →location in zip folder: 12-17-20 Upload - Sage Rider Gauge Data – select the 5 and 6 wells
Summary

- **The BH5 is a vertical observation well with external gauges measuring reservoir pressure ~ equidistant laterally from producing wells (pressure for frac and depletion)**
- **The BH6 is the slant observation well with external gauges measuring reservoir pressure closer laterally to Producing wells. (pressure starts later due to various science projects run in the slant prior to gauges.)**
- **These 2 wells are located between lateral wells that were stimulated in the Upper Wolfcamp A/Y and Middle Wolfcamp A.**

This is tough to navigate, I have included plots for both observation wells to save time that could be made with public data. Please find (HFTS2 Observation well reservoir pressure measurement of staggered Wolfcamp development) atached

- **I am sparsely plotting the data as daily points instead of at high resolution gauge frequency.**
- **The offset wells are denoted by arrows and labeled on the log**
- **Depletion vs. initial pressure by gauge is shown on the log**
- **Conclusions are fractures grow up**

Click to Download
Study upward vertical growth of fracs.pdf
34.9 MB

Click to Download
HFTS2 Observation well reservoir pressure measurement of staggered Wolfcamp development.pdf
865 KB

GTI ENERGY
solutions that transform

REPORT
GTI ENERGY PROJECT NUMBER 22315

HFTS-2 Final Report

DE-FE0031577

Report Issued:
December 5, 2022

Prepared For:
Mr. Gary Covatch
Project Manager
US Department of Energy
National Energy Technology Laboratory
3610 Collins Ferry Road
Morgantown, WV 26505
304-285-4589
Gary.Covatch@NETL.DOE.GOV

GTI Energy Technical Contacts:
Mr. Jordan Ciezobka
Sr. Manager, R&D
847-768-0924
jciezobka@gti.energy

Dr. Debotyam Maity
Sr. Engineer, R&D
847-768-0523
dmaity@gti.energy

1700 S. Mount Prospect Rd.
Des Plaines, Illinois 60018
www.gti.energy

File Name: DE-FE0031577_HFTS-2_FINAL_REPORT

Signature Page

Print or typed First M. Last	*Signature*	*Date*
AUTHOR:		
	Title:	
REVIEWED BY:		
	Title:	
APPROVED BY:		
	Title:	

Legal Notice

This information was prepared by GTI Energy for U.S. Department of Energy.

Neither GTI Energy, the members of GTI Energy, the Sponsor(s), nor any person acting on behalf of any of them:

a. Makes any warranty or representation, express or implied with respect to the accuracy, completeness, or usefulness of the information contained in this report, or that the use of any information, apparatus, method, or process disclosed in this report may not infringe privately-owned rights. Inasmuch as this project is experimental in nature, the technical information, results, or conclusions cannot be predicted. Conclusions and analysis of results by GTI Energy represent GTI Energy's opinion based on inferences from measurements and empirical relationships, which inferences and assumptions are not infallible, and with respect to which competent specialists may differ.

b. Assumes any liability with respect to the use of, or for any and all damages resulting from the use of, any information, apparatus, method, or process disclosed in this report; any other use of, or reliance on, this report by any third party is at the third party's sole risk.

c. The results within this report relate only to the items tested.

Table of Contents

Table of Figures

Page

List of Tables

Abstract

This report delves into the research program, identified tasks, various studies, observations, results, and conclusions under the Hydraulic Fracturing Test Site (HFTS-2) project. This test site is located in Loving County close to the Texas, New Mexico border. The program targeted the Wolfcamp formation in Delaware Basin. The aim of the project was to improve our understanding of hydraulic fracturing processes to not only optimize unconventional resource development in US Basins but to minimize environmental footprint as well. Various new diagnostic technologies were demonstrated at this site, including distributed acoustic microseismic, high resolution strain using Rayleigh frequency band (DSS-RFS), and in-fill proppant logging tool. Significant conclusions from this study include: 1) lateral and vertical fracture growth mapping as well as proppant transport behavior, 2) Use of DSS-RFS as a diagnostic tool to understand cluster level behavior, 3) Validation of proppant log, both at core scale as well as in-fill well implementation, and 4) New modeling tools to map far-field strain response using distributed strain sensing data. Specifically, far-field fracture distribution is influenced by linear fracture corridors defined by the stress-state as well as clustering behavior influenced by spatio-temporal effects. Depletion impacts on new stimulation was demonstrated and technically quantified. Significant vertical fracture height growth was observed. However, our understanding is limited by available gauge data availability. Numerical strain modeling techniques have been developed and demonstrated to help understand observed strain response behavior. Finally, proppant log has been further validated as a useful tool to map propped zones within the SRV. It has also shown very strong correlation with observed drawdown behavior at this test site. This report will detail many of these studies as well as technical results and conclusions from said studies. These include general subsurface characterization work, completion designs as implemented, studies looking at fracture geometry, high resolution microseismic study including source mechanisms, advanced DSS-RFS studies including drainage characterization, core characterization results, proppant analysis (core and in-fill child well), geochemistry, etc.

Executive Summary

The HFTS-2 project addresses the environmentally prudent development of shale oil and gas resources which require the drilling and completing of tens-of-thousands horizontal wells in multiple vertically stacked geologic horizons. Non optimal development can result in drilling substantial number of unnecessary wells resulting in waste of resources such as water, steel casings, and other infrastructure. It adds to emissions issues and land footprint. Too few wells from the perspective of well spacing and inefficient hydraulic fracturing leaves valuable resources in the ground which may be extracted later at potentially higher financial and environmental cost. These two scenarios have billion-dollar development implications as well as significant environmental implications, as each scenario leads to added emissions and land footprint. Understanding of the hydraulic fracturing geometry, which informs the well spacing, is vital to addressing this optimization problem and is the focal point of the HFTS program (both HFTS-1 project in the Permian Midland, and HFTS-2 project in the Permian Delaware).

Funded by the US Department of Energy (US-DOE) through the National Energy Technology Laboratory (NETL) and managed by GTI Energy, the HFTS-2 project is a public private partnership inclusive of sixteen industry participants comprised of producing and service companies. The partnership leverages industry funding and subject-matter expertise and facilitates immediate technology transfer leading to rapid adoption of learnings.

A highly instrumented field test site operated by Occidental, with Shell an interest partner, enabled the collection of a research-quality dataset over the course of 4 years. The field test site is in the Permian Delaware Basin in Loving County Texas and consists of eight new producing wells, two existing parent wells, and two new dedicated science/observation wells drilled during the course of the project. The eight new producing wells are landed in various Wolfcamp horizons and have lateral lengths of about 7,500 feet with laterals spaced 660 feet apart horizontally. Permanent fiber optic cables extending the entire length of the well were installed in two producing wells and in one observation well and were extensively utilized during field testing for fracture diagnostics and testing of new technologies.

The comprehensive research dataset includes microseismic surveys, 1,500 ft of whole core of which 950 is drilled through hydraulically fractured reservoir, diagnostic formation injection tests (DFIT), fluid characterization, advanced logs, geochemistry, downhole gauges, varying completions, and many advanced fiber optic surveys. These data were integrated and used to characterize HF geometry/dimensions and resulting depletion profiles, leading to improved completion design and well spacing, and a better understanding of parent well depletion effects on child well performance.

Project Data is publicly available on https://edx.netl.doe.gov/group/gti-hfts-2

The analysis and integration of the comprehensive HFTS-2 diagnostics dataset provide insights for optimal well placement and completions and improves understanding about the effects of parent well depletion. This dataset can be used to blind test and develop subsurface workflows for unconventional resources. Key learnings from HFTS-2 and the new technologies tested at the site can be applied to the environmentally prudent development of other unconventional plays.

The collected core and research quality dataset will be mined for many years to come and will lead to additional learnings and insights.

Published Art

Summary

With broad industry participation in the HFTS-2 project, various papers and articles have been published over the past few years. This section provides a listing of all such relevant articles, and

includes those by the project team and other HFTS consortium members, as well as those which have utilized HFTS-2 dataset for their respective study.

Reference to publications

1. Ciezobka, J., et al. 2020. Overview of Hydraulic Fracturing Test Sites (HFTS) in the Permian Basin and Summary of Selected Results (HFTS-I in Midland and HFTS-II in Delaware). https://doi.org/10.15530/urtec-2020-1544
2. Tan, Y., et al. 2020. Geomechanical Template for DAS Fiber Strain Patterns During Hydraulic Fracturing. https://doi.org/10.2118/201627-MS
3. Ciezobka, J. 2021. Overview of Hydraulic Fracturing Test Site 2 in the Permian Delaware Basin (HFTS-2). https://doi.org/10.15530/urtec-2021-5514
4. Bessa, F., et al. 2021. Subsurface Characterization of Hydraulic Fracture Test Site-2 (HFTS-2), Delaware Basin. https://doi.org/10.15530/urtec-2021-5243
5. Gale, J., et al. 2021. Fracture Description of the HFTS-2 Slant Core, Delaware Basin, West Texas. https://doi.org/10.15530/urtec-2021-5175
6. Grechka, V., et al. 2021. Microseismic at HFTS2: A Story of Three Stimulated Wells. https://doi.org/10.15530/urtec-2021-5517
7. Tan, Y., et al. 2021. Mechanism of Microseismic Generation During Hydraulic Fracturing - With Evidence from HFTS 2 Observations. https://doi.org/10.15530/urtec-2021-5296
8. Zakhour, N., et al. 2021. HFTS-2 Completions Design and State-of-the-Art Diagnostics Results. https://doi.org/10.15530/urtec-2021-5242
9. Ugueto, G. A., et al. 2021. An Integrated View of Hydraulic Induced Fracture Geometry in Hydraulic Fracture Test Site 2. https://doi.org/10.15530/urtec-2021-5396
10. Zhang, Z., et al. 2021. Hydraulic fracture characterization by integrating multidisciplinary data from the Hydraulic Fracturing Test Site 2 (HFTS-2). https://doi.org/10.15530/urtec-2021-5039
11. Vissotski, A., et al. 2021. Analysis of Completion Design Impact on Cluster Efficiency and Pressure-Based Well Communication in HFTS-2 Delaware Basin. https://doi.org/10.15530/urtec-2021-5289

10. Wang, J., et al. 2021. Observations and Modeling of Fiber-Optics Strain on Hydraulic Fracture Height Growth in HFTS-2. https://doi.org/10.15530/urtec-2021-5295

13. Ugueto, G. A., et al. 2021. A New Fracture Diagnostic Tool for Unconventionals High Resolution Distributed Strain Sensing via Rayleigh Frequency Shift during Production in Hydraulic Fracture Test 2. https://doi.org/10.15530/urtec-2021-5408
14. Maity, D., et al. 2021. A Systematic Interpretation of Subsurface Proppant Concentration from Drilling Mud Returns: Case Study from Hydraulic Fracturing Test Site (HFTS-2) in Delaware Basin. https://doi.org/10.15530/urtec-2021-5189

15. Pudugramam, V. S., et al. 2021. Analysis and Integration of the Hydraulic Fracturing Test Site -2 (HFTS-2) Comprehensive Dataset Venkateswaran. https://doi.org/10.15530/urtec-2021-5241

16. Gulliver, D., et al. 2021. Novel Geochemistry Determined From High Pressure, High Temperature Simulation Experiments of Hydraulic Fracture Test Site 2. https://doi.org/10.15530/urtec-2021-5219

17. Bourne, S., et al. 2021. Inference of Induced Fracture Geometries Using Fiber-Optic Distributed Strain Sensing in Hydraulic Fracture Test Site 2. https://doi.org/10.15530/urtec-2021-5472

18. Zhao, Y., et al. 2021. Key Learnings from Hydraulic Fracturing Test Site - 2 (HFTS-2), Delaware Basin. https://doi.org/10.15530/urtec-2021-5229

19. Tan, Y., et al. 2022. Interpretation of HFTS 2 Microseismic Data Using Bedding-Plane-Slip Mechanism. https://doi.org/10.2118/209232-PA

20. Turner, A., et al. 2022. Integration of Time Lapse Geochemistry to Enhance Subsurface Characterization at Hydraulic Fracture Test Site II. https://doi.org/10.30632/SPWLA-2022-0086

21. Cao, M., et al. 2022. Impact of Complex Fracture Networks on Well Productivity: A Case Study of the Hydraulic Fracturing Test Site #2. https://doi.org/10.2118/209131-MS

22. Maity, D., et al. 2022. Quantifying Proppant in the SRV Along a Fractured Well at the Hydraulic Fracturing Test Site: A Proppant Log Case Study from Permian-Delaware Basin. https://doi.org/10.15530/urtec-2022-3704106

23. Maity, D., et al. 2022. Novel Proppant Logging Technique for Infill Drilling of Unconventional Shale Wells. https://doi.org/10.2118/209790-PA

24. Guerrero, J. O., et al. 2022. High Resolution HFTS2 Slant Core Imaging through X-Ray Computed Micro Tomography. https://doi.org/10.15530/urtec-2022-3709572

25. Wang, J., et al. 2022. Deep-Learning-Based Prediction of Post-Fracturing Permeability Field for Development Strategy Optimization in Unconventional Reservoirs. https://doi.org/10.15530/urtec-2022-3723603

Background

Introduction

The Hydraulic Fracture Test Site 2 - Delaware Basin (HFTS-2) project provides the opportunity to address the "billion-dollar problem" or the optimal development of a "stacked pay" resource which requires simultaneous drilling and completion of tens-of-thousands of wells across multiple geologic horizons, also known as "cube development". Too many wells result in a waste of resources such as water, steel casings, and other infrastructure. It adds to emissions issues and land footprint. Too few wells from the perspective of well spacing leaves valuable resources in the ground. Research results from this project are expected to have positive impact on economic, environmental and resource recovery factors.

At the HFTS-2, in excess of $30 million was used to perform hydraulic fracturing research focusing on various horizons of the Wolfcamp formation at a field site operated by Occidental Petroleum, with Shell as a joint venture (JV) partner. In addition to the field research data collected by the project, Occidental provided a significant amount of background data to support research efforts, for about a dozen existing wells in the test area as well as access to previously collected core. Additional technical and laboratory support was provided by the program members.

Building on learnings and unanswered questions from Hydraulic Fracture Test Site 1 (HFTS-1) in the Permian Midland basin, the HFTS-2 used eight new producing wells and two existing parent well to perform hydraulic fracturing research. Multiple science wells were drilled to sample and characterize the subsurface, including the collection of 540 feet of core in a vertical pilot hole and 950 feet of high-angle through-fracture core. The project installed permanent fiber optic cables in 3 wells (two horizontal and one vertical) enabling spatial and temporal hydraulic fracturing propagation, geometry development, and depletion monitoring. Additional advanced diagnostics included a significant formation evaluation program on the vertical whole core, microseismic survey using multi array tools capable of moment tensor inversion, multi-well time-lapse geochemistry analysis, analysis of proppant distribution in producing child and slant core well, and others.

The HFTS-2 project comprises a series of coupled analytic and field experiments where research quality data are acquired in dedicated research wells through full instrumentation at and in proximity of hydraulically fractured wells. Furthermore, the unique site design provides a great opportunity to understand the effect of reservoir depletion, as many child-well stages overlapped parent well areas. The extensive dataset acquired was integrated and used to calibrate subsurface models and characterize hydraulic fracture (HF) geometry and proppant distribution. Diagnostics and modeling efforts enabled comprehensive calculations of HF vertical

and lateral extent and production depletion profiles, as well as quantification of the HF growth bias for child well stages that overlapped parent wells (Zhao et al 2020).

Results from the HFTS program culminate in the development of a series of optimization procedures for increased drilling and completion efficiency reducing the environmental footprint by producing the reservoir from fewer well pads and fracturing stages.

Test Site

The HFTS-2 field test site is located in the Permian Delaware Basin in Loving County Texas, Block 55 (Fig 1 left and center panels) and is operated by Occidental with Shell being a JV partner. The research well package consists of 8 new producing wells, 2 existing parent wells, and 2 new dedicated science/observation wells drilled specifically for this project. The 8 new producing wells are landed in various Wolfcamp horizons and have lateral lengths of about 7,500 feet. The lateral sections of the wells are spaced about 660 feet apart. The 2 existing parent wells are also in the Wolfcamp formation and have lateral lengths of about 5,000 feet. The 2 new science wells were drilled from the same pad which is positioned between the B3H and B4H laterals (Figure 1 right panel). One science well is a vertical pilot hole used to characterize the reservoir through the collection of mud and drill cutting samples, electric logs, and whole and sidewall cores. The well was also used to house diagnostic instrumentation including permanent fiber optic cables (FO), pressure & temperature gages, and conventional microseismic tools. The second science well is a slant well which was drilled after all wells were stimulated and was used to collect whole cores through the created fractures. The slant core well was also instrumented with pressure and temperature gauges to monitor reservoir depletion during production.

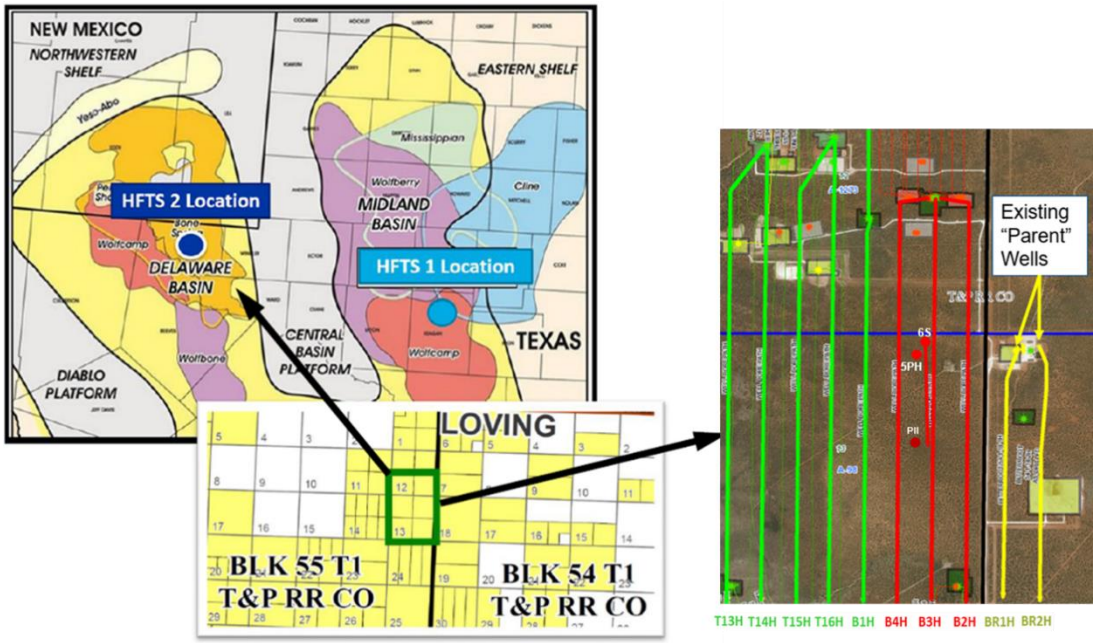

Fig 1—Location of HFTS 2. Loving County Texas block 55. Right insert is a plan view of existing (2) and new (8) horizontal wells, including 2 new science wells. Vertical 5PH and slant 6S wells (red dots).

The eight-horizontal well package consisted of 5 new uncompleted horizontal test wells (T13H, T14H, T15H, T16H, and B4H) drilled prior to project commencement, and 3 new horizontal test

wells drilled beginning in Q4 2018 (B3H, B2H and B4H) once the project started. Since the 3 new wells were drilled after the HFTS-2 project started, it allowed for modification of the data acquisition program for these wells, and as such, open hole logs were acquired in each well including quad combo and image logs, and permanent fiber optic cables were installed in 2 of the 3 horizontal wells. In B3H and B4H, FO pressure gauges were included in the toe and heel section of the wells. The FO pressure gauges were mounted externally on the casing and were ported to the casing inside to record casing pressure in the toe and heel of the well. All the producing horizontal test wells, including the 2 parent wells, are landed in the various horizons of the Wolfcamp formation. Fig 2 shows a front view of the test wells indicating the relative position of the horizontal wells and the vertical pilot and slant core well.

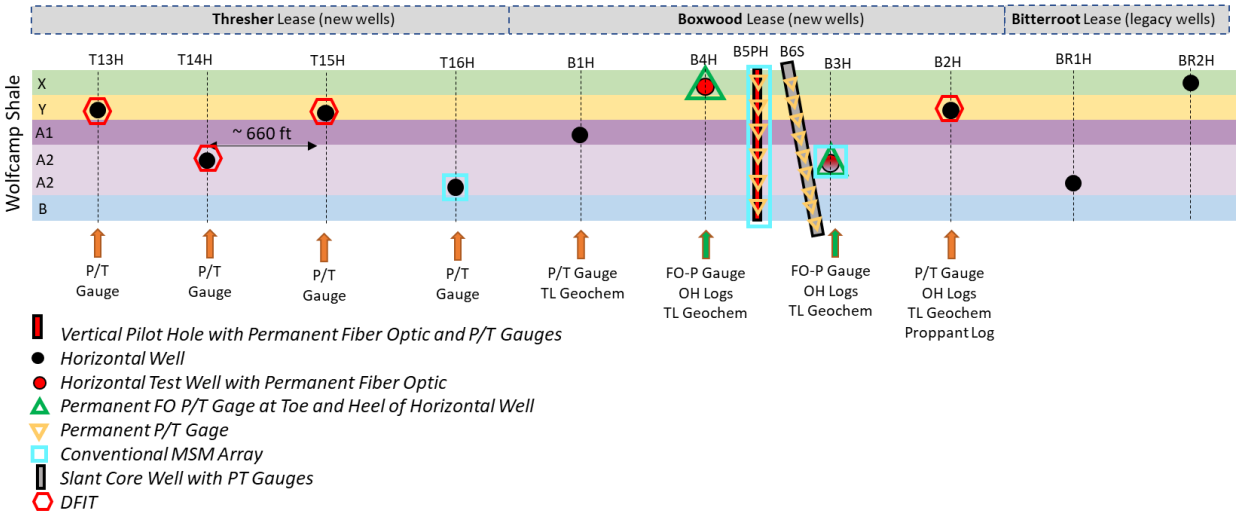

Fig 2—Test wells at HFTSII-Delaware Research Site – Permian Basin – West Texas

Fig 2 also shows a summary of various installed diagnostic instrumentation and data collected in each test well. Note that all the horizontal test wells are now on production and have been equipped with artificial lift (gas lift) and bottom hole pressure gauges.

Following the drilling and casing of all test wells, a gyro survey was run in B3H and B4H to reduce chances of collision when drilling the slant core well, B6S. A cable mapping log was also run in the B3H and the B4H to locate the position of the FO cable on the outside of the casing to allow oriented perforating away from the FO cable. To our knowledge, this is the first project which utilizes 3 fiber optic wells, including a vertical and horizontal well, to collect FO data. Next, a Diagnostic Fracture Injection Test (DFIT) was pumped in the B2H, T13H, T14H, and T15H, with pressure recorded for a few weeks using high resolution surface pressure gauges. The wells were then fracture stimulated and fracture treatments were monitored using conventional microseismic tools and fiber optic diagnostics, including Distributed Temperature, Acoustic, and Strain Sensing, DTS, DAS, and DSS. Post fracturing, the fracture plugs were drilled out, tubing was installed with bottomhole pressure gauges, and all wells were put on production. After a few months of production, the slant core well was drilled between the B3H and B4H wells and about 950 feet of core was collected, with the intention of capturing fractures from the B3H well.

After the well was drilled, 12 pressure gauges were installed. Fig 3 shows the project timeline and the sequence of field operations and various testing.

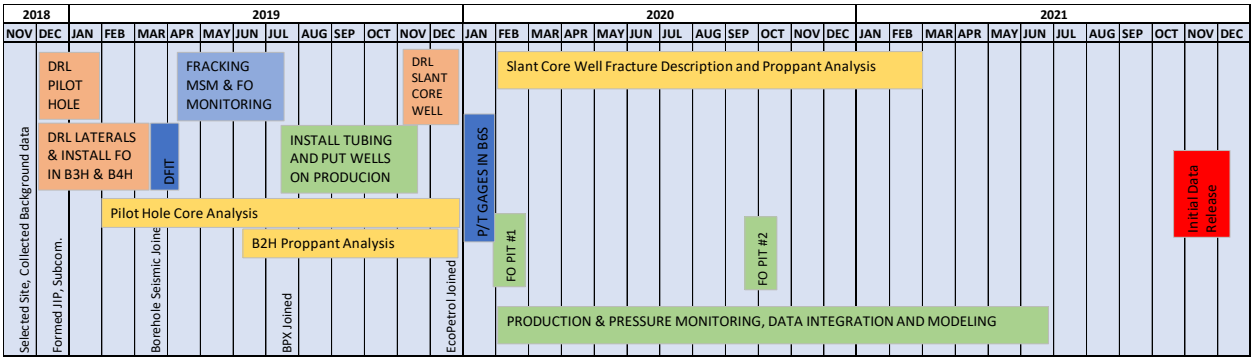

Fig 3—Project Timeline

Project structure

The HFTS-2 project is managed by GTI with DOE being the primary sponsor and NETL administering and managing the project for DOE and performing specific research. In addition to project management, GTI is also responsible for project budget, performing specific research including proppant analysis and data integration, and industry outreach to solicit industry membership and technology transfer.

The test site host, Occidental, is responsible for managing day-to-day field operations of the test site, including management of vendors and subcontractors for field and laboratory work. In addition to hosting the test site, Occidental also provided a large background dataset for 20 nearby wells (including the 8 test wells) and hosted multiple project workshops in the Woodlands. Fig 4 shows a detailed project structure and roles.

Six technical subcommittees shown in Fig 5, were created to provide technical input and direction for specific areas of the project. The subcommittees comprise members from DOE/NETL, GTI, the test site host, and all the industry members. Each subcommittee has a chair (or co-chairs) either from Occidental or Shell, or both, which leads the subcommittee. The subcommittee chairs provide guidance on specific items based on input from the subcommittee to the Technical Advisory Group, which then makes decisions regarding the direction of the overall research program.

Industry membership is comprised of 16 producing and service companies shown in Fig 6, which provide cost sharing to the project in the form of cash or in-kind contributions. The technical HFTS-2 program was designed by GTI and experts from the industry through multiple workshops and meetings. Initial planning also included identification of technology and knowledge gaps and research needed for minimization of environmental impacts and improved efficiency of hydraulic fracturing.

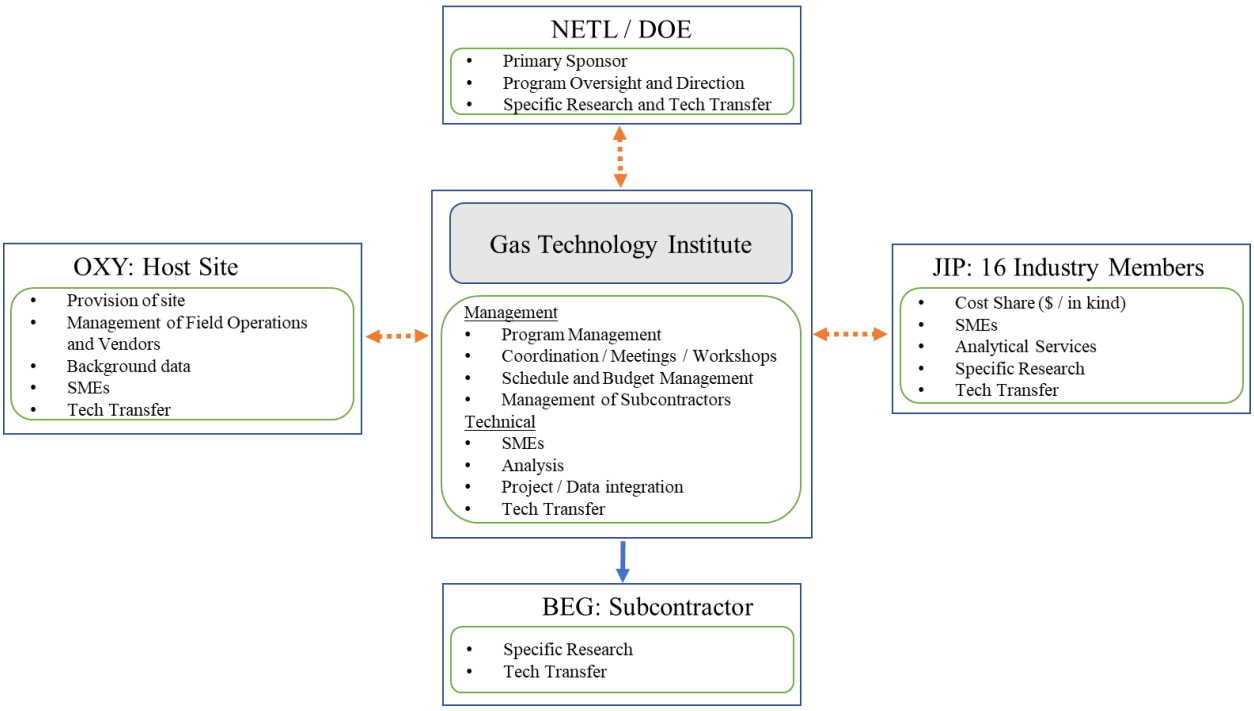

Fig 4—HFTS-2 Project Structure and Roles.

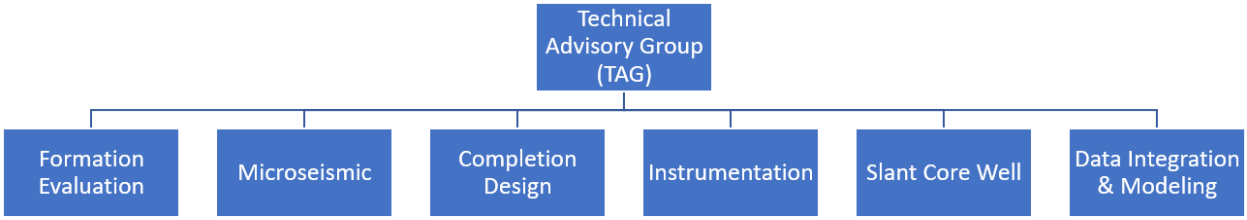

Fig 5—List of technical subcommittees

Fig 6—HFTS-2 Industry Members.

Subsurface Characterization

Authors: Fadila Bessa*, Kanay Jerath, Chris Ginn, Patrick Johnston, Yu Zhao, Tim Brown, Ruben Lopez, James Kessler, Brian Nicklen, Vinay Sahni

Summary

Hydraulic Fracturing Test Site-2 (HFTS-2) is a field-based research experiment performed in the Wolfcamp Formation of the Permian (Delaware) Basin. This section focuses on integration, advanced geological characterization, and 3D subsurface modeling of the comprehensive HFTS-2 dataset. The study showcases a multidisciplinary reservoir characterization approach that incorporates geology, petrophysics, geochemistry, geomechanics, microseismic, and subsurface engineering analysis. Subsurface characterization of organic-rich mudstone formations requires understanding complex hydraulic fracture network growth in relation to inherent lithology, geomechanical properties, and interaction with pre-existing natural fractures. This paper section presents a characterization workflow incorporating pre- and post-stimulation subsurface data, unique to the HFTS-2 dataset. The study integrated: (1) rock properties from logs, cores, and thin sections; (2) natural and hydraulic fracture descriptions from cores and image logs; (3) local and regional stresses; (4) geomechanics; (5) microseismic; (6) fiber optic (FO) and bottomhole pressure gauge (BHPG) response; and (7) produced fluids analysis. During a stimulation treatment, creation of the stimulated rock volume (SRV) is influenced by several subsurface factors. Key contributing factors include structural context, stress conditions, lithology, facies architecture, pre-existing natural fractures, and geomechanical properties. The HFTS-2 subsurface data integration indicates that the SRV is comprised of a complex juxtaposition of hydraulic fracture swarms, as evidenced by image logs analysis, core description, and microseismic monitoring. The HFTS-2 microseismic event density was used to generate 3D heat maps that serve as a representative SRV footprint, corroborated by secondary datasets. These maps were further integrated with petrophysical and geomechanical characteristics, as well as responses from Fiberoptic and bottom hole pressure gauges, to estimate the lateral and vertical dimensions of the effective fractures. The geological characterization for the HFTS-2 dataset combined with 3D modeling for petrophysical and geomechanical properties provides a strong foundation for subsurface simulation and optimization studies. The workflow improved our understanding of HFTS-2 hydraulic fracture propagation and characteristics in relation to offset pressure depletion and interaction with pre-existing natural fractures. Analysis showed that fracture geometry varies by stage and by well, and a complex fracture network is generated with varying fracture density. The multidisciplinary workflow presented herein for integration and characterization serves as a foundation to evaluate completion efficiency and estimate areal and vertical stimulation and depletion extent for projects. The workflow and learnings can also be transferred to other plays.

Introduction

Hydraulic Fracture Test Site-2 (HFTS-2) is located in Loving County, Delaware Basin, TX (Fig 7). The site is operated by Occidental and comprises multiple horizontal production wells, a vertical pressure monitoring well, and a slant well. All wells target or penetrate the Lower Permian Wolfcamp Formation.

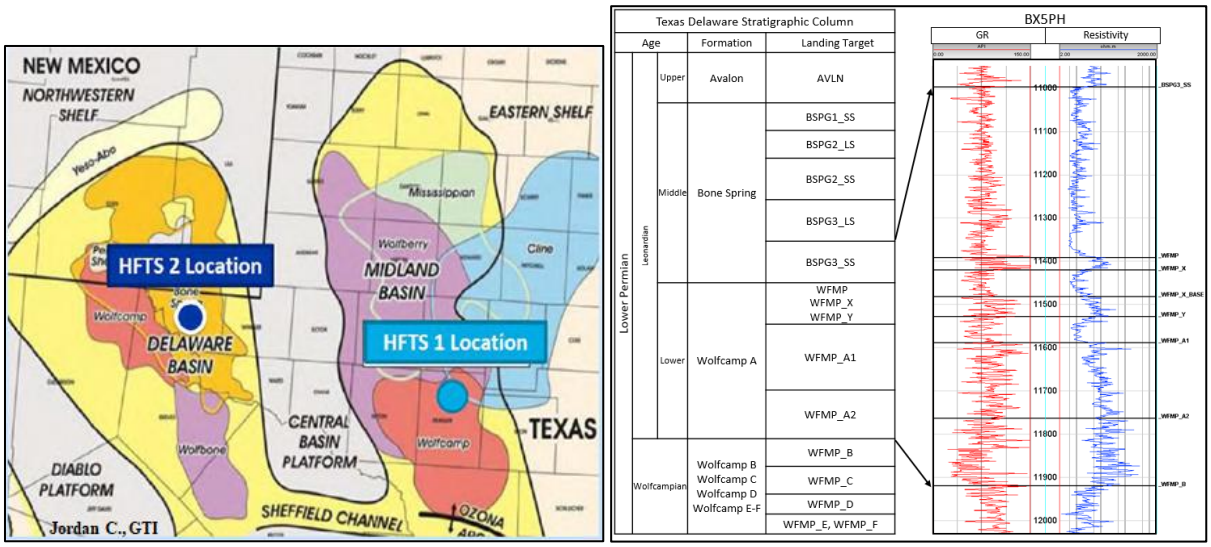

Fig 7—Location map on the left; Regional stratigraphic column and landing target on the right

The Delaware Basin is a structural sub-component of the greater Permian Basin, having formed during the Late Paleozoic (Hills, 1984). The basin deepens to the east along a dominantly monoclinal dip until encountering its terminus at the structural uplift of the Central Basin Platform, as shown in Fig 7. The magnitude of sea level change during Early Wolfcamp time was as high as 700 ft (Reid et al., 1995), leading to significant reciprocal sedimentation patterns in the deep basin. As a result, the depositional patterns of Late Wolfcampian and Early Leonardian time alternated from carbonate-dominated to siliciclastic-dominated packages, as well as significant mixed fan deposits in the organic-rich Wolfcamp A source rock (Kyale et al., 2020). The Wolfcamp A is divided into two landing zones: WFMP_A2 and WFMP_A1 (Fig 7). Overlying the Wolfcamp A are the WFMP_X and WFMP_Y siltstones that are capped by a regionally extensive mudstone above the Wolfcamp Formation. The Bone Spring Three Sandstone (BSPG3_SS) sits conformably on top of the Upper Wolfcamp well targets of HFTS-2 and represents additional reservoir potential for fracture stimulation. The HFTS-2 operation (Fig 8) involved drilling and completing four horizontal wells (BX1H, BX2H, BX3H, and BX4H), and coring a vertical well (BX5PH) and a slant well (BX6S). The primary objectives of the HFTS-2 project were to understand subsurface controls and operational impacts on fracture development, evaluate stimulated rock volume geometry, and estimate completion efficiency.

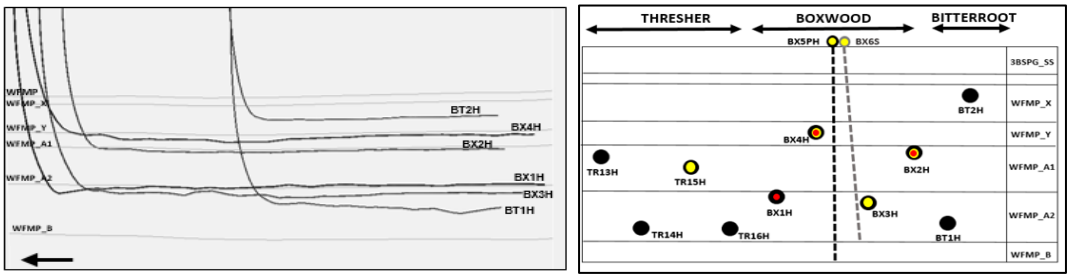

Fig 8—Left: Side view of study wells and landing zones. Right: Gun barrel view of study area and wells with image logs (5 yellow dots) and with microseismic data (3 red dots).

Methodology

Data Collection

The region around the HFTS-2 project area has good petrophysical data coverage and detailed seismic interpretation. An extensive pre- and post-stimulation subsurface dataset, unique to the HFTS-2, was analyzed and integrated in our reservoir and fracture characterization study, including:

1. Triple- and Quad-Combo open hole logs
2. Image logs in BX2H, BX3H, BX4H, BX5PH, and BX6S (Fig 8)
3. Microseismic monitoring of three horizontal wells (BX2H, BX1H, and BX4H)
4. Eight bottomhole pressure gauges in the vertical well (BX5PH) and 12 gauges in the slant well (BX6S) (Zakhour et al., 2021)
5. Fiber optic data from the four horizontal wells (BXH1, BX2H, BX3H, and BX4H)
6. Pre-stimulation core and thin sections from the vertical well (BX5PH) covering most Wolfcamp benches and a post-stimulation core in Wolfcamp A1 and A2 from the slant well (BX6S).

Core Planning and Acquisition

Several key factors in the HFTS-2 coring operations for the vertical well (BX5PH) and the slant well (BX6S) led to successful results in core recovery and core quality:

Core planning involved the discussion of coring objectives, procedures, and core handling protocols including: a) core interval details, b) estimated timing for spudding/coring, c) hole size and core size (diameter), d) target formation, e) core run length/number of runs, f) coring tool and jam mitigation system, g) mud system, h) trip out of the hole schedule, i) core laydown procedure, j) core handling area identification and requirements, k) core transportation to the laboratory, l) coring and core handling protocols, m) dry run of the coring and core handling, and n) Coring & Wellsite Core Handling Checklist document.

Coring operations for the vertical well (BX5PH) and the slant well (BX6S) were carried out safely and successfully. Completion of each coring run was followed by: a) pulling the core out of the hole at a controlled speed to prevent damage due to gas expansion, b) core barrel transfer from its vertical position in the derrick to a horizontal position in the core processing area, c) core inner barrel marking and core gamma measurement, d) inner barrels cut into 3-ft lengths using a band saw, and stabilization of the core in the inner barrel with shims, e) both ends of the core segments were capped using a rubber cap and seal with several wraps of duct tape and a stainless-steel hose clamp. All 3-ft inner barrel core sections were placed into secure core crates, refrigerated onsite, and transported to the laboratory for analysis.

For the vertical pilot hole core (BX5PH), there were 4 coring runs with an overall 76% core recovery. The second run recovery was 4% due a core catcher failure. Sidewall core samples were taken in this interval to cover the lost section. For the slant well (BX6S), the recovery was 100% in 9 runs. The first 6 runs were cut above the Boxwood-3H offset as per objective. The coring assembly built a tendency of 1.5°/100 ft, which had to be adjusted with a directional

correction from 13,500–13,750 ft. At this point coring resumed for the final 3 runs below the Boxwood-3H offset. A summary of the coring runs for both wells and the slant BX6S coring trajectory are included in Fig 9.

Coring Summary

Well:	BX5PH	BX6S
Hole Size:	6 3/4	6 3/4
Core OD:	3 1/2"	3" (JMS 3.0)
Mud system:	OBM	OBM
# runs:	4	9
Formation:	BSPG3 SS Wolfcamp X,A1, A2, B	Wolfcamp A1 Wolfcamp A2
Footage recovered:	549'	949'
Total recovery:	76%	100%

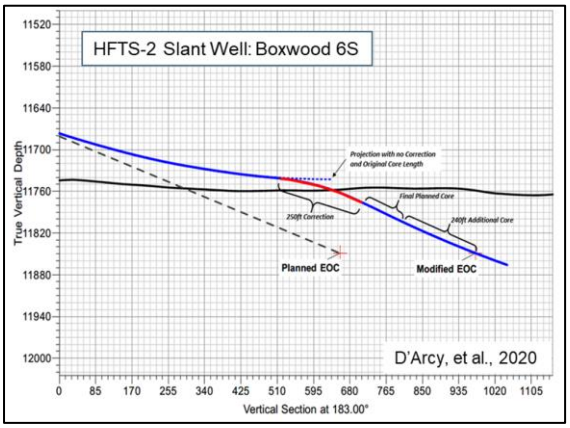

Fig 9—Left: Coring information for BX5PH and BX6S; Right: BX6S coring trajectory

Multi-Disciplinary Workflow

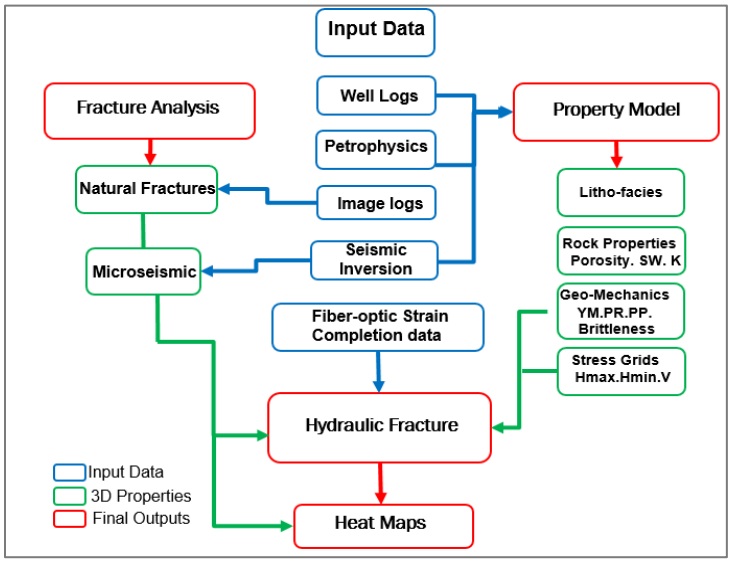

Fig 10—Streamlined workflow for understanding rock properties and fractures geometry

Predicting fracture geometry for hydraulic stimulation of unconventional reservoirs has been a challenge in the industry. Fracture density, extent, and connectivity all depend on the subsurface conditions (Gale et al., 2014; Maity, 2018). Therefore, understanding complex hydraulic fracture network growth requires subsurface data analysis and integration of lithology, rock mechanical properties, pre-existing natural fracture network, stresses, and pore pressure.

The process, shown in Fig 10, starts with assimilating all the available geoscience and engineering data for the study area (Bessa et al., 2019). The integrated workflow utilized for understanding fracture geometry and extent includes key components such as property modeling, natural fractures, and the hydraulic fracture network. Heat map evaluation was also

used to understand inter-well communication and subsequently define zones of high fracture density and potential high production performance. In this project, reservoir characterization involved integration of all Boxwood, Thresher, and Bitterroot wells followed by 3D reservoir property distribution, which formed the foundation of the simulation and completion models.

Discussion and Results

Inferences from Data

Rock Type Characterization

The stratigraphic sections in HFTS-2 consist of Wolfcamp (X, Y, A1, A2, B) and 3rd Bone Spring (sand, and limestone) formations (Fig 7). The HFTS-2 mudstones are tight rocks, with a porosity range of 2% to 7% and ultra-low permeability in the micro- to nano-Darcy range. To characterize such variation, special core measurement techniques were performed in the vertical well BX5PH on a whole core, slabbed core, and plug samples to distinguish rock types using their density, mechanical properties, and chemostratigraphy. The special analysis results were evaluated and compared to regular core and thin section descriptions and to petrophysical mineralogy.

Fig 11 shows rock type analysis in the cored intervals. Rock type analysis from different sources (eight CoreHD lithofacies, six thin section rock types, and well logs) enabled grouping them into three major lithofacies: a) siltstone/mudstone-rich silica, b) mudstone-rich carbonate, and c) limestone. They are consistent with the mineral content variation, which makes multi-well lateral correlation and 3D facies distribution easier.

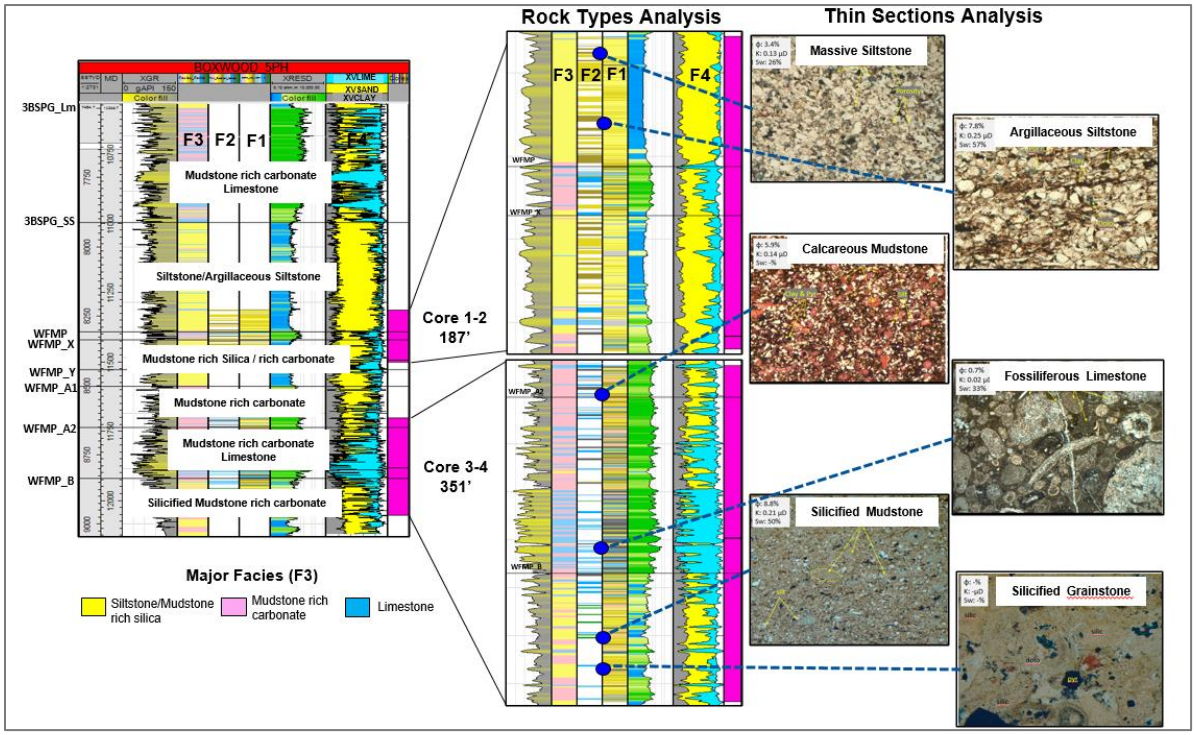

Fig 11—Rock types and facies definition. (F1) Eight cores HD Plus - lithofacies. (F2) Six thin sections - rock types. (F3) Three combined facies from petro-mineralogy logs, F1, and F2. (F4) Three petro-minerals from logs and geochemistry data.

Well Logs and Petrophysical Analysis

Wolfcamp reservoirs in the Delaware Basin are characterized by geologic and petrophysical heterogeneity at a variety of scales. Therefore, the data acquisition plan for log, rock, and fluid data for HFTS-2 project was prepared to address the heterogeneity at the different scales. From pore scale to field scale, diverse but complementary data were acquired to be able to address and integrate the subsurface characterization at all levels. Fig 12 below provides further details on the key data acquired from wireline well logs and cores.

	LOG Data type		LOG Data type
VERTICAL PILOT WELL (Boxwood 55-1-12 Unit 5PH)	Quad combo with Dipole Sonic	HORIZONTAL WELLS (Boxwood 2H, 3H & 4H)	Quad Combo with Dipole Sonic
			Oil Image Log
	NMR (T1-T2 & standard mode)	SLANT WELL (Boxwood 55-1-12 Unit 6S)	Quad Combo with Dipole Sonic
	Elemental Spectroscopy		Oil Mud Imaging log
	Azimuthal Resistivity		
	Oil Mud Imaging log		Logging While Drilling Ultrasonic Image log

Core/Rock Data type	Primary Application
Dual Energy CT Scan Photography (WL, UV, Hi-Res)	Sedimentological and Textural Features
Autoscan (FTIR, Impulse Hammer, Permeability, Sonic)	Elemental Composition, Rock Strength and Anisotropy
XRF (major & trace elements, facies model)	Elemental Composition including Trace Elements
End-cap Gas Analysis	Gas Composition
Rotary Sidewall Core Analysis	Porosity, Water Saturation, Permeability
Rock Mechanics	Rock Strength, Poroelasticity
Thin Section Scans	Rock and Pore Classification
Fracture Description and Fluid Inclusion Analysis	Fracture and Stress Orientation, Fault Identification
XRD Mineralogy	Mineral Composition
Routine and Crushed Core Analysis	Porosity, Water Saturation, Permeability
Source Rock Analysis	Organic Matter Type, Content and Maturity
Time Lapse Geochemistry	Fluid Compartment Identification and Production Allocation

Fig 12—Left: Summary of key data acquired from wireline well logs and core; Right: Special core analysis performed in HFTS-2.

The primary application of the well logs was to provide the subsurface properties listed below, which serve as critical inputs into the geologic model:

1. Organic content: quantity, type, and maturity
2. Lithology
3. Storage capacity
4. Fluid distributions and properties
5. Pore pressure profile
6. Flow properties
7. Elastic properties
8. Geochemical properties of produced oils and core extracts

All the above properties were calculated using the general guidelines and methodology discussed by Newsham, et al. in their 2019 SPWLA Organic-Mudstone Petrophysics Tutorials series (Newsham et al., 2019a, b, c). Additionally, these properties were calibrated with other available data sources, such as core measurements, PVT samples, DFITs, as appropriate, providing a high level of confidence. Fig 13 shows an integrated petrophysical interpretation snapshot of the key development intervals and interpreted wireline logs from well BX5PH. In

addition to the pilot well core, wireline logs were deployed in three horizontal wells and the cored slant well to characterize the variability of near-wellbore rock properties. Fig 14 below shows an example of an interpreted horizontal log.

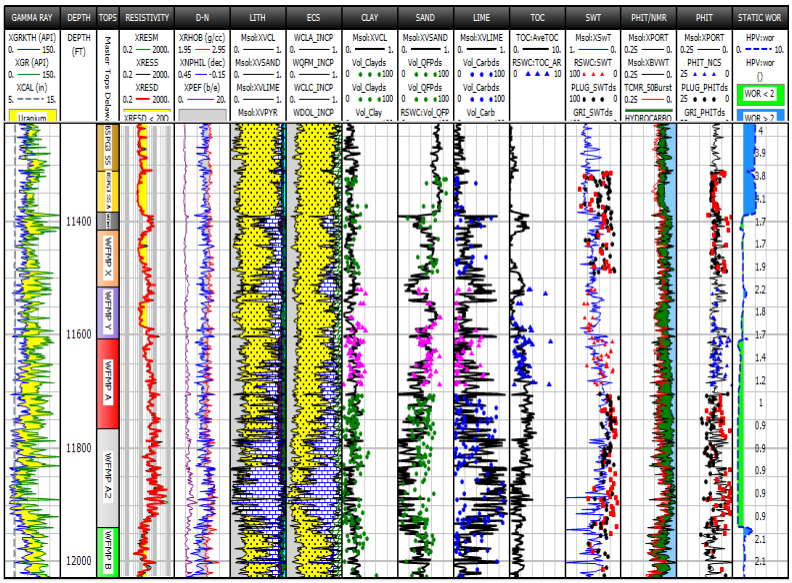

1: Spectral and Total Gamma Ray logs
2: Depth
3: Stratigraphic Formation Tops
4: Resistivity logs
5: Bulk Density, Neutron Porosity, Photoelectric Factor logs
6: Inverted Lithology from log interpretation
7: Vendor-processed Lithology using Lithoscanner log
8: Volume of Clay with core calibration
9: Volume of Quartz with core calibration
10: Volume of Calcite with core calibration
11: Total Organic Carbon with core calibration
12: Total Water Saturation with core calibration (Mismatch due to water loss during core processing)
13: Total Porosity with Bulk Volume of Water from logs and NMR Total Porosity with core calibration
14: Total Porosity from log interpretation with core calibration
15: Static Water/Oil Ratio calculated using OIP and WIP

Fig 13—Left: Integrated petrophysical interpretation in vertical pilot well BX5PH; Right: Log tracks from left to right.

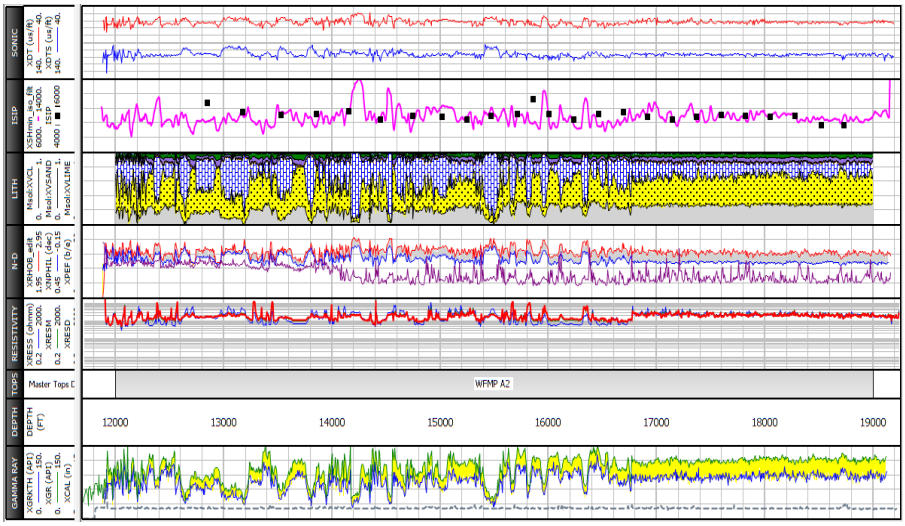

Fig 14—Left: Integrated petrophysical interpretation in horizontal well; Right: Track descriptions from bottom to top.

Fracture Description (Slant Core)

This brief fracture description review serves as an introduction to a more detailed analysis of the fracture description Fracture/ Completion Diagnostics section (Gale et al., 2021).

A total of 949.25 ft of 3-in. diameter core was recovered from 9 core runs in the BX6S well. Cores 1-6 captured rock intervals above the nearby stimulated BX3H well, and Cores 7-9 were from

below it (Fig 15). The team followed established fracture description methods as described and deployed in the previous HFTS-1 project in the Midland Basin (Gale et al., 2018).

Four main fracture types were observed: hydraulic, natural, core-handling, and drilling-induced. Of the 1,261 fractures identified, 500 were described as hydraulic fractures. These fractures were often very planar, devoid of surface morphology, and smooth. However, there were some examples of hydraulic fractures with more complicated morphologies, including steps, kinks, plumose structures, and twist-hackles. The dominant orientation of the hydraulic fractures was 80°, mirroring the local Shmax orientation. Two sets of subvertical opening-mode fractures with blocky calcite cement were observed. Set 1 natural fractures display a dominant NE-SW orientation, while Set 2 natural fractures are oriented WNW-ESE. Kinematic apertures on most of these Set 1 and Set 2 fractures are small, averaging less than 1.5 mm. Natural fracture characteristics observed are similar to previous studies from the greater Permian Basin (Forand et al., 2017; Ginn et al., 2017). Core-handling and drilling-induced fractures were present in all nine cores. Drilling-induced fractures are sometimes seen to have curviplanar, saddle-like surface morphologies, while core-handling fractures display characteristically sharp, jagged, and irregular breaks. Other features present in lesser numbers include a subvertical set of calcite-filled natural fractures of different orientations, bed-parallel natural fractures with fibrous calcite cement (“beef”), and faults with normal/oblique slip in Core 6.

All clam-shelled core barrels and whole-core open fracture faces were cleaned, and sludge samples were collected and catalogued for proppant analysis. Further discussion on proppant analysis will follow in Core Characterization - Proppant section (Maity, 2021).

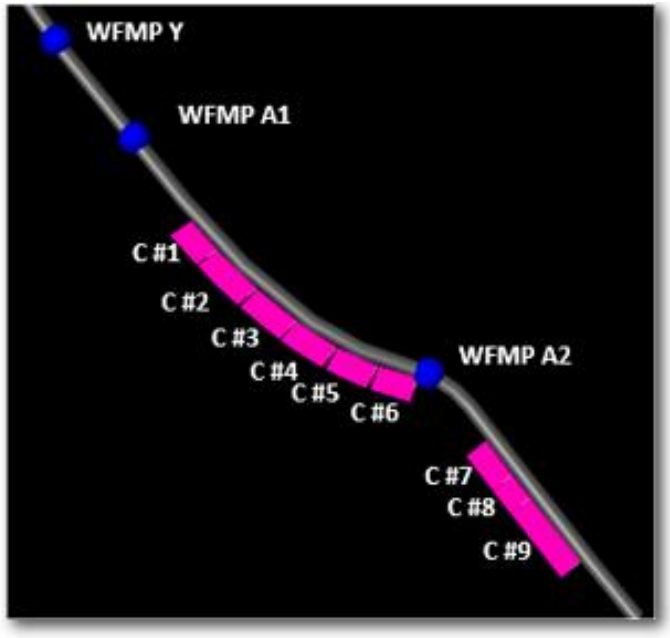

Fig 15—Slant well BX6S core layout

Microseismic Analysis

A full description of the microseismic acquisition and processing is provided in Microseismic Data Analysis section (Howell, 2021) and is summarized in Fig 16. While the geometry consists of

a 5-array design, events located for the toe-ward stages are less constrained due to the static acquisition. To minimize the acquisition effects, the catalogue was filtered to remove poor quality events defined by their location uncertainty, source parameters, and relative stage-timing. Moreover, to identify probable fluid-driven events, estimates of the average hydraulic fracture propagation velocities from the cross-well strain analysis (Gale et al., 2018) were used to define the dynamic fracture front and categorize events based on this boundary. The cleaned catalogue was used to provide estimates of SRV from event-density using statistical analysis and 3D heat maps.

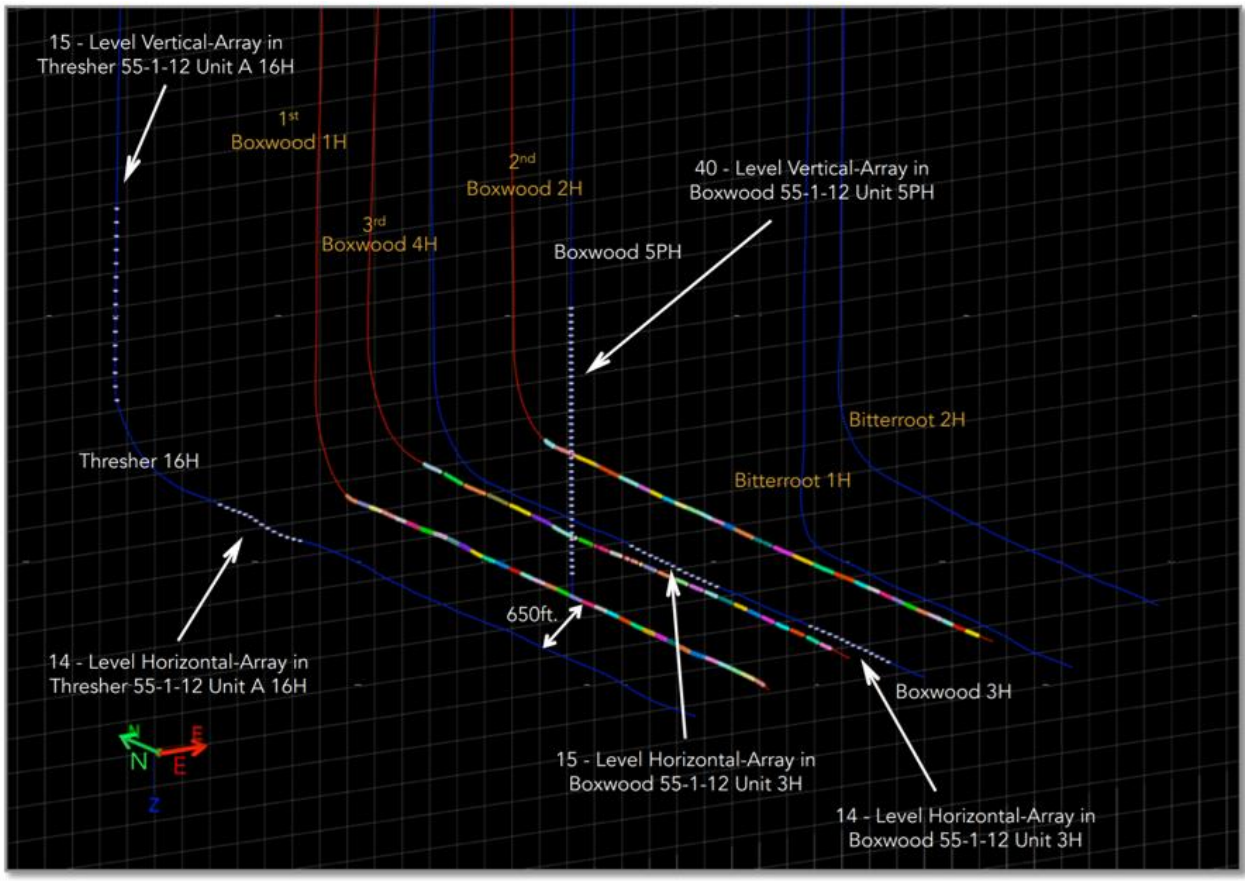

Fig 16—HFTS-2 microseismic monitoring data

Stress Characterization for Fracture Modeling

The initial state of stress is required for both hydraulic fracture models and discrete fracture models that describe the stimulated reservoir volume (SRV). The initial stress state describes the pore pressure (Pp) and the three principal stresses, σ1, σ2, σ3, represented in the cartesian reference system as overburden (S_v), minimum principal horizontal stress (S_{hmin}), and maximum principal horizontal stress (S_{hmax}). The failure mechanism is defined by the relative magnitude of the three principal stresses. The failure mechanisms defined by Andersonian mechanics are normal faulting ($S_v > S_{hmax} > S_{hmin}$), strike-slip faulting ($S_{hmax} > S_v > S_{hmin}$), or reverse faulting ($S_{hmax} > S_{hmin} > S_v$). Pore pressure was modeled using the effective stress, normal compaction trend Eaton method from compressional velocity well data (Thiercelin and Plumb, 1994). The

method utilized the Terzaghi effective stress principle to estimate pore pressure from calculation of overburden and estimate of effective stress such that:

$$Pp = \sigma v - \sigma v'$$

Eq. 1

where σ_v is the overburden stress estimated from bulk density well log data and the estimate of the trend of density to the ground surface, and σ_v' is the effective stress estimated from the Eaton normal compaction trend method using compressional velocity well log data. The Eaton pore pressure model must be calibrated in onshore basins with estimates or measurements of formation pressure. In this case, we utilize the interpretation of late time falloff pressures in diagnostic fracture injection tests (DFIT).

The state of stress was modeled using isotropic and plane-strain poroelastic stress models (Thiercelin and Plumb, 1994), as shown in Equations 2 and 3, respectively:

$$\sigma 3 = \frac{\nu}{1-\nu}(\sigma v - \alpha Pp) + \alpha Pp$$

Eq. 2

$$\sigma 3 = \frac{\nu}{1-\nu}(\sigma v - \alpha Pp) + \frac{\varepsilon h E}{1-\nu^2} + \frac{\varepsilon H \nu E}{1-\nu^2} + \alpha Pp$$

Eq. 3

where:

σ_3 = least horizontal principal stress,
ν = Poisson's ratio,
E = Young's modulus,
σ_v = maximum principal stress,
α = Biot's coefficient,
Pp = pore pressure,
ε_h = minimum tectonic strain, and
ε_H = maximum tectonic strain.

In addition to pore pressure and overburden stress, elastic and poroelastic rock properties are calculated at the well log scale for input into the stress models. Those rock property models are generated from existing proprietary models developed from a database of core and log data from across the Permian Basin.
In conclusion, the stress characterization was implemented at nine wells in the study area. The stress models indicate the failure mechanism is generally normal faulting transitioning to strike-slip failure in the shallow formations of the Leonardian section above the interval of interest. In all wells, the failure mechanism in the Wolfcamp Y up through the Third Bone Spring Sand is normal faulting. That is, both principal horizontal stresses are less than the overburden such that Sv = σ_1, Shmax = σ_2, and Shmin = σ_3. For each of the nine wells, the well-based curves for Pp, Shmin, Shmax, Sv, Poisson's ratio, Young's modulus, and Biot's coefficient were exported for input into fracture models. The results of this workflow provide the initial state of stress that are initialized in both hydraulic fracture models and DFN models.

Fiber Optic Data Analysis

Using two horizontal wells (BX3H and BX4H) and one vertical well (BX5PH) instrumented with permanent fiber optic cable (FO), a near-wellbore survey and a far-field survey were conducted to achieve better understanding of spatial and temporal hydraulic fractures characteristics. The detailed FO data analysis and interpretation is discussed in Fiber Optic Data Analysis section (Zakhour et al, 2021; Pudugramam et al., 2021).

Data Integration

Natural and Hydraulic Fractures Interpretation

A comprehensive fracture description on the HFTS-2 study interval was compiled by integrating fracture interpretations from three separate sources, namely, pre-stimulation image logs from Boxwood wells and post-stimulation image logs from Boxwood wells and CT scans on slant well core to differentiate in-situ fractures from those induced by core barrel extraction and to define sealed and open fracture networks, bedding planes, and lithology changes. The methodology used the above data to define (1) fracture sets, (2) fracture types, (3) fracture intensity, and to compare them to engineering data to better understand hydraulic fracture behavior in a stimulated, naturally fractured rock (Bessa et al., 2019). Two major fracture sets were defined based on their orientation and effectiveness during stimulation (Fig 17):

Set 1: Oriented 70–100°, and most likely reactivated during stimulation. These are identified as conductive hydraulic fractures with a high frequency of fractures oriented 80° following stress maximum direction, confirmed by image log induced fractures, microseismic monitoring data, and HFTS-2 FO data (Fig 17).

Set 2: Oriented 30–60° and described as resistive fractures, confirmed by image log induced fractures, core description, and outcrop studies.

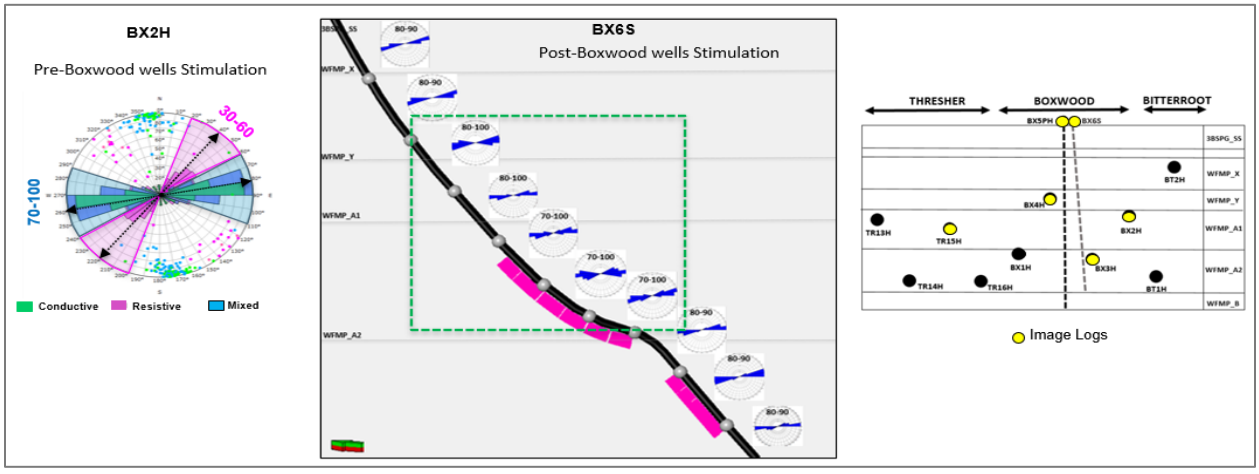

Fig 17—Fracture analysis: fracture sets and orientation from image logs. Right: Gun barrel view of the study wells and image log locations. Left: Defined fracture sets and fracture types in a horizontal well. Middle: Hydraulic fractures from image logs on the slant well.

Fracture analysis from image logs and cores indicates that HFTS-2 rocks are highly naturally fractured. These natural fractures, when reactivated during stimulation, may contribute to the creation of stimulated rock volume (Fig 17, Fig 18) (Weng et al., 2011; Lacazette et al., 2014).

A comparison of fracture descriptions from image logs and cores (Fig 18) shows consistency in hydraulic fractures' and fractures swarms' orientations (70–100°). However, core and CT scan fracture descriptions reveal a higher intensity of hydraulic fractures than those captured by the image log.

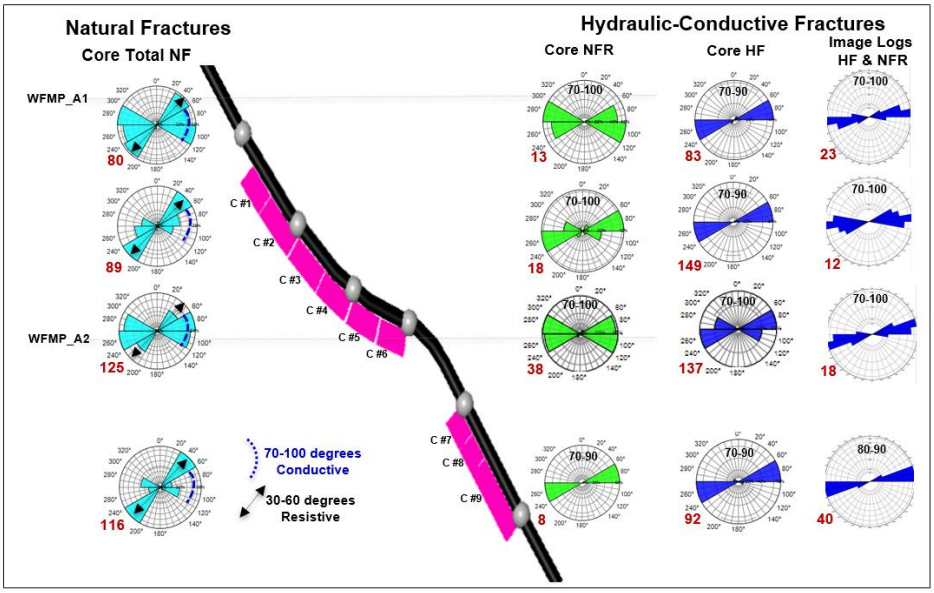

Fig 18—Core and image logs fracture description comparison on slant well: natural fractures (NF), reactivated natural fractures (NFR) during stimulation, and hydraulic fractures (HF). Fracture count = red numbers.

Data analysis of the sequence of drilling and stimulation timing helped to understand the succession of pre- and post-stimulation events, fracture network extension, and well-to-well communication. Fig 19 is a simplified schematic showing sequential timing of operations in the study area.

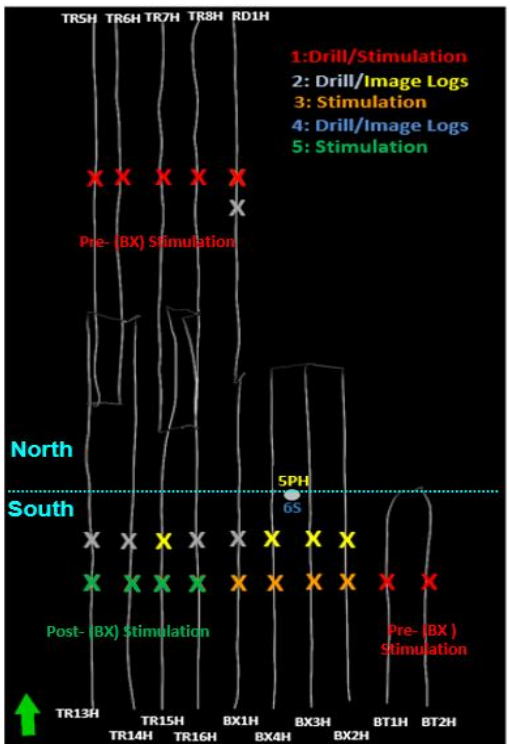

Fig 19—Schematic showing the sequence of operations

Hydraulic Fracture Lateral Growth Interpretation

Independent assessment using a proprietary mud return proppant log and a conductive fractures intensity log on BX2H showed the clear impact of BTR1H and BTR2H stimulation on the BX2H well. This is indicated by a high proppant content in the BX2H mud log return and a high intensity of re-activated natural fractures (Fig 20). The eastward bias of microseismic events after BX2H was stimulated is in line with the pre-stimulation image logs.

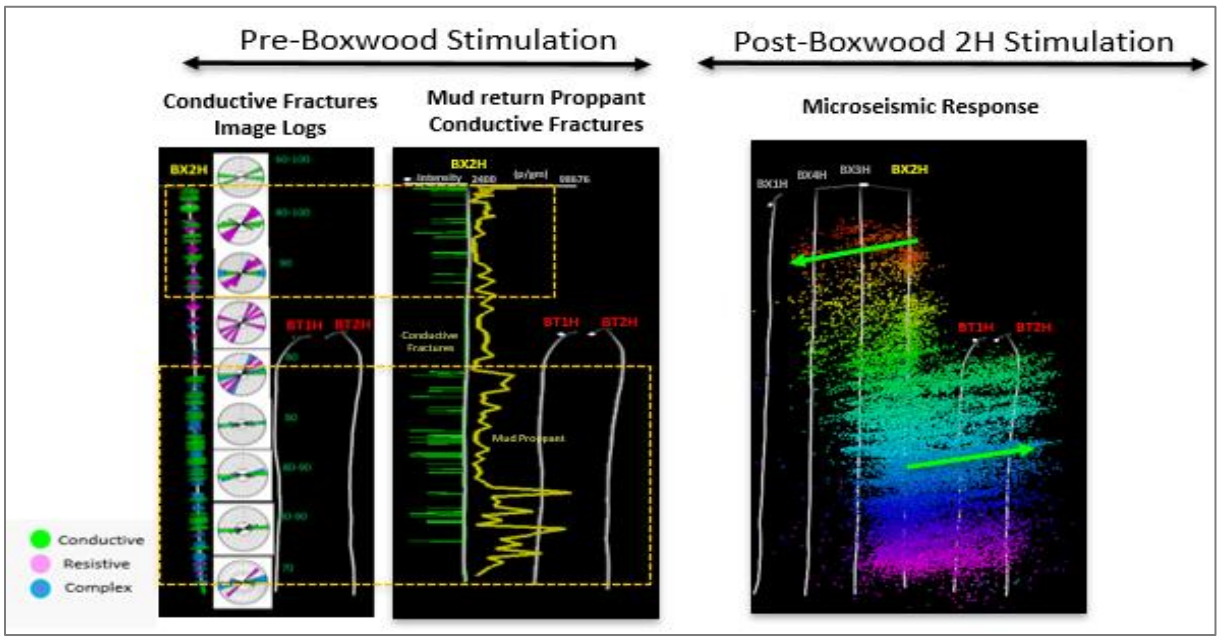

Fig 20—Parent well influence on "first child". Left: Comparison of conductive natural fractures and proppant volume in mud log returns on BX2H from Bitterroot. Right: Microseismic event patterns indicating Bitterroot stimulation impact on Boxwood wells.

Hydraulic Fractures Vertical Growth Interpretation

A multi-disciplinary integrated approach was used to understand the principal factors affecting the fractures' growth and extent during a hydraulic fracture stimulation. The contributing factors, in addition to the natural fracture network described above, include rock mechanical properties, lithology, and stress changes (Fig 21). These were compared to FO strain signals (captured by BX5PH sensors), and to microseismic event density. FO strain and microseismic events were analyzed separately, and they agree with each other. They are not a direct indicator of hydraulic fracture height and effectiveness, but they do indicate the total strain of rock under stress and temperature changes during stimulation.

The analysis of cross-well strain data acquired on the BX5PH well shows two major types of induced strain: a) mechanically induced strain related to induced fractures, and b) thermally induced strain related to rock elastic or ductile deformation. More far-field FO data analysis results are discussed in Appendix D: Analysis and Integration of the Hydraulic Fracturing Test Site-2 (HFTS-2) Comprehensive Dataset section (Pudugramam et al., 2021). A mechanically induced strain interval of 970 ft has very good agreement with microseismic event density, lithology, and stress profile from 3rd Bone Spring Sand to Wolfcamp A2.

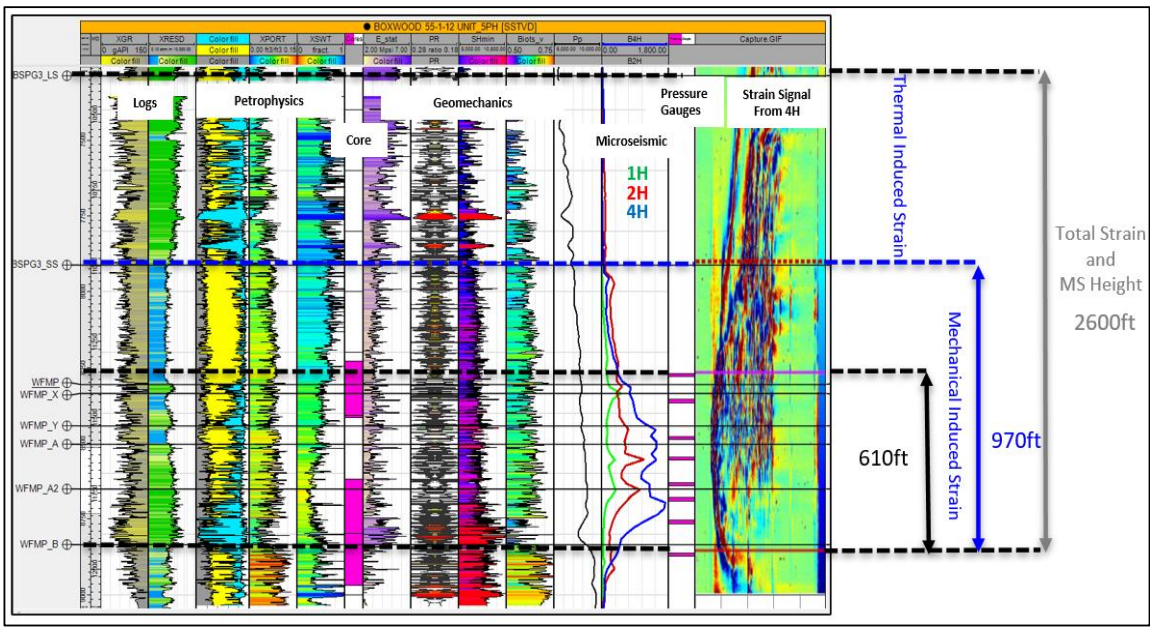

Well	Monitor	Total Strain vertical Height (ft)	Mechanical Induced Strain height (ft)
B1H	B5PH	1800	900
B2H	B5PH	1200	800
B3H	B5PH	2400	700
B4H	B5PH	2600	1000

Fig 21—Multidisciplinary integration for hydraulic fracture vertical growth. Table shows FO mechanically and thermally induced strain height for all four horizontal wells.

Quantification of Fracture Size from Heat Maps

Heat maps represent the density of any object related to hydraulic fractures (Bessa et al., 2019). They can be created from microseismic events and/or hydraulic fracture density extracted from a stimulation model. In this project, they were utilized to convert microseismic event density to a representative 3D fracture footprint (Cipolla et al., 2011). They are effective visualization tools for evaluating completion type and well spacing. In this case study, heat maps were generated (Fig 22) using the available microseismic events to estimate fracture size and SRV geometry. They also helped to correlate fracture geometries with field observations such as FO strain and stimulated natural fracture network. Heat maps helped to define the high density of events related to stimulated rock and to estimate hydraulic fracture size (Campbell et al., 2018; Pankaj et al., 2018; Xu et al., 2009; Trowbridge et al., 2017; Wang et al., 2018). Northern and southern sectors of HFTS-2 wells were evaluated separately because of Bitterroot's pre- stimulation impact on Boxwood wells. Heat map assessment of stimulation sequential time indicated: (a) high fracture activity in the southern part of Boxwood wells and their eastward tendency, (b) fracture size asymmetry as a function of landing depth and their interaction with successive stimulations, and (c) high fracture density and connectivity from the upper Wolfcamp A2 to top of Wolfcamp (Fig 23). The microseismic heat map grid helped to estimate fracture sizes (Fig 24) and compare them to those from FO strain and the completion fracture model. The comparison shows a reasonable corroboration from different data outputs (Trowbridge et al., 2017; Wang et al., 2018; Stegent and Candler, 2018).

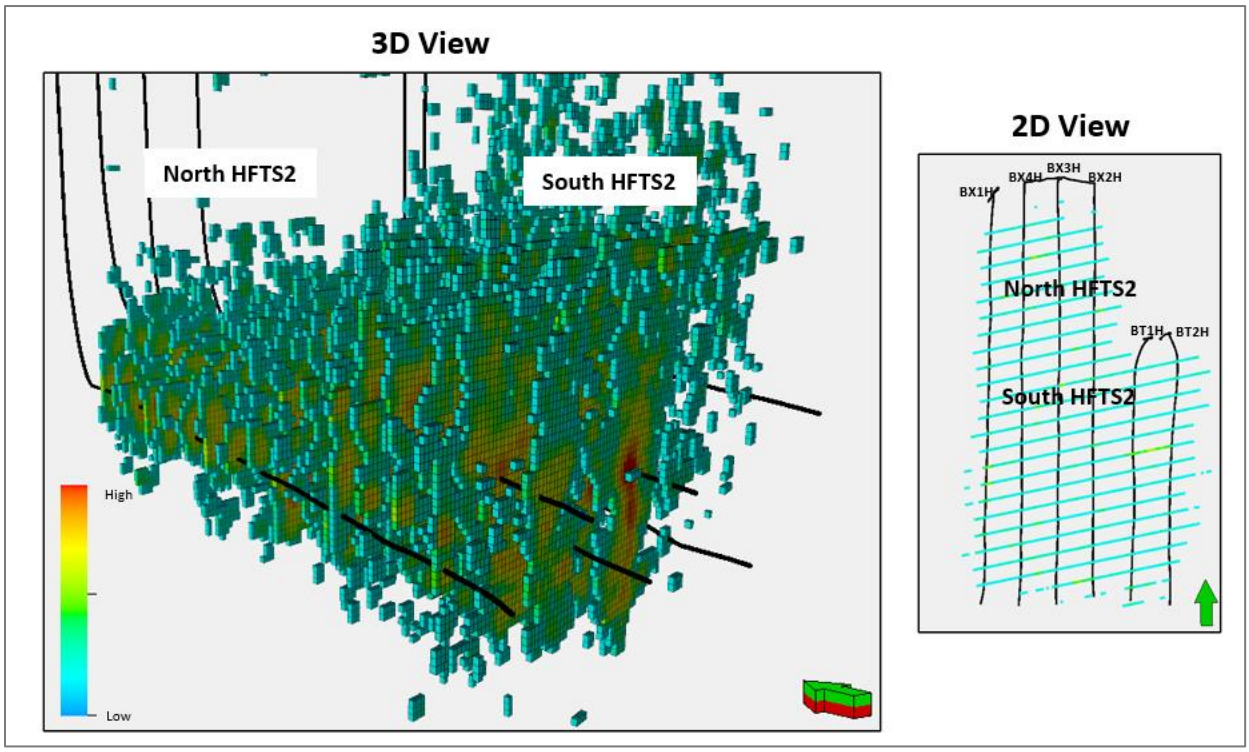

Fig 22—Left: 3D view of heat map grid showing high hydraulic fracture density and fracture size. Right: 2D view of selective section from heat map grid in North and South HFTS-2 sector.

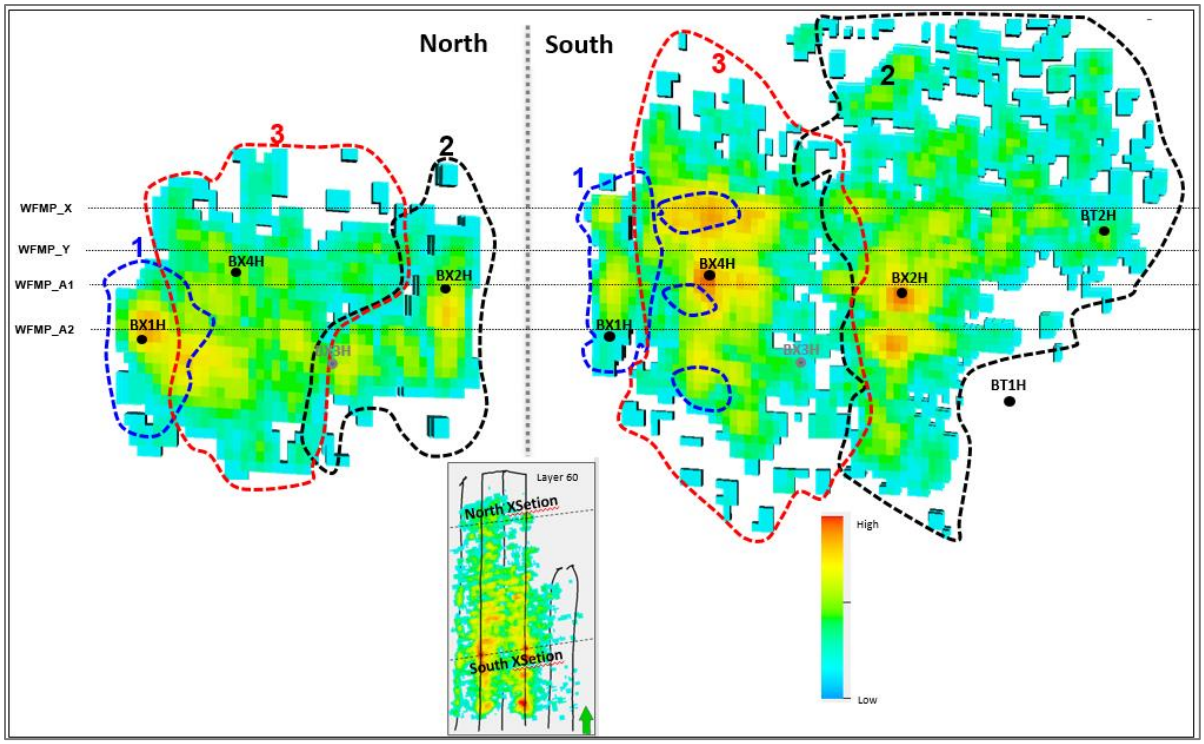

Fig 23—Areal and cross-sectional view in stimulation sequential timing of 3D heat maps grid generated for HFTS-2 area. The numbers and colors (blue, black, red) correspond to relative stimulation time successively.

Fractures Dimensions from 3D MS Heat Maps

Wells	South				North			
	East (ft)	West (ft)	Up (ft)	Down (ft)	East (ft)	West (ft)	Up (ft)	Down (ft)
Boxwood 1H	867	90	370	70	160	120	250	80
Boxwood 2H	856	398	290	193	340	730	282	190
Boxwood 4H	591	296	220	280	572	335	120	280

Microseismic 2D Heat Maps in stimulation sequential timing

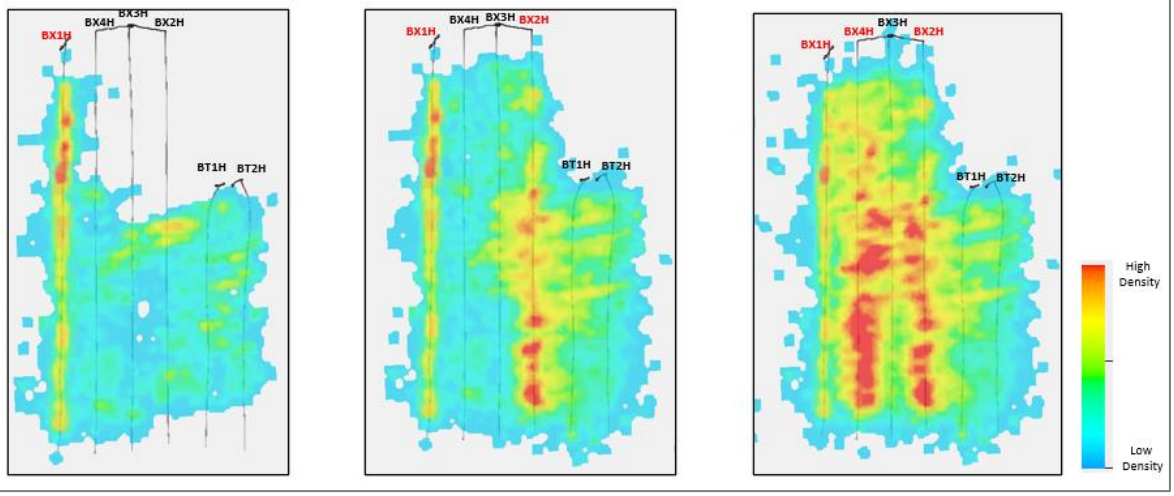

Fig 24—2D view of heat maps in sequential stimulation from left to right (red well name corresponds to stimulated well). Above: Fracture size estimation by well and by zone (south, north).

Conclusions

The integrated workflow described in this section provides a comprehensive understanding of the key parameters that influence hydraulic fracture growth in complex, organic-rich shales.

Prediction of hydraulic fracture network complexity in a shale system requires a detailed understanding of the combined effect of several factors. The factors influencing creation of hydraulic fractures include the structural context, the natural fracture network, geomechanical properties, lithology, and stress conditions.

A methodology is presented for characterizing matrix and fracture properties for dynamic numerical simulation and completion optimization.

Core analysis data and wireline logs provide critical data for integrated reservoir characterization at different scales and serve as essential inputs to the geomodel.

Special core analysis and thin sections were integrated for facies definition and to understand rock properties' heterogeneity.

Image logs and core data were utilized to comprehend hydraulic and natural fracture densities, distribution, and interaction during stimulation treatment.

Pre- and post-fracture data were analyzed to understand reservoir and hydraulic fracture characteristics. Post-stimulation microseismic events' eastward bias is in line with pre-stimulation image logs for stages that overlap parent wells. Image logs were used for parent well hydraulic fracture tracking and were evaluated using GTI's proppant log.

The far-field cross-well strain data acquired on the vertical fiber well, BX5PH, during the treatment of horizontal wells indicates that mechanically induced strains associated with the height of hydraulic fractures cover from the 3rd Bone Spring Sand to Wolfcamp A2, which aligns well with microseismic event distribution and pressure depletion profile from gauges on the BX5PH well.

Multidisciplinary integration was performed to understand vertical and lateral fracture growth. Mechanical strain signals are in line with microseismic event density, rock petrophysics, and the minimum stress profile.

For the study area, microseismic data was utilized to generate three-dimensional heat maps and understand hydraulic fractures' interaction and asymmetry as a function of stimulation sequence and timing. The study also demonstrates how heat maps can be used to better understand effective/conductive geometry and help estimate hydraulic fracture size and inter-well communication for spacing decisions.

The workflow presented here is not limited to the given area or formation. It can be applied to improve understanding and optimize fractured well performance for most unconventional fields.

Fracture Geometry

Authors: ***Gustavo A. Ugueto, Magdalena Wojtaszek, Paul T. Huckabee, Alexei A. Savitski, Artur Guzik, Ge Jin, J. Andres Chavarria, Kyle Haustveit***

Summary

Until relatively recently, most of our understanding about the geometry of hydraulically induced fractures in unconventional reservoirs has been inferred by patterns observed via microseismic monitoring. Important information, such as fracture-azimuth, fracture-length, height-growth, and other geometric data has been determined from microseismic "event clouds", which in turn has been used to interpret a stimulated reservoir volume (SRV). It is important to note that relatively limited microseismic results have been acquired in conjunction with other diagnostics and validated in a consistent manner.

The Hydraulic Fracture Test Site 2 (HFTS-2) in the Permian Delaware Basin provides a unique opportunity to compare the frac geometry interpretations derived from multiple frac diagnostic tools and at multiple scales. The integrated view that emerges from all the frac diagnostic tools is that in HFTS-2 the geometries of hydraulically induced fractures are not random and with a highly complex branching architecture as it is sometimes assumed. In fact, the fracs are mostly vertical, parallel planar domains, and both vertically and horizontally asymmetrical. The hydraulically induced fractures have a very consistent azimuth with a strike that matches SHmax. At the distance corresponding to the spacing between nearby wells in HFTS-2, ~ 660 ft, the pattern of strain-rate interceptions observed from Low Frequency Distributed

Acoustic Sensing (LF-DAS) shows far-field dimensions that are consistent with the stage length dimensions at the stimulated well. In general, larger stages with higher number of clusters create larger number of interceptions and wider stimulated intervals than that of shorter stages with fewer clusters. The hydraulically induced fractures also show a clear tendency to preferentially grow upwards as shown by the microseismic data, by the relative lower number of LF-DAS interceptions in nearby deeper wells and finally by the observed LF-DAS strain patterns in the vertical observation well. In the near field, the geometries of the fracture domains are also consistent. As shown by the distributed strain-change measurements obtained during production via the monitoring of Rayleigh Frequency Shift (RFS), each cluster has a separate, non-overlapping, frac-zone-domain that are generally centered around the locations of each perforation cluster. Overall, the hydraulically induced fractures in HFTS-2 are interpreted as occurring in swarms associated with individual clusters, each with its own unique geometry but with similar predictable geometric and propagation tendencies.

The comprehensive frac diagnostic program in HFTS-2, the well-pad layout that permits the investigation of the impact that nearby producing wells has on frac geometry, together with an innovative Design of Experiment (DofE) that includes sequential-fracing, consistent cluster-to-cluster distances and few single-perforation-cluster stages, has allowed us to gain a unique perspective about the geometry of induced hydraulic fractures on this pad. The HFTS-2 dataset

has also provided us with a better understanding of the applicability and limitations of different diagnostic tools.

Introduction

New valuable insights about frac geometry, such as fracture-azimuth, velocity of fracture propagation, hydraulic length and height can be determined and cross validated using an assortment of tools. Monitoring the creation of hydraulic induced fractures using a variety of frac diagnostic tools is a relatively expensive but necessary step for achieving successful unconventional reservoir development and to avoid under or over capitalization. Unfortunately, no single diagnostic tool can provide all the necessary information required to understand frac geometry. Misinterpretation of diagnostic data can lead to costly erroneous development decisions, thus the need for corroboration of the information provided by different and complementary diagnostic tools. Therefore, following a consilience approach is essential. In recent years, the monitoring of pressure, temperature and strain interactions between wells is providing new and detailed information about frac geometry not available before. In the Hydraulic Fracture Test Site 2 (HFTS-2) the combination of some of these technologies with traditional frac geometry diagnostic tools such as microseismic and the ground truth provided by post stimulation core-through are revealing unique information about the propagation tendencies of the fractures generated while stimulating the Wolfcamp in the Permian Delaware Basin.

Frac Geometry from Microseismic

Until relatively recently, most of the understanding about the geometry of hydraulically induced fractures in unconventional reservoirs has been inferred from poorly calibrated fracture growth models or the interpretation of patterns observed via microseismic monitoring only. Unfortunately, relatively limited microseismic results have been validated in any consistent manner (Warpinski et al. 2016). Microseismic events are mainly created as a result of shear slippage around hydraulically induced fractures. In shale reservoirs with very low matrix permeability, shear slippage occurs around the altered stresses near the tip of the hydraulic fractures, as well as, where pore pressure changes in conductive natural fractures or micro permeable layers causes the rock to exceed its shear failure envelope. Based on this, Mayerhofer et al. 2008 and others introduced workflows that equate the cloud of microseismic events to a Stimulated Rock Volume (SRV). Unfortunately, this interpretation of the microseismic cloud does not fully account for the fact that microseismic events can have significant position uncertainty, thus given the impression of a widely spread and rather homogenous SRV. This is particularly evident in datasets created by stages with closely spaced clusters. In these stages it is impossible to associate events with individual clusters. In addition, the fact that rock can also fail without generating enough acoustic energy to be detected by geophones located at a relative long distance (apparent aseismic fracturing) and finally the fact that new fractures can also interact and reopen priorly created hydraulically induced fractures is frequently ignored when interpreting SRV using microseismic only. One of the objectives of HFTS-2 was to compare and reconcile microseismic results with other diagnostics. To achieve this the DofE for HFTS-2 included: single perforation cluster stages, sequential fracing and the investigation of frac geometries on potentially stimulated and not stimulated rocks. All this was done with the

objective of simplifying the signals from the different diagnostic tools so to gain a deeper knowledge about frac geometry. In HFTS-2 a very comprehensive microseismic dataset was acquired using 5 separate multi-geophone arrays deployed in three wells, Thresher 16H (T16H), Boxwood 3H (B3H) and in the vertical observation well Boxwood 5PH (Grechka et al. 2021).

Fig 25 shows the plan view of all the microseismic events detected during the stimulation of Boxwood 1H (B1H), Boxwood 2H (B2H) and Boxwood 4H (B4H).

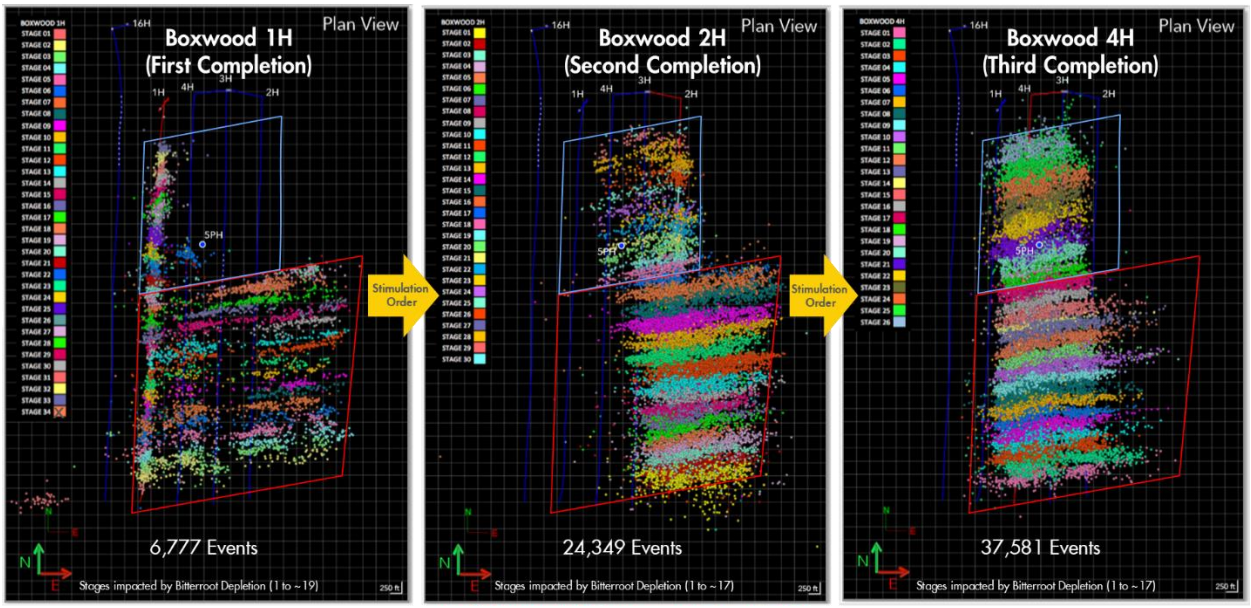

Modified from Borehole Seismic presentation June 14th, 2019

Fig 25—Plan View of all the microseismic events in HFTS2. Events are presented following the sequential fracing order in which the wells were stimulated: B1H, B2H and B3H. The dataset clearly shows the spatial and temporal effect of completion order, preexisting fractures and depletion have on the number and locations of microseismic events.

Two distinctive regions of events can be recognized on this dataset. All the toe stages (red polygon) show preferential Eastward growth, particularly for the events associated with B1H and B2H stimulation. This was somewhat expected as East of the Boxwood wells there are a couple of preexisting producers. All the stages that exhibit such pattern are grouped here under a red polygon. In contrast, the heel stages show a very different pattern. The events from these stages, grouped here under a blue polygon, do not extent as much Eastward. The preexisting producers, not shown in Fig 25 (Bitterroot wells), have shorter lateral length mostly only overlapping the toe 2/3 of the stages in the Boxwood wells. The blue polygon encloses events from stages that are not impacted by preexisting hydraulic fractures and or depletion. Fig 25 also shows the time and spatial evolution of the microseismic events in HFTS2. The number of events increases as stimulation progresses from B1H to B2H and finally B4H, 6,777 during stimulation of B1H, 24,349 during B2H and finally 37,581 events during the stimulation of B4H. It is worth noting that events associated with the B1H stimulation show very little lateral extend. These B1H heel stages occur in the not yet stimulated area, which is also an area without pre-existing hydraulic fractures (blue polygon). As the stimulation progresses and more hydraulic fractures are now present during the stimulation of B2H and B4H, the number of events also increases given the impression of a denser fracture network. Both the event patterns in the blue and red polygons, as well as the temporal effects observed in this dataset strongly suggest that detectable

microseismicity is strongly controlled by preexisting hydraulic fractures and their stress state. When new stimulation frac geometry coincides with preexisting fractures (with and without depletion), a lot of events become detectable and with higher magnitude in depleted regions. In contrast, when stimulation occurs in un-depleted and un-fractured areas less events are observed. Fig 26 illustrates the interpreted SRV associated with events shown in Fig 25. This classical, only microseismic based interpretation of the SRV provides a somewhat erroneous description of the SRV, as it does not account for aseismic fracturing and the impact that the aforementioned depletion and the stress state in prior hydraulic induced fractures can have in the generation of detectable events.

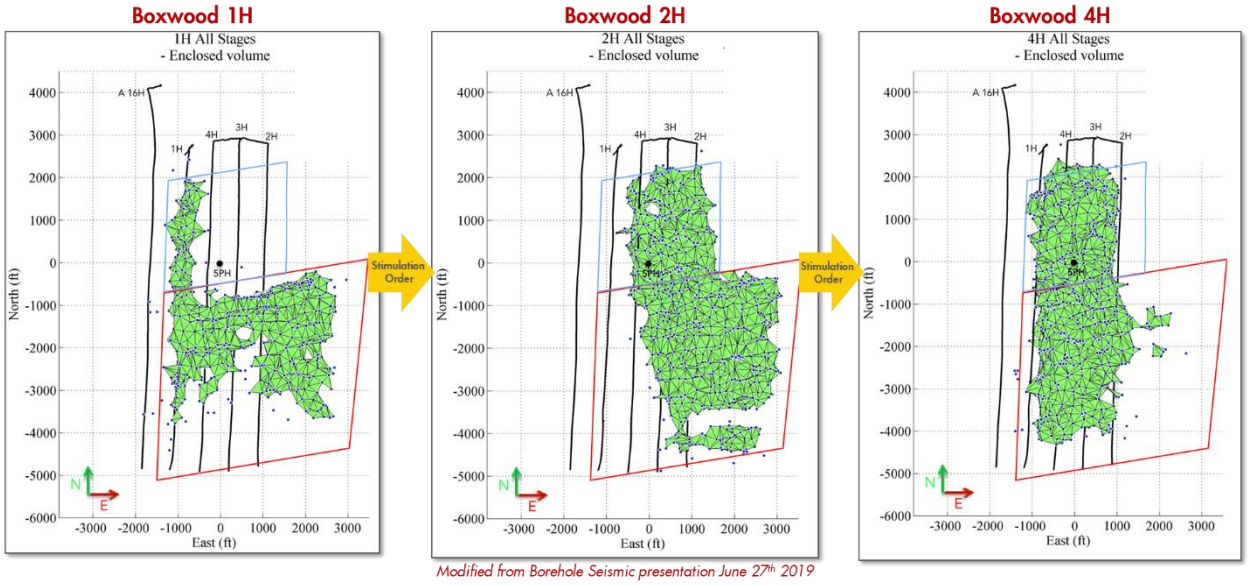

Fig 26—Microseismic only interpreted SRV and its evolution following stimulation order: B1H, B2H and B3H

Cross-Well-Monitoring, Strain Interactions during Stimulation, LF-DAS (Far-Field Frac Geometry Insights)

Fiber Optic (FO) technology such as Low Frequency Distributed Acoustic Sensing (LF-DAS) and Distributed Strain Sensing (DSS) can determine the timing and location of intercepting hydraulically induced fractures at high spatial and temporal resolution. Following the initial observation of DAS cross-well responses by Webster et al. (2013), Jin and Roy (2017) documented how LF-DAS can be used to monitor the occurrence of strain perturbations in the far-field due to the fracture propagation from the stimulation of individual clusters and stages from nearby plug-and-perf (PnP) wells. More recently, Ugueto et al. 2019, Hull et al. 2020, Wu et

al. 2021 and others have also highlighted the use LF-DAS to evaluate fracture geometry across a variety of unconventional reservoirs and completion types.

In order to better understand the LF-DAS signals and the geometries of induced hydraulic fractures in the far-field, the DofE in HFTS2 included several, relatively simple, single cluster stages. Fig 27a shows the LF-DAS observed in B3H during the stimulation of Stage 19 in B4H.

In Fig 27a the top panel displays the LF-DAS strain-rate as a color map in the not-yet-stimulated B3H. The x-axis is time, approximately 3 hours for this stage. The y-axis is measured depth, where only the impacted portion of the horizontal section of the B3H is displayed. The colors represent the axial strain-rate along the wellbore. In this color display, the green color roughly corresponds to no changes in strain-rate, while the warmer (yellow/red) and cooler (blue) colors representing intervals in which the wellbore are either extending or compressing respectively. As it is customary with this type of display, the bottom panel shows the time synchronized hydraulic fracturing treatment from the nearby well that is being stimulated (Stage 19 in B4H). In this single cluster stage, we first observed a narrowing region of extending strain rate (mostly yellow and red) as the hydraulic fractures progressively approach B3H (between time "1" and "b"). A change in strain-rate pattern occurs at time "b". This is interpreted as representing the time when the induced hydraulic fractures intercept the observation well (B3H). After this time, we see a single, mostly extending region with well-defined dimensions that represents the portion of the well containing the intercepting hydraulic fractures, in this case all from a single cluster stage. This zone is surrounded by a mostly compressing regions (blue) which represents a halo "stress shadow" region around the propagating hydraulic fractures. In this example the pattern of strain rate also changes as a two step-down and step-up rate tests were also conducted during Stage 19. After the stimulation in B4H Stage 19 ends, time "2", the LF-DAS pattern reverses in polarity almost immediately. Regions that were mostly extending are now compressing and those compressing are now starting to relax. From this type of display, we can measure and map a variety of properties, such as: frac-azimuth, frac-zone-domain width, time/volume to interception, velocity of propagation, etc. From the interpretation of the single perforation clusters stages, we conclude that in the far-field, at distances of ~660 ft, induced hydraulic fractures are contained within a single well defined frac-zone-domain with a width not much wider than the gauge length used in the acquisition of LF-DAS in the HFTS2 dataset (~5m ~ 16ft). Fig 27b shows the calculated frac-azimuth from two single cluster stages (Stages 14 and 19 in B4H). In these two stages, where the location of the fractures is precisely known, the calculated azimuth (~N80E) is remarkably consistent despite that these stages being separated in the B4H wellbore by more than 1000 ft and 4 multi-cluster frac stages, therefore indicating that individual clusters generate induced hydraulic fracture domains that are planer and parallel.

Fig 28 shows a typical example of the LF-DAS signals obtained from the stimulation of a multi-cluster, six perforation cluster stage (B2H Stage 6) observed at two different nearby wells B3H and B4H. Fig 28a shows strain-rate patterns corresponding with the interception of at least 4, possibly 5 frac-zone-domains. Based on the relative spacing between the intercepting patterns, individual frac-zone-domains are assigned to each cluster from B2H Stage 6. Perforation Cluster 1 (PC1) is interpreted as arriving first, followed by PC 5, then PC 6 and finally PC 3. All the induced hydraulic fractures for the entire stage arrived relatively early, indicating a rapid propagation of the B2H fractures toward B4H located ~1320 ft away. The example also shows

the occurrence of interference between active clusters. As subsequent fractures arrive at B4H, the strain-rate pattern from nearby cluster changes, fractures that were showing extending strain-rate suddenly start compressing, thus indicating the complex propagation tendencies of multi-cluster stages. At the end of this stage there are at least 3 well defined frac-zone-domains at the B4H location. Fig 28b shows the LF-DAS strain-rate pattern from the same stage (B2H Stage 6) at the B3H well. In this well located at ~660 ft away, strain-rate patterns corresponding to only two intercepting frac-zone-domains are observed. Comparing with the timing of the interceptions at B4H, the B2H Stage 6 interceptions occur later. This is a recurring pattern in the HFTS-2 dataset. In general, the frac-zone-domain from B2H stages intercept early in B4H which is relatively far-away than in the closer but deeper well B3H. This again suggest easier and faster propagation upwards when fractures are initiated in the Wolfcamp (Permian Delaware Basin).

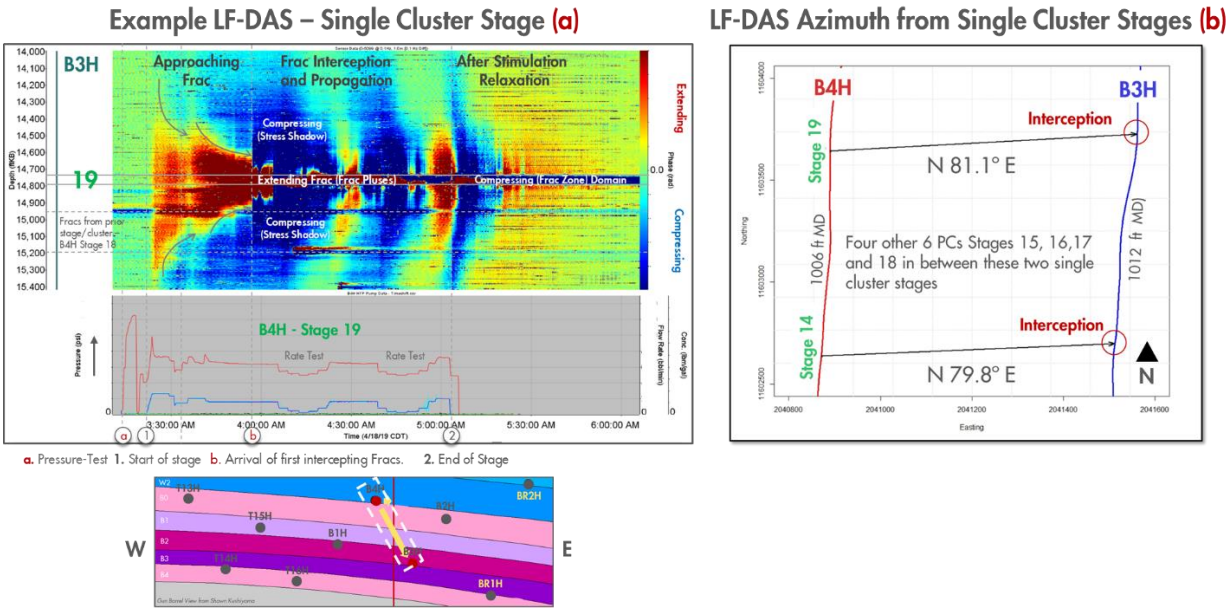

Fig 27— Example LF-DAS signal acquired during the stimulation of a single cluster stage B4H Stage 19 (a). (b) show a plan view of the vectors from a couple of single perforation cluster stages and the interpreted location of the interception in the nearby, not-yet completed well B3H. (b) also shows the corresponding calculated azimuth for these two single cluster stages ~ N80E.

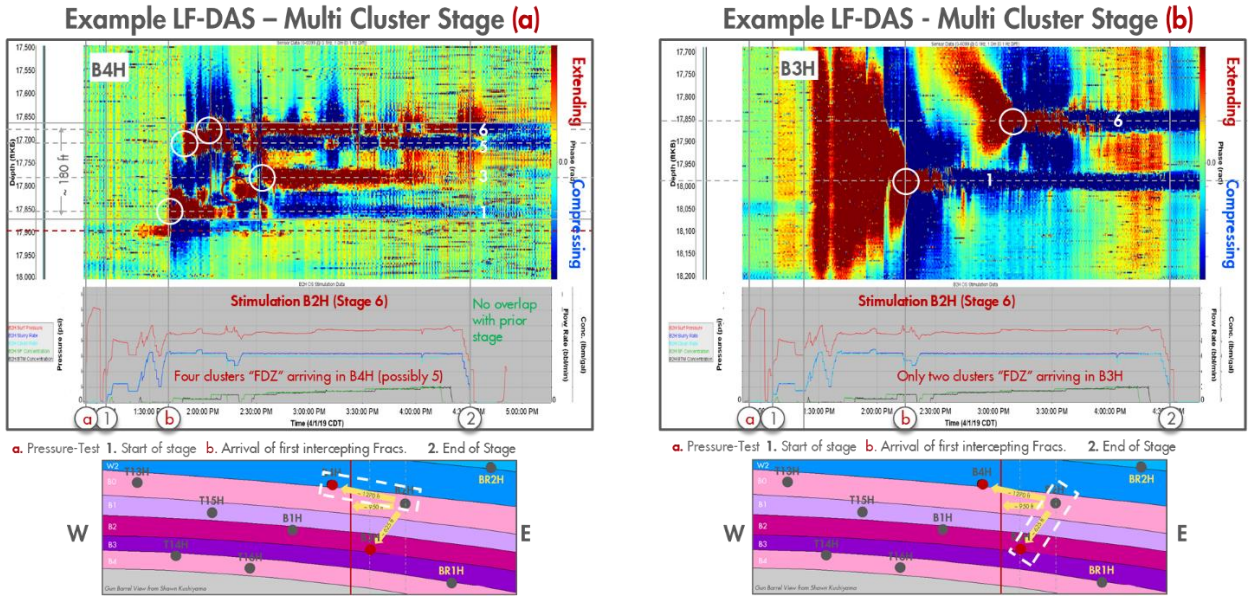

Fig 28— Example of LF-DAS signals from one stage (B2H Stage 6) in two different, not yet stimulated wells, B4H and B3H. (a) shows the time and location of 4 to 5 interpreted interceptions in B4H, while (b) shows the occurrence of only two interceptions in B3H. In (a) we can see a Far Field Stage Length (FFSL) of ~ 180 ft.

In multi-cluster stages, the interpretation of the LF-DAS strain-rate patterns and allocation of frac-zone-domains to individual clusters is somewhat speculative. However, recent geomechanical modeling of strain-rate by Zhang et al. 2020, Shahri et al. 2021 and Bourne et al. 2021 provide credibility to the LF-DAS interpretations and the allocation of signals to individual clusters. In all these papers the strain-rate results, modeled from first principles, seem to match very well the observations and interpretations of the LF-DAS signals both from single and multi-cluster stages. Fig 29 shows a plan view and the number of the interpreted hydraulic fracture interceptions of B1H into B4H and B3H, of B2H into B3H and B4H and finally between B4H and B3H. The data is shown in the order that HFTS-2 wells were stimulated B1H, B2H and B4H. To facilitate the comparison with microseismic this figure also shows the stages that are impacted and those not impacted by the nearby depletion from the preexisting Bitterroot wells, red and blue polygons respectively. This figure shows the far field propagation tendencies between the induced hydraulic fractures. When stimulating B1H we observe many more interceptions in B4H than in B3H. This makes sense given the well spacing with B4H and B3H, ~660 ft and ~1320 ft respectively. Interestingly there are far more interceptions in B3H across the blue polygon stages than in the red polygon confirming that it is relatively easier to propagate fracture downwards in absence of depletion, blue polygon stages. The occurrence of likely shallow depletion made upwards propagation easier. During stimulation of B2H we observed greater number of interpreted interceptions in both B3H and B4H, but still there are more interceptions in the blue polygon than in the red polygon area. Finally, during the stimulation of B4H we see similar number of interceptions in the blue and red polygon. Similar to microseismic dataset there is a

temporal and spatial distribution of the mapped LF-DAS strain-rate interceptions confirming that depletion and preexisting fractures have some control on fracture geometry.

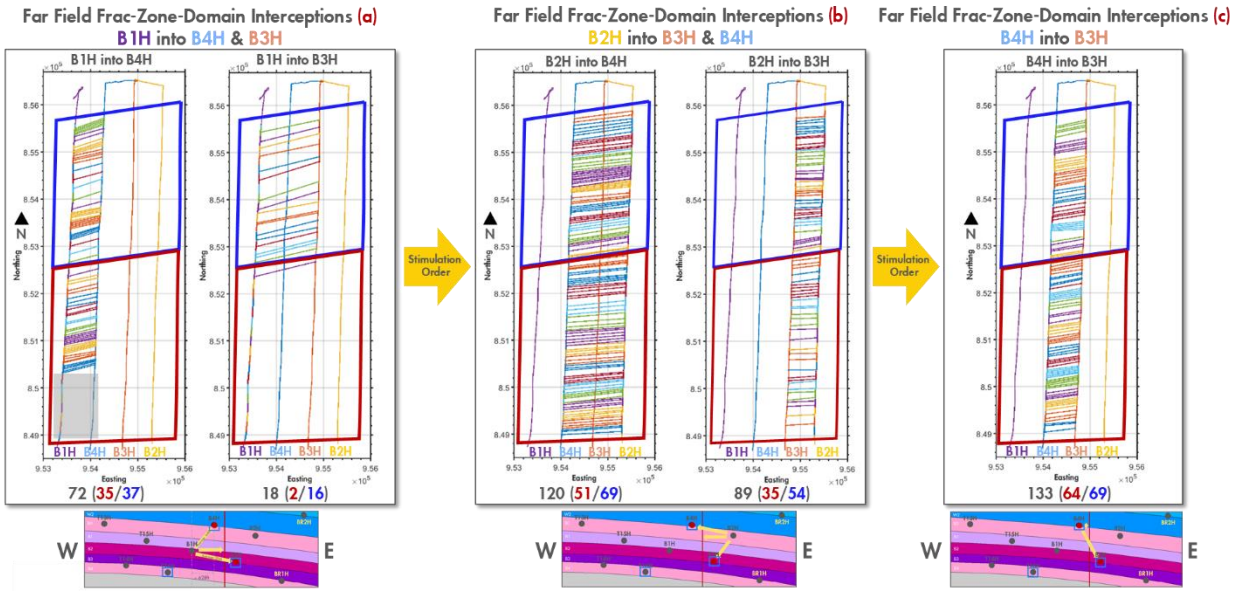

Fig 29—Plan view of the LF-DAS interpreted interceptions during the stimulation of B1H, B2H and B4H.

Fig 28 and Fig 29 also show that the frac-zone-domains from different stages do not overlap. This indicates that in the presence of good isolation a Far Field Stage Length (FFSL) can be calculated for stages showing multiple interceptions (Fig 28a). Fig 30a shows the far field stage length dimensions observed in the B4H offset well while stimulating B1H. These stages show stage length dimension distributions in the far field with an average stage length in B4H of around 200 ft for both 6 PCs and 12 PCs stages. This matches the stage length in B1H for both these two types of stimulation designs as shown by the reference lines in the whisker plots. In B1H the 12 PCs Stages have similar stage length as the frac-to-frac cluster spacing from this design is half of that from the 6 PC stages. Fig 30b and Fig 30c shows the whisker diagrams of the distribution of FFSL from B2H. This reveals that FFSL also matches the stage lengths of 6 PCs and 10 PCs stages in B2H. In B2H, as the cluster-to-cluster spacing was kept constant, the FFSL shows clear stage length differences from the two main designs. Finally, Fig 30d shows the FFSL

of the B4H stages. As in the B2H, the far-field stage length matches that of the stimulation design.

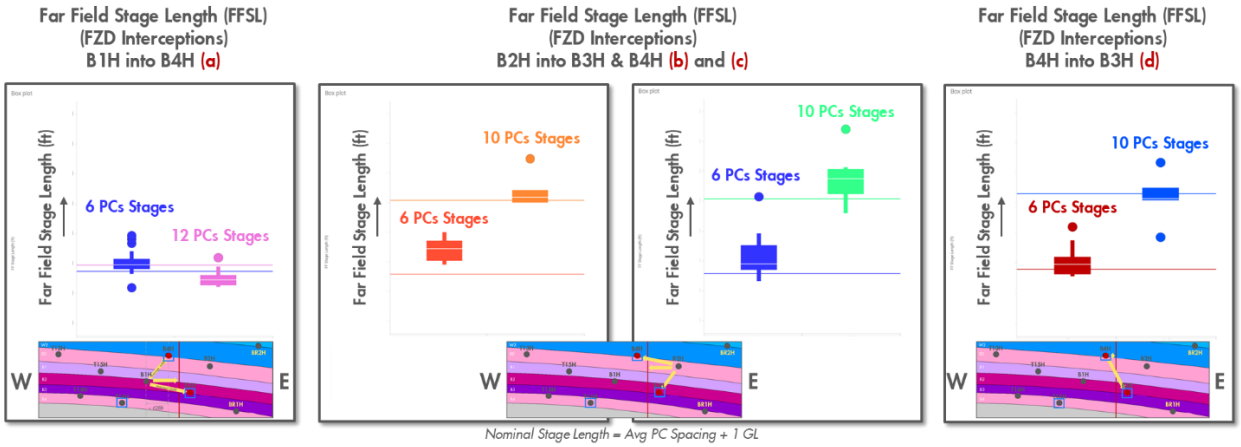

Fig 30—Whisker diagrams of the Far Field Stage Length (FFSL) dimensions from LF-DAS interceptions corresponding to the stimulation of B1H, B2H and B4H.

All this indicates that in the HFTS-2 dataset, the pattern of strain interceptions observed from Low Frequency Distributed Acoustic Sensing (LF-DAS) represent the far-field dimensions of the stages and are also consistent with the stage length dimensions at the stimulated well.

Comparison Microseismic and LF-DAS (Lateral Extend and SRV Insights)

The HFTS-2 dataset provides a unique opportunity to compare the interpreted geometries from microseismic and from LF-DAS strain interceptions. Fig 31 shows several co-display examples of the interpreted vectors corresponding to LF-DAS strain interceptions together with the clouds of microseismic events for the same stages. Fig 31a shows the comparison for a single cluster stage (B4H Stage 19). This perspective view in the direction of the fracture plain shows good correspondence between LF-DAS and microseismic. Both datasets support the occurrence of a single vertical frac-zone-domain. However, microseismic data suggests an SRV that is significantly wider than that observed by LF-DAS. We believe that this apparent inconsistency is likely the consequence of position uncertainty and, to a lesser degree, due to shear slippage in preexisting critically stressed nearby fractures. Fig 31b shows an example (plan view) of the results from the co-displaying LF-DAS interception vectors and the microseismic cloud in one multi-cluster stage (Stage 24 in B4H). Typically, we observed a rather wide, amorphous microseismic clouds without the resolution required to identify the more planar nature suggested by the LF-DAS interceptions. Fig 31c and Fig 31b shows the result from two B1H stages. In Stage 18, Fig 31c, the number of events increasing towards the depleted Bitterroot well while the LF-DAS suggest few interceptions in B4H and only one cluster intercepting B3H. This suggests that some of the microseismic in the red-polygon stages are the result of pressure connection between few frac-zone-domains (one or two) in B1H with some of the preexisting Bitterroot fracs. Fig 31d shows the opposite, a microseismic cloud of events with a small areal extent while LF-DAS suggest interceptions in both B4H and B3H, respectively. In this stage, B1H Stage 33, in an area with no preexisting fracs and no depletion, the SRV interpretation from

microseismic will be pessimistic. Conversely, in B1H Stage 18 and within the red polygon, the SRV would probably be too large.

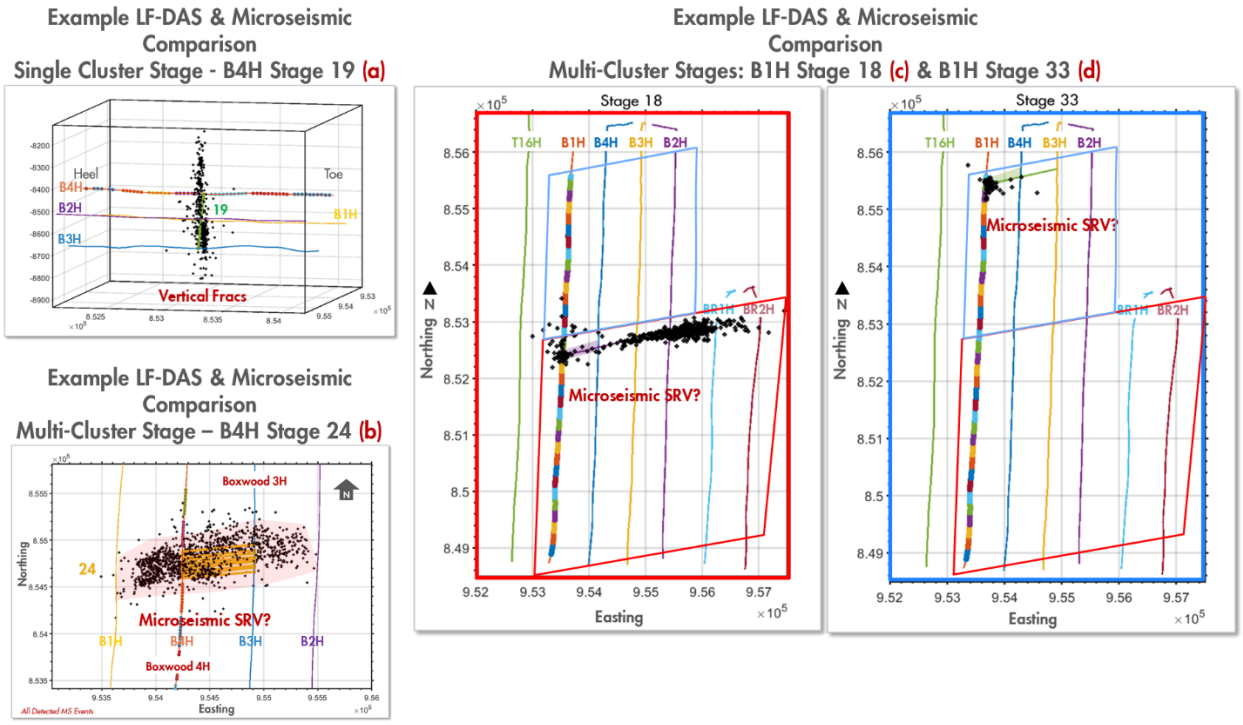

Fig 31—Example of comparison of LF-DAS interceptions and microseismic events for few stages: Single perforation cluster stage, B4H Stage 19 (a). Multi-cluster stage, B4H Stage 24 (b) and for two B1H stages, Stage 18 in an area impacted by depletion and preexisting fractures and Stage 33 in an area not stimulated by any nearby well, (d) and (c) respectively.

Cross-Well-Monitoring, Strain Interactions during Production, DSS-RFS (Near-Wellbore Frac Geometry Insights)

Most of the LF-DAS studies in unconventional reservoirs to date have focused on the monitoring of offset wells during stimulation on nearby wells. So far, little attention has been paid to monitoring strain changes during production. A new FO diagnostic method, Distributed Strain Sensing based on Rayleigh Frequency Shift (DSS-RFS), first demonstrated for oil and gas applications in the Hydraulic Test Site 2 (HFTS-2) provides us with new insights about the characteristics of the fractures in the near-wellbore-region (NWR) during production (Jin et al. 2021 and Ugueto et al. 2021). Fig 32 shows the strain-changes (Δe) in B4H after removing temperature changes from a DSS-RFS acquisition during a test performed in February 2020. Fig 32a shows the strain-changes together with the measured downhole pressures for the entire well and tested period. Fig 32b shows the average shut in strain-change (day 3) for a depth range corresponding to a single stage with 10 perforations clusters (PCs). This average strain-

change curve shows well defined peaks matching the position of 8 out of the 10 PCs for that stage. These peaks correspond to the stimulated and producing clusters.

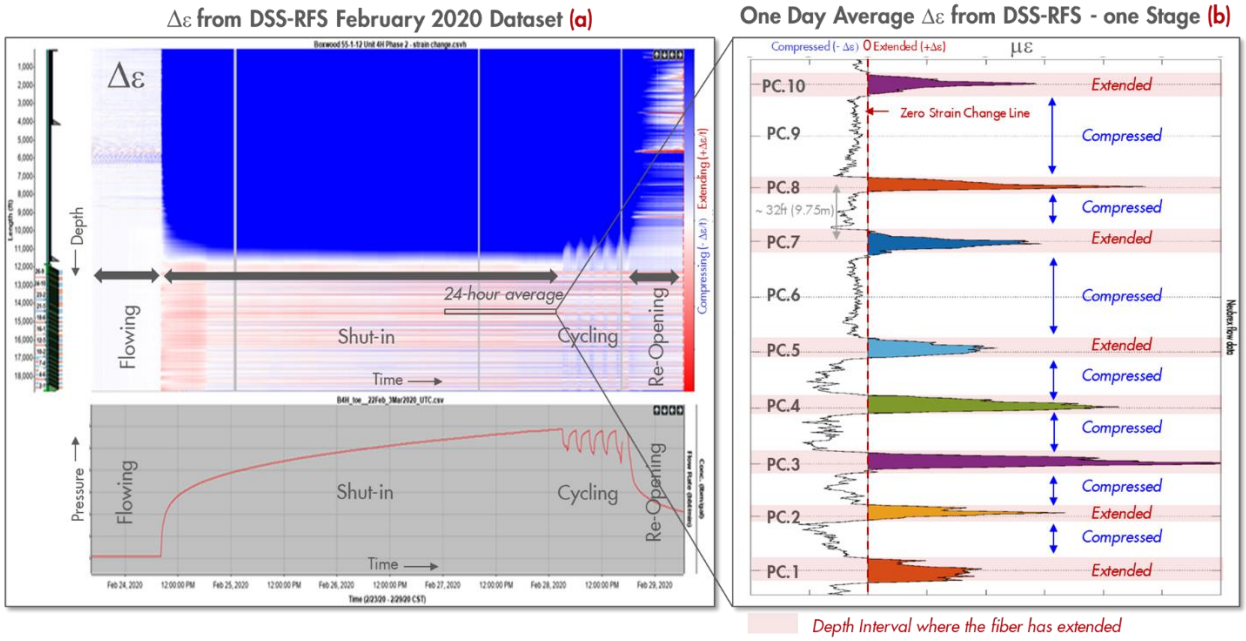

Fig 32—Strain changes and downhole pressures acquired during shut-in and reopening test conducted in FO instrumented well in HFTS2. (b) shows the 24-hours average strain-change response across a single stage with multiple clusters.

The shape and magnitude of the strain-change peaks can be related to the geometry of individual conductive fractures in the near wellbore region. In HFTS-2 we have discrete frac-zone domains for most clusters. The width of the frac-zone-domain changes cluster to cluster and is significantly different for the two main types of stimulation designs tested in B4H (Jin et al. 2021 and Ugueto et al. 2021). On average we see frac-domain-zone widths of around 12.5ft (~ 3.5m). This data shows that in the presence of good isolation between clusters, a multi-cluster stage will create individual fracture networks at each cluster with well-defined characteristics.

P/T Gauges and LF-DAS in Vertical Observation Well B5PH and Comparison with Microseismic (Frac Height Insights – Vertical SRV)

Vertical observation wells provide the best configuration to monitor the growth and geometry of vertical hydraulically induced fractures in unconventional reservoirs. Understanding how hydraulically induced fractures propagate through the different stratigraphic layers is essential. Frac modeling is typically used to predict frac height. This approach relies on a detailed and accurate knowledge of the rock properties and stresses of the reservoir and surrounding layers. Such knowledge is seldomly available. Direct observation of vertical fracture growth using diagnostics can provide the best possible indication of frac height, as well as essential data to calibrate geomechanical models.

The monitoring fracture driven pressure interactions between wells are also expanding our knowledge about the extent of fractures between nearby wells. In HFTS-2 we use the pressure

gauges installed in the vertical observation well, Boxwood 5 Pilot Hole (B5PH), to monitor amongst other things, the intensity of poro-elastic effects due to the creation of mostly vertical fractures during the stimulation of the Boxwood wells. An array of 8 P/T gauges were deployed in B5PH. Fig 33 shows an overview of the pressure response recorded during the stimulation of the HFTS2 wells.

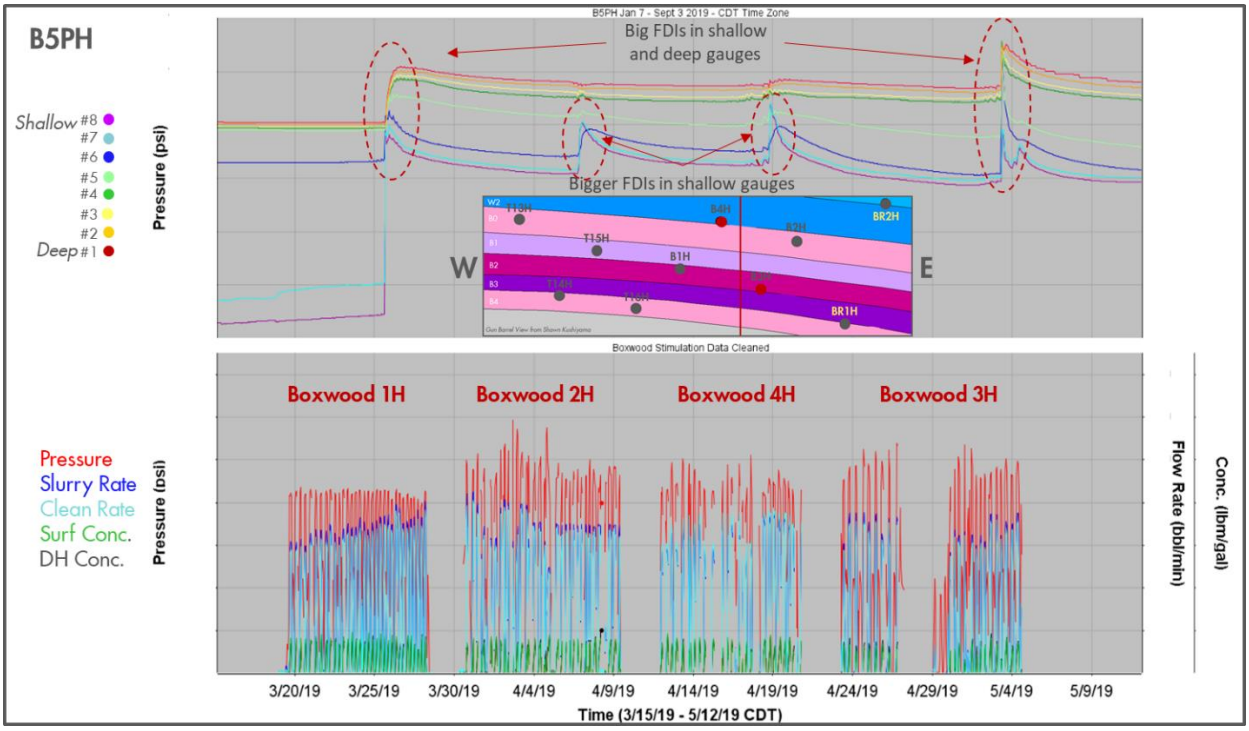

Fig 33—Pressure responses in P/T Gauge in B5PH during the sequential-fracing of B1H, B2H, B4H and B3H.

Pressure interactions in the B5PH aligned well with the fracture propagation azimuths suggested by LF-DAS interceptions. In general, all the shallow gauges (#8, #7 and #6) show comparable and larger pressure increases during stimulation of the wells but only the deeper wells B1H and B3H cause significant pressure increases in the deeper gauges (#1, #2, #3 and #4), thus supporting the shallow growth tendencies observed from the other HFTS-2 datasets (Microseismic and LF-DAS). Fig 34 shows a more detailed view of the pressure interactions in B5PH during stimulation of Stage 21 in B4H. For this stage the first pressure interaction occurs in gauge #6, which is closer in depth to the landing zone for well B4H, but larger pressure increases, around 700 psi, occur in the shallow gauges #7 and #8.

In B5PH, in addition to the P/T gauge array, a FO cable was deployed to monitor vertical strain-changes during stimulation and production. Unlike the point measurements provided by the pressure gauges, measuring strain in vertical deployed fibers allows to monitor the vertical growth of fractures. Fig 34 shows the LF-DAS signals recorded during stimulation of Stage 21 in B4H. Recent work from Zhang et al. 2020 and Bourne et al. 2021 indicate that LF-DAS strain rate in vertical wells provides information about the vertical growth of the fracture tips generated in single and multi-cluster stages. The maximum height of the fractures and vertical velocity of frac

propagation can be determined when vertical fractures from different stages pass by and project a strain-rate signal in the FO instrumented vertical well. In Fig 34 we can observe the front of a series of fractures propagating through the stratigraphy, first at the same layer where B4H is located and then asymmetrically upwards and downwards. The pattern of strain-change signals after the stimulation ends also indicates the occurrence of additional, post-stimulation, upwards growth. These frac growth tendencies are not seen only on this stage but also in other stages on this well, as well as in B1H, B2H and B3H.

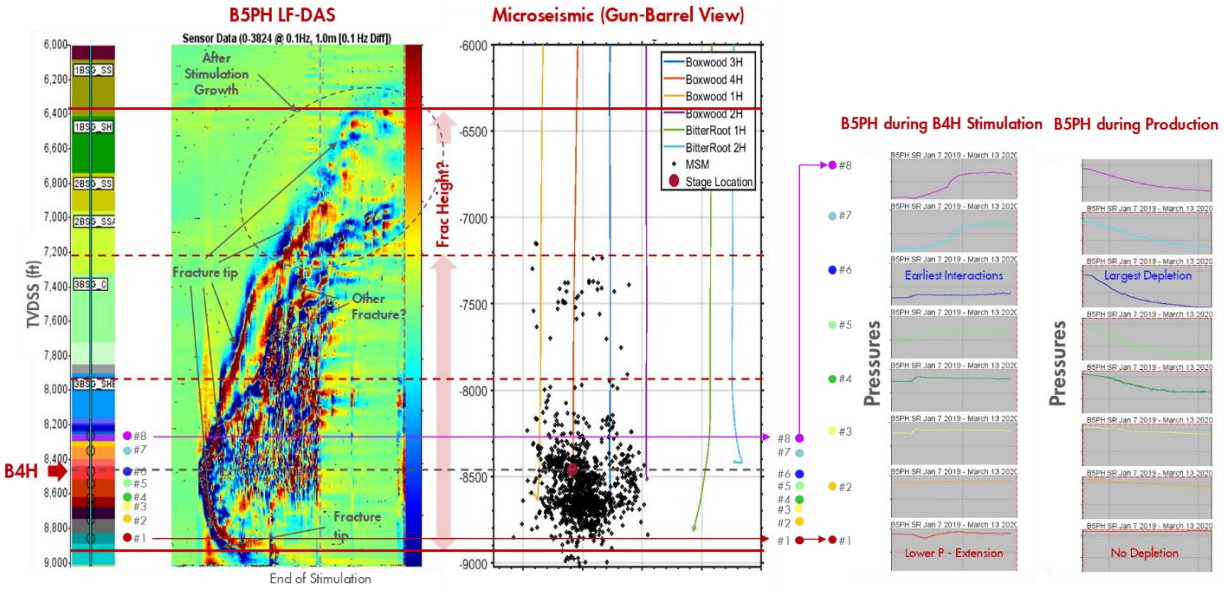

Fig 34—Comparison of LF-DAS, microseismic and pressure responses in vertical observation well B5PH during the stimulation of Stage 24 in B4H.

LF-DAS in B5PH indicate frac heights larger than those from microseismic events. Fig 34 shows a comparison of LF-DAS and a gun-barrel view of all the microseismic events recorded during B4H Stage 24. In this stage, most of the microseismic events occur in the Wolfcamp layers with few events occurring above and on a separate cloud. LF-DAS sees continuous growth between these two clouds indicating that all events are the result from the continuous propagation of the fracs in this stage. The discontinuity in the microseismic cloud is likely to be the results of the capacity of the rock in this interval (between the Wolfcamp and the 3BSG Lime) to generate detectable events. Furthermore, the high resolution, continuity and sensitivity of the LF-DAS measurements allow to better determine the extent of the fractures across layers with contrasting stress and rock properties. Again, the combination of all these diagnostics provided a more consistent and confident interpretation of the frac height in HFTS-2.

Fractures in the Post Stimulation Core-Through B6S (Natural, Hydraulic and Reactivated Natural Fractures)

Outside of a direct mineback, post stimulation core-throughs are probably the most ground-truth information we can possibly get about the nature and geometry of natural and hydraulically induced fractures. In HFTS-2 post stimulation cores were acquired in B6S (Gale et

al. 2021). Fig 35a shows an example of the fracture description and corresponding unwrapped CT-Scan of a 3 ft section in Core 1 (B6S). In this section a swarm of 5 hydraulic fractures has been identified. Such swarms are commonly observed across all the 6 post stimulation cores in HFTS-2. In B6S a total of 500 out of a total 1261 fractures were classified as hydraulic. Fig 35c shows the lower hemisphere stereograms for cores 1, 2 and 3. In addition to the hydraulic fractures (black projections) two datasets of natural fractures constitute the bulk of the fractures encountered in B6S (light and dark blue great circles). It is difficult to state how many of the natural fractures are reactivated by the stimulation, but many of the fractures observed are not parted. Other natural fractures may have come apart as a result of core handling. All these suggest that majority of open fractures observed post stimulation are hydraulic. This information together with the observations of discrete frac-zone-domains both in the near and far-field, allows us to interpret SRVs that are different from the commonly held view in which reactivated natural fractures provide the bulk of the fracture network and the effective surface area required to justify the production observed in frac stimulated unconventional wells.

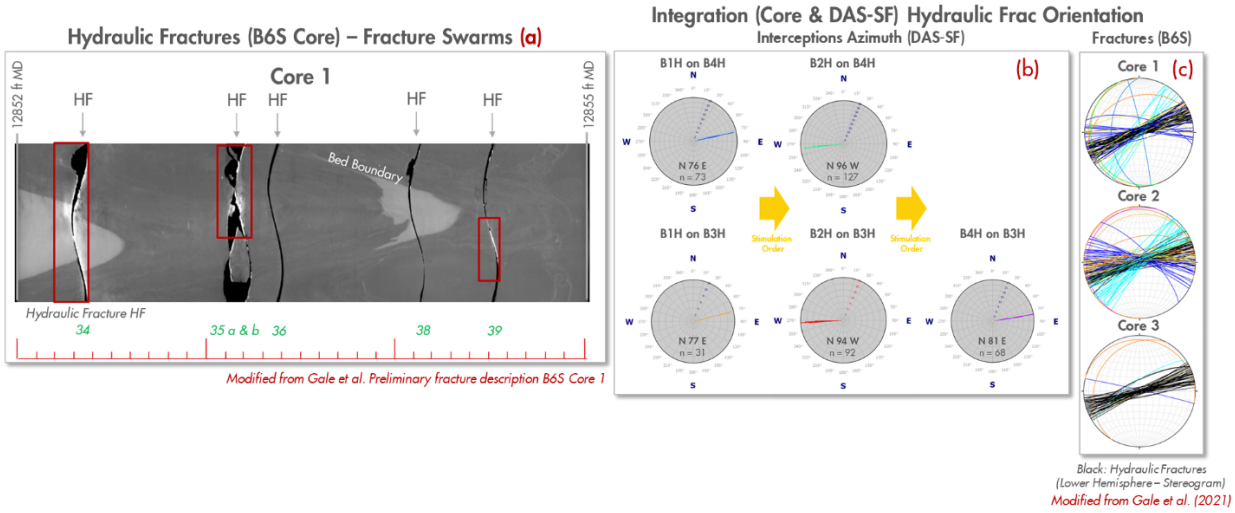

Fig 35—Example core description of 3 ft section of Core 1 in B6S (a) and comparison of the azimuths interpreted LF-DAS interceptions (b) and lower hemisphere stereogram, great circles, from fractures in Cores 1, 2 and 3 (c).

The occurrence of frac swarm matches the observations made via strain in both the near and far field that suggest the occurrence of discrete and parallel frac-zone-domains. However, in both the HFTS-1 and in the Eagle Ford projects, the frac swarm spacing does not seem to match cluster spacing. This is believed to be the result that post-stimulation core-throughs capture the superimposed effects of fracturing of many nearby wells and not only the well closest to the well location where the cores have been taken. Nevertheless, the azimuth of hydraulic fractures in the B6S matches that obtained by LF-DAS. Fig 35b shows the rose diagrams from the interpreted interceptions mapped during the stimulation of B1H, B2H and B4H.

Although the occurrence of fracture swarms induced by hydraulic stimulation are no longer in dispute, there is a lot of ongoing discussions and investigations about the mechanisms that create fracture swarms. Recent work by Savitski 2019 provides a mechanism for the creation of such swarm. Ongoing work at the national labs are both helping to explain, model, and upscale

the frac swarms too. We believe that datasets such as those provided by HFTS-2 project can and should be used to further understand the nature of these swarms and how to represent them in frac and reservoir models. Even though they only represent a small volume of the stimulated rock, core-throughs together with other diagnostics can provide insights to help understand the nature of hydraulic fracturing. Moreover, in HFTS-2, the information provided by core-throughs and all other complementary high confidence diagnostics is consistent.

Conclusions

Hydraulically induced fractures in HFTS-2 are interpreted as occurring in swarms associated with individual clusters, each with its own unique geometry but with similar predictable geometric and propagation tendencies. In fact, the following can be concluded about the geometries of hydraulic induced fractures in HFTS-2:

- Fracs are not random and do not have a complex branching architecture.
- Frac domains are mostly planar & parallel with similar azimuth matching SH_{Max}.
- Frac domains have well defined discrete near and far-field widths.
- Frac domains are vertical and asymmetrical, exhibiting strong shallow growth tendencies controlled by initial stress state and depletion in shallower formations.
- Frac domains are also lateral asymmetrical and with lateral growth that it is strongly controlled by preexisting fracs and depletion.

In HFTS-2, a great deal was also learned about the different diagnostic tools, these are some of the conclusions and recommendation regarding frac diagnostics:

- No single diagnostic tool can provide all the necessary information required to understand frac geometry.
- Misinterpretation of diagnostic data can lead to costly erroneous development decisions, thus following a consilience approach is essential.
- Valuable insights about frac geometry can be determined using an assortment of new tools such as LF-DAS, DSS-RFS as well as P/T gauges for FDI and SWPM.
- Vertical observation wells provide the best configuration to monitor the frac height and vertical fracture growth.
- Numerical modeling can and should be used to understand the signals and observations from frac diagnostics.
- The insights from multiple frac diagnostics must and should be used to calibrate frac models.

Without a doubt, HFTS-2 has advanced our understanding about the geometry of hydraulic fractures in general and in the Permian specifically. Very few of us expected to see the rather large frac-heights and the spatial and temporal nature of microseismic and strain-rate interception events observed in the HFTS-2 datasets. The information from HFTS-2 is helping us

to understand the limitations of different diagnostics and the valuable insights that multiple diagnostics can bring when analyzed together.

In HFTS-2 we have gained a great amount of new knowledge about hydraulic geometries and SRV. Now, it is imperative that we complement this effort with a comparable understanding of effective frac dimensions. Monitoring pressure decline in the far field, conducting regular pressure interference tests and determining the production from individual clusters and stages would provide insights to help us understand the Drainage Rock Volume (DRV). These should be the challenge for other follow-up data acquisition programs in HFTS-2 and for new integrated diagnostic pilot projects in Permian and elsewhere.

Microseismic Data Analysis

Summary

At HFTS-2 site, a multi-array, multi-well microseismic monitoring program was implemented. The aim was to perform fracturing diagnostics at the pad scale. A geometry design with 5 static monitoring arrays was established to acquire and process the signals during stimulation of 3 laterals at the site (B1H, B2H, B4H). The data was instrumental in understanding fracture propagation (lateral as well as vertical height growth) and was useful in cross-validating observations from permanently installed fibers, particularly vertical response in B5PH fiber. Details regarding the data acquisition and analysis, as well as advanced interpretation with fiber response in the vertical pilot well are further elaborated through articles in *Appendix A* and *Appendix B* respectively.

Advanced Fiberoptic Analysis (DSS-RFS)

Authors: Gustavo A. Ugueto, Magdalena Wojtaszek, Somnath Mondal, Artur Guzik, Dana Jurick, Ge Jin

Summary

Fiber Optic monitoring in unconventional reservoirs has proven to be an invaluable diagnostic tool for assessing both near-wellbore stimulation effectiveness and to help describe the far-field frac geometries created by hydraulic fracture stimulation. Unfortunately, gaining any detailed qualitative and quantitative understanding of the near wellbore frac geometry or cluster/stage productivity during production via Fiber Optic (FO) has proven to be more difficult, particularly in wells producing liquids. A new FO diagnostic method, Distributed Strain Sensing based on Rayleigh Frequency Shift (DSS-RFS), first demonstrated for oil and gas applications in the Hydraulic Fracture Test Site 2 (HFTS-2) provides new insights about the characteristics of near-wellbore-region (NWR) during production. DSS-RFS is different from other FO strain measurements because it relies on accurate measurement of frequency shifts of Rayleigh backscattered spectrum obtained by scanning the fiber with a coherent optical time-domain reflectometer with a range of laser frequencies using a tunable-wavelength laser system. Changes in strain are measured with an extremely high spatial resolution of 20 cm and with high signal-to-noise ratios over long distances. In HFTS-2, strain changes for the entire wellbore have been measured twice during scheduled shut-in and reopening operations (February 2020 and September 2020). After removing temperature effects, consistent strain changes have been observed at the location of most perforation clusters. These are caused by near-wellbore fracture aperture changes due to pressure increases during shut-in within the near-wellbore fracture network. The strain-change patterns from the DSS-RFS during shut-in correlate very well with the location of clusters and allow for the definition of extending intervals with positive strain signals at each cluster and slightly compressing intervals with negative strain signals between the clusters and in the non-stimulated intervals. The locations of the measured positive strain peaks also show good correspondence to DAS acoustic intensity measurements acquired during the stimulation. The geometry and magnitude of the strain changes differ significantly between the two tested completion designs in the same well. During shut-in and reopening each cluster exhibit its own strain-change / pressure path. In addition, the September 2020 dataset also revealed the existence of small but measurable strain changes as consequence of pressure decline during production. These strain changes also correlate well with the presence of producing clusters, but the strain-rate signals are opposite to that obtained during shut-in and reopening operations. Although we are still in the early stages of exploring the potential of this novel FO technique, we believe that the highly detailed information contained in the measurement of strain changes using DSS-RFS during production can significantly improve our understanding of near-wellbore hydraulic fracture characteristics and the relationships between stimulation and production from unconventional oil and gas wells.

Introduction

Unraveling the complex interplay between the wells, stimulation and subsurface in unconventional reservoirs requires an in-depth knowledge of the reservoir properties, frac

geometries (both hydraulic and effective), the monitoring of well and reservoir pressures and a detail understanding of the production for selected stages and perforation clusters through time. Obtaining such information for many stages and wells is currently cost prohibitive. However, a concentrated and comprehensive data acquisition program within a dedicated test site can provide insights about the stimulation/subsurface interplay. The objective of a dedicated Integrated Fracture Diagnostics Pilot (IFDP) such as HFTS-2 is to learn in few instrumented and observation wells so that the information gained can be applied to many other wells and pads with similar reservoir conditions. This approach towards de-risking unconventional development can provide critical information not available by other means. We believe this information would allow to balance the capital investment against the required economic returns that we get from production (Ugueto et al. 2018).

Traditionally rate allocation within a well with many production entries has been done via Production Logging Tools (PLT). Unfortunately, the current generation of PLT devices have proven unreliable and inadequate in determining the relatively low flow rates expected from individual perforation clusters in unconventional wells with hundreds of potential inflow entries. The need for tractoring or Coil Tubing (CT) to convey the PLT in horizontal wells and the inability to monitor logging/QC the data in real time has diminished the impact and value that production profiling and PLT logging could have in understanding unconventional reservoirs. Long horizontal sections made PLT tractoring and CT conveyance operations very costly and potentially risky. As a result, very few PLTs have been acquired in unconventional wells. In the rare occasions when production logs have been acquired, many clusters appear to be not producing with two-thirds of production being allocated to only one third of the perforation clusters (Miller et al. 2011). A new generation of modern and configurable PLT devices is now available (Donovan et al. 2019). Although these new tools can provide better quality production profiling and could provide better metering of the overall flow within the wellbore, differentiating the contribution of individual clusters may still prove difficult for PLTs.

FO technology have been identified as a possible solution to obtaining reliable production profiling in unconventional wells. Successful production profiling via Distributed Acoustics Sensing (DAS) have been reported in gas producing wells (Ugueto et al. 2018). Regrettably, many gas and most liquid producing wells do not generate strong enough DAS signals while flowing thus limiting the use of this technology for production profiling. Jin et al. 2019 documented a jointly inverted DTS transient temperature signal and DAS flow-velocity measurements to provide a production allocation profile across an entire well. Identification of producing clusters and possible production profiling using multiple short duration transient DTS, and DAS signals have also been proposed by Attia et al. 2019, Lawrence et al. 2021 and Wu et al. 2021. However, all these new FO production profiling data acquisition protocols and workflows rely on collecting signals during short shut-in reopening cycles lasting only few minutes. The data from these tests may not represent the flowing condition during continuous stable flow. Therefore, there is still a need to develop new workflows and algorithms using high

fidelity FO data that can be related to the production characteristics of individual perforation clusters.

DSS-RFS Explained

Distributed Strain Sensing Rayleigh Frequency Shift (DSS-RFS) uses Rayleigh backscatter in a non-engineered single mode fiber (SM) to measure strain changes along the fiber. The principle of the DSS-RFS method is described as follow (Jin et al. 2021): When an optical fiber is manufactured, random inhomogeneities of the glass density are created in the fiber core. The random density heterogeneities manifest as a variation of refractive index along the fiber. For a certain laser frequency, the constructive and destructive interferences between the Rayleigh backscatters causes irregular but unique amplitude fluctuations in the coherent optical time-domain reflectometer along the fiber length. For each discrete fiber segment, a unique Rayleigh scattering spectrum is obtained by scanning the fiber with a coherent optical time-domain reflectometer with a range of laser frequencies using a tunable-wavelength laser system. This unique Rayleigh scattering spectrum shifts in frequency if the temperature and/or strain of the fiber section changes, which causes the spacing and optical delay to vary between the scatterers (Kishida et al. 2014). This measuring principle is conceptually illustrated in Fig 36a & Fig 36b.

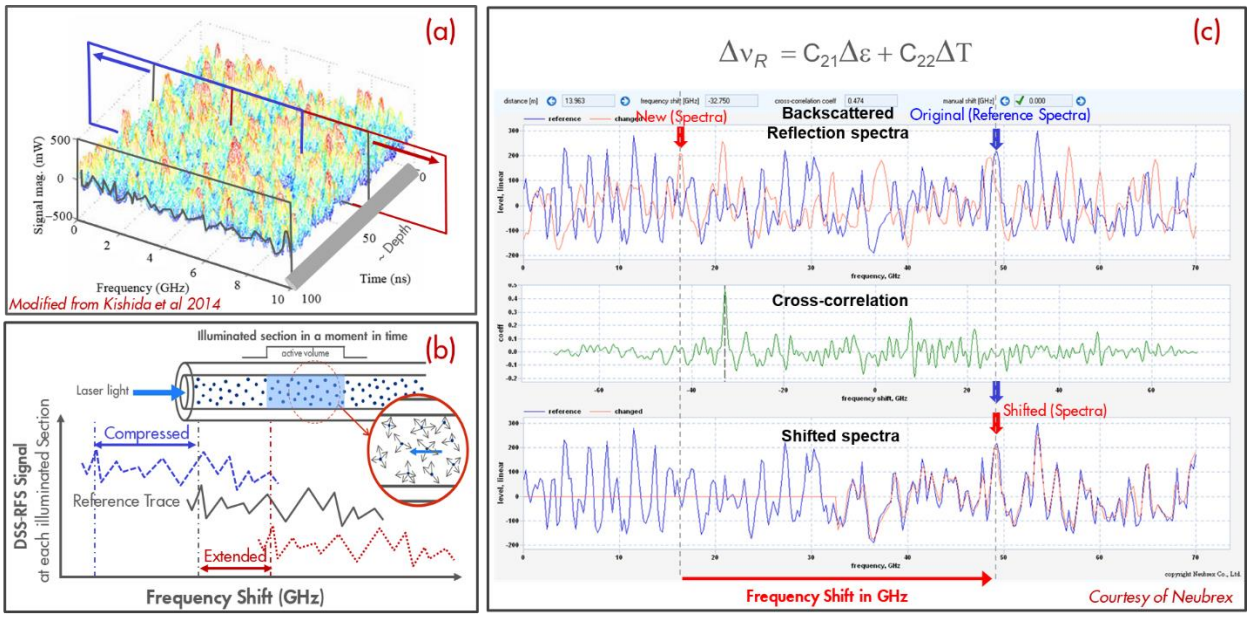

Fig 36—Illustration of Rayleigh Frequency Spectrum RFS. Conceptual response of along a fiber length (a) and for a single illuminated fiber segment (b). Example single spectra and cross-correlation workflow (c)

Fig 36c shows two reflected spectra for a given fiber segment, reference signal (blue) and new signal (red) as well as the shifted spectra after applying Neubrex frequency shift correlation algorithms. Like many other FO strain monitoring systems, DSS-RFS measures relative strain changes instead of absolute strain along the fiber. However, when compared with other DSS methods, DSS-RFS has some distinctive advantages. DSS-RFS has higher measuring sensitivity than strain measured using Brillouin optical time domain reflectometry (BOTDR), <1 με vs. > 1 με. DSS-RFS has higher spatial resolution than Low-Frequency DAS (LF-DAS), ~20 cm vs. ~3-8

m, and finally, DSS-RFS does not have the fiber sensing length restrictions of commercially available Fiber Bragg Grating (FBG) based DSS systems, 8-20km vs. ~100-500m.

The relationship between Rayleigh back-scatter spectrum frequency shift and temperature and strain change can be presented as:

$$\Delta\nu_R = C_{21}\Delta\varepsilon + C_{22}\Delta T$$

Eq. 4

Where $\Delta\nu_R$ is the frequency shift of the Rayleigh back-scattering spectrum at a certain section of the sensing fiber, which is referred to as RFS in this paper. $\Delta\varepsilon$ and ΔT are the strain and temperature changes of the fiber section being interrogated, respectively. C_{21} and C_{22} are coefficients determined by fiber structure and materials. Although RFS can be caused by either temperature or strain variations, the temperature variations can be independently measured using Distributed Temperature Sensing (DTS) at the same time and in the same cable where RFS is being measured. If the temperature variation can be accurately measured or it is small enough to be ignored, then the strain changes can be measured in a fully distributed manner using the RFS. Because the pattern of the Rayleigh scattering spectrum is unique for each section of sensing fiber and does not change over time, the pattern can be used to recognize the location and strain changes in sequential data acquisitions. This enables long term time-lapse strain change monitoring using the DSS-RFS without having to do continuous strain measurements (Jin et al. 2021).

DSS-RFS During Shut-in / Reopening Test Feb-2020

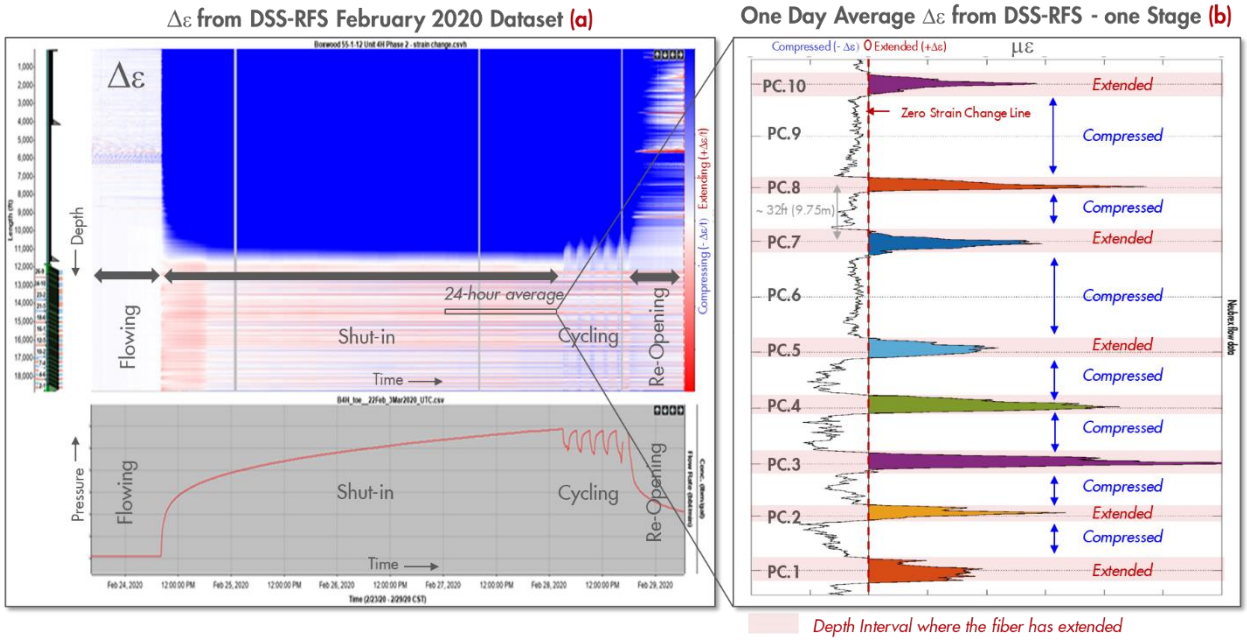

Fig 37—(a) Strain changes and downhole pressures acquired during shut-in and reopening during a test conducted in FO instrumented well in HFTS2. (b) shows the 24-hour average strain-change response across a single stage with multiple clusters.

In February 2020, DSS-RFS data was acquired at one of the two FO instrumented wells in Hydraulic Fracture Test Site 2 (HFTS-2). The RFS was measured on a single-mode fiber using a NeubrexVR SR7000 Rayleigh interrogator unit, which has a sensitivity of 0.075 GHz, equivalent to 0.5 με or 0.06 deg. C. The spatial resolution of the measurement is 20 cm, with a time sampling interval of 150 seconds. Fig 37 shows the strain-changes ($\Delta\varepsilon$) after removing temperature changes from a DSS-RFS acquisition during a shut-in and reopening test performed in February 2020. The test began after establishing a baseline measurement during normal flowing conditions, then the well was shut- in for 4 days and opened again in a series of 2-hour shut-in and 1-hour producing cycles. Finally, the well was re-opened and DSS-RFS was acquired for approximately 6 hours. Fig 37a shows the strain-changes together with the measured downhole pressures. Fig 37b shows the average strain-change from day 3 across a depth range corresponding to a single stage with 10 perforation clusters (PCs). This average strain-change curve shows well defined peaks matching the position of 8 out of the 10 PCs for that stage.

This DSS RFS data allows for the definition of intervals where extension has occurred corresponding to active clusters with positive strain-change signals and slightly compressed intervals with negative strain-change signals between the clusters, as well as for interval with in-active clusters.

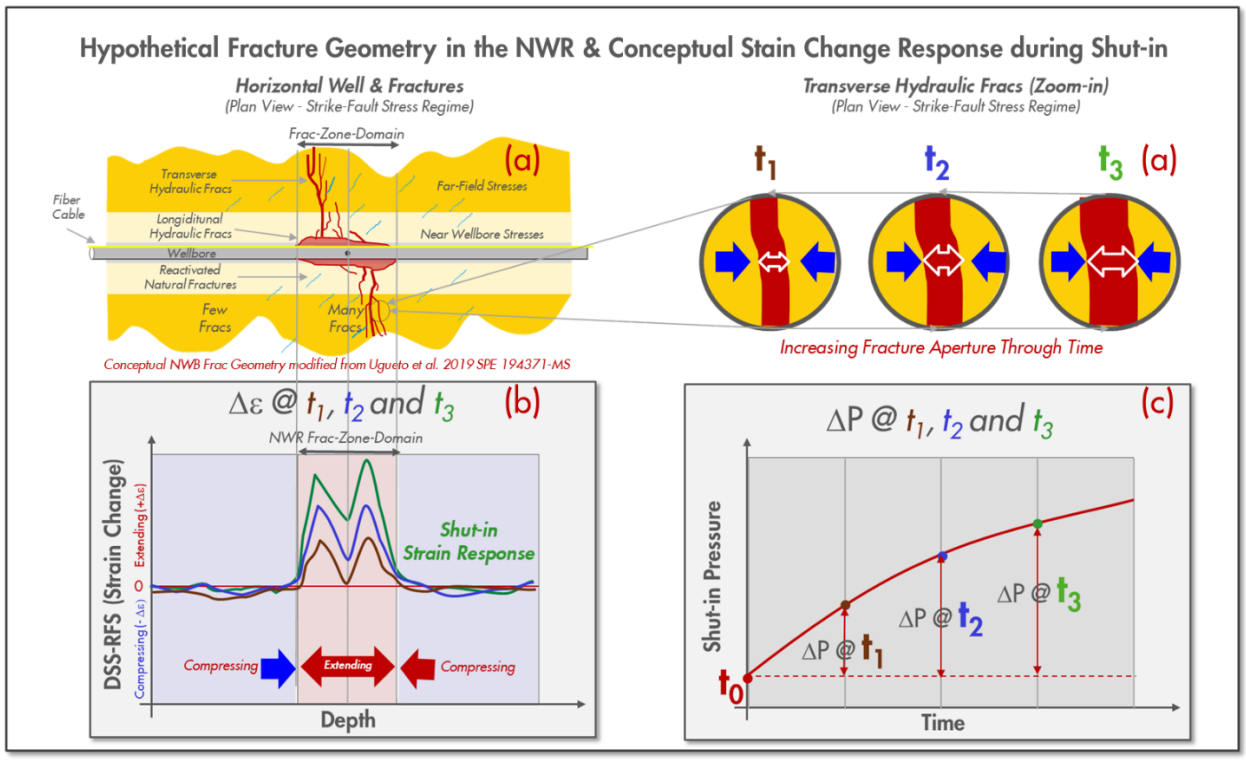

Fig 38—Hypothetical Fracture Geometry in the Near-Wellbore-Region around a single cluster (a) and conceptual strain and pressure changes during a production shut-in (b).

These signals are interpreted to be caused by fracture aperture changes due to pressure increases during shut-in within the fracture network in the NWR. Fig 38 shows a hypothetical representation of the near-wellbore environment showing a Frac-Zone-Domain consisting of

hydraulic fractures generated around a single perforation cluster. The figure also shows the conceptual evolution of strain changes through time corresponding to the change in pressures within each of the fractures connected to the wellbore as result of shut-in the well. The width of the extending zone corresponds to the dimension of the frac domain created by the stimulation in the NWR. The positive strain changes after a temporary shut-in can be interpreted as fracture aperture increases caused by pressure recharging of the connected fracture network in the NWR. After the shut-in, the pressure in the fractures and the matrix pore space begin to equilibrate, decreasing the pressure drawdown between the reservoir matrix and fracture fluid, this leads to an increase in fracture aperture. This elastic mechanical response generates strain perturbations near the producing hydraulic fractures, which are detected and captured by the DSS-RFS measurements (Jin et al. 2021). Although this fracture aperture change occurs along the entire connected fracture length, the DSS-RFS measured strain changes are mostly affected by the aperture change in the fractures closer to the fiber deployed behind casing in the NWR. Fig 39 shows the average strain-change during the shut-in (day 3) in the February 2020 dataset for the entire well compared to the production period before the shut-in. Positive strain-change peaks occur across the great majority of clusters. Conversely, the space between the stages and at the heel of the well show strain changes close to zero.

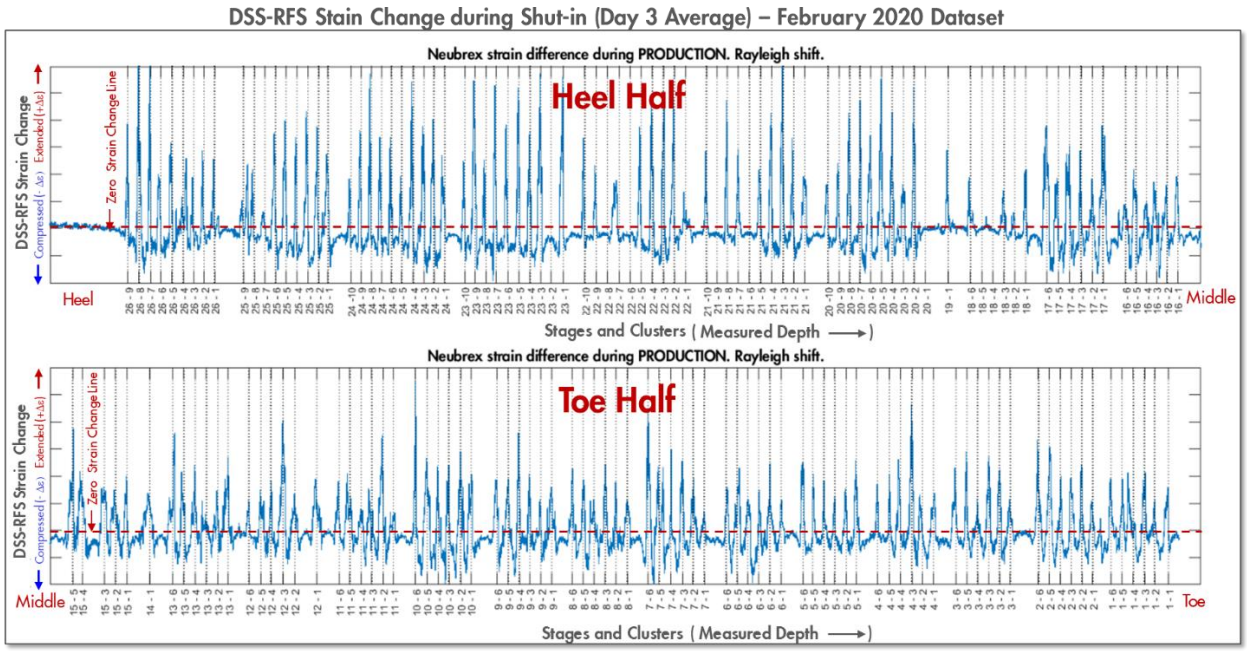

Fig 39—One day average strain-change profile across toe and heel half of FO instrumented well B4H in HFTS2-February 2020 dataset (shut-in day 3).

The acoustic intensity of the DAS signal during hydraulic fracture stimulation can serve as a good estimate of stimulation distribution efficiency and to allocate slurry to individual clusters. Fig 40 shows the comparison between the DAS acoustic intensity measurements during stimulation and DSS-RFS measurements during the February 2020 dataset for two treatment stages. In stage A, very limited DAS signal can be observed at clusters 6 and 9 during stimulation, and no positive strain changes are observed in the DSS-RFS during shut-in. The lack

of DAS during stimulation and strain change peak during shut-in suggest there is no frac-zone-domain associated with these two clusters. In stage A, clusters 6 and 9 were perforated but they screened out very early in the treatment. Stage B shows five signals in both the DAS during stimulation and DSS-RFS during shut-in. However, the spacing between the signals is different as perforation of cluster 4 was skipped due to cable mapping uncertainty around this segment of the wellbore. These two stages illustrate the high level of correspondence between placement of the frac during stimulation and the presence of active fracs during production. In this dataset the correspondence between DAS signal during stimulation and DSS-RFS during production is greater than 95%. Clusters that do not develop a positive strain change during shut-in are less likely to be the clusters that contribute to production. Hence, DSS-RFS can be used to determine the cluster efficiency during production. Fig 40 also shows that intervals with high DAS acoustic intensity signal in Stage B, at each cluster, are significantly wider than the ones in Stage A. A similar trend can be observed in the strain change measurements, with positive strain peaks in Stage B being wider and of smaller magnitudes. Because the clusters spacing are similar between these two stages, this observation supports the interpretation of Ugueto et al. 2019, who hypothesized that part of the DAS acoustic intensity signals during stimulation is also generated by the near-wellbore-region instead of the perforations only. The spatial consistency between the DAS acoustic signals during stimulation and the DSS-RFS strain changes during production indicates that DAS acoustic intensity is also controlled by the conditions in the NWR. The quality of cement between PCs, the intensity of the treatment (rate per cluster) and the rock quality all ultimately impact the characteristics of the fractures created around each cluster.

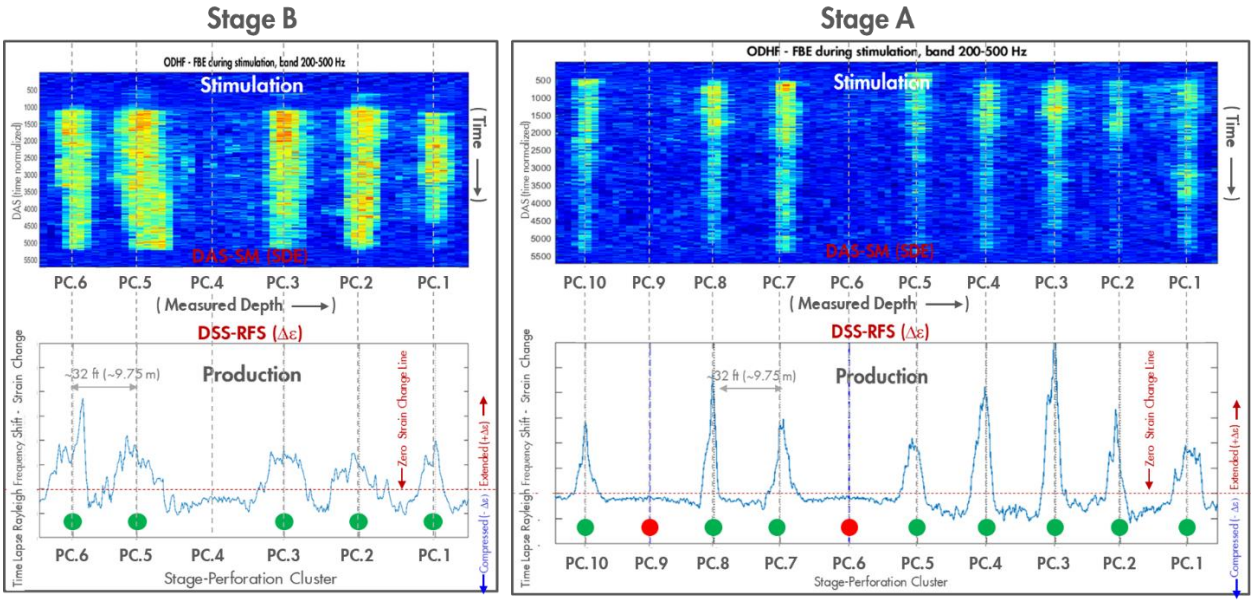

Fig 40—Comparison between DSS-RFS strain-change profiles during production shut-in and DAS acoustic intensity during stimulation for two stages. Stage A has 10 equally space perforation clusters and Stage B only has 5 clusters. Stage B was originally planned as 6 PCs stage, but PC 4 was skipped due to FO cable mapping uncertainties.

This also explains the spatial migration of DAS acoustic intensity signal near the perforation clusters during stimulation, which is commonly observed and are clearly seen at cluster 5 of

Stage B. The consistency of the DSS-RFS measurements with the DAS intensity during injection also supports our interpretation that the extensional strain signals during shut-in are associated with highly conductive fracture zones in the NWR. Therefore, the shape and magnitude of the strain-change curve can be attributed to the geometry and connectivity of the fracture-zone-domain in the NWR. Several attributes can be measured from the DSS-RFS strain-change peaks. For example, the width of frac-zone-domain in the NWR can be measured. Similarly, the area of each peak can be measured by integrating the positive strain change for each perforation cluster. Fig 41 shows strong dependence of these two attributes in relation to the main two type of stimulation designs tested in this well (6 PCs Stages and 9-10 PCs Stages).

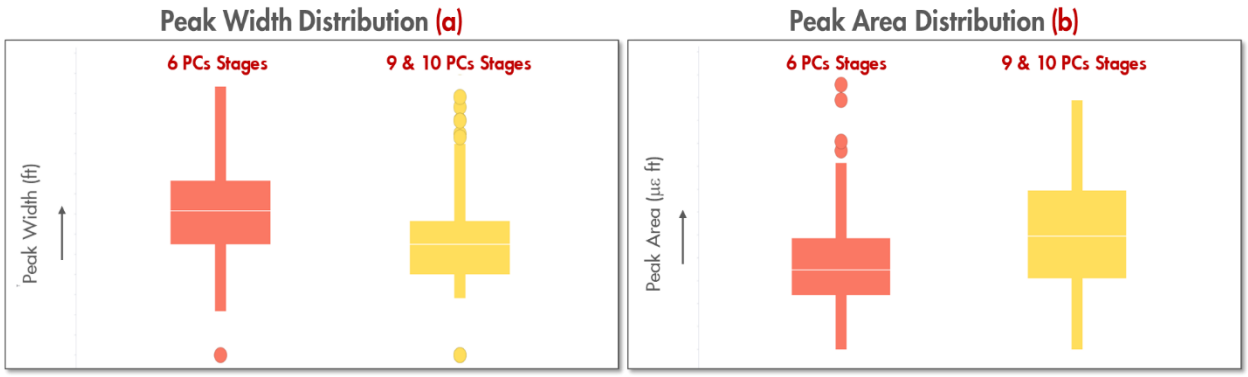

Fig 41—Example of attributes and corresponding population distribution statistics extracted from DSS-RFS strain-change profiles for the main two type of completion designs tested in HFTS-2 well.

As observed in Fig 40 the peak width of 6 PCs stages is wider that those from 9 and 10 PCs stages, in average 15ft (4.6m) and 11ft (3.2m) respectively. Conversely, the peak area of the 6 PCs stages is smaller than that of 9 and 10 PCs stages. Many other attributes can be mapped from the DSS-RFS signals but these simple statistics from relatively large samples (n=101 for 6 PCs and n=68 for 9-10 PCs stages) clearly indicate that the frac geometry and probably the production of these two designs is different.

Using DSS-RFS, strain changes can be continuously monitored at each perforation cluster during the shut-in and reopening operations. Fig 42 shows the strain changes for one perforation cluster (Fig. 42a) and for all the clusters in one stage (Fig. 42b) for the February 2020 dataset. This data indicates a strong correlation between the strain changes in the NWR as the rate of pressure increase progresses during shut-in and later decreases during reopening for each cluster. Every cluster exhibits its own “pressure strain change path”. Assuming that the observed strain changes are mostly due to elastic deformation of the fractures in the NWR and resulting from the pressure changes in the wellbore, the measured strain changes can serve as proxy to the pressure changes in the near-wellbore fracture zone. However, during the shut-in period of a multi-cluster horizontal well, the interaction between the borehole and the near-wellbore fractures can be complicated due to the expected variety of conductivities between borehole and fractures in the NWR. This combined with the different recharging rates by the reservoir

matrix into the fractures and possibly the occurrence of crossflow can also impact the pressure strain change path of the near-wellbore fractures.

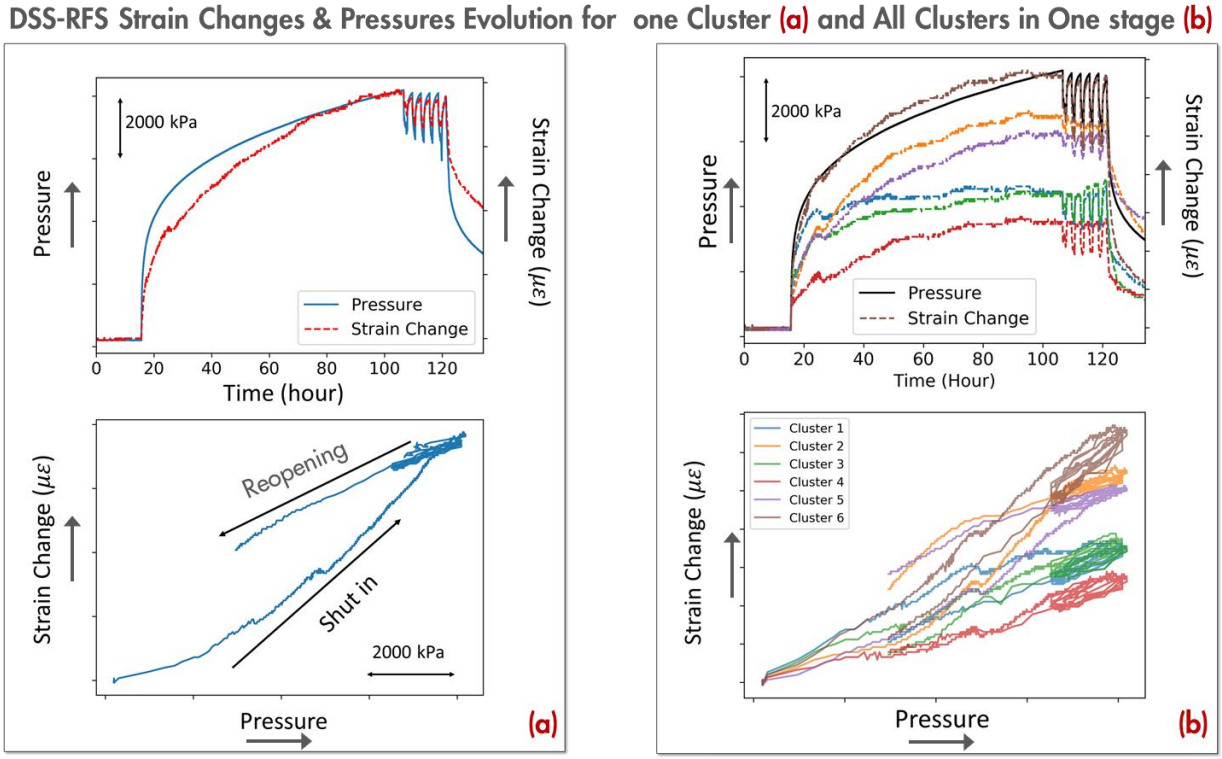

Fig 42—DSS-RFS strain-change time evolution and comparison with wellbore pressure for one cluster (a) and for all the clusters in one stage (b).

After the well is reopened, fractures with lower connectivity or higher recharging rates to the borehole may show larger discrepancies on the pressure-strain relationship curves between the shut-in and reopening paths, as illustrated in the lower panels of Fig 42a & Fig 42b. We believe that these different "pressure strain change path" curves that include shut-in and reopening can be numerically modeled to explain and quantify the near-wellbore fracture properties and production information from this type of dataset (Liu et al. 2021).

DSS-RFS Shut-in and Reopening Test Sep-2020 and Comparison with Feb-2020 Dataset

In September 2020 a second DSS-RFS dataset was acquired in HFTS-2 with the objective of determining if the new signals were like those obtained in February 2020 and to quantify any changes in the observations after 7 months of additional production. Fig 43 shows the strain changes from February 26th and September 17th, 2020, over the entire well. This comparison was made using the DSS-RFS changes corresponding to the same amount of pressure built-up (1000 psi) for both shut-in periods. The strain changes results are very consistent, showing positive strain-change peak associated with cluster locations, no strain across non-stimulated intervals and smaller negative strain changes between the clusters.

Fig 44 shows the comparison of the February and September datasets for one stage with 9 PCs. In general, the location and shape of the positive strain-change peaks are similar, but overall, the maximum strain changes are smaller in the September dataset. The strain change signals

from some clusters are almost identical in PC1 and PC2, but in other cluster such as PC8 and PC9 show lesser peak width and area in the September dataset. These changes reflect the evolution of the frac-zone-domain in the NWR over the additional 7 months of production. Therefore, confirming that DSS-RFS can be used for time-lapse observations.

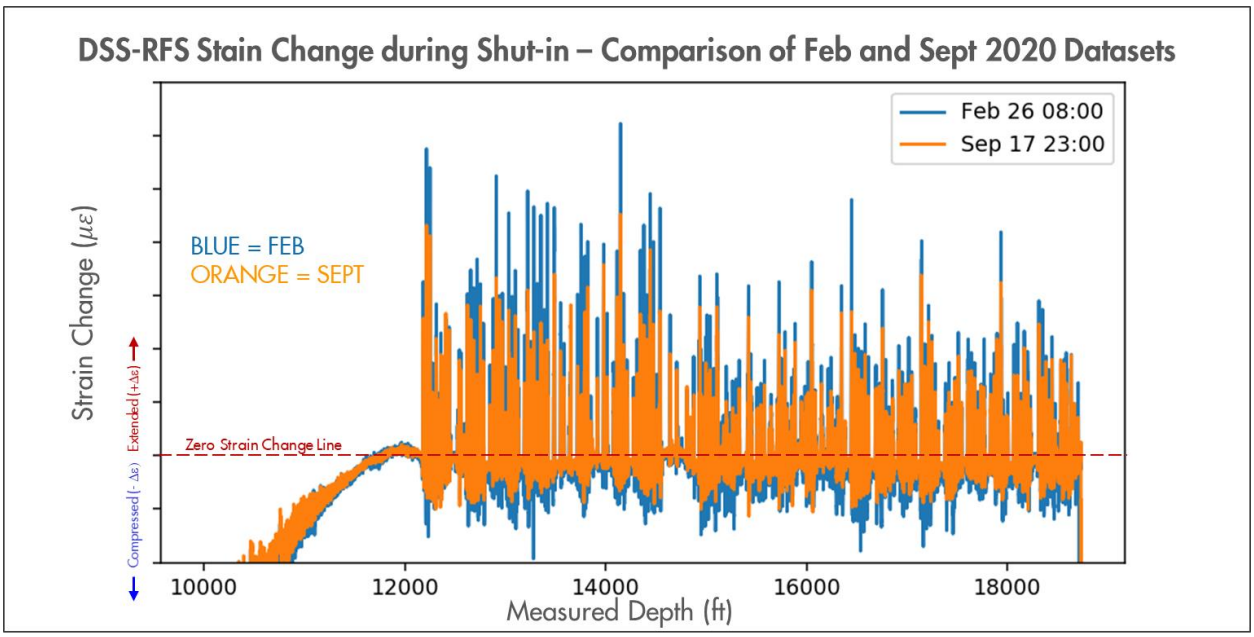

Fig 43—Comparison across the entire B4H well of the DSS-RFS strain-change profiles during shut-in on the same HFTS2 well during two separate acquisitions seven month apart, February and September 2020.

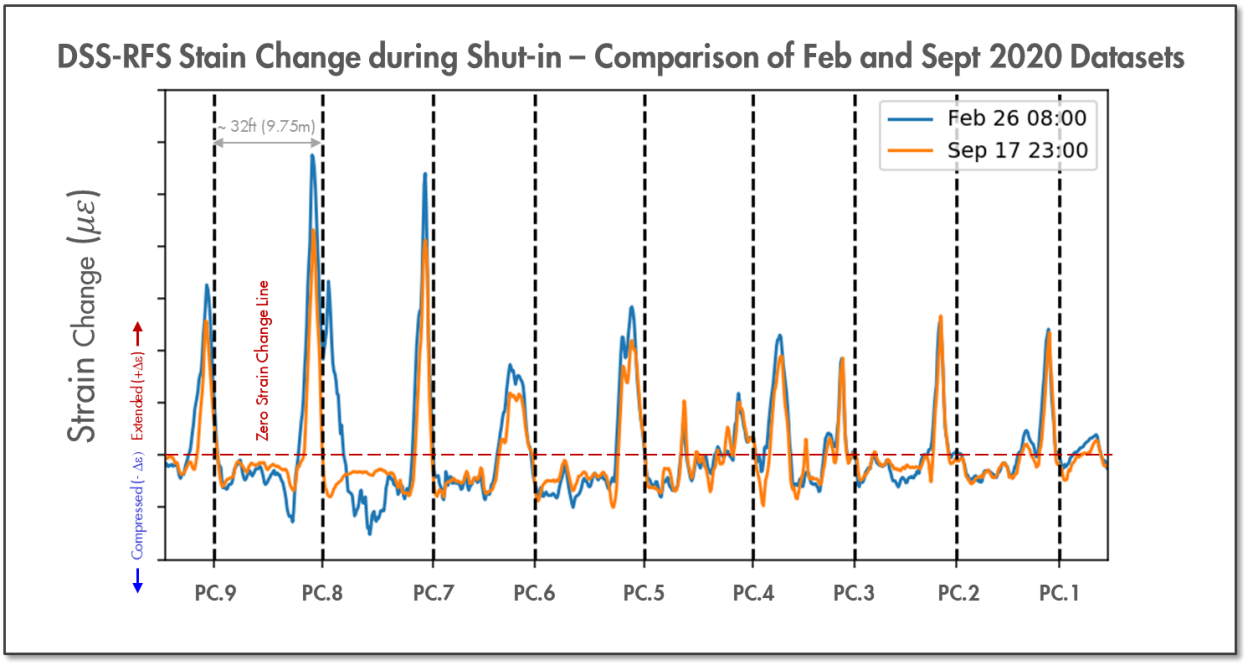

Fig 44—Comparison across one stage of the DSS-RFS strain-change profiles during shut-in for two separate acquisitions seven month apart, February and September 2020.

Fig 45 shows the comparison between two attributes from the shut-in in February and September datasets. Overall, the strain-change peaks are 24% to 32% smaller in September with the data corresponding to stages with larger number of clusters showing the bigger differences. The strain change area attribute shows a somewhat similar result but larger difference between the two datasets, indicating a reduction of 36% and 48% during the additional 7 months of production, with the bigger changes occurring on the stages with larger number of clusters. These changes can be the results of production over 7 months. We note that in this well the total liquid rate and pressure have declined by around 37% and 24% respectively over the same

period, thus supporting the hypothesis that the observed strain-changes reflects the changing conditions in the well due to depletion.

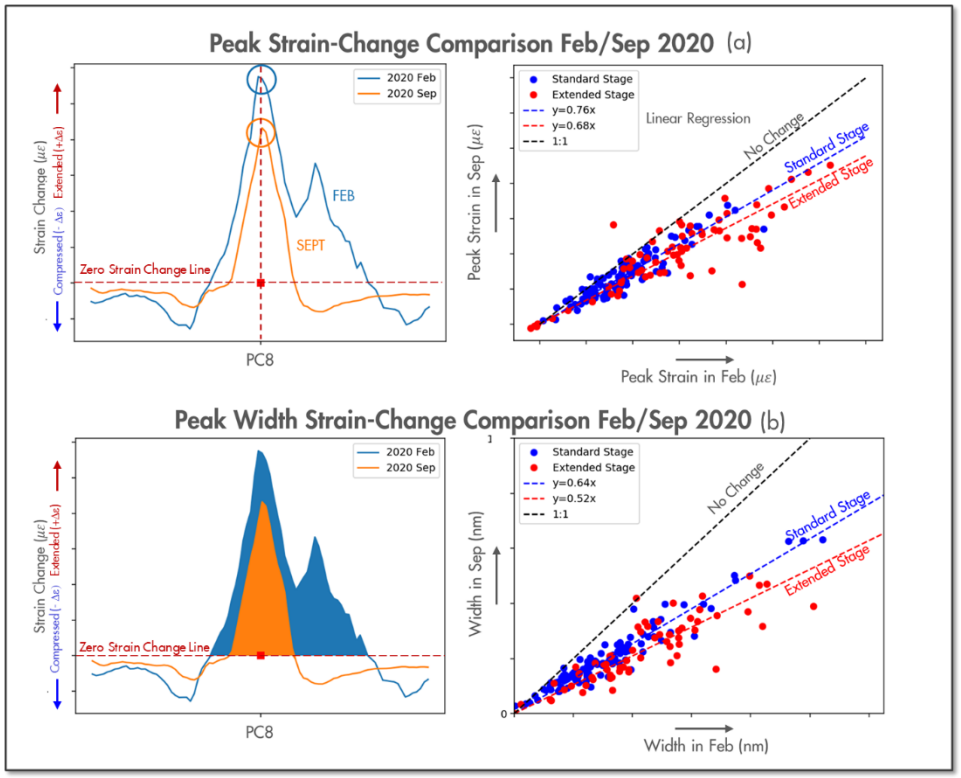

Fig 45—Changes in DSS-RFS strain-change for attributes: maximum peak and area, after 7 months of production.

The comparison of the pressure strain-change paths corresponding to individual clusters seem to indicate that most productive clusters remain the same after 7 months of production. Fig 46 shows the pressure strain-change paths for all clusters in an entire stage. Strain-change for each cluster is plotted against the pressure change (delta pressure) during the shut-in (pressure built-up) and reopening (pressure decline). In this stage, both datasets show no strain-change signals in the non-stimulated clusters (PC6 and PC7). The pressure strain-change paths for PC1 and PC9 are similar in both datasets, generally showing a low slope and similar path during shut-in and reopening. This response probably represents low producing clusters. Other PC2, 3, 4 and 5 have paths that represent productive clusters. Only two PCs (8 and 10) show paths that are different in the February and September datasets. This stage is representative of other stages in this well

where characteristics of the pressure strain-change paths from February and September are similar for most of the clusters.

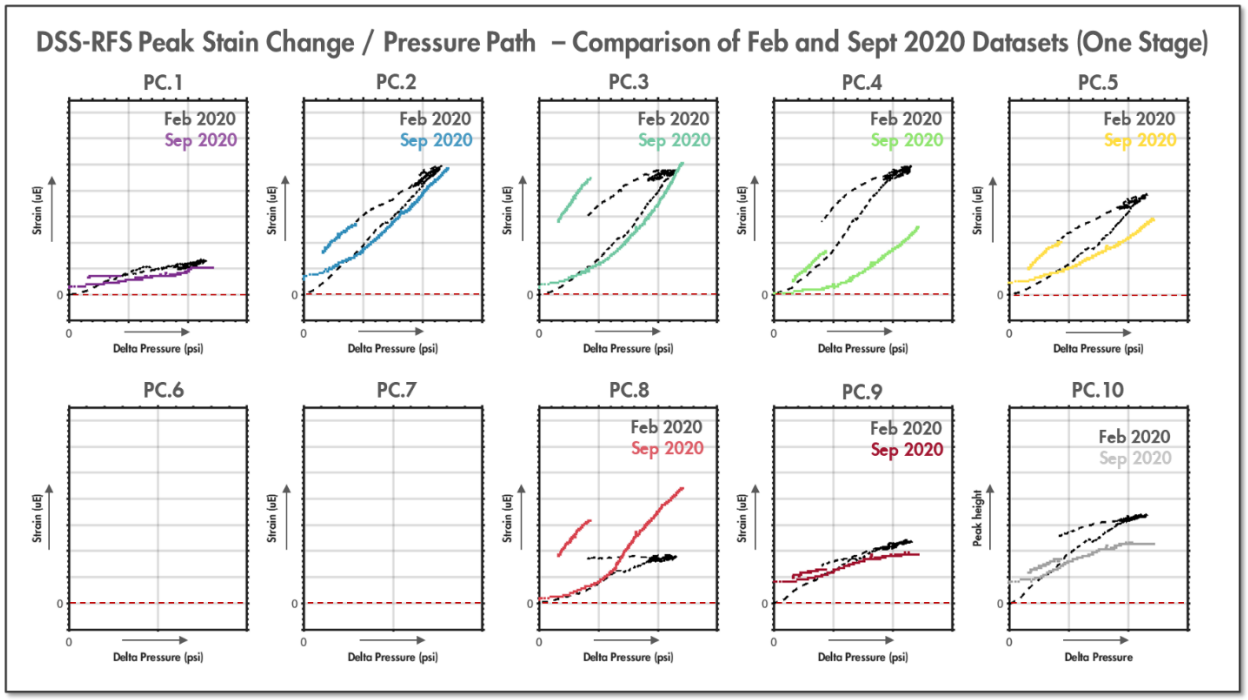

Fig 46—DSS-RFS strain-change time evolution for all clusters in one stage and comparison between the pressure strain-change path acquired in February and September 2020 datasets.

DSS-RFS during Stable Production – September 2020 Dataset

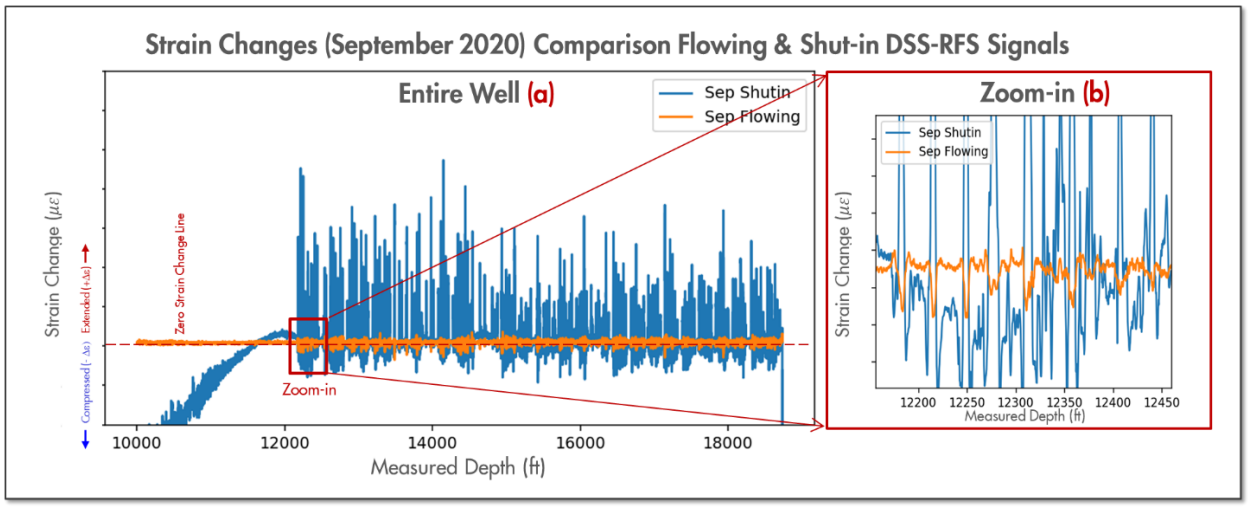

Fig 47—DSS-RFS Strain-change profile during stable flowing conditions and comparison with the strain-change profile during shut-in (September 2020 Dataset).

An additional objective of the September dataset was to look for the existence of any high-fidelity strain-change signals that could be obtained by monitoring DSS-RFS during stable production. We expected the signals to be small given the anticipated low rate of decline within the observation period of only one day (corresponding ~30-40 psi/day pressure decline).

Fig 47a shows the one-day strain-changes while flowing (Sep 14th) and the signals acquired later during shut-in (Sep-17th) for the entire well. Fig 47b shows the signals across one stage. As expected, the signals obtained while flowing are small and show strain-changes that are opposite to that acquired during shut-in, but remarkably these signals also match very well the location of active clusters. Fig 48 explains the hypothetical strain response during stable production. Like the strain-changes recorded during shut-in we expect these signals during stable flow to be the result of the elastic deformation of the fractures in the NWR. These negative strain-change signals are the consequence of the reduction in aperture of the fractures as fluids are being drained from connected fractures and somewhat recharged by the reservoir.

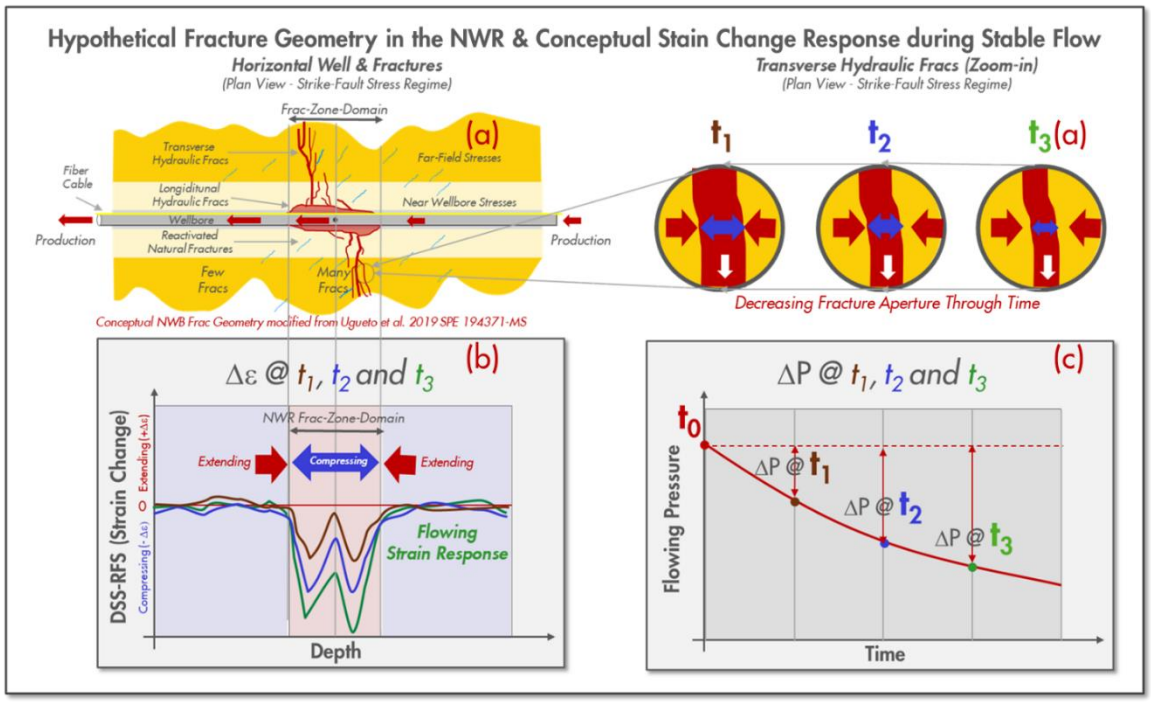

Fig 48—Hypothetical Fracture Geometry in the Near-Wellbore-Region around a single cluster (a) and conceptual strain and pressure changes during stable flow (b and c).

To facilitate the comparison of the shut-in strain-changes resulting from relatively large pressure perturbation during shut-in (~1000 psi) against the smaller perturbation during stable flow (~30-40 psi), the strain-changes during flow were flipped and amplified by applying a somewhat arbitrary -13.3 scaling factor. Fig 49 shows the comparison of the strain-rate signals, shut-in and flowing, for a 9 PCs and 6 PCs stages after applying the scaling factor. Although the signals obtained during stable flow are noisier, in general there is great correspondence between the characteristics of the frac-zone-domains at each cluster. However, both shut-in and flowing

datasets suggest wider frac-zone-domains for the 6 PCs than for 9PCs stages. Also, the relative intensity of the peaks matches very well between flowing and shut-in acquisitions.

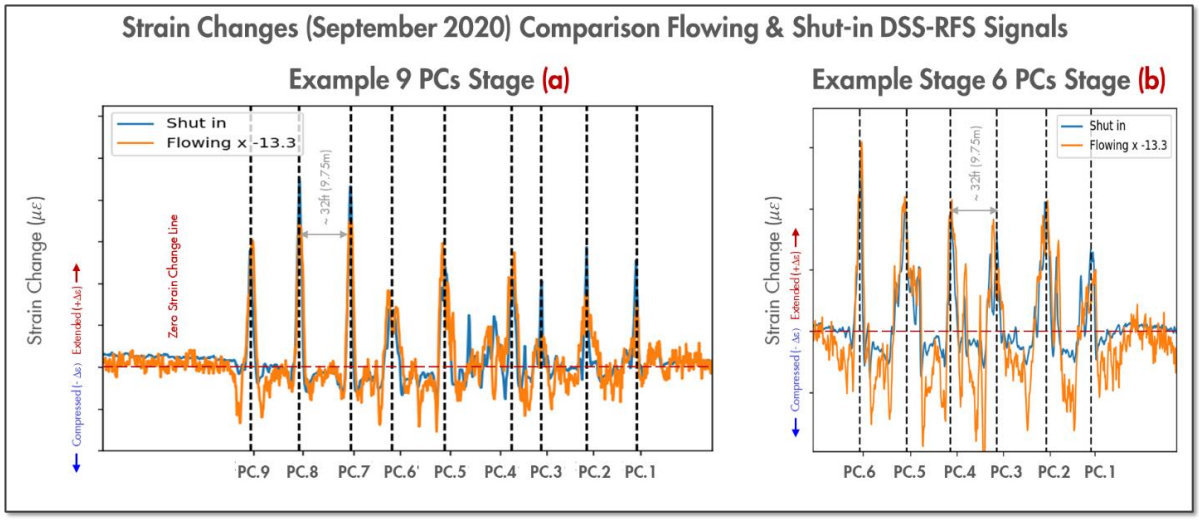

Fig 49—Comparison of DSS-RFS strain-change profiles obtained during shut-in (blue) and flipped/amplified profile acquired during stable flow (orange) for two stages with different number of clusters.

The detailed comparison of the attributes for all the clusters indicates somewhat larger, wider geometry during flowing than that observed during shut-in, suggesting a slightly larger frac-zone-domain during drainage. Fig 50 shows the geometry comparison for two clusters and corresponding statistics. Like the observations made for the shut-in datasets, the data also suggest some difference between the 9-10 PCs and 6 PCs stages.

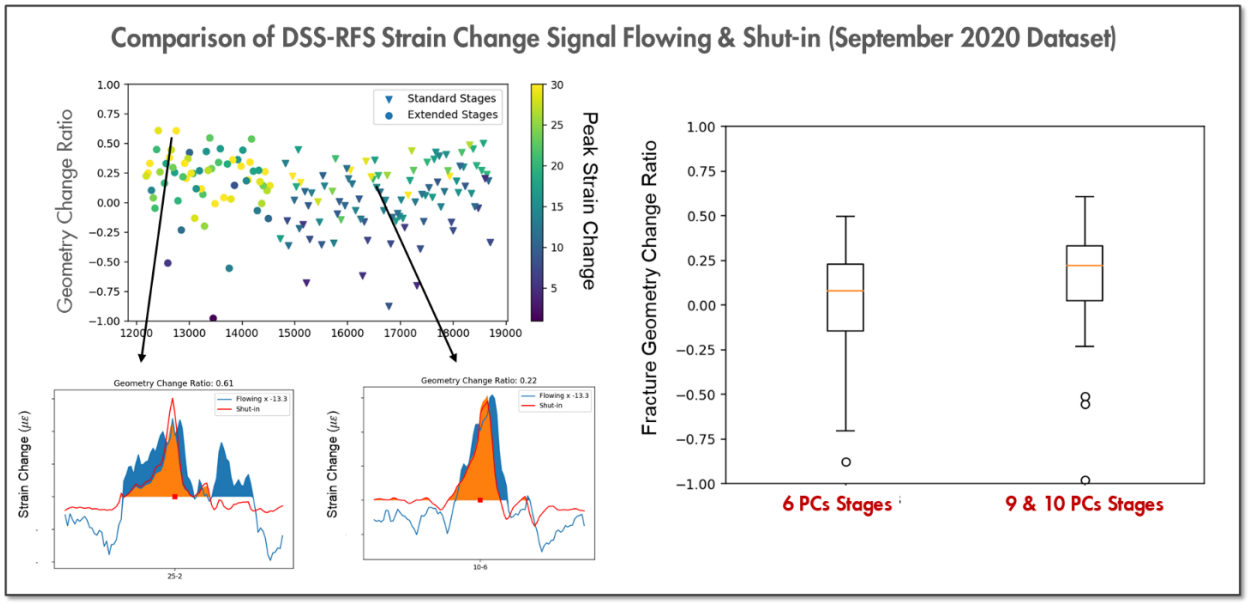

Fig 50—Comparison of DSS-RFS strain-change attributes and corresponding statistics for two types of stimulation design

As flowing pressure inside the well is similar across most clusters, we expect these signals obtained during stable flow to provide the best indication of the relative production from all the clusters. These signals can be acquired without the need to shut-in the well thus minimizing impact on well production and therefore enabling a more frequent time-lapse collection of these type of DSS-RFS signals. We anticipate that both the acquisition of the multiple flowing and shut-in/reopening datasets will provide unique information required to better understand important aspects of the production and productivity of individual cluster never obtained before.

Conclusions

In this section we introduce the use of DSS-RFS during production to evaluate near-wellbore fracture characteristics related to frac geometry in the NWR and cluster productivity for unconventional wells with hundreds of potential inflow entries. We believe this breakthrough application of strain monitoring provides important information related to the near borehole pressure changes at each perforation cluster.

The strain changes obtained via DSS-RFS can be determined at high spatial resolution of 20 cm and with high temporal sampling rates.

This high-fidelity production related data can be acquired during stable flow as well as during shut-in and reopening well operations.

The observed strain-change variations are interpreted to be the result of near-wellbore fracture aperture changes over time and space.

The shape and magnitude of the strain change peaks are related to the geometry of conductive near-wellbore fracture zones.

In HFTS-2 we observed near-wellbore “frac-zone-domains”: with average widths ranging between 15ft (4.6m) and 11ft (3.2m).

In HFTS-2, significant differences can be observed between the two main types of stimulation and completion designs.

The time dependent relation between borehole pressure and strain changes can provide important insights into near-wellbore fracture conductivity and reservoir recharge rate.

We anticipate that the innovation described here in using distributed fiber-optic strain sensing measurements will improve our understanding of the near-wellbore hydraulic fracture characteristics and the interaction between stimulation design and production yield in unconventional reservoirs.

Fracture/ Completion Diagnostics

Summary

At HFTS-2 site, multiple diagnostic datasets were used to understand completion quality and effectiveness, as well as fracture growth, particularly vertical height growth above target zone of interest. Various studies have been released which cover these topics in significant detail. A summary of completion designs, and state-of-the-art diagnostic results are shared in Appendix C and Appendix D. Impact of completion design on cluster efficiency is further discussed in Appendix E. Hydraulic fractures were characterized using DAS and microseismic observations and have been shared in Appendix F. Modeling of fracture height growth (strain response) is demonstrated in Appendix G and Appendix H.

Core Characterization - Fracture

Authors: Julia Gale, Sarah Elliott, Bethany Rysak, et al.

Summary

This section provides an overview of the results from the fracture description work carried out on the slant core (through the stimulated volume) acquired above and below B3H well. Nine, 3-inch-diameter whole cores from the slant well were examined for fractures prior to slabbing, together with a CT scan of the core. We used criteria developed during the HFTS-1 project to identify hydraulic, natural, drilling-induced, and core-handling fractures. Material collected from a few fracture faces was cleaned, sieved, and examined under a microscope to look for proppant. A total of 1261 fractures, including 500 hydraulic fractures, were described in 948 feet of core. Hydraulic fractures are not evenly distributed through the cores; they tend to occur in clusters. Many are remarkably planar, smooth, and featureless, while others have twist hackles, steps, plumose, and kinks. Natural, subvertical fractures, mostly less than 1 mm in width, sealed with blocky calcite, are oriented NE-SW (Set 1) and WNW-ESE (Set 2). Two Set 1 fractures have drusy cement on parted faces and were possibly open prior to drilling. A few subvertical sealed fractures with different orientations are also present. Bed-parallel natural fractures, most having fibrous cement (beef), and some showing top-to-north bed-parallel shear are present. Faults with normal/oblique movement were found in one part of the core. Drilling induced and core-handling breaks were identified in all cores and were also noted to have reactivated some natural fractures. The results from this work will allow hydraulic fracture distribution relative to the stimulated well to be assessed. The number of fractures is generally greater than the number of perforations, but these can be compared for different stages and perforation clusters. Surface features provide information about the direction of hydraulic fracture propagation and about segmentation and bifurcation that might increase the number of fracture strands. Reactivation of natural fractures, including bedding-parallel fractures, occurs although the mechanism of parting is mostly unknown. The wider HFTS-2 project makes use of this fracture description to improve hydraulic fracture modeling (geomechanics and engineering), to help explain pressure depletion and fiber optics observations (reservoir depletion and frac geometry), to help verify indirect fracture diagnostic techniques such as microseismic monitoring (geophysics), and to help calibrate horizontal well image logs.

Introduction

Improved understanding of hydraulic fracture growth and interaction with geologic discontinuities is needed to optimize drilling and completions strategies. Natural fractures are typically present in most shales and are one of the most important types of discontinuity (Gale, et al., 2007; 2014). The HFTS-1 project in the Midland Basin showed that useful insights about growth and interaction could be obtained through direct observation of hydraulic fractures in core taken through a stimulated volume (Gale et al., 2018; 2019). The study presented here focuses on the fracture description for the HFTS-2 slant core.

For this study, we focus on fracture description in a slant core taken in two sections, one above and one below a stimulated well. Details of the configuration of the wells and the hydraulic fracturing are given in 2021 URTeC papers from the HFTS-2 special session or from other

sections of this final report. There were nine cores totaling 948 ft in length; six cores (1-6) were situated above the stimulated well and 3 cores (7-9) were situated beneath. The angle of the slant core from horizontal decreased steadily from 14° to just 3° for the section above the stimulated well but was more consistent in the section below (14-16°). In this section we present characteristics of the main fracture types but are restricted from showing fracture distributions and depth information due to a non-disclosure agreement.

Methods Used

Fractures in all nine cores were characterized, described, photographed and orientations measured. Methods are like those described in Gale et al. (2018), including criteria for distinguishing between the different fracture types. Fracture orientations were measured using an iPad with a GeoID application and then corrected for magnetic declination and finally rotated into their in-situ orientations. Rotations and plotting of stereograms were done using Richard Allmendinger's free 'Stereonet' software available at: http://www.geo.cornell.edu/geology/faculty/RWA/programs/stereonet.html.

Fracture types included natural fractures, drilling-induced fractures, core-handling fractures, and hydraulic fractures. Interpretation of fracture type was done by synthesizing all the observations direct from core with those from a CT scan of the whole core. In addition, an uncertainty estimate accompanied each interpretation. Where a cemented natural fracture is now parted, we identified the natural fracture set and the reason for parting: hydraulic fracture reactivation, drilling induced reactivation or core-handling breakage. Typically, the reason for parting has high uncertainty. We collected material from all parted fractures and made qualitative observations on any possible proppant observed during the fracture description work.

Key Results

We documented a total of 1261 fractures in the slant core. Some fractures have additional, subsidiary breaks, particularly at the apices of core pieces where the tips are weak. These small breaks are commonly, although not always, parallel to bedding. These were not included in the overall fracture count. Hydraulic fractures, and two main sets (Set 1 and Set 2) of calcite-filled, subvertical natural fractures were identified. These fracture types, including their orientations, are like those seen in the HFTS-1 project (Gale et al 2018; 2019). Other natural fractures with different orientations are also present but are not as common as the main sets. Bed-parallel natural fractures, most having fibrous cement (beef), occur in all cores except Core 1. Several faults were found in Core 6 and evidence of bed-parallel shear in bed-parallel fractures was seen in Core 9. Drilling-induced and core-handling breaks were identified in all cores and were also noted to have reactivated some natural fractures. Typically, drilling-induced breaks are close to normal to the core axis.

Orientations of fractures are presented as stereographic projections by core (Fig 51). Hydraulic fractures show a strong preferred orientation of ENE-WSW in most cores, and other fracture types also have consistent orientations. The core divisions are of course arbitrary, but some differences are notable. For example, the range of orientations of the various structures is much greater in Core 6, part 1 than in the preceding and following cores, and the hydraulic fractures (black) are grouped in two distinct orientations in Core 6, part 2. It is possible that the apparent

differences in fracture orientations in Core 6 relative to the other cores is due to measurement error because of difficulty in orienting this core. Here, the angle from horizontal was only 3°, making the bedding planes lie close to the core axis. This, together with the fact that in this section the core tracked through massive carbonates with no bedding visible, made determination of way up challenging. The low angle to bedding meant that the core stayed in these carbonates for 10s of feet. Further comments about orientation are made within the descriptions of the main fracture types.

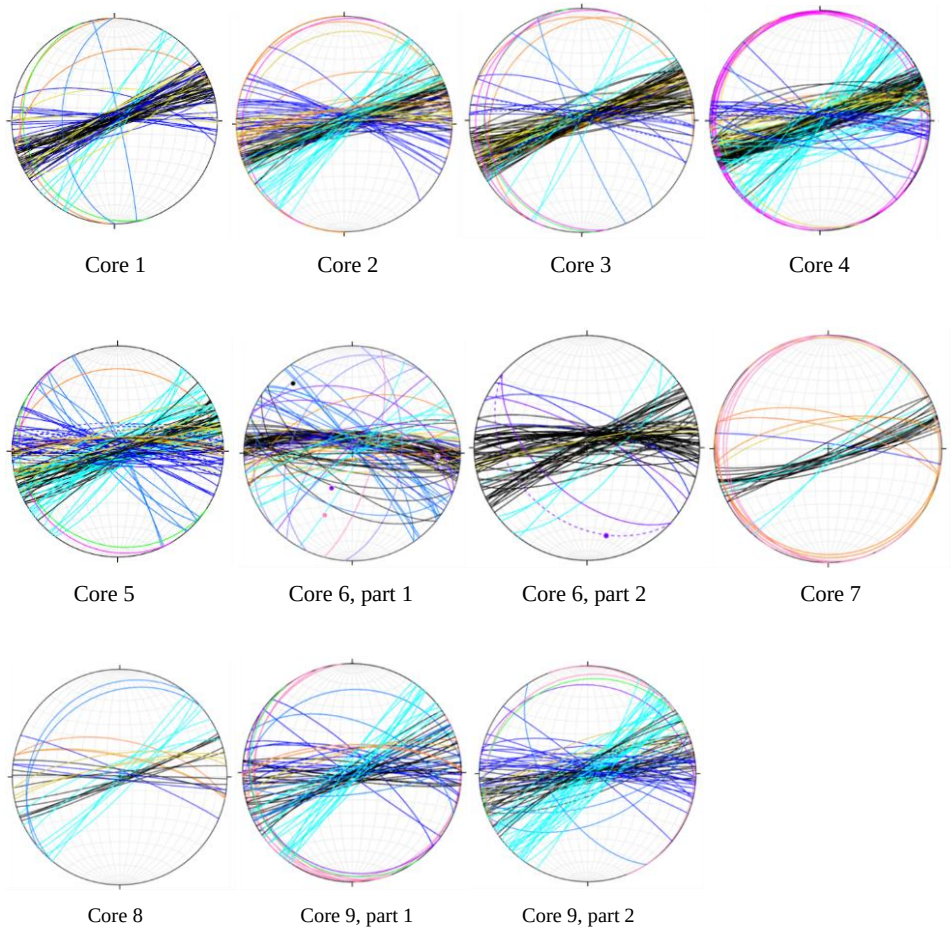

Fig 51—Stereographic projections of structures by core. Black = hydraulic fracture; Light blue = Set 1 natural fracture; Dark blue = Set 2 natural fracture; Powder blue = unassigned natural fracture set; pink = bed-parallel fracture; lilac = fault; mustard = drilling induced fracture; orange = core-handling fracture; green = bedding; dots are measured slickenside lineations.

Hydraulic Fractures

There are 500 hydraulic fractures interpreted, distributed as follows: Core 1, 39; Core 2, 44; Core 3, 78; Core 4, 76; Core 5, 40; Core 6, 104; Core 7, 33; Core 8, 20; Core 9, 66. Hydraulic fractures are not evenly distributed through the cores; they tend to occur in clusters. For example, there is a wide cluster toward the end of core 6. Fracture surface characteristics in the HFTS-2 slant core are like those described for fractures in the HFTS-1 core (Gale et al, 2018). Many are remarkably

planar, smooth, and featureless (Fig 52a); those cutting coarse carbonate lithologies tend to be slightly irregular and rough (Fig 52b); others have twist hackles, steps and/or plumose commonly seen where the fracture cuts through different lithologies (Fig 52c,d,e). Some planes change orientation slightly (Fig 52f) so that two or even three orientations are measured. Changes of this kind may not necessarily occur at bedding planes — they may divert along strike.

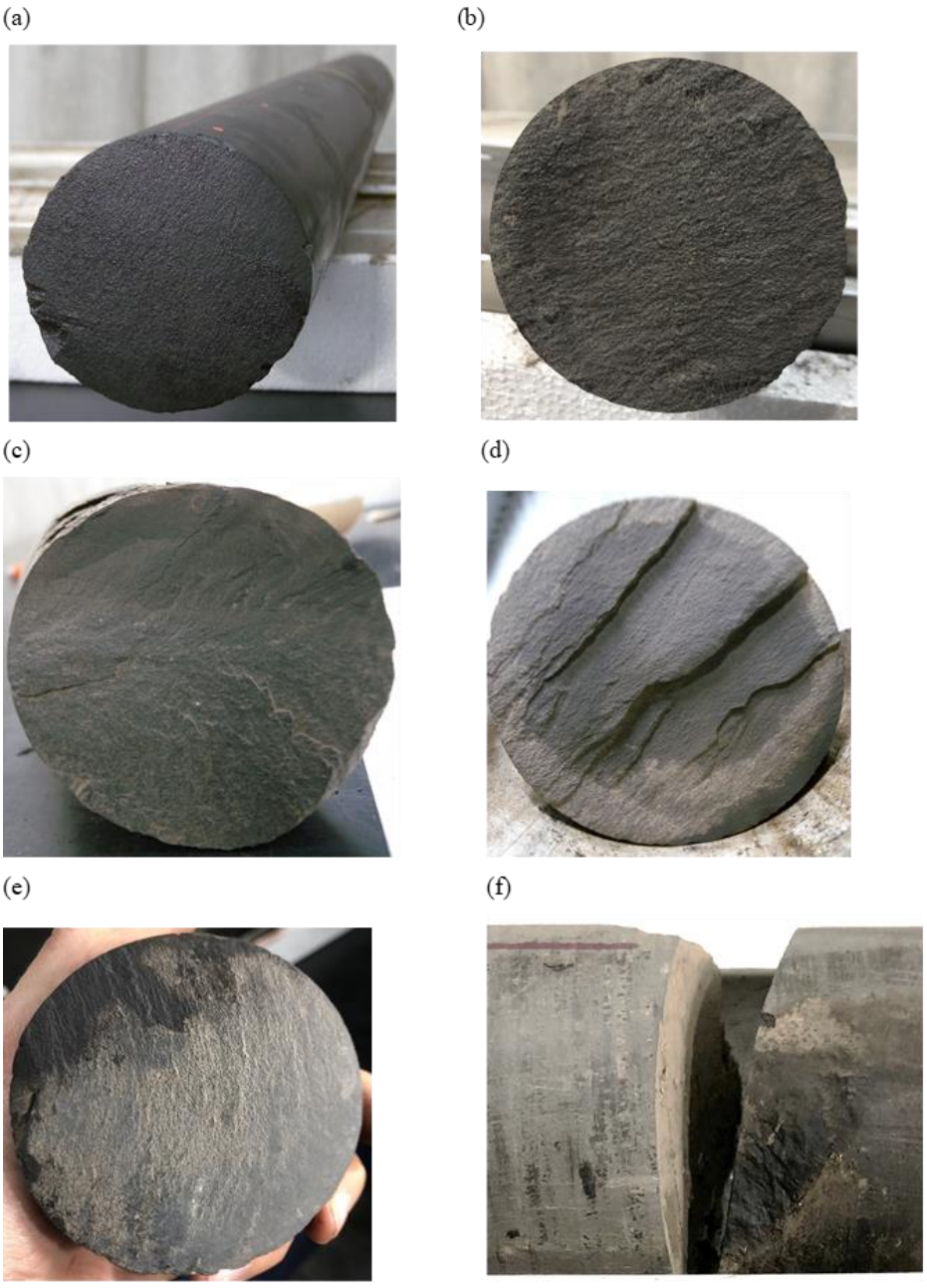

Fig 52—Hydraulic fractures: (a) Core 2, planar, smooth, featureless, (b) Core 6, rough face in carbonate, (c) Core 6, mudrock above with twist hackles, carbonate below with rougher surface and step, (d) Core 3, with marked steps oblique to bedding, (e) Core 4, plumose (f) Core 6, subtle change in orientation (face on right).

Doublets are quite common, for example there are three in part of Core 3 (Fig 53) and there are some triplets, a 4-fracture swarm, and even a 5-fracture swarm (Fig 54).

(a)

(b)

(c)

Fig 53—Hydraulic fracture doublets in three tubes from Core 3: (a) in middle of tube, (b) above the yellow foot marker), (c) center left of tube.

(a)

(b)

Fig 54—(a) Four-fracture swarm in Core 2. The four HFs are the leftmost fractures, the two on the right (uphole) are interpreted as drilling induced. This swarm contained some fine sand patches (see Fig 61). (b) Five-fracture swarm in Core 6.

There are some examples of hydraulic fractures reactivating natural fractures, including one location in Core 8 where a bed-parallel natural fracture is reactivated (Fig 55).

Fig 55—Bed-parallel natural fracture (BPF) filled with fibrous calcite (beef) is parted along both faces. The fractures bounding the section with parted beef are hydraulic fractures (HF). Our interpretation is that the hydraulic fracture caused reactivation of the natural fracture. Core 8.

Natural Fractures

Subvertical fractures filled with blocky calcite and striking NE-SW (termed Set 1) and WNW-ESE (termed Set 2) are dominant and are similar in character to those described in the HFTS-1, Midland Basin (Gale et al., 2019). They are mostly less than 1 mm in width. Except for two Set 1 fractures in Core 9 that have drusy cement on parted faces (Fig 56) most of the natural fractures were likely not open in the subsurface prior to well stimulation and drilling.

Fig 56—Drusy calcite cement on both the uphole (left) and downhole (right) faces of a Set 1 fracture in Core 9. Interpretation is that this fracture was possibly open in the subsurface. The reason for fracture reactivation in this case is likely core handling.

Cross-cutting relations are observed in several places and mostly show Set 1 predates Set 2 (Fig 58a), but in a couple of cases Set 1 appears to postdate Set 2 (Fig 57). This may mean that the timing of development of the two sets overlap, although Set 1 mostly came first. There are

significant numbers of subvertical, calcite-filled fractures in orientations other than for Set 1 or Set 2. Timing of these is uncertain, but some can be seen to postdate Set 1.

(a) (b)

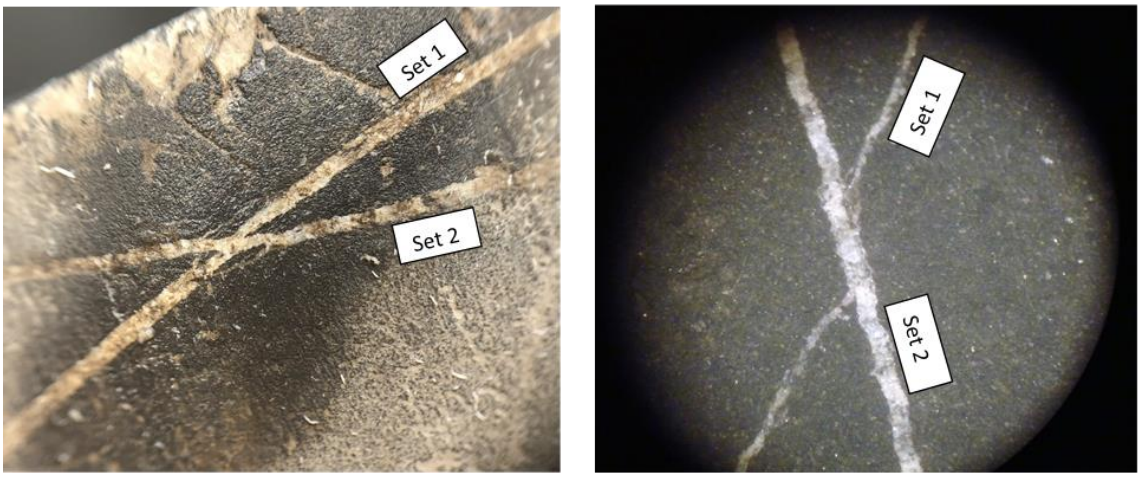

Fig 57—(a) Typical cross-cutting relation in Core 2 where Set 1 (0.75 mm wide) is cut by Set 2. (b) Less common cross-cutting relation where a Set 1 fracture diverts along a Set 2 fracture for ~ 1 mm, then resumes. The portion of the Set 2 where the diversion occurs is wider than the rest of that fracture, which is 0.265 mm wide. The Set 1 fracture has 2-3 strands. Photos through hand lens.

Bed-parallel fractures

(a)

(b)

Fig 58—(a) Discontinuous, bed-parallel fractures with blocky fill. Core 4, (b) Thick (1 cm) beef in Core 9. Labels are for core-handling breaks.

There are some narrow bed-parallel fractures filled with blocky calcite (Fig 58a), but also several large (> 5 mm thick) bed-parallel fractures filled with fibrous calcite (beef) (Fig 55 and Fig 58b). Fibers are commonly oblique and mostly indicate top to the north shear.

Observed Faults

There are several faults in Core 6 showing normal displacement on moderately dipping planes, and a fault zone with two phases of calcite cement (Fig 59a). The fault consists of a wide (4 cm), early, zone with mixed, blocky calcite and host rock with some planar shear bands, orientation 032°/58°, which is cut by a 1-cm-thick zone of calcite that has a strong, pervasive, mineral lineation trending 23°/092° (not slickensides). The later zone is oriented 350°/71°. The mineral lineation does not lie in the later fault plane, but is oblique to it, lying close to the earlier fault plane.

Two bed-parallel fractures with beef show evidence of shear in Core 9. Polished surfaces with slickensides parallel to the core axis indicate top-to-the-north movement (Fig 59). An

accumulation of calcite cement with porosity occurs where the fracture steps down to the north to create a pull-apart structure (Fig 59).

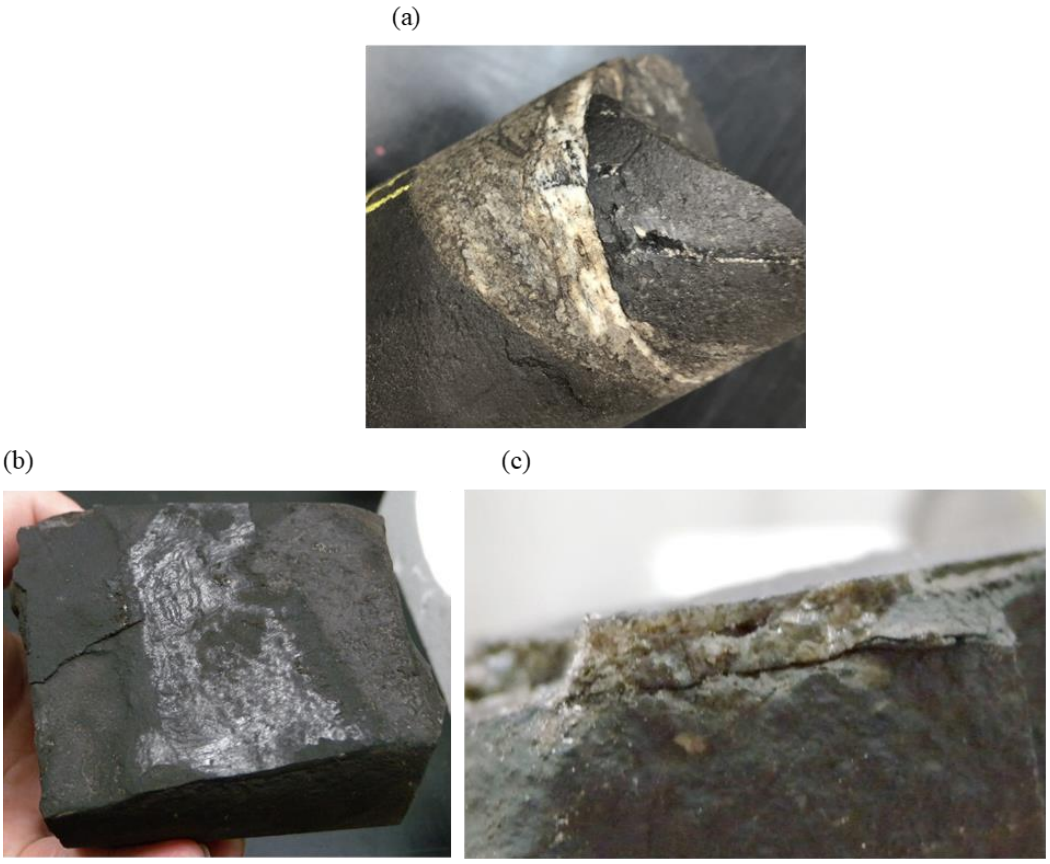

Fig 59—(a) Fault zone up to 4 cm thick with blocky and fibrous cement in Core 6. (b) Bed-parallel fracture face with slickensides and polish and (c) cement with pore in releasing step of bed parallel fracture #1085 in Core 9 at 13,917.90 ft. Cement is 4 mm thick here.

Drilling-induced and core-handling fractures

Both drilling-induced and core handling fractures are present, with characteristics previously described in Gale et al. (2018) and summarized here. Drilling-induced fractures are typically at a high angle to the well bore and parallel to SHmax. They commonly have a core-symmetric, curviplanar, saddle shape and tend to be smooth. Core-handling fractures are more irregular, and rougher, and can break across the core, commonly stepping at bedding planes, or along bedding. In both drilling-induced and core-handling fractures, surface plumose markings may emanate from a point source within the core; in natural and hydraulic fractures, plumose markings would have no relation to core margins, barring coincidence. Other evidence of

breakage points within the core includes core-rimming plumose markings and raised knobs (tangs) at the core margin.

Proppant Observations

Material collected from parted fractures consists of drilling mud, aluminum shavings from the core barrel, shale and other lithic particles, calcite, and rarely proppant that was pumped during the hydraulic fracturing of adjacent wells. The material is preserved should a future study require it, but we did not undertake a systematic analysis as this was beyond the scope of work. Separately, Maity et al. (2021) examined the material collected from each core tube, and on the outside of the core.

We observed very fine sandy material in several locations, although none was identified unequivocally as proppant. This material, consisting of small patches, was observed in cores 1, 2, 4, 5, 6, 7, but not in 3, 8, or 9. There were no sand packs, although there was a deposit of thick, gritty mud in one hydraulic fracture in Core 6 (Fig 60).

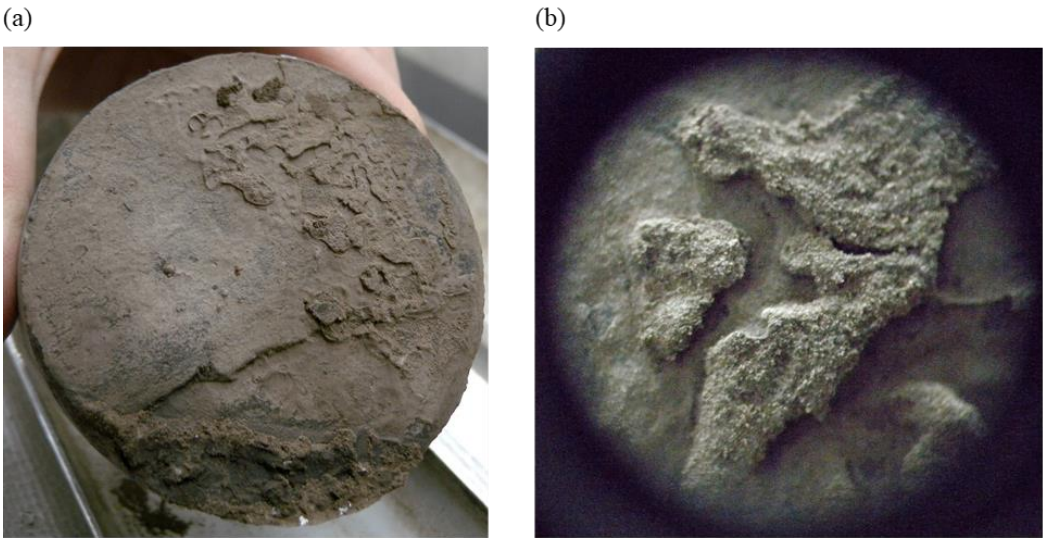

Fig 60—Patches of gritty/sandy mud (a) on fracture face (b) close-up of patch using hand lens, field of view ~1 cm.

Semiquantitative analysis was done for some samples from fractures at the top of Core 2 (see Fig 54a) to establish the character of the fine sand. Most of the sand was in the 63-120 μm size range (Fig 61), which is smaller than the proppant mesh size pumped. In keeping with findings by Elliott et al. (2018), because proppant at any given size range typically contains a lot of much smaller grains, we interpret the sand as proppant. These smaller grains are the most likely to be

transported long distances in the pumped fluid. Fractures that have surface irregularities such as steps and twist hackles are likely a trap for this sand (Fig 61c).

(a)

(b)

(c)

Fig 61—(a) fracture face showing sand patches (b) close-up of patch, field of view ~1 cm. (c) cleaned face showing steps and twist hackles.

Discussion

The overall findings from this study in terms of fracture types and distribution are like those from the HFTS-1 study Gale et al. (2018). The main difference is the presence of bed-parallel natural fractures, which were absent in the core from HFTS-1. Studies of these bed-parallel fractures suggest they are related to overpressuring during rapid burial (Ginn et al., 2017). The

contrast between the Delaware Basin and Midland Basin burial histories, with the Delaware Basin being much deeper, is the likely reason for the difference.

The reasons for clustering of hydraulic fractures are beyond the scope of this section and are the subject of a separate study on fracture segmentation. We make the general observation that more hydraulic fractures are observed than would be predicted from the estimated number of perforations in the stimulated well. Surface features provide information about the direction of hydraulic fracture propagation and about segmentation and bifurcation that might increase the number of fracture strands. Our hypothesis is that large numbers of clustered hydraulic fractures are partly due to segmentation and bifurcation. Fracture bifurcation, which was directly seen in the HFTS-1 core, appears not to have been clearly captured in the HFTS2 core; points (lines) of bifurcation are inferred to occur just outside the core where there are closely spaced doublets. The results from this work will allow hydraulic fracture distribution relative to the stimulated well to be assessed.

For natural fractures we use the term parted to refer to a fracture whose faces are now separated, and the term open to refer to a fracture that had some porosity in the subsurface. Where parted, the mechanism of parting is mostly unknown, and could be due to hydraulic fracturing, drilling, or core-handling. Reactivation of natural fractures, including bedding-parallel fractures, occurs although the mechanism of parting is mostly unknown.

Conclusions

The HFTS-2 project successfully acquired 948 ft of core, covering the reservoir interval above and below a hydraulic fracture stimulation. A total of 1261 fractures, including 500 hydraulic fractures, were observed. Hydraulic fractures are clustered, with groups of up to five fractures spaced just a few centimeters apart. Pairs of fractures, termed doublets, are common. Many are remarkably planar, smooth, and featureless, while others have twist hackles, steps, plumose, and kinks. These surface features give indications that hydraulic fractures become segmented during growth, which could account for the large number observed.

Natural, subvertical fractures, mostly less than 1 mm in width, sealed with blocky calcite, are oriented NE-SW (Set 1) and WNW-ESE (Set 2), with a few showing other orientations. Two Set 1 fractures have drusy cement on parted faces and were possibly open prior to drilling. Bed-parallel natural fractures, most having fibrous cement (beef), and some showing top-to-north bed-parallel shear are present. Faults with normal/oblique movement were found in one part of the core. Drilling induced and core-handling breaks were identified in all cores, and likely reactivated some natural fractures.

Core Characterization - Proppant

Authors: Debotyam Maity & Jordan Ciezobka

Summary

In the past, we have developed and shared a unique workflow for subsurface proppant detection and quantification from cores or drilling mud return samples at the Hydraulic Fracturing Test Sites (HFTS – 1 Midland Basin). In this study, we extend our work to include an analysis of samples from a through-fracture core collected at HFTS-2 test-site in Delaware Basin. The broad objectives were firstly, to determine the spatial distribution of proppant in the created SRV along the cored interval; secondly, introduce new proppant attributes such as relative particle size distributions to better understand proppant settling characteristics; and finally, recognize the controlling factors driving the observed proppant distribution. Approximately 340 sludge samples containing proppant were collected from whole cores drilled through a hydraulically fractured reservoir. This represents more than 950 ft. of cored SRV of nearby stimulated horizontal wells. Samples were prepared and analyzed for proppant, with particles below mesh 20 size fraction used in the analysis. Representative subsamples were mapped using high-resolution optical imaging. The scans were processed using an image processing algorithm which uses Hough Transform along with other optical attributes associated with sand-like particles within a machine learning framework to detect proppant. Finally, select samples were further tested using high resolution scanning electron microscopes with compositional analysis to validate the imaging results as required. In line with our observations from the first two cores from Permian-Midland test site, we observe vertical proppant distribution to be defined by stress contrast at bed boundaries such as carbonate layers. Significant proppant starts showing up at ~ 25 ft. above the nearby producer being sampled at a lateral offset of ~ 75 ft. from said producer. We see a broad correlation between hydraulic fracture clusters in the core and significant propped zones. Using DAS interpretation, we see a good match between proppant placed at perforation clusters and far-field observations at the core. Finally, we observe a strong correlation between observed fracture and proppant distribution on one hand and pressure drawdown response measured using gauges placed along the slant core well. This study helps validate our original workflow meant for both qualitative as well as quantitative assessment of proppant presence near stimulated wells. Further, we demonstrate improvements in interpretation by using modified attributes key to understanding proppant height growth and settling characteristics. Finally, we validate proppant distribution results with pressure drawdown response. This method has been successfully modified for drilling mud return samples as well as cuttings analysis to further expand its applicability and potential use cases, providing a proppant

log along the entire lateral of a new in-fill or offset well. We believe this technology holds the key towards systematically optimizing the development of shale reservoirs.

Introduction

This study pertains to the approximately 950 ft. of through fracture core along a slant core-through well. The test area already had pre-existing producing laterals (BR1H and BR2H drilled southwards; TR5H, TR6H, TR7H and TR8H drilled northwards) as is highlighted in Fig 62.

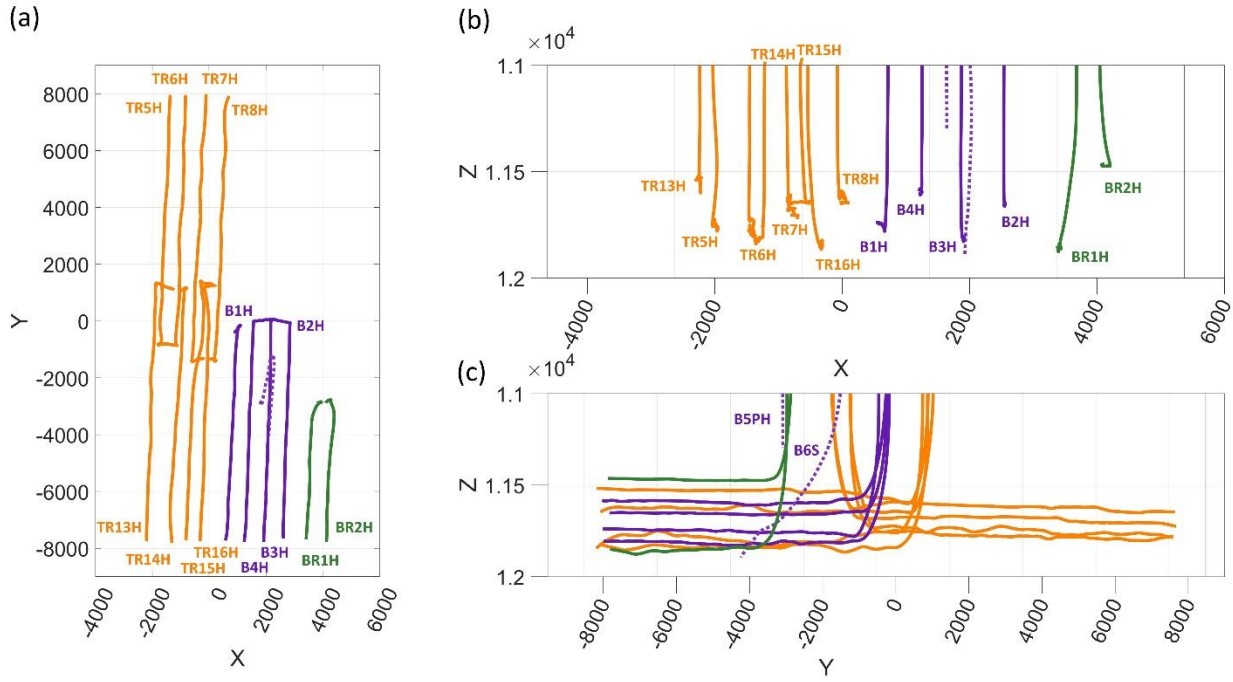

Fig 62—HFTS-2 site wells shown as (a) top view, (b) gun-barrel view, and (c) side view. The proppant log was run of through fracture core collected along B6S science well.

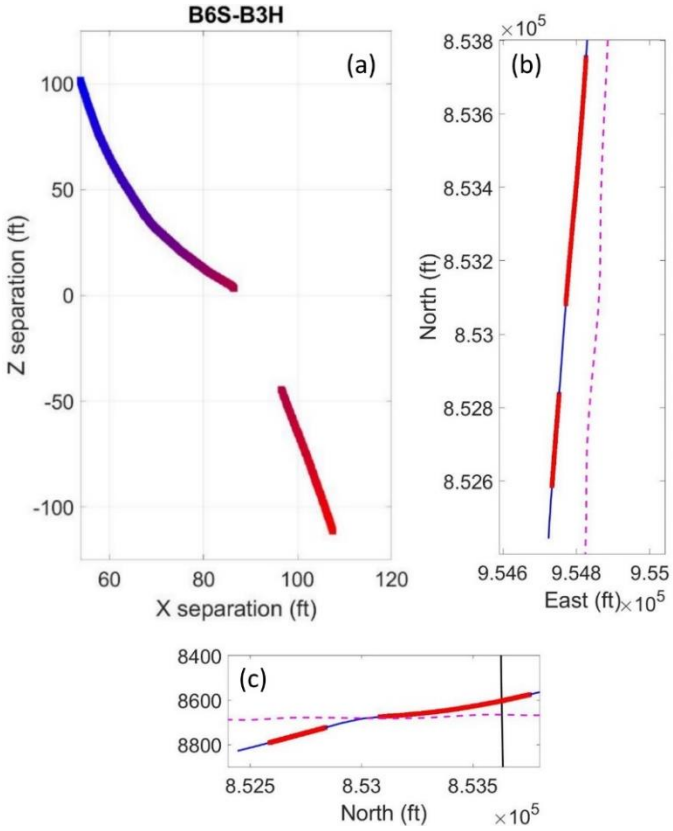

Fig 63—(a) Relative core location w.r.t. B3H well sampled by the B6S core. Subplots (b) and (c) highlight the map and side view. Dotted insert indicates location of B3H well and red inserts show the location of the core.

In addition to the significant core analysis and fracture characterization work from core samples collected along B5PH pilot well and B6S slant well, the project installed permanent fiber optic cables in 3 wells to monitor near wellbore signals during fracturing and to collect cross-well strain measurements and for production monitoring (Jin et al. 2021). Two fibers are in the B3H and B4H laterals and one in vertical B5PH pilot hole. Permanent P/ T gauges were placed at the heel and toe of both B3H and B4H laterals. Furthermore, pressure and temperature gauges were placed in the B5PH well to monitor pressure drawdown during production. Additional advanced diagnostics included a significant formation evaluation program on the vertical whole core (Zhao et al. 2021), multiple well logs in horizontal wells, multi-array MTI capable microseismic survey (Grechka et al. 2021), multi-well time-lapse geochemistry analysis, among others. In this study, we will reference observations from some of these diagnostics to interpret and validate observations from the proppant log run for the B6S slant core. Due to trajectory build-up and subsequent correction, the actual cored interval is split between two intervals. The first interval is located above and up to the nearby parent well (B3H). The second cored interval is located below the B3H landing depth with a depth offset of approximately 50 ft. Fig 63 shows map and side view as well as approximate distance of coring points (3 ft. tubes) from the B3H. We also

note that the core stays to the west of the B3H. Multiple fracture stages in B3H straddle this interval including standard (6 clusters/ stage) as well as extended (8 clusters/ stage) designs.

Applied Methods

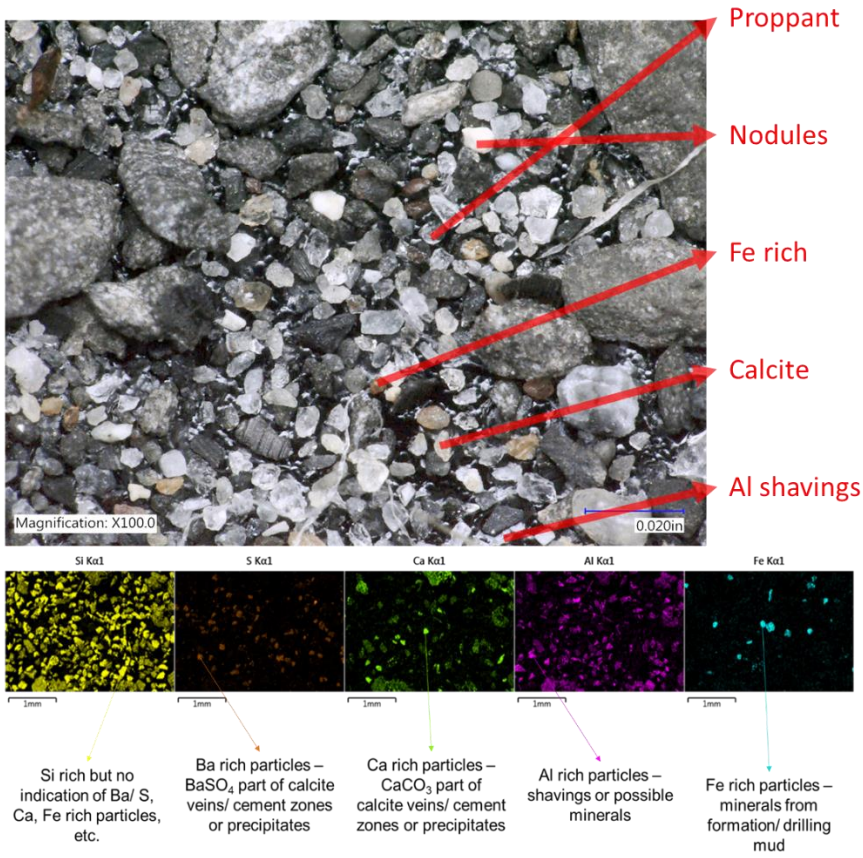

Fig 64—Interpretation of SEM-EDS results at a sample QC location showing preponderance of proppant particles but other minerals with similar optical characteristics as well [Maity and Ciezobka, 2021b].

The details of the workflow have been shared in past publications by the authors (Maity et al., 2018; Maity and Ciezobka, 2019a, b). However, some modifications were implemented to improve the applicability considering smaller sand particle sizes which were pumped into these wells. The basic workflow involved sample collection from the inside of the core tubes as well as surface of the cores, shipment of samples to GTI lab in Illinois, sample preparatory steps including washing, drying, sieving, sub-sampling, etc., before imaging analysis. Since we are only concerned with smaller particles, material smaller than Mesh 20 (< 840 µm) is screened out and sub-sampled using a riffler. We use high resolution bench scale imaging tools to image these sub-samples and run these images through a proprietary classification algorithm to identify all "proppant" and "proppant-like" particles from each sub-sample. Since the approach is based on imaging, the resolution limits the size of particles that can be accurately identified. Mesh 100 particles, which are of interest to us, can range in size from Mesh 70 to Mesh 140, i.e., 200 µm to 100 µm.

With this workflow, we can capture most of the proppant and provide a reasonably accurate quantitative indication of number of particles present in the imaged sample. Apart from the

imaging workflow discussed, for quality control, SEM-EDS analysis is incorporated to accurately discriminate actual proppant from other proppant-like particles such as calcites and sulphates. Our baselining tests with proppant as well as mineral cements from subsurface samples show that the imaging workflow can sometimes find it hard to sort proppant from other minerals which have similar optical characteristics such as translucency, etc. This is particularly the case when the particles are very small (≤ 100 µm). While we would typically not expect Mesh 100 sand particles to fall in such a small size range, actual samples from field suggest that a significant distribution of Mesh 100 sand falls in this smaller size range and can go as small as 60 µm. Thus, this quality control step is applied on selected samples to cover samples with low to high proppant counts. The results from this QC process are further used to obtain a more accurate distribution of proppant versus other mineral particles in the samples and is useful in our interpretations. The correction is done by identifying an applicable correction factor from the controlled SEM results and implementing the correction on rest of the dataset. Fig 64 shows an example SEM scan results panel with various mineral identifications and their interpretation for the QC process (Maity & Ciezobka, 2021b). The plot also highlights a high-resolution microscopic image of the same sample and the corresponding particles likely observed in the visible spectrum as well. The microscopic image is useful in understanding the challenge associated with classifying these particles using optical imaging techniques.

Observations

Fig 65 highlights proppant distribution observed along the B6S cored interval. We have a total of 9 core sections dividing the two intervals. Significant proppant seems to start showing up at core 3 but then drops subsequently before starting to rise again proximal to the producing lateral both above (core 6) and below (cores 7, 8 and 9). We can also observe significant local peaks in the distribution as well.

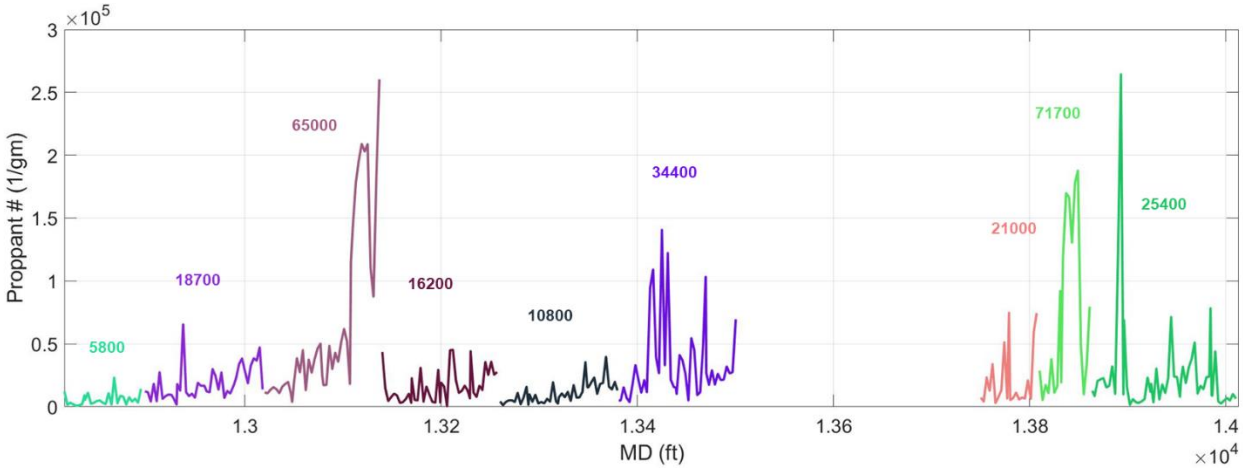

Fig 65—Observed proppant distribution along the cored interval in B6S well. The colors indicated individual core sections and the numbers indicate the average normalized proppant counts for these sections. The proppant count normalization is achieved by scaling the actual counts for each sample by the weight of the sample.

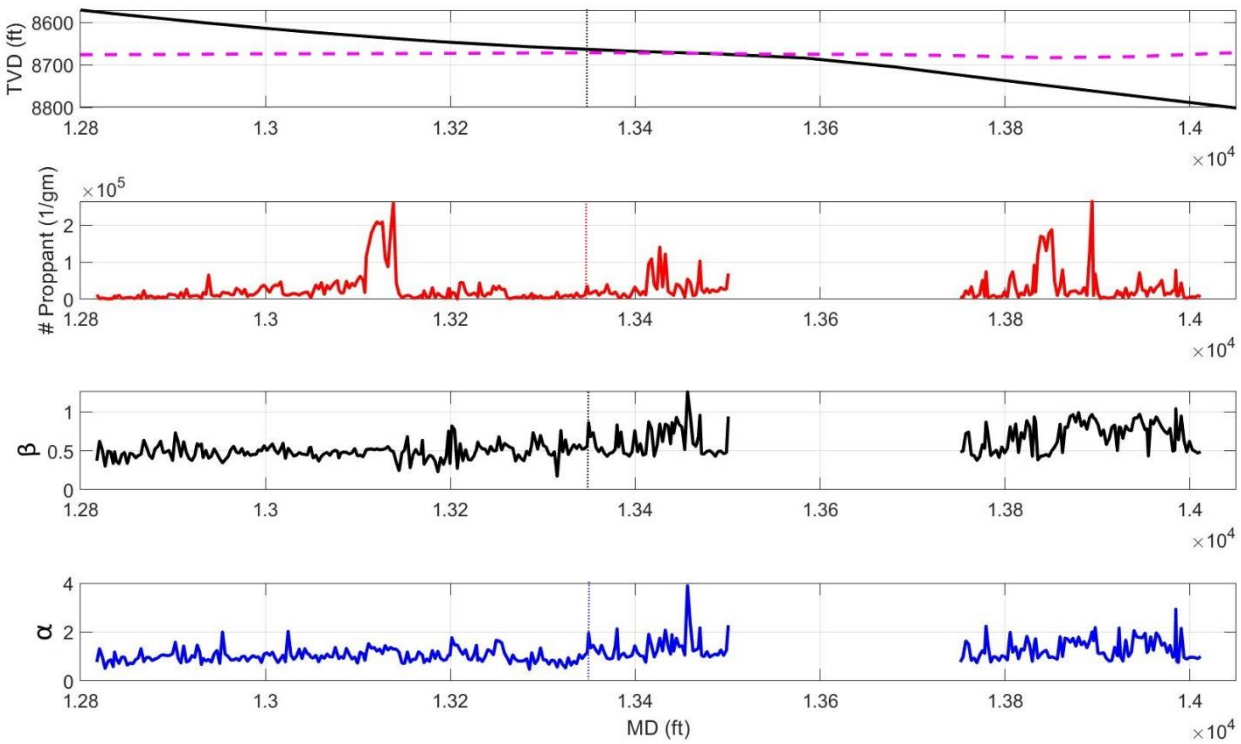

Fig 66—Wellbore trajectories (B6S slant well and B3H lateral) with various proppant log parameters from this study.

Apart from absolute proppant counts, other derived parameters such as particle type ratio (proppant versus other minerals as identified or α) as well as relative proppant size distribution (β), are both useful for accurate interpretation of the log (Maity & Ciezobka, 2022). These can be defined as follows:

$$\alpha_i = \frac{Number\ of\ proppant\ particles_i}{Number\ of\ other\ mineral\ particles_i}$$

Eq. 5

$$\beta_i = \frac{C_{125-150} + C_{150-175}}{C_{100-125} + C_{125-150} + C_{150-175}}$$

Eq. 6

Note that C represents proppant counts tabulated within size ranges as per the specified subscripts. Fig 66 highlights these parameters for the proppant log evaluated for this cored interval. In multiple datasets, if the sample preparation protocols are appropriate and consistent, we have observed the relative proppant abundance to be a strong indicator of proppant presence in the pre-stimulated rock. For this dataset, we see a significant increase in the relative proppant abundance ratio at depths larger than 13350 ft. MD. Similarly, relative proppant size distribution is a good indicator of proppant presence as well. Sampling locations with lower proppant counts but high values of above-mentioned parameters are indicative of proppant presence, just not in large quantities at that location. Also, we do see proppant or fractures at shallower depths, however below this depth, proppant indicator values suggest predominance of proppant particles in these samples. There are various factors which could be at play here, for example, proppant settling behavior vs. lateral growth, presence of significant frac barriers, or

fracture properties as well. A possible interpretation for the peak observed at ~ 13110 ft. MD is that the zone is influenced by fractures propagating from other wells in the development that are laterally farther away from the sampling locations and therefore, have predominantly smaller proppant particles. This is reflected in the lower corresponding α and β values.

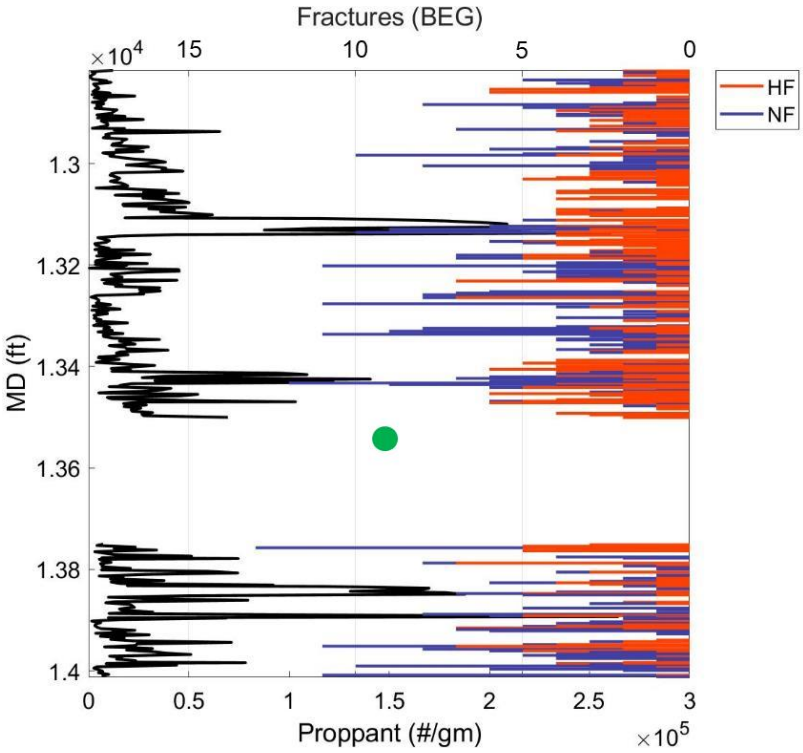

Fig 67—Hydraulic (HF) and natural (NF) fractures identified by BEG tallied per core tube (3 ft. sections). We see more hydraulic fractures in the first 6 core sections (Cores 1 through 6) and less hydraulic fractures in the last 3 cores (Cores 7 through 9). However, we see more proppant in the last three core sections (below the notional B3H lateral represented by green insert).

The core has been extensively characterized including a complete characterization of fractures by BEG (Gale et al., 2021). It is instructive to view the overall distribution of proppant particles with depth as compared to the hydraulic and natural fracture counts or density with depth. For this core, Fig 67 shows both these datasets plotted out in depth. We do observe some correlation between locations which are dominated by hydraulic fractures vs significant proppant peaks in the distribution. At the same time, locally, many locations with hydraulic fractures do not show significant proppant.

Formal observations and Results

There are some broad similarities between proppant distribution behavior observed in this core vs. other cores from HFTS-1 project in Midland Basin (Maity & Ciezobka, 2021a). Specifically, we see clear evidence of changes in lithology or stresses to be strongly correlated to higher proppant distribution counts. This observation is scale independent, i.e., it holds for zones with very low as well as very high proppant counts. Similarly, many of the high proppant distribution outliers can be correlated with significant variation of hydraulic fracture orientation at those

locations from the prevailing horizontal stress orientation which suggests that complex fracture distribution and morphology is a key driving factor (Maity & Ciezobka., 2020).

Fiber data (cross-well distributed strain sensing) at the site suggests that majority of these hydraulic fractures propagate along fracture corridors which are well aligned with the prevailing stress orientation (Huckabee et al., 2022). Thus, we can use fracture orientations as per classification and extrapolate these orientations back to the B3H parent well to see whether there is any association between observed far-field fractures and B3H clusters. There are implicit assumptions here which may not be strictly applicable. For example, that all these fractures are associated with B3H and not some of the other wells in the pad or that the extrapolation method provides accurate results. However, this approach is useful since it helps tie near field proppant placement (such as from DAS proppant placement analysis or hydraulic fracture profiling) and far field proppant distribution observed in our study. Near vs. far-field proppant association is achieved by fracture association as described above. Specifically, the criteria used is for the extrapolated fracture propagation path (from orientation) to intersect within ± 10 feet of any originating cluster.

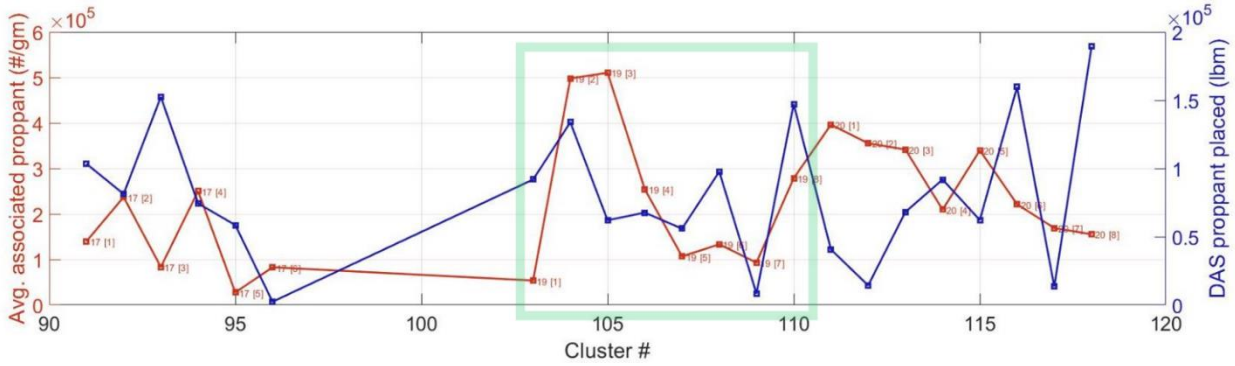

Fig 68—Connectivity based cluster proppant placement comparison between near-field (DAS derived proppant allocations) and far-field (proppant log) observations.

From Fig 68, we can see that the best correlation is observed between clusters 103 to 110 which corresponds to a specific stage in well B3H. Incidentally, this stage corresponds to section of the core closest to B3H in a vertical sense. This suggests that as we move away from the depth of the injection zone, the far-field proppant distribution begins to vary significantly from near-field proppant placement as interpreted from DAS data. Another interpretation could be around the impact of the other wells on the observed data at the sampling locations. As discussed earlier, these hydraulic fractures or proppant could be associated with other wells in the pad. We can consider well B4H, and the fractures associated with stages in B4H as well. Since this well is landed higher than the sampling locations, we would expect intersecting hydraulic fractures from B4H to have significant proppant due to proppant settling behavior. Part of the diagnostic dataset includes cross-well communication response through strain measurements (DSS) during fracturing of B4H well as measured in B3H well lateral. We can map intersection points along B3H fiber with the corresponding cluster locations in B4H well (Fig 69). This exercise clearly shows that for stages 16, 17 and 20, there could be some impact of fractures from B4H in our observations at the sampling location along B6S core well. Specifically, the large proppant peak

observed across stage 20 may indeed be associated with B4H instead of B3H well. On the other hand, for stage 19, which corresponds to clusters 103 through 110, we see a very sparse distribution of B4H fracture systems mapped using DSS response at B3H. This suggests that clusters 103 through 110 (Fig 68) from B3H completions have a more pronounced impact on far-field proppant distribution.

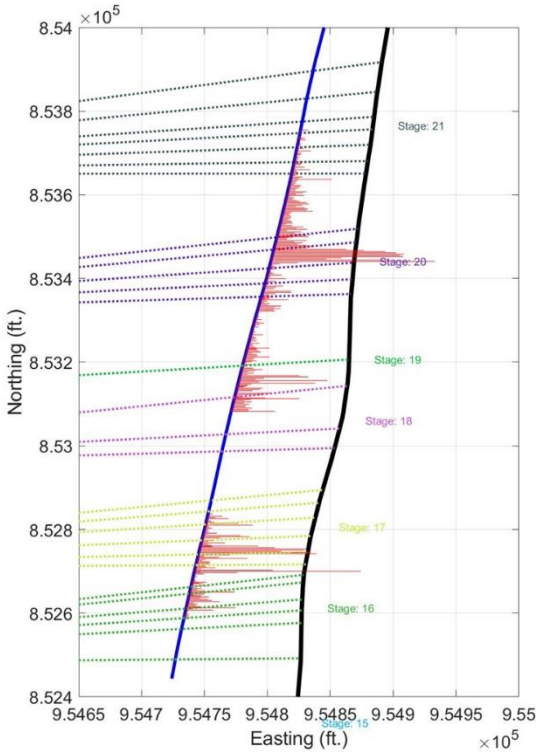

Fig 69—Potential impact of B4H fractures on observations at B6S cored interval. B4H →B3H connections are based on observed fracture intersections in B3H fiber from distributed strain sensing (DSS) data.

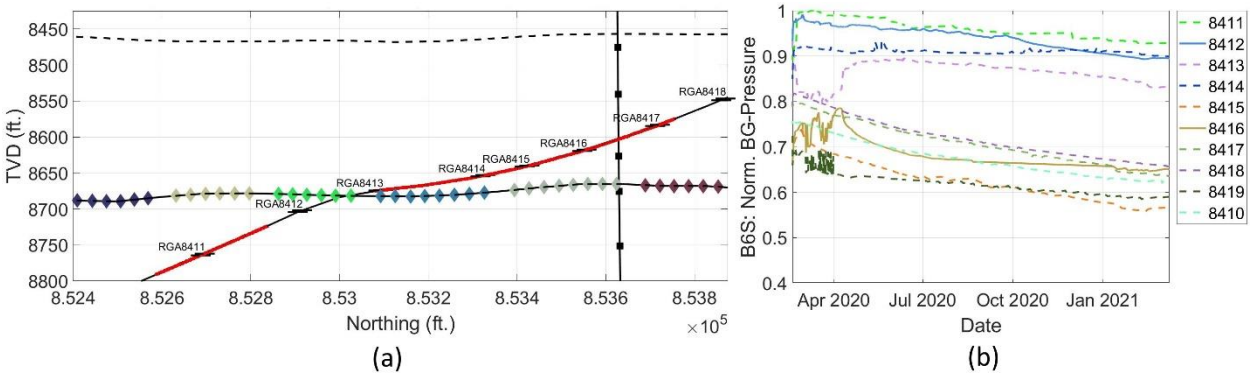

Fig 70—Observed pressure drop across various gauges placed in B6S core well.

Additionally, pressure gauges were placed in the B6S slant well to monitor production drawdown behavior as these wells were brought online. If we simply consider the observed pressure drop over a given period once pressures have stabilized as drawdown, we can compare

that with observed fracture as well as proppant distribution along those locations in B6S slant well. In addition, petrophysical logs can provide useful insights into types of formation or changes in lithology which can also be compared with the observed drawdown behavior. Another useful parameter set to investigate is the distance of the measurement location from nearby producer. This includes both vertical as well as lateral offset which can in turn have some influence on observed proppant distribution. We can use various methods to understand if there are any dependencies between these variables though not in a causal manner. The way to do this is to use various available regression techniques, such as decision trees, etc. Fig 70 highlights the location of some of these pressure gauges along B6S well and the measured pressure during production phase (Fig 70b).

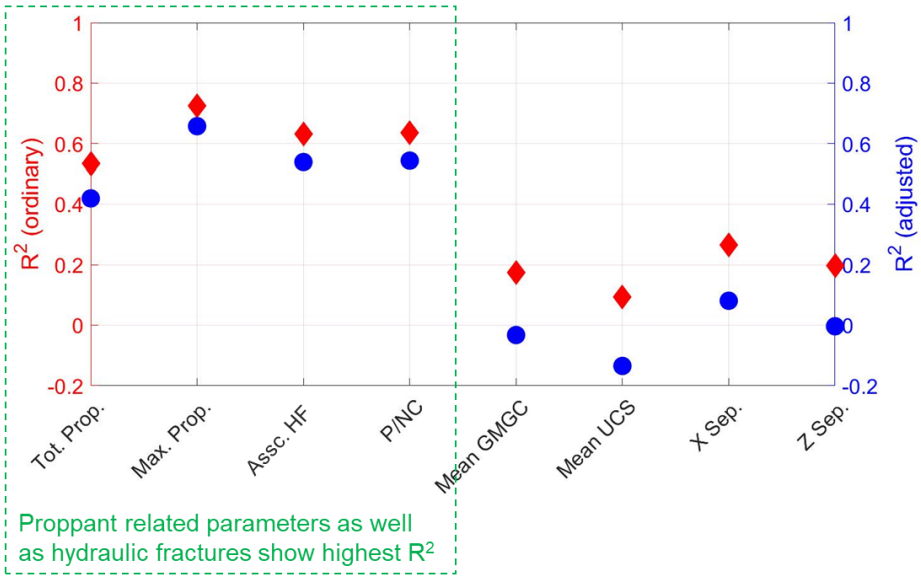

Fig 71—Coefficients of determination for various predictors when modeling pressure drawdown. Far-field proppant and associated hydraulic fractures highly correlated with observed pressure response at the B6S gauge locations.

With the caveat that correlation does not mean causation, we do observe strong positive correlation between pressure drop or drawdown observed at the gauges and the observed proppant distribution or associated hydraulic fractures far-field. If we use bi-variate regression analysis, maximum observed proppant at the gauge location shows an adjusted R^2 of ~ 0.63 when correlated with pressure drop. Associated hydraulic fractures show an adjusted R^2 of ~ 0.54 (Fig 71). A more rigorous approach is to build non-linear multi-variate models to better understand which properties show the highest impact on observed pressure drop behavior. One approach is to use boosted regression analysis which is a non-linear decision tree with binary splits for regression. The final predictive model is composed with weighted combination of multiple trained regression trees. The model is generated by fitting an ensemble of learners for regression. It uses a gradient boosting strategy applied for least squares (LSBoost) algorithm to boost the learning process. In each step of LS boosting, the ensemble fits a new learner to the difference between the observed response and aggregated prediction for all learners generated

previously. The fit is to minimize mean squared error, which is the cost function. The results are highlighted in Fig 72.

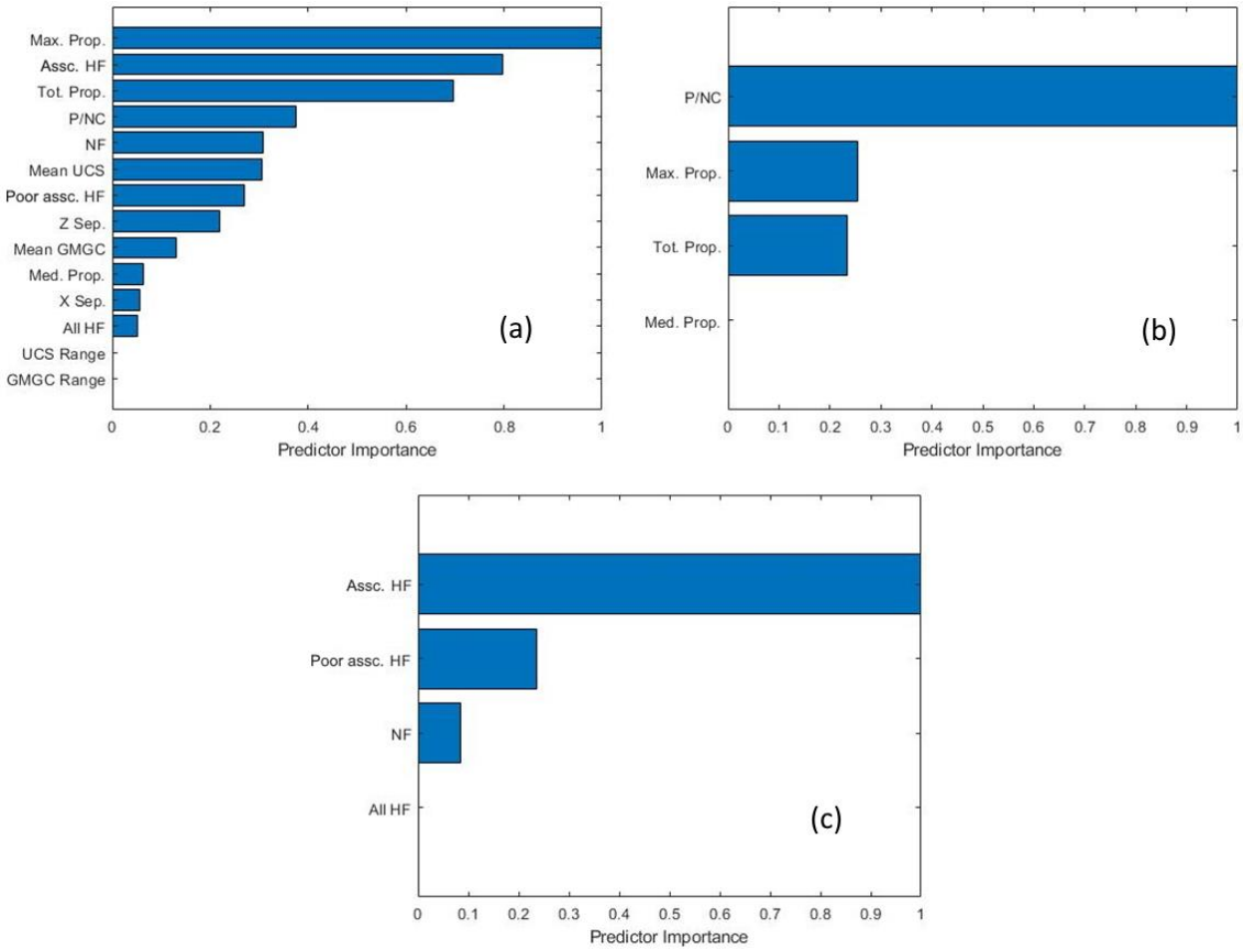

Fig 72—Predictor importance tests showing proppant and associated hydraulic fractures to be the most important predictors. We also see relative proppant ratio (P/NC) to be a good predictor as well.

By iterating through the various predictors, we can identify the most significant predictors which have the highest impact on the prediction mismatch between the actual pressure drop and the modeled pressure drop from the boosted regression tree. Fig 72a shows predictor importance values where all possible parameters are used for the model design. These include proppant and fracture related parameters, as well as rock properties such as gamma ray and unconfined compressive stress, as well as physical location of the monitoring gauges with respect to treatment well (B3H). The rms error for this model was low at ~ 60 psi. Fig 72b shows predictor importance values where only proppant related parameters are used. We get a similarly low rms error for this model as well (~ 70 psi). The third mode (Fig 72c) uses fracture related parameters and shows a reasonably good prediction with rms error of ~ 200 psi. It is worth noting that since the actual dataset is small (with 6 pressure monitoring locations along the cored interval), it was synthetically expanded by randomly perturbing the data points slightly and making sure that

final dataset showed similar distribution of predictor properties as those compiled from the original 6 data points.

Discussion

With this case study and its observations, a relevant question could be whether a baseline threshold for proppant data is necessary. In our opinion, based on past studies, a more appropriate approach is to use all three proppant indicators variables, i.e., normalized proppant counts, α, and β parameters to understand proppant presence and behavior.

For analysis of drainage response (pressure drop) based on gauge data and correlating observed response with various directly and indirectly measured properties in the cored interval, a start time is selected after interference tests, etc., i.e., are complete and once the depletion has stabilized. The end point is also selected such that there are no significant events between the two. Other methods, such as decline curve analysis, etc., may be more suitable for a more robust analysis.

Finally, proppant and fracture distribution seem to govern the local drawdown behavior as evidenced from the pressure gauges installed in B6S well. Thus, irrespective of which wells these fractures and associated propped sections relate to, the local drawdown will be agnostic to such relationships. This is useful since it opens the door for using similar systematic proppant log profiles from in-fill child wells captured during drilling process (Maity and Ciezobka, 2022) to be used to map and validate drawdown as predicted using hydraulic fracture simulators.

Conclusions

This case study has provided useful insights into proppant distribution behavior, possible factors influencing said behavior, as well as potential ways in which this information can be used as a diagnostic data point for understanding completion quality.

Our study suggests that apart from hydraulic fractures present at the sampling locations, the most significant factor influencing proppant distribution seems to be the variations in lithology and stresses within the reservoir. Furthermore, majority of hydraulic fractures observed can be associated with corresponding clusters in B3H well. At the depth of the B3H lateral, which was being sampled, the proppant placed (as evaluated using distributed fiber-optic hydraulic fracture profiling) correlates well with observed proppant at the core location.

Pressure drawdown behavior can be reconciled with the location of gauges and presence/ absence of fractures/ proppant at those locations. Thus, normalized, and accurate proppant log could potentially be a useful proxy for drainage predictability in previously stimulated zones.

Various studies incorporating proppant logging results, including this one, suggests that it can be a very useful tool for assessing stimulated/unstimulated (drained/undrained) zones during drilling of child or infill wells and therefore, can be used as a data point to inform optimal proppant placement strategies in those wells.

Cluster Level Drainage Interpretation – Fiber-Optic Observations

Authors: Debotyam Maity & Jordan Ciezobka

Summary

In this study, we highlight various distributed acoustic surveys conducted at the site over time which provide insights into cluster level efficiencies and their relationship with perforation efficiencies for test site wells. We use observations from novel Rayleigh frequency shift technique (DSS-RFS) to understand strain change during well shut-in and flow periods as part of pressure interference tests. We have observed a strong relationship between perforation and cluster efficiencies as well as independent far-field observations based on core-through studies which suggest that perforation efficiency is key to optimizing fracture stimulation in horizontal well laterals. Finally, observations from DSS-RFS surveys provide insights into clusters along the wellbore where the drainage or productivity may have been sub-optimal and are likely candidates for re-stimulation or other approaches to be implemented in the future.

Introduction

Problem definition

Hydraulic fracturing is a well-established stimulation technique particularly useful in tight hydrocarbon reservoirs such as shales to improve well productivity by artificially creating propped fractures which allow enhanced fluid flow into the wellbore. While many techniques are available, two most used methods include plug-and-perf and sliding sleeve techniques (Stegent et al., 2011). Of these two, most unconventional shale wells use the plug-and-perf technique where a frac plug is pumped down on wireline along with perforating guns to the specific depth or zone of interest (stage). Once the plug is set, the guns are triggered so that the zone can be perforated. The gun is then removed from the well and the fracture stimulation treatment is pumped downhole along with the frac ball leading the treatment to seal the plug and create necessary stage isolation. A major uncertainty in plug-and-perf completion strategy is perforation efficiency when phasing is used, i.e., shots are sequentially oriented along different angles along the well axis. Since these wells are horizontal long laterals, it is hard to centralize gun systems in the wellbore and therefore, generally cause significant variances in perforation tunnel lengths and diameters. These variances can cause preferential fluid flow and erosion along some perforations but limited to no flow for other perforations within a cluster or stage (Li et al., 2018; Liu et al., 2018). In addition, other issues such as mechanical damage during perforating (Halleck et al., 1998) or geomechanical stresses (Waters and Weng, 2016) can also have an impact on fracture initiation and growth. Acoustic, distributed acoustic sensing (DAS), and other imaging techniques have shown poor perforation efficiencies in real-world unconventional well completions (Robinson et al., 2020; Pakhotina et al., 2020). While some methods have been proposed to improve perforation efficiencies such as improving perforation techniques (Cuthill et al., 2017), or using optimized pumping schemes such as rate fluctuations

(Ciezobka et al., 2016), it is necessary to evaluate and understand individual perforation as well as cluster level efficiencies and productivity from these intervals.

In this study, we make use of the significant amount of diagnostic data collected at the test site including fiberoptic distributed acoustic and temperature sensing or DAS/ DTS data (Zhao et al., 2021), far-field distributed strain sensing or DSS (Bessa et al., 2021), distributed strain sensing using Rayleigh frequency shift technique or DSS-RFS method (Ugueto et al., 2021), high quality step-down testing, etc., to provide a valuable dataset to systematically analyze and evaluate perforation or cluster level efficiencies during fracturing as well as to better understand productivity. Fig. 73 shows a gun-barrel view of the wells at the test site and identifies two horizontal wells with permanently installed fiberoptics (box inserts). Also identified is the core well (B6S) which was used to identify post fracturing far-field hydraulic fractures at this site (Gale et al., 2021). Specifically, we have the two instrumented horizontal wells B3H and B4H with DAS/ DTS observations. In addition, B4H well was also instrumented for DSS-RFS surveys for two pressure interference tests (PIT-1 and PIT-2) run during February 2020 and September 2020.

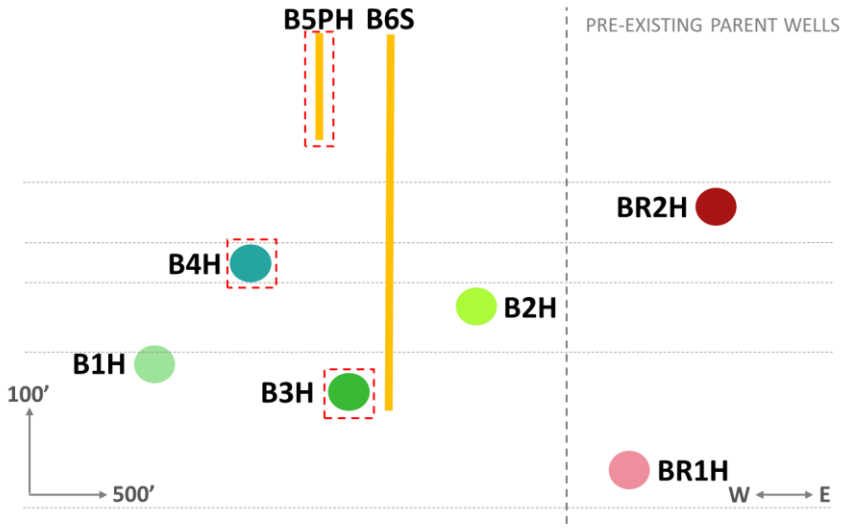

Fig. 73—Gun-barrel view of test wells at the HFTS-2 site in Delaware Basin. The wells bounded by red boxes indicate instrumented wells with permanent fiber installations. B6S is a slant core well drilled to identify and characterize far-field fractures associated with B3H well lateral.

Specifically, we will look at the stage designs for two of the test wells (B3H, B4H), the stimulation response across the stage clusters as well as overall perforation and cluster efficiencies. We will look at evidence of inefficiencies from far-field through fracture coring observations. Finally, we will use observations from DAS as well as DSS-RFS surveys to understand cluster-level efficiencies and longer-term productivity trends across B4H lateral.

Data & Interpretation

Understanding Cluster vs. Perforation Efficiencies

Two wells of interest at HFTS-2 site are the B3H and B4H laterals. The unique part of the test involved permanently installed optical fibers along the casings of these wellbores which were

cemented in place and then used for observations during stimulation as well as during production of these wells. Multiple fracture stimulation designs were tested including standard designs, aggressive limited entry designs, tapered cluster designs, etc. Fig. 74 shows the average perforations shot per cluster across various B3H and B4H stages. In general, extended stages have fewer perforations per cluster, including tapered designs when compared with standard stages.

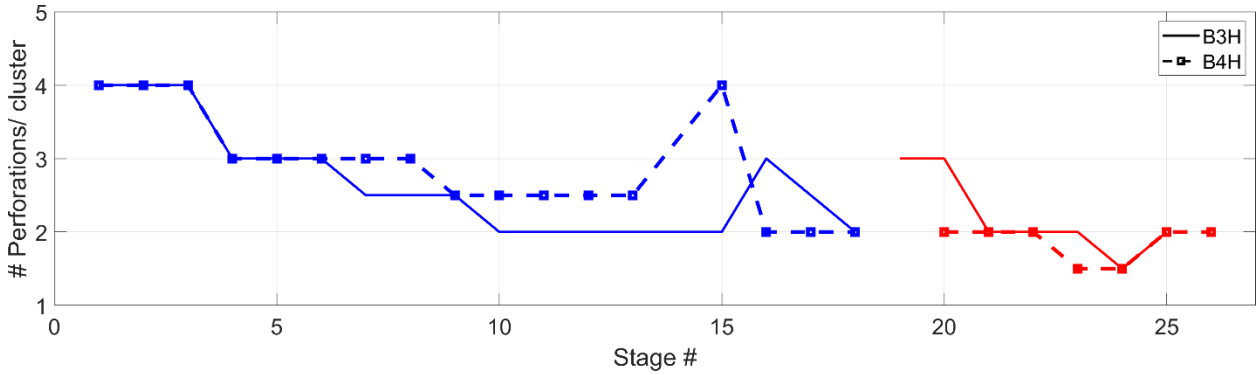

Fig. 74—B3H and B4H cluster designs including standard (blue) and extended (red) stage lengths.

While many stage designs were tested at the HFTS-2 site, broadly, we can classify them into two designs, i.e., standard stages having 5 to 6 clusters and extended stages having 8 to 10 clusters (Zakhour et al., 2021). Cluster efficiency in terms of proppant placement or fluid placement using DAS observations suggests a larger variance for extended length stages (> 6 cluster) vs. the standard stages (<= 6 clusters). Here, proppant allocation is made using the following correlation for i^{th} cluster of any stage:

$$Proppant\ placed_i = \sum_{i=1}^{m} Proportion_i \times Clean\ fluid\ rate \times Proppant\ concentration \quad \text{Eq. 7}$$

Here *m* indicates the total number of clusters in any specific stage. We can visualize fluid uptake by normalizing uptake observed per cluster with assumed uptake for uniform distribution for all clusters in any stage. The results are highlighted in Fig. 75. Note 100% uniformity corresponds to

proppant uptake as predicted based on uniform distribution of proppant across all clusters for specific stages. Thus, the largest deviation among clusters governs the spread in these plots.

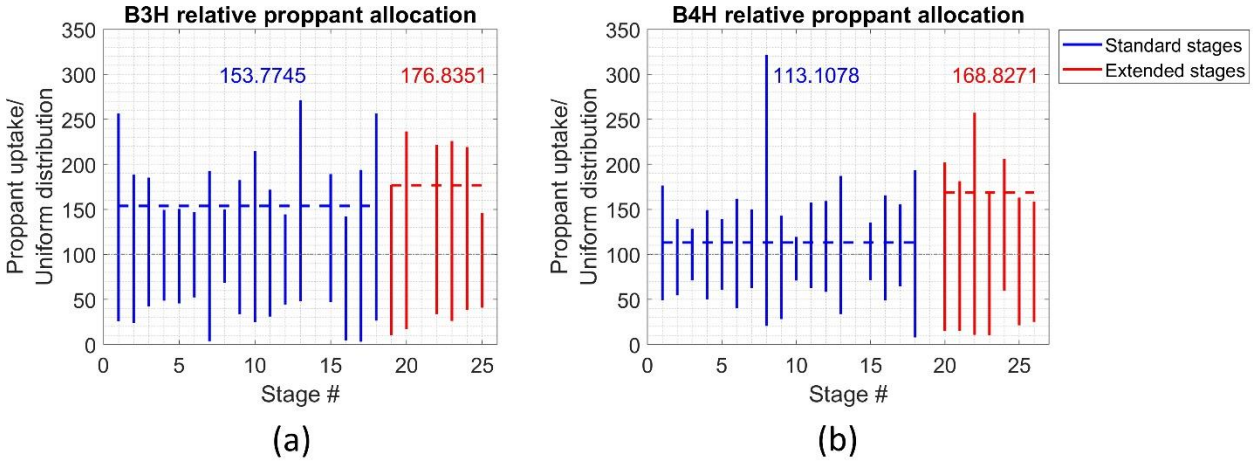

Fig. 75—Min-max spread in proppant distribution across clusters for each stage in (a) B3H and (b) B4H wells. The dotted colored inserts and corresponding values indicate the median uptakes. Note that 100% uniformity indicates that the observed distribution is the same as uniform distribution.

We can observe that the spread in proppant distribution across clusters is much larger for extended stage lengths compared to standard stage lengths. For B3H well, the difference is approximately 13% (177% for extended stage lengths vs. 154% for standard stages) whereas for B4H well, it is almost 33% (169% for extended stage lengths vs. 113% for standard stages). Based on the minimums observed in the proppant allocation spreads for extended stages when compared with the standard stages, B4H distribution suggests that significant clusters may have taken minimal proppant or fluid contributions during fracturing and may have unopened or poorly communicating perforations. This contrasts with the standard stage designs which had 5 or 6 perforations per cluster.

Cluster efficiency as observed from DAS response during hydraulic fracturing, is significantly impacted by the individual perforation efficiency as well as perforation design (i.e., size, spacing, orientation, etc.) . Specifically, more perforations we have per cluster, the higher the observed cluster efficiency is expected to be. This is because more perforations per cluster allows higher likelihood of at least one or a few of the perforations to be open and taking fracturing fluid. On the other hand, fewer perforation shots per cluster increases the likelihood of lower cluster efficiency showing up in our observations given that individual perforation efficiencies can be low. In short, if individual perforations do indeed remain closed and non-communicating, it should show up more strongly in clusters with fewer perforations. This relationship can be studied further in a probabilistic sense. Depending on number of perforations per cluster, n, we can identify the cluster efficiency limit for given perforation efficiency by extrapolating for n. Fluid flow through a cluster will be negligible to zero if all perforations are closed. This is a highly unlikely scenario but provides us with a general boundary value to compare. Defining

efficiency in a probabilistic sense, the probability of single perforation being closed can be calculated easily from observed perforation efficiency as:

$$P(perf.closed) = 1 - perf.efficiency$$

Eq. 8

So, if we have *n* perforations per cluster,

$$P(all\ perfs.closed) = (1 - perf.efficiency)^n$$

Eq. 9

Since a single open perforation in a cluster will provide 100% cluster efficiency. Thus, we have a relationship for cluster efficiency as follows:

$$P(one\ perf.open) = 1 - P(all\ perfs.closed) = 1 - (1 - perf.efficiency)^n$$

Eq. 10

This provides an upper limit for cluster efficiencies for given perforation efficiencies. The lower limit is provided by the perforation efficiency and cluster efficiency equivalence line which is observed if we had a single perforation in each cluster.

For stage level perforation efficiency, we use data from controlled step-down tests conducted during pumping of hydraulic fracturing treatments to estimate perforation friction and likely number of open perforations. On the other hand, cluster efficiency is obtained using hydraulic fracture profiling during pressure pumping based on DAS response. Note that we use a threshold of <2% proppant placed to indicate either very poor or no injection through the entire duration of pumping. This has been validated by visually analyzing waterfall plots of such stages or clusters from our database. Fig. 76 shows two examples of acoustic waterfall plots of stages at the test site. We note that cluster 3 in Stage A and cluster 2 as well as 7 in stage B have < 2% proppant placed and show minimal acoustic response.

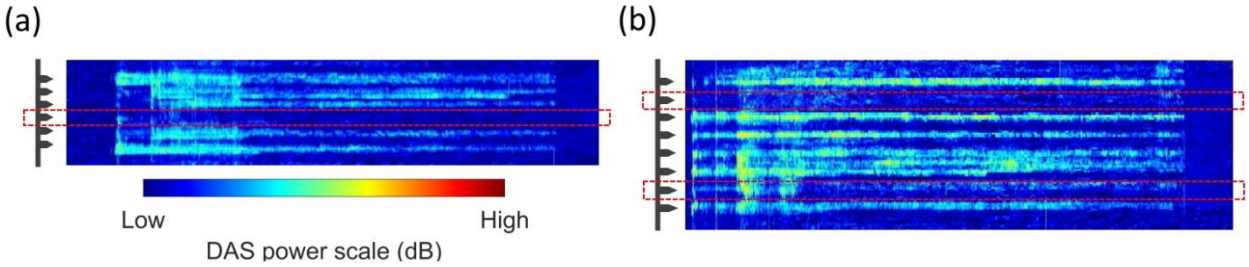

Fig. 76—DAS frequency response spectrum for representative stages, (a) stage A with minimal flow in 3rd cluster and (b) stage B with minimal flow in 2nd and 7th cluster.

Using DAS allocation threshold of 2%, we can calculate estimated cluster efficiency values for various DAS monitored stages at HFTS-2 site. Perforation efficiencies are calculated using step down analysis (Massaras et al., 2007). Various stages for wells B3H and B4H were analyzed to calculate open perforations during pressure pumping. Fig. 77 shows a cross-plot of perforation vs. cluster efficiency for various stages with calculated perforation and cluster efficiency data using the described approach. The plot also shows efficiency relationship cutoff overlays for various cluster designs ranging from n = 1 perforation/ cluster to n = 4 perforations/ cluster.

These overlays highlight the envelop of maximum cluster efficiency mathematically possible for given perforation efficiencies.

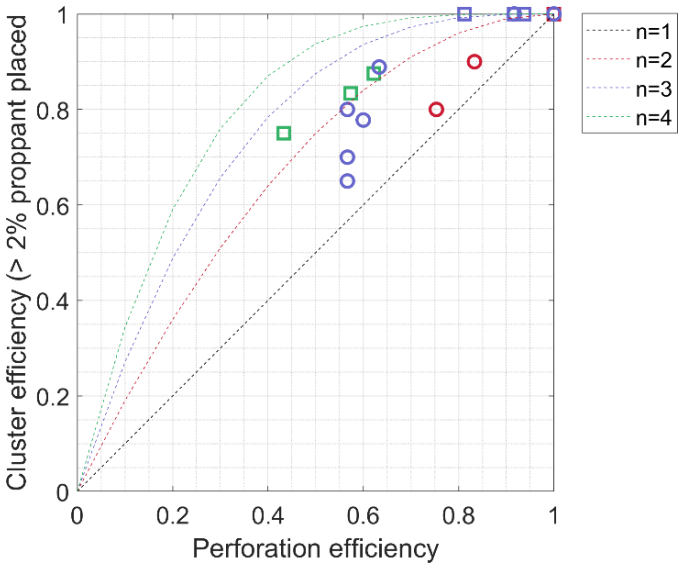

Fig. 77—Perforation efficiency vs. cluster efficiency observations for stages from instrumented HFTS-2 wells. The overlays indicate limits to stage-wise cluster efficiency for given perforation efficiency. Each marker corresponds to data for a specific stage. The marker colors are indicative of the actual perforation count per cluster for a given stage and varies from 1 to 4 as implemented in B3H and B4H wells.

Thus, as expected, we observe cluster efficiency values to be higher than perforation efficiency but also note that a significant proportion of perforations are likely not taking adequate fluid causing reduced perforation-level fracturing efficiency resulting in fewer fractures emanating from the treated wellbore and bypassed zones of rock mass which lack adequate fracture stimulation.

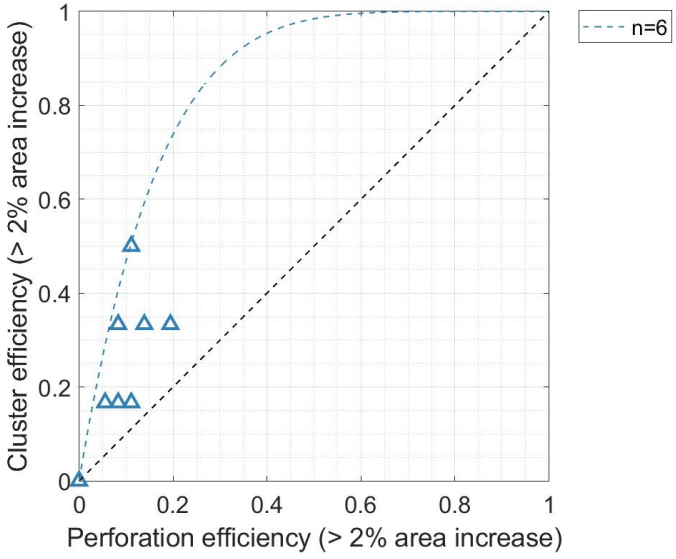

Fig. 78—Perforation efficiency vs. cluster efficiency observations using ultrasonic downhole imaging for stages from HFTS-1 Phase 3 well. The overlay indicates limits to stage-wise cluster efficiency for given perforation efficiency

considering the 6 perforations/ cluster design used in this well. Each marker corresponds to data for specific stages in this well.

As mentioned in the introduction to this study, ultrasonic wellbore imaging can be used to directly measure perforation opening or entry hole diameters (EHD) after fracture stimulation to estimate perforation erosion and therefore, estimate cluster level or perforation efficiencies. Such a study was conducted at HFTS-1 Phase 3 site in Eagleford Shale to log for perforation erosion of a pre-existing producer. Fig. 78 highlights estimated perforation vs. cluster efficiencies for this well. Perforation efficiency is measured as percentage of perforations in a stage that eroded more than 5% in area whereas cluster efficiency is estimated by tabulating the number of clusters in each stage where at least one perforation that eroded more than 5%. Since there was no "before" survey, i.e., perforation profiling before stimulation of this producer, the initial EHD estimates are based on baseline charge specifications and EHD design used during original completions. We note that the general observations still hold true even for this dataset, concretely, cluster efficiencies are higher than perforation efficiencies and fall within the estimated envelop. However, the data, particularly perforation efficiencies, are skewed towards lower values. With downhole ultrasonic imaging, there is a strong underprediction of effective clusters as well as perforation efficiencies because we assume that only increase above the design perforation diameter (increase in perforation area) corresponds to perforation erosion. However, from experience and other studies around variability in entry hole diameters (Snyder et al., 2021), we know that a significant number, if not most perforations have lower entry hole diameters compared to specifications.

Far-field observations

Far field observations from through fracture core sampling have shown clear evidence of significant sections of the rock with reduced hydraulic fracture density vs. other zones. Fig. 79 shows observations from multiple example cores which show hydraulic fractures along cored intervals at three separate test sites in Permian-Midland and in Permian-Delaware Basin from within the Wolfcamp formation (Gale et al., 2018; Gale et al., 2021). We can see that in all the three cases, whether the corresponding stages were high or low cluster spacing designs, significant sections far-field have low hydraulic fracture density. While some of these variations could be geology or stress driven, another factor impacting far-field hydraulic fracture

distribution is reduced perforation efficiency of associated stages for the sections being sampled.

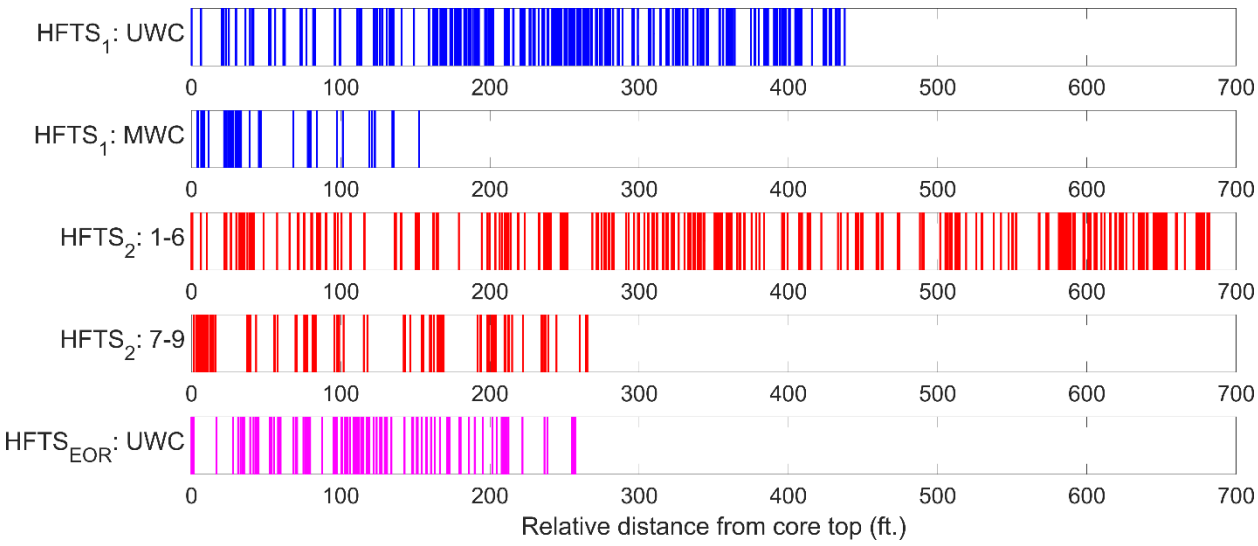

Fig. 79—Observed hydraulic fractures in cored intervals from 3 slant core wells in the Permian Basin. These are the HFTS-1 and HFTS-1 EOR sites in Permian-Midland Basin and HFTS-2 site in Permian-Delaware basin. Note sections with very low fracture density and minimal stimulation vs. other highly fractured sections.

Far-field proppant distribution in child wells when compared to the parent wells also suggests significant non-uniformity in proppant or conductive fracture distribution with significant zone seemingly having reduced connectivity (Maity & Ciezobka 2021b). Studies have also suggested that observed far-field hydraulic fracture distribution is strongly driven by cluster spacing considerations (Maity et al., 2018; Maity & Ciezobka, 2021a; Wu et al., 2021). This is particularly true for conductive fracture zones from one well out to the sampling location at a specific lateral offset. The authors in their previous work (Maity & Ciezobka, 2021a) have demonstrated that observed far-field hydraulic fractures are clustered. Thus, despite the far-field hydraulic fracture count far exceeding the number of stage perforations, the actual number of far-field fracture clusters do follow the number of perforation clusters at the wellbore, especially considering other nearby wells and propagating fracture clusters from those wells. For example, in case of HFTS-1 upper Wolfcamp and middle Wolfcamp cores from Midland Basin, fracture clusters were identified to be separated by approximately 14 ft. to 20 ft. (Maity & Ciezobka 2021a, Maity & Ciezobka 2021c). This can be tied back to the possible hydraulic fractures associated with multiple wells and the average cluster spacing in those wells. More transverse fracture growth would cause more fracture clusters far-field and potentially overlap among clusters as well. While average cluster characteristics are informative, we can clearly observe sections with minimal fracture density vs. other zones with very high hydraulic fracture density as well. Many of the relatively sparse or low-density intervals are associated with clusters which may have poor perforation or cluster efficiencies overall. Thus, significant variability in far-field fracture distribution suggests scope for maximizing or improving far-field fracture coverage by modifying the hydraulic fracture design elements such as cluster spacing, perforations shots per

cluster, advanced perforating strategies such as oriented perforating, modified treatment design, etc., to name a few.

Thus, both near wellbore observations such as friction calculations, DAS response during pumping of stages, Downhole ultrasonic imaging, as well as far-field sampling and observations suggests that perforation efficiencies can be relatively low, particularly where the stimulation program is not specifically designed to optimize perforation level efficiencies. However, these observations are a snapshot in time, specifically when the stages are pumped, and the fractures are created in the reservoir. It is necessary to better understand how these clusters behave over a longer duration as the wells are in production. This is further investigated in the next section by making use of a novel technique applied to the monitoring of unconventional wells using fiberoptic monitoring of low frequency DAS signals (Jin et al., 2021).

Strain change response at clusters during interference tests

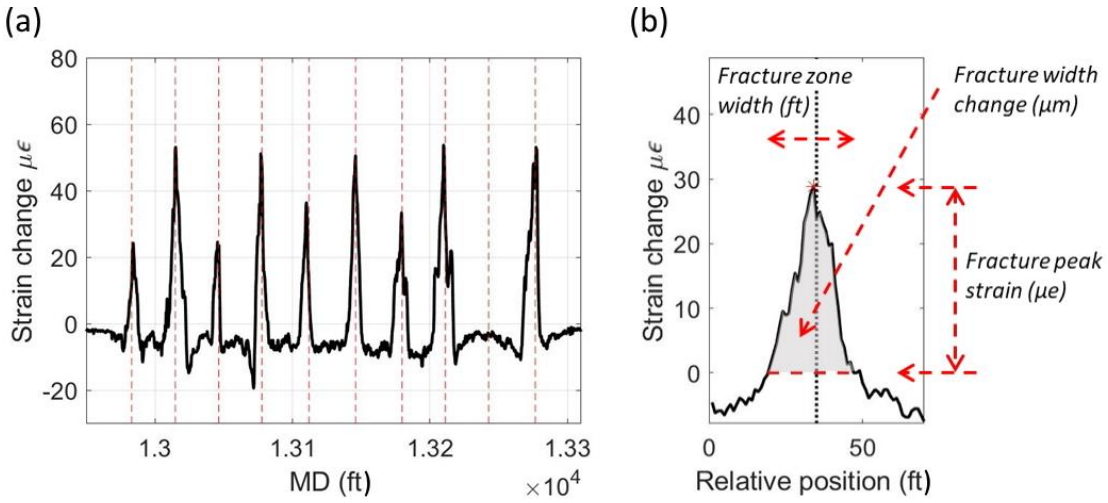

Fig. 80—(a) DSS-RFS results for a specific stage at HFTS-2 site and (b) response for a specific cluster highlighting some attributes of interest (based on Ugueto et al., 2021).

A novel study at the HFTS-2 site in Delaware Basin involved the use of high-resolution distributed strain sensing using Rayleigh frequency shift (DSS-RFS) method (Kishida et al., 2014; Jin et al., 2021). This technique measures Rayleigh frequency shift and inverts the observations for strain change at the fiber by using independent temperature measurements using DTS. It provides very high spatial resolution (0.2 m) and very high strain sensitivity (0.5 με). While a rigorous discussion around the concepts as well as observations from this test is beyond the scope of this paper, we will identify and elaborate on observations from this dataset which will help understand near wellbore connectivity between the formation and the wellbore and how individual clusters are impacted due to depletion. Two separate pressure interference tests were performed approximately 6 months apart and as part of the tests, well B4H was shut-in for an extended period and were subsequently allowed to flow again (Ugueto et al., 2021). With the well instrumented with pressure gauges, both the pressure and corresponding strain response could be monitored during these shut-in and flow periods. The strain response in general showed a very high degree of correlation with the cluster locations indicating a response

associated with the pressurization and de-pressurization of fractures at these clusters (Ugueto et al., 2021). For this study, the two parameters of interest for us are the fracture zone width of the strain response and the peak strain change observed along the cluster of interest (Jin et al., 2021; Ugueto et al., 2021). Fig. 80 shows strain profile associated with a selected stage from the test site and strain attributes as mentioned earlier.

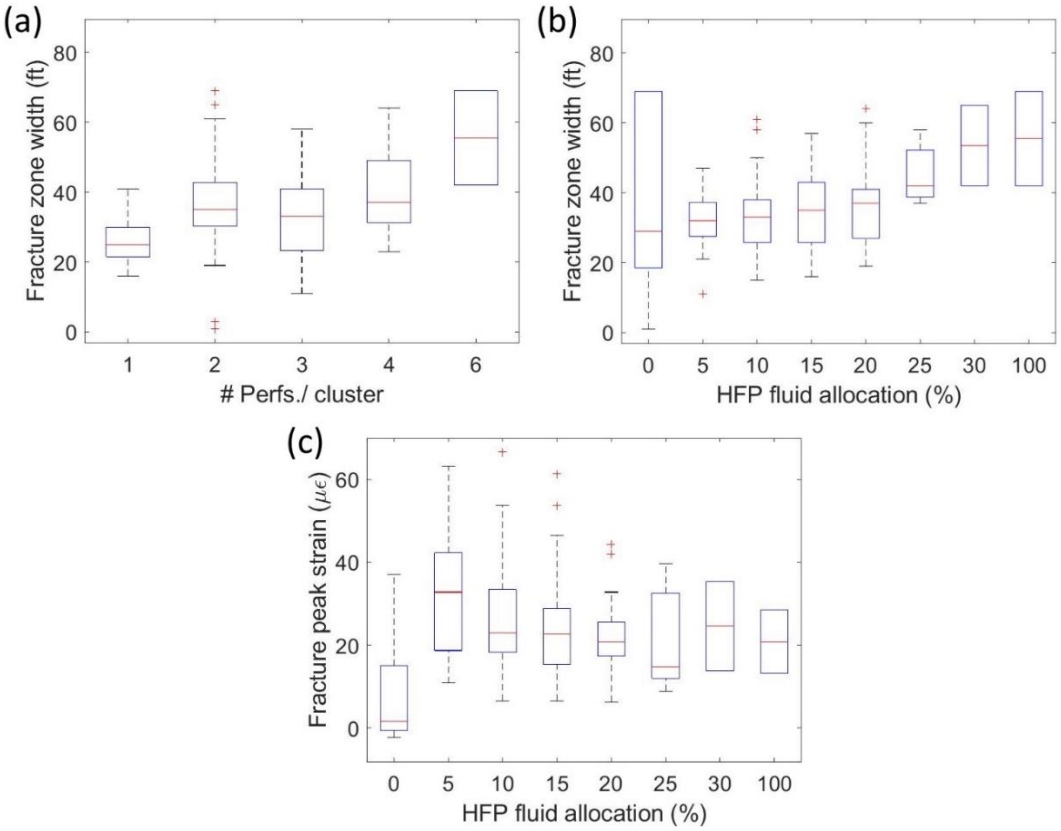

Fig. 81—Derived fracture zone width attribute compared with (a) number of perforations/ cluster and (b) derived fluid allocations from hydraulic fracture profiling using DAS response Eq. 8. In addition, (c) peak strain response is also mapped against derived fluid allocations from DAS profiling and shows an inverse relationship when compared with fracture zone width attribute.

These parameters are governed by the cluster design considerations as well as stimulation effectiveness across said clusters. As an example, Fig. 81 shows the fracture zone width compared with the number of perforations across clusters as well as the fluid uptake observed at these clusters based on DAS fluid allocations discussed earlier. Thus, there is evidence from observations that higher fluid pumped through a specific cluster may create a wider fracture zone due to higher fluid flow throughput associated with said clusters and accompanying erosional effects. Furthermore, as we get clusters with more perforation shots, due to perforation spacing, the fracture zone width gets wider. Consequently, we also observe a

general inverse relationship between peak strain and fracture zone width attributes (Fig. 81b & c).

However, it is important to note that the strain response due to pressurization during shut-in or due to stress release during flow is likely also influenced by the nature of the rock itself. As mentioned earlier, during the DSS-RFS survey, the collected strain response data can be combined with wellbore pressure which acts as a proxy for applied stress within the fracture zones to better understand the stress strain relationship. In addition, changes in temperatures and associated thermal alterations can also influence stress deformation characteristics (Pellet and Selvadurai, 2016). Lab experiments provide ample validation for these correlations (Zhou et al., 2016; Hu et al., 2016). Fig. 82a shows the strain behavior observed at the cluster locations along the monitored fiber for B4H well at HFTS-2 site. It also shows the corresponding pressure build-up behavior during shut-in of the producing well, B4H (red dotted curve). Fig. 82b shows the Stress (pressure) vs. strain observations for various representative clusters at this well. Thus, it is possible to carefully analyze the stress-strain loading-unloading hysteresis characteristics and interpret the observations with respect to variations in fluid saturation levels. This can provide insights into cluster level productivity characteristics during the production phase of the well and potentially provide a temporal productivity response attribute for the clusters. It is important to note that any such analysis aimed towards better understanding of fiber response during production period should also require careful consideration of thermal effects as well.

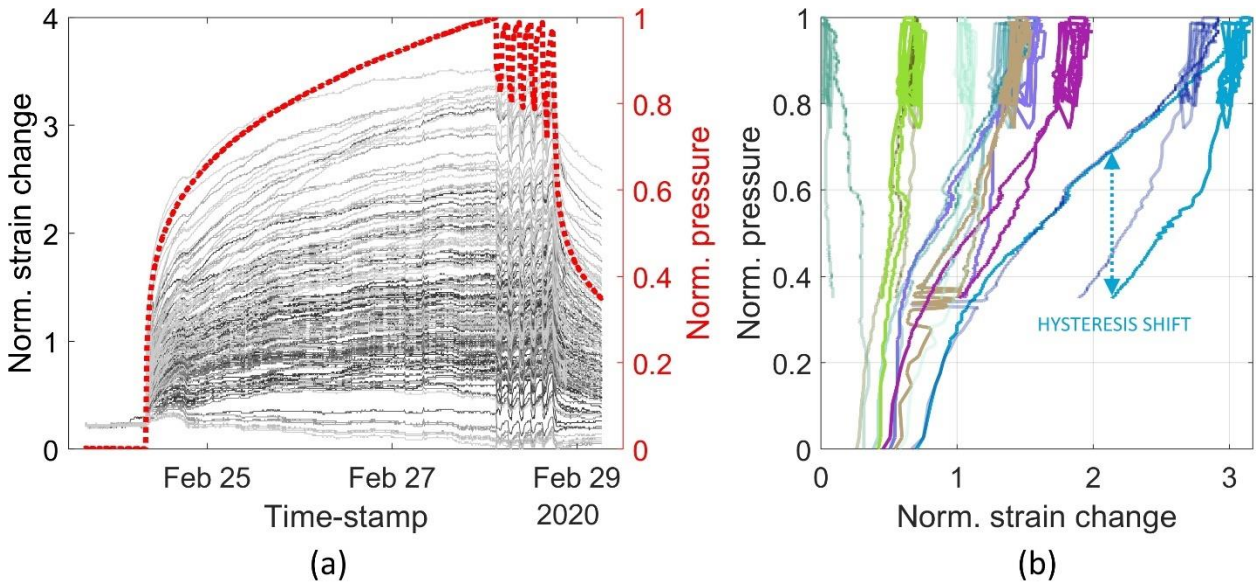

Fig. 82—Strain change behavior observed using DSS-RFS survey across B4H during the first pressure interference test. Subplot (a) shows the strain change across various clusters as well as the wellhead pressure build-up during the test and (b) shows pressure vs. strain response for a few clusters along this well lateral.

To begin with, let us consider this test well and analyze how the stress-strain hysteresis characteristics during shut-in and flow-back periods compares with changes in near-wellbore lithology across this well lateral. To do this systematically, we can calculate hysteresis response attributes that can be used as a proxy for how divergent the hysteresis response is. Fig. 82b highlights one of the ways to accomplish this, i.e., observing the shift in loading vs. unloading

curves at the same reference strain change observed with the fiber. Other options could include calculating area under the loading-unloading curve or maximum pressure, or stress differential observed. In Fig. 83, the normalized hysteresis shift attribute is plotted against normalized observed gamma ray counts from wireline logging run prior to well stimulation. The hysteresis shift parameter was averaged for each stage due to high variance observed in cluster level data. We can clearly see that across most of the lateral, lower hysteresis shifts seem to be associated with higher gamma count zones (clay/ organics or TOC rich) whereas very high hysteresis shifts seem to be associated with low gamma zones towards the heel (carbonate rich). In the section between 14000 ft. and 15000 ft. MD, we see a mismatch in behavior. However, we note that a part of this zone showed significantly lower cluster efficiency levels with reduced stimulation coverage from 14400 ft. to 14750 ft. This likely creates a zone with reduced overall drainage.

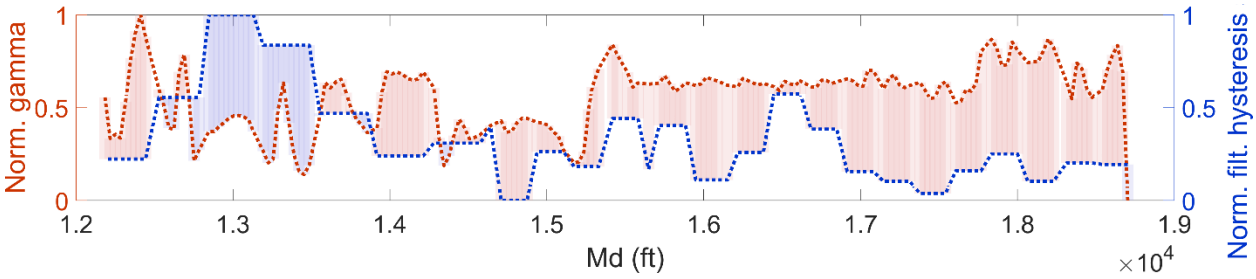

Fig. 83—Normalized hysteresis shift parameter compared with the lithological variability observed through gamma ray log. Strain response attribute has been scaled up to stage level. Note the distinct differences in rock properties between the tail half (clay rich, high gamma counts) vs. heel half (heterogeneous with significantly higher gamma variability) of the well.

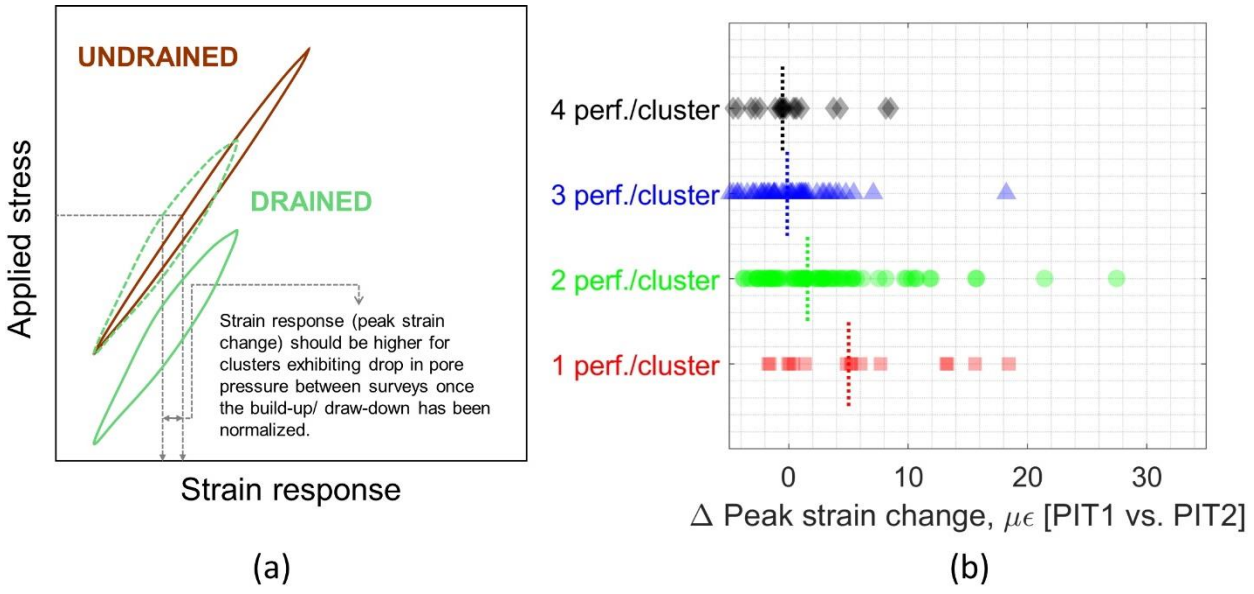

Fig. 84—Subplot (a) shows notional representation of expected strain response behavior due to drainage and associated pore pressure changes and (b) observed differences in peak strain change response over two separate surveys classified by cluster design.

We can also consider the observed strain response between two separate DSS-RFS surveys in time and use the observed differences to interpret cluster level productivity behavior. For example, we have already touched upon the impact of varying fluid saturation levels or pore pressure changes on the stress-strain function. For the sake of discussion, we can discount the impact of other factors, such as thermal effects for now. Since drainage and associated lower pore pressures show smaller strain response for given amount of applied stress (Fig. 84a), clusters that produce the most during any given period should show the largest drop in peak strain response between the two DSS-RFS observations (Ma and Zoback, 2017; Jiang et al., 2018). Since various completion designs were tested (Fig. 74), we can segment our analysis to look at standard and extended stages separately (Fig. 84b). The observations suggest that during this period between the two interference tests when the DAS-RFS surveys were done, clusters with lower perforation counts (extended stages) drained more compared to those with higher perforation counts (standard stages). In addition to changes in the peak strain change between two surveys, a divergent trend is observed in the fracture zone widths as well (Fig. 85). This makes intuitive sense since higher drainage creates a pore pressure gradient, and consequently, a saturation gradient proximal to the hydraulic fractures. The higher relative saturation levels should create higher peak strain values for equivalent applied stress levels.

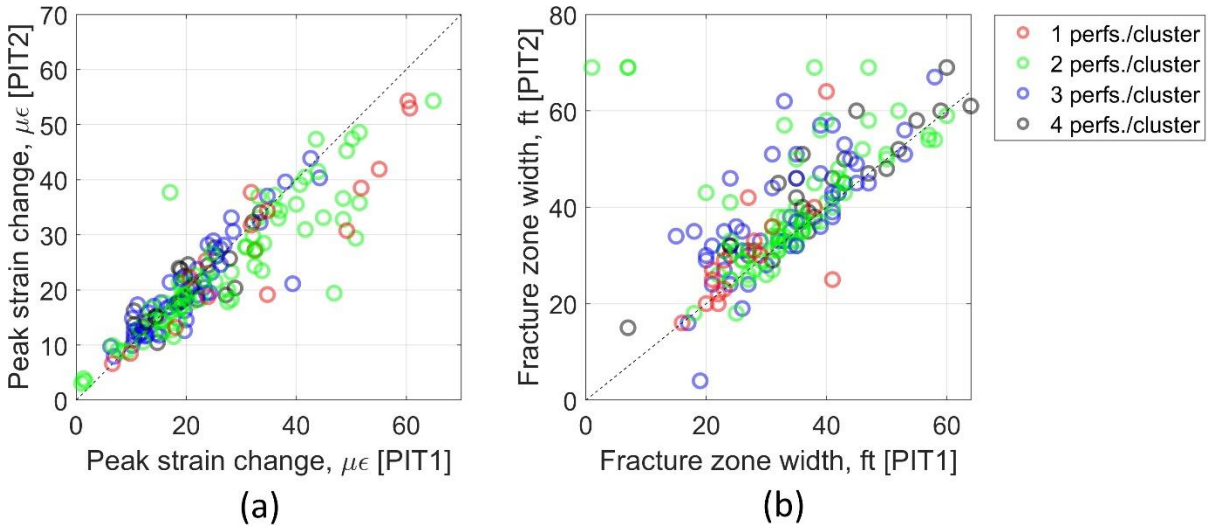

Fig. 85—Comparison of DSS-RFS observations from two separate surveys (PIT1 vs. PIT2) at same pressure build-up with (a) peak strain change and (b) fracture zone width distributions. Note that for many clusters, for same level of stress build-up, peak strain change dropped, and fracture zone width increased.

If we consider sample clusters and observe the strain build-up curves during the first and the second surveys, we can validate the lowering of strain change response through the hysteresis behavior (Fig. 86). Both the higher slopes associated with later build-up as well as larger hysteresis loops indicate substantial drop in saturation and corresponding pore pressure changes in the monitored cluster locations.

If we consider sample clusters and observe the strain build-up curves during the first and the second surveys, we can validate the lowering of strain change response through the hysteresis behavior (Fig. 86). Both the higher slopes associated with later build-up as well as larger

hysteresis loops indicate substantial drop in saturation and corresponding pore pressure changes in the monitored cluster locations.

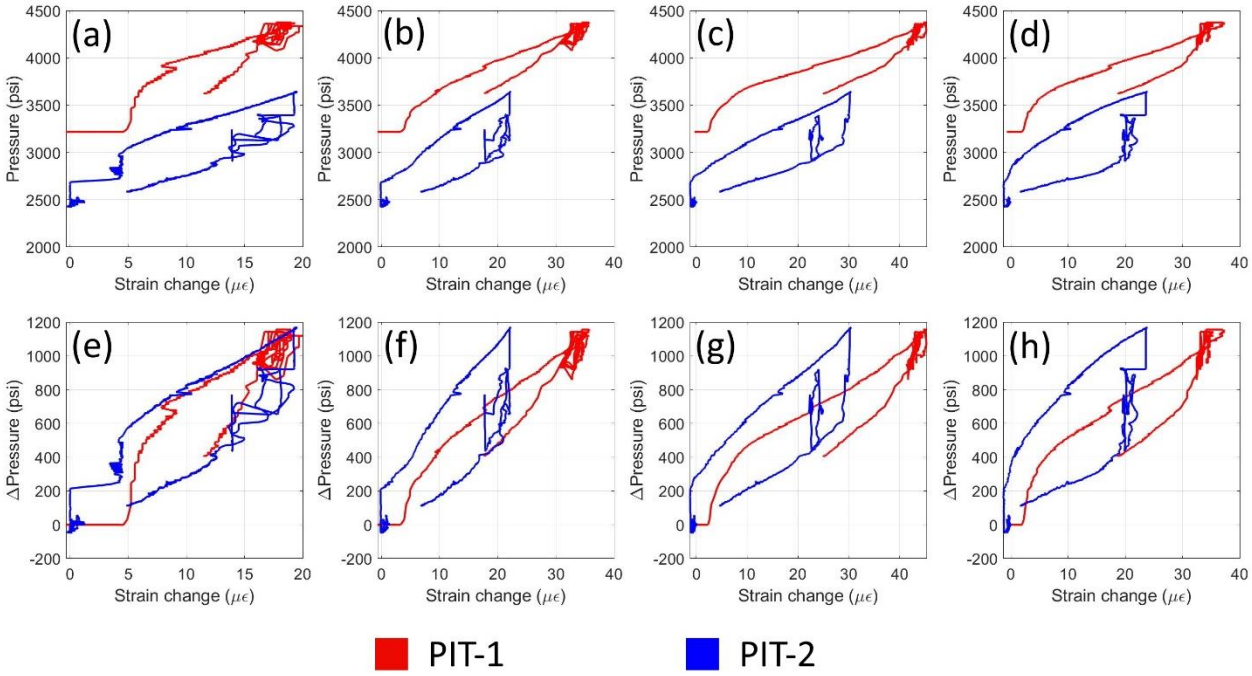

Fig. 86—Example strain build-up observations across two DSS-RFS surveys (red vs. blue) clearly indicating significant drop in pore pressure due to drainage (a, b, c, d) as well as reduced saturations indicated by the increase in hysteresis shifts during strain build-up and draw-down cycles (e, f, g, h) for four example clusters. Note larger slopes at moderate strain build-ups for the second test indicating lower saturations. Subplots (a) and (e) indicate a cluster with minimal changes observed between the two surveys.

Numerical modeling

Simple numerical modeling approaches can be used to validate strain observations from DSS-RFS surveys as well as various interpretations regarding changes in strain behavior due to depletion over given period. Fig. 87 shows an example of such a model and results of stress or strain changes due to changing rock properties (associated with depletion or lowering of pore pressures) or due to varying fracture widths (associated with fluid flow and erosional effects during fracturing). For simplicity, we use a static modeling framework and vary either the properties of the model space or the width of the included fracture at the center of the model space (Fig. 87a) to obtain stress or strain change distributions. The mapping location is at the center of the fiber placed along the edge of the fracture as shown in Fig. 87a.

We understand that rock strength is a direct function of effective stress which is influenced by changes in pore pressure of the rock. The effect of pore pressure change is seen in Fig. 87b. Note that increasing saturation or pore pressure has a direct impact on rock moduli with lower young's Modulus (Lin et al., 2005; Du et al., 2016) and higher Poisson's Ratio (Carcione and Cavallini, 2002; Zhang et al., 2017). Results indicate that decreasing pore pressure would cause a drop in strain response as hypothesized in Fig. 84a, and the data from the site follows this observation (Fig. 86e, f, g & h). In addition, increasing fracture width reduces the peak strain

across the fracture zone (Fig. 87c) and correspondingly, must correlate with higher fluid or proppant transport causing higher erosional effects (Fig. 81).

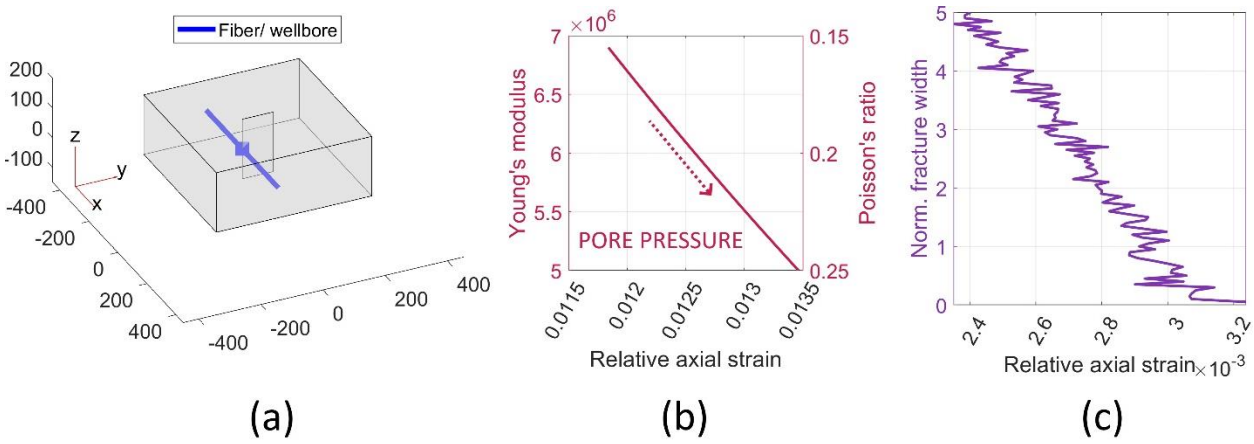

Fig. 87—Numerical modeling results to understand strain behavior due to varying fracture and rock properties. Subplot (a) shows the model space including the instrumented wellbore and fracture or cluster being studied. Subplot (b) shows the impact of varying pore pressure on observed strain at the wellbore and (c) shows the impact of varying fracture width.

Evaluating cluster level drainage characteristics

Thus, apart from the cluster level fluid or proppant uptake estimates from DAS hydraulic fracture profiling which is traditionally used to understand cluster efficiency during fracturing (Richter et al., 2019; Hull et al., 2020), we can potentially use time variant DSS-RFS strain profile shifts to evaluate cluster level productivity at later times. A possible framework for such an analysis is as follows:

1. For a given period during which the clusters are in production, continued drainage should cause a drop in the peak strain change values across said clusters for similar degrees of pressure build-ups. In addition, we can use the change in hysteresis shifts between surveys to predict drainage as well.
2. Since the observations are over a given period, it does not imply that other clusters with lower peak strain change response aren't productive. They may have already produced significantly and moved on to more of a boundary dominated flow condition prior to the first survey. This would cause a significant drop in productivity and consequently, lack of observable changes in the strain response.
3. It is likely a fair assumption that clusters which have taken significant fluid or proppant during fracturing will produce well. At the same time, clusters showing significant drops in peak strain response are likely still producing at the time of the second DSS-RFS

survey. Thus, clusters which fall outside of these two criteria are prime candidates for zones with poor primary stimulation response.

4. Alternatively, if we acquire the first DSS-RFS survey right after bringing the well into production, we will not have to use DAS derived allocations as a proxy measure of initial cluster productivity.

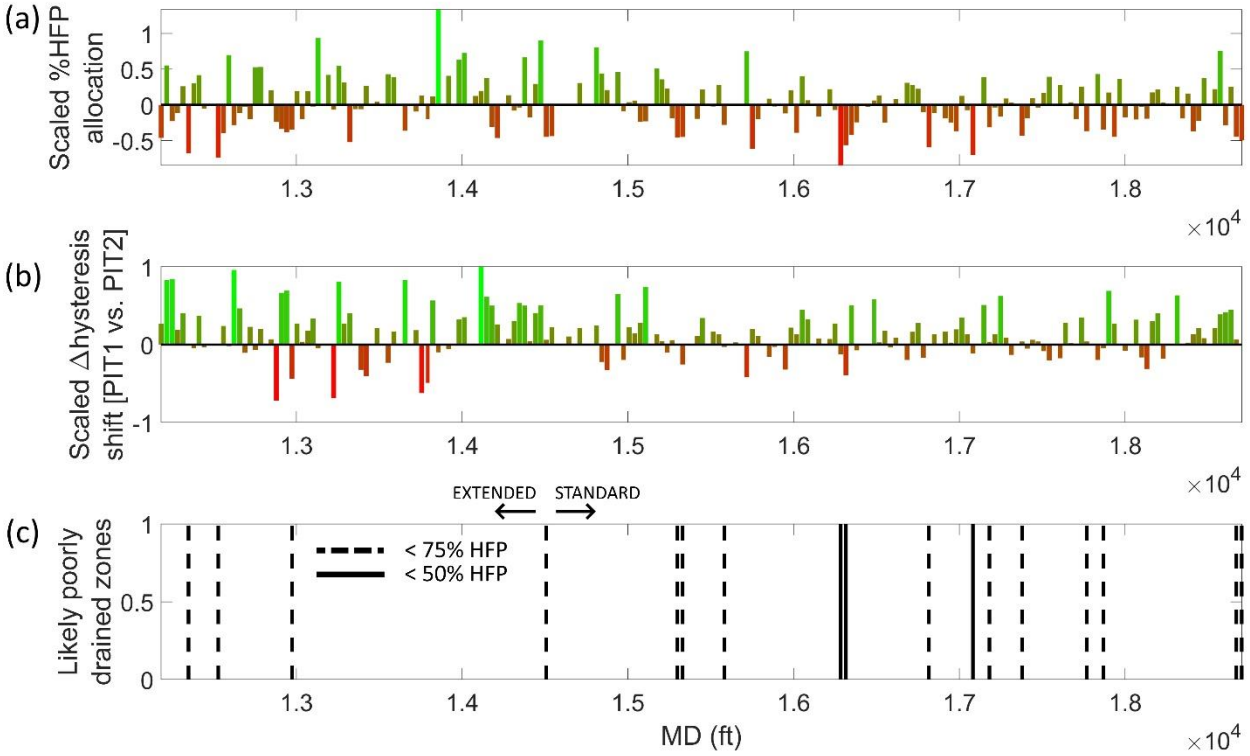

Fig. 88— (a) DAS derived fluid allocation attribute and (b) DSS-RFS derived attribute indicative of poorly drained zones and (c) identified likely poorly drained clusters based on defined thresholds for the two attributes (< 50% HFP or < 75% HFP and ≤ 0 hysteresis shift).

Fig. 88 shows two primary attributes from the above framework, namely the scaled fluid allocations from DAS survey during fracturing and the peak strain change difference between the two DSS-RFS surveys. It also highlights clusters which can be classified as likely poorly drained based on values of these two attributes. Specifically, if the fluid allocations are below either 50% (solid) or 75% (dotted) of uniform distribution levels and if the hysteresis shift is zero or negative, the clusters are classified as poorly drained. As already highlighted, this framework makes significant assumptions by discarding the impact of other relevant factors such as impact of varying temperatures on the fiber response.

Conclusions

This case study used data and observations from HFTS-2 test site in Delaware Basin to evaluate and interpret near wellbore connectivity post fracturing using perforation as well as cluster level efficiencies. In addition, new fiberoptics based diagnostic technique was used to understand longer term cluster level productivity. Analysis of perforation efficiency and correlation with observed cluster efficiencies from DAS analysis during pressure pumping provides ample

evidence that the two are strongly correlated. Thus, high cluster efficiencies do not necessarily indicate correspondingly high perforation efficiencies. Since far field through-fracture sampling have shown a good degree of correlation between fracture distribution and perforation efficiencies, we believe perforation efficiencies, rather than cluster level efficiencies, to be a key parameter for effective well stimulation, particularly as we have more perforations in individual clusters.

In addition, in this case study, we used DSS-RFS survey data from two pressure interference tests to understand drainage characteristics across clusters in the instrumented well. Specifically, the strain response during pressure build-up and subsequent drawdown can be interpreted to understand the drainage characteristics at those clusters which are influenced by the fluid saturations and pore pressure changes. While the complex interplay between strain response in fractures with rock properties, thermal characteristics, etc. imply that inversion for useful information, such as cluster level drainage or productivity is a complex undertaking which will require robust forward modeling workflow and inversion techniques in future.

In-fill Well Proppant Log Study

Authors: Debotyam Maity & Jordan Ciezobka

Summary

During the development of an unconventional play, wells are drilled and completed in batches and depending on the development plans, current and expected energy market trends, as well as other developmental considerations, new wells are drilled and hydraulically fractured later near existing producing laterals. This creates challenges in terms of optimizing resource recovery and reducing inter-well communication. A novel approach is proposed which utilizes systematic composite sampling and analysis of drilling mud returns to look for and quantitatively identify sand particles. The workflow involves cleaning, drying, and segregation of samples into sizes of interest to us (size distribution of pumped proppant in offset parent wells). These samples are imaged at very high resolution and analyzed for grains using characteristic optical imaging properties to classify proppant sand particles using computer vision algorithms. Further analysis, such as elemental compositional analysis is used to validate the results from imaging workflow. We present a case study from the Permian Basin where a new child well was used as a test case to prove this technology at the Hydraulic Fracturing Test Site (HFTS-2) in Delaware Basin. We introduce new proppant parameters that help identify sustained proppant zones vs. localized propped fractures. We have used additional diagnostics and data collected at the test site to validate observations from the proppant log and have successfully interpreted significantly propped vs. unpropped zones. A key finding from this test has been the significant proppant transport distances observed away from parent wells. Observable proppant was found at a lateral distance of approximately 1400 ft for one set of parent wells and more than 3000 ft for another set of parent wells. While a major limitation of this technique is the sampling rate, given adequate sampling, the proposed technology represents a systematic and one-of-a-kind interpretation of spatial proppant distribution while drilling in-fill wells. It provides us with unique opportunities to better understand the current state of the reservoir being targeted including zones which are likely highly drained relative to others and how the planned hydraulic fracturing of child wells can be improved.

Introduction

Hydraulic fracture stimulation involves pumping large quantities of sand to prevent these fractures from collapsing back once pumping has ceased during the flow back or production phase. Fracturing effectiveness is a key contributor to the overall stage and eventually, well productivity. The aim is to uniformly propagate, and prop-open hydraulic fractures along the horizontal wellbore to limit run-away fractures. This helps improve productivity of individual stages but at the same time, also limits issues associated with inter-well fracture driven interactions. Better understanding of the distribution of hydraulic fractures, and more importantly propped fractures, can be very useful for completion diagnostics. It can help understand and optimize fracturing designs (Bartko et al. 2013; Perfetto et al. 2013) and calibrate fracture models as well (Offenberger et al. 2013). When it comes to the underlying question of directly or indirectly evaluating fractures, proppant transport and proppant distribution, various techniques have been proposed or used. Some applications are geared

towards near wellbore surveillance. Acoustic imaging tools can directly map fractures and their properties can be used to predict presence of hydraulic fractures when logging in-fill wells (Craig et al. 2021). Another approach to directly map near-well proppant placement is the use of proppant tracers and logging at far-field in-fill well locations using pulsed or compensated neutron tools to identify proppant (King and Leonard 2011; Liu et al. 2015; Zhao et al. 2019). While this technique is promising, it is primarily limited to understanding near-wellbore proppant placement and cluster efficiencies and not far-field. This is due to typically small amounts of traceable proppant in the mix pumped during fracturing. Far-field techniques to map hydraulic fractures include use of microseismic (Maxwell and Cipolla 2011; Warpinski et al. 2013), distributed strain sensing using fiberoptics (Bourne et al. 2021), or techniques using electromagnetics where coated ceramic particles are pumped during fracturing (Palisch et al. 2017), etc. to name a few. Logging while drilling (LWD) techniques have also been used or proposed in the past. LWD ultrasonic imaging techniques can help identify induced fractures for subsequent optimization (Amorocho and Langford 2020). Finally, surface sampling and analysis from the rig site has also been proposed for advanced gas and elemental analysis to identify fractures (Chiniwala et al. 2018).

Attempts towards better understanding of subsurface proppant concentration within the stimulated zone using through fracture core sampling has been successfully demonstrated in the past (Maity and Ciezobka 2019a, b). Once a long horizontal well has been hydraulically fractured, a new core well can be drilled in proximity of the original well to sample the created fracture systems. Subsequently, samples collected from the core barrels as well as from the surface of the cores and fractures can be systematically analyzed for proppant or sand particles. The genesis of the proppant log concept is essentially an extension of the proppant analysis work that was done as part of the Hydraulic Fracturing Test Site (HFTS-1) in the Permian-Midland Basin. This first of its kind study was to test the application of proppant log technique on mud return samples. With core samples, the sampling process can be controlled since the process is well established regarding sampling protocols. However, the challenge of scaling up from core samples to drilling mud-returns is significant since with mud returns, factors such as sampling protocols, sampling frequency or log resolution, and improved verification techniques are key in obtaining accurate logging results and interpreting those results. For example, mud additives such as barites can have a significant influence over the results and verification techniques need to be expanded to maintain applicability. With this study, we not only attempt to provide the best possible answers to some of these relevant questions but also provide results to validate the applicability of this technique under field conditions. In this study, we utilized drilling mud return samples for a new child well in proximity of a pre-existing parent well at the HFTS-2 site in Permian-Delaware Basin. This in-fill child well was part of operator's standard development plans and not drilled specifically under HFTS-2 program. The motivation was to validate the concept of proppant log and its applicability using a real world in-fill well as an example. This methodology can be applied to any in-fill well with additional benefits of having minimal surface footprint, equipment needs, and personnel training requirements. Given that in-fill drilling is now an often-used approach by the industry to maximize resource recovery, this technique can be applied for all such wells of opportunity to gain useful insights around

original completions, existing fracture network and ways to optimize completion of these new in-fill wells.

Test Site

HFTS-2 is a large collaborative field-based research program in the Permian Delaware Basin (Ciezobka 2021). The test program involved eight new producing wells and two existing parent wells with two science wells drilled specifically to sample and characterize the subsurface. Coring program involved more than 540 ft of vertical core through a pilot hole and approximately 950 ft of through fracture core along a slant core-through well. The test area already had pre-existing producing laterals (BR1H and BR2H drilled southwards; TR5H, TR6H, TR7H and TR8H drilled northwards) and one of the new wells being drilled as part of the test program (B2H) acted as the child well which was logged during drilling (Fig. 89). In terms of lateral length, the parent wells are much shorter than the new in-fill wells and provide a great opportunity to carry out controlled testing of the proppant log technique. The distance of the new lateral with respect to the pre-existing laterals is approximately 275 ft above and 690 ft to the west of well BR1H and approximately 150 ft below and approximately 1400 ft to the west of well BR2H. These parent wells were standard sand completions with 20 to 22 fracture stages and approximately 200 ft inter-stage separation. These were plug and perf slickwater completions (Zakhour et al. 2021). Each stage typically had 6 clusters and mesh 100 sand was exclusively pumped as part of the stimulation.

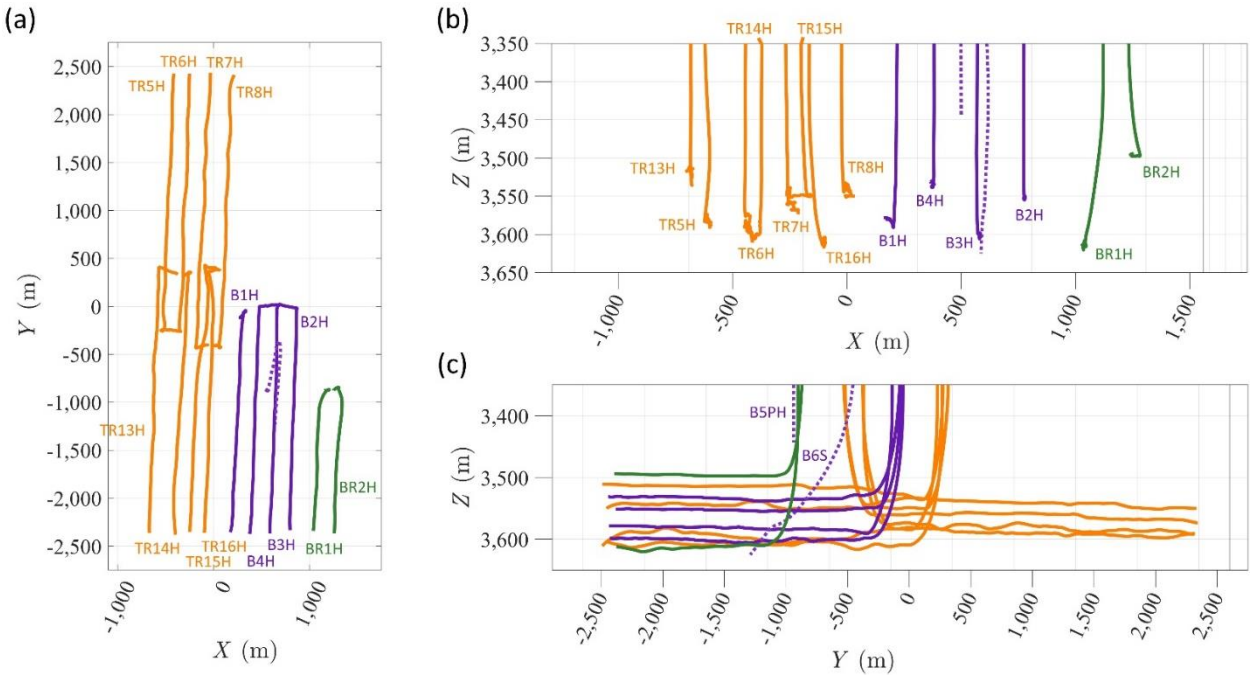

Fig. 89—HFTS-2 site wells shown as (a) top view, (b) gun-barrel view, and (c) side view. Horizontal well B2H acted as the child well and wells BR1H/ BR2H to the east of the new pad and TR7H/ TR8H to the west were the parent laterals with expected impact on new drill B2H well. B5PH was the pilot hole drilled at the test site and well B6S was a slant core through well drilled to sample fractures proximal to well B3H.

In addition to the significant core analysis and fracture characterization work from core samples collected along B5PH pilot well and B6S slant well, the project installed permanent fiber optic cables in 3 wells to monitor near wellbore signals during fracturing and to collect cross-well strain measurements as well as for production monitoring (Jin et al. 2021). These include two fibers along the B3H and B4H laterals and along vertical B5PH pilot hole. Permanent pressure and temperature gauges were placed at the heel and toe of both B3H and B4H laterals. Furthermore, pressure and temperature gauges were placed in the B5PH well to monitor pressure drawdown during production. Additional advanced diagnostics included a significant formation evaluation program on the vertical whole core (Zhao et al. 2021), multiple petrophysical logs in horizontal wells, multi-array moment tensor inversion capable microseismic survey (Grechka et al. 2021), multi-well time-lapse geochemistry analysis, among others. We will reference observations from some of these diagnostics to interpret and validate observations from the proppant log run for the B2H horizontal well.

Applied Methods

Detailed methodology has been shared by the authors in prior articles (Maity and Ciezobka 2019a, b). In this section, we provide an outline of the sampling methodologies that can potentially be used at drill sites as well as a broad overview of the analysis technique and workflow we follow to generate a proppant log. Specifically, modifications made to the analysis technique to work with smaller particles such as mesh 100 which are now routinely pumped in modern fracturing treatments will be discussed. During the drilling process, mud returns are fed through a shale shaker for solids control. Cuttings of various sizes are removed, and the screened mud is returned to the pits for re-use (Fig. 90).

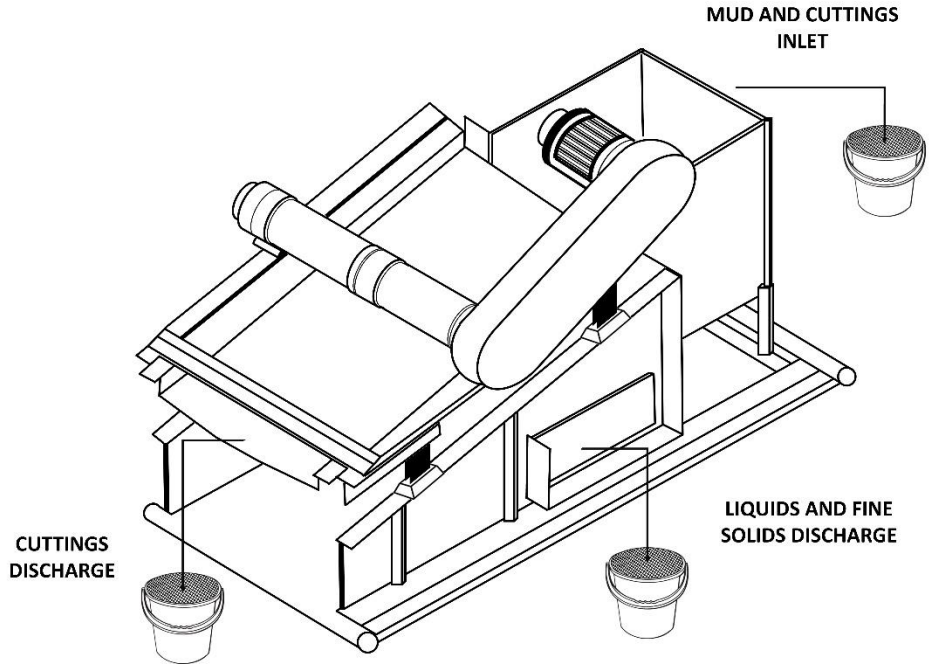

Fig. 90—Potential sample collection points at the shale shaker.

Sampling

As the mud returns are processed through the shaker at the rig site, samples can be collected at various points such as from the possum belly as a slip stream, the mud stream as it flows through the screens on to the catch pan, or at the cuttings discharge (Fig. 90). The material can be collected in a bucket and a screen may be used to eliminate larger materials that we are not interested in. The samples can be composite, i.e., material is collected over a depth interval (drilling duration) in these sampling buckets and then a small amount is transferred in tagged jars. Alternatively, the samples can be spot, i.e., the material is collected at specific drilling depths in tagged jars directly from the slip streams. Both composite and spot sampling approaches have been tested and found to work in field conditions. Fig. 90 shows a schematic of a shaker set-up and potential locations of sampling as described.

Authors have previously discussed sample preparation protocols in detail for material collected from cores (Maity et al. 2018). A similar approach is used to prepare and image the drilling mud return samples as well. Samples are washed in soap solution and continuous agitation to remove residual oil and mud on a mesh 200 screen. The screen size used depends on the particles of interest and mesh 200 screen is considered adequate for proppant or sand particles in the mesh 100 or mesh 40-70 category. A larger screen (mesh 20) is used to remove larger particles in the samples, if any. The washed samples are dried in an industrial oven and weighed for cataloging. The material is then sub-sampled for imaging and analysis. Each sub-sample to be imaged is weighed separately to normalize identified proppant distribution with respect to weight and the material is imaged at very high resolutions (≥ 4,800 dpi) using bench scale tools to provide scans that can be further processed to detect sand particles which are of interest to us. Unlike the earlier studies with core samples, this increase in imaging resolution is useful since it allows classification of proppant and proppant-like particles as small as 60 microns (≤ mesh 200). As will be discussed later, the lower threshold of 60 microns is needed since pumped sand at the correct size specification still have significant quantities of smaller tail end fractions.

Apart from the actual samples, relevant baseline samples are also analyzed to make sure that results can be qualified based on other chemicals that may be added to the mud stream. As an example, Barite ($BaSO_4$) is pumped as a mud additive during drilling as a weighting agent, but it does show optical characteristics like silica (SiO_2) particles making any interpretation difficult. Thus, baseline barite pumped needs to be optically as well as chemically analyzed to be able to identify and correct for these particles in actual drilling mud return samples since our interest is primarily in proppant particles. For accurate identification and correction, we use chemical compositional analysis (energy dispersive spectroscopy) technique with a scanning electron microscope as will be discussed later.

Proppant Detection

Once the high-resolution sample images have been captured, they are run through a classification algorithm to identify all “proppant” and “proppant-like” particles from each sub-sample. Since the approach is based on imaging, the resolution limits the size of particles that can be accurately identified. Mesh 100 particles, which are of interest to us, can range from

mesh 70 to mesh 140 screen sizes, i.e., approximately 200 microns to 100 microns. If larger size sand was pumped in the original completions of the parent wells, the size range we are looking for is appropriately larger. The first step is to identify distinct particles in the images. Since most of the particles are round or elliptical in shape, we can use Hough transform to detect them (Rizon et al. 2005). Then specific "proppant-like" characteristics, or properties are computed and used by the algorithm which include roundness, translucence, hue, size, entropy, darkness, etc. Detailed methodology has been shared by the authors in prior articles (Maity and Ciezobka 2019a, b).

While the imaging workflow provides an estimate of proppant count, there are additional ways in which we validate and interpret the results. Apart from the actual proppant particle counts, we are also identifying and tabulating the number of other mineral particles which have proppant like characteristics. Past proppant log studies at the core scale as well as synthetic sampling (where proppant is mixed with calcite in laboratory setting) have shown the relative distribution of proppant particles when compared to other minerals as identified by this workflow is a strong indicator of presence of proppant particles. Mathematically, this is calculated by taking the ratio of the identified proppant counts to other mineral counts for i^{th} sample in question as shown in Eq. 5. Another relevant parameter of interest is the relative abundance of larger particles in specific size fractions within the samples. For mesh 100 sand particles pumped during fracturing, the expected size range is 105 microns to 210 microns. For our samples, the imaging workflow provides an overall particle size distribution based on each identified proppant particle by binning at different size intervals. Assuming a bin size of 25 microns, the total number of particles in each bin can be separately tabulated and relative abundance of larger particles can be calculated as per Eq. 6.

This relationship, specifically, which bins to use, will depend on the size distribution of particles pumped and later observed during the in-fill logging process. The imaging workflow used in the proppant log analysis as highlighted in Fig. 91 works best for particles larger than 100 microns and for this reason, we look at size distributions higher than 100 microns size cutoff. Larger particles identified as proppant have a lower degree of uncertainty associated with their classification. In the same vein, particles classified as proppant have a much lower degree of uncertainty associated with their classification when compared to other mineral particles. Thus, these two parameters, α and β, are very useful in identifying zones with significant proppant or identifying sudden onset of propped zones in high resolution sampling. Trivially, we look for actual proppant counts in conjunction with the α and β parameters. Low proppant counts but high α, β values are indication of presence of significant proppant. However low α, β values positively identify zones without significant proppant. The true strength of such integrated interpretation can be observed when we have much higher sampling resolution (< 25 ft) and is beyond the scope of this case study.

The actual proppant counts also need to be corrected in case there is a significant misclassification of proppant particles due to mud system additives use, sample collection or preparation biases, or larger lateral separation from parent wells. To accurately classify proppant particles, particularly at these lower size ranges, it becomes necessary to utilize compositional

analysis tools to adjust or validate the results from imaging analysis, as is highlighted in the workflow (Fig. 91).

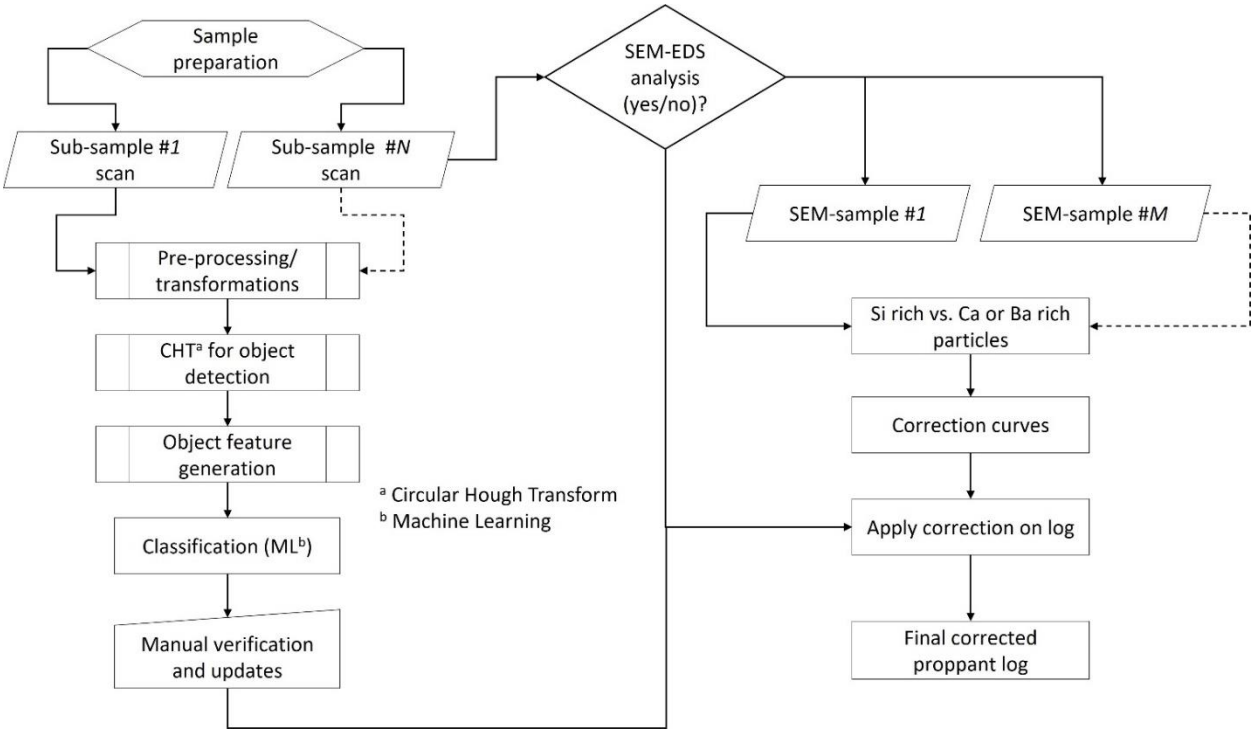

Fig. 91—Proppant analysis workflow used post the sample preparation phase including SEM analysis to correct proppant log based on compositional analysis.

SEM EDS Analysis

For quality control, scanning electron microscopy with energy dispersive spectroscopy (SEM-EDS) technique is incorporated to accurately discriminate actual proppant from other proppant-like particles such as calcites and sulphates. This technique has been routinely used for soil or mud analysis in the past (Liu et al. 2015). Our baselining tests with proppant as well as mineral cements from subsurface samples show that the imaging workflow can sometimes find it hard to sort proppant from other minerals which have similar optical characteristics such as translucence, hue, etc. This is particularly the case when the particles are very small (≤ 100 microns). While we would typically not expect mesh 100 sand particles to fall in such a small size range, actual samples from field suggest that a significant distribution of mesh 100 sand falls in this smaller size range and can go as small as 60 microns. One contributing factor could be relatively large lateral offsets of 100's to 1000's of feet from the clusters which could cause more fines to be sampled. Another factor is proppant crushing which can create particles size distributions in these smaller ranges. This tends to cause systematic over-prediction or under-prediction of particles. Thus, SEM-EDS analysis is applied on selected samples to cover examples with low to high proppant counts. The result from this analysis provides us with an accurate distribution of proppant versus other mineral particles in the samples and is useful in making our interpretations more robust and quantitative. The correction is done by identifying an

applicable correction factor from the controlled SEM results and implementing the correction on rest of the dataset.

Specifically, samples are carefully selected based on relative proppant distributions as well as absolute proppant counts to get a wide range of possible data points for the correction curves. For example, we can select samples with high and low proppant counts as well as high and low relative proppant distribution vs. other minerals to provide us with enough data points for our correction curve. We have observed a positive correlation between relative distribution of proppant in our optical analysis vs. results from SEM-EDS analysis.

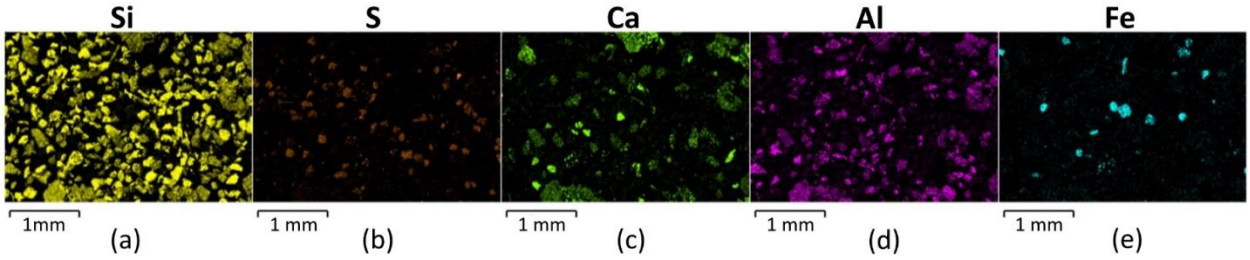

Fig. 92—SEM-EDS results for a typical sample showing particles being (a) Silicon rich, (b) Barium or Sulfur rich, (c) Calcium rich, (d) Aluminum, and € Iron rich. Silicon rich particles indicate sand, sulfur rich are Barite from either the mud system or from within the formation. Calcium rich particles indicate calcites, likely from within the formation.

Energy dispersive spectroscopy (EDS) analysis involves preparing a sample pedestal with a small amount of sample to be analyzed. Actual imaging involves high resolution SEM followed by use of an EDS detector to get a surface or near-surface chemical composition depending on the scanning voltage being used. Fig. 92 shows an example SEM scan results panel with various mineral identifications and their interpretation for the verification process. Silica rich particles are indicative of sand whereas Calcium or Barium rich particles indicate Calcites or Barites which could be from mud systems or from the formation itself. Composition curves from EDS mapping can be used to predict relative abundance of silica or proppant sand vs. other minerals. Fig. 93 shows the relative abundance of proppant particles for carefully selected samples from this dataset. This is further used to obtain a regression curve for application on the entire dataset so that the results from optical imaging can be corrected for any observed high or low counting biases in the analysis.

Once the proppant counts have been corrected using the SEM-EDS workflow, it is useful to do a material balance test to see if the identified particle counts are realistic and within the expected range based on the total sample weight being analyzed. Specifically, we cannot have more particles than what would be possible given the total sample weight being analyzed. Since total dried sampled weights are tabulated, the normalized proppant or mineral counts (i.e., number of proppant particles or other mineral particles per gram of sample) can be scaled up as per the

total sample weight. A cross-plot of total proppant-like particle identified vs. sample weight indicates a strong positive correlation between the two (Fig. 94).

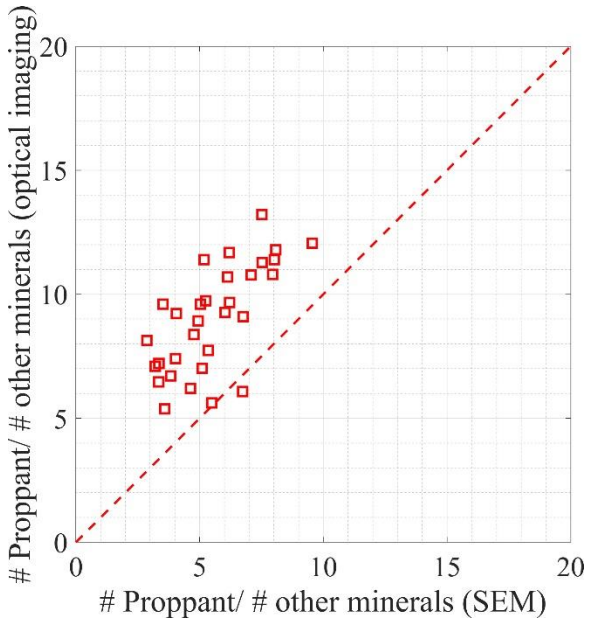

Fig. 93—Relative proppant distribution vs. other minerals such as calcites or sulfates from optical imaging analysis vs. SEM-EDS analysis for selected samples. Note that despite the distribution not following 1:1 trend line, we see a strong positive correlation in the data subset which provides us with a correction curve through regression analysis to update proppant counts across the entire dataset. Such correction also resolves overprediction of particles from workflow.

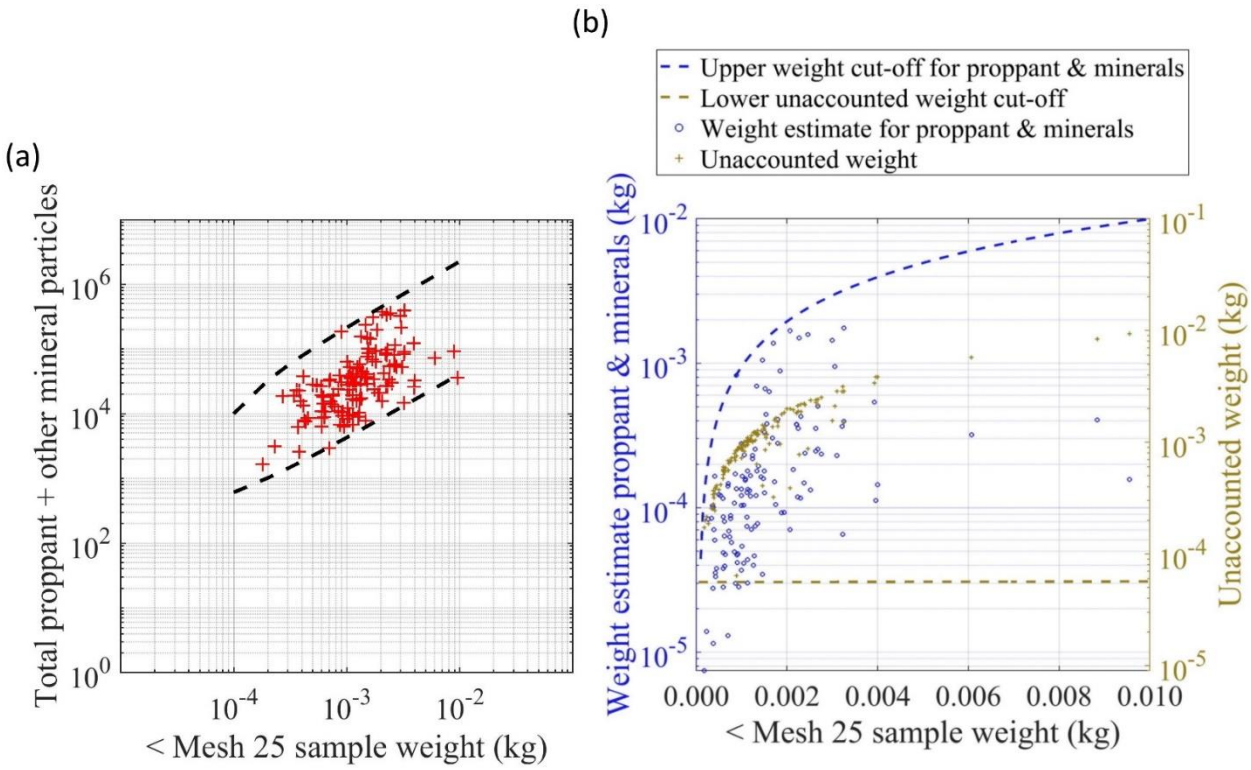

Fig. 94—Tallying proppant log results with sample weights. (a) shows the actual identified particles along with distribution envelop (top and bottom dotted inserts). The upper envelope is used in (b) to calculate estimate of proppant and other mineral weights as an upper limit which is cross-checked with total sample weight to estimate the lower limit of unaccounted weight to make sure we are not overestimating proppant particles.

If we assume average particle size of 150 microns based on observed results for this dataset and a particle density of 2.5 g/cc, we can estimate the approximate mass of proppant and proppant like mineral particles for a given upper limit using the cutoff shown by the top insert in Fig. 94a. Negative unaccounted weight would indicate a severe overestimation of particles. From Fig. 94b the unaccounted weight remains positive for upper envelop cut-off and the actual unaccounted weight indicates presence of other material in the samples, such as shale particles.

Observations

As discussed in the introduction, well B2H was logged for proppant at pre-selected depths to identify zones with significant sand concentrations along the well. Two sampling rates were tested for this case study. Initial samples were captured at a rate of one sample every 30 ft. After the first three hundred meters of measured depth (*MD*), the sampling rate was increased to one sample every 90 ft. The sampling rates as well as the identified proppant counts (# proppant particles in sample) are shown in Fig. 95 for reference. We note that the proppant counts (i.e., # proppant particles) for the log are calculated as normalized with respect to the total sample weight imaged and analyzed so that we have counts normalized per kilogram of sample at any logged location. Simply put, normalization is achieved by dividing the number of identified proppant particles in the imaged subsample by the weight of the imaged subsample. Also note that the notional positioning of the nearby parent laterals BR1H/ BR2H as well as TR7H/ TR8H has been highlighted for context. We do observe a widely varying proppant distribution across

the logged lateral. However, at first glance, it appears that the toe end of the child well has significant proppant particles when compared to the rest of the well. In addition, the segments overlapping the expected perturbed zones associated with the pre-existing wells does indicate higher proppant counts compared to the nearby un-perturbed segments.

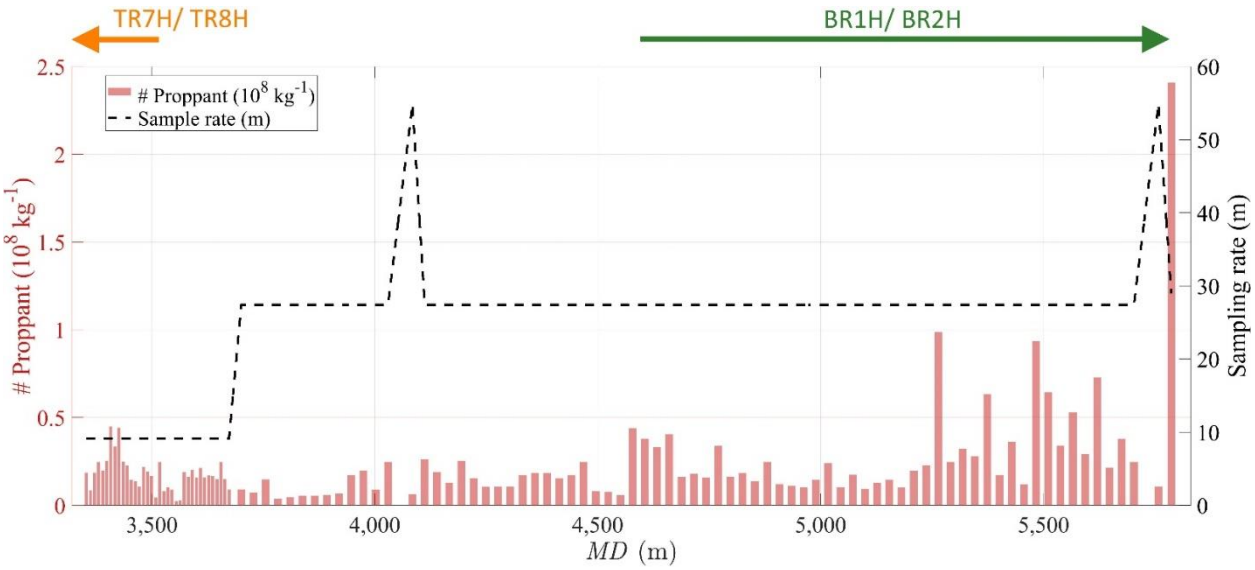

Fig. 95—Identified normalized proppant counts at logged locations in child well B2H. Also identified are the likely perturbed zones associated with the pre-existing parent laterals (BR1H/ BR2H pair & TR7H/ TR8H pair). We observe higher proppant concentrations due to more proppant identified towards toe half of new well B2H across the parent BR1H and BR2H laterals.

Apart from absolute proppant counts, other derived parameters such as particle type ratio (proppant versus other minerals as identified) as well as relative proppant size distribution, are both useful for accurate interpretation of the log. In multiple datasets, if the sample preparation protocols are appropriate and consistent, we have observed the relative proppant abundance parameter (α from Eq. 1) to be a strong indicator of proppant presence in the pre-stimulated rock. For this test, we see a significant increase in the relative proppant abundance ratio in the perturbed zone associated with the parent laterals as is seen in Fig. 96. Similarly, relative proppant size distribution (β from Eq. 2) is a good indicator of proppant presence as well. Sampling locations with lower proppant counts but high α and β parameters are indicative of proppant presence, just not in large quantities at that location. It is interesting to note that while we do see very high α and β parameter values across the toe half, we don't see similar elevated values across the heel of the well which is impacted by TR7H and TR8H parent wells. A likely explanation for this is the extremely large lateral offset of more than 3000 ft which should cause majority of the larger proppant particles to have already settled out before the fracturing fluid reaches these distances. There are multiple ways to develop a thresholding or normalization criteria such that we can use all these proppant measures to decide locations that are associated with propped fractures and likely significantly drained versus other locations that are relatively

unpropped or zones with other issues (such as localized proppant screen-out). However, further discussion around these interpretation approaches is beyond the scope of this report.

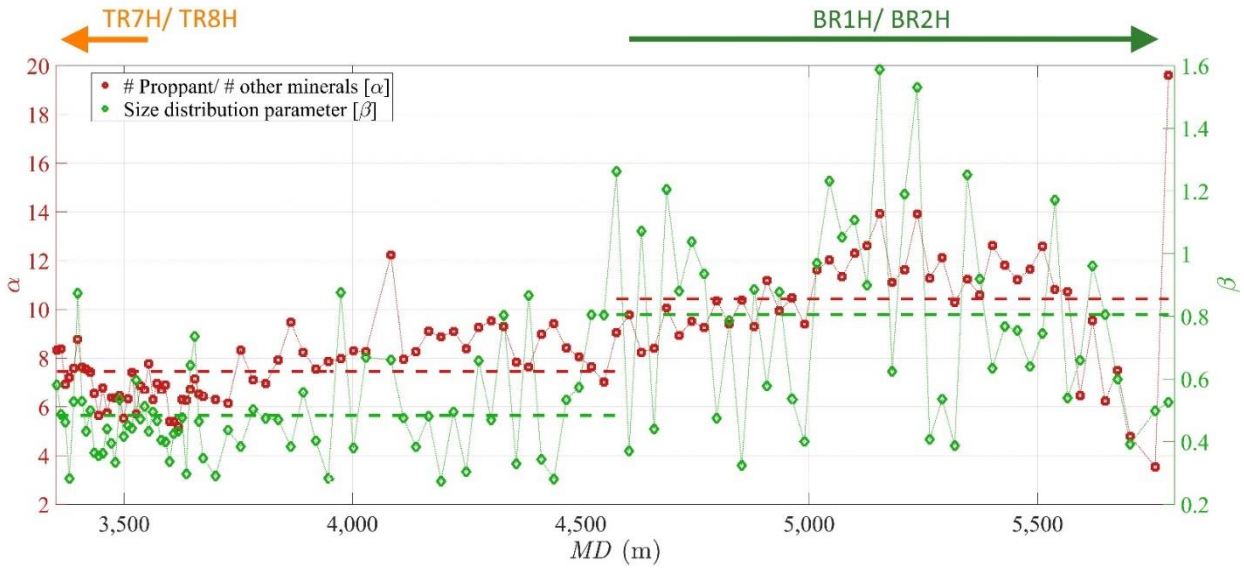

Fig. 96—Imaging parameters derived from identified proppant counts as defined in Eq. 5 and Eq. 6. Note that both parameters show a distinct increase in average values as we move into the perturbed zone associated with the BR1H/ BR2H parent wells. The change in average values is highlighted with the dashed lines.

OBMI Log

For further validation, we can consider the open hole oil based micro imager (OBMI) results and interpretations to correlate possible hydraulic fractures with observed proppant distribution from this log. OBMI tool uses microresistivity imaging in oil-based nonconductive mud systems to image the invaded zone along the drilled wellbore. It is used to interpret the orientation and structural dip of fractures and faults which intersect the well. To interpret hydraulic fractures from OMBI data, we consider subvertical fractures and their distribution in the new child well, B2H, and compare the location of fractures with the identified proppant distribution shown in Fig. 95. The proppant and fracture distribution along B2H are shown in Fig. 97 and we can see a strong correlation between zone where significant and likely hydraulic fractures begin (toe half, i.e., laterally proximal to BR1H/ BR2H wells as well as the heel end) and the initiation of significant proppant particles. This further validates the broader proppant particle distribution,

as well as derived proppant parameters such as relative proppant abundance (α), which is a strong indicator of presence of proppant particles.

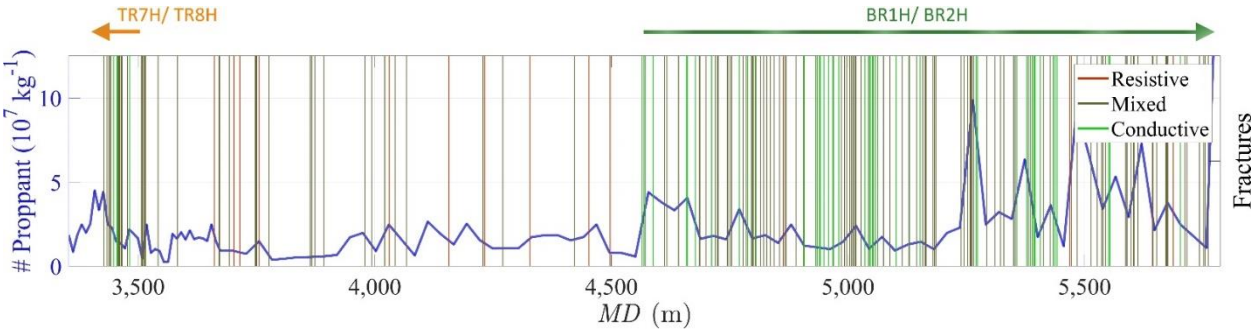

Fig. 97—Validation through presence of sub-vertical fractures proximal of proppant peaks as identified from the image log. Fracture colors indicate image log interpretation results regarding fracture conductivity with conductive fractures indicating likely hydraulic fractures.

We note that there are sections along the parent B1H/ B2H laterals where proppant counts identified were relatively low, for example, from 16000 ft to 17000 ft measured depth. However, since we see very high relative proppant counts as well as abundance of larger proppant particles along this section (Fig. 96), we interpret these depths and sections to be proppant rich. Additionally, we observe significant proppant peaks in the heel end of the B2H lateral at the shallowest measured depths along the sampled interval. These peaks also correlate with significant subvertical conductive fractures as observed from the image log interpretation (Fig. 97). Clearly the BR1H/ BR2H parent laterals cannot explain this observation. Recent work by Craig et al. (2021) suggests that the most likely explanation is that these fractures are associated with another set of preexisting parent laterals (TR7H/ TR8H) to the west of the pad that we have highlighted in this study. Fig. 98 shows a schematic representation of these wells and the likely hydraulic fracture corridors, or windows with expected intersection along the B2H child well based on identified in-situ stress state. Importantly, these observations suggest that proppant is transported to significant distances from the treatment well. In case of BR1H/ BR2H parent laterals, approximately 1400 ft, and in the case of TR7H/ TR8H parent laterals, approximately 3000 ft of transverse fracture growth and proppant transport. Also, based on independent observations (to be discussed in later sections), we believe that some of these propped zones could have a significant impact on fracture growth in child wells and could affect well productivity as well as inter-well communications during stimulation as well as during production stages. We also note that the pre-existing TR7H/ TR8H wells with likely associated

fractures and proppant at the heel of the child well are both at similar vertical landing depths when compared to new B2H child lateral being logged.

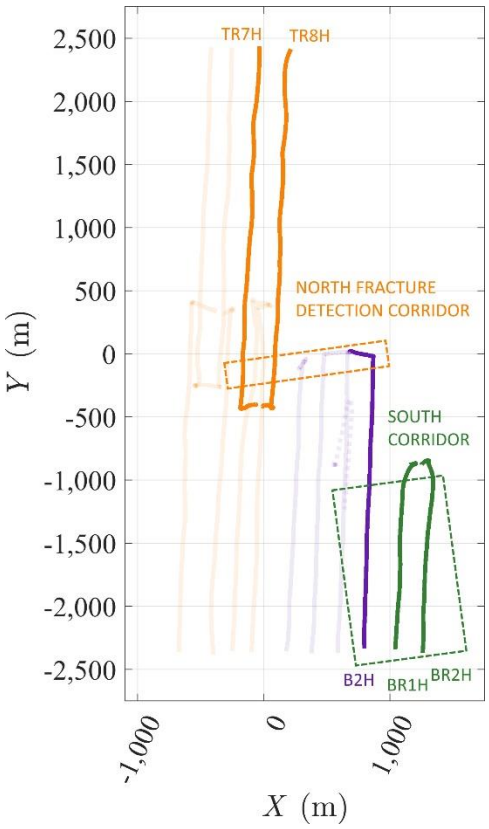

Fig. 98—BR1H/BR2H as well as TR7H/TR8H fracture intersection corridors at B2H based on prevalent fracture orientations/ stress state of approximately 16° ENE (After Craig et al. (2021).

Fracture Gradients

The interpreted fracture gradients from the pump shut-in for various stages can also be a good indicator of significant impact of proximal parent wells on the stimulation of child well stages (Roussel et al. 2021). We can map out the fracture gradients for various test wells, i.e., B1H, B2H, B3H and B4H, using instantaneous shut-in pressure (ISIP) calculations from pressure pumping data. A visual comparison of ISIP behavior suggests that there is a clear impact of parent BR1H/ BR2H drainage zones on the stimulation of B2H child well. The effect is obvious across the toe-half of B2H along the BR1H/ BR2H wells as seen in Fig. 98. Here the calculated ISIP values for each stage along the four wells are mapped vs. the measured depth of said stage relative to each wellhead. Additionally, the notional representation of proximal BR1H/ BR2H parent wells is with respect to the B2H ISIP trace. Lower fracture gradients or ISIPs are indicative of lower reservoir pressures due to depletion and thus likely much higher differential stresses and is a clear indication of impact due to BR1H/ BR2H drainage zone overlap. It is worth noting that we do not see significant impact on fracture gradients for rest of the test wells, i.e., B3H, B4H and B1H, which are at much larger lateral offsets from the BR1H/ BR2H wells (Fig. 99). There could be other factors influencing local ISIP behavior such as changing lithology or pad scale faulting (Ma

and Zoback, 2017), however, the overall trend shows distinct change between B2H and other wells in the pad across the parent laterals which makes our interpretation valid. In summary, while we do not have pre-stimulation image logs or proppant logs for B3H, B4H and B1H wells, it can be argued that the impact of the pre-existing parent laterals is much higher in case of B2H which is the most proximal to BR1H/ BR2H pair among the wells in this pad (Fig. 98).

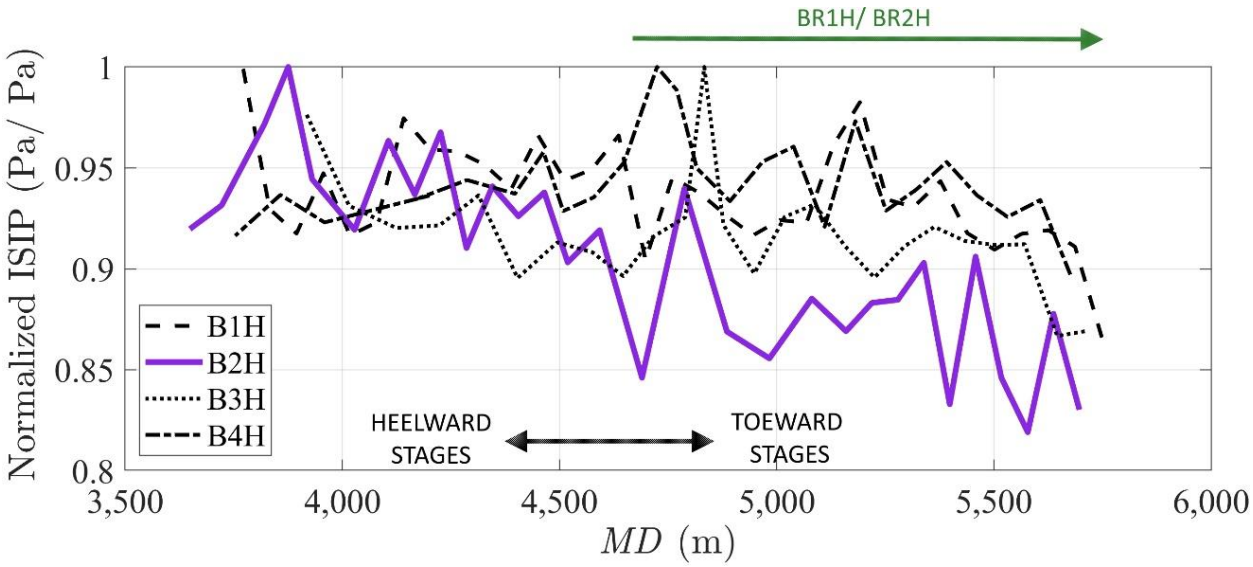

Fig. 99—Identified fracture gradients for various stages for wells B1H through B4H at HFTS-2 site. Data corresponding to each stage is plotted at relevant MD of that stage along corresponding well. Note the distinctly low fracture gradients for B2H stages across BR1H/ BR2H parent producing laterals, i.e., the toe half. The relative locations of the wells can be referenced from Fig. 89. Note that the plotted pressures for each well are normalized by scaling them to the maximum stage ISIP pressure observed for given well.

Microseismic Interpretations

Apart from observed fracture gradients, we also expect the pre-existing BR1H/ BR2H wells to influence the fracture growth behavior in the new child well. If we expect no significant propped fractures from parent wells intersecting the child well (B2H), we expect fracture growth towards (B3H) and relatively more uniform fracturing on both flanks of the well. On the other hand, with significant propped fractures from parent wells intersecting child well (B2H), we would expect reduced fracture growth towards B3H, i.e., more skewed fracturing towards the parent wells. Due to expected variations in fracture growth behavior across the B2H well, we can verify whether expressions of such growth can be observed in various datasets, such as microseismic event distributions as well as cross-well strain response behavior or cross-well communication.

First, we look at the variability in microseismicity across the pad (Fig. 100). There could be significant issues with this dataset such as acquisition geometry related biases or impact of velocity model uncertainties or anisotropies unaccounted for in the inversion algorithms. However, the microseismic surveys were well controlled, multi-array (three whip arrays) acquisition. Thus, we can assume that the results, particularly the relative microseismicity distribution, have not been significantly impacted by said uncertainties. We use an "event density" parameter to display the spread of microseismicity observed during fracturing of B2H

stages. This parameter is computed by sub-dividing the monitored space into evenly spaced grids 50 ft across and identifying all microseismic events with hypocenters falling within the search grid intervals. In addition to the event density parameter, Fig. 100 also maps out the proppant log distribution observed for B2H using yellow bars with the length of the bars indicating relative proppant counts from the log. Despite the larger sampling interval associated with the proppant log data (one sample every 90 ft), we do see that local peaks in the proppant data seems to correlate with identifiable microseismic event spread features propagating towards the parent BR1H/ BR2H wells, some of which are identified for reference in Fig. 100. We note that due to the acquisition geometry, i.e., distance to two of the microseismic arrays, we did not record significant events proximal of the toe-ward stages in B2H and this leads to fewer events close to the toe of the well. Also, for the high confidence events (Fig. 100b), we use a cutoff of travel time misfit < 2.5 milliseconds and at least phase arrival data from two arrays used for source location triangulation to limit the catalog for display.

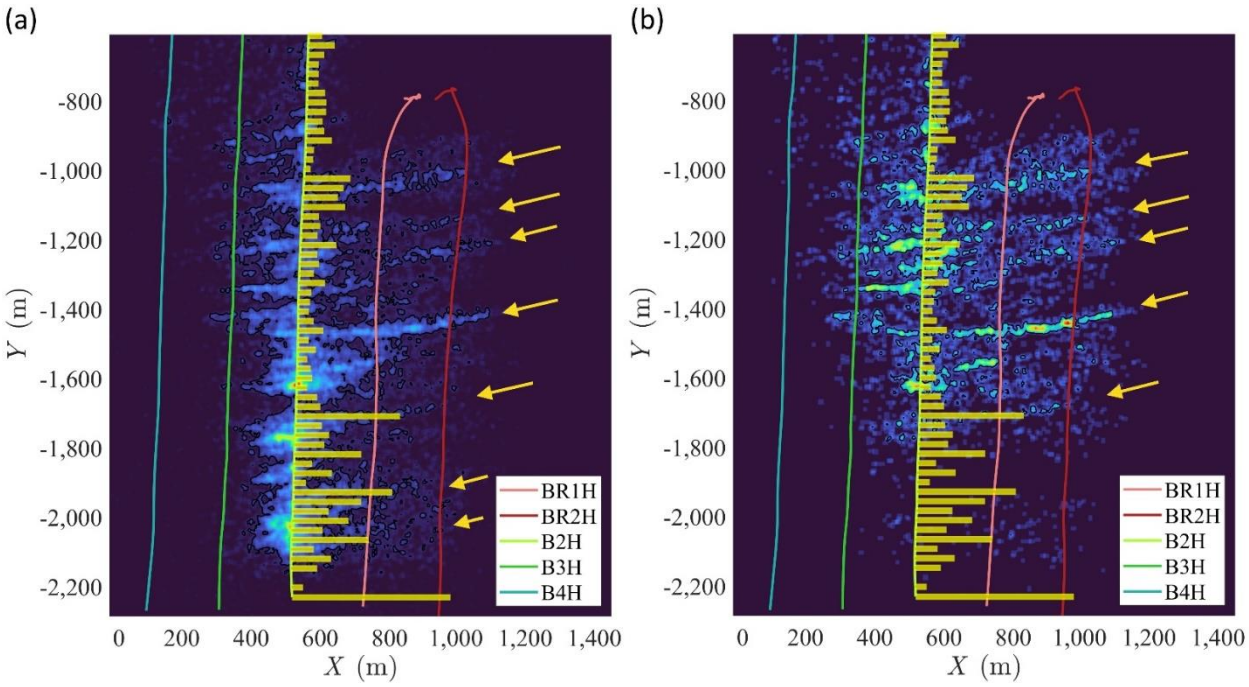

Fig. 100—Microseismicity distribution during B2H well stimulation for stages across BR1H/ BR2H producers. Subplot (a) shows microseismicity mapped using entire event catalog whereas (b) shows microseismicity based on high confidence events (travel-time misfit < 2.5 milliseconds and data from minimum two of the three arrays used for inversion). Arrows indicate match between local peaks in proppant distribution (yellow horizontal bars) and the seismicity features connecting B2H with BR1H/ BR2H laterals.

We can consider the source mechanisms from moment tensor inversion of microseismic waveforms observed during treatment of B2H well. This is useful to investigate considering we have significant variability in proppant distribution across the likely perturbed zone due to parent laterals and we expect that there may be variability in preferential growth towards BR1H/ BR2H wells. Failure modes can suggest likely fracture re-activations and expected fracturing behavior, i.e., growth eastward towards pre-existing laterals or westward. Identifying events that are double couple (DC) versus compensated linear vector dipole (CLVD) could indicate zones

where most fractures show shear failure with the former versus areas where we tend to see tensile or opening mode failure with the latter (Sileny et al. 2009). Typically, we expect the microseismicity to be dominated by shear failures as has been observed in many of the field microseismic datasets. However, as we can see in Fig. 101, the toe end of the well shows a preponderance of CLVD or opening mode tensile failures. Only high-quality inversion results are used in mapping the results with a confidence of higher than 0.5 and a condition number smaller than 70 (Baig and Urbancic 2010; Grechka et al. 2021).

More opening mode failure towards the toe end of B2H indicate re-activation of pre-existing fractures during the child well stimulation which would suggest a relatively higher impact of BR1H/ BR2H completions in this section compared to the middle of well B2H. Moreover, we would expect more propped fractures where we have tensile fracturing due to re-pressurization with fluid injection causing higher pore pressures across the fracture planes compared with more shear fracturing where we see relatively unpropped fracture due to higher minimum in-situ stresses (Agharazi and Kashikar 2016). Note that the difference in the two sections is relative with significant tensile fracturing likely occurring across the entire lateral as is expected during typical hydraulic fracturing operations. This transition in relative failure mode distributions seems to occur somewhere between hydraulic fracture stages 11 and 13 in well B2H (Fig. 101).

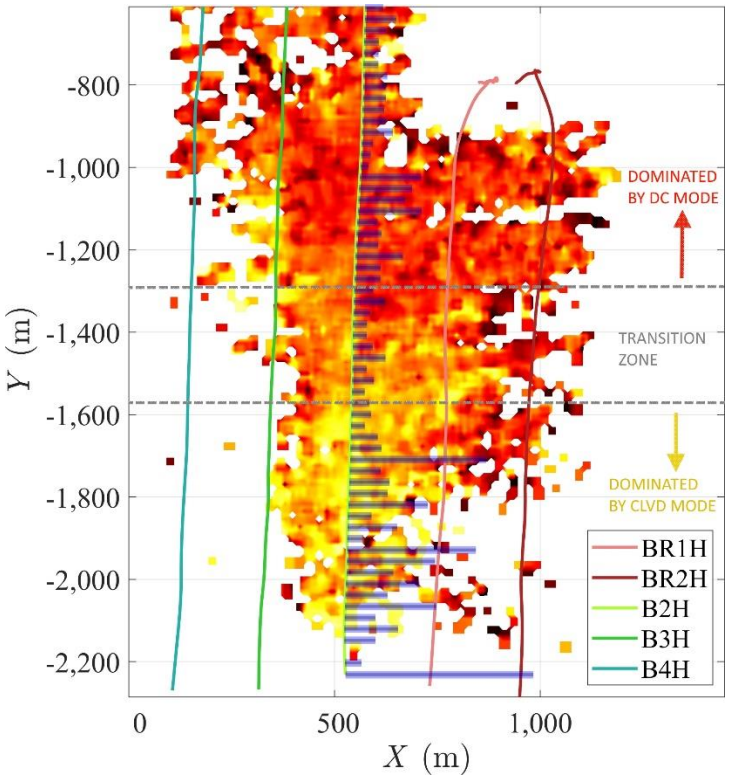

Fig. 101—Variation in source mechanisms of microseismic events as we move from toe towards the middle of the B2H child well. The blue horizontal bars represent the relative distribution of proppant data from this study. The mechanisms are averaged over grid dimensions of 100 ft × 100 ft and displayed as a heat map. Zones dominated by shades of yellow represent more of CLVD or opening mode failure whereas zones dominated by shades of red represent more of DC or shear failure.

Distributed Cross-Well Strain Surveys (DXSS) Surveys

Another dataset that was investigated is the cross-well communication between wells B2H and B3H while B2H was being hydraulically fractured. This was done using permanently installed fiber in well B3H used to monitor B2H treatments using cross-well strain measurements (Zhao et al. 2021). As already indicated, BR1H/ BR2H fractures intersecting B2H will cause preferential fracture growth towards the parent laterals (eastward) and reduced cross-well communication with the B3H well which is west of the B2H producer (Fig. 89). One measure of cross-well communication is to observe and sum over the number of fracture arrivals interpreted based on a flip in polarity of strain response at the observation well (Zhang et al. 2020). Another approach is to sum the strain change measured in the observation fiber during the fracturing operations of the given stage in treatment well (B2H). Fig. 102 shows both these parameters mapped at the depths associated with the corresponding stages in well B2H for reference. As already mentioned, the actual cross-well strain measurements were made along the fiber in B3H. The proppant log for this section is also mapped and shows varying behavior across the displayed interval.

We note that in the zone with fewer significant pre-existing propped fractures from BR1H/ BR2H parents as interpreted from proppant log, i.e., from 15000 ft to 17200 ft measured depth, fractures are growing more uniformly in a relative sense when compared to the toe end of the well from 17200 ft to 18750 ft measured depth. The toe-end sections show significant propped zones and fewer fractures growing westward towards B3H indicating much higher preferential growth eastward towards the BR1H/ BR2H parent wells causing skewed fracture growth patterns. The lower summed strain response in the toe end section also corresponds with fewer interpreted fractures observed along this section in B3H well. Also of note is that the data resolution, while varying between the two datasets, should be broadly comparable (100's of feet).

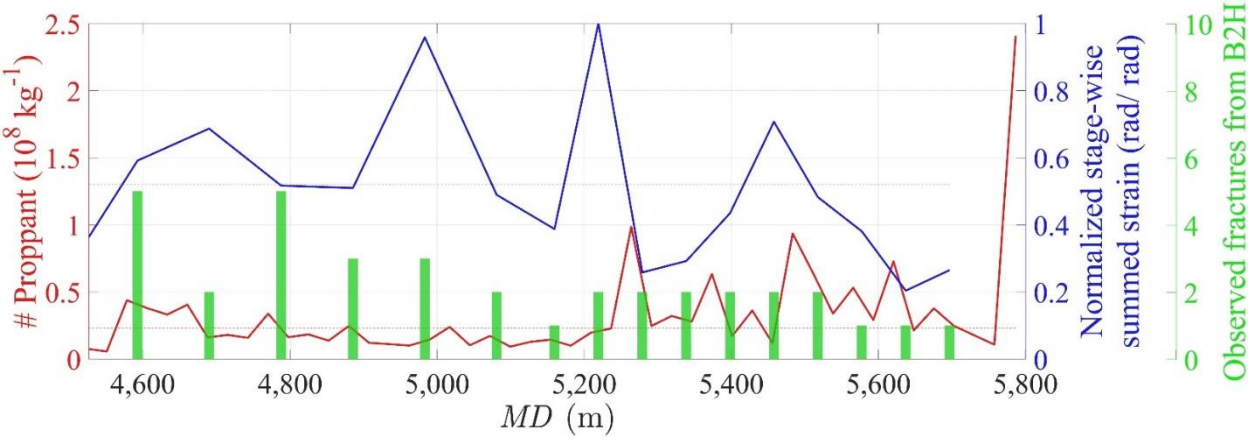

Fig. 102—Cross-well strain response parameters observed in well B3H fiber during treatment of B2H stages. Each data point along the blue curve, i.e., summed strain response, as well as each green bar, i.e., identified fracture arrivals, represents data for corresponding B2H stages. The data is plotted along well B2H with an overlay of proppant log data (red curve). Note that this entire depth interval is situated across the BR1H/ BR2H laterals. The blue dotted line indicates mean values of strain parameter for all B2H stages as measured at B3H fiber.

Conclusions

Based on our observations from this case study, we have found that propped fractures are differentially distributed across the B2H well under study with more propped fractures towards the toe end compared to the heel end. More broadly, various independent observations provide evidence towards validity of proppant logging technique using mud return samples as a useful diagnostic tool to identify propped as well as perturbed zones. Proppant log technique provides a much more accurate representation of near well propped zones when compared with traditional techniques such as post drill image logs, and that too at a fraction of the cost. Our high-level conclusions are as follows:

- Proppant-log provides indication of presence of pre-existing hydraulic fractures from prior fracture stimulation associated with proximal parent wells, particularly fractures with significant propped zones being intercepted by new child well lateral.
- While higher sampling rates could be more revealing, even a relatively low sampling rate of 90 ft provides useful diagnostic information. Relatively high-resolution logs at sampling every 20 ft should be doable at standard drilling rates.
- Analysis of data from this case study suggests that the parent wells have had a significant impact on the proximal new child well drilled at the HFTS-2 site. This includes both the BR1H/ BR2H wells to the east and the TR7H/ TR8H wells to the west of the new development. This translates to observable proppant transport over more than 3000 ft in case of the TR7H/ TR8H laterals and approximately 1400 ft for the BR1H/ BR2H wells. To the best of authors knowledge, this is the first case study to have demonstrated proppant transport across such large lateral separations through actual proppant sampling techniques.
- The impact of prior stimulation observed along the child well varies along the length of the stimulation overlap. Proppant log provides useful insights to better understand said impact. The other datasets which do provide similar insights, such as microseismic or DSS profiles, are very expensive to acquire and process unlike proppant logging approach. Thus, while the traditional geophysical techniques are limited to pilot studies, proppant logging can be a routine data acquisition tool to understand pre-existing stimulation effectiveness and help inform new in-fill well stimulation.

Thus, with proppant log, we see value during drilling of in-fill wells provided the parent wells are already fracture stimulated. In most shale plays this is indeed the case. Older wells generally are spaced further apart, and most mature field development programs involve drilling new in-fill wells to maximize resource recovery. However, understanding impact of depletion due to pre-existing wells on new child wells can be a very hard challenge (Lindsay et al. 2018; Rezaei et al. 2019). Proppant log can be a useful potential tool to help overcome this challenge. Specifically, this method helps identify locations where significant propped or “mother” fractures exist. These can have an adverse effect in terms of cross-well communication and have potential productivity impacts. There is scope for modifying completion strategies based on zones with “mother” fractures. As an example, pumping of relevant diverting agents to temporarily close off highly conductive, preexisting, hydraulic fractures or modifying completion strategies, such as cluster

or perforation density. Further, it can be used as a predictive tool to understand inter-well communication between parent-child pairs. Finally, proppant log can be a useful tool in assessing well spacing. This tool provides good value proposition in that it does not require rig downtimes and expensive tools associated with traditional logging or coring operations. Thus, for a typical proppant log run at moderate sampling rates (sampling every 20 to 30 feet), while we are sacrificing resolution, we get a usable proppant log at a fraction of the cost associated with typical e-logs.

Geochemistry

Authors: ***Djuna Gulliver, Kara Tinker, Preom Sarkar, Nicholas Means, Wei Xiong, Alexandra Hakala, Christina Lopano, Scott Leleika, Amanda Harmon, Jordan Ciezobka***

Summary

A standard method in unconventional oil and gas production is the process of hydraulic fracturing followed by a shut-in period, in which the fracture fluid remains pressurized in the reservoir for up to three weeks before production begins. Despite this widely used process, very little is known about what occurs in the reservoir during this shut-in process. In order to properly delineate potential reservoir reactions that may occur during shut-in that would lead to corrosion and scaling events, experiments were conducted in high pressure, high temperature reactors to simulate conditions of the Wolfcamp Shale in the Delaware basin. Experimental design allowed the assessment of the effect of proppant, microbiology, and time on the fluid chemistry and shale mineralogy in the reservoir.

Results suggest the biggest impact on fluid chemistry and shale mineralogy during shut-in is time. Analyses demonstrate dissolution of the shale material, with maximum dissolved ions occurring after 7 days of the shut-in period. After 21 days, results suggest precipitation occurs. The Delaware Basin is demonstrated to be high in sulfate content, which further increases in the fluid due to dissolution reactions during shut-in. The pressure vessel experiments suggest there was no significant contribution to reactions from microbiology during the shut-in period. However, early production samples demonstrate a significant selection of the microorganism *Caminicella*, a genus of which has previously been correlated to corrosion and sulfide production. Results suggest shut-in conditions may provide high sulfate concentrations that could later be utilized by a shifted microbial community to drive potential well infrastructure failure. This is the first study to incorporate microbiology, mineralogy, and fluid chemistry to investigate the fundamental geochemical reactions that occur during shut-in and early phase production of the Delaware Basin. Results from this study can complement observations from the Hydraulic Fracture Test Site 2 observations.

Introduction

Hydraulic fracturing has increased US domestic oil and gas production, with dry gas production estimated at 26 trillion cubic feet (Tcf) and tight oil production estimated at 2.67 billion barrels in 2020 ("Frequently Asked Questions (FAQs) - U.S. Energy Information Administration (EIA)," n.d.). The process of hydraulic fracturing is most commonly coupled with horizontal drilling, followed by injection of fluid and proppant (called fracture fluid or "frac fluid") and a shut-in period. During the shut-in period the injection fluid/proppant remains pressurized in the hydraulically fractured well for up to 3 weeks. After the shut-in period, production begins, and a large volume of oil/gas associated water is generated. This water has the chemical characterization close to that of the injection fluid. Over time, as production continues, the chemical composition of the fluid changes to higher salinity and is referred to as produced fluid.

Despite this widely utilized method of unconventional oil and gas production, not much is understood of the biogeochemical processes that occur during the shut-in period. The basic

geochemistry at the end of the shut-in period suggests various dissolution and precipitation reactions (Osselin et al., 2019), although it is unknown when and to what extent this occurs. In addition, previous observances of fouling, corrosion, and souring have been attributed to reservoir microbiology (Daly et al., 2016; Liang et al., 2016; Lipus et al., 2017). However, there has been no explicit study of abiotic versus biotic reactions occurring within hydrocarbon reservoirs.

Here, we present results from a simulation experiment designed to test the effect of proppant, microbiology, and time on biogeochemical processes in the reservoir during the shut-in period. These high pressure, high temperature laboratory experiments were conducted in parallel to the Hydraulic Fracture Test Site 2 (HFTS-2) field demonstration, allowing a detailed delineation of the change in geochemistry, microbiology, and mineralogy, to be compared to observations from the field site. Additionally, the microbial community from the first 35 days of production during HFTS-2 was assessed. Results from this study can complement observations from HFTS-2. This work can be utilized to mitigate risks of corrosion and scaling events that may occur during the shut-in and early production period, thus reducing the number of occurrences of well failure.

Methods

Experiments were conducted in high pressure, high temperature reactors to simulate reservoir conditions of the Wolfcamp Shale in the Delaware basin. The shut-in simulation was run at 210 ^{0}F and 5000 psi with injection fluid, shale, and proppant collected from HFTS-2. This experiment ran: 1) duplicate reactors with shale, proppant, and fluid, 2) a reactor with only shale and fluid, and 3) a sterilized reactor with shale, proppant, and fluid (Table 1). Reactors were sacrificed and sampled for analysis after 1 day, 3 days, 7 days, and 21 days. This experimental design allowed the assessment of the effect of proppant, microbiology, and time on the reservoir during the shut-in period. To minimize material alteration between the reactors due to sterilization procedures, autoclaved and filter-sterilized synthetic saline fluid was used to wash shale chips three times for all reactors (biotic and abiotic). Proppant was washed with synthetic saline fluid for abiotic reactor (Reactor 4). Fluid samples for the sterile reactors (Reactor 4) were filter sterilized, while the remaining reactors (Reactor 1-3) utilized unfiltered fluid.

Table 1—Experimental Matrix for Shut-In Simulations

Run time	Reactor 1	Reactor 2 (Duplicate)	Reactor 3 (No Proppant)	Reactor 4 (Abiotic)
1 day	Fracture fluid, shale chips, proppant	Fracture fluid, shale chips, proppant	Fracture fluid, shale chips	Sterile fracture fluid, sterile shale chips, sterile proppant
3 days	Fracture fluid, shale chips, proppant	Fracture fluid, shale chips, proppant	Fracture fluid, shale chips	Sterile fracture fluid, sterile shale chips, sterile proppant
7 days	Fracture fluid, shale chips, proppant	Fracture fluid, shale chips, proppant	Fracture fluid, shale chips	Sterile fracture fluid, sterile shale chips, sterile proppant

21 days	Fracture fluid, shale chips, proppant	Fracture fluid, shale chips, proppant	Fracture fluid, shale chips	Sterile fracture fluid, sterile shale chips, sterile proppant

Major cations and anions were detected using ion chromatography (IC) on a ThermoFisher (Thermofisher, Waltham, MA) ICS-5000+ with AS11-HC column for anion quantification and CS16 column for cation quantification. All samples were run in triplicate and the standard error of IC measurements reported here was less than 3%. Additionally, every 10–20 samples, a cation/anion control sample (Sigma Aldrich, St Louis, USA) with known certified concentrations was added during measurements and all control samples demonstrated an accuracy within 95–105%. Dissolved silica and chromium were measured using inductively coupled plasma optical emission spectroscopy (ICP-OES) on an Optima 7300 DV (Perkin Elmer, Waltham, MA), which is a dual-view spectrometer with solid state SCD detectors. U.S. EPA Method 6010D was employed for analysis with one duplicate, one standard recovery, and one spike recovery. Sample solutions were nebulized using a glass Seaspray concentric nebulizer and a glass Baffled Cyclonic spray chamber (Glass Expansion, Pocasset, MA) using 5 ppm yttrium as an online internal standard. Calibration standards were purchased from Inorganic Ventures (Christiansburg, VA) and are traceable to NIST standard reference materials.

Mineralogy was analyzed via scanning electron microscopy (SEM) and X-Ray Diffraction (XRD). For the SEM imaging, post-reaction samples were air-dried and imaged via a back-scatter detector (BSE) on a scanning electron microscope (SEM, Quanta 600F, FEI). Elemental spot analyses were performed with energy dispersive X-Ray spectroscopy (EDS, Oxford). For XRD analysis, each sample was ground using a zirconium lined ball mill (powder size < 5µm). Each specimen was spiked with a ~ 10 wt.% corundum (α-Al_2O_3) internal standard and homogenized in a mortar and pestle using acetone as a lubricant. The ground sample material was backloaded into a 10 mm diameter stainless steel cavity spin mount for analysis. The samples were run on a PANalytical X'Pert Pro with an X'Celerator detector at 45 kV, 40 mA utilizing copper X-rays. The samples were scanned between 4-70° 2θ at using a step size of 0.033°/step and a 1000 sec count time. The resulting XRD patterns were compared against the ICDD database (PDF-4+) using the X'Pert HighScore program to identify the mineral phases present. The mineral phases were quantified via Rietveld fitting of the crystallographic parameters (converted from PDF-4+) in the X'Pert HighScore program using semi-automatic fitting of the background, crystallographic structural information, and profile fitting parameters for each phase individually. The quantitative results (Table 4) were derived after renormalizing to 100% using the internal standard to quantify the amorphous content of the material in addition to the crystalline phases.

Mineral saturation indices (SI = log Q/K) were calculated based on the aqueous chemistry data in Geochemists' Workbench with the thermo_pitzer database, which is suitable for high salinity fluid. This database does not include C and Si species so minerals containing C or Si were not calculated. Selected saturation indices were listed from high SI to low SI in Table 5.

DNA was extracted from the samples using a modified version of the DNeasy Powersoil kit (Qiagen, Hilden, Germany). We amplified extracted DNA using universal primers targeting the V4 region of the 16S rRNA gene, as previously described (Caporaso et al., 2011, 2012). We were

unable to amplify to a detectable concentration from the shut-in reactors. However, we were able to quantify and amplify DNA from produced fluid collected directly from HFTS-2. Therefore, we opted to complete our microbial analysis directly on the produced fluid from HFTS-2. We concurrently extracted four kit blanks and completed negative PCR control to confirm no contamination occurred and visualized all samples on the Agilent Bioanalyzer to confirm DNA quality. Libraries were prepared according to the manufacturer's instructions before sequencing on an Illumina Miseq (Illumina, San Diego, CA) using a 300 cycle V2 Nano kit. The resulting 16S rRNA gene sequences were analyzed using QIIME2 version 2021.20 (Bolyen et al., 2019). We also measured the microbial load of the HFTS-2 produced water samples using previously described qPCR methodology (Tinker et al., 2020).

Results Overview

Shut-in Simulation Geochemistry

Cation, anion, and organic acid analysis was completed via IC and ICP (Table 2/ Table 3). Reactors 1 and 2 did not have enough fluid present after 21 days, and therefore were not able to be analyzed for dissolved ions. Most of the ions were in the form of sodium, chloride, and sulfate, with some contribution from calcium and magnesium.

Overall, there were minimal differences in concentrations of dissolved cations and anions between all four reactors during each time point, with most relative standard deviation within 20% for all reactor samples on a given sample period. The exception was chloride concentration, which had a relative standard deviation up to 28%, with the abiotic reactor 4 demonstrating high dissolved chloride compared to the reactor 1.

Although there was no significant geochemical change between the reactors of each sample period, a distinct geochemical trend did emerge with time. The concentration of cations and anions increased steadily from the 1-day reactors to the 3-day reactors, and from the 3-day reactors to the 7-day reactors, with the largest increase in dissolved cations and anions occurring between the 3-day and 7-day reactors. The 7-day reactors have the highest TDS values across all samples. Then, from the 7-day to the 21-day reactors, the cations and anions decrease to concentrations like the 1-day and 3-day reactors.

Sulfate was especially elevated in both the initial fracturing fluid and the reactor samples, ranging from 1605 mg/L – 4593 mg/L, with the lowest concentration coming from the frac fluid and the highest from the 7-day reactor 3 sample. This sulfate concentration is significantly higher than previously reported for the Bakken and Marcellus regions, but is within the range of the Permian Midland Basin (Tinker et al., 2020). Despite the high sulfate frac fluid, within 1 day, the sulfate concentrations increased by as much as 787 mg/L. The sulfate concentration nearly doubled after 7 days with a high concentration of 4593 mg/L, before decreasing to about 2450 mg/L after 21 days.

Table 2—Cation concentrations in mg/L of shut-in reactors

Cation	Day	Frac Fluid	Reactor 1	Reactor 2 (Duplicate)	Reactor 3 (No Proppant)	Reactor 4 (Abiotic)
Lithium	1	0.1	0.2	0.1	0.2	0.2
	3		0.2	0.2	0.3	0.2
	7		0.3	0.3	0.5	0.4
	21				0.3	0.2
Sodium	1	695.5	1292.0	904.3	1326.4	1557.6
	3		1311.9	1300.2	1327.9	1887.1
	7		1794.5	1978.3	2854.3	2930.2
	21				1457.4	2132.5
Ammonia	1	2.7	1.9	5.9	1.9	2.4
	3		1.9	2.6	2.0	2.6
	7		7.4	6.5	7.2	4.9
	21				6.8	5.7
Potassium	1	11.1	19.3	13.5	16.6	16.7
	3		16.8	15.8	20.2	20.6
	7		26.5	26.8	37.2	29.1
	21				18.9	19.9
Magnesium	1	171.0	252.5	183.4	236.7	234.5
	3		231.9	207.3	274.1	276.7
	7		347.5	357.7	520.7	373.6
	21				201.5	194.6
Calcium	1	235.6	317.7	317.2	275.4	242.4
	3		330.4	300.9	313.8	277.1
	7		373.2	384.3	485.2	327.6
	21				385.6	386.9
Strontium	1	3.7	5.6	4.9	5.1	4.4
	3		5.5	5.3	5.0	5.2
	7		6.2	6.5	7.1	6.1
	21				6.2	6.5
Barium	1, 3, 7, 21	ND	ND	ND	ND	ND
*Chromium	1, 3, 7, 21	ND	ND	ND	ND	ND
*Silica	1	3.9	6.5	5.9	5.4	5.4
	3		6.0	6.2	5.9	6.5
	7		7.6	7.9	8.4	7.4
	21				8.0	7.8
pH	1	8.0	8.4	8.1	8.2	8.0
	3		7.7	7.7	7.8	7.6
	7		7.6	7.3	7.3	7.2
	21				7.5	7.4
Alkalinity	1	129.2	30.8	105.6	36.4	23.6
	3		22.0	20.4	26.0	21.6
	7		26.4	34.8	34.3	30.0
	21				34.8	28.0

* Analyzed via ICP-OES

Table 3—Anion and organic acid concentrations in mg/L of shut-in simulation reactors

Anion	Day	Frac Fluid	Reactor 1	Reactor 2 (Duplicate)	Reactor 3 (No Proppant)	Reactor 4 (Abiotic)
Fluoride	1	0.9	1.7	1.0	1.6	1.3
	3		1.3	1.2	1.8	1.4
	7		2.6	2.6	0.0	0.0
	21				0.8	0.5
Chloride	1	720.4	1434.9	970.5	1444.1	1767.7
	3		1265.4	1235.9	1462.9	2321.7
	7		1913.5	2150.2	3108.3	3445.1
	21				1656.4	2672.3
Bromide	1	1.5	2.6	1.8	2.4	2.3
	3		2.3	2.2	2.9	3.0
	7		3.8	3.3	5.5	4.5
	21				2.7	2.9
Nitrate	1	10.7	17.7	12.1	15.6	15.4
	3		15.9	14.2	19.1	19.4
	7		25.3	26.3	37.5	29.6
	21				18.0	18.4
Sulfate	1	1604.9	2391.0	1862.1	2235.4	2263.4
	3		2539.1	2435.0	2549.9	2482.2
	7		3178.2	3365.7	4592.9	3585.2
	21				2436.5	2469.6
Phosphate	1	1.5	1.2	1.7	1.0	0.9
	3		1.2	1.1	1.7	0.5
	7		0.5	2.2	0.6	0.2
	21				0.2	0.0
Thiosulfate	1	0.0	0.2	0.2	0.2	0.2
	3		0.2	0.2	0.2	0.2
	7		0.3	0.1	0.5	0.6
	21				0.2	0.3
Acetate	ND	ND	ND	ND	ND	ND
Propionate	ND	ND	ND	ND	ND	ND
Formate	ND	ND	ND	ND	ND	ND
Butyrate	ND	ND	ND	ND	ND	ND
Succinate	ND	ND	ND	ND	ND	ND
Oxalate	ND	ND	ND	ND	ND	ND

Shut-In Simulation Mineralogy

XRD analysis was performed on the initial shale and all samples from reactor 3 to determine bulk mineral content. Only reactor 3 was utilized for this analysis, as the other reactors contained proppant, which would reduce an ability to see bulk mineral changes in the shale without a

competing signal. A majority of all the shale consisted of quartz and clay, with minor carbonate contributions (Table 4). It should be noted that it is difficult to ascertain if mineralogic variation is due to sampling (only about 0.5g of material is used in the XRD analysis), or the result of reaction. However, in conjunction with the aqueous chemistry, the decrease in carbonates in the shale reactor as determined by XRD is consistent with the trends of rapid dissolution followed by precipitation over the course of the reaction. Specifically, the carbonates appear to decrease in the shale mineral content within just one day of the shut-in simulation, decreasing from over 15% to under 5% before increasing to similar levels as the initial shale after 7 days of simulation. This again suggests dissolution of the shale matrix within 24 hours of the shut-in period, followed by precipitation after 7 days of shut-in.

SEM imaging of the shale samples further suggested that the shale in all reactors has a clay matrix with minor contribution from other minerals. The initial shale showed evidence of diagenetic alterations, with most of the pyrite already oxidized and only a small amount of Ba-containing celestite (Sr, Ba)SO_4 observed (Fig 103a) in the parent rock material. These alterations and sulfate precipitates may be a result of diagenetic reactions with the reservoir before the cores were extracted for this experiment. After incubation in the reactors, secondary mineral precipitates were observed across most samples. The new precipitates included Ca-phosphate minerals (Fig 103b) and anhydrite ($CaSO_4$), as well as a significant amount of NaCl (Fig 103d). The NaCl may have been a result of evaporation of high salinity residual fluid left on the samples during the preparation methods for SEM imaging. Some Fe-Ni-Cr were imaged (Fig 103c), but it is unknown whether these minerals were formed during reaction in the shut-in or caused by metal shavings during the initial coring of the shale. Lastly, silver sulfate minerals were observed in the sample from Reactor 2 after 21 days of incubation (Fig 103e). Silver sulfate has thus far not been reported as a mineral in shale. It was present in limited amounts after incubation, suggesting a small amount of silver may be released from the shale during rock-fluid interactions of the shut-in period. Also present in limited amounts were rare earth elemental precipitates (not pictured), consisting of Ce and La.

Mineral saturation was calculated using the fluid chemistry data listed in Table 2/ Table 3, to predict expected mineralization that would occur as the shut-in fluid equilibrated. Calculated mineral saturation indices are listed in Table 5 in the order of high to low, demonstrating that most of the supersaturated minerals are Ca-phosphate containing minerals. This correlates with the secondary mineral precipitation detected in the reactor samples from the SEM images. Anhydrite was also calculated to be is supersaturated, which was also detected in the SEM imaging. Combined results from the fluid chemistry, XRD, SEM imaging, and saturation indices calculations suggest that early shut-in reactions were dominated by dissolution of ions such as calcium, barium, strontium, and sulfate, followed by a secondary precipitation between 7 and 21 days.

Table 4—Quantitative X-ray diffraction results, using the initial shale and the shale from reactor 3. Reactor 3 was used to prevent proppant from biasing the silica values. All values are in wt. %.

	Initial Shale	1 day	3 day	7 day	21 day
Albite	4	4	2	5	3
Calcite	12	3	8	12	12
Dolomite	4	1	2	3	1
Muscovite/Illite	16	13	8	15	11
Pyrite	2	1	2	1	1
Quartz	45	47	38	36	43
*Amorphous	18	30	39	28	29

* The amorphous content is calculated from the internal standard normalized quantified results and is calculated assuming the sum of all phases is 100 wt.%. e.g., Amorphous = 100% - Sum Crystalline phases (wt.%).

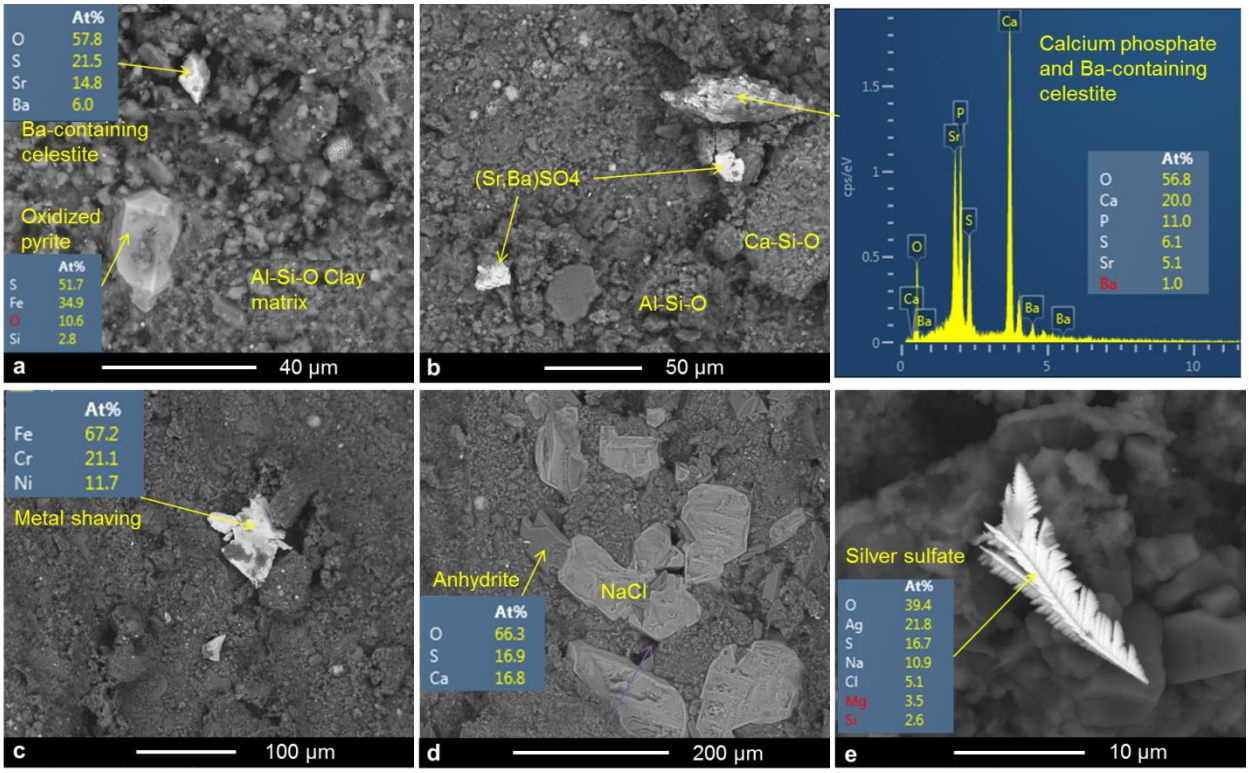

Fig 103—SEM images of a) pre-reaction shale sample; b), c), d) shale sample reacted for 21 days from Reactor 3; e) shale sample reacted for 21 days from Reactor 2.

Table 5—Calculated mineral saturation indices using thermo-pitzer database. Dissolved solids in mg/kg, Charge imbalance in %, and all other entries in log Q/K.

Sample ID	R1-1D	R1-3D	R1-7D	R2-1D	R2-3D	R2-7D	R3-1D	R3-3D	R3-7D	R3-21D	R4-1D	R4-3D	R4-7D	R4-21D	frac fluid
Dissolved solids	6242	6209	8212	4645	5972	8849	5955	6467	12467.2	6652	6490	7772	11339.4	8386	3779
Charge imbalance error	-1.41	-0.38	0.51	0.52	-0.60	0.13	0.32	-1.54	0.30	-0.91	-0.04	-0.73	-0.18	-0.54	-0.70
Water type	Na-SO_4	Na-SO_4	Na-SO_4	Na-SO_4	Na-SO_4	Na-SO_4	Na-SO_4	Na-SO_4	Na-SO_4	Na-SO_4	Na-Cl	Na-Cl	Na-Cl	Na-Cl	Na-SO_4
Fluorapatite	27.15		24.04	26.76	24.03	24.40	26.04	25.48	23.51	23.46	25.25	23.74	21.88	22.89	25.80
Hydroxyapatite	20.93		16.92	20.41	17.19	17.01	19.59	18.63	16.09	16.66	18.73	16.80	14.50	16.06	19.44
Whitlockite	11.17		9.04	11.01	9.16	9.28	10.45	10.06	8.64	8.90	9.98	8.97	7.68	8.55	10.45
Brucite	1.53	0.14	-0.05	0.84	0.00	-0.59	1.03	0.29	-0.45	-0.40	0.76	-0.05	-0.73	-0.59	0.68
Anhydrite	0.30	0.33	0.38	0.28	0.29	0.39	0.22	0.30	0.51	0.37	0.16	0.20	0.30	0.34	0.15
Celestite	-0.10	-0.09	-0.07	-0.17	-0.10	-0.06	-0.16	-0.14	-0.05	-0.07	-0.24	-0.19	-0.14	-0.12	-0.27
Fluorite	-0.13	-0.27	0.04	-0.43	-0.34	0.04	-0.20	-0.14	0.18	-0.69	-0.38	-0.34	-0.19	-0.81	-0.67
Gypsum	-0.18	-0.14	-0.09	-0.20	-0.18	-0.08	-0.25	-0.18	0.04	-0.10	-0.32	-0.27	-0.18	-0.14	-0.32
Bassanite	-0.34	-0.31	-0.26	-0.36	-0.35	-0.25	-0.42	-0.34	-0.13	-0.27	-0.48	-0.44	-0.34	-0.31	-0.49

Production Fluid Microbiology from HFTS 2

No DNA was amplified to a detectable amount from any of the shut-in reactor samples. However, production fluid was sampled during different days of production during the HFTS-2 project, and the microbial community was assessed (Fig 104). The diversity was calculated to determine the quantity of various species of microorganisms inhabiting the system, with a low diversity demonstrating few species present, and a high diversity demonstrating many different species present. The microbial load was measured via qPCR as a method of determining the relative microbial population size of the system.

The unreacted proppant and the fracture fluid that was used for injection during the hydraulic fracturing process had high levels of diversity, with Shannon Indices of 3.6 and 4.9 and Chao 1 indices of 29 and 52, respectively. Additionally, the microbial load was relatively high, with $3x10^6$-$5x10^7$ 16S rRNA gene copies/mL of sample. This suggests that the fluid injected in the Delaware formation for hydraulic fracturing had a high microbial population that was composed of a large variety of species.

The diversity of the microbial community was comparatively high for the first day of production, with a Shannon Index of 4.4 and a Chao Index of 100. The microbial load on the first day of production was also high, with over 10^6 16S rRNA gene copies/ mL of sample. However, the samples taken at day 5 and day 7 of production had microbial loads too low to complete sequencing, suggesting a decrease of microbial population. The microbial load increased after 12 days of production. This increase is accompanied by a significant decrease in diversity, with a Shannon Index as low as 1 and a Chao Index as low as 15. As the production continued, the diversity decreased to a low range of 0-0.82 Shannon Indices and 10-13 Chao Indices, while microbial load remained between 10^5-10^9 16S rRNA gene copies/mL sample. This suggests early production drove a change in the microbial community, in which a high population of a high variety of species initially inhabited the system, following by an overall decrease in the microbial population 7 days after production began, and finally resulting in a rebound of the microbial population completely dominated by a single microorganism.

The taxonomy of each sample was assessed via 16S rRNA sequencing (Fig 104). The starting frac fluid and proppant had several different common environmental microorganisms that are not typically found in subsurface environments (Tatar, 2018). This suggests the microbial community from these samples was representative of the groundwater and sand used to make the fracture fluid. After the conclusion of the shut-in period, the microbial community appeared to shift. This shift was already apparent by the first day of production, with *Caminicella* representing as much as 35% of the relative abundance and *Desulfovibrio* representing 12%. The remaining 53% of the community was represented by "Other", which represents 77 different species that each contributed <3% relative abundance each. As production continued, the relative abundance of *Caminicella* significantly increased, representing 90%-100% of the detected relative abundance. Although currently little is known about *Caminicella*, a species of this genus has previously been isolated from a Pacific Rise hydrothermal vent and is a thermophilic heterotrophic anaerobe (Alain, 2002). Since *Caminicella* appeared to become highly selected in the HFTS-2 production well, more DNA assessment should be completed to determine the microbial functional potential of this microorganism in this system. Desulfitibacter was also present in lower relative

abundances, representing up to 9% of the relative abundance in the day 12 sample. Desulfitibacter is also understudied, although a species of this genus has previously been found to be a sulfite reducing anaerobe (Nielsen et al., 2006).

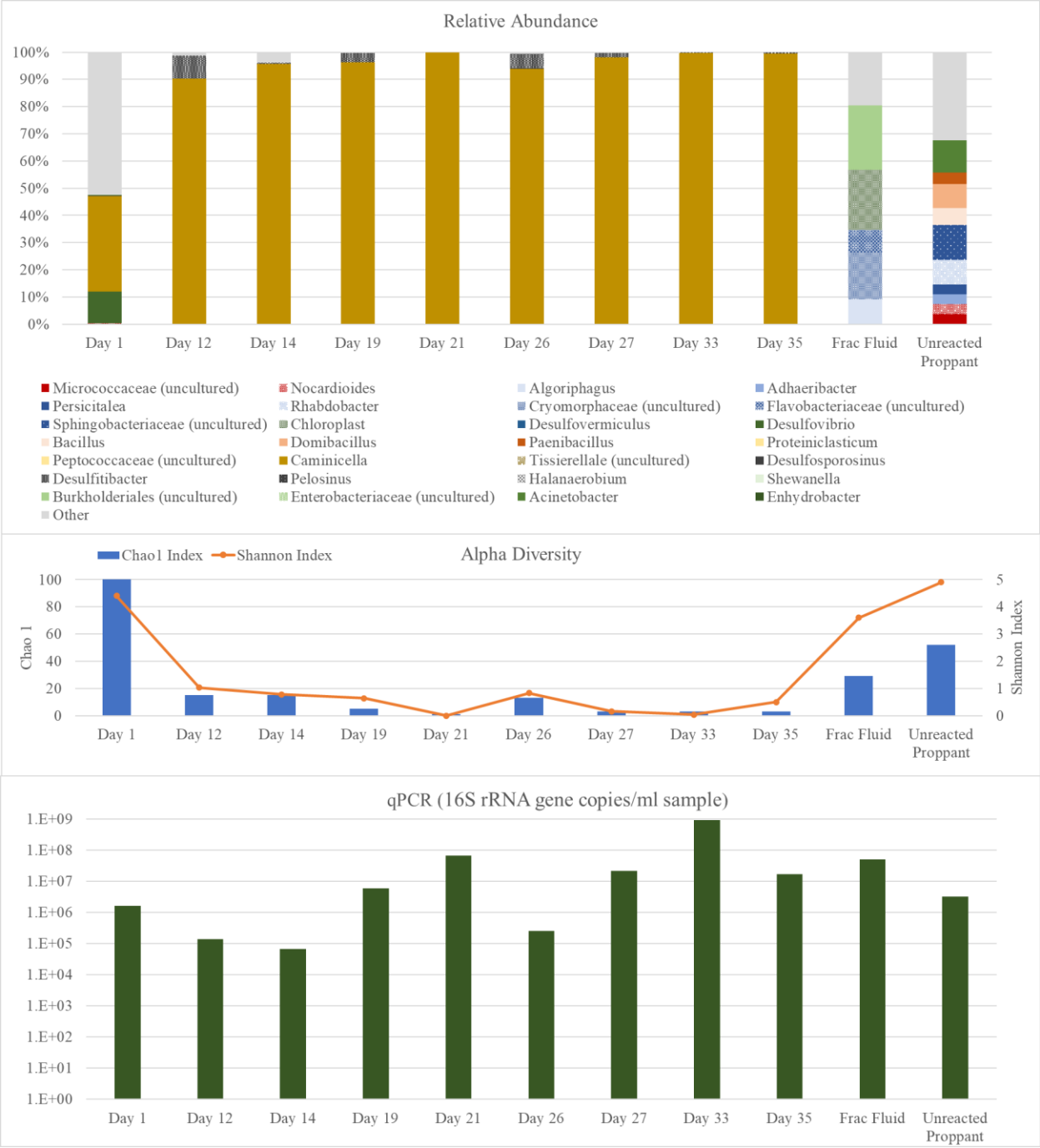

Fig 104—Relative abundance, alpha diversity, and qPCR analysis of sample during HFTS 2 production. All relative abundance is listed at the genus level, and all listed genus is above 3% relative abundance, with the remaining genus grouped in "Other".

Discussion

In this study, we assessed the geochemical, mineralogical, and microbiological changes that would be expected to occur during the shut-in period at HFTS-2 with simulation experiments. In addition, we assessed the microbiological changes that occurred during the first 35 days of production from HFTS-2 produced fluid samples. To our knowledge, this is the first study to delineate the change of microbial community during production in the Delaware Basin, and the first study to assess the geochemistry, mineralogy, and microbiology that would occur during the shut-in period.

Analysis of the fluid chemistry suggests the highest dissolved ions concentration occurred at 7 days, before decreasing to levels of the original fracture fluid. This suggests a pattern of dissolution followed by precipitation. SEM analysis and saturation indices demonstrate later formation of calcium sulfate (in the form of anhydrite) and calcium phosphate minerals, while XRD analysis demonstrates dissolution of carbonate minerals within 1-3 days of shut-in followed by precipitation of these minerals. These results suggest maximum dissolution of the shale may occur within 7 days, and optimal permeability of the reservoir may occur before 21-days. Correlation with production would have to be completed to demonstrate optimal shut-in period phases.

Fluid chemistry results also demonstrate high sulfate concentrations within the initial fracture fluid that increases significantly during the first 7 days of shut-in. Sulfate is known to cause scaling problems in unconventional oil and gas systems (Kamal et al., 2018). Additionally, if this high sulfate fluid is left in a biological system, there is a high risk of microbial reduction to hydrogen sulfide, which will reduce the quality of the product, increase risk of infrastructure failure, and increase worker hazards (Booker et al., 2017). Significant consideration in the fate and transport of sulfate should be made for the Delaware Basin.

During the shut-in simulation experiments, microbial loads were too low to analyze, suggesting minimal impact from microbiological processes during the shut-in period of the HFTS-2 production well. However, the results from our analysis of HFTS-2 field samples during production demonstrate the microbial community changes after shut-in. We found that within 1 day of production the microbial shifts towards a different composition, one that ultimately is completely overtaken by *Caminicella*. *Caminicella* is currently not well characterized, with only one documented species (Stipanicev et al., 2014). The known species has the ability to produce hydrogen sulfide, acetate, hydrogen, and high concentrations of carbon dioxide (Stipanicev et al., 2014). Additionally, this species was found abundant on carbon steel with magnesium and calcium deposits (scaling) and was suggested to be associated with corrosion in the form of pitting (Stipanicev et al., 2014). Given *Caminicella's* high relative abundance and microbial load in the HFTS-2 production well, and the high sulfate content demonstrated from the shut-in simulation experiments, the enrichment of this microorganism could lead to a high risk of corrosion and hydrogen sulfide production. Further work should be completed to determine the microbial functional potential of this microorganism.

Previous research demonstrates not only a large variation of biogeochemistry between basins (Tinker et al., 2020), but also variation within the same basin (Tinker et al., 2020). Thus, this work represents the geochemistry, mineralogy, and microbiology of the HFTS-2 well in the Delaware

Basin and should not be used as expected results from other shale plays. Additional research is needed to determine the site-specificity of this study.

Conclusion

- During shut-in, dissolution of the shale is expected to occur within 1 day, with maximum dissolution within 7 days, followed by a secondary precipitation of minerals after 7 days.
- Fluid chemistry demonstrates a high concentration of sulfate compared to other shale plays, and consideration should be given to potential scaling, corrosion, or H_2S occurrences.
- Microbiology is not expected to drive major reactions during the shut-in period of systems representative of HFTS-2
- During the first 35 days of HFTS-2 production, the microbial community became highly enriched in a poorly characterized anaerobic heterotrophic microorganism, *Caminicella*.

A species of *Caminicella* has been previously demonstrated to lead to sulfide production and corrosion, and the selection of this microorganism coupled with the high sulfate content in the HFTS-2 well could lead to increased risk of infrastructure failure.

Results and Discussions

This joint DOE-industry project has been instrumental in furthering the optimization of unconventional oil and gas developments and helped answer some very pressing questions long plaguing the industry.

This was one of the first instances where multiple horizontal and vertical fiber-optic cables were deployed to understand both lateral and vertical fracture propagation. This is key in optimizing multi-bench developments such as the Wolfcamp shale. Observations provide key understanding on significant fracture height growth, fracture communication, as well as production drawdown behavior.

This site was also one of the first examples where a new strain measurement technique (DSS-RFS using Rayleigh Frequency Shift) was run in an unconventional O&G setting. This technology provides high resolution mapping of strain change response which can be used to map and understand behavior across individual clusters for hydraulic fracture stages. Insights from this study have demonstrated the value and potential use cases for this technique within the industry.

Finally, GTI developed Proppant Logging technique was applied on an in-fill well and results and observations have validated its use case and efficacy in understanding propped zones at in-fill locations. The study also demonstrated proppant transport behavior wherein possible proppant associated with pre-existing wells were identified at lateral distances of more than 2000 ft. This was a major technology spin-off which has been validated at the site.

The test also provided opportunity for the operator to analyze the rich dataset in a comprehensive manner and contextualize the observations against their existing operations in Delaware Basin. Some of their key learnings are highlighted in the following discussion.

Summary

Hydraulic fractures (HF) play a dominant role in oil and gas production from unconventional reservoirs, fracture characteristics, geometry, and extent are generally not well known and are typically inferred from various monitoring methods or subsurface models. The Hydraulic Fracturing Test Site-2 (HFTS-2) is a field-based research experiment performed in the Wolfcamp formation of the Permian (Delaware) Basin.

HFTS-2, a unique joint industry program (JIP) that brings together government, academia, and industry, focused on field data acquisition and interpretation and built a comprehensive HF research dataset that includes microseismic (MS), 1,500 ft of core, diagnostic formation injection tests (DFIT), fluid characterization, advanced logs, geochemistry, downhole gauges, varying completions, and permanent fiber optic (FO) cable in vertical and horizontal wells. These data were integrated and used to characterize HF geometry/dimensions and resulting depletion profiles, gain insights for completion design, and achieve a better understanding of parent well depletion effects on child well performance.

The analysis and integration of the comprehensive HFTS-2 diagnostics dataset provide insights for optimal well placement and completions and improves understanding about the effects of

parent well depletion. This dataset can be used to blind test and develop subsurface workflows for unconventional resources. Key learnings from HFTS-2 and the new technologies tested can easily be transferred to other unconventional plays.

Introduction

The Hydraulic Fracturing Test Site-2 (HFTS-2) is a field-based, cost-shared research and development program in the Permian Basin. Fig 7 shows the location map for the HFTS-2 project in the Permian Delaware Basin, which is approximately 140 miles away from the HFTS-1 project (Ciezobka et al., 2018). Occidental is the host and operator for the HFTS-2 project, where the US Department of Energy (DOE) through the National Energy Technology Laboratory (NETL) and 16 consortia members have funded >$20 million for science data acquisition and interpretation in addition to the funds required for drilling, completions, and facilities for horizontal wells. HFTS-2 offered a unique opportunity to understand the hydraulic fracturing process better in unconventional reservoirs. The primary objectives included: a) evaluate various completion designs; b) characterize HF geometry/dimensions and resulting depletion profiles, with and without parent wells' influence; c) identify and test new technologies; and d) build a comprehensive HF diagnostics dataset.

HFTS-2 Dataset Overview

The HFTS-2 test site is located in Loving County, Texas, and several horizontal wells were drilled in different formations (mostly primary Delaware Basin drilling targets) approximately 700 ft away from each other. The HFTS-2 project successfully acquired state-of-the-art diagnostics data through the joint efforts of several operators and service companies. Fig 105 provides an overview of the HFTS-2 comprehensive dataset. The yellow circles with numbers represent the stimulation order of the horizontal wells. The black solid triangles represent the two legacy Bitterroot wells in the east that were drilled and completed about three years before the child wells (Boxwood-1H, -2H, -3H, and -4H). The hydraulic fracturing test and research focused on the four child wells with over 100 stimulated stages and varying completion designs in the Upper and Middle Wolfcamp formations.

Two science wells drilled as a part of the HFTS-2 program, Boxwood-5PH (vertical pilot hole) and -6S (slant well), were used to acquire ~550 ft of unstimulated whole core and ~950 ft of post-frac SRV core, respectively. Two horizontal wells (Boxwood-3H and -4H) and one vertical well (Boxwood-5PH) were instrumented with permanent fiber optic (FO) cable. New FO technologies were tested and demonstrated through unique near-wellbore and far-field surveys that provided spatial and temporal insights for HF propagation and depletion monitoring. FO was used both for stimulation monitoring (HF profiling and vertical/lateral coverage) and for production monitoring (well interference and production logging). In addition, BHP gauges were installed in all horizontal wells (fiber wells had heel and toe P/T gauges), and arrays of P/T gauges were installed in the vertical and slant science wells. Conventional microseismic (MS) surveys were collected from three wells indicated by blue squares in Fig 105 during stimulation of selected

wells, and the data were compared with FO-based MS. The comprehensive dataset also includes DFIT acquired in five wells, PVT, advanced logs, and Timelapse Geochem.

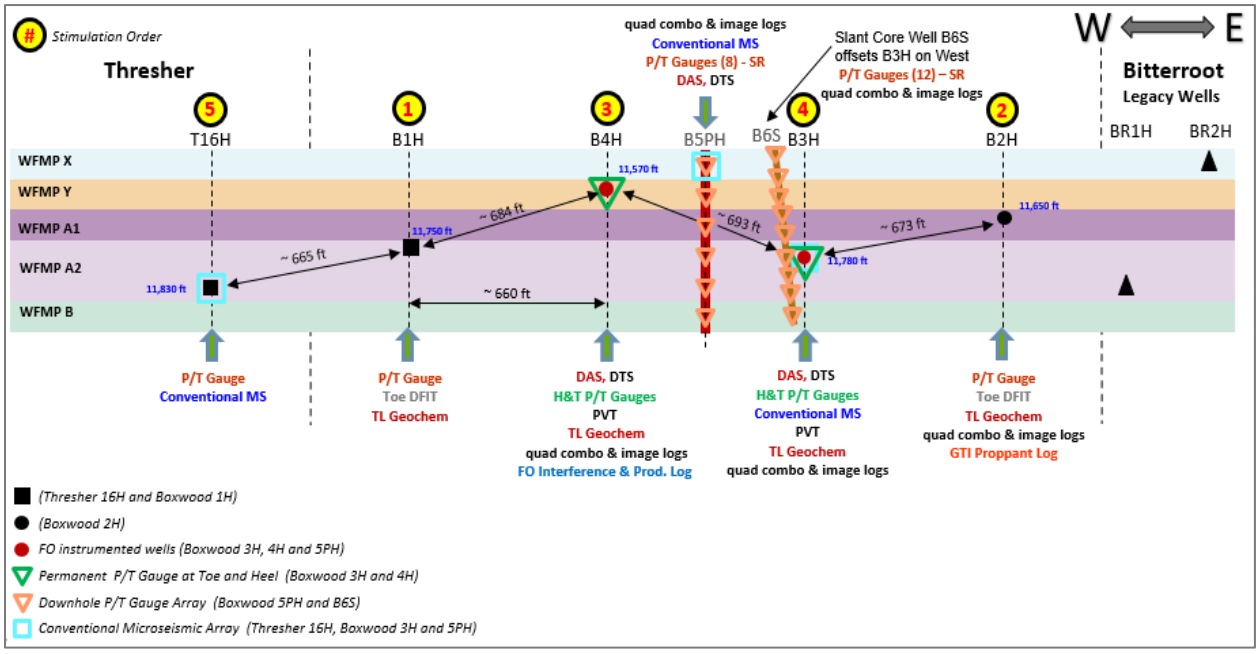

Fig 105—Overview of the HFTS-2 dataset

The unique site design offered a great opportunity to understand the effect of depletion better, as more than half of the child well stages overlapped parent well areas. The extensive dataset acquired was integrated and used to calibrate subsurface models and characterize HF geometry/dimension. Diagnostics and modeling efforts enabled thorough calculations of HF vertical and lateral extent and production depletion profiles, as well as quantification of the HF growth bias for child well stages that overlapped parent wells.

HFTS-2 Fiber Optic Overview

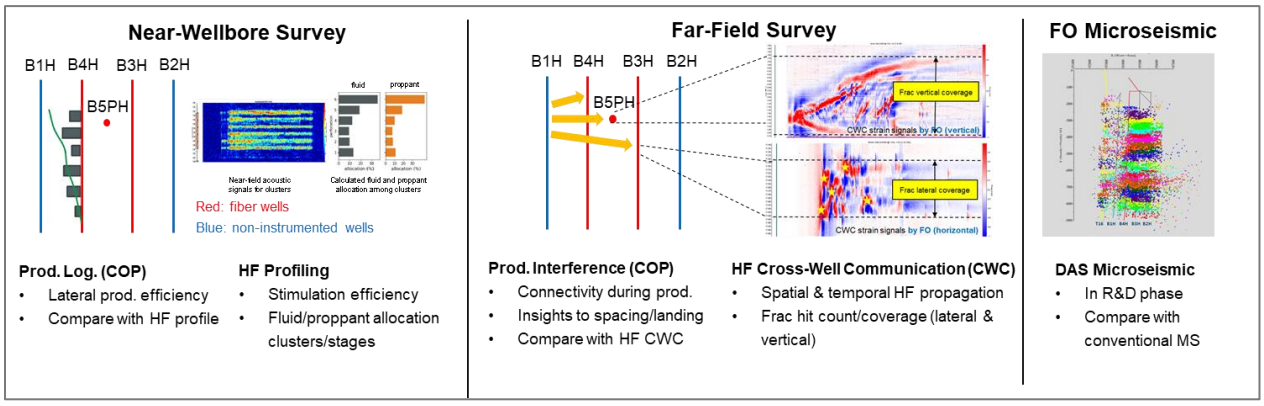

Fig 106—Applications of FO technologies at HFTS-2

What really differentiates HFTS-2 and other programs (e.g., HFTS-1) is the broad applications of advanced FO technologies that were not previously available. The unique design of permanent FO installation on three wells (two horizontal and one vertical) enabled spatial and temporal hydraulic fracturing propagation and depletion monitoring. This is the first known demonstration in the industry that could help characterize SRV and depletion and calibrate subsurface models. Moreover, the tailor-made multi-strand cable allowed FO data acquisition by multiple vendors at the same time for performance and technology comparison. The collaborative nature of HFTS-2 facilitated the sharing of learnings and interpretations regarding the new FO technology among consortium members.

Fig 106 shows the applications of FO technologies at HFTS-2. The red lines and dots represent the fiber wells, and the non-instrumented wells are indicated in blue. Through near-wellbore surveys, Distributed Acoustic Sensing (DAS) and Distributed Temperature Sensing (DTS) data were acquired during the stimulation of two horizontal fiber wells (Boxwood-3H and -4H). The resulting hydraulic fracture profile (i.e., fluid/proppant allocation among perforation clusters; see Fig 107) enabled quantitative assessments of stimulation distribution effectiveness (SDE) of various stimulation schemes (e.g., aggressive/extreme limited entry, tapered perforations, extended stage length) relative to a baseline configuration. A comprehensive analysis is discussed in detail in Zakhour et al., 2021.

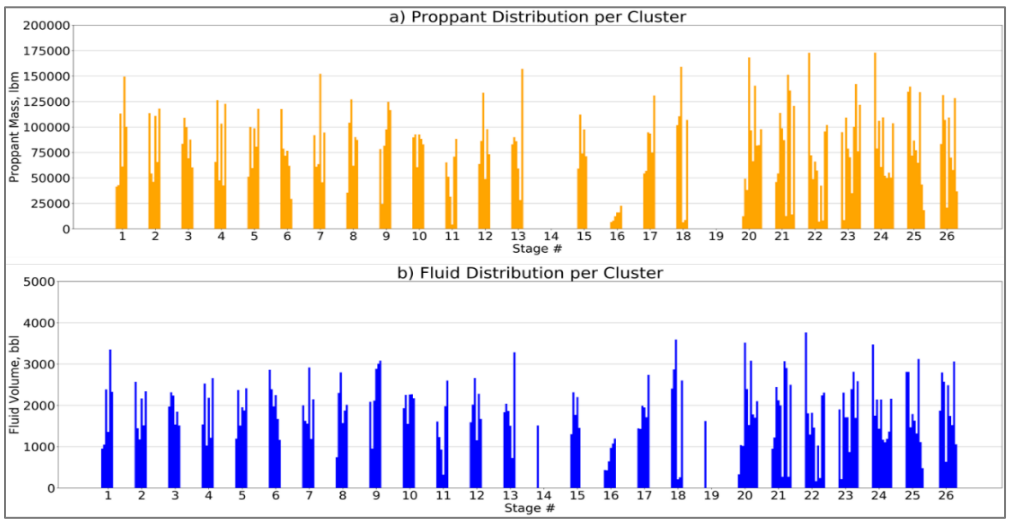

Fig 107—Hydraulic fracture profile (fluid and proppant distribution among perforation clusters) for Boxwood-4H

In Feb. 2020, an FO-based well interference test and production log was conducted for Boxwood-4H based on the proprietary procedure developed by ConocoPhillips (Jin et al., 2019). Through joint inversion of low-frequency DAS and DTS data, a production log at the cluster/stage level was delivered with statistical non-uniqueness considered. The results showed that most stages were active for production, and the heel extended stages appeared to contribute more. During this test and another similar test in Sept. 2020, a new FO-based strain monitoring technique termed DSS-RFS (Distributed Strain Sensing - Rayleigh Frequency Shift), was tested and demonstrated its potential to gain insights on time-dependent fracture property changes in the near-wellbore region. The near-wellbore strain changes based on DSS-RFS data

acquired during two tests over a 7-month period show high consistency and a strong correlation with the near-wellbore DAS acquired during stimulation (see Fig 108), which provides high-resolution and valuable information for fracture property changes after 7 months of production. Moreover, since the shallowest P/T gauges on the Boxwood-5PH and -6S wells were installed near the bottom of the 3rd Bone Spring Sand, the application of DSS-RFS technique on the vertical fiber well Boxwood-5PH in the Sept. 2020 test enables the use of strain depletion profiling as a proxy to understand the vertical depletion better in shallower formations that are not covered by conventional diagnostics during the production phase.

Through far-field surveys, cross-well strain data were acquired using low-frequency DAS (LF-DAS) to monitor response on the fiber wells to activities on the offset wells. This provided a great opportunity to achieve a better understanding of horizontal and vertical fracture propagation characteristics (see Fig 109). During stimulation of offset wells, the frac hits on the horizontal fiber wells were observed and counted, indicating planar fracture propagation in the Wolfcamp formation. Through integrated data analysis with other diagnostics (e.g., MS, image logs, and SRV core), the Shmax orientation is suggested to be 80° for subsurface modeling and reservoir simulation. On the other hand, the strongest strain responses acquired on the vertical fiber well Boxwood-5PH covered vertical strain of more than 2,000 ft from 2nd Bone Spring to the Wolfcamp-B formation for the offset wells landed in Wolfcamp-Y, -A1, and -A2. The cross-well strain on a vertical fiber well is rarely reported in the industry, and the observations from Boxwood-5PH at HFTS-2 indicates that LF-DAS is very sensitive to small strain changes induced by rock deformation and could capture signal response not detectable by other diagnostics (e.g., MS, pressure gauges). Therefore, the vertical coverage of cross-well strain data should be the upper bound on hydraulic fracture height.

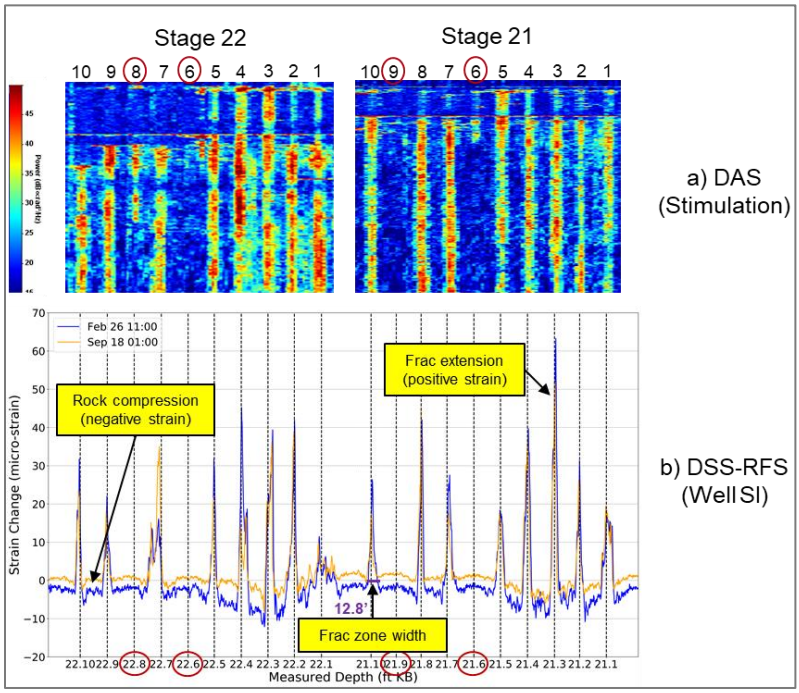

Fig 108—DAS (stimulation) vs. DSS-RFS (well shut in) for Stages 21 and 22 on Boxwood-4H. There is great correlation between the two independent datasets acquired in different stages of the well's life cycle by different vendors. For red-circled clusters that were poorly treated, there was no identifiable positive strain change as the BHP increased.

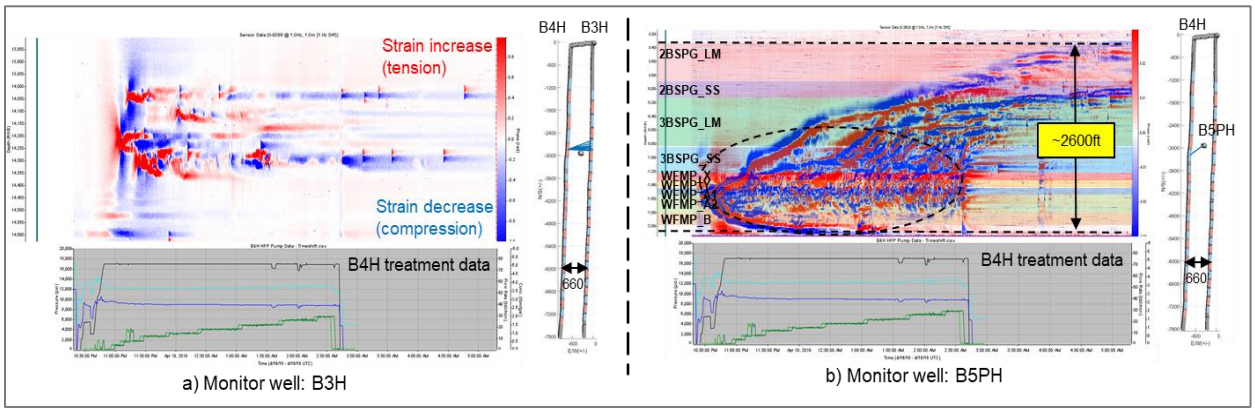

Fig 109—Far-field cross-well strain data on Boxwood-3H and -5PH during treatment of Stage 21 (10 clusters, 20 perforations) on Boxwood-4H

Data Acquisition Highlights

The HFTS-2 consortium acquired and built a comprehensive subsurface dataset to enhance internal workflows and benchmark interpretations. A detailed subsurface characterization of HFTS-2 is discussed in Bessa et al., 2021. Several consortium members collaborated for lab services and joint data analysis. Fig 110 shows that two science wells (Boxwood-5PH and Boxwood-6S) were drilled for acquiring pre- and post-frac data, respectively.

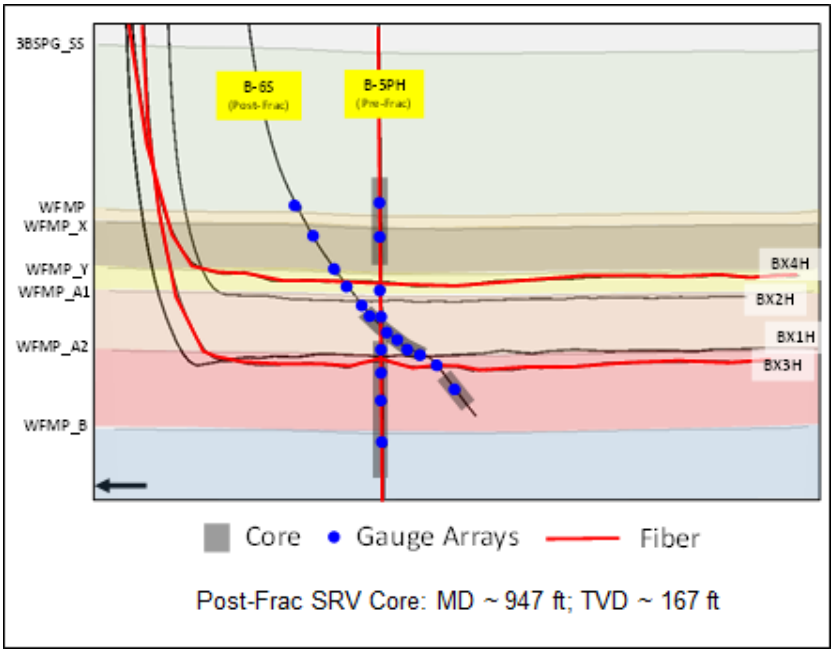

Fig 110—Core, FO, and BHP data acquisition at HFTS-2

About 540 ft of whole core and logs were acquired from the vertical well Boxwood-5PH before the drilling and completion of other Boxwood wells. Special core measurement techniques were used to distinguish rock types, and the well logs provided critical subsurface properties along with other available data sources. Eight P/T gauges were deployed in Boxwood-5PH from the bottom of 3rd Bone Spring to the top of Wolfcamp-B for well stimulation and pressure depletion monitoring.

In the slant well Boxwood-6S, about 950 ft of SRV core was recovered in 9 coring runs with a close approach to the Boxwood-3H wellbore. Several subject matter experts conducted comprehensive core analysis and fracture description. Various types of fractures (hydraulic, natural, drilling-induced, core handling-induced) were counted and analyzed, and the dominant orientation of conductive hydraulic fractures was 80°, which aligned well with other diagnostics (MS, FO, image logs). A more detailed fracture description of the slant core is covered in Gale et al., 2021. There are also 12 P/T gauges in Boxwood-6S from the bottom of the 3rd Bone Spring to the middle of Wolfcamp-A2.

For MS data acquisition, excellent geophone arrays were deployed to detect event locations in all dimensions. The interpretation of the acquired microseismic data was utilized for fracture growth/dimension estimation and workflow blind tests by integrating with other diagnostics.

The conventional MS was also compared with the FO MS to understand the performance of new technology better.

Data Integration and Selected Results

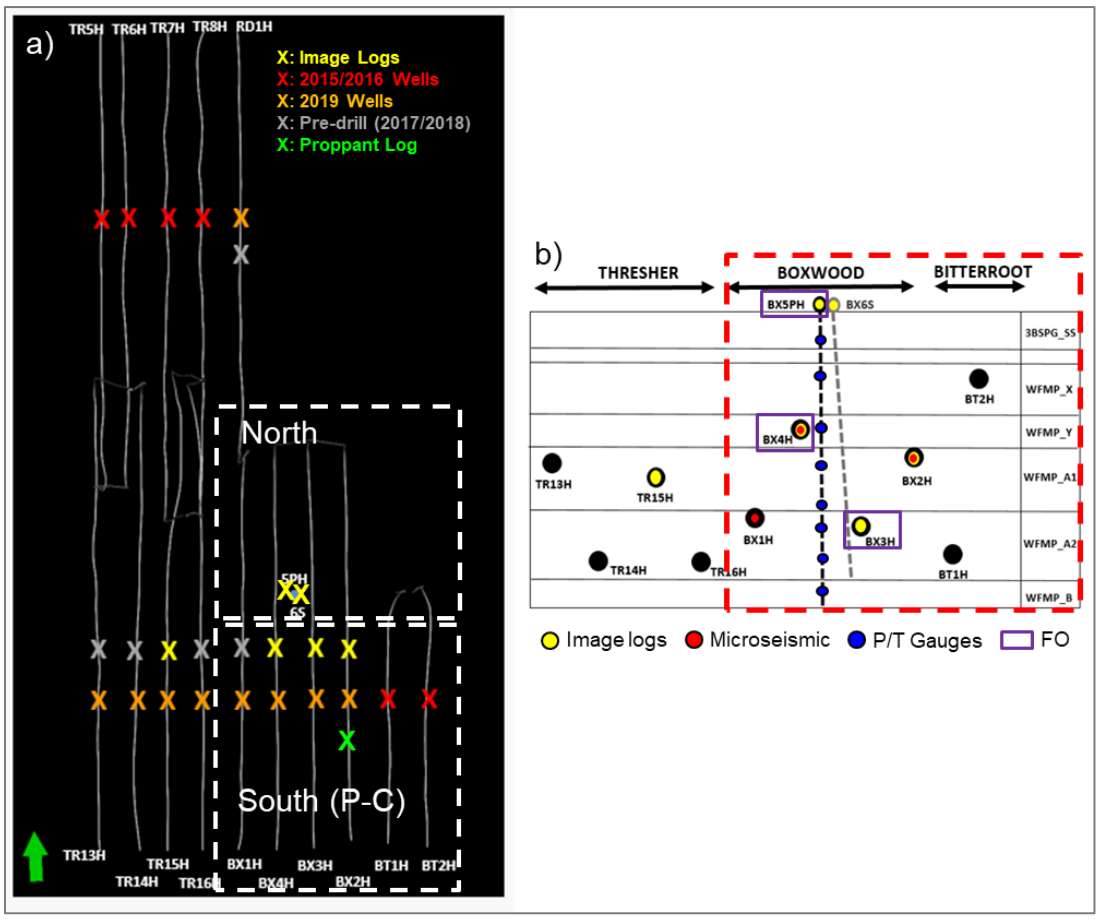

Fig 111—Schematic of the HFTS-2 wells: a) Plan view, b) Gun barrel view

Integration of the comprehensive dataset acquired at HFTS-2 provides a unique opportunity to gain insights on the depletion effect of parent wells on child wells and the corresponding well performance characteristics. Selected results and high-level key takeaways are provided in this section. The analysis and interpretation of the comprehensive HFTS-2 dataset is covered in detail in Pudugramam et al., 2021.

Fig 111 shows the schematic of the HFTS-2 wells. The two red crosses indicate two parent wells that were completed in 2015-2016, and the orange crosses are the wells that were drilled and completed later as part of the HFTS-2 program. The North sector represents the area where the two science wells were drilled and where there is no depletion effect from the parent wells, whereas the South sector is the area with classic parent-child effects.

The extensive dataset enabled the calculation of hydraulic fracture dimensions and helped with the depletion estimation for all the wells. Fig 112a shows the example of Boxwood-2H, which is the nearest child well to the parent wells, to illustrate the areal coverage of hydraulic fractures.

The blue and orange bars represent the westward and eastward fracture half-lengths from diagnostics estimation and simulation results, which indicate a clear eastward fracture growth preference in the South sector for the stages that overlapped the parent wells. The tubing head pressure data on the parent wells also showed strong frac hit responses during the child well stimulation. Even before the stimulation, the image log and proppant log on the Boxwood-2H indicated the effects of hydraulic fractures from the parent wells.

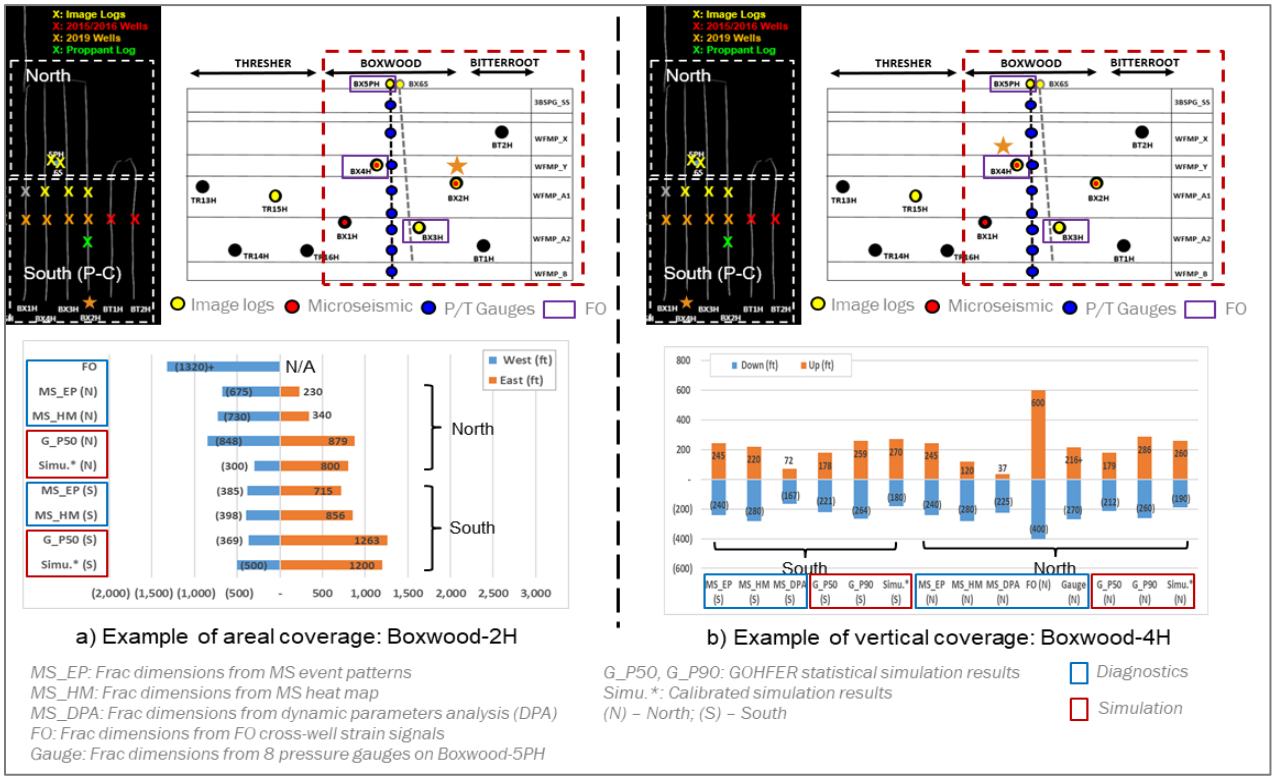

Fig 112—Examples of areal and vertical coverage of the hydraulic fractures

Since there is no depletion effect from the parent wells in the North sector, the MS events showed a westward fracture growth trend for the Boxwood-2H stages, which is probably due to the earlier stimulation effect of Boxwood-1H. Although frac hits were detected on the two fiber wells for all the Boxwood-2H stages during its stimulation, the fewer frac hits detected on the Boxwood-3H for the stages in the South sector than those in the North sector further confirmed the strong depletion effect from the two parent wells in the South sector. The revelation of asymmetric fracture geometry in different areas at HFTS-2 played a key role in subsequent fracture modeling and reservoir simulation. This suggests that a well spacing sensitivity study would be helpful for optimization in other unconventional development projects with parent-child effects.

Fig 112b shows a similar example of Boxwood-4H for the vertical coverage of hydraulic fractures, and the calculations have been done for all the wells. For the pre-frac vertical science well Boxwood-5PH that was drilled in the North sector, both the FO and the eight pressure gauges showed clear frac hits during the stimulation of the four Boxwood child wells. The

strongest pressure gauge response was observed in the 3rd Bone Spring Sand, and the severity decreased towards the Wolfcamp-B. As mentioned previously, FO is very sensitive to small strain changes, and vertical strain response could cover the entire 3rd Bone Spring for child well stimulations.

During the production phase, a large pressure drop was seen from the lower 3rd Bone Spring Sand all the way to the Wolfcamp-A1 based on the pressure gauges (see Fig 113). There was medium pressure depletion in Wolfcamp-A2, but no depletion in Wolfcamp-B. Although there is not much coverage of pressure gauges for shallower formations above the bottom of the 3rd Bone Spring, the strain depletion test using DSS-RFS technology with FO conducted on the Boxwood-5PH well indicated vertical production depletion from the 3rd Bone Spring Sand to the middle Wolfcamp-A2 for all the wells.

During the FO-based well interference test in Feb. 2020, no identifiable flow communication was observed between Boxwood-4H and offset wells based on the analysis of DAS data. The short well shut-in and open durations (hours) made it difficult to interpret the recorded pressure gauge data on Boxwood-5PH and Boxwood-6S. To verify the well connection, a dedicated pressure interference test with longer shut-in and open durations (3-6 days) was conducted on the Boxwood-3H and -4H wells in Sept. 2020. Strong pressure response was observed in four gauges (from Wolfcamp-X to -A2) on the vertical well for the Boxwood-4H shut-in, whereas no identifiable response was seen in pressure gauges on the slant well. For Boxwood-3H shut-in and open activities, eight gauges (from 3rd Bone Spring Sand to Wolfcamp-A2) on the slant well showed strong response.

The rich diagnostics dataset acquired at HFTS-2 provided comprehensive calibration for modeling workflows, and the calibrated models can be used for well performance forecasts, well spacing/landing optimization in primary benches, and depletion study in secondary benches. Regarding the performance characteristics of child wells, Boxwood-2H is the best performer, whereas Boxwood-3H is the worst performer, and Boxwood-1H and -4H have similar performance. This observation is in line with the calibrated model forecast and multiple

contributing factors. For instance, Boxwood-3H had most operational issues during stimulation, while Boxwood-2H had the fewest issues.

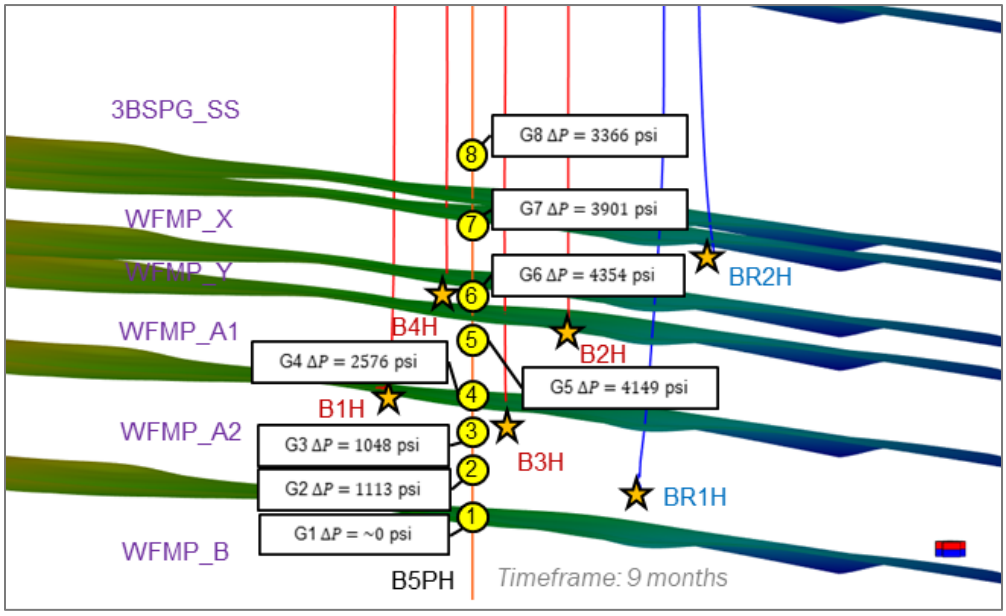

Fig 113—Pressure depletion from gauges on Boxwood-5PH for 9 months of production.

Conclusions

This section presents a high-level summary of key learnings from the HFTS-2 project. The main site-specific takeaways include:

- With the unique design of the three fiber wells, advanced FO technologies (DAS/DTS/DSS-RFS) were tested and demonstrated effective and high-resolution stimulation and production monitoring. FO MS was compared with conventional MS, and its 3D accuracy needs to be further verified.
- Through near-wellbore surveys, the hydraulic fracture profile generated from DAS data enabled quantitative assessments of stimulation distribution effectiveness of various completion designs, and an FO-based production log was obtained using LF-DAS.
- Through far-field surveys, the cross-well strain data during well stimulations indicated planar fracture propagation in the Wolfcamp formation, and the Shmax orientation was

found to be ~80° through integrated data analysis (e.g., FO, MS, image logs, and SRV core).

- The DSS-RFS technology showed the potential to gain insights on time-dependent fracture property changes, and the strain change results aligned well with near-wellbore DAS signals acquired during stimulation.
- Fracture descriptions of the slant core provided a better understanding of geometry and spatial distribution of hydraulic and natural fractures in the SRV.
- Various diagnostics (e.g., FO and MS) and calibrated subsurface models showed a strong depletion effect in the South sector, and there was an eastward fracture growth bias in child wells for stages that overlapped parent wells.
- Areal coverage (half-length) of hydraulic fractures from diagnostics (e.g., MS, FO cross-well strain, pressure gauge responses, image logs) and simulation results indicated connections between child wells during stimulation. Two well interference tests did not show well flow communication, probably due to weak pressure/strain signals and complex subsurface changes during production.
- Vertical coverage of hydraulic fractures during stimulation was monitored using a vertical pilot well. Both FO and the pressure gauges showed clear frac hits during the stimulation of child wells. Vertical strain coverage should be an upper bound of hydraulic fracture. The stronger mechanical strain signals from 3rd Bone Spring Sand to Wolfcamp-B showed good correlation with MS event intensities and geomechanical properties.
- During production, gauges on the two science wells showed a large pressure drop from the lower 3rd Bone Spring Sand to the Wolfcamp-A1. There was medium pressure depletion in Wolfcamp-A2, but no depletion in Wolfcamp-B. This observation is in line with the strain depletion profile obtained using DSS-RFS technology with FO on the vertical well.

Reference List

Agharazi A. and Kashiker S. 2016. What Microseismicity Tells Us About Re-fracturing – An Engineering Approach to Re-fracturing Design. *Hydraulic Fract J,* **3** (1).

Ahmed A., Jared B., Matthew L., et al. 2019. Validating Refrac Effectiveness with Carbon Rod Conveyed Distributed Fiber Optics in the Barnett Shale for Devon Energy. Paper presented at the SPE Hydraulic Fracturing Technology Conference and Exhibition, The Woodlands, Texas. https://doi.org/10.2118/194338-MS.

Alain, K. 2002, Caminicella sporogenes gen. nov., sp. nov., a novel thermophilic spore-forming bacterium isolated from an East-Pacific Rise hydrothermal vent. *International Journal of Systematic and Evolutionary Microbiology*, 52(5): 1621–1628, https://doi.org/10.1099/ijs.0.02142-0.

Amorocho, C., Langford, C. 2020. Characterizing Fractures to Improve Hydraulic Fracturing Efficiency in Shale Reservoirs Through use of an LWD Ultrasonic Imager Designed for Oil-Based Mud Environments. Paper presented at the International Petroleum Technology Conference, Dhahran, Saudi Arabia. https://doi.org/10.2523/IPTC-19845-ABSTRACT.

Baig, A. and Urbancic, T. I. 2010. Microseismic moment tensors: A path to understanding frac growth. *Lead Edge*, **29** (3): 320-324. http://dx.doi.org/ 10.1190/1.3353729.

Bartko, K., Salim, A., Saldungaray, P. et al. 2013. Hydraulic Fracture Geometry Evaluation Using Proppant Detection: Experiences in Saudi Arabia. Paper presented at the SPE Saudi Arabia Section Technical Symposium and Exhibition, Al-Khobar, Saudi Arabia. https://doi.org/10.2118/168094-MS.

Bessa, F., Sahni, V., Liu, S., et al. 2019. Integrated Natural and Hydraulic Fracture Modeling: A Permian Basin Wolfcamp Case Study. Paper presented at the SPE/AAPG/SEG Unconventional Resources Technology Conference, Denver, Colorado.

Bessa, F., Jerath, K., Ginn, C., et al. 2021. Subsurface Characterization of Hydraulic Fracture Test Site-2 (HFTS-2), Delaware Basin. Paper presented at the SPE/AAPG/SEG Unconventional

Resources Technology Conference, Houston, Texas. https://doi.org/10.15530/urtec-2021-5243.

Bolyen, E., Rideout, J. R., Dillon, M. R., et al. 2019. Reproducible, interactive, scalable and extensible microbiome data science using QIIME 2. *Nature Biotechnology*, **37**(8): 852–857. https://doi.org/10.1038/s41587-019-0209-9.

Booker, A. E., Borton, M. A., Daly, R. A., et al. 2017. Sulfide Generation by Dominant Halanaerobium Microorganisms in Hydraulically Fractured Shales. *mSphere*, **2**(4): e00257-17. https://doi.org/10.1128/mSphereDirect.00257-17.

Bourne, S., Hindriks, K., Savitski, A. A. 2021. Inference of Induced Fracture Geometries Using Fiber-Optic Distributed Strain Sensing in Hydraulic Fracture Test Site 2. Paper presented at the SPE/ AAPG/ SEG Unconventional Resources Technology Conference (URTeC). Houston, Texas. https://doi.org/10.15530/urtec-2021-5472.

Campbell, W., Wicker, J., and Courtier, J. 2018. Natural and Hydraulic Fracture Density Prediction and Identification of Controllers. Paper presented at the SPE/AAPG/SEG Unconventional Resources Technology Conference, Houston, Texas. https://doi.org/10.15530/URTEC-2018-2934611.

Caporaso, J. G., Lauber, C. L., Walters, W. A., et al. 2012. Ultra-high-throughput microbial community analysis on the Illumina HiSeq and MiSeq platforms. *The ISME Journal*, **6**(8): 1621–1624. https://doi.org/10.1038/ismej.2012.8.

Carcione, J. M., Cavallini, F. 2002. Poisson's ratio at high pore pressure. *Geophys Prospect*, **50**: 97-106. https://doi.org/10.1046/j.1365-2478.2002.00299.x.

Chiniwala, B., Palakurthi, A. K., Easow, I. et al. 2018. Measurement and Analysis of Wellbore Micro Losses and Rock Properties While Drilling: A Novel Approach to Identification of Fractures in the Osage and Meramec Formations of Anadarko Basin. Paper presented at the SPE/AAPG/SEG Unconventional Resources Technology Conference, Houston, Texas. https://doi.org/10.15530/URTEC-2018-2896976.

Ciezobka, J., Maity D., Salehi I. 2016. Variable Pump Rate Fracturing Leads to Improved Production in the Marcellus Shale. Paper presented at SPE Hydraulic Fracturing Technology Conference and Exhibition, The Woodlands, Texas. https://doi.org/10.2118/179107-MS.

Ciezobka, J., Courtier, J., and Wicker, J. 2018. Hydraulic Fracturing Test Site (HFTS) – Project Overview and Summary of Results. Paper presented at the SPE/ AAPG/ SEG Unconventional Resources Technology Conference, Houston, Texas. http://doi.org/10.15530/urtec-2018-2937168.

Ciezobka, J. 2021. Overview of Hydraulic Fracturing Test Site 2 in the Permian Delaware Basin (HFTS-2). Paper presented at the SPE/ AAPG/ SEG Unconventional Resources Technology Conference (URTeC). Houston, Texas. https:// doi.org/10/15530/urtec-2021-5514.

Cipolla, C. L., Weng, X., Mack, M. G., et al. 2011. Integrating Microseismic Mapping and Complex Fracture Modeling to Characterize Hydraulic Fracture Complexity. Paper presented at the SPE Hydraulic Fracturing Technology Conference, The Woodlands, Texas. https://doi.org/10.2118/140185-MS.

Cuthill, D., Yang, W., Hardesty, J. 2017. Improved Hydraulic Fracturing Perforation Efficiency Observed with Constant Entry Hole and Constant Penetration Perforating System. Paper presented at the SPE Hydraulic Fracturing Technology Conference and Exhibition, The Woodlands, Texas. https://doi.org/10.2118/184878-MS.

Craig, D. P., Hoang, T., Li, H. et al. 2021. Defining Hydraulic Fracture Geometry Using Image Logs Recorded in the Laterals of Horizontal Infill Wells. Paper presented at the SPE/ AAPG/ SEG Unconventional Resources Technology Conference (URTeC). Houston, Texas. https:// doi.org/10.15530/urtec-2021-5031.

Daly, R. A., Borton, M. A., Wilkins, M. J., et al. 2016. Microbial metabolisms in a 2.5-km-deep ecosystem created by hydraulic fracturing in shales: *Nat Microbiol*, **1**:16146, https://doi.org/10.1038/nmicrobiol.2016.146.

Du, S., Shi Y., Guan P., Zhang Y. 2016. New inspiration on effective development of tight reservoir in secondary exploitation by using rock mechanics method. *Energy Explor*, **34**(1): 3-18. https://doi.org/10.1177/0144598715623661.

Elliott, S. J., and Gale, J. F. W. 2018. Analysis and distribution of proppant recovered from fracture faces in the HFTS slant core drilled through a stimulated reservoir. Paper presented at the SPE/AAPG/SEG Unconventional Resources Technology Conference, Houston, Texas. https://doi.org/10.15530/urtec-2018-2902629.

Forand, D., Heesakkers, V., & Schwartz, K. 2017. Constraints on natural fracture and in-situ trends of unconventional reservoirs in the Permian Basin, Paper presented at SPE/AAPG/SEG Unconventional Resources Technology Conference, Austin, TX.

Frequently Asked Questions (FAQs) - U.S. Energy Information Administration (EIA), n.d.: <https://www.eia.gov/tools/faqs/faq.php>.

Gale, J. F. W., Laubach, S. E., Olson, J. E., et al. 2014. Natural fractures in shale: A review and new observations. *AAPG Bulletin*, **98**11): 2165-2216.

Gale, J. F. W., Elliott, S. J., Laubach, S. E. 2018. Hydraulic fractures in core from stimulated reservoirs: core fracture description of HFTS slant core, Midland Basin, West Texas. Paper presented at the SPE/AAPG/SEG Unconventional Resources Technology Conference, Houston, Texas. https://doi.org/10.15530/urtec-2018-2902624.

Gale, J. F. W., Elliott, S. J., Li, J. Z., et al. 2019. Natural fracture characterization in the Wolfcamp Formation at the Hydraulic Fracture Test Site (HFTS), Midland Basin, Texas. Paper presented at the SPE/AAPG/SEG Unconventional Resources Technology Conference (URTeC), Denver, Colorado. https://doi.org/10.15530/urtec-2019-644.

Gale, J. F. W., Elliott, S. J. Rysak, B. G., et al. 2021. Fracture Description of the HFTS-2 Slant Core, Delaware Basin, West Texas. Paper presented at the SPE/AAPG/SEG Unconventional Resources Technology Conference, Houston, Texas. https://doi.org/10.15530/urtec-2021-5175.

Ginn, C. L., Wilkins, S. J., and Liu, X. 2017. Fracture Characteristics of the Wolfcamp Formation, Delaware Basin, TX. AAPG Search and Discovery Article #90291. Paper presented at AAPG Annual Convention and Exhibition, Houston, Texas.

Glenn D., Sagar K., Elizabeth T., et al. 2019. Third Generation Production Logging Technologies Enhance Inflow Profiling in Deepwater Gulf of Mexico Reservoirs. Paper presented at the SPE Annual Technical Conference and Exhibition, Calgary, Alberta, Canada. https://doi.org/10.2118/196188-MS.

Grechka, V., Howell, B., Li, Z. et al. 2021. Microseismic at HFTS2: A Story of Three Stimulated Wells. Paper presented at the SPE/ AAPG/ SEG Unconventional Resources Technology Conference (URTeC). Houston, Texas. https://doi.org/10.15530/urtec-2021-5517.

Halleck, P. M., Robins, J., Pekot, L., et al. 1998. Mechanical Damage Caused by Perforations May Affect Fracture Breakdown. Paper presented at the SPE Eastern Regional Meeting, Pittsburg, Pennsylvania. https://doi.org/10.2118/51051-MS.

Hills, J. M. 1984. Sedimentation, tectonism, and hydrocarbon generation in Delaware basin, West Texas and southeastern New Mexico. *AAPG Bulletin*, **68**: 250–267.

Hu Y., Deng, H., Wang, W., et al. 2016. Influence of Moisture Content and Stress Cyclic Loading Amplitude on the Dynamic Characteristics of Sandstone. *Electron J Geotech Eng*, **21**(15): 4857-4871.

Huckabee, P., Ugueto, G., Haustveit, K., et al. 2022. Completions and Stimulation Experimental Design, Execution, Analysis & Application for the Permian Delaware Basin Hydraulic Fracture Test Site 2. Paper presented at the SPE Hydraulic Fracturing Technology Conference and Exhibition (HFTC). The Woodlands, Texas. https://doi.org/10.2118/209172-MS.

Hull, R., Woerpel, C., Trujillo, K., et al. 2020. Hydraulic fracture characterization using fiber optic DAS and DTS data. Paper presented at the SEG Annual Conference and Exhibition, virtual. https://doi.org/10.1190/segam2020-3425789.1.

Jiang, C., Liu, T., Zhang, D., et al. 2018. An experimental study of deformation and fracture characteristics of shale with pore-water pressure and under triaxial cyclic loading. *R Soc Open Sci*, **5**(8): 180670. https://doi.org/10.1098/rsos.180670.

Jin, G., Friehauf, K., Roy, B. et al. 2019. Fiber Optic Sensing-Based Production Logging Methods for Low-Rate Oil Producers. Paper presented at the SPE/AAPG/SEG Unconventional Resources Technology Conference, Denver, Colorado. https://doi.org/10.15530/urtec-2019-943.

Jin, G., Ugueto, G., Wojtaszek, M. et al. 2021. Novel Near-Wellbore Fracture Diagnosis for Unconventional Wells Using High-Resolution Distributed Strain Sensing during Production. *SPE J*, 1-10. https://doi.org/10.2118/205394-PA.

Kamal, M. S., Hussein, I., Mahmoud, M., et al. 2018. Oilfield scale formation and chemical removal: A review. *Journal of Petroleum Science and Engineering*, **171**: 127–139, https://doi.org/10.1016/j.petrol.2018.07.037.

King, G. E., Leonard, D. 2011. Utilizing Fluid and Proppant Tracer Results to Analyze Multi-Fractured Well Flow Back in Shales: A Framework for Optimizing Fracture Design and Application. Paper presented at the SPE Hydraulic Fracturing Technology Conference, The Woodlands, Texas. https://doi.org/10.2118/140105-MS.

Kishida, K., Yamauchi, Y., and Guzik, A. 2014. Study of Optical Fibers Strain-Temperature Sensitivities Using Hybrid Brillouin-Rayleigh System. *Photonic Sens* **4**(1): 1–11. https://doi.org/10.1007/s13320-013-0136-1.

Kvale, E. P., Bowie, C. M., Flenthrope, C., et al. 2020. Facies variability within a mixed carbonate-siliciclastic sea-floor fan (upper Wolfcamp formation, Permian, Delaware Basin, New Mexico). *AAPG Bulletin*, **104**: 525-563.

Lacazette, A., Dershowitz, W., & Vermilye, J. 2014. Geomechanical and Flow Simulation of Hydraulic Fractures Using High-Resolution Passive Seismic Images. Paper presented at the SPE/ AAPG/ SEG Unconventional Resources Technology Conference (URTeC). Denver, Colorado. https://doi.org/10.15530/urtec-2014-1935092.

Li, Y., Chen, X., Zhao, Z., et al. 2018. Influence of perforation erosion on multiple growing hydraulic fractures in multi-stage fracturing. *Nat Gas Ind B,* **5**(1): 8-15. https://doi.org/10.1016/j.ngib.2017.11.002.

Liang, R., Davidova, I. A., Marks, C. R., et al. 2016. Metabolic Capability of a Predominant Halanaerobium sp. in Hydraulically Fractured Gas Wells and Its Implication in Pipeline Corrosion. *Frontiers in Microbiology*, **7**. https://doi.org/10.3389/fmicb.2016.00988.

Lin, M. L., Jeng, F., Tsai, L., et al. 2005. Wetting weakening of tertiary sandstones - microscopic mechanism. *Environ*, **48**(2): 265-275. https://doi.org/10.1007/s00254-005-1318-y.

Lindsay, G., Miller, G., Xu, T. et al. 2018. Production Performance of Infill Horizontal Wells vs. Pre-Existing Wells in the Major US Unconventional Basins. Paper presented at the SPE Hydraulic Fracturing Technology Conference, The Woodlands, Texas. https://doi.org/10.2118/189875-MS.

Lipus, D., Vikram, A., Ross, D., et al. 2017. Predominance and Metabolic Potential of Halanaerobium spp. in Produced Water from Hydraulically Fractured Marcellus Shale Wells. *Applied and Environmental Microbiology*, **83**(8): e02659-16. https://doi.org/10.1128/AEM.02659-16.

Liu, Y., Li, Y., Li, Q. et al. 2015. Micro- to Nanoscale Morphologies and Chemical Components of Soils Investigated by SEM-EDS for Forensic Science. *J Chem*, **4** :1-5. http://dx.doi.org/10.1155/2015/734560.

Liu, J., Zhang, F., Gardner, R. P. 2015. A method to evaluate hydraulic fracture using proppant detection. *Appl Radiat Isot*, 105:139-143. https://doi.org/10.1016/j.apradiso.2015.08.003.

Liu, L., Li L., Elsworth D., et al. 2018. The Impact of Oriented Perforations on Fracture Propagation and Complexity in Hydraulic Fracturing. *Processes*, **6**(11): 213. https://doi.org/10.3390/pr6110213.

Liu, Y., Jin, G., Wu, K. 2021. New Insights on Near-Wellbore Fracture Characteristics from High-Resolution Distributed Strain Sensing Measurements. Paper Presented at Unconventional Resources Technology Conference, Houston, Texas. https://doi.org/10.15530/urtec-2021-5436.

Ma, X., Zoback, M. D. 2017. Lithology-controlled stress variations and pad-scale faults: A case study of hydraulic fracturing in the Woodford Shale, Oklahoma. *Geophys*, **82** (6): ID35-ID44. https://doi.org/10.1190/GEO2017-0044.1.

Maity, D., Ciezobka, J. and Eisenlord, S. 2018. Assessment of In-situ Proppant Placement in SRV Using Through-Fracture Core Sampling at HFTS. Paper presented at the SPE/ AAPG/ SEG Unconventional Resources Technology Conference (URTeC). Houston, Texas. http://dx.doi.org/10.15530/urtec-2018-2902364.

Maity, D. 2018. Microseismicity Analysis for HFTS Pad and Correlation with Completion Parameters. Paper presented at the SPE/ AAPG/ SEG Unconventional Resources Technology Conference (URTeC). Houston, Texas. https://doi.org/10.15530/URTEC-2018-2902355.

Maity, D. and Ciezobka, J. 2019a. Designing a robust proppant detection and classification workflow using machine learning for subsurface fractured rock samples post hydraulic fracturing operations. *J Petrol Sci Eng*, **172** :588-606. http://dx.doi.org/10.1016/j.petrol.2018.09.062.

Maity, D. and Ciezobka, J. 2019b. An interpretation of proppant transport within the stimulated rock volume at the hydraulic-fracturing test site in the Permian Basin. *SPE Res Eval & Eng*, **22** (2): 477-491. http://dx.doi.org/10.2118/194496-PA.

Maity, D. and Ciezobka, J. 2020. A data analytics framework for cored fracture imaging and novel characterization workflow – Application on samples from Hydraulic Fracturing Test Site (HFTS) in the Midland Basin. Paper presented at the Hydraulic Fracturing Technology Conference (HFTC). The Woodlands, Texas. http://dx.doi.org/10.2118/199754-MS.

Maity, D., Ciezobka, J. 2021a. Digital Fracture Characterization at Hydraulic Fracturing Test Site HFTS-Midland: Fracture Clustering, Stress Effects and Lithologic Controls. Paper presented at the SPE Hydraulic Fracturing Technology Conference, Virtual. https://doi.org/10.2118/204174-MS.

Maity, D., Ciezobka, J. 2021b. A Systematic Interpretation of Subsurface Proppant Concentration from Drilling Mud Returns: Case Study from Hydraulic Fracturing Test Site (HFTS-2) in Delaware Basin. Paper presented at the SPE/AAPG/SEG Unconventional Resources Technology Conference, Houston, Texas. https://doi.org/10.15530/urtec-2021-5189.

Maity, D., Ciezobka, J. 2021c. Diagnostic assessment of reservoir response to fracturing: a case study from Hydraulic Fracturing Test Site (HFTS) in Midland Basin. *J Pet Explor Prod Technol*, **11**: 3177-3192. https://doi.org/10.1007/s13202-021-01234-x.

Maity, D. and Ciezobka, J. 2022. Novel Proppant Logging Technique for Infill Drilling of Unconventional Shale Wells. *SPE Res Eval & Eng*., 1-14. https://doi.org/10.2118/209790-PA.

Massaras, L. V., Dragomir, A., Chiriac, D. 2007. Enhanced Fracture Entry Friction Analysis of the Rate Step-Down Test. Paper presented at the SPE Hydraulic Fracturing Technology Conference, College Station, Texas. https://doi.org/10.2118/106058-MS.

Matthew Lawrence and Ahmed Attia (2021). "Comparing and Combining Camera, Tracer and Distributed Temperature and Acoustic Sensing DAS+DTS for a Holistic Understanding of Stimulation and Production Performance". DOI: 10.2118/204188-MS

Maxwell, S. C., Cipolla, C. 2011. What Does Microseismicity Tell Us About Hydraulic Fracturing? Paper presented at the SPE Annual Technical Conference and Exhibition, Denver, Colorado. https://doi.org/10.2118/146932-MS.

Mayerhofer, M., Lolon, E., Warpinski, N., et al. 2008. What is Stimulated Rock Volume?. Paper presented at the SPE Shale Gas Production Conference, Fort Worth, Texas. https://doi.org/10.2118/119890-MS.

Miller, C. K., Waters, G. A., & Rylander, E. I. 2011. Evaluation of Production Log Data from Horizontal Wells Drilled in Organic Shales. Paper presented at the North American Unconventional Gas Conference and Exhibition, The Woodlands, Texas. https://doi.org/10.2118/144326-MS.

Newsham, K., Comisky, J., Chemali, R. 2019. Tutorial: Organic Mudstone Petrophysics, Part 1: Workflow to Estimate Storage Capacity, *Petrophysics - The SPWLA Journal of Formation Evaluation and Reservoir Description*, **60**(1): 4–15. https://doi.org/10.30632/PJV60N1-2019t1.

Newsham, K., Comisky, J., Chemali, R. 2019. Tutorial: Organic Mudstone Petrophysics, Part 2: Workflow to Estimate Storage Capacity, *Petrophysics - The SPWLA Journal of Formation Evaluation and Reservoir Description,* **60**(2): 181–207. https://doi.org/10.30632/PJV60N2-2019t1.

Newsham, K., Comisky, J., Chemali, R. 2019. Tutorial: Organic Mudstone Petrophysics, Part 3: Workflow to Estimate Storage Capacity, *Petrophysics - The SPWLA Journal of Formation Evaluation and Reservoir Description,* **60**(2): 351–371. https://doi.org/10.30632/PJV60N3-2019t1.

Nielsen, M. B., Kjeldsen, K. U., & Ingvorsen, K. 2006. Desulfitibacter alkalitolerans gen. nov., sp. nov., an anaerobic, alkalitolerant, sulfite-reducing bacterium isolated from a district heating plant. International *Journal of Systematic and Evolutionary Microbiology*, **56**(12): 2831–2836. https://doi.org/10.1099/ijs.0.64356-0.

Offenberger, R., Ball, N., Kanneganti, K. et al. 2013. Integration of Natural and Hydraulic Fracture Network Modeling with Reservoir Simulation for an Eagle Ford Well. Paper presented at the SPE/ AAPG/ SEG Unconventional Resources Technology Conference (URTeC). Denver, Colorado. https://doi.org/10.1190/urtec2013-049.

Osselin, F., Saad, S., Nightingale, M., et al. 2019. Geochemical and sulfate isotopic evolution of flowback and produced waters reveals water-rock interactions following hydraulic fracturing of a tight hydrocarbon reservoir. *Science of The Total Environment*, **687**: 1389–1400. https://doi.org/10.1016/j.scitotenv.2019.07.066.

Pakhotina, J., Zhu, D., Hill, A. D. 2020. Evaluating Perforation Erosion and its Effect on Limited Entry by Distributed Acoustic Sensor DAS Monitoring. Paper presented at the SPE Annual Technical Conference and Exhibition. https://doi.org/10.2118/201538-MS.

Palisch, T., Al-Tailji, W., Bartel, L. et al. 2017. Far-Field Proppant Detection Using Electromagnetic Methods – Latest Field Results. Paper presented at the SPE Hydraulic Fracturing Technology Conference (HFTC), The Woodlands, Texas. https://doi.org/10.2118/184880-MS.

Pankaj, P., Morrell, J. C., Pope, T., et al. 2018. Introducing Hydraulic Fracture Heat Maps: Deriving Completion Changes to Increase Production in the Wolfcamp Formation. Paper presented at the SPE Annual Technical Conference and Exhibition, Dallas, Texas. https://doi.org/10.2118/191442-MS.

Pellet, F. L., Selvadurai, A. P. S. 2016. Rock damage mechanics, Chapter 3 in Rock Mechanics and Engineering (65-107). Boca Raton, Florida. CRC Press. https://doi.org/10.1201/b20273-4.

Perfetto, R., Saldungaray, P., Martocchia, F. et al. 2013. Fracture Optimization Applying a Novel Traceable Proppant and a Refined Mechanical Earth Model in the Congo Onshore. Paper presented at the International Petroleum Technology Conference, Beijing, China. https://doi.org/10.2523/IPTC-16581-MS.

Pudugramam, S., Zhao, Y., Bessa, F., et al. 2021. Analysis and Integration of the Hydraulic Fracturing Test Site-2 (HFTS-2) Comprehensive Dataset. Paper presented at SPE/SEG/AAPG Unconventional Resources Technology Conference, Houston, Texas.

Reid, A., Reid, S. A. T., Walker, D. A., et al. 1995. Practical applications of sea level fluctuations, paleontology, paleogeography and environment of deposition applied to the search for small (but numerous) stratigraphic traps. Carbonate Facies and Sequence Stratigraphy: Practical Applications of Carbonate Models. *PBS-SEPM Publication* **95**(36): 81-82.

Rezaei, A., Dindoruk, B., Soliman, M. Y. 2019. On parameters affecting the propagation of hydraulic fractures from infill wells. *J Petrol Sci Eng*, **183** :106255. https://doi.org/10.1016/j.petrol.2019.106255.

Richter, P., Parker, T., Woerpel, C., et al. (2019). Hydraulic fracture monitoring and optimization in unconventional completions using a high-resolution engineered fibre-optic Distributed Acoustic Sensor. *First Break*, **37**(4): 63-68. https://doi.org/10.3997/1365-2397.n0021.

Rizon, M., Yazid, H., Saad, P. et al. 2005. Object Detection using Circular Hough Transform. *Am J Appl Sci*, **2** (12): 1606-1609. https://doi.org/10.3844/ajassp.2005.1606.1609.

Robinson, S., Littleford, T., Luu, T., et al. 2020. Acoustic Imaging of Perforation Erosion in Hydraulically Fractured Wells for Optimizing Cluster Efficiency. Paper presented at the SPE Hydraulic Fracturing Technology Conference and Exhibition, The Woodlands, Texas. https://doi.org/10.2118/199718-MS.

Roussel, N., Swan, H., Snyder, J. et al. 2021. Evaluation and Insights from Instantaneous Shut-in Pressures. Paper presented at the SPE/ AAPG/ SEG Unconventional Resources Technology Conference (URTeC). Houston, Texas. https://doi.org/10.15530/urtec-2021-5681.

Sahni, V., Zhao, Y., Pudugramam, S., Liu, S. 2021. Key Learnings from Hydraulic Fracturing Test Site - 2 (HFTS-2), Delaware Basin. Paper presented at the SPE/ AAPG/ SEG Unconventional Resources Technology Conference, Houston, Texas. https://doi.org/10.15530/urtec-2021-5229.

Savitski A. 2020. On a poroelastic nature of multi-stranded hydraulic fractures in heterogeneous Unconventional rocks. Paper presented at the 54th U.S. Rock Mechanics/Geomechanics Symposium.

Sileny, J., Hill, D. P., Eisner, L. et al. 2009. Non-double-couple mechanisms of earthquakes induced by hydraulic fracturing. *J Geophys Res*, **114**: B08307. https://doi.org/10.1029/2008JB005987.

Snyder, J., Cramer, D., White, M. 2021. Improved Treatment Distribution Through Oriented Perforating. Paper presented at the SPE Hydraulic Fracturing Technology Conference and Exhibition, The Woodlands, Texas. https://doi.org/10.2118/204203-MS.

Shahri, M., Tucker, A., Rice, C., et al. 2021. High Fidelity Fiber-Optic Observations and Resultant Fracture Modeling in Support of Planarity. Paper presented at the SPE Hydraulic Fracturing Technology Conference and Exhibition. https://doi.org/10.2118/204172-MS.

Stegent, N. A., Ferguson, K., Spencer, J. 2011. Comparison of Frac Valves vs. Plug-and-Perf Completion in the Oil Segment of the Eagle Ford Shale: A Case Study. Paper presented at

the Canadian Unconventional Resources Conference, Calgary, Alberta. https://doi.org/10.2118/148642-MS.

Stegent, N., & Candler, C. 2018. Downahole Microseismic Mapping of More Than 400 Fracturing Stages on a Multi-well Pad at the Hydraulic Fracturing Test Site (HFTS): Discussion of Operational Challenges and Analytic Results. Paper presented at the SPE/SEG/AAPG Unconventional Resources Technology Conference, Houston, Texas. https://doi.org/10.15530/URTEC-2018-2902311.

Stipanicev, M., Turcu, F., Esnault, L. et al. 2014. Corrosion of carbon steel by bacteria from North Sea offshore seawater injection systems: Laboratory investigation: *Bioelectrochemistry*, **97**: 76–88. https://doi.org/10.1016/j.bioelechem.2013.09.006.

Tatar, A. 2018. Microbial Enhanced Oil Recovery, in Fundamentals of Enhanced Oil and Gas Recovery from Conventional and Unconventional Reservoirs: *Elsevier*, 291–508. https://doi.org/10.1016/B978-0-12-813027-8.00010-2.

Thiercelin, M. J., & Plumb, R. A. 1994. Core-Based Prediction of Lithologic Stress Contrasts in East Texas Formations. *SPE Formation Evaluation*, **9**: 251-258. https://doi.org/10.2118/21847-PA.

Tinker, K., Gardiner, J., Lipus, D., et al. 2020. Geochemistry and Microbiology Predict Environmental Niches With Conditions Favoring Potential Microbial Activity in the Bakken Shale. *Frontiers in Microbiology*, **11**: 1781. https://doi.org/10.3389/fmicb.2020.01781.

Tinker, K., Lipus, D., Sarkar, P., et al. 2020. The Geochemistry and Microbial Ecology of Produced Waters from Three Different Unconventional Oil and Gas Regions. Paper presented at the Unconventional Resources Technology Conference, Houston, Texas. doi:10.15530/urtec-2020-2979.

Trowbridge, S., Wicker, J., Courtier, J., et al. 2017. Application of Microseismic to Assess Hydraulic Fracture Behavior in Relation to Completion Design and Landing Zone. Paper presented

at the Unconventional Resources Technology Conference, Houston, Texas. https://doi.org/10.15530/urtec-2017-2674376.

Ugueto C. G. A., Wojtaszek, M., Huckabee, P. T. et al. 2018. Accelerated Stimulation Optimization via Permanent and Continuous Production Monitoring Using Fiber Optic. Paper presented at the SPE/AAPG/SEG Unconventional Resources Technology Conference, Houston, Texas. https://doi.org/10.15530/urtec-2018-2901897.

Ugueto, G., Huckabee, P., Wojtaszek, M. et al. 2019. New Near-Wellbore Insights from Fiber Optics and Downhole Pressure Gauge Data. Paper presented at the SPE Hydraulic Fracturing Technology Conference and Exhibition, The Woodlands, Texas. https://doi.org/10.2118/194371-MS.

Ugueto, G. A., Todea, F., Daredia, T., et al. 2019. Can You Feel the Strain? DAS Strain Fronts for Fracture Geometry in the BC Montney, Groundbirch. Paper presented at the SPE Annual Technical Conference and Exhibition, Calgary, Alberta, Canada. https://doi.org/10.2118/195943-MS.

Ugueto, G. A., Wojtaszek, M., Mondal, S., et al. 2021. New Fracture Diagnostic Tool for Unconventionals: High-Resolution Distributed Strain Sensing via Rayleigh Frequency Shift during Production in Hydraulic Fracture Test 2. Paper presented at the SPE/AAPG/SEG Unconventional Resources Technology Conference, Houston, Texas. https://doi.org/10.15530/urtec-2021-5408.

Wang, I. H., Fairfield, R., Courtier, J., et al. 2018. Using Stage Level Microseismic Analysis to Gain Insight into Fracture Efficiency and Completion Effectiveness. Paper presented at the SPE/AAPG/SEG Unconventional Resources Technology Conference, Houston, Texas.

Warpinski, N. R., Mayerhofer, M. J., Agarwal, K., Du, J. 2013. Hydraulic-Fracture Geomechanics and Microseismic-Source Mechanisms. *SPE J*, **18** (04): 766-780. https://doi.org/10.2118/158935-PA.

Warpinski, N., & Wolhart, S. 2016. A Validation Assessment of Microseismic Monitoring. Paper presented at the SPE Hydraulic Fracturing Technology Conference, The Woodlands, Texas. https://doi.org/10.2118/179150-MS.

Waters G., Weng X. (2016). The Impact of Geomechanics and Perforations on Hydraulic Fracture Initiation and Complexity in Horizontal Well Completions. Presented at the SPE Annual Technical Conference and Exhibition, Dubai, UAE. https://doi.org/10.2118/181684-MS.

Webster, P., Cox, B., and Molenaar, M. 2013. Developments in Diagnostic Tools for Hydraulic Fracture Geometry Analysis. Paper presented at the SPE/AAPG/SEG Unconventional Resources Technology Conference, Denver, Colorado. https://doi.org/10.1190/urtec2013-025.

Weng, X., Kresse, O., Cohen, C. E., et al. 2011. Modeling of Hydraulic Fracture Network Propagation in a Naturally Fractured Formation. *SPE Prod & Oper*, **26**(4): 368–380. https://doi.org/10.2118/140253-PA.

Wu, K., Liu, Y., Jin, G., et al. 2021. Fracture Hits and Hydraulic-Fracture Geometry Characterization Using Low-Frequency Distributed Acoustic Sensing Strain Data. *J Pet Technol*.

Wu, Y., Hull, R., Tucker, A., et al. 2021. Hydraulic Fracturing Diagnostics Utilizing Near and Far-Field Distributed Acoustic Sensing DAS Data Correspondences. Paper presented at the SPE Hydraulic Fracturing Technology Conference and Exhibition. https://doi.org/10.2118/204205-MS

Wu, Y., Richter P, Hull, R., et al. 2020. Hydraulic Frac-Hit Corridor (FHC) Monitoring and Analysis with High-Resolution Distributed Acoustic Sensing (DAS) and Far-Field Strain (FFS) Measurements. *First Break*, **38**(6): 65–70. https://doi.org/10.3997/1365-2397.fb2020045.

Wood, T., Leonard, R., Senters, C., et al. 2018. Interwell Communication Study of UWC and MWC Wells in the HFTS. Paper presented at the SPE/AAPG/SEG Unconventional Resources Technology Conference, Houston, Texas. https://doi.org/10.15530/URTEC-2018-2902960.

Xu, W., Le Calvez, J. H., & Thiercelin, M. J. 2009. Characterization of Hydraulically-Induced Fracture Network Using Treatment and Microseismic Data in a Tight-Gas Sand Formation: A

Geomechanical Approach. Paper presented at the SPE Tight Gas Completions Conference, San Antonio, Texas. https://doi.org/10.2118/125237-MS.

Zakhour, N., Jones, M., Zhao, Y. et al. 2021. HFTS-2 Completions Design and State-of-the-Art Diagnostics Results. Paper presented at the SPE/ AAPG/ SEG Unconventional Resources Technology Conference (URTeC). Houston, Texas. https://doi.org/10.15530/urtec-2021-5242.

Zhang, D., Gamage, R. P., Perera, M. S. A., et al. 2017. Influence of Water Saturation on the Mechanical Behavior of Low-Permeability Reservoir Rocks. *Energies*, **10**: 236. https://doi.org/10.3390/en10020236.

Zhang, Z., Fang, Z., Stefani, J. et al. 2020. Modeling of Fiber Optic Strain Responses to Hydraulic Fracturing. *Geophys*, **85** (6): 1-22. http://dx.doi.org/10.1190/geo2020-0083.1.

Zhao, B., Panthi, K., Mohanty, K. 2019. Tracer Eluting Proppants for Shale Fracturing. Paper presented at the SPE/AAPG/SEG Unconventional Resources Technology Conference, Denver, Colorado. https://doi.org/10.15530/urtec-2019-478.

Zhao, Y., Bessa, F., Sahni, V. et al. 2021. Key Learnings from Hydraulic Fracturing Test Site - 2 (HFTS-2), Delaware Basin. Paper presented at the SPE/ AAPG/ SEG Unconventional Resources Technology Conference, Houston, Texas. https://doi.org/10.15530/urtec-2021-5229.

Zhou, Z., Cai, X., Zhao, Y., et al. 2016. Strength characteristics of dry and saturated rock at different strain rates. *T Nonferr Metal Soc*, **26**(7): 1919-1925. https://doi.org/10.1016/S1003-6326(16)64314-5.

Appendix A: Microseismics at HFTS2: A Story of Three Stimulated Wells

Authors: Vladimir Grechka, Bo Howell, Zhao Li, et al.

Summary

A microseismic data set was acquired at Hydraulic Fracturing Test Site 2 (HFTS2) in the Delaware Basin (Texas, USA) by the HFTS2 consortium as a part of data-collection program designed to help maximize the efficiency of hydraulic fracturing, understand the impacts of nearby depleted zones, and increase the production of hydrocarbons. Advanced methods of microseismic monitoring applied at HFTS2 include 1) native synchronization of five monitor arrays, 2) real-time location of microseismic events, 3) joint event-hypocenter/ velocity-model inversion that locates microseismic events simultaneously with constructing azimuthally anisotropic velocity models, 4) high-resolution reservoir imaging, utilizing microseismic events as downhole sources. HFTS2 microseismic data set illustrated the influence of geologic complexity, variations in treatment designs, and the presence of parent wells on the efficiency of hydraulic fracturing. Three Wolfcamp wells, B1H, 2H, and 4H, were stimulated sequentially, exhibiting very different patterns of microseismicity. When the B1H well is stimulated, its toe stages quickly reacted to the presence of depleted Bitterroot section to the east of the Boxwood pad, extending microseismic events over 3,000 ft to the east. This behavior changes dramatically after the treatment passes the Bitterroot section at the toe, and the heel stages in 1H showed tight microseismic grouping around the stimulated well, indicative of treatment of virgin reservoir rock. The B2H demonstrates this same pattern of behavior between the toe and heel stages of the well, suggesting that the depleted Bitterroot section remains easier to refracture than adjacent non-depleted rock. Microseismic activity associated with B4H treatment is distinctly different from those in Boxwood wells 1H and 2H. The events generated during stimulation of 4H are hardly influenced by the depleted Bitterroot section and fill the space between the previously stimulated 1H and 2H wells. Overall, microseismic patterns suggest that treatment fluids tend to find the weakest passages through geologic formations, and the relative well positions and treatment sequence have a significant impact on fracture geometry, as indicated by microseismic event locations.

Introduction

Hydraulic fracturing has been employed on a massive scale in the unconventional reservoirs in pursuit of production enhancement for decades. With increasing use of hydraulic fracturing and the transition to infill drilling, the scale of complexity for pad development has increased significantly. Not only must one take into consideration local geology and stresses, but placement of infill wells in section with parent wells which presents additional challenges due to interaction with depleted zones. One of the objectives of the HFTS2 consortium has been research the impact of treatment methods and techniques used for production optimization. A distinguished method widely used to evaluate these impacts and better understand the local stresses and geology is microseismic acquisition.

Microseismic events are small earthquakes with magnitudes ranging from -3 to -0.5 that indicate rock failure or movement. The rock failure associated with these events is caused by the injection of pressurized fracturing fluid, characterizing a hydraulic fracture and those are

potential conduits for the fluid flow in the rock. Stimulation grants the wellbore recovery factor increase. To keep these conduits open during production, proppant is usually added to the fracturing fluid so they can settle in the fractures keeping them open for fluid flow.

Average dimensions of the fracture extension are drastically influenced by nearby depleted zones. In the case of the HFTS2 pad, the Bitterroot wells increased the observed fracture lengths extension to the east by a range of 1700 ft to 3000 ft observed on B1H and B2H. Fracture height growth was dominant upwards in the stratigraphic section. Events were observed as far up as the Bone Spring Lime in the B4H and B2H treatment.

The most significant take away from the HFTS2 project was the strong influence of depleted zones in fracture geometry development caused by Bitterroot parent wells. The shallower BR2H has stronger influence than deeper BR1H. Many microseismic events were observed cascading directly towards the BR 2H when the first offsetting stages were treated. Additionally, significant height growth of fractures from the treatment of the B4H well is worth noting. Approximately 33% of microseismic events observed were in the Bone Springs Sand and 2% were in the Bone Spring Lime.

High-frequency, high-resolution seismic volumes were derived from the HFTS2 data using the microseismic events as sources. High-quality microseismic events were selected and the 3-component seismogram is migrated. These volumes have a resolution far superior to those recovered from the conventional surface seismic due to the source nature and locations, providing a powerful tool for reservoir studies.

Methods

Acquisition Geometry

A geometry design with 5 static monitoring arrays was established to acquire and process the microseismic data for HFTS2, to ensure that interpretation for all 3 wells would remain consistent. Starting on March 18th of 2019, 3 individual completions of 1-mile laterals drilled in the Wolfcamp and Wolfcamp B were monitored with this arrangement. These arrays were static throughout the entire operation, except for a redeployment at 2H stage 5 landing back at same position into the B5PH. The sampling rates were the same for all arrays at one sample every 0.25 ms.

The 40-level vertical array in the B5PH was deployed with 50 ft receiver spacing totaling 2000 ft of array extension. Two horizontal arrays in the B3H were deployed as a single split-whip array with 100 ft receiver spacing to the toe of the well. The horizontal arrays had 1300 ft and 1400 ft of length, respectively, and they are separated by an interconnect cable of 1500 ft. For T 16H, a single split-whip array with 100 ft spacing were deployed to straddle the heel part of the well, where one array was in the horizontal part of the well and the other was in the vertical part of the well. The vertical and horizontal array had 1300ft and 1400ft of length, respectively, and separated by an interconnect cable of 1500ft. The geophones being deployed were standard Geospace DS150, with magnetic coupling in the vertical sections and gravity coupling with no magnetic components for the horizontal arrays.

Fig A 1 illustrates the position of the treatment and monitor wells. On the first half of acquisition, referred to as the “toe half”, we primarily had events detected on the B3H horizontal arrays. As

the completion progressed, the events were easily detected by B5PH array. Events in the "heel half" were detected by T 16H arrays as the completions progressed towards the heels of the wells.

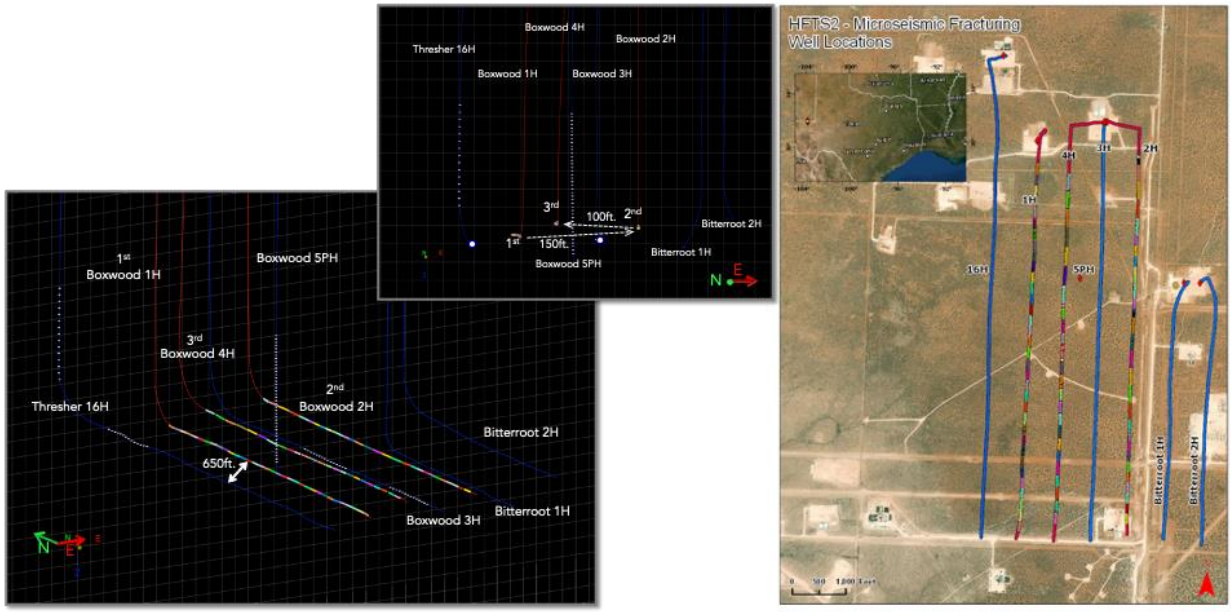

Fig A 1—The HFTS2 geometry and well locations on the figures on the left and center; well locations on the right.

All data was natively synchronized on a single recording system including all channels on all arrays. In other words, every single channel for all the receivers in all the monitor wells was connected to and recorded by a single acquisition system, as if they were a single array, and merged into a single trace gather in the processing phase. This specific setup is critical because the native sample is not recoverable, if each array is recorded independently and merged according to GPS time stamps. Our acquisition setup eliminates the possibility of any synchronization uncertainty, commonly associated with GPS systems.

Geometry and Processing

Clearly identifiable P- and S-wave arrivals must be evident from a given array for that data to be incorporated into the processing and locating of that event. For this reason, data from the array most distant from an event was usually excluded from multi-array event location. In the HFTS2 project, this meant that events associated with the "toe half" stages excluded data from the T16H array. Similarly, horizontal arrays in the B3H were used to process "heel half" stages only if the sources generated clearly identifiable P- and S-wave arrivals. Triggering, the first step in our proprietary processing workflow, detects microseismic events in the continuously recorded data. The algorithm based on image-processing will automatically classify the continuous data and categorize them based on the noise level, where data segments with medium-to-low noises are likely to contain microseismic events with visible P- and S-waves. The highest quality events direct P- and S- waves arrivals times, were used for velocity model building. The key differentiator of our processing is that we built the velocity model based on both perforation

shots and microseismic events. This process is described in detail in Grechka and Yaskevich (2014).

The advantage of incorporating microseismic events to constrain the velocity model is that we the significant increase sampling of the reservoir as opposed to the traditional method of using just perforation shots. Events carry the information of the velocity model along their ray path. By adding them to the velocity model building, we improve the sampling of the velocity variations in different azimuths and geological formations eliminating extrapolation of the observed reservoir character along many different azimuths, that could introduce potentially significant errors in event locations. This allows us to construct a layered azimuthally anisotropic velocity model, which can fit the travel time data of both perforation shots and events. During post-processing, additional high-quality events are incorporated to further constrain the velocity model, and all the events are reinverted using this final velocity model. To eliminate the unknown origin times, we only used sources with both P- and S- waves picked in at least one vertical and one horizontal array.

The second path is to locate the events using joint inversion or tomography and calculate its properties (high quality events used for velocity model building also pass through this step) and those are the events that are posted during real-time on the BHS Portal. Because of time constrains, during real-time we are usually not able to go over every trigger file, so we performed a complete processing during "post-processing" where more events were added to the already located events for the wells.

Additionally, as a quality control process, we review the picked times of located events and reprocess the events that didn't pass our misfit threshold. The misfit is the root-mean-square (RMS) average of the difference between picked arrival times and model-predicted arrival times. The predicted arrival times are calculated via two-point dynamic ray tracing using the final velocity model. The misfit value is calculated using

$$Misfit = \sqrt{\frac{\sum_{all\ picked\ arrivals}\left(t_{picked} - t_{computed}\right)^2}{Number\ of\ arrivals}}$$

Eq. A 1

For the HFTS2 project, we used a threshold of 2.5 ms. Events with misfits above 2.5 ms were reviewed and reprocessed when necessary. Events with misfits above 2.5 ms will be reviewed and reprocessed if necessary. If a reprocessed event still didn't pass the misfit threshold, it's usually because of the misidentified arrivals related to a high level of noise.

Two velocity models were computed for each treatment well – one each for the toe and heel sections. The motivation of building 2 velocity models for each treatment well is that events at the toe stages set on the rock that has not been fracked yet, while the heel stages were in a part where the rock is more likely stimulated.

To quality control the velocity model, we relocated the perforation shots to compare the model-predicted relocations using the final velocity model with the known perforation locations, as seen in Fig A 2. Those errors can be used to quantify the upper bounds of location error for the microseismic events. Due to the respective differences in source nature and signature,

perforation shots are primarily located using only P-waves while microseismic events are located using S-waves arrivals. Slower S-waves have more moveout, consequently provide better constraint on the location of hypocenters.

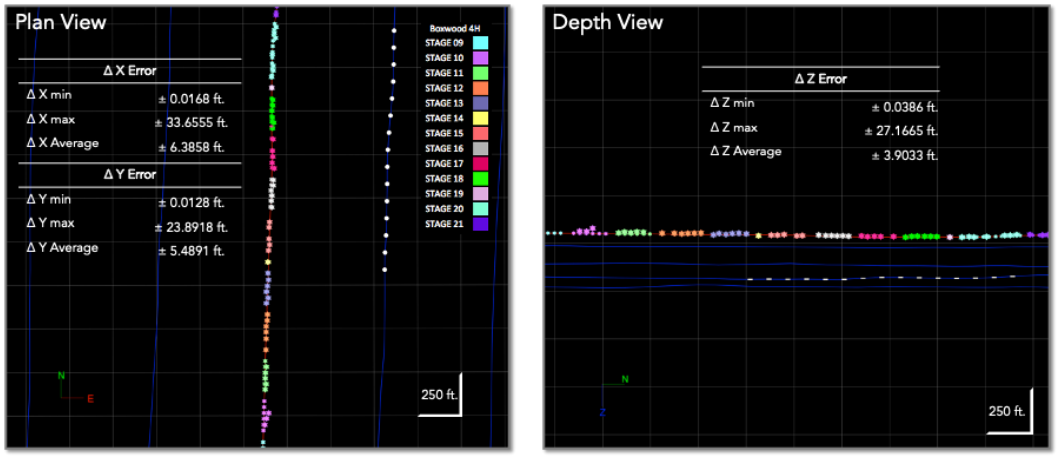

Fig A 2—Perforation shot relocation showing the known source locations and the results of the relocation; left side plan view, showing the x/y relocation and the right side shows a side view showing the relocation in depth. Tables show their associated errors.

Fig A 3 contains an example of a microseismic event seismogram or trace gather. Note that this event was detected on 4 arrays, all of which were used to compute its hypocenter. The 5PH vertical array displays a parabolic moveout with a minima around 7395 ft. Similar observations can be made on other arrays. In other words, the hyperbolic moveout on each array

demonstrates that the hypocenter is very well constrained, besides a well-constructed velocity model was used to locate.

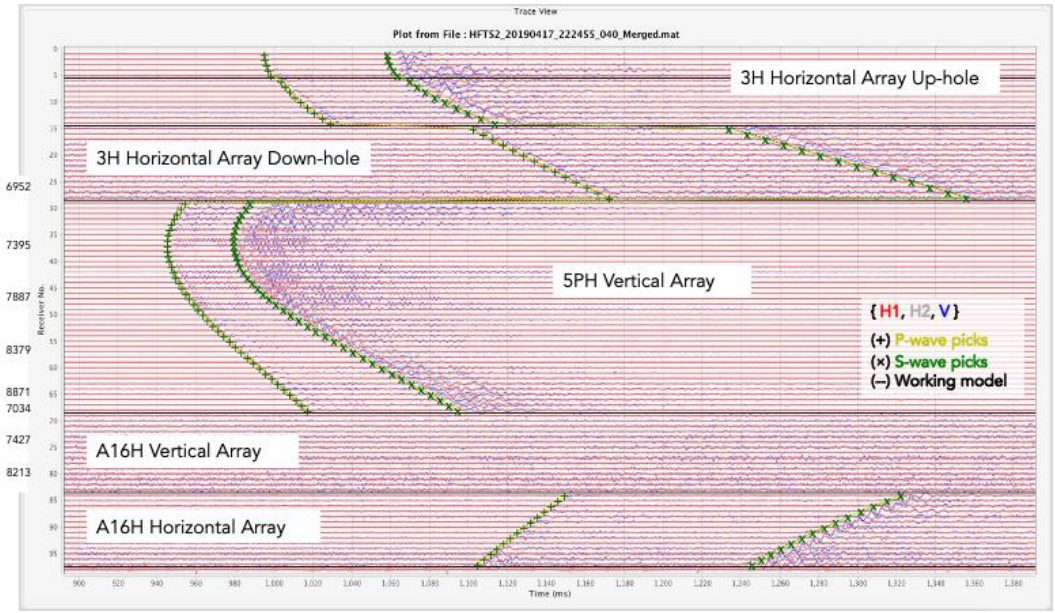

Fig A 3—A seismogram, or trace gather, of a shallow event for the HFTS2 project.

Imaging

After being located, microseismic events are used as sources to illuminate the subsurface, Grechka et al (2017). First, we selected high-quality events that would be used to image a volume of the reservoir that contain the treatment wells. We selected high quality events with high SNR, so they don't add noise to the migrated volume. Based on the geometry and spatial distribution of the microseismic events, one volume was created to the south of the B5PH, referred to as the "southern volume", and another volume was created to the north, referred to as the "northern volume". Each image volume had a different ray fold in accordance with locations of microseismic events. The spatial extent of image volumes is selected to reflect the optimally illuminated region. Both volumes had a grid size of 5x5x5 ft.

The southern volume was computed using 407 events from B4H stages 13 to 16. Note that those events were illuminating the subsurface likely stimulated by the B1H and B2H treatment. The calculation of northern volume involves 386 events from B4H stages 24 to 26. These events illuminated a region, which is stimulated by not only B1H and B2H but also B4H stages 21 to 23.

Using those sources to image the subsurface we applied a 3D Kirchhoff pre-stack depth migration to the squared-phase trace data and create volumes for P- and fast S-waves. For further technical information on the processing methodology (Grechka et al., 2017). After further analysis of the frequency content and image quality, the fast S-wave volume was used for interpretations. The microseismic volume derived from the fast S-wave have a remarkably

high spatial resolution of approximately 12 ft due to the high-frequency nature of microseismic sources (50-400 Hz).

Next, fractures were extracted from image volumes using Geoteric. We investigated if the microseismic volumes displayed the major discontinuities that can be tied with surface seismic and nearby well-logs. We identified possible seismic stratigraphic terminations as well as discontinuities that are likely to be related to fractures. Additionally, we overlayed microseismic events to the volume to correlate them and to further investigate the discontinuities.

Results & Observations

Microseismic

Fig A 4 shows the entire microseismic dataset processed for the HFTS2 project, and Fig A 5 the manually selected subset of data containing only the highest quality events, referred to as the representative dataset. The representative dataset is obtained by applying a series of cut-offs to the dataset to filter out events with processing limitations, like large offsets, or other types of limitation in geometry, which may cause poorly constrained hypocenters. The representative dataset only includes events detected by at least one vertical and one horizontal array. Events with misfits larger than 2.5 ms were excluded. Fig A 6 displays the event locations for the B1H well, which was the first well to be treated. B1H is also the furthest well from the Bitterroot wells located about 3000 ft away to the east. Activity captured during the treatment of the "toe half" of the B1H is observed to extend towards the depleted region associated with the Bitterroots. Conversely, events from the "heel half" stages of B1H are near the treatment well, consistent with what is observed in stimulations of virgin reservoir rock. Note that the absence of events north of Bitterroot wells was not associated with geometry limitations.

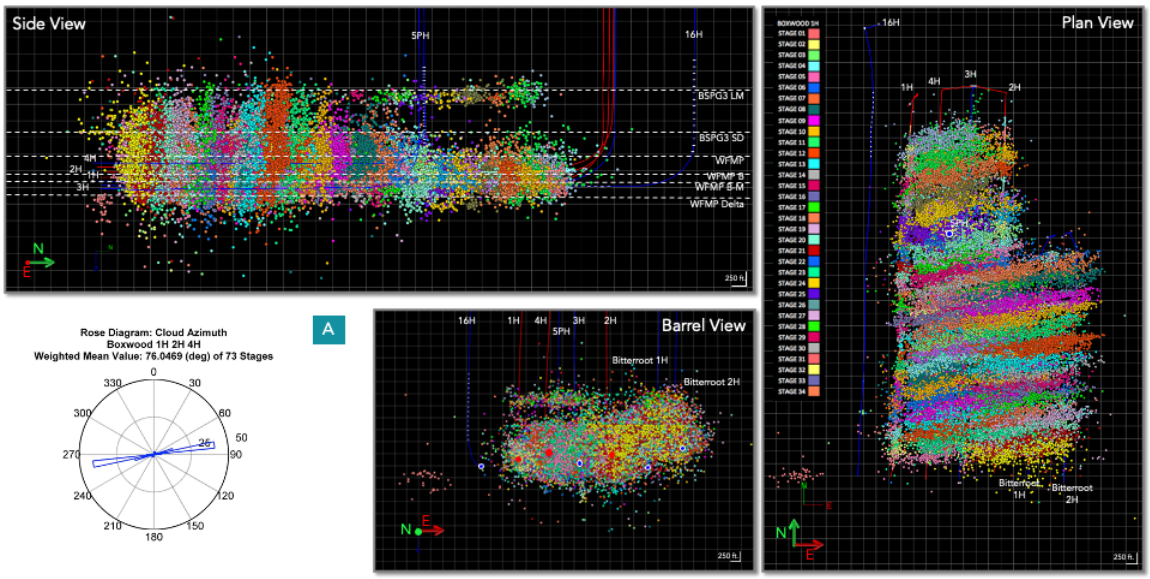

Fig A 4—The entire process dataset for the HFTS2 project. Top left figures show a side view, bottom view a gun barrel view and right-side plan view. Rose diagram shows the event cloud azimuth, for the entire project.

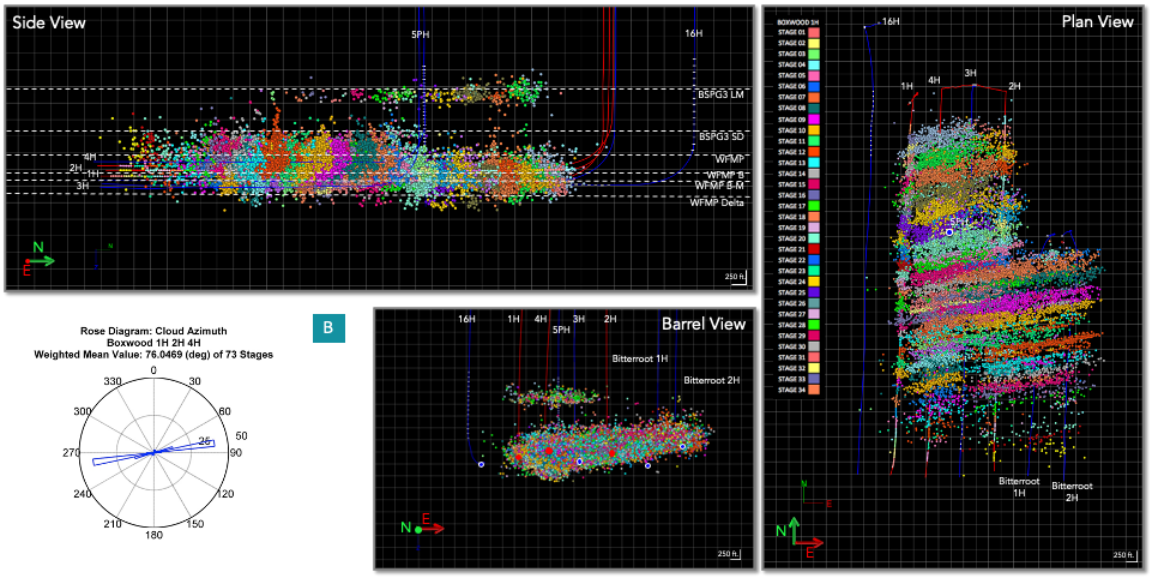

Fig A 5—Representative dataset for the HFTS2 project. Top left figures show a side view, bottom view a gun barrel view and right-side plan view. Rose diagram shows the event cloud azimuth for the entire project.

The B2H was the next well to be completed and the closest well to the depleted region 1100 ft to the east. In Fig A 7, a similar trend in event locations to the 1H can be observed for the B2H, demonstrate a significant preference for eastward growth towards the Bitterroot wells. However, stimulation of the heel stages triggered events back to the west between the B1H and 2H. This reversal in the direction of half-length asymmetry for the B2H is compelling evidence that, absent a nearby depleted zone, the B2H preferentially develops length towards the recently completed B1H. This suggests that the microseismic events tend to be triggered on the rocks that are easier to refracture as previously fractured zones, rather than to fracture virgin reservoir, regardless of the state of depletion. Note that the shallow Wolfcamp formation was the primary conduit for communication from the B2H to the Bitterroot wells, and the total event count for

the B2H, the well closer to the depleted zone, was higher than the more distant B1H. The treatment of the B2H also produced more events than 1H.

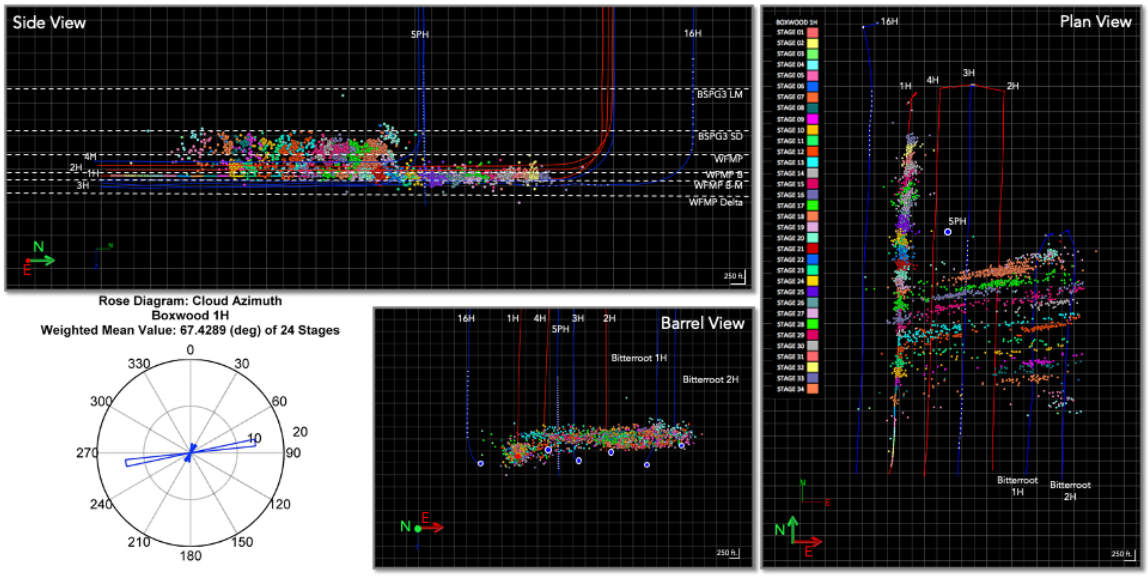

Fig A 6—Representative dataset for the B1H well. Top left figures show a side view, bottom view a gun barrel view and right-side plan view. Rose diagram shows the B1H event cloud azimuth.

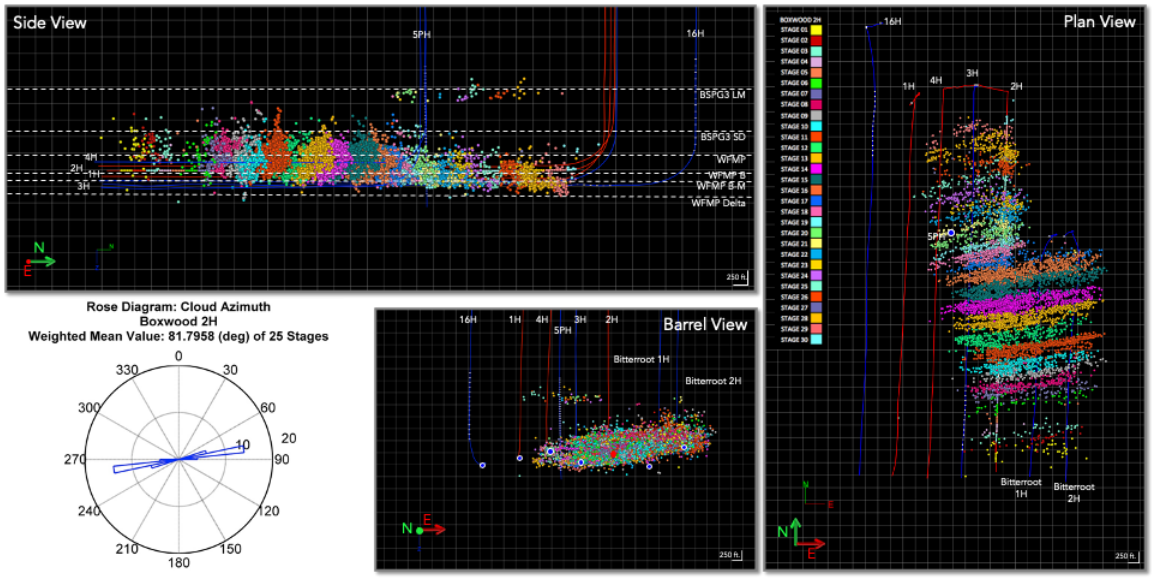

Fig A 7—Representative dataset for the B2H well. Top left figures show a side view, bottom view a gun barrel view and right-side plan view. Rose diagram shows the B2H event cloud azimuth.

B4H was the last well to be completed, and microseismicity trend from its treatment were distinctly different from the B1H and 2H wells, as seen in Fig A 8. Most of the events associated with the 4H were located between the B1H and 2H regardless of position relative to the

Bitterroot wells. This suggests that pressure walls were created on both sides of the 4H by the stimulations of the 1H and 2H, effectively containing length development.

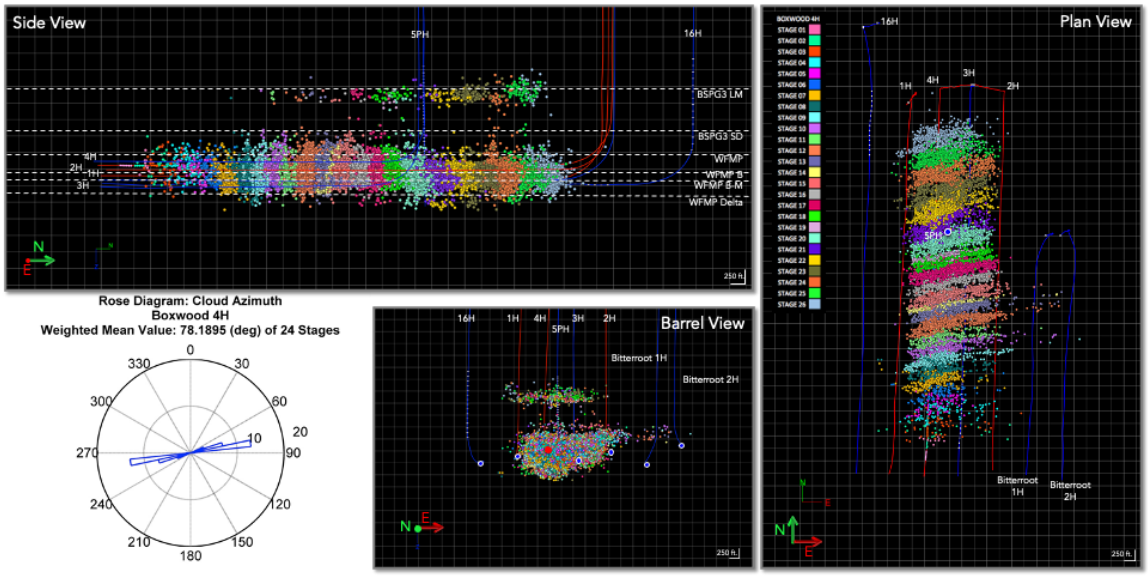

Fig A 8—Representative dataset for the B4H well. Top left figures show a side view, bottom view a gun barrel view and right-side plan view. Rose diagram shows the B4H event cloud azimuth.

Additionally, low magnitude microseismic events were located in shallow formations at the top of the Bone Springs Lime, indicating this containment encouraged more height growth. Interestingly, an aseismic zone was observed in the middle and bottom sections of the Bones Springs Lime, where few, if any events were triggered. This lack of events was not associated with any geometry limitations, as the hypocenter was well constrained.

Finally, all three Boxwood wells displayed a similar absence of westward length development beyond the B1H, towards T16H. Events were restricted to the area of B1H, 4H, 2H and BR 1H and 2H. This indicates that these regions were easier for the microseismic events development since there was no former cause to prevent the hydraulic fracturing to progress towards the west.

Imaging results

Four volumes were created for the microseismic imaging analysis: two derived from P-waves (Fig A 9) and two from fast S-waves (Fig A 10). These volumes exhibit higher resolution and detail when compared to surface seismic volumes. Major reflectors were observed in the microseismic volumes and that can be tied with surface seismic as well as well-logs. The result of the fracture extraction performed using Geoteric is included in Fig A 11. Despite differences in microseismic pattern between the "heel half" and "toe half" stages of the Boxwood wells, the fracture density observed in the northern and southern volumes are similar This is likely since all events selected as sources for the microseismic volumes were associated with the B4H stimulation, which captures the of the subsurface after the treatment of B1H and 2H. Although one might notice

that the northern volume appears to be more continuous comparing to the southern volume, which has phases being terminated multiple times.

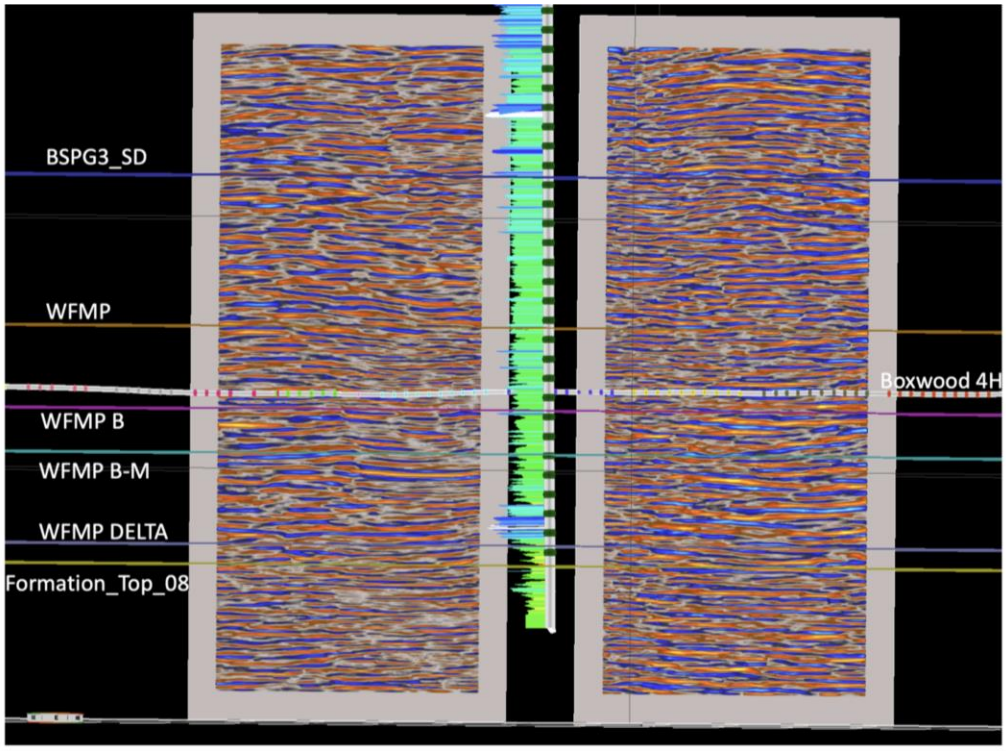

Fig A 9—Cross-section showing the microseismic imaging volumes derived from P-waves. The cross-section on the left and right are the southern and the northern volumes, respectively.

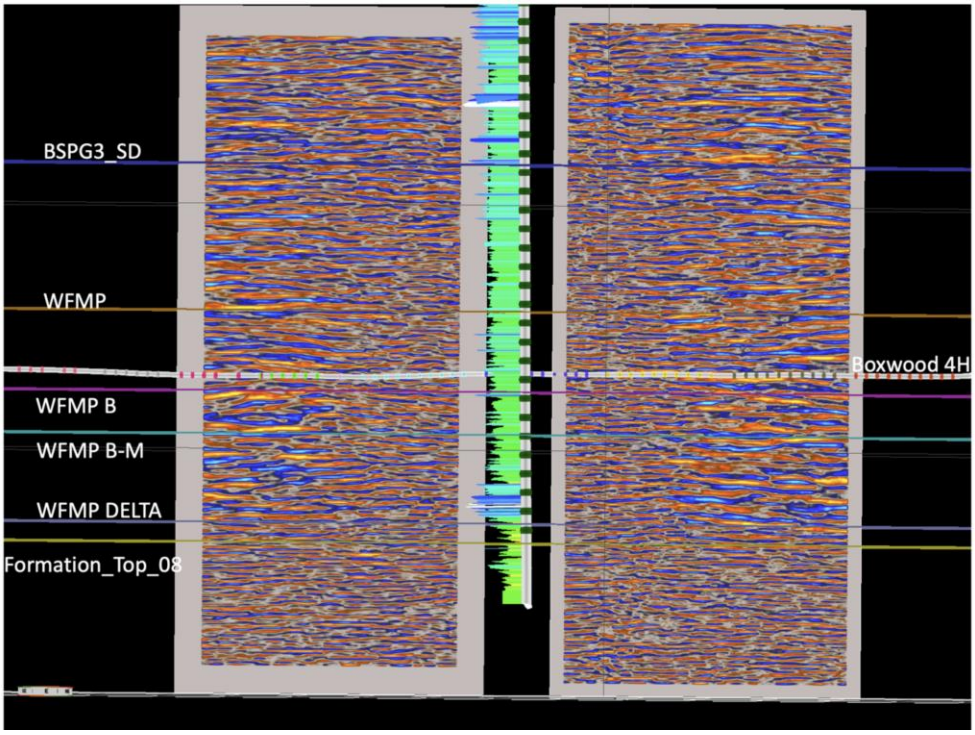

Fig A 10—Cross-section showing the microseismic imaging volumes derived from fast S-waves. The cross-section on the left and right are the southern and the northern volumes, respectively.

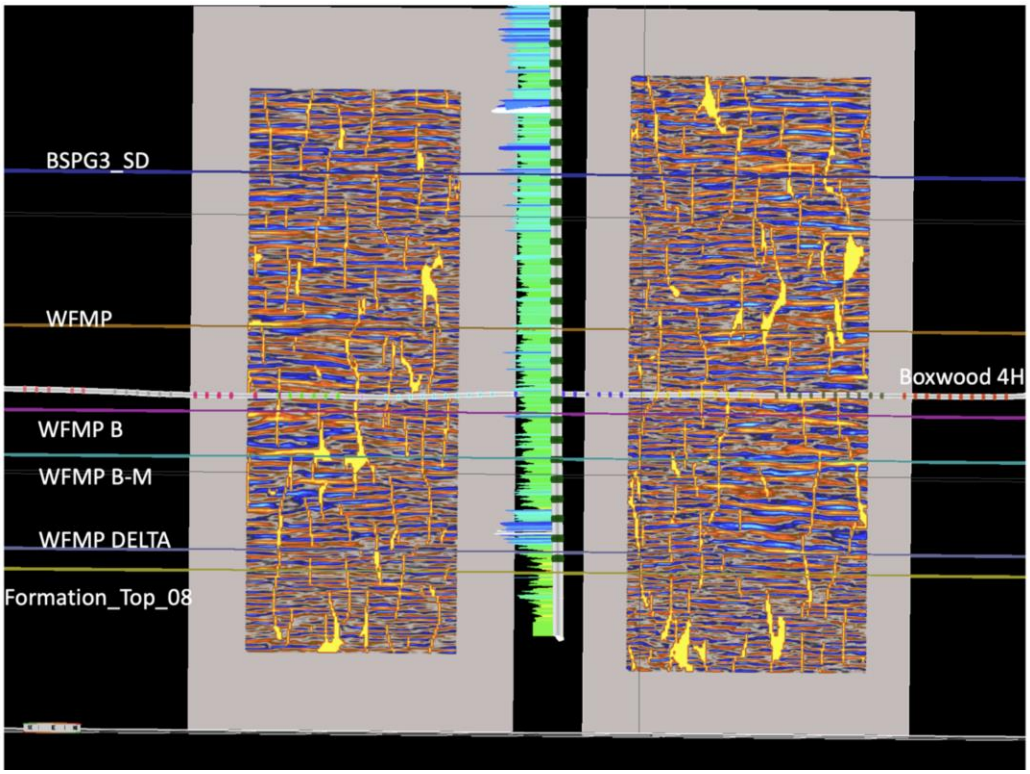

Fig A 11—Results from the fracture extraction performed using Geoteric on the microseismic imaging volumes derived from fast S-waves. The cross-section on the left and right are the southern and northern volumes, respectively.

Discussion and Conclusions

We recognize that microseismic events have grown towards the Bitterroots wells because this region is easier to be refracked. It is evidenced by the different imprint from toe and heel stages for B1H and 2H, where the heel stages show more common microseismicity pattern of a virgin reservoir rock treatment.

We also believe that the distinct behavior of microseismic events from B4H is due to the creation of a pressure wall from the treatments of B1H and B2H, which forced stimulation to be triggered in between those wells.

In respect to the shallow events in the Bone Spring Lime formation, we infer that they are a consequence of the pressure wall formed by the stimulation of B1H and 2H. Once more fluid is pumped into the subsurface, it increases the pressure of the surroundings and affecting the fracture to growth upwards. It is interesting to mention that a fiber cable was deployed in the B5PH monitor well. Fractures hits were detected on it during the treatment of the B4H for stages close to the monitor well. This observation agreed with the microseismic results, and it confirmed our hypothesis. Additionally, the geophone array deployed in the same monitor well had an increase of 6 times in the average noise level for stage 22.

Microseismic imaging is a powerful tool to unveils high-resolution details of the reservoir. Reflectors can be delineated and tied with other geophysical data. Integration of different data types, such as surface seismic, well logs, and fiber-optic data, can be helpful when interpreting the extracted fractures.

References

Grechka, V., 2010. Data-acquisition design for microseismic monitoring, *The Leading Edge* **29**: 278-282. https://doi.org/10.1190/1.3353723.

Grechka, V., and Heigl, W. M. 2017. Microseismic monitoring: SEG, Geophysical References series, no. 22.

Grechka, V., Z. Li, B. Howell, H. et al. 2017. High-resolution microseismic imaging: *The Leading Edge*, **36**: 822–828. https://doi.org/10.1190/tle36100822.1.

Grechka, V., Li, Z., Howell, B. et al. 2018. Microseismic imaging of unconventional reservoirs. Paper presented at the SEG Annual International Meeting. https://doi.org/10.1190/segam2018–2995627.1.

Grechka, V., and Yaskevich, S. 2014. Azimuthal anisotropy in microseismic monitoring: A Bakken case study. *Geophys*, **79**(1): KS1–KS12. https://doi.org/10.1190/geo2013-0211.1.

Grechka, V., Li, Z., Yathams, S., et al. 2020. Microseismic reservoir imaging in the Permian Basin. Paper presented at the SEG Annual Meeting. https://doi.org/10.1190/segam2020-3399804.1.

Appendix B: Mechanism of Microseismic Generation During Hydraulic Fracturing – With Evidence From HFTS 2 Observations

Authors: Yunhui Tan, Jiehao Wang, Peggy Rijken, Zhishuai Zhang, Zijun Fang, Ruiting Wu, Ivan Lim Chen Ning, Xinghui Liu

Summary

The objective of this study is to understand how microseismic events are generated during hydraulic fracturing, as well as the role of geomechanical conditions (i.e., stress and mechanical stratigraphy) in this process. In the industry, microseismic event clouds have been generally used as an "outer-boundary" of the "stimulated reservoir volume (SRV)". However, by comparing with other surveillance data (Low frequency Distributed Acoustic Sensing, or LF-DAS strain) in the Hydraulic Fracturing Test Site (HFTS) 2 experiment, we show that this assumption is fundamentally flawed. The HFTS 2 data has three unique observations that have not been commonly observed in other datasets: 1. Due to influence of offset pad depletion, microseismic data shows that hydraulic fractures from the child well can propagate over 3000 ft into the depleted low stress zone. 2. By comparing microseismic and horizontal fiber LF-DAS strain data, we observe that microseismic event cloud does not necessarily reflect the created hydraulic fracture volume. Particularly, the extent of microseismic event clouds near heel stages are much shorter than what is shown with LF-DAS strain data. 3. Microseismic event magnitudes are larger in the depleted regions. Through geomechanical analysis, we demonstrate that the "bedding-plane-slip" model is likely the mechanism for microseismic generation during hydraulic fracturing. This model successfully explains the above field observations from HFTS 2 experiment. We also provide a quantitative relationship connecting the microseismic event magnitude with fracture width increment and layer mechanical property contrast.

Introduction

Although microseismic monitoring has been applied to hydraulic fracturing since the beginning of the shale revolution, understanding of the mechanism generating microseismic events remains poor. What exactly causes microseismic events and how they are connected to the hydraulic fracturing propagation process is still debated and consensus among the industry has not been reached (Rutledge et al., 2016; Rutledge 2019; Teran and Thornton 2019). Three major theories have been proposed to explain the mechanism of microseismicity generated during hydraulic fracturing: tensile opening, natural fracture slip or bedding plane slip.

Tensile opening is the most intuitive mechanism that seems to be consistent with the mode I opening of hydraulic fracturing (Baig and Urbancic 2010). If this mechanism explains a majority of the microseismic events, the microseismic cloud should trace the hydraulic fracture tip thus reflecting the propagation speed of hydraulic fractures. Furthermore, the source mechanism should follow the characteristic patterns of tensile opening source mechanism. However, evidence from microseismic source mechanism studies show that tensile opening cannot be the dominant mechanism and most microseismic events with quality inversion show double-couple patterns. Most seen source mechanisms are Dip-Slip or Horizontal-Slip (DSHS) with one nodal

plane horizontal and the other one usually follows the hydraulic fracture propagation direction (Duncan et al., 2013; Tan and Engelder 2016).

The natural fracture slip theory states that the microseismic events are either induced in the natural fractures by either a decrease in effective normal stress due to elevated pressure, or an increase in shear stress along the fracture planes (Bussetti et al., 2014; Yang and Zoback 2014). If the events are caused by the increase of pressure due to injection of fracturing fluid, the microseismic events are categorized as "wet events" and can represent the real fracturing volume (i.e., SRV) (Tan et al., 2014a). If the microseismic events are caused by increase of shear stress due to stress shadowing of the hydraulic fractures, the events are "dry events". This is a very attractive theory since the natural fractures are usually treated as Discrete Fracture Networks (DFN) in the hydraulic fracturing model. Stress shadowing can be calculated using net pressure from hydraulic fractures combined with a finite element simulator or analytical estimation. In theory, the microseismic events can be synthetically calculated combining these two pieces of information. However, there are limited successes using this approach to predict microseismic events. The first challenge is that it cannot explain the DSHS events. Many natural fractures are generally vertical in normal stress environments and are often observed in the shale outcrops or cores (Tan et al., 2014b). There is very little shear stress along the vertical natural fracture planes.

The bedding plane slip model is the least intuitive but has gained much attention in recent years (Rutledge et al., 2016; Kahn et al., 2017; Hull et al., 2017; Rutledge 2019). This model states that the microseismic events are generated along bedding planes either by offset of hydraulic fractures in the vertical direction or termination against bedding planes (Rutledge et al., 2013; Stanek and Eisner, 2013; Tan and Engelder, 2016). It can also be generated due to the differential width of hydraulic fractures in neighboring high/low stress layers. This model can explain microseismic focal mechanisms that are consistent with the DSHS events observed (Tan and Engelder, 2016). This model is also able to predict the microseismic events created along beddings planes with large mechanical property contrasts.

People have been puzzled by the observation that in many cases microseismic events show dramatic difference in number of events. In some areas there are tens of thousands of microseismic events during hydraulic fracturing, while in some other areas there are barely any events detected. The timing of microseismic events also show dramatic differences. Sometimes the events are clustered during the break-down period of the stage while other events occur only at the end of the stage (Tan 2015).

The HFTS 2 project is an ideal dataset to test these theories regarding to microseismic event generation. The site installed multiple surveillance tools (microseismic, fiber and pressure/temperature gauges) and later cores were retrieved from a slant well drilled through the stimulated reservoir volume (SRV). In this study, we will use the bedding plane slip model to

explain the spatial and temporal distribution of the microseismic events recorded. We will also evaluate event magnitude distribution using a fracture simulation model.

Data Overview

There are numerous other publications describing the experiment design of HFTS 1&2 projects (e.g., Ciezobka and Reeves 2021). Many important learnings were obtained from the HFTS 1 project regarding how fractures propagate and the role of geomechanics in that process (Wang et al., 2019). The HFTS 2 pad was stimulated in the sequence of B1H, B2H and B4H from toe to heel using plug and perf techniques. Two parent wells (BR1H, BR2H) next to the pad to the east have been stimulated and on production for a few years, which has great impact on the microseismic event distribution during the child well stimulation. As shown in Fig B 1, a suite of monitoring tools was deployed in this pad: B3H and B4H were instrumented with fiber in the horizontal section; B5PH was instrumented with fiber in the vertical direction along with pressure and temperature gauges.

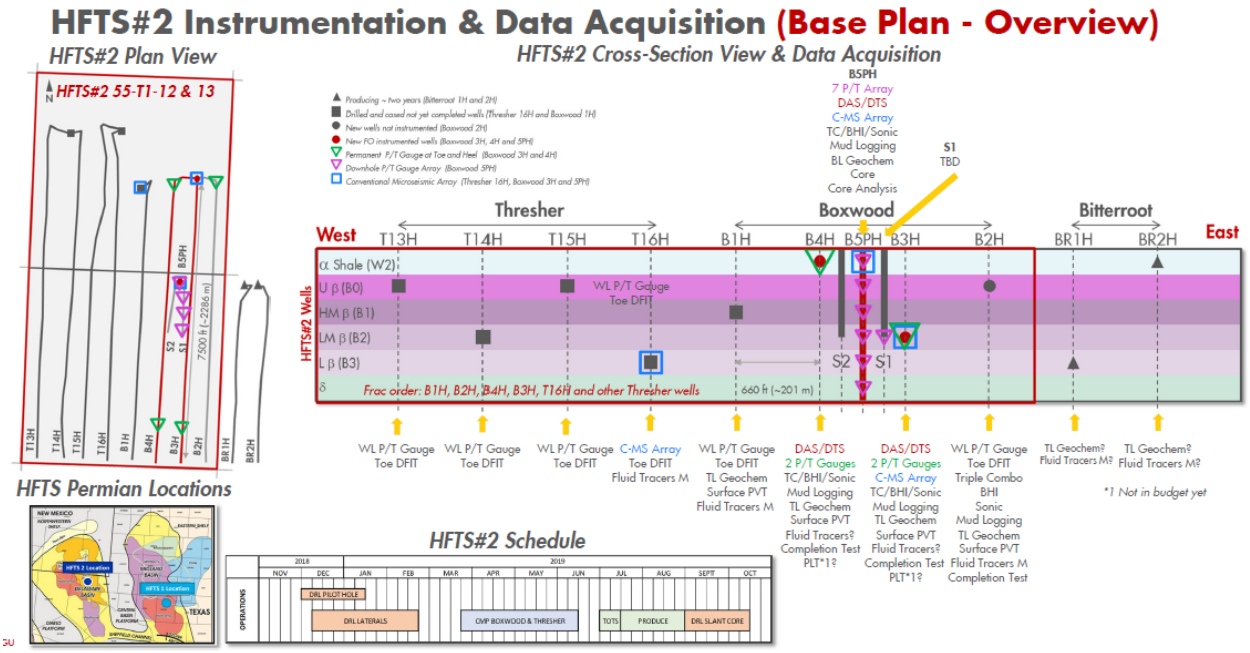

Fig B 1—overall monitoring plan and well geometry of the HFTS2 project.

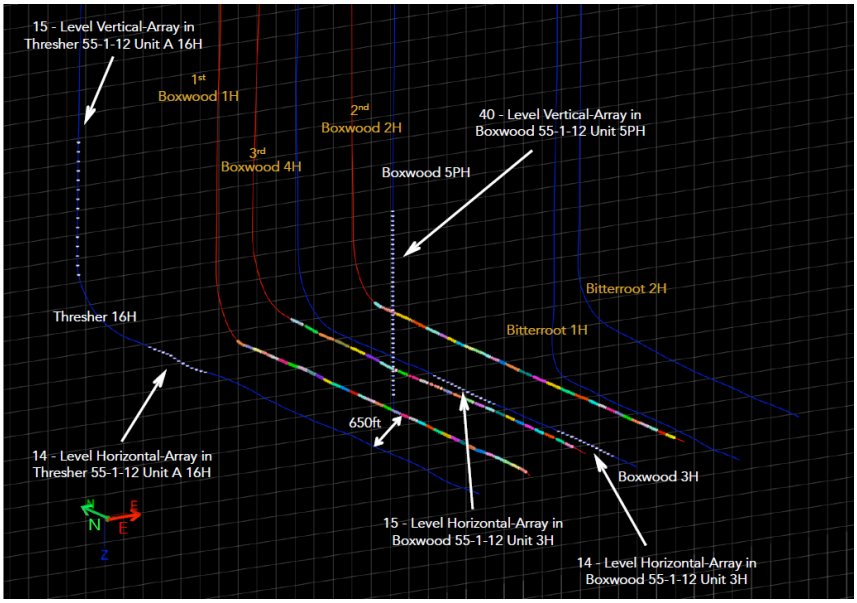

Fig B 2—microseismic monitoring geophone setup of the HFTS 2 project.

The microseismic monitoring design is shown in Fig B 2. There are 3 wells with downhole geophone arrays: B3H, B5PH, and T16H. Two arrays were deployed in B3H and T16H each to maximize the area being monitored both in horizontal and vertical directions. The geophone arrays were not moved during the operation, and hence the microseismic event completeness was not changed during the entire operation. B3H was not monitored as it was stimulated after pulling the geophones out of the wellbore.

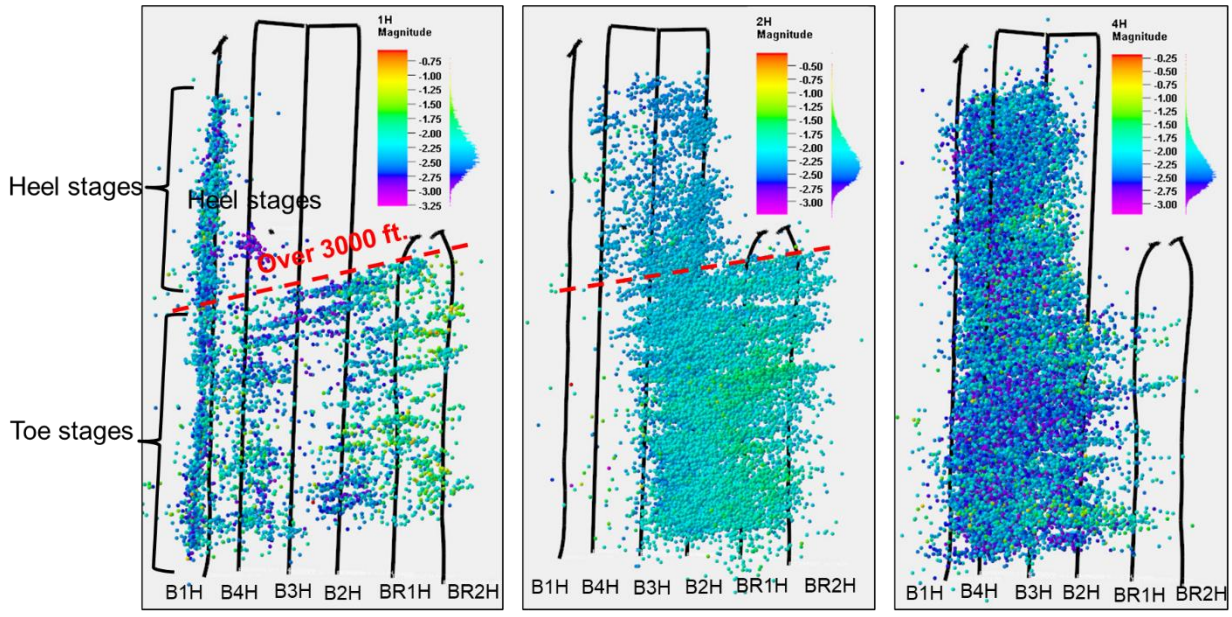

Fig B 3—map view of the microseismic events of the 3 wells stimulated (left B1H, middle B2H, right B4H). All wells showed some level of interference from parent wells (BR1H & BR2H). Color indicates the event magnitudes. Warmer color means larger event magnitudes.

Fig B 3 shows the map view of microseismic events of the 3 wells monitored. The most obvious observation is the strong impact of the two parent wells to the east of the pad. All 3 wells' microseismic events were aggregated to the east into the depleted region. Event bias in the depleted area was more severe for B1H because it was stimulated first. Since the parent wells were shorter than the child wells, the strong bias of microseismic events were only observed in the toe side of the child wells. In B1H, the microseismic data showed extensive lateral growth into the parent wells in the first 19 stages. The microseismic cloud covered over 3000 ft. in lateral length. Considering the B1H well is the furthest from the parent wells, the lateral growth distance was exceptional. It is also very surprising to see the heel stages (after Stage 19) only showed microseismic events very close to the wellbore. The lateral length is only one to two hundred feet. Why there is such a dramatic difference in the lateral length of microseismic events besides the influence of parent depleted well? Does the small microseismic volume around later (heel) stages reflect the actual SRV? These questions will be addressed later in this paper.

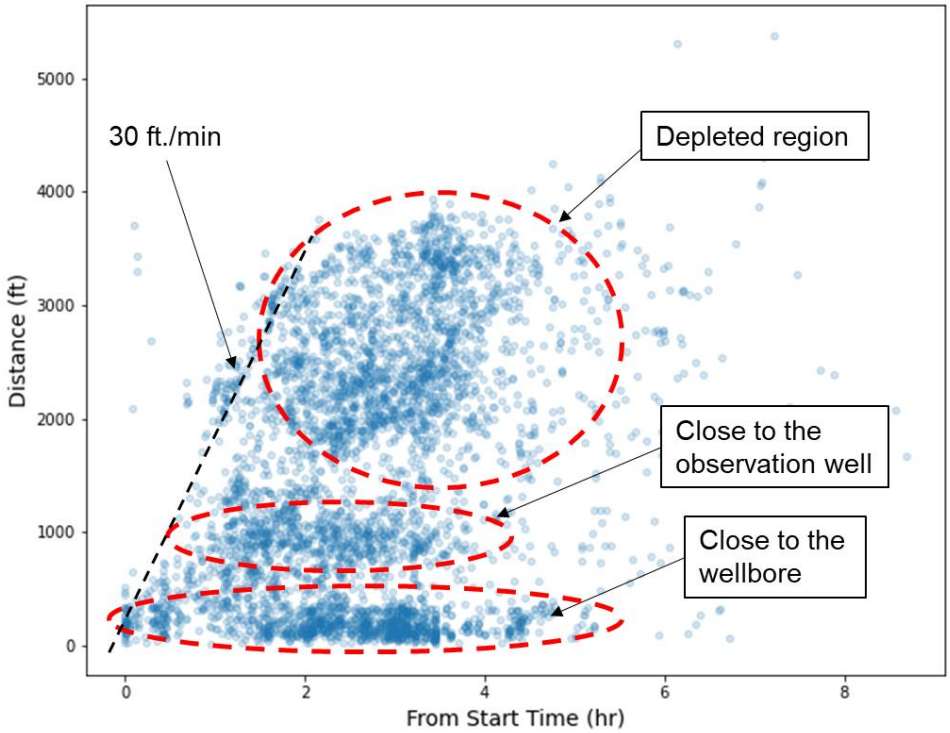

Fig B 4—distance of microseismic events from the perforation as a function of time. Vertical axis is the distance from the perforation location.

Fig B 4 shows the distance vs. time plot of the microseismic events for B1H. In this plot we overlay the Stage 1-19 which are affected by the depleted parent well. We can see 3 distinct groups of events clustered at certain distances from the perforation locations. In addition to the two event clusters that are close to the wellbeing stimulated and located in the depleted regions, there is another event cluster in between, observed from the geophones in the B3H well horizontal section. The geophone array likely picked up some small events very close by. The

microseismic propagation speed of B1H toe stages shown in Fig B 4 can be as much as 30 ft/min.

The B2H microseismic event cloud also showed some interesting patterns. It showed similar bias towards the parent depleted wells in the toe side stages. However, the later stages on the heel side also showed a tendency of microseismic propagation towards B1H. Whereas on the east side of the B2H well there were barely any microseismic events. We usually assume symmetric bi-wing fractures unless there is a depleted region close by. Why the microseismic event cloud is more prone to the stimulated region close to B1H instead of the un-stimulated region east of B2H?

The B4H microseismic events were less impacted by the depleted parent wells. But the microseismic event cloud was not symmetric either. They are laterally more prone to the east B2H well side. To the west of the B1H well, there were very few microseismic events located.

Another important difference between these 3 wells was the microseismic event number. B1H had about 6000 events recorded, while B2H had about 20000 events and B4H had about 26000 events recorded. Why there are more events in the later treated wells?

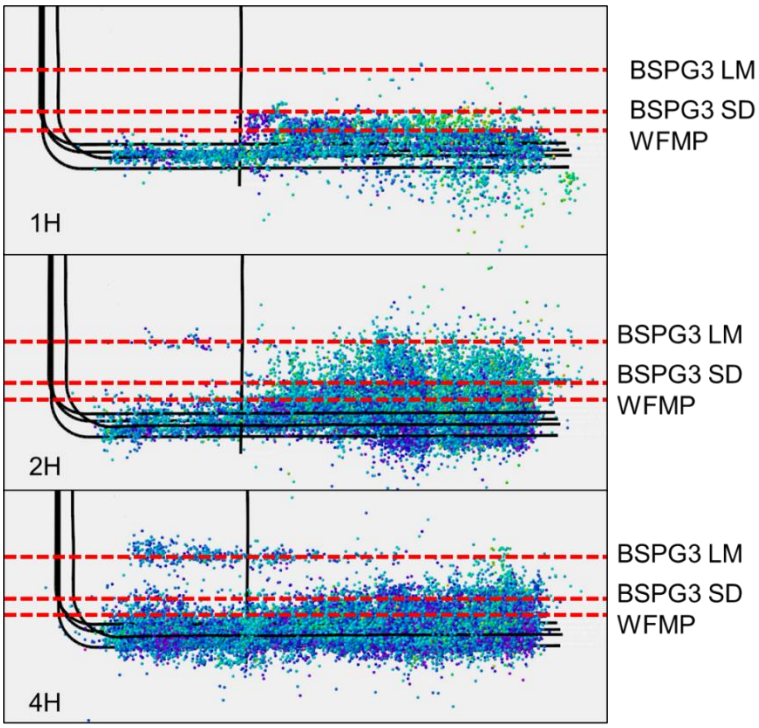

Fig B 5—side view of the microseismic events of 3 wells stimulated

Along the vertical direction, there were also dramatic differences between toe/heel stages and among the three wells (Fig B 5). In B1H, the toe stages showed larger depth range than the heel stages. In B2H and B4H, not only they showed much larger microseismic height distribution, but also an isolated group of microseismic events much higher than the main event cloud (around BSPG3 LM). This group of events seems to be more concentrated in the heel stages of B2H and B4H. B4H showed more high events than B2H. One obvious question is: are those events caused by hydraulic fractures propagating that high? If so, why there is a quiet zone in between? If not,

how can we explain the high microseismic events observed? In Fig B 5, we also label the depth of formations. The high events reside on top of BSPG3 LM layer. One obvious question is: what is the relationship between the geology and the microseismic events? The cross-well fiber optics strain data is useful in answering above questions. Fig B 6 and Fig B 7 present the comparison between microseismic and fiber optics strain data on the same scale. A more comprehensive demonstration of such integration of the data can be found in (Zhang et al. 2021). Fig B 6 shows a stage from B1H. This is a later stage which only showed limited microseismic cloud extension around the wellbore. However, we can clearly see that fiber data from B3H showed a heart shape extension zone indicative of arrival of hydraulic fracture tips (Zhang et al. 2020; Tan et al., 2020). Therefore, the hydraulic fracture has at least reached the B3H well to the east towards end of pumping. Likewise, on vertical fiber we see that the strain signal showed much higher growth than the microseismic event cloud. The distance between this stage and vertical monitoring well B5PH is quite far. But the signal pattern followed what we typically expect of vertical monitoring LF-DAS strain (Tan et al. 2021). Details of height growth modeling of B1H well can be found in another study (Wang et al. 2021). The interpretation of pressure gauge data for hydraulic fracturing are discussed in (Vissotski et al., 2021).

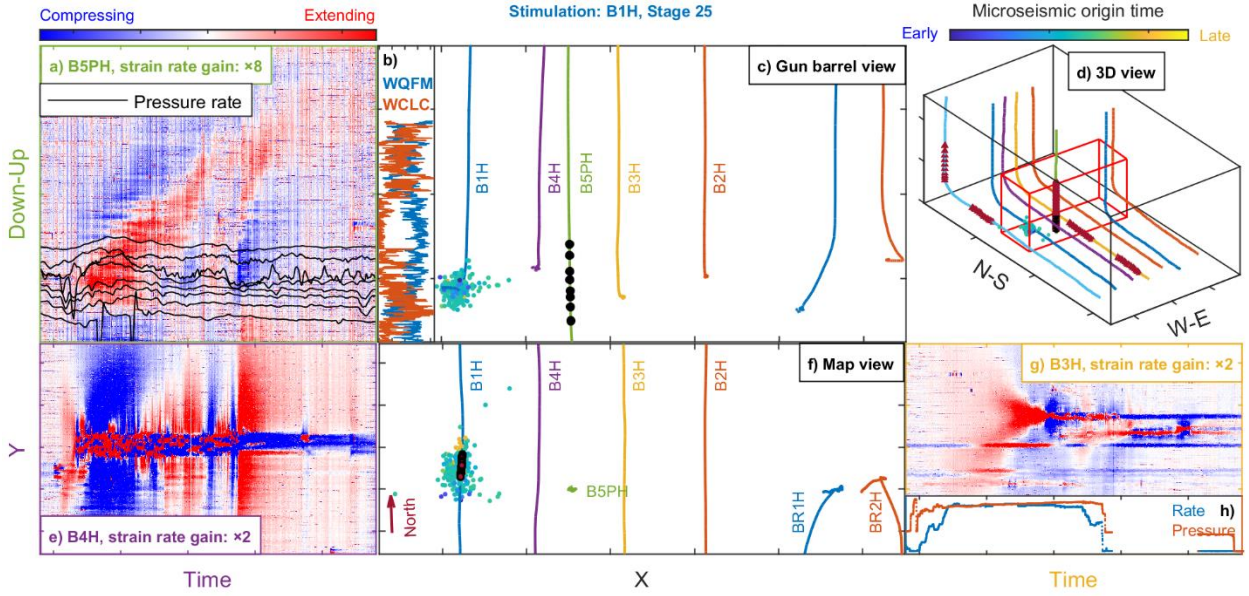

Fig B 6—comparison between microseismic and fiber observations of B1H Stage 25. More integrated demonstration of such data can be found in (Zhang et al. 2021)

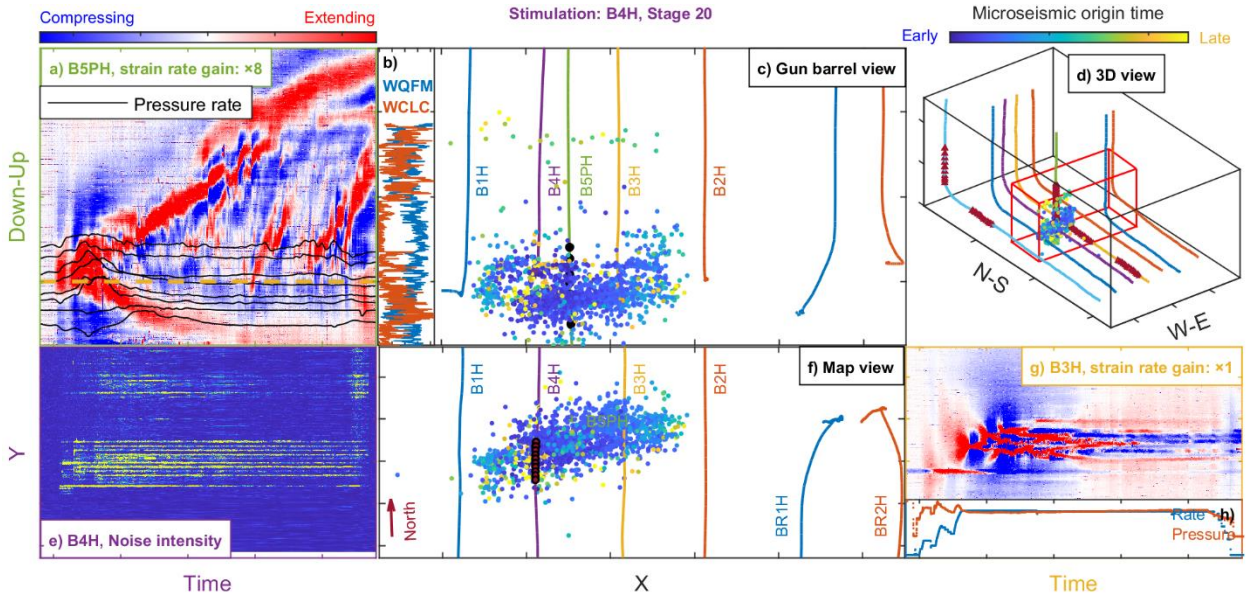

Fig B 7—comparison between microseismic and fiber observations of B4H Stage 20. More integrated demonstration of such data can be found in (Zhang et al. 2021)

Fig B 7 showed the comparison between microseismic data and DAS data for a stage in B4H. Since B4H is installed with fiber, we can obtain the high frequency DAS noise signal which is indicative of the perforation efficiency. From the comparison of low frequency DAS strain data of vertical well B5PH and microseismic events, we can see that the hydraulic fracture propagated higher than the depth of the highly isolated microseismic event cloud. Therefore, the microseismic events are real "wet events". The formation in the middle is just very quiet.

Model and Method

From previous observations, we can see that it is very challenging to explain all the different phenomena observed. In this section, we try to propose a conceptual model which can reconcile these observations. The model is shown in Fig B 8. This model assumes that the microseismic

events are generated along bedding planes where there is a sharp contrast in the mechanical properties between neighbor rock formations.

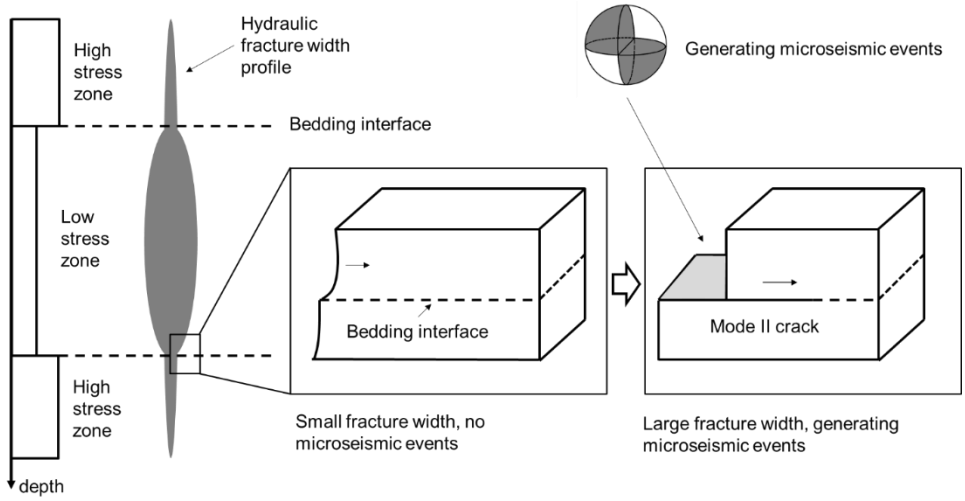

Fig B 8—conceptual model of the bedding plane slip microseismic generation model

The difference of this model from previous bedding plane slip models (Stanek and Eisner 2013, 2017; Rutledge et al., 2013) is that it does not require the hydraulic fracture to be terminated or off-set along the bedding planes. If the hydraulic fracture terminates along the bedding plane, it will just be a special case of no hydraulic fractures in the high stress layers.

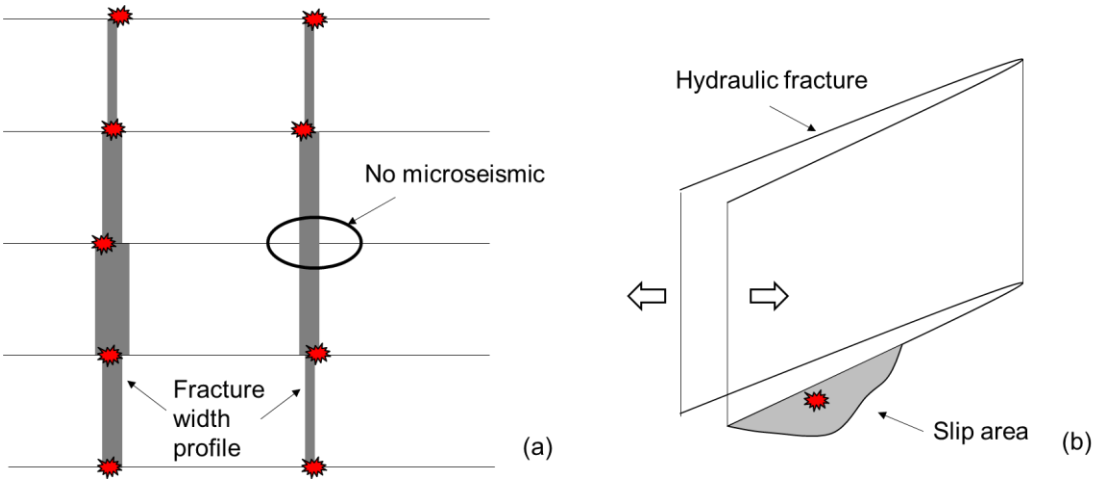

Fig B 9—Conceptual model illustrating connection between fracture width profile and microseismic event generation. Red stars represent the microseismic events. (a) Quiet zones where no microseismic is generated along bedding plane when there is no width difference； (b) slip area and microseismic event generation.

There are two major factors in this model controlling the microseismic magnitude: fracture width and layer mechanical property contrasts. If there is no mechanical property contrast, there will be very few microseismic events even with impactful fracture width (Fig B 9**Error! Reference source not found.**). On the other hand, if there are mechanical property contrasts between

neighboring layers but fracture width is very small, the magnitudes of microseismic events might be below the detection limit of a typical geophone array.

Following this model, the relationship between fracture width and microseismic event magnitudes can be calculated using these following equations.

To calculate the magnitude of the microseismic event M_w, we need to know the seismic moment M_0.

$$M_w = \frac{2}{3}(log_{10}M_0 - 9.1)$$

Eq. B 1

Moment can be calculated using this equation:

$$M_0 = \mu AD$$

Eq. B 2

Here μ is the shear modulus, A is the slip area and D is the slip distance. To determine these two parameters, we need to use Linear Elastic Fracture Mechanics (LEFM) theory (Whittaker et al., 1992).

$$D = \frac{K_{IIc}}{4\mu}\sqrt{\frac{c}{\pi}}[(2k+3)sin\frac{\pi}{2} + sin\frac{3\pi}{2}]$$

Eq. B 3

In this equation, c is the fracture length, K_{IIc} is the mode II fracture toughness, μ is the shear modulus, k is a constant related to the loading condition. Rearranging this equation, we can get the fracture length from the slip distance:

$$c = \frac{16\mu^2\pi}{K_{IIc}^2(k+1)^2}D^2$$

Eq. B 4

According to our model, the relative width difference between two layers determines the driving slip distance. We use a parameter ε to represent the level of width difference due to mechanical contrast between layers. ε varies between 0 and 100%. 0 represents the case where there is no difference between the two layers (homogeneous). 100% means the fracture is terminated/arrested against that bedding plane. The effective width increment is:

$$D = D_0 * \varepsilon$$

Eq. B 5

The slip area is a function of the fracture length. We assume it obeys the square root of fracture length multiplied by a shape factor α. For simplicity, we use 1 here, which means it is an isosceles triangle. The K_{IIc} is assumed to be rather low since we are considering a weak bedding interface.

$$A = \alpha c^2$$

Eq. B 6

Table B 1—parameters used for microseismic event magnitude calculation

Parameters	Value range
Fracture width increment D_0	0.1-4 mm
Width difference ε	0-100%
Shear modulus μ	1GPa
Shape factor α	1
Mode II fracture toughness K_{IIc}	0.1MPam$^{1/2}$

Using the parameters listed in **Error! Reference source not found.** and equations above, we can get the relationship between fracture incremental width and the microseismic event magnitude, shown in Fig B 10.

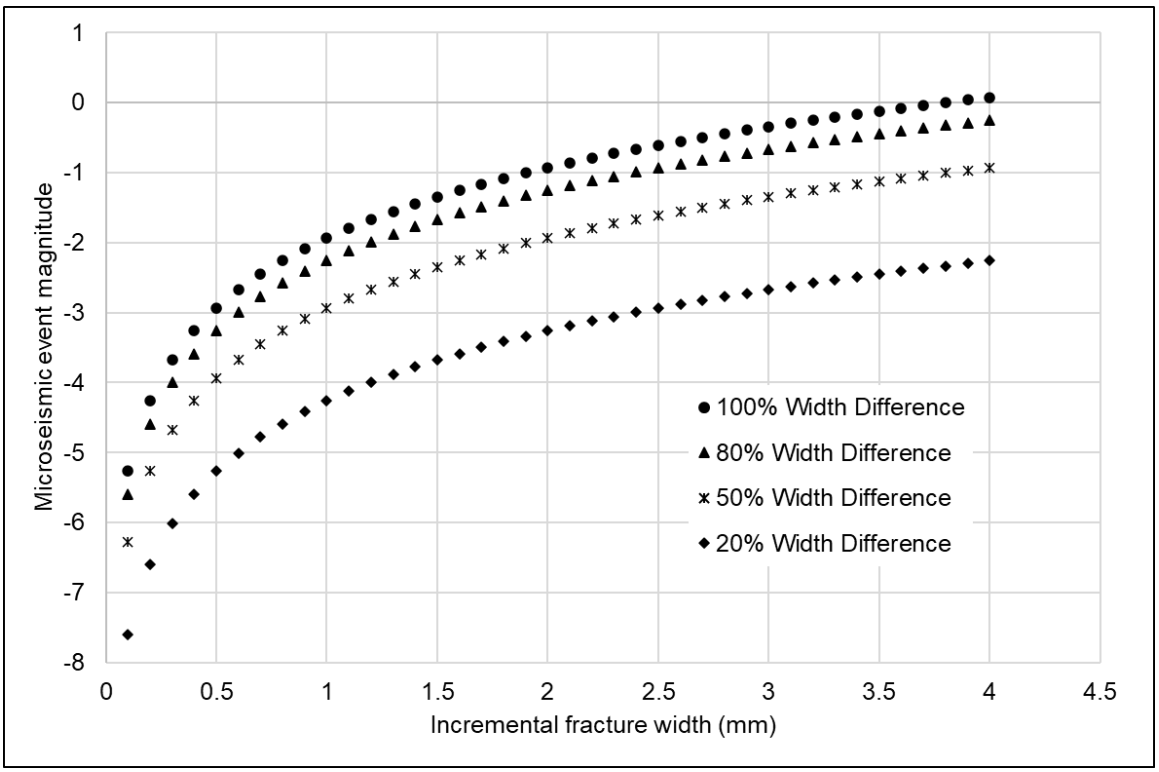

Fig B 10—calculated microseismic event magnitude with incremental fracture width

From Fig B 10, it is easy to observe that both incremental fracture width and mechanical property contrast determine the event magnitude. This explains why some areas have a much high number of microseismic events while others have very few. For example, in the case of homogeneous rock formations, there will be no detectable events. Also from this calculation, we can see that the range of microseismic event magnitudes can be anywhere from -8 to 0, given different fracture width increment values. Since most geophones arrays have detection limit

between -3 and -2, the microseismic events highlight the hydraulic fractures with incremental width of 0.5 mm or above, and for width difference between layers over 50%. When the mechanical contrast is below 20%, there will be barely any microseismic event generated above magnitude -2. Obviously, this is a rough estimate. But it provides a quantitative relationship connecting the microseismic event magnitudes with hydraulic fracture width and geomechanical properties.

Please note that the incremental fracture width is not the total fracture width. It is the incremental width change that resulted in a sudden slip along the bedding planes. Here we adopt the stick-slip slip pattern like natural earthquakes (Brace and Byerlee, 1966). To know exactly how much incremental width occurs in each step is beyond the scope of this paper. But we can safely assume it is a fraction of the total fracture width. Further research needs to be performed to understand the relationship between the stick-slip distance and the total fracture width.

Key Results

We applied this model to the HFTS 2 data to explain the observations mentioned above. This is achieved by combining fracture modeling and logical reasoning. The answers specific to each question are provided below.

Question 1. Why are the event magnitudes larger in the depleted parent wells (BR1H & BR2H) regions?

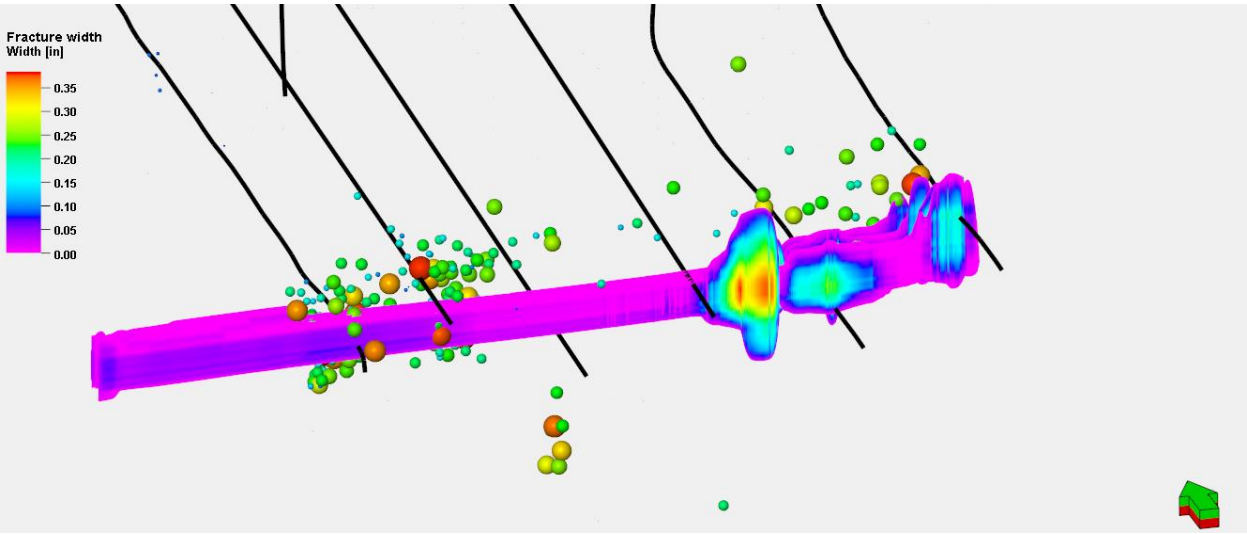

Fig B 11—simulated fracture width profile and the microseismic events observed for B1H Stage 2. Microseismic events are scaled according to their magnitudes.

We simulate the fracture width profile using the real stress profile and pumping schedule under the influence of depleted wells (BR1H and BR2H). The width profile of one stage is shown in Fig B 11. In this figure we can see that the depleted regions have much higher fracture width, thus inducing much larger microseismic events. This is consistent with the pattern observed from Fig B 3. The simulated width is on the order of 0.1-0.2 inch (2.5 to 5 mm) in the depleted region. The

incremental width is a fraction of the total width. Based on the relationship predicted between fracture incremental width and microseismic event magnitude in Fig B 10, the resulting microseismic event magnitude from our model is below -1, consistent with what was observed in Fig B 12.

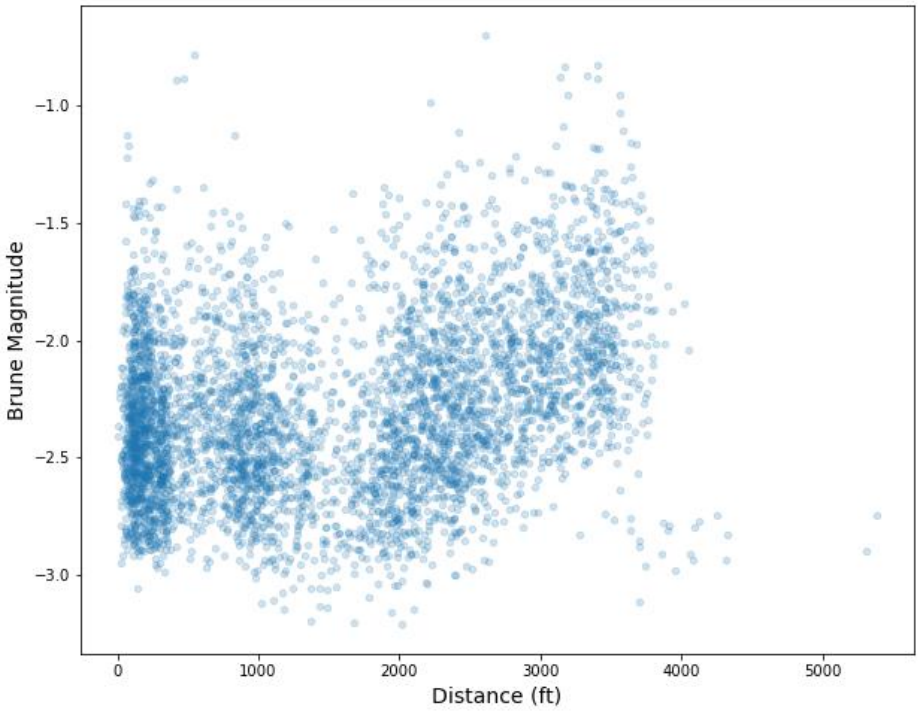

Fig B 12—magnitude of B1H well microseismic events as a function of distance from the perforation.

Also, we plot the magnitude of microseismic events as a function of distance from the perforation location (Fig B 12). We can also see that the low magnitude events are missing at the location of farther distances. This is likely caused by the detection limit of the geophone arrays. The closest geophones are in B3H, as shown in Fig B 2.

Question 2. Why are the microseismic events of the heel stages in well B1H limited around wellbore?

From the fiber LF-DAS data we already know that there are hydraulic fractures intersecting B4H and B3H during those heel side stages where there are no microseismic events (Fig B 3). Therefore, the microseismic data from B1H does not show the entire SRV. Using our model, it is likely because either the hydraulic fracture width in the late stages is smaller than what is required to generate detectable events, or there are fewer mechanical contrasts in this region. It

is difficult to estimate the change of geomechanical properties as there is only one vertical well with log information. However, we can make some deductions about the fracture width.

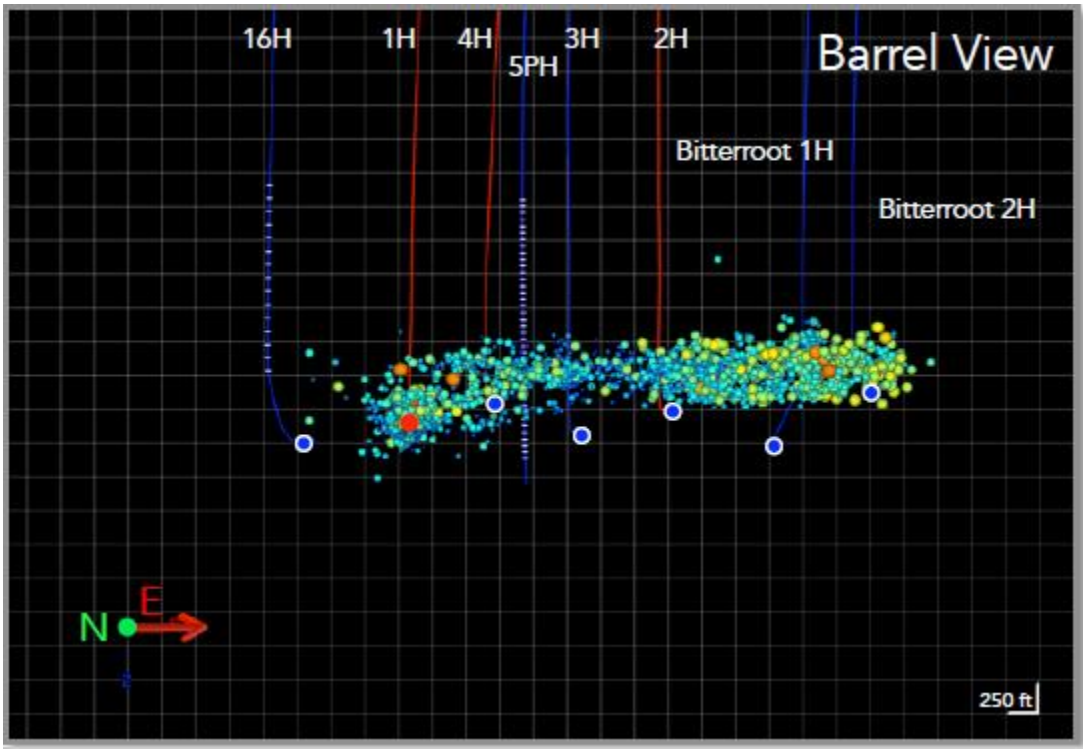

Fig B 13—Gun barrel view of microseismic events in B1H. Microseismic events are filtered with multiple receivers and 2.5ms misfit cutoff.

Due to the influence of depleted parent wells, the toe stages were heavily biased towards the depleted regions (Fig B 3 and Fig B 4). From Fig B 13, we can also see that the microseismic events from B1H were moving upward toward BR2H. This is because BR2H was put on production earlier and has produced more reservoir fluids than BR1H. The microseismic events were migrating toward this more depleted region. We can safely assume due to the influence of depleted region, the hydraulic fractures in the toe side stages have much larger length than height. The heel side stages were not influenced by the depleted regions, and hence the hydraulic fractures were much higher as shown in the fiber optics strain in the vertical well (Fig B 6). The volume pumped in each stage was roughly the same. If the fracture area is larger, by mass balance, the width is smaller, leading to smaller microseismic events according to our model. Therefore, it is likely that the fracture width of B1H heel stages was below the value needed to create detectable microseismic events.

Question 3. Why are B2H microseismic events biased toward the west in the heel stages?

From fiber optics strain data, we know that the hydraulic fractures from B1H have propagated past B4H and B3H in the heel stages (Fig B 6). However, these hydraulic fractures are just not shown by the microseismic events. Following the bedding plane slip model that we have proposed above, the microseismic event magnitude is a function of fracture width. If there are

existing hydraulic fractures in a region, adding additional volume will further increase the width of these existing hydraulic fractures, leading to more microseismic events.

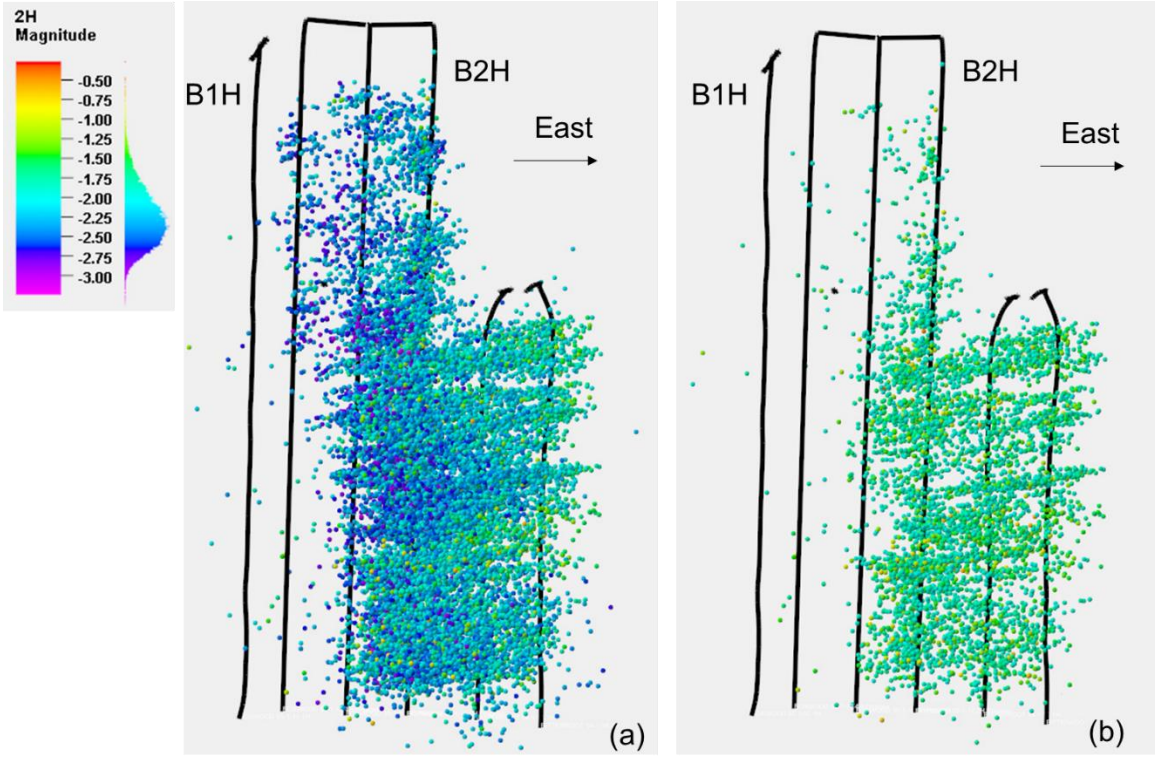

Fig B 14—comparison of microseismic events of B2H well. (a) no filter applied; (b) only showing microseismic events with magnitude > -2.0

If we filter the microseismic events of B2H with a high magnitude pass, we can see that the high magnitude events are clustered around the wellbore along the heel stages, much like what is observed in B1H. The microseismic events west to the B2H wellbore were just above the detection limit of geophone array. We can deduct that by adding additional volume of B2H well, the hydraulic fractures from previous B1H were further widened. The increased fracture width produced larger magnitude microseismic events, which made previously undetectable events now detectable. The lack of microseismic events west to B1H wellbore location is because the hydraulic fracture was not wide enough, which also provides additional evidence to Question 1.

Question 4. Why are microseismic events shown in the B2H and B4H heel stages high above wellbore depth with a quiet zone in the middle?

From fiber optics strain data of the vertical observation well (B5PH), we know that the hydraulic fractures were propagating over 1000 ft. above the wellbore. The isolated microseismic event group is likely to be directly related to the hydraulic fractures and not caused by stress transfer or fault reactivation. The key question is: why there is a quiet zone in the middle? From our model, there are two main drivers for microseismic event generation: fracture width increment and mechanical property variation between layers. From Question 2 and 3 we concluded that the hydraulic fractures were narrower in the heel stages of B1H. Another factor might be the

rock is more homogenous in this region. There was not enough mechanical property contrast between layers to cause detectable microseismic event until BSPG3 LM.

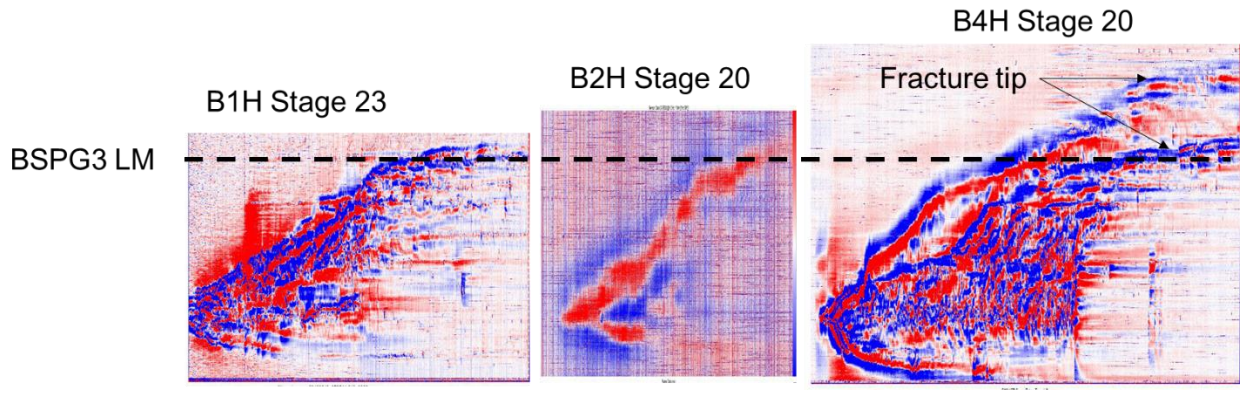

Fig B 15—Comparison of the DAS strain data in B5PH of B1H, B2H and B4H. The vertical scale is the same for 3 wells.

By comparing B2H and B4H, we can see that there are more microseismic events located higher in B4H than B2H (Fig B 5). Like our argument in Question 3, additional fracture fluid would further increase the fracture width, hence inducing more microseismic events. The stimulation was in the sequence of B1H, B2H and B4H, and hence more microseismic events are expected in the later wells. Another important difference is B4H is landed higher than B1H and B2H (Fig B 13). From Fig B 15, we can see larger height growth in B4H compared with B2H and B1H in the heel stages. Also, from B4H LF-DAS strain plot there appears to be two fracture tips. The lower fracture tip is likely caused by the high stress layer in BSPG3LM, which further validates our model that microseismic events are caused by layer mechanical contrasts.

Conclusions

Although microseismic monitoring has been applied to hydraulic fracturing for a long time in the industry, fundamental understanding of the mechanism of microseismic event generation remains poor. The HFTS 2 experiment provides a unique opportunity to understand the geomechanical conditions with data from different surveillance techniques. In this paper we proposed a bedding plane slip model connecting between the microseismic magnitude with two other parameters: incremental fracture width and mechanical layer contrasts. When there is not enough contrast in mechanical layers or fracture widths, the microseismic only represents a subset of the SRV. We demonstrated that this model can be used to explain many of the unexpected phenomena observed during stimulation, particularly under the influence of the parent depleted wells.

References

Baig, A. and Urbancic, T. 2010. Microseismic moment tensors: A path to understanding frac growth. *The Leading Edge*, **29**(3): 320-324. https://doi.org/10.1190/1.3353729.

Brace, W.F. and Byerlee, J.D. 1966. Stick-slip as a mechanism for earthquakes. *Science*, **153**(3739): 990-992. https://doi.org/ 10.1126/science.153.3739.99.

Busetti, S., Jiao, W. and Reches, Z.E. 2014. Geomechanics of hydraulic fracturing microseismicity: Part 1. Shear, hybrid, and tensile events. Geomechanics of Hydraulic Fracturing Microseismicity Part 1. *AAPG Bull*, **98**(11): 2439-2457. https://doi.org/10.1306/05141413123.

Ciezobka, J. and Reeves, S. 2021. Overview of Hydraulic Fracturing Test Sites (HFTS) in the Permian Basin and Summary of Selected Results (HFTS-I in Midland and HFTS-II in Delaware). Paper presented at Latin America Unconventional Resources Technology Conference. https://doi.org/10.15530/urtec-2020-1544.

Duncan, P.M., Barker, W.B., Eisner, L., et al. 2013. Microseismic monitoring in early Haynesville development. In Geology of the Haynesville Gas Shale in East Texas and West Louisiana, AAPG. 219-236 https://doi.org/10.1306/13441852M1053605.

Hull, R.A., Leonard, P.A. and Maxwell, S.C. 2017. Geomechanical investigation of microseismic mechanisms associated with slip on bed parallel fractures. Paper presented at Unconventional Resources Technology Conference, Austin, Texas. https://doi.org/10.15530/URTEC-2017-2688667.

Kahn, D., Roberts, J. and Rich, J. 2017. Integrating microseismic and geomechanics to interpret hydraulic fracture growth. Paper presented at Unconventional Resources Technology Conference, Austin, Texas. https://doi.org/10.15530/URTEC-2017-2697445.

Rutledge, J., Weng, X., Yu, X., et al. 2016. Bedding-plane slip as a microseismic source during hydraulic fracturing. Paper presented at SEG Annual Meeting. https://doi.org/10.1190/segam2016-13966680.1.

Rutledge, J., 2019. Is bedding-plane slip a common microseismic source during hydraulic fracturing? Paper presented at SEG Annual Meeting. https://doi.org/10.1190/segam2019-3215935.1.

Stanek, F. and Eisner, L. 2013. New model explaining inverted source mechanisms of microseismic events induced by hydraulic fracturing. Paper presented at SEG Annual Meeting. https://doi.org/10.1190/segam2013-0554.1.

Staněk, F. and Eisner, L.. 2017. Seismicity induced by hydraulic fracturing in shales: A bedding plane slip model. *J Geophys Res*: *Solid*, **122**(10): 7912-7926. https://doi.org/10.1002/2017JB014213.

Tan, Y., Chai, C. and Engelder, T. 2014a. Use of S-wave attenuation from perforation shots to map the growth of the stimulated reservoir volume in the Marcellus gas shale. *The Leading Edge*, **33**(10): 1090-1096. https://doi.org/10.1190/tle33101090.1.

Tan, Y., Johnston, T. and Engelder, T. 2014b. The concept of joint saturation and its application. *AAPG Bull*, **98**(11): 2347-2364. https://doi.org/10.1306/06231413113.

Tan, Y. and Engelder, T., 2016. Further testing of the bedding-plane-slip model for hydraulic-fracture opening using moment-tensor inversions. *Geophys*, **81**(5): KS159-KS168. https://doi.org/10.1190/geo2015-0370.1.

Tan, Y., Wang, S., Rijken, P., et al. 2020. Geomechanical Template for DAS Fiber Strain Patterns During Hydraulic Fracturing. Paper presented at SPE Annual Technical Conference and Exhibition. https://doi.org/10.2118/201627-MS.

Tan, Y., Wang, S., Rijken, M., et al. 2021. Geomechanical Template for Distributed Acoustic Sensing Strain Patterns during Hydraulic Fracturing. *SPE J*, **26**(02): 627-638. https://doi.org/10.2118/201627-PA.

Teran, O.J. and Thornton, M.P. 2019. Microseismic Bedding-plane Slip Theory–[Requires] a Very Slippery Slope or a Very Large SHmax. Paper presented at the Unconventional Resources Technology Conference, Denver, Colorado. https://doi.org/10.15530/urtec-2019-997.

Vissotski, A., Singh, A., Rijken, P. et al. 2021. Analysis of completion design impact on cluster efficiency and pressure-based well communication in HFTS-2 Delaware Basin. Paper presented at Unconventional Resource Technology Conference. https://doi.org/10.15530/urtec-2021-5289.

Wang, S., Tan, Y., Sangnimnuan, A., et al. 2019. Learnings from the Hydraulic Fracturing Test Site (HFTS)# 1, Midland Basin, West Texas—A Geomechanics Perspective. Paper presented at Unconventional Resources Technology Conference, Denver, Colorado. https://doi.org/10.15530/urtec-2019-1570.

Wang, J., Tan, Y., Wang, S., et al. 2021. Observations and Modeling of Fiber-Optics Strain on Hydraulic Fracture Height Growth in HFTS-2. Paper presented at Unconventional Resources Technology Conference. https://doi.org/10.15530/urtec-2021-5295.

Weng, X., Chuprakov, D., Kresse, O., et al. 2018. Hydraulic fracture-height containment by permeable weak bedding interfaces. *Geophys*, **83**(3): MR137-MR152. https://doi.org/10.1190/geo2017-0048.1.

Whittaker, B.N., Singh, R.N. and Sun, G. 1992. Rock fracture mechanics. Principles, design and applications. Elsevier.

Yang, Y. and Zoback, M.D. 2014. The role of preexisting fractures and faults during multistage hydraulic fracturing in the Bakken Formation. *Interpretation*, **2**(3): SG25-SG39. https://doi.org/10.1190/INT-2013-0158.1.

Zhang, Z., Fang, Z., Stefani, J., et al. 2020. Modeling of Fiber Optic Strain Responses to Hydraulic Fracturing. *Geophys*, **85**(6): 1-22. https://doi.org/10.1190/geo2020-0083.1.

Zhang, Z., J. DiSiena, D. Bevc, I., et al. 2021. Hydraulic fracture characterization by integrating multidisciplinary data from the Hydraulic Fracturing Test Site 2 (HFTS-2). Paper presented at Unconventional Resources Technology Conference, Houston, Texas. https://10.15530/urtec-2021-5039.

Appendix C: HFTS-2 Completions Design and State-of-the-Art Diagnostics Results

Authors: Nancy Zakhour, Matt Jones, Yu Zhao, Kate Orsini, Vinay Sahni

Summary

Various completion schemes were tested as part of the Hydraulic Fracture Test Site-2 (HFTS-2) project. The wells were instrumented with permanent fiber optic (FO) cable, and unique near-wellbore and far-field region surveys were acquired to evaluate spatial and temporal hydraulic fracture characteristics. The state-of-the-art diagnostics included substantial monitoring of both the well stimulation and longer-term production performance. The objective was to evaluate and improve stimulation distribution effectiveness (SDE) for different completion designs based on the diagnostics results. A hydraulic fracturing (HF) profile (i.e., proppant/fluid allocation among clusters) was obtained using near-wellbore Distributed Acoustic Sensing (DAS) data acquired during stimulation. Statistical analysis provided a quantitative assessment of SDE for the different completion designs. A novel workflow was developed to assess time-lapse fracture property changes at the cluster and stage levels based on Distributed Strain Sensing (DSS) data acquired during the production phase. These time-lapse fracture property changes were compared with the HF profile. Based on the statistical analysis, Rate Per Cluster (RPC) during proppant slurry placement appears to be a primary completion design variable, rather than the typical Rate Per Perf (RPP). If RPC was not maintained at a certain level, the likelihood of uneven distribution increased dramatically. The stage configurations that created low RPC while maintaining high RPP did not show improved SDE. The strain change results based on DSS data during the production phase indicated near-wellbore fracture property changes (e.g., aperture changes during well shut-in and flow periods) and aligned well with near-wellbore DAS signals acquired during stimulation. More importantly, fracture property changes based on DSS data acquired during two tests over a 7-month period show high consistency and good alignment with the near-wellbore HF profile. This workflow quantitatively evaluates SDE for different completion designs using diagnostic results and could help optimize completion strategy for future development projects. The analysis and interpretation of results demonstrate the technical feasibility of using permanent fiber optic cable for stimulation and production monitoring and indicate a strong correlation between proppant/fluid allocation and time-lapse near-wellbore fracture property changes.

Introduction

The Hydraulic Fracture Test Site-2 (HFTS-2) is a cost-shared, field research program located in the Delaware Basin of West Texas, specifically in Block 55 of Loving County. Occidental is the host company and operator of the program, and the 18 consortia members all acquired a rich data set consisting of microseismic (MS) data, 1,500 ft of whole core (including 1,000 ft of SRV core), DFIT data, PVT data, quad combo and image logs, proppant logs, geochemical data, pressure/temperature (P/T) data from 28 bottomhole gauges, and fiber optic data from 1 vertical pilot well and 2 horizontal wells.

The primary objective of the Completions Design of Experiments (DoE) for the HFTS-2 study was to evaluate the stimulation distribution effectiveness (SDE) of various stimulation schemes relative to a baseline configuration. This baseline had a ~190 ft geometric stage length (SL)

containing 6 perforation clusters (PC) with a perforation cluster spacing (PCS) of 32 ft. Each PC had 4 perforations for a total of 24 perforations per stage, and each perforation had an average entry hole diameter (EHD) of 0.41 in. This baseline configuration is compared to more Aggressive Limited Entry (ALE) practices achieved by reducing the number of perforations per cluster. Additionally, tapered perforations to reduce heel-side bias were tested along with Extended Stage Length (ESL) with 10 PCs per stage at ~330 ft SL using ALE practices.

While stages treated with fewer PCs tend to have a higher SDE and better well performance, the underlying issue for most E&P operators is the economics. Although productivity may be improved by completing a well with shorter stages and fewer PCs per interval, the cost of doing so can outweigh the benefits. This dilemma begs the question of how horizontal wells in unconventional formations can be completed with longer stages and fewer intervals throughout the lateral while maintaining an effective stimulation with uniform distributions of proppant and fluid volumes, which is precisely what this study addresses.

The second objective of the Completions DoE was to establish an improved understanding of Stimulated Rock Volume (SRV) to drive enhanced field development programs by optimizing well spacing, drilling and completion configurations and strategies, and mitigating parent-child influence on performance and economics.

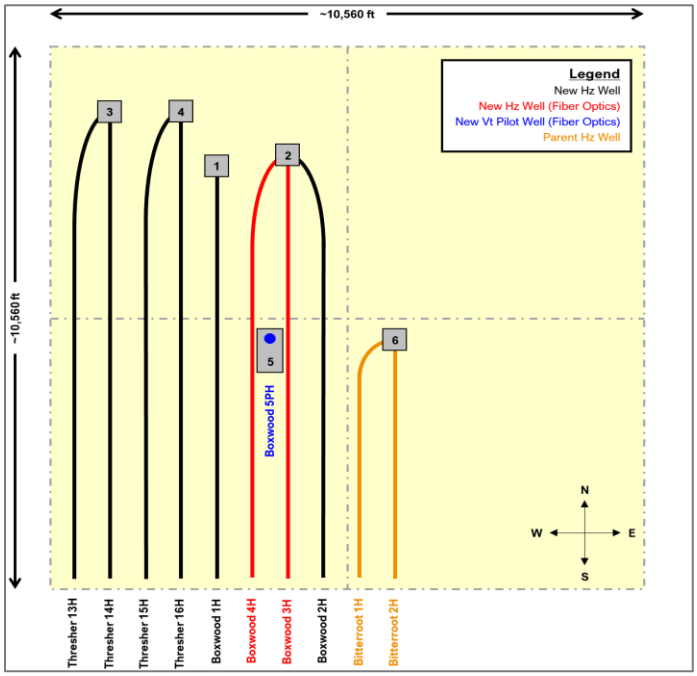

Fig C 1—Simplified map of the area of operations for HFTS-2.

In total, there were 5 new horizontal wells and 1 new vertical pilot well that constituted the project at the time of hydraulic stimulation. The well placement is shown in Fig C 1. The primary horizontal wells of interest (Boxwood-1H, -2H, -3H, -4H, and Thresher-16H) were bracketed to the west by drilled, uncompleted "child wells" and to the east by previously completed, producing "parent wells." The wells to the west (Thresher-13H, -14H, and -15H) were used to

collect DFIT's data as well as pressure data using installed pressure gauges. Similarly, the wells to the east (Bitterroot-1H and -2H) were not considered part of the project, but they are shown to indicate their proximity to the primary horizontal wells of interest, as potential depletion effects on SDE were a consideration in the initial planning phases of the Completions DoE. The vertical pilot well (Boxwood-5PH) was placed between the middle and heel sections of the Boxwood-3H and -4H laterals. All of the horizontal child wells had approximately 7,500 ft of lateral length to complete, and the parent wells had approximately 4,500 ft of completed lateral length.

To define the relationship between the primary wells of interest and illustrate the instrumentation used for data acquisition and diagnostic purposes, a simplified stratigraphic cross-section is shown in Fig C 2**.** The horizontal wells were positioned strategically in the Wolfcamp X (WFMP_X), Wolfcamp Y (WFMP_Y), Wolfcamp A1 (WFMP_A1), and Wolfcamp A2 (WFMP_A2) target intervals with an approximate horizontal spacing of 660 ft between laterals. The Boxwood-5PH vertical pilot well traverses all the target intervals in the Wolfcamp A formation and lands within the upper portion of the Wolfcamp B (WFMP_B) formation.

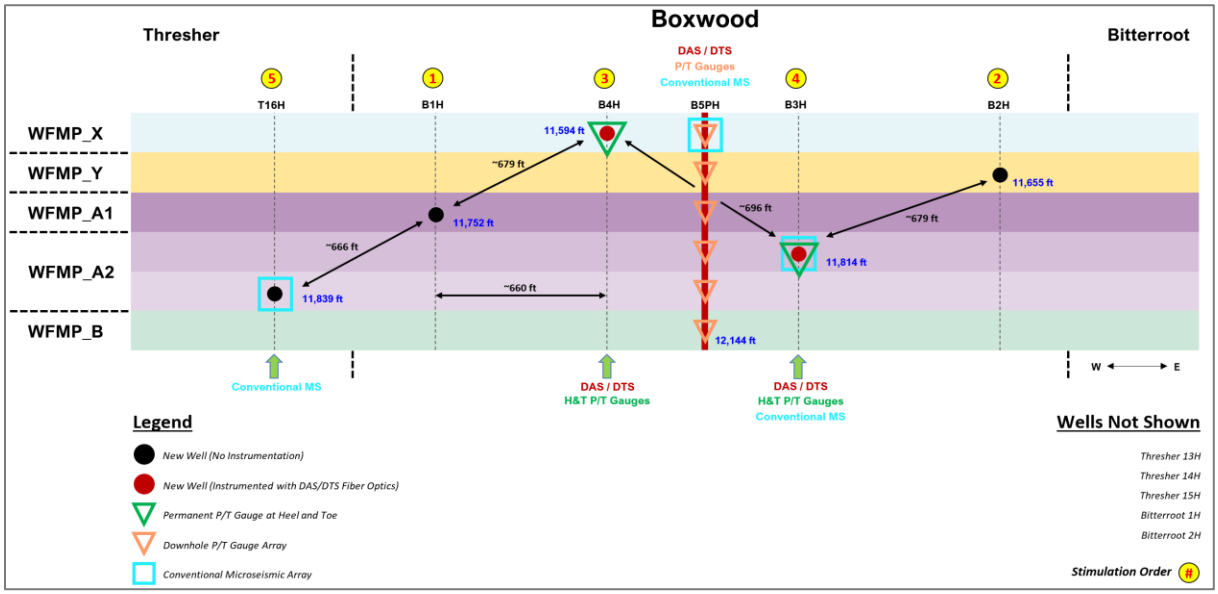

Fig C 2—Simplified stratigraphic cross-section of the wells of interest for the hydraulic stimulation portion of HFTS-2.

Microseismic (MS) arrays were installed in Boxwood-3H, -5PH, and Thresher-16H for 3D acoustic imaging to provide insights into fracture half-length, height, azimuth, and SRV. The Boxwood-3H, -4H, and -5PH wells were each equipped with a multi-mode fiber optic cable behind casing for DAS and DTS profiling. The data acquired included HF profiling on Boxwood-3H and -4H as well as far-field cross-well strain (FF CWS) monitoring for the Boxwood-1H, -2H, and Thresher-16H wells as they were stimulated. The FF CWS data acquired on the horizontal wells provide insights regarding minimum fracture half-lengths and azimuth, while the FF CWS data acquired from the vertical pilot well provide insights regarding fracture height in addition to azimuth. Lastly, the Boxwood-3H, -4H, and -5PH wells were also equipped with downhole P/T gauges, which provided data for fracture pressure matching on the horizontal wells and fracture propagation pressures on the vertical pilot well. The P/T gauges on the horizontal wells were

located at the heel and toe of the laterals. The P/T gauges on the vertical pilot well were selectively placed throughout the target intervals and isolated by packers.

Although zipper fracs are typically preferred for efficiency and reduced cycle times, the horizontal wells were stimulated through single-well operations, or "stack fracs." Boxwood-1H was stimulated first, followed by Boxwood-2H second and Boxwood-4H third. Then the MS array in Boxwood-3H was retrieved prior to its stimulation. The MS array was then retrieved from Thresher-16H, and it was subsequently completed along with the remaining Thresher-13H, -14H, and -15H wells to the west. The order of operations is shown with yellow circles in Fig C 2 and in the Gantt Chart below in Fig C 3.

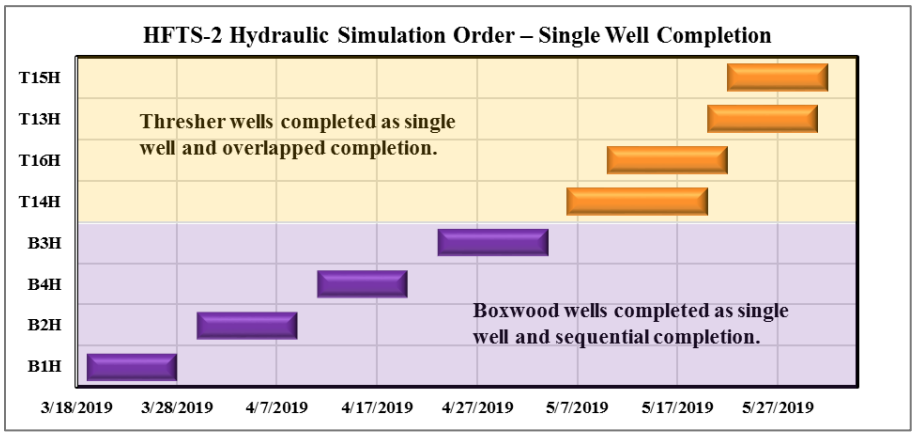

Fig C 3—Hydraulic stimulation sequencing Gantt Chart.

Not all of the horizontal wells were equipped with the same casing design configuration. Boxwood-2H, -3H, and -4H were newly drilled wells that employed a 5 ½" × 5" tapered production casing string, while the previously drilled Boxwood-1H and Thresher-16H were equipped with a 7" × 4 ½" liner design. These details, along with the maximum allowable surface treating pressures (MASTP) and nominal inner diameters (IDs), are listed below in Fig C 4.

Well Name	Vertical Casing Description	Vertical Casing Nominal ID (in)	Horizontal Casing Description	Horizontal Casing Nominal ID (in)	MASTP (psig)
Boxwood 1H	7", 29#, C-110/P-110 HC, BTC	6.184	4-1/2", 13.5#, P-110 HC, CDC HTQ	3.920	8,900
Boxwood 2H	5-1/2", 23#, P-110 HC, CDC HTQ	4.670	5", 18#, P-110 HC, CDC HTQ	4.276	12,200
Boxwood 3H	5-1/2", 23#, P-110 HC, CDC HTQ	4.670	5", 18#, P-110 HC, CDC HTQ	4.276	12,200
Boxwood 4H	5-1/2", 23#, P-110 HC, CDC HTQ	4.670	5", 18#, P-110 HC, CDC HTQ	4.276	12,200
Thresher 16H	7", 29#, C-110/P-110 HC, BTC	6.184	4-1/2", 13.5#, P-110 HC, CDC HTQ	3.920	8,900

Fig C 4—Casing design details for the horizontal wells of interest in HFTS-2.

Completions Design of Experiments (DoE)

With the goal of improving SDE, the objectives of the Completions DoE focused on evaluating different stage configurations with varying degrees of LE as well as alternative perforating

techniques designed to reduce the over-stimulation of PCs closest to the heel. Eleven separate full-stage designs were conceptualized at the outset of the project, as shown in Fig C 5. The configuration denoted as "1PC" was designed to be a single point of injection that was included in the diagnostics portion of the DoE for the purpose of DAS amplitude calibration.

The baseline completion configuration consisted of a geometric 6 PC design with 32-ft spacing between PCs. This constituted a 192-ft effective stage length with 4 perforations per PC for a total of 24 perforations per stage, which was typically treated at 60–70 bpm. Perforation entry hole diameters (EHD) usually ranged from 0.38 to 0.41 in., which resulted in a total perforation friction value of 600–1,000 psi at the end of treatment depending on the magnitude of perforation erosion and the number of PCs still active.

Stage Design	PCs per Stage	Perfs per Cluster	Perfs per Stage	Perf Taper Design	Cluster Spacing (ft)	Effective Stage Length (ft)	Rate per Perf (bpm/perf)	Rate per Cluster (bpm/cluster)	Planned Non-FO Stages	Planned FO Stages	Planned Wells
6 x 24	6	4	24	None	32	192	2.5	10	29	6	B1H, B2H, B3H, B4H
6 x 18	6	3	18	None	32	192	3.3	10	6	9	B2H, B3H, B4H
6 x 15	6	2.5	15	2H, 3T	32	192	4	10	6	9	B2H, B3H, B4H
6 x 12	6	2	12	None	32	192	5	10	0	9	B3H, B4H
8 x 24	8	3	24	None	32	256	2.5	7.5	0	2	B3H
8 x 16	8	2	16	None	32	256	3.8	7.5	0	3	B3H
9 x 18	9	2	18	1H, 2M, 3T	32	288	3.3	6.7	0	2	B4H
10 x 20	10	2	20	None	32	320	3	6	5	4	B2H, B3H, B4H
10 x 15	10	1.5	15	1H, 2T	32	320	4	6	5	3	B2H, B3H, B4H
12 x 24	12	2	24	None	16	192	2.5	5	10	0	B1H
12 x 24	12	2	24	None	12	144	2.5	5	2	0	B2H
1PC	1	6	6	None	None	None	Variable	Variable	1	3	B2H, B3H, B4H

***Note: Limited Entry values are based on a designed slurry rate of 60 bpm.

Fig C 5—Stage configurations conceptualized at the outset of the hydraulic stimulation portion of HFTS-2.

While it is entirely appropriate to discuss and evaluate different stage configurations according to perforation friction, this approach can become complicated when designs with tapers are introduced, as not all PCs within the stage will have the same number of perforations. To simplify comparison between designs, the Completions DoE focused on Rate Per Perf (RPP) and Rate Per Cluster (RPC) to delineate stage configurations in terms of LE aggressiveness and addressed configurations with tapered perforations in a binary manner.

The primary objective was to evaluate the SDE provided by the 6 × 24 baseline configuration and then test configurations with increasingly more aggressive LE RPP values to determine if SDE could be improved. Stages with tapered perforations were also included to eliminate, or at least reduce, the heel-side bias observed in other studies. To determine if extended stage lengths (ESL) with more PCs and relatively aggressive LE RPP values could lead to a high degree of SDE and potentially fewer stages required to complete a horizontal well, these types of configurations were included in the DoE, as well. Lastly, a slant well was planned to be drilled through the SRV for coring and fracture analysis following hydraulic stimulation and the period of initial production, so several stages with varying LE designs were strategically placed along the lateral of the Boxwood-3H well.

As a controlled variable, spacing between PCs was designed to be kept constant at 32 ft on the Boxwood-3H and -4H wells for all stage configurations. Proppant and fluid volumes were also kept constant at 83,333 lb./PC and 1,833 bbl./PC, respectively. The DoE program also tested several stage configurations with substantially more PCs and tighter PC spacing, but these could only be performed on Boxwood-1H and -2H, which did not have fiber optic cable behind casing.

That necessitated perforating within casing cable protectors (CCPs) to protect the cable during stimulation. These configurations were not held to the same sand and fluid volumes per PC as described above. All proppant used was 100% WTX Regional 100 Mesh.

Operational Execution

Prior to stimulating any of the new horizontal wells, fiber optic cable mapping was conducted on Boxwood-3H and -4H to determine the relative bearing (RB) of the CCPs behind the casing. This is a critical component in the stimulation process for wells equipped with fiber optic cable, as the mapping results are used to prescribe perforating gun orientation angles to avoid shooting through and damaging the cable. The logs illustrating the RB of the CCPs for Boxwood-3H and -4H are shown in Fig C 6, which shows how the cable makes one or more full revolutions along the length of the lateral from the toe to the heel on both wells.

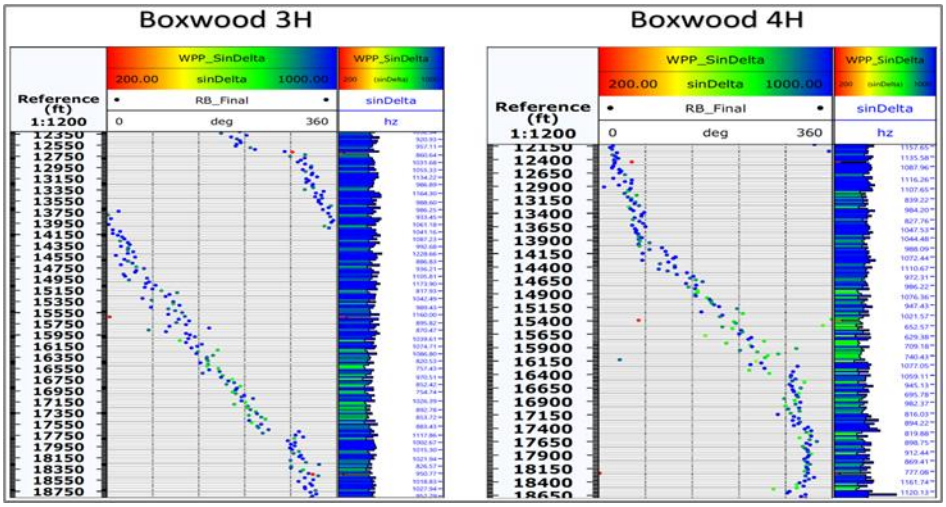

Fig C 6—RB mapping results of the CCPs on the Boxwood-3H and -4H wells (logs courtesy of Schlumberger).

While mapping the RB of the CCPs is relatively straightforward, determining which PCs should be omitted from the perforating plan is more complex. To ensure that the fiber survives the hydraulic stimulation process so DAS/DTS data can be collected during production, an overabundance of caution was used in planning the perforation process, requiring the removal of some previously planned PCs. All the perforation orientations on the Boxwood-3H and -4H wells were performed using eccentric weight bars and a rigorous QC process on location prior to every plug-and-perf run. Therefore, all PCs were successfully perforated with no damage to the fiber.

The first horizontal well to be stimulated was Boxwood-1H. This well was not equipped with fiber optics for DAS/DTS data acquisition for hydraulic stimulation profiling, so the diagnostics were done with MS monitoring from the Boxwood-3H, -5PH, and Thresher-16H wells along with FF CWS monitoring on the Boxwood-3H, -4H, and -5PH wells. The stimulation details and perforation details for this well are given in Fig C 7 and Fig C 8. The 12 × 24 stage groups were strategically placed in the toe and heel sections of the lateral so any depletion effects caused by the Bitterroot-1H and -2H wells to the east could be observed and delineated. A 34th stage was

planned for the well, but due to operational issues encountered on the final plug-and-perf run, that stage was omitted.

Boxwood 1H - Actual Stimulation Design

Stage	Stage Design	PCs per Stage	Perfs per Cluster	Perfs per Stage	Perf Taper Design	Perf Phasing (deg)	Perf Orientation (deg CW)	PC Spacing (ft)	Top Perf (ft MD)	Bottom Perf (ft MD)	Effective Stage Length (ft)	Average Treating Rate (bpm)	Average RPP (bpm/perf)	Average RPC (bpm/cluster)	Proppant (lbs)	Fluid (bbls)
1	6 x 24	6	4	24	None	60	None	33	18,778	18,942	196	43	1.8	7.2	508,750	11,039
2	6 x 24	6	4	24	None	60	None	33	18,575	18,739	196	53	2.2	8.9	509,670	11,270
3	6 x 24	6	4	24	None	60	None	33	18,373	18,536	196	57	2.4	9.6	505,850	11,475
4	6 x 24	6	4	24	None	60	None	33	18,170	18,334	196	53	2.2	8.9	510,830	11,440
5	6 x 24	6	4	24	None	60	None	33	17,967	18,131	196	57	2.4	9.5	506,810	11,387
6	12 x 24	12	2	24	None	0	0	16	17,756	17,931	191	60	2.5	5.0	505,640	11,138
7	12 x 24	12	2	24	None	0	0	16	17,554	17,728	190	60	2.5	5.0	502,290	11,380
8	12 x 24	12	2	24	None	0	0	16	17,351	17,526	191	58	2.4	4.9	498,350	11,149
9	12 x 24	12	2	24	None	0	0	16	17,151	17,323	188	63	2.6	5.3	515,750	11,125
10	12 x 24	12	2	24	None	0	0	16	16,945	17,120	190	58	2.4	4.8	503,650	11,320
11	6 x 24	6	4	24	None	60	None	33	16,751	16,914	196	56	2.3	9.3	504,070	10,706
12	6 x 24	6	4	24	None	60	None	33	16,548	16,712	196	66	2.8	11.0	504,080	10,965
13	6 x 24	6	4	24	None	60	None	33	16,345	16,509	196	69	2.9	11.5	499,610	11,054
14	6 x 24	6	4	24	None	60	None	33	16,143	16,306	196	61	2.5	10.1	500,440	11,102
15	6 x 24	6	4	24	None	60	None	34	15,940	16,109	203	61	2.5	10.1	507,930	11,071
16	6 x 24	6	4	24	None	60	None	33	15,737	15,901	196	71	2.9	11.8	506,800	10,994
17	6 x 24	6	4	24	None	60	None	33	15,534	15,698	196	62	2.6	10.3	500,780	11,264
18	6 x 24	6	4	24	None	60	None	33	15,332	15,495	196	59	2.4	9.8	508,140	11,002
19	6 x 24	6	4	24	None	60	None	33	15,129	15,293	196	62	2.6	10.3	505,780	10,913
20	6 x 24	6	4	24	None	60	None	32	14,926	15,087	193	61	2.6	10.2	506,540	11,025
21	6 x 24	6	4	24	None	60	None	33	14,723	14,887	196	70	2.9	11.7	513,510	11,140
22	6 x 24	6	4	24	None	60	None	33	14,521	14,684	196	65	2.7	10.8	507,990	10,873
23	6 x 24	6	4	24	None	60	None	33	14,318	14,482	196	63	2.6	10.5	510,150	10,407
24	6 x 24	6	4	24	None	60	None	33	14,115	14,279	196	63	2.6	10.6	502,530	10,943
25	12 x 24	12	2	24	None	0	0	16	13,905	14,079	190	71	2.9	5.9	503,390	10,958
26	12 x 24	12	2	24	None	0	0	16	13,702	13,877	191	66	2.8	5.5	499,820	11,524
27	12 x 24	12	2	24	None	0	0	16	13,499	13,675	192	64	2.7	5.3	500,580	10,717
28	12 x 24	12	2	24	None	0	0	16	13,296	13,471	190	65	2.7	5.4	504,240	10,746
29	12 x 24	12	2	24	None	0	0	16	13,094	13,268	190	67	2.8	5.6	505,380	10,845
30	6 x 24	6	4	24	None	60	None	33	12,899	13,063	196	66	2.8	11.0	500,560	10,672
31	6 x 24	6	4	24	None	60	None	33	12,696	12,860	196	66	2.7	10.9	504,530	11,729
32	6 x 24	6	4	24	None	60	None	33	12,493	12,657	196	66	2.8	11.1	506,640	11,131
33	6 x 24	6	4	24	None	60	None	33	12,291	12,454	196	69	2.9	11.6	501,060	10,937

Fig C 7—Stimulation details for Boxwood-1H.

Perforation Charge Details - Boxwood 1H

Gun Size (in)	Perf Density (spf)	Perf Phasing (deg)	Charge Name	Pentration Depth (in)	Perf Diameter (in)	Explosive Load (grams)	Test Casing Specification
2-3/4	6	60	150 MaxForce - Frac, RDX, IS	22.5	0.35	15	4-1/2 in, 13.5 lb/ft, P-110

Fig C 8—Perforation charge details for Boxwood-1H.

Next was the stimulation of the Boxwood-2H well. As shown in Fig C 1, this well was closest to the Bitterroot-1H and -2H producing parent wells, making it more susceptible to depletion effects than the other new horizontal wells. The stimulation objectives for Boxwood-2H were twofold. First, because the well shared the same casing design as Boxwood-3H and -4H, it was to be used as a test case for some of the more aggressive LE stage designs and oriented perforations, as well as the 1PC single point injection, to understand how these configurations might behave from a rate and pressure perspective. Second, as this well was offset by depletion towards the toe and by unstimulated rock towards the heel, it provided a great opportunity to collect MS and FF CWS data with different stage configurations in both settings. The stimulation details and perforation details for this well are given in Fig C 9 and Fig C 10 of the Appendix. The stage configurations in the first half of the lateral were replicated in the second half. Stage 15, which has a 9 × 14 configuration, was meant to be a 10 × 15 configuration with ESL, tapered

perforations, and an aggressive LE RPP value. Unfortunately, one of the perforating guns could not be fired during the plug-and-perf run, so a modified stage design was implemented.

Boxwood 2H - Actual Stimulation Design

Stage	Stage Design	PCs per Stage	Perfs per Cluster	Perfs per Stage	Perf Taper Design	Perf Phasing (deg)	Perf Orientation (deg CW)	PC Spacing (ft)	Top Perf (ft MD)	Bottom Perf (ft MD)	Effective Stage Length (ft)	Average Treating Rate (bpm)	Average RPP (bpm/perf)	Average RPC (bpm/cluster)	Proppant (lbs)	Fluid (bbls)
1	6 x 24	6	4	24	None	60	None	31	18,612	18,768	188	78	3.2	12.9	507,720	11,016
2	6 x 24	6	4	24	None	60	None	31	18,416	18,573	188	75	3.1	12.5	505,690	10,861
3	6 x 24	6	4	24	None	0	0	30	18,224	18,377	183	71	2.9	11.8	501,800	11,278
4	6 x 18	6	3	18	None	60	None	31	18,024	18,178	184	65	3.6	10.8	504,810	12,153
5	6 x 18	6	3	18	None	60	None	31	17,828	17,985	188	57	3.2	9.6	506,750	11,254
6	6 x 18	6	3	18	None	0	0	31	17,633	17,789	188	58	3.2	9.7	507,840	11,442
7	6 x 15	6	3	15	2H,3T	0	0	31	17,437	17,594	188	70	4.6	11.6	509,000	11,291
8	6 x 15	6	3	15	2H,3T	0	0	31	17,241	17,398	188	74	4.9	12.4	507,680	10,795
9	6 x 15	6	3	15	2H,3T	0	0	31	17,045	17,202	188	70	4.7	11.7	502,240	12,415
10	6 x 15	6	3	15	2H,3T	0	0	31	16,849	17,006	188	67	4.5	11.2	503,590	12,004
11	10 x 20	10	2	20	None	0	0	31	16,529	16,810	313	72	3.6	7.2	744,370	16,800
12	10 x 20	10	2	20	None	0	0	31	16,208	16,490	313	67	3.4	6.7	789,530	19,437
13	10 x 20	10	2	20	None	0	0	31	15,888	16,169	313	67	3.4	6.7	788,010	17,500
14	10 x 15	10	2	15	1H,2T	0	0	31	15,568	15,846	309	67	4.5	6.7	793,690	17,486
15	9 x 14	9	2	14	1H,2T	0	0	35	15,247	15,527	315	44	3.1	4.9	789,910	21,105
16	10 x 15	10	2	15	1H,2T	0	0	31	14,927	15,208	313	62	4.1	6.2	794,710	17,653
17	12 x 24	12	2	24	None	0	0	12	14,761	14,891	142	63	2.6	5.3	408,130	9,081
18	6 x 24	6	4	24	None	60	None	31	14,571	14,728	188	66	2.7	10.9	506,650	11,118
19	6 x 24	6	4	24	None	60	None	31	14,375	14,532	188	64	2.7	10.7	499,820	11,383
20	6 x 18	6	3	18	None	60	None	31	14,179	14,336	188	69	3.8	11.5	503,130	10,769
21	6 x 18	6	3	18	None	60	None	31	13,983	14,140	188	63	3.5	10.6	507,920	11,033
22	6 x 18	6	3	18	None	0	0	31	13,788	13,944	188	65	3.6	10.9	503,370	11,136
23	6 x 15	6	3	15	2H,3T	0	0	31	13,593	13,749	187	67	4.4	11.1	502,530	11,037
24	6 x 15	6	3	15	2H,3T	0	0	30	13,396	13,548	182	68	4.5	11.3	505,690	10,693
25	10 x 20	10	2	20	None	0	0	31	13,076	13,357	313	65	3.3	6.5	795,910	17,441
26	10 x 20	10	2	20	None	0	0	31	12,755	13,037	313	68	3.4	6.8	792,560	17,904
27	1PC	1	6	6	None	60	None	None	12,715	12,716	None	30	5.0	30.0	0	2,234
28	10 x 15	10	2	15	1H,2T	0	0	31	12,395	12,676	313	67	4.5	6.7	793,770	17,277
29	10 x 15	10	2	15	1H,2T	0	0	31	12,074	12,351	307	66	4.4	6.6	791,470	17,408
30	12 x 24	12	2	24	None	0	0	11	11,909	12,036	138	64	2.7	5.3	406,700	8,364

Fig C 9—Stimulations details for Boxwood-2H.

Perforation Charge Details - Boxwood 2H

Gun Size (in)	Perf Density (spf)	Perf Phasing (deg)	Charge Name	Pentration Depth (in)	Perf Diameter (in)	Explosive Load (grams)	Test Casing Specification
3-1/8	6	60	230 MaxForce - Frac, RDX, IS	31.6	0.41	23	4-1/2 in, 13.5 lb/ft, P-110

Fig C 10—Perforation charge details for Boxwood-2H.

Next came the completion of Boxwood-4H, which was the first stimulation in the project involving DAS/DTS data acquisition for SDE assessment. As shown in Fig C 6, the FO cable made a full 360° revolution from the toe to the heel. Accordingly, each stage had a prescribed perforation orientation with perforation guns set to 0° phasing, and all PCs were designed to be placed in the direct center of the CCPs behind casing to protect the fiber during perforating as well as during stimulation. The progression of stage configurations through the lateral was established to evaluate the 6 × 24 base case design and then implement stages with more aggressive LE configurations to determine if an improvement in SDE could be achieved. Stages with tapered perforations were also included to determine if heel-side bias could be eliminated, or at least reduced. Configurations with ESLs were also included to determine if a relatively high degree of SDE could be maintained on stages covering more lateral footage with a higher

number of PCs. The stimulation details and perforation details for this well are given in Fig C 11 and Fig C 12.

Boxwood 4H - Actual Stimulation Design

Stage	Stage Design	PCs per Stage	Perfs per Cluster	Perfs per Stage	Perf Taper Design	Perf Phasing (deg)	Perf Orientation (deg CW)	PC Spacing (ft)	Top Perf (ft MD)	Bottom Perf (ft MD)	Effective Stage Length (ft)	Average Treating Rate (bpm)	Average RPP (bpm/perf)	Average RPC (bpm/cluster)	Proppant (lbs)	Fluid (bbls)
1	6 x 24	6	4	24	No	0	120	32	18,540	18,703	195	58	2.4	9.6	508,130	11,423
2	6 x 24	6	4	24	No	0	135	32	18,313	18,476	195	60	2.5	9.9	508,290	11,210
3	6 x 24	6	4	24	No	0	135	33	18,065	18,229	197	65	2.7	10.8	509,270	11,418
4	6 x 18	6	3	18	No	0	135	33	17,834	18,000	199	57	3.2	9.5	507,890	11,144
5	6 x 18	6	3	18	No	0	150	32	17,607	17,768	193	68	3.8	11.3	507,880	11,314
6	6 x 18	6	3	18	No	0	150	33	17,378	17,542	197	59	3.3	9.9	435,780	12,301
7	6 x 18	6	3	18	No	0	120	33	17,147	17,313	200	63	3.5	10.6	508,730	11,430
8	6 x 18	6	3	18	No	0	120	33	16,915	17,081	200	73	4.1	12.2	505,850	11,296
9	6 x 15	6	3	15	2H,3T	0	120	33	16,684	16,848	197	60	4.0	9.9	522,880	14,124
10	6 x 15	6	3	15	2H,3T	0	120	34	16,448	16,617	202	54	3.6	8.9	506,850	12,438
11	6 x 15	6	3	15	2H,3T	0	90	32	16,218	16,380	195	63	4.2	10.5	311,240	8,667
12	6 x 15	6	3	15	2H,3T	0	75	40	15,950	16,152	242	66	4.4	11.0	503,110	11,370
13	6 x 15	6	3	15	2H,3T	0	45	34	15,717	15,885	202	66	4.4	10.9	503,180	11,253
14	1PC	1	6	6	No	0	45	None	15,649	15,650	None	10	1.7	9.9	0	1,512
15	5 x 20	5	4	20	No	0	30	41	15,419	15,582	203	66	3.3	13.1	413,920	9,041
16	6 x 12	6	2	12	No	0	15	31	15,174	15,331	188	49	4.1	8.2	81,843	4,752
17	6 x 12	6	2	12	No	0	0	33	14,939	15,107	201	54	4.5	9.1	505,070	11,261
18	6 x 12	6	2	12	No	0	330	33	14,709	14,875	198	55	4.6	9.2	493,217	11,935
19	1PC	1	6	6	No	0	330	None	14,643	14,643	None	14	2.3	14.0	0	1,620
20	10 x 20	10	2	20	No	0	285	33	14,280	14,575	328	69	3.4	6.9	832,850	18,481
21	10 x 20	10	2	20	No	0	270	33	13,918	14,213	328	75	3.7	7.5	834,150	17,747
22	10 x 20	10	2	20	No	0	240	34	13,554	13,856	336	66	3.3	6.6	672,020	16,123
23	10 x 15	10	2	15	1H,2T	0	240	33	13,193	14,390	1,229	69	4.6	6.9	836,560	18,196
24	10 x 15	10	2	15	1H,2T	0	225	31	12,848	13,131	314	71	4.7	7.1	838,830	17,929
25	9 x 18	9	2	18	1H,2M,3T	0	210	32	12,529	12,784	288	69	3.8	7.6	770,600	16,537
26	9 x 18	9	2	18	1H,2M,3T	0	210	32	12,184	12,444	292	65	3.6	7.2	744,120	17,739

Fig C 11—Stimulation details for Boxwood-4H.

Perforation Charge Details - Boxwood 4H

Gun Size (in)	Perf Density (spf)	Perf Phasing (deg)	Charge Name	Pentration Depth (in)	Perf Diameter (in)	Explosive Load (grams)	Test Casing Specification
3-1/8	6	60	230 MaxForce - Frac, RDX, IS	31.6	0.41	23	4-1/2 in, 13.5 lb/ft, P-110

Fig C 12—Perforation charge details for Boxwood-4H.

Stage 15, which was a 5 × 20, was specifically designed to omit a PC for one CCP that had an orientation angle vastly different than the others in that stage. Several stages had proppant and fluid volumes less than others with the same configuration. Several stages were cut short to avoid damaging the fiber when significant acoustic energy was observed between CCPs. Ultimately, all 26 stages were perforated and stimulated with no damage to the fiber.

Boxwood-3H was the next well to be completed in this project, but first the MS array that had been installed to monitor the stimulation of the other wells had to be removed. This left one MS array in Boxwood-5PH and one in Thresher-16H during hydraulic stimulation of Boxwood-3H. FF CWS data could still be captured from the fiber optic cables on Boxwood-4H and -5PH. Like Boxwood-4H, the stimulation plan for Boxwood-3H was to evaluate the SDE of the 6 × 24 base case design followed by configurations with more aggressive LE techniques to determine if improvements could be made. Stages with tapered perforations were also included to reduce the effects of heel-side bias, along with ESL configurations, aggressive RPP LE, and more PCs. Stages with varying configurations were placed consecutively along the lateral where the slant well would later be drilled for coring and fracture analysis purposes. The stimulation details and perforation details for this well are given in Fig C 13 and Fig C 14.

There were two misfires that occurred on Stage 1 and Stage 23 plug-and-perf runs during the hydraulic stimulation of Boxwood-3H. Stage 1 was intended to be a 6 × 24 configuration, but it

was modified during operations to be a 5 × 20 configuration, similar to Stage 15 on Boxwood-4H. Stage 23 was intended to be a 10 × 20 configuration, but it was modified to be a 9 × 18. The Boxwood-3H well was significantly more difficult to treat than Boxwood-4H due to the large amounts of acoustic energy observed between CCPs on many stages. As a result, several stages were cut short to preserve the fiber. Regrettably, the fiber was severed during Stage 21, which eliminated the ability to read data below the damaged point, including DAS/DTS and P/T data from the gauge at the toe (see Fig C 15).

Boxwood 3H - Actual Stimulation Design

Stage	Stage Design	PCs per Stage	Perfs per Cluster	Perfs per Stage	Perf Taper Design	Perf Phasing (deg)	Perf Orientation (deg CW)	PC Spacing (ft)	Top Perf (ft MD)	Bottom Perf (ft MD)	Effective Stage Length (ft)	Average Treating Rate (bpm)	Average RPP (bpm/perf)	Average RPC (bpm/cluster)	Proppant (lbs)	Fluid (bbls)
1	5 x 20	5	4	20	No	0	135	32	18,668	18,795	160	50	2.5	10.0	407,700	11,661
2	6 x 24	6	4	24	No	0	135	33	18,441	18,605	197	72	3.0	12.0	505,120	11,216
3	6 x 24	6	4	24	No	0	120	33	18,194	18,359	198	65	2.7	10.9	502,520	11,092
4	6 x 18	6	3	18	No	0	120	32	17,968	18,130	195	67	3.7	11.1	505,200	11,420
5	6 x 18	6	3	18	No	0	120	32	17,743	17,903	192	63	3.5	10.5	505,080	11,379
6	6 x 18	6	3	18	No	0	75	32	17,514	17,675	193	67	3.7	11.2	505,450	11,253
7	6 x 15	6	3	15	2H,3T	0	60	32	17,290	17,452	195	63	4.2	10.5	507,560	11,372
8	6 x 15	6	3	15	2H,3T	0	30	32	17,063	17,222	191	67	4.5	11.2	505,170	12,150
9	6 x 15	6	3	15	2H,3T	0	30	33	16,836	16,999	196	72	4.8	12.1	507,400	13,404
10	6 x 12	6	2	12	No	0	0	32	16,610	16,771	194	58	4.8	9.6	168,040	8,094
11	6 x 12	6	2	12	No	0	345	32	16,384	16,545	193	63	5.2	10.4	289,620	8,578
12	6 x 12	6	2	12	No	0	330	33	16,152	16,318	199	58	4.9	9.7	504,200	11,317
13	6 x 12	6	2	12	No	0	315	33	15,920	16,085	199	67	5.6	11.1	145,450	6,027
14	1PC	1	6	6	No	0	270	None	15,857	15,858	None	13	2.2	13.1	0	1,422
15	6 x 12	6	2	12	No	0	300	32	15,634	15,794	191	58	4.8	9.6	503,680	11,182
16	6 x 18	6	3	18	No	0	285	32	15,390	15,550	192	58	3.2	9.7	255,343	7,634
17	6 x 15	6	3	15	2H,3T	0	270	33	15,162	15,327	198	63	4.2	10.5	504,680	11,043
18	6 x 12	6	2	12	No	0	240	33	14,932	15,096	197	62	5.1	10.3	513,827	11,384
19	8 x 24	8	3	24	No	0	225	33	14,631	14,864	267	70	2.9	8.7	672,320	15,397
20	8 x 24	8	3	24	No	0	210	33	14,332	14,563	263	72	3.0	9.0	673,340	15,315
21	8 x 16	8	2	16	No	0	210	33	14,038	14,267	263	67	4.2	8.3	202,580	8,185
22	8 x 16	8	2	16	No	0	180	33	13,743	13,972	261	70	4.4	8.7	662,740	15,152
23	9 x 18	9	2	18	No	0	150	36	13,384	13,677	330	69	3.8	7.6	747,020	17,290
24	10 x 15	10	2	15	1H,2T	0	135	33	13,028	13,322	327	72	4.8	7.2	840,480	18,956
25	8 x 16	8	2	16	No	0	120	34	12,730	12,966	270	56	3.5	7.0	20,598	2,954

Fig C 13—Stimulation details for the Boxwood 3H.

Perforation Charge Details - Boxwood 3H

Gun Size (in)	Perf Density (spf)	Perf Phasing (deg)	Charge Name	Pentration Depth (in)	Perf Diameter (in)	Explosive Load (grams)	Test Casing Specification
3-1/8	6	60	230 MaxForce - Frac, RDX, IS	31.6	0.41	23	4-1/2 in, 13.5 lb/ft, P-110

Fig C 14—Perforation charge details for the Boxwood 3H.

The last horizontal well to be completed in the HFTS-2 project was Thresher-16H. Prior to its stimulation, the MS array that had previously been installed was removed, as was the one in Boxwood-5PH. This limited its data acquisition program to only FF CWS data from Boxwood-3H and -4H, albeit in a diminished capacity as a result of the fiber damage in the Boxwood-3H well during stimulation. Thresher-16H was completed with 36 stages of the 6 × 24 base case design.

There was a strong desire for the FO cables on the Boxwood-3H and -4H wells to survive the hydraulic stimulation so that DAS/DTS data could be acquired during production. The CCPs were designed to provide a certain level of protection to the fiber from the abrasive frac slurry, but this was only for a minimal distance on either side of the PC perforated in the middle of each protector. Any lack of cement isolation between CCPs that allowed unintended, intra-stage flow provided a substantial risk of fiber damage (see Fig C 16). On both wells, but especially on Boxwood-3H, several stages had to be terminated earlier than planned to mitigate this risk. These problematic stages seemed to coincide with sections along the lateral having greater

degrees of relative inclination changes as well as stages between the change and the heel (see Fig C 17). This suggests that the cement isolation problem is compounding once it begins, meaning all subsequent stages are more likely to experience similar issues.

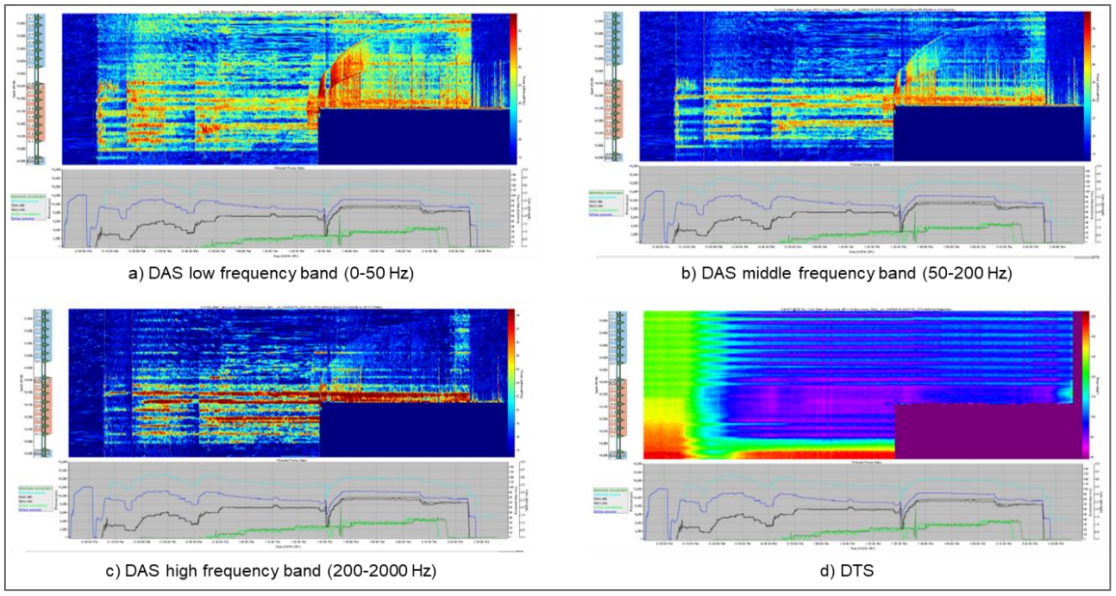

Fig C 15—Fiber was severed during the stimulation of Stage 21 of Boxwood-3H, which led to losing 66% of lateral coverage towards the toe.

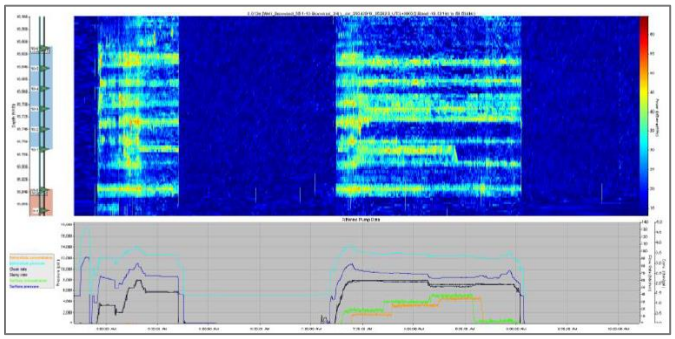

Fig C 16—Stage 10 of the Boxwood-3H well showing intra-stage flow between PCs, as indicated by DAS responses.

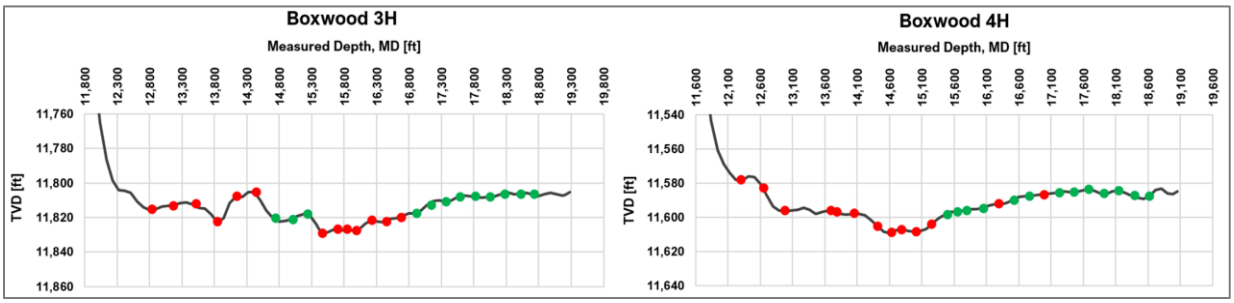

Fig C 17—Exaggerated wellbore profiles of Boxwood-3H and -4H showing stages with observable intra-stage communication based on DAS responses.

Methodology and Workflow

In the HFTS-2 project, unique near-wellbore and far-field surveys were acquired on the three fiber wells, Boxwood-3H, -4H, and -5PH, to evaluate spatial and temporal hydraulic fracture characteristics (see Fig C 18). Near-wellbore Distributed Acoustic Sensing (DAS) and Distributed Temperature Sensing (DTS) data were acquired during the stimulation of two horizontal fiber wells (Boxwood-3H and -4H). The hydraulic fracturing (HF) profile (i.e., fluid/proppant allocation among perforation clusters) was obtained using DAS Frequency Band Extracted (FBE) data, and statistical analysis provided quantitative assessments of stimulation distribution effectiveness (SDE) for different completion designs. In addition, time-lapse fracture property changes were assessed at the PC and stage levels based on Distributed Strain Sensing (DSS) data acquired during the production phase and was compared with the HF profile.

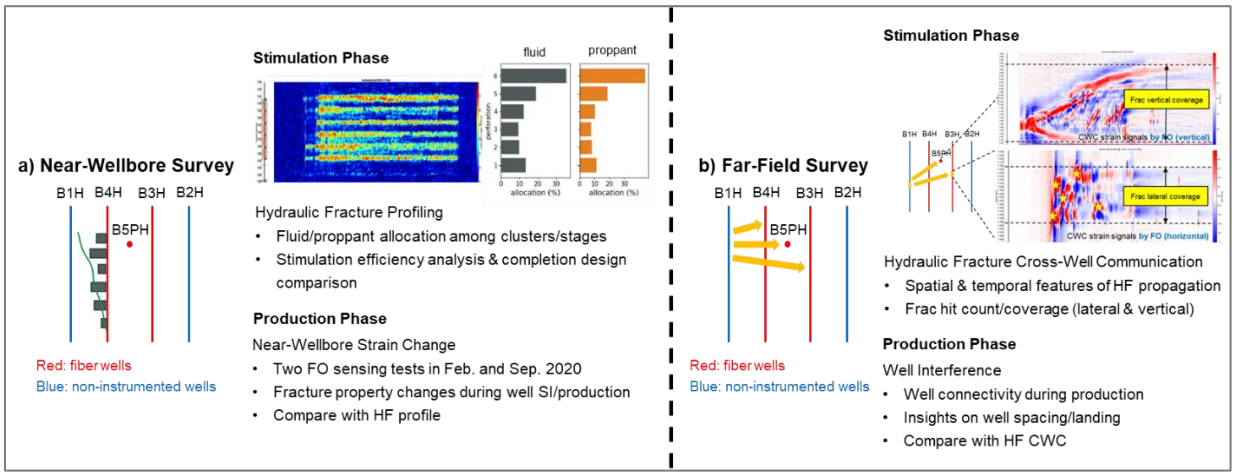

Fig C 18—Near-wellbore and far-field surveys with fiber wells.

Results: Completion Design Evaluation via DAS/DTS

The integration of DAS, DTS, and hydraulic fracturing treatment data allows a detailed and comprehensive analysis of SDE across PCs (Molenaar and Cox 2013; Holley and Kalia 2015; Wheaton et al. 2016; Ugueto et al. 2016, 2019). Qualitative and quantitative information gained through the integrated analysis supports an improved understanding of whether the PCs within a stage were treated evenly as planned, and how different completion designs, and operational issues affect stimulation efficiency.

Near-Wellbore DAS/DTS Interpretation and Analysis:

Fig C 19 shows a typical example of near-wellbore DAS/DTS and treatment data acquired during the stimulation of Stage 7 on Boxwood-4H consisting of 6 PCs, 18 perforations, and 32-ft PCS. The three time-synchronized panels in Fig C 19 consist of DAS, DTS, and treatment data listed from top to bottom. With the start of injection on the stage, DAS clearly showed high-energy signal responses indicated by warmer colors and corresponding to fluid and proppant placement for the 6 PCs, annotated as 7.1 to 7.6 from toe to heel. The DAS energy signals remained active for all clusters until the end of the treatment, when the pumps were shut down. Due to the injection of fracturing fluid with a relatively lower temperature, the DTS temperature

waterfall map in the middle showed a cool-down effect indicated by cooler colors in the near-wellbore region during the treatment of the 6 PCs followed by a warm-back effect shortly after the end of treatment.

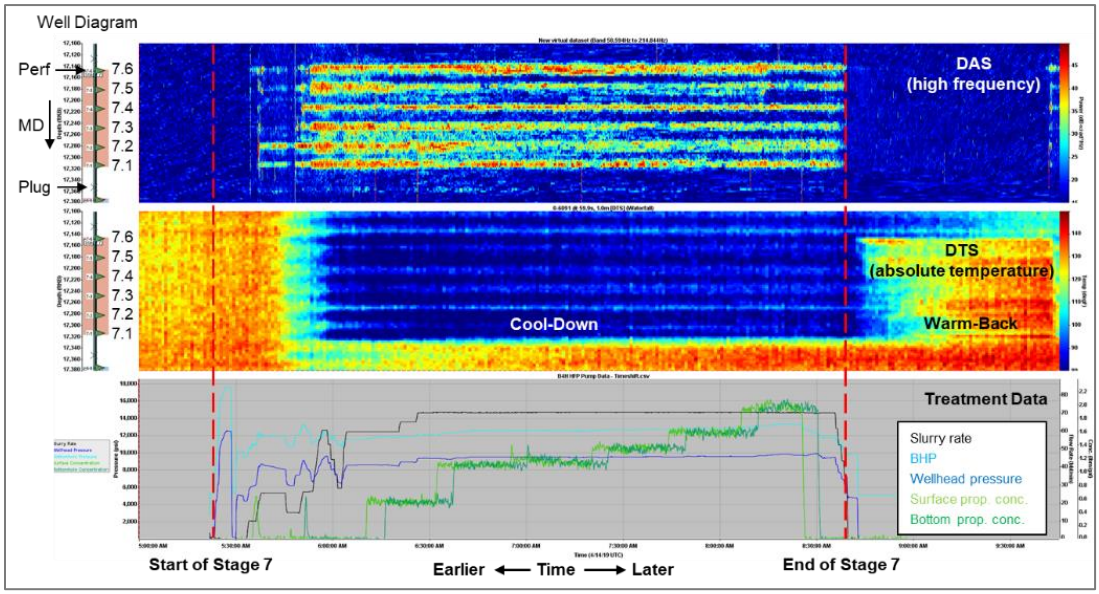

Fig C 19—Near-wellbore DAS/DTS and treatment data acquired during the stimulation of Stage 7 (6×18) on Boxwood-4H. Data integration indicates six independent hydraulic fractures were created during the treatment.

The integrated analysis of near-wellbore DAS/DTS and treatment data can be used to better understand the adverse impacts of completion operational issues. These operational issues can include plug failures, poor cement bonding behind casing, operational challenges leading to mid-stage shutdowns, and others (see Fig C 20).

There is an understanding within the completions community that operational efficiency is critical to ensuring proper placement of the fracturing treatment within a given stage. Fig C 20a shows that all the PCs in Stage 6 received treatment early in the stage, as evidenced by high DAS energy signals. After pumping resumed after the mid-stage shutdown caused by a pump reliability issue, DAS energy signals were clearly lost for a single heel PC, which remained inactive during the rest of the treatment, while the other PCs remained active and may have taken additional fluid and proppant beyond the designed amounts. Fig C 20b and Fig C 20c shows the lack of isolation during the treatments of Stage 8 and Stage 11 based on clear DAS/DTS responses in the previous stages. Specifically, the DAS/DTS response lag in Stage 7 during the treatment of Stage 8 indicates flow behind casing, potentially due to poor cement bonding or a longitudinal fracture connection. Alternatively, the immediate and stronger DAS/DTS response in Stage 10 when Stage 11 was being stimulated implies a probable plug leak or failure. In Fig C 20d, the reduced frac job size during the treatment of Stage 16 led to only 16% of actual proppant placement compared to the original design. Fig C 20e to Fig C 20g show similar adverse impacts of operational inefficiency on the treatment of PCs and

fluid/proppant placement. The observations and interpretations from Fig C 19 and Fig C 20 are applicable to most stages on the Boxwood-3H and -4H wells.

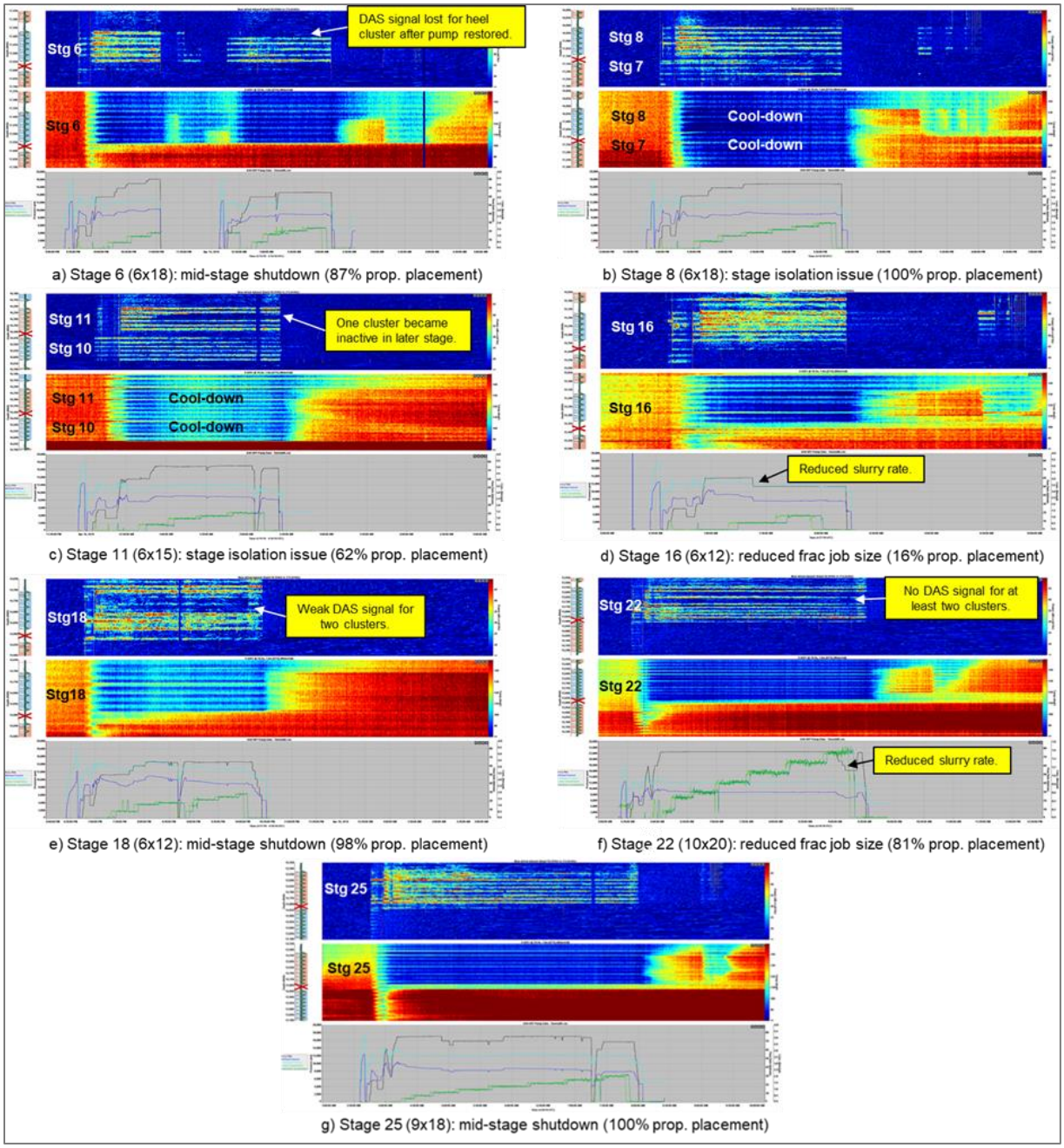

Fig C 20—Near-wellbore DAS/DTS and treatment data for 7 stages with operational issues on Boxwood-4H. Actual percentage of proppant placement is shown under each image. The red cross located on the left portion of each display represents the plug location between stages.

Fig C 21 shows that almost all the stages on the Boxwood-1H and -2H wells were treated as designed without much deviation. However, a fair number of stages on the Boxwood-3H (~32%) and Boxwood-4H (~15%) wells received less proppant than designed, which coincides with the stages that experienced issues during the stimulation, partly due to operational problems and partly due to suspected cement isolation issues. This observation is aligned with the production

performance characteristics of the Boxwood wells: Boxwood-2H is the best performer, whereas Boxwood-3H is the worst performer, clearly highlighting the impact of operational efficiency and success on well productivity and overall performance.

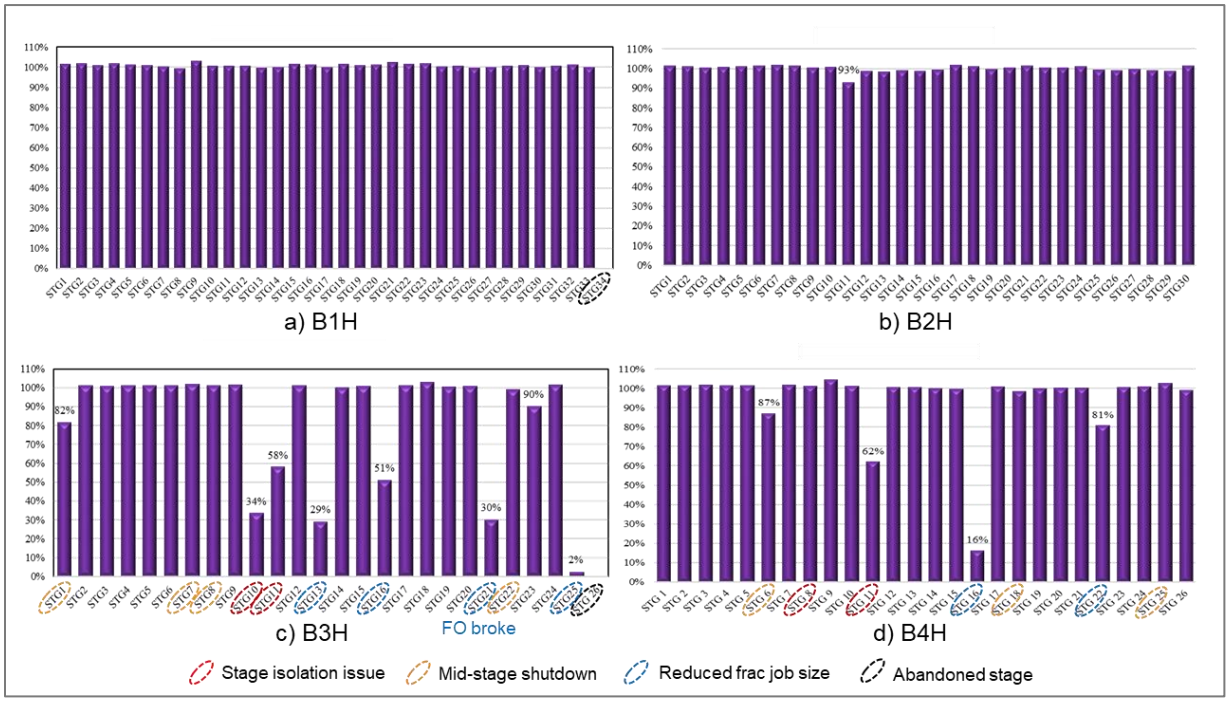

Fig C 21—Actual percentage of proppant placement by stage for the Boxwood wells.

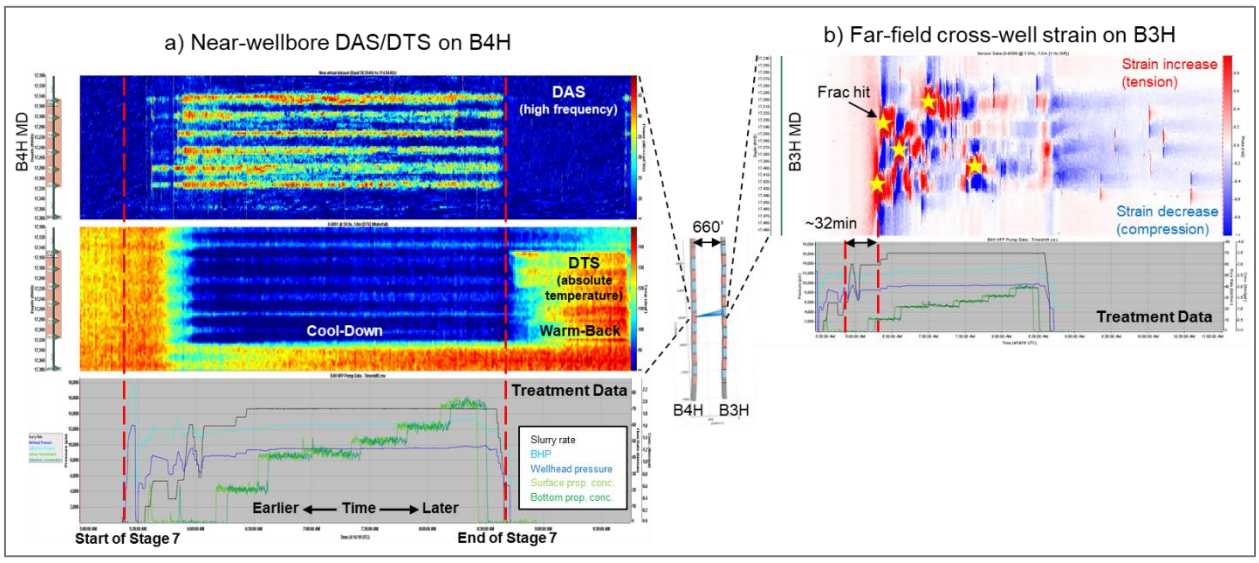

Fig C 22—a) Near-wellbore DAS/DTS data during treatment of Stage 7 on Boxwood-4H. b) Five frac hits (marked by yellow stars where there is significant tension while the surrounding rocks are being compressed simultaneously) are seen on Boxwood-3H from the Boxwood-4H treatment.

The unique layout of the two horizontal fiber wells allowed the acquisition of FF CWS data from one fiber well when another fiber well was being treated. Fig C 22 shows the integration of near-wellbore DAS/DTS acquired during the treatment of Stage 7 on Boxwood-4H and the FF CWS data recorded by the offset monitoring well Boxwood-3H. Near-wellbore DAS/DTS (Fig C 22a) clearly shows that 6 hydraulic fractures were initiated during the treatment of Stage 7 on Boxwood-4H, while only 5 frac hits (indicated by the yellow stars in Fig C 22b) were interpreted based on FF CWS signals on Boxwood-3H. Provided that similar geological stresses exist, the smaller number of frac hits on the offset well could potentially reflect the stimulation inefficiency and resulting non-uniform distribution of energy and fluid/proppant placement among the PCs.

Stimulation Efficiency Analysis and Completion Design Comparison via DAS:

Through the integration of fracture stimulation data and relative amplitudes of DAS FBE data, fluid and proppant distribution among PCs can be calculated based on mass balance (Li et al. 2020). The resulting hydraulic fracture profile (HFP) shown in Fig C 23 enables further analysis of stimulation efficiency as well as comparison of various completion designs in a more detailed and quantitative manner.

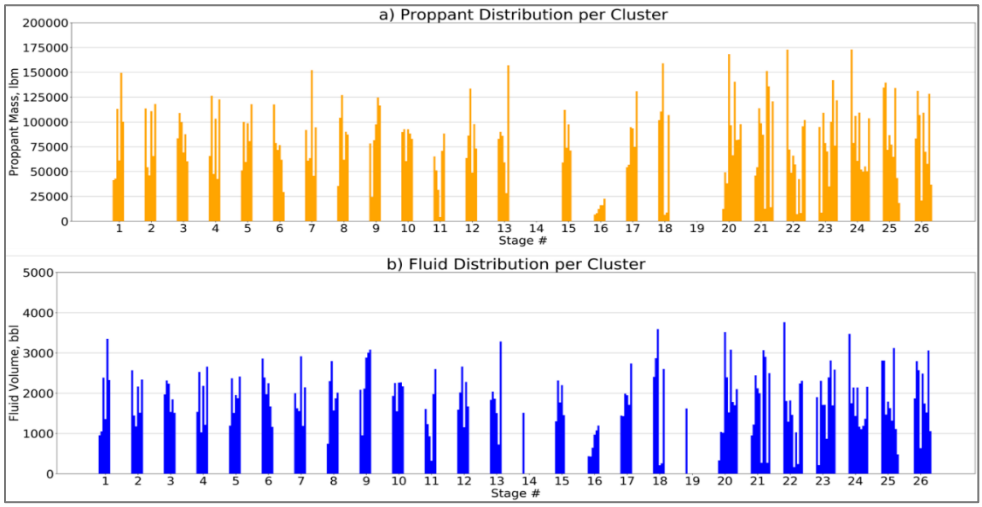

Fig C 23—Hydraulic fracture profile (HFP) for Boxwood-4H (i.e., fluid and proppant distribution among PCs).

During the treatment of each stage, the preferred and recommended scenario is to stimulate all PCs efficiently by achieving an even distribution of fluid and proppant throughout the interval. Realistically, a number of factors influence the chance of success, such as completion designs and PC configurations along with heterogeneity and anisotropy of geological and geomechanical properties in the formation. There are multiple ways to evaluate stimulation efficiency quantitatively.

Fig C 24 shows boxplots with percentages of actual proppant placed per PC divided by the percentage of designed proppant per PC for both the Boxwood-3H and -4H wells. For example, the baseline design that consisted of 6 PCs per stage would require ~16% proppant placement per PC. However, if the HFP showed only 10% placement in a particular PC, that would be a

62.5% (10/16) efficiency, as opposed to the designed 16% proppant, which would have been 100% efficiency.

Ideal values are 100%, representing perfect proppant allocation. The two bounds at 50% and 150% group the clusters into three categories, with those receiving more than 150% planned proppant considered "super-clusters," while those receiving less than 50% planned proppant are "poorly treated." The small range of spread indicates relatively uniform treatment for most stages on the Boxwood-3H and -4H wells. The pie charts in Fig C 24 show the proportion of PCs within the three categories for standard stages (mostly 5-6 PCs/Stage) and extended stages (8-10 PCs/Stage). The results indicate better SDE in standard stages than in extended stages on the Boxwood-4H well. On Boxwood-3H, though, the proportions of the three categories are similar for both standard and extended stages, which is more than likely attributable to the more frequent operational issues encountered on the standard stages leading to similar results.

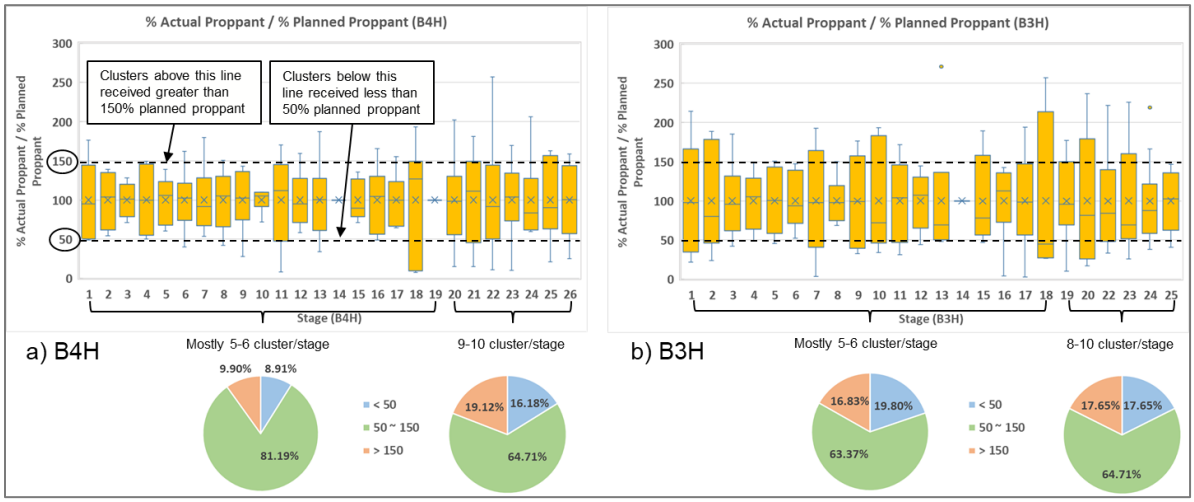

Fig C 24—Percentage of actual proppant placed per PC divided by the percentage of designed proppant per PC for Boxwood-3H and -4H. The Boxwood-4H well shows better SDE than Boxwood-3H, which is consistent with well performance.

Another metric developed for improving SDE evaluation is referred to as the proppant distribution metric (PDM), which is defined as the ratio of minimum to maximum actual PC proppant placement for each stage. PDM can be employed to evaluate various completion designs more concisely to analyze key performance drivers for SDE. The value of PDM can be between 0 and 1, with higher PDM values implying better stimulation efficiency. Fig C 25 shows average treatment Rate Per Cluster (RPC) for all stages on the X-axis and the corresponding PDM on the Y-axis. Among the stages with the same completion design, operational issues appear to add higher risk to stimulation efficiency, leading to a lower PDM value. By calculating the Pearson's correlation (ρ) between PDM and RPC, we observe a strong positive correlation ($\rho = 0.61$) between PDM and RPC for stages on the Boxwood-4H well, and a consistent but weak positive correlation ($\rho = 0.31$) for stages on the Boxwood-3H well. All the circled stages encountered operational issues and were removed for the correlation calculations. Higher RPC values (10-13 bpm/PC) appear to improve SDE, especially for stages with a higher number of

PCs/Stage (e.g., ESL), as all the stages on the Boxwood-3H and -4H wells were treated at an average rate of 60-70 bpm, regardless of PC count.

The correlation between PDM and average treatment Rate Per Perforation (RPP) is shown in Fig C 26**.** There is a weak negative correlation ($\rho = -0.30$) between RPP and PDM for the stages on the Boxwood-4H well, and an inconsistent and very weak positive correlation ($\rho = 0.11$) for the stages on the Boxwood-3H well. This statistical analysis of HFP and SDE clearly shows that RPC is a more effective metric and design variable than RPP, which is used more commonly in the industry. Excessively high values of RPP (greater than 4 bpm/perf) tend to produce uneven proppant distribution, probably due to erosional effects. If RPC was not maintained at a certain level (greater than 10 bpm/PC), the likelihood of uneven proppant distribution increased dramatically. The stage configurations that created low RPC while maintaining high RPP did not show improved SDE. In addition, no obvious effects of tapered PC schemes or perforation orientation/phasing was observed during the treatments of the Boxwood-3H and -4H wells. Note that the completion design for both wells was based on 32-ft PC spacing, which was a fixed variable due to the fiber optic clamping and protection system.

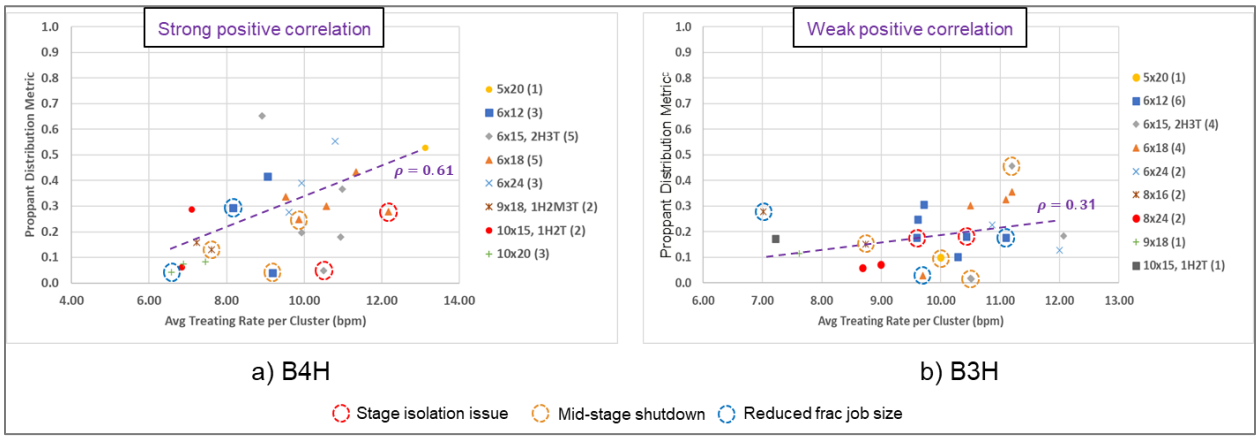

Fig C 25—Average treatment Rate Per Cluster (RPC) vs. proppant distribution metric (PDM). All stages are marked by different symbols and colors, and those with operational issues are circled individually.

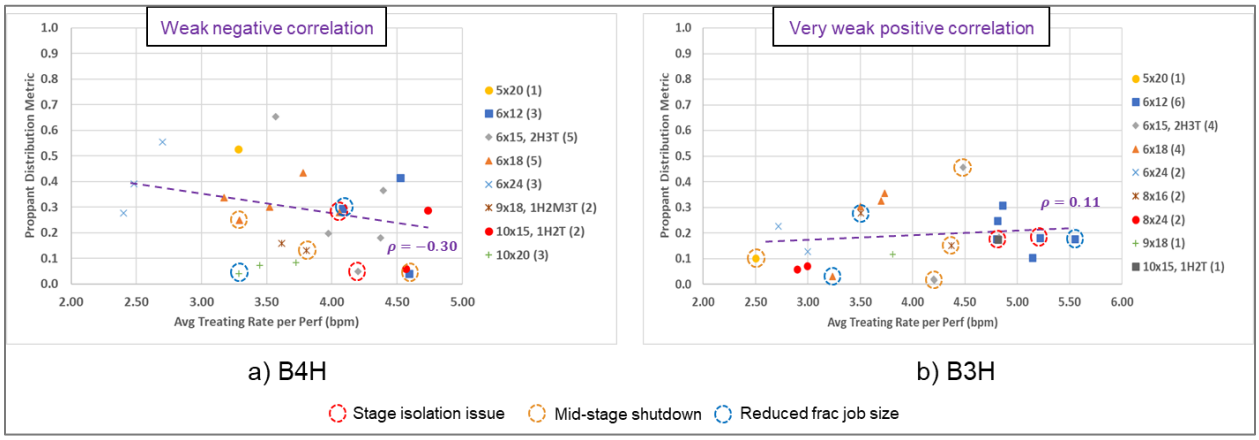

Fig C 26—Average treatment Rate Per Perforation (RPP) vs. proppant distribution metric (PDM). All stages are marked by different symbols and colors, and those with operational issues are circled individually.

Production always provides the ultimate assessment of SDE for different completion designs, but no conventional production logging was conducted in this HFTS-2 project. To fill this gap, the DSS data acquired during the production phase of the Boxwood wells enables further analysis of fracture property changes in the near-wellbore region potentially associated with SDE and longer-term production performance.

Results: Near-Wellbore Frac Property Changes via DSS

Fiber Optic Sensing Tests:

In Feb. 2020, a unique FO-based well interference and production logging test was implemented on the HFTS-2 wells. This test was inspired by the proprietary procedure developed by ConocoPhillips (Jin et al. 2019). Fig C 27 shows the test execution schedule in which four Boxwood wells (-1H, -2H, -3H, and -4H) and one Bitterroot well (Bitterroot-1H) were cycled "Open" and "Shut-in" for a few hours after an extended period of stable production. Because the FO cable was installed and operating reliably on Boxwood-4H, this well was the primary target for monitoring and FO data acquisition during the test. After overcoming several operational challenges, the test was completed successfully, and the data were collected as planned. Through comprehensive analysis of the DAS data and pressure gauge responses, no identifiable well interference was observed between Boxwood-4H and the offset wells. The near-wellbore strain change data acquired using newly developed FO technique, DSS-RFS (Distributed Strain

Sensing - Rayleigh Frequency Shift) (Jin et al. 2021), were analyzed to gain insights on time-dependent fracture property changes when the Boxwood-4H well was shut in or producing.

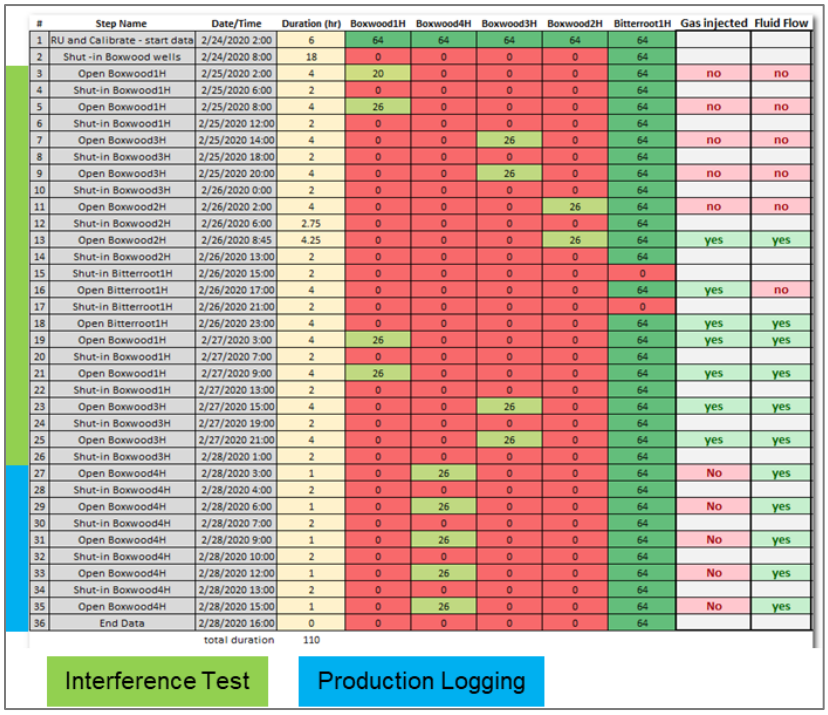

#	Step Name	Date/Time	Duration (hr)	Boxwood1H	Boxwood4H	Boxwood3H	Boxwood2H	Bitterroot1H	Gas injected	Fluid Flow
1	RU and Calibrate - start data	2/24/2020 2:00	6	64	64	64	64	64		
2	Shut -in Boxwood wells	2/24/2020 8:00	18	0	0	0	0	64		
3	Open Boxwood1H	2/25/2020 2:00	4	20	0	0	0	64	no	no
4	Shut-in Boxwood1H	2/25/2020 6:00	2	0	0	0	0	64		
5	Open Boxwood1H	2/25/2020 8:00	4	26	0	0	0	64	no	no
6	Shut-in Boxwood1H	2/25/2020 12:00	2	0	0	0	0	64		
7	Open Boxwood3H	2/25/2020 14:00	4	0	0	26	0	64	no	no
8	Shut-in Boxwood3H	2/25/2020 18:00	2	0	0	0	0	64		
9	Open Boxwood3H	2/25/2020 20:00	4	0	0	26	0	64	no	no
10	Shut-in Boxwood3H	2/26/2020 0:00	2	0	0	0	0	64		
11	Open Boxwood2H	2/26/2020 2:00	4	0	0	0	26	64	no	no
12	Shut-in Boxwood2H	2/26/2020 6:00	2.75	0	0	0	0	64		
13	Open Boxwood2H	2/26/2020 8:45	4.25	0	0	0	26	64	yes	yes
14	Shut-in Boxwood2H	2/26/2020 13:00	2	0	0	0	0	64		
15	Shut-in Bitterroot1H	2/26/2020 15:00	2	0	0	0	0	0		
16	Open Bitterroot1H	2/26/2020 17:00	4	0	0	0	0	64	yes	no
17	Shut-in Bitterroot1H	2/26/2020 21:00	2	0	0	0	0	0		
18	Open Bitterroot1H	2/26/2020 23:00	4	0	0	0	0	64	yes	yes
19	Open Boxwood1H	2/27/2020 3:00	4	26	0	0	0	64	yes	yes
20	Shut-in Boxwood1H	2/27/2020 7:00	2	0	0	0	0	64		
21	Open Boxwood1H	2/27/2020 9:00	4	26	0	0	0	64	yes	yes
22	Shut-in Boxwood1H	2/27/2020 13:00	2	0	0	0	0	64		
23	Open Boxwood3H	2/27/2020 15:00	4	0	0	26	0	64	yes	yes
24	Shut-in Boxwood3H	2/27/2020 19:00	2	0	0	0	0	64		
25	Open Boxwood3H	2/27/2020 21:00	4	0	0	26	0	64	yes	yes
26	Shut-in Boxwood3H	2/28/2020 1:00	2	0	0	0	0	64		
27	Open Boxwood4H	2/28/2020 3:00	1	0	26	0	0	64	No	yes
28	Shut-in Boxwood4H	2/28/2020 4:00	2	0	0	0	0	64		
29	Open Boxwood4H	2/28/2020 6:00	1	0	26	0	0	64	No	yes
30	Shut-in Boxwood4H	2/28/2020 7:00	2	0	0	0	0	64		
31	Open Boxwood4H	2/28/2020 9:00	1	0	26	0	0	64	No	yes
32	Shut-in Boxwood4H	2/28/2020 10:00	2	0	0	0	0	64		
33	Open Boxwood4H	2/28/2020 12:00	1	0	26	0	0	64	No	yes
34	Shut-in Boxwood4H	2/28/2020 13:00	2	0	0	0	0	64		
35	Open Boxwood4H	2/28/2020 15:00	1	0	26	0	0	64	No	yes
36	End Data	2/28/2020 16:00	0	0	0	0	0	64		
		total duration	110							

Fig C 27—Execution schedule of FO-based well interference and production logging test in Feb. 2020. Sufficient fluid flow was the top operational priority, and for that reason, choke size was increased from 20/64" to 26/64" after step #3, and gas lift was supplied on offset wells after step #11.

To confirm the results from the Feb. 2020 test, a second FO sensing test was conducted in Sept. 2020. Fig C 28 shows the execution schedule, in which the extended shut-in time offered a better opportunity to confirm the well interference after 7 months of production. Overall, the test was executed similarly to the February test, with precautions to avoid unnecessary facility shut-ins and automation constraints. DSS-RFS data were acquired on all three fiber wells during

the Sept. 2020 test, which enabled the investigation of time-lapse fracture property changes in the near-wellbore region.

			B1H		B4H		B3H		B2H	
	Date	Event Description	Status	Inj	Status	Inj	Status	Inj	Status	Inj
Day 1	9/14/20 12:00 PM		Producing	350	Producing	500	Producing	550	Producing	350
Day 2	9/15/20 12:00 PM	Shut-in B4H	Producing	350	Shut-in	0	Producing	550	Producing	350
Day 3	9/16/20 12:00 PM		Producing	350	Shut-in	0	Producing	550	Producing	350
Day 4	9/17/20 12:00 PM		Producing	350	Shut-in	0	Producing	550	Producing	350
Day 5	9/18/20 12:00 PM	Shut-in B3H	Producing	350	Shut-in	0	Shut-in	0	Producing	350
Day 6	9/19/20 12:00 PM		Producing	350	Shut-in	0	Shut-in	0	Producing	350
Day 7	9/20/20 12:00 PM		Producing	350	Shut-in	0	Shut-in	0	Producing	350
Day 8	9/21/20 12:00 PM	Flowback B4H	Producing	350	Producing	500	Shut-in	0	Producing	350
Day 9	9/22/20 12:00 PM		Producing	350	Producing	500	Shut-in	0	Producing	350
Day 10	9/23/20 12:00 PM		Producing	350	Producing	500	Shut-in	0	Producing	350
Day 11	9/24/20 12:00 PM	Flowback B3H	Producing	350	Producing	500	Producing	550	Producing	350

Fig C 28—Execution schedule of the FO sensing test in Sept. 2020. Duration of shut-in periods on the Boxwood-3H and -4H wells was a matter of days (similar to conventional pressure interference test), as opposed to a matter of hours.

DSS-RFS Interpretation and Integration with Near-Wellbore DAS:

The analysis and interpretation of DSS-RFS data acquired in the two FO sensing tests can provide critical, high-resolution information for near-wellbore fracture property changes after 7 months of production. Fig C 29 shows the conceptual explanations for near-wellbore strain change during shut-in and production periods (Jin et al. 2021).

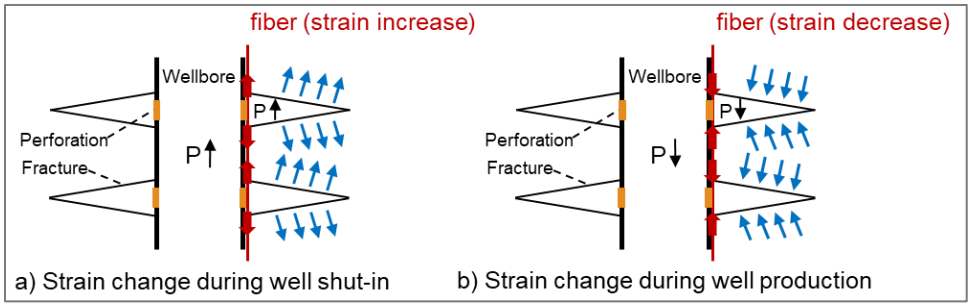

Fig C 29—Conceptual explanations for near-wellbore strain change during shut-in and production periods. a) Hydraulic fractures reopening and generating positive strain changes (extension) as BHP builds up after the well is shut in. b) Hydraulic fractures closing and generating negative strain change (contraction) as BHP declines when the well is producing.

Since the entire FO cable on the Boxwood-4H well was fully operational during the two tests, the analysis and interpretation of DSS-RFS data are specific to that well. Fig C 30 shows the BHP buildups during shut-in periods in the Feb. 2020 and Sept. 2020 tests. Because near-wellbore strain change is highly related to BHP changes, two separate time stamps of when the BHP buildup reached 1,000 psi in these tests were selected for comparison. Fig C 31 integrates near-

wellbore strain change data at the selected time stamps with DAS data acquired during well stimulation for Stages 21 and 22 on the Boxwood-4H well.

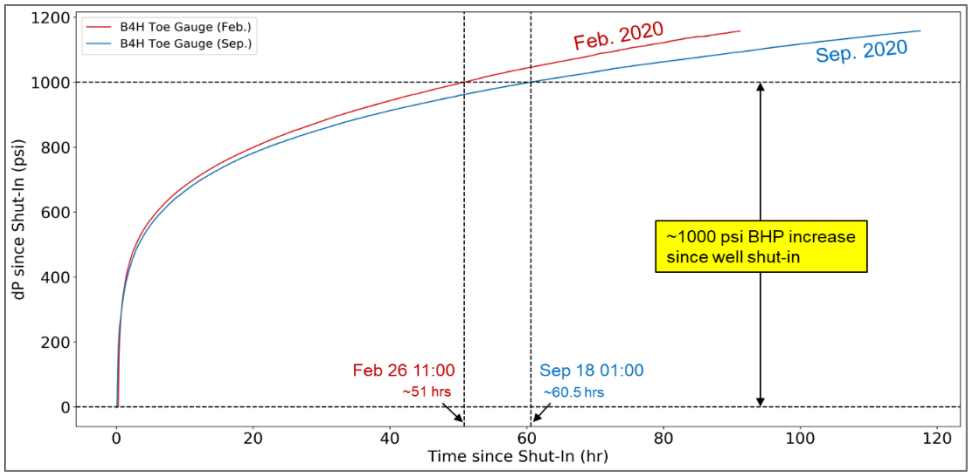

Fig C 30—BHP buildup while Boxwood-4H was shut in during the Feb. 2020 and Sept. 2020 tests. The total liquid production rate before the Feb. 2020 test was higher than before the Sept. 2020 test, so the BHP buildup rate is faster during the Feb. 2020 test than the Sept. 2020 test.

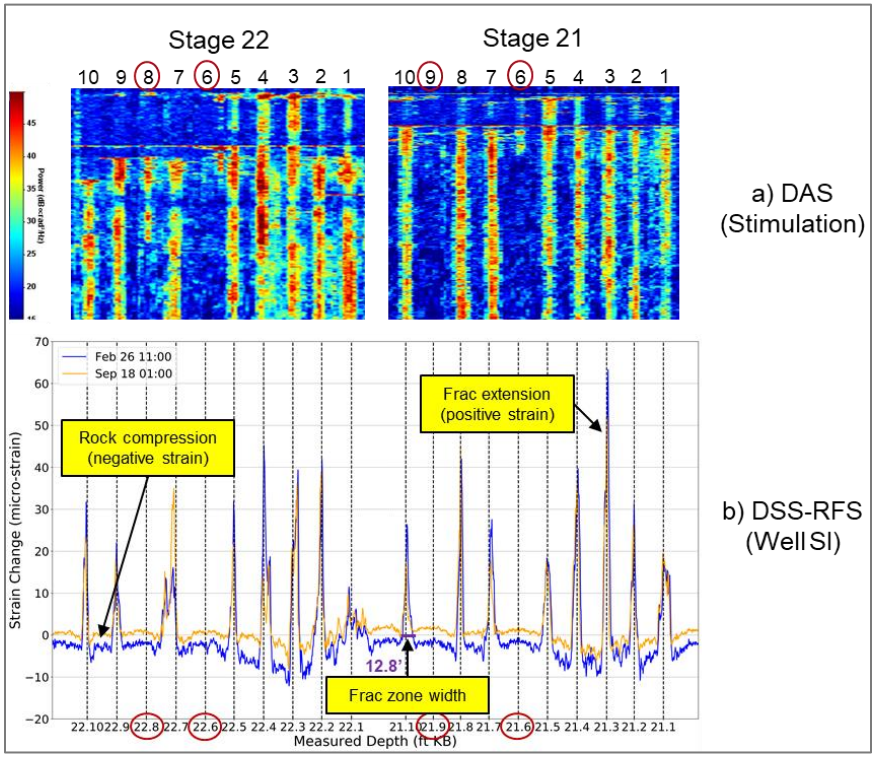

Fig C 31—DAS (stimulation) vs. DSS-RFS (well shut in) for Stages 21 and 22 on the Boxwood-4H well. There is significant correlation between the two independent datasets acquired in different stages of the well life cycle by different vendors. For red-circled clusters that were poorly treated, there is no identifiable positive strain change as the BHP builds up.

Near-wellbore DAS in Fig C 31a shows that the four red-circled PCs were poorly treated, based on very weak or non-existent DAS energy responses during stimulation. In Fig C 31b, the blue

and yellow curves represent strain changes in the near-wellbore regions of Stages 21 and 22, respectively, at the two selected time stamps shown in Fig C 30. With such a consistent and repeatable pattern, the amplitude of near-wellbore strain change on Feb. 26, 2020, is larger than that on Sept. 18, 2020, for most PCs, even though BHP buildup is the same, potentially due to complex time-lapse changes in the near-wellbore region and different production rates prior to the test. The fracture zone width was estimated based on the range of positive strain change for each PC. For instance, the fracture zone width for PC 10 in Stage 21 is 12.8 ft. The integral of the strain change value and fracture zone width gives the fracture aperture change, which is an important parameter of fracture geometry and plays a key role in fracture performance.

Despite achieving the same BHP buildup at the selected timestamps, greater strain change is observed in the Feb. 2020 test than the Sept. 2020 test, and such was the case for most of the stages on the Boxwood-4H well (see Fig C 32a), especially for the PCs belonging to the extended stages (9-10 PCs/Stage), as shown in Fig C 32b.

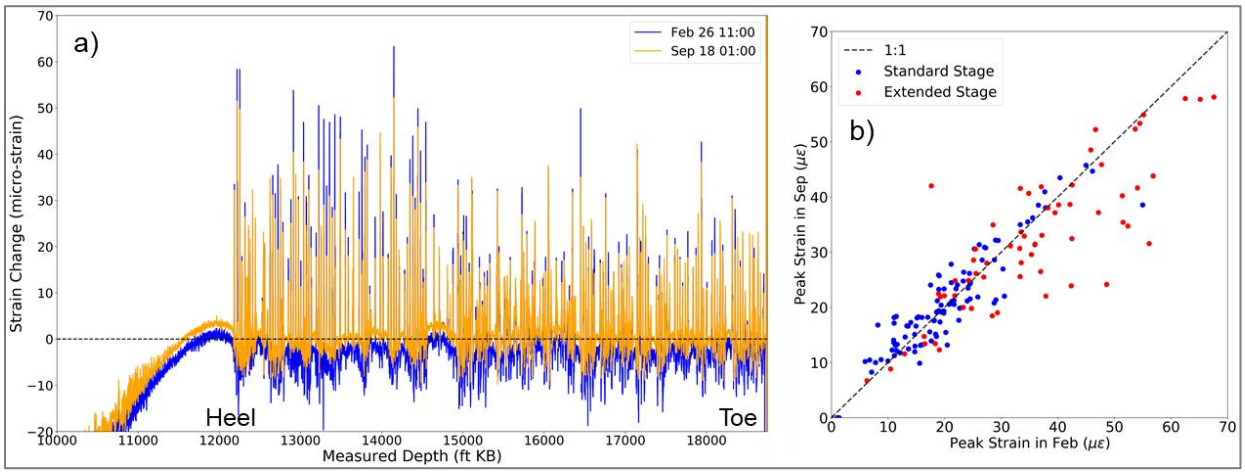

Fig C 32—a) Strain change comparisons along the lateral of Boxwood-4H. b) Peak strain change comparisons for all PCs. Larger strain change differences between the two tests for extended stages (9-10 PCs/Stage) than standard stages (mostly 5-6 PCs/Stage) indicates more fracture extension decay in extended stages after 7 months of production.

Strain Change Comparison Between Shut-in and Production Periods:

During the Sept. 2020 test, DSS-RFS data were also acquired for a short period when all Boxwood wells were in a state of stable production before Boxwood-4H was shut in. Fig C 33a compares the well shut-in and production strain changes along the lateral of Boxwood-4H, and Fig C 33c shows a closeup for Stages 20 and 21. Due to the short measurement time and the small BHP drawdown, clear strain change in the near-wellbore region during production is observed, but with much smaller amplitude and reversed polarity when compared with the

strain change during the well shut-in period. Fig C 34 shows the strong correlation between shut-in and production peak strain change values for both standard and extended stages.

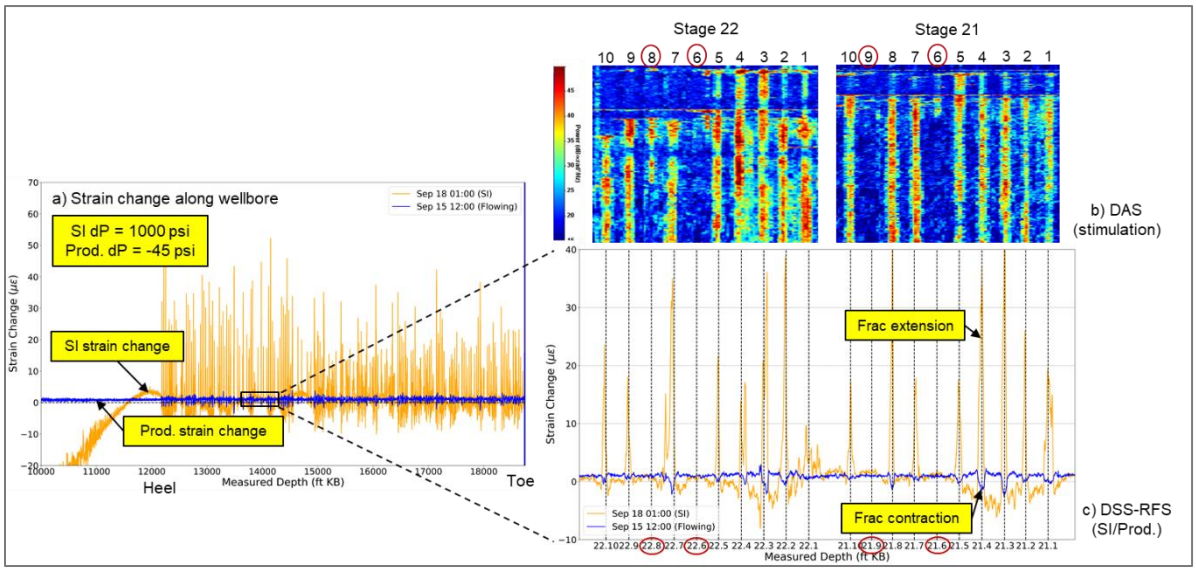

Fig C 33—Shut-in and production strain change comparison for Boxwood-4H. There is good agreement between DAS energy response during the stimulation and strain change during well shut-in and production periods.

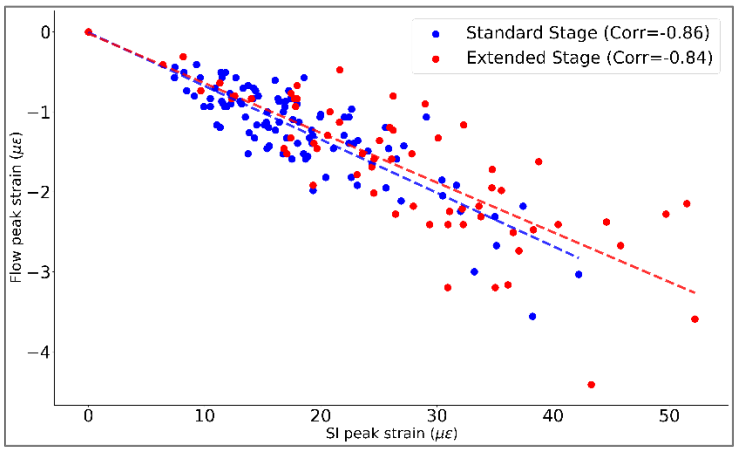

Fig C 34—Shut-in (X-axis) and production (Y-axis) peak strain change comparison for all PCs on Boxwood-4H. The strong correlation indicates that fractures showing larger extension during BHP buildup after well shut-in also experience larger contraction when the well is producing.

Time-Lapse Fracture Property Changes vs. Hydraulic Fracture Profile:

Since no conventional production logging was conducted on the Boxwood wells during this project, the comparisons in Fig C 35 and Fig C 36 attempt to link stage treatment to possible stage production performance associated with cumulative fracture aperture changes, which show desirable alignment with the HF profile (i.e., proppant distribution). In general, the stages that received less proppant due to operational issues show smaller fracture aperture changes during the shut-in periods. It is interesting to note the inconsistency between proppant allocation and fracture aperture changes for Stages 16 and 18 of Boxwood-4H, which have the same completion design. The analysis illustrated in Fig C 34 to Fig C 36 reveals that better SDE

was achieved in Stage 16 than Stage 18, which would partially explain why Stage 18 received more proppant than Stage 16, but it experienced less fracture extension as the BHP built up.

The difference between the dark and light green bars in Fig C 35 indicates larger fracture aperture reduction and possible productivity decay in extended stages with more PCs per stage after 7 months of production. This may be due to the low SDE during the treatment of extended stages, where the calculated proppant distribution metric appears to be below 0.2, as shown in Fig C 35 and Fig C 36.

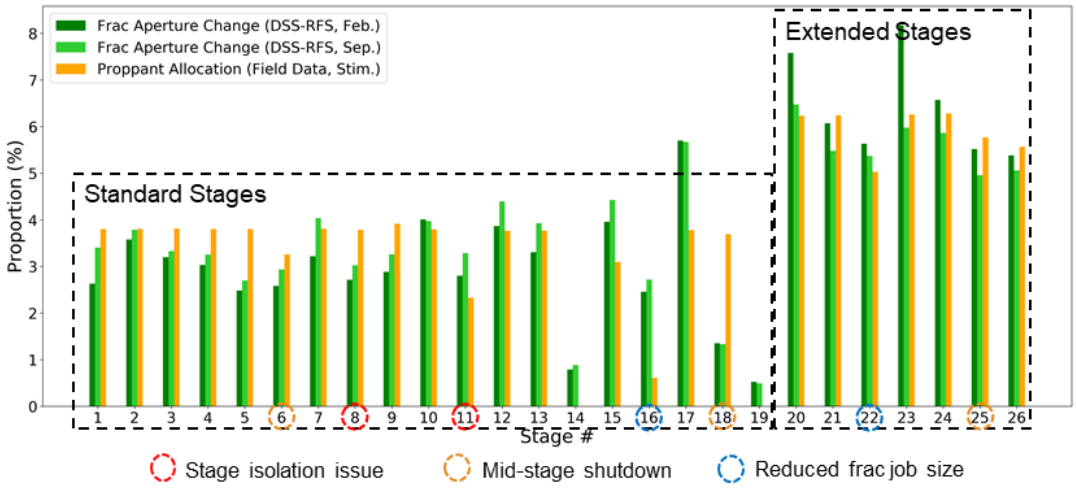

Fig C 35—Time-lapse fracture aperture changes vs. proppant allocation for all stages of Boxwood-4H. Fracture aperture change was calculated based on near-wellbore strain change value and fracture zone width during the shut-in period.

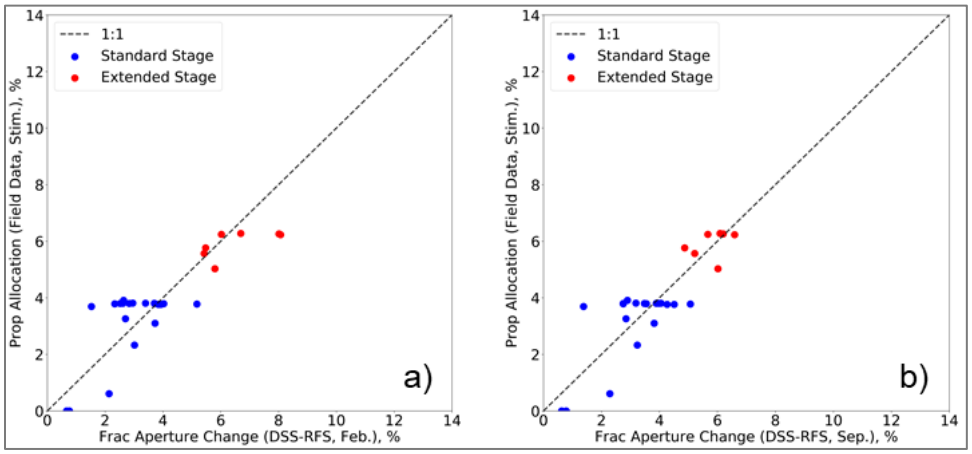

Fig C 36—Fracture aperture changes (X-axis) vs. proppant allocation (Y-axis) for all stages of Boxwood-4H: a) Feb. 2020 test results; b) Sept. 2020 test results.

Conclusions

- Even distribution of proppant and fluid was best achieved with geometric PC schemes that targeted 2.5–3.0 bpm/perf and 10.0–12.5 bpm/PC.
- Based on the statistical analysis of hydraulic fracturing profiles with effective limited entry practices, Rate Per Cluster (RPC) during proppant slurry placement appears to be a primary completion design variable rather than Rate Per Perforation (RPP), which is the typical default consideration.
- If RPC is not maintained above 10 bpm/PC, the likelihood of uneven distribution increased dramatically. The stage configurations that created low RPC while maintaining high RPP did not show improved SDE.
- All stages on the Boxwood-3H and -4H wells were treated with an average rate of 60-70 bpm, regardless of PC count. Higher RPC values (10.0 – 12.5 bpm/PC) could help improve SDE, especially for extended stages.
- No obvious effect of tapered PC schemes or perforation orientation/phasing was observed during the treatment of the Boxwood-3H and -4H wells.
- Based on near-field DAS/DTS data, completion operational issues (e.g., poor cement bonding behind casing, mid-stage shutdowns, and plug failures) add the risk of degradation of SDE.
- The strain change results based on DSS data acquired during production clearly indicate near-wellbore fracture property changes (e.g., aperture changes during well shut-in and flow periods) and are aligned well with near-wellbore DAS signals acquired during stimulation.
- Fracture property changes based on DSS data acquired during two tests 7 months apart show high consistency and good alignment with near-wellbore hydraulic fracturing profiles.

References

Holley, E. H., & Kalia, N. 2015. Fiber-Optic Monitoring: Stimulation Results from Unconventional Reservoirs. Paper presented at the Unconventional Resources Technology Conference, San Antonio, Texas. https://doi.org/10.15530/URTEC-2015-2151906.

Jin, G., Friehauf, K., Roy, B., et al. 2019. Fiber Optic Sensing-Based Production Logging Methods for Low-Rate Oil Producers. Paper presented at the Unconventional Resources Technology Conference, Denver, Colorado. https://doi.org/10.15530/urtec-2019-943.

Jin, G., Ugueto, G., Wojtaszek, M., et al. 2021. Novel Near-Wellbore Fracture Diagnosis for Unconventional Wells Using High-Resolution Distributed Strain Sensing during Production. *SPE J*: 1–10. https://doi.org/10.2118/205394-PA.

Li, X., Zhang, J., Grubert, M., et al. 2020. Distributed Acoustic and Temperature Sensing Applications for Hydraulic Fracture Diagnostics. Paper presented at the Hydraulic Fracturing Technology Conference, The Woodlands, Texas. https://doi.org/10.2118/199759-MS.

Molenaar, M. M. & Cox, B. E. 2013. Field Cases of Hydraulic Fracture Stimulation Diagnostics Using Fiber Optic Distributed Acoustic Sensing (DAS) Measurements and Analyses. Paper presented at the Unconventional Gas Conference and Exhibition, Muscat, Oman. https://doi.org/10.2118/164030-MS.

Murphy, W. B., & Juch, A. H. 1960. Pin-Point Sand Fracturing – A Method of Simultaneous Injection into Selected Sands. *J Pet Technol*, **12**(11): 21–24. https://doi.org/10.2118/1415-G.

Somanchi, K., Brewer, J., & Reynolds, A. 2017. Extreme Limited Entry Design Improves Distribution Efficiency in Plug-n-Perf Completions: Insights from Fiber-Optic Diagnostics. Paper presented at the Hydraulic Fracturing Technology Conference, The Woodlands, Texas. https://doi.org/10.2118/184834-MS.

Ugueto, G., Huckabee, P., Molenaar, M., et al. 2016. Perforation Cluster Efficiency of Cemented Plug and Perf Limited Entry Completions; Insights from Fiber Optic Diagnostics. Paper presented at the Hydraulic Fracturing Technology Conference, The Woodlands, Texas. https://doi.org/10.2118/179124-MS.

Ugueto, G. A., Huckabee, P. T., Molenaar, M. M., et al. 2016. Perforation Cluster Efficiency of Cemented Plug and Perf Limited Entry Completions; Insights from Fiber Optics Diagnostics. Paper presented at the Hydraulic Fracturing Technology Conference, The Woodlands, Texas. https://doi.org/10.2118/179124-MS.

Ugueto, G., Huckabee, P., Wojtaszek, M., et al. 2019. New Near-Wellbore Insights from Fiber Optics and Downhole Pressure Gauge Data. Paper presented at the Hydraulic Fracturing Technology Conference, The Woodlands, Texas. https://doi.org/10.2118/194371-MS.

Wheaton, B., Haustveit, K., Deeg, W., et al. 2016. A Case Study of Completion Effectiveness in the Eagle Ford Shale Using DAS/DTS Observations and Hydraulic Fracture Modeling. Paper

presented at the Hydraulic Fracturing Technology Conference, The Woodlands, Texas. https://doi.org/10.2118/179149-MS.

Appendix D: Analysis and Integration of the Hydraulic Fracturing Test Site-2 (HFTS-2) Comprehensive Dataset

Authors: Venkateswaran Sriram Pudugramam, Yu Zhao, Fadila Bessa, Jake Li, Nancy Zakhour, Tim Brown, Jichao Han, Iwan Harmawan, and Vinay Sahni

Summary

Hydraulic Fracturing Test Site-2 (HFTS-2) is a field-based research experiment performed in the Permian (Delaware) Basin. The unique aspect of this program was the acquisition of a unique, comprehensive, diagnostic dataset. Additionally, shorter parent wells drilled three years before the child wells offered clear distinction between the stages influenced by parent-child effects and the stages without any effects. The goal of this study was to analyze and integrate this comprehensive diagnostic dataset to understand the areal and vertical extent of hydraulic fractures (HF). The paper also provides insights on the effects of parent wells' depletion on child well HF geometry based on various monitoring methods and subsurface models. Areal and vertical coverage for all HFTS-2 wells during stimulation and depletion was estimated based on analysis and interpretation of diagnostics and advanced modeling results. HFTS-2 diagnostics included microseismic (MS), pre- and post-stimulation logs and cores, bottomhole gauges, and fiber optic (FO) data. The diagnostics results (MS, FO, image logs) were integrated and used to calibrate subsurface models. Additional field tests were designed and implemented for depletion monitoring. The tailored program for monitoring depletion included vertical and slant well pressures, interference testing, and vertical strain depletion trial. Specifically,

Areal Coverage: Conventional MS (and FO MS) were used to compute HF dimensions, which were compared with diagnostics (FO strain, gauge, image logs) observations and calibrated subsurface models. A post-production interference test did not show offset well communication.

Vertical Coverage: Vertical coverage during stimulation was monitored using a vertical monitoring well. The stronger mechanical strain signals showed good correlation with MS event intensities, geomechanical properties, and gauge inferences. Vertical depletion was estimated based on vertical/slant well gauges and strain depletion tests.

Parent-Child Effects: Diagnostics and calibrated subsurface models show asymmetry in child well fracture geometries for stages that overlap parent wells. Child well image logs serve as a good indicator for parent well HF tracking. Child well MS events had an eastward bias, in line with pre-stimulation image logs, and was confirmed by parent well frac hits.

The dataset presents a unique, over-constrained problem space to compare independent techniques to arrive at HF metrics (i.e., stimulation height and/or half-length), unlike a single-source dataset, in which calibration is done using available data to guide predictions. The asymmetry in HF geometry seen in the stages influenced by parent-child effects offers unique

insights into well spacing and landing, which are key capital decisions the unconventional resources industry is seeking to optimize.

Introduction and Objectives

The Hydraulic Fracture Test Site-2 (HFTS-2) is a cost-shared, field-scale R&D program in the Permian (Delaware) Basin. Occidental is the host and operator of this program with 18 consortia members. The dataset acquired in the program included microseismic (MS), 1,500 ft of whole core including 1,000 ft of SRV core, DFIT, PVT, Quad Combo and image logs, proppant logs, geochemical data, 28 bottomhole gauges' P/T data in production and science wells, varying completions, and fiber optic cable in two horizontal wells and one vertical well. The unique aspects of the program are the one-of-a-kind, comprehensive dataset and the application and demonstration of fiber optic (FO) technology for stimulation and production monitoring and fracture diagnostics. The two horizontal parent wells, drilled 3 years prior, are shorter than the four child wells, thereby offering a clear distinction between the stages influenced by parent-child effects and the stages without any depletion effects. The asymmetry in fracture geometry, which influences well spacing and landing decisions, is a critical piece of the puzzle to optimize capital expenditure and reduce the environmental footprint of the unconventional resources industry.

Project Area

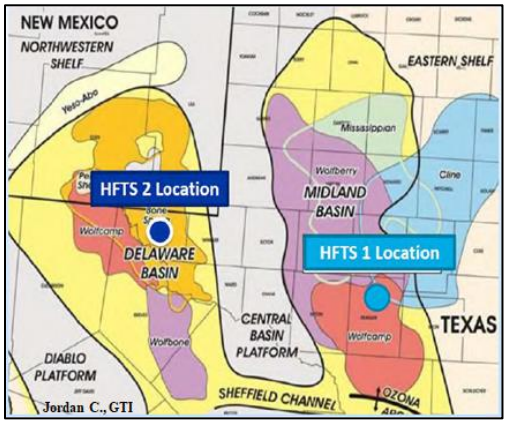

Fig D 1—Location of the HFTS-2 project area

The Hydraulic Fracture Test Site-2 (HFTS-2) is in the Delaware Basin about 140 miles west of the HFTS-1 project area (Fig D 1). The HFTS-2 project area includes two parent horizontal wells (BR1H and BR2H) drilled and completed three years before the child wells, four horizontal Boxwood wells (BX1H, BX2H, BX3H, and BX4H) spanning the Wolfcamp-X to Wolfcamp-A formations. The average lateral length of the parent wells is 60% of the four child wells, so a portion of the lateral length on the child wells was affected by depletion. The project area also includes a vertical well (B5PH) drilled before the child well stimulation, and one slant core well (B6S) drilled after the child well stimulation, covering up to the Wolfcamp-B bench. The vertical well (B5PH) also had fiber optic cable installed, as did two adjacent horizontal wells (BX3H and

BX4H). The setup and interpretation of near-wellbore DAS/DTS data is covered in detail in another paper (Zakhour et al., 2021).

There are 8 bottomhole gauges on the vertical well (B5PH) and 12 bottomhole gauges on the slant well (B6S). About 500 ft of whole core was recovered from the vertical well (B5PH) prior to the hydraulic fracturing of the child wells. About 1,000 ft of SRV core was recovered from the slant core well (B6S) after the child wells were fractured. The child horizontal wells have a rich dataset that includes heel and toe P/T gauges, Quad Combo and image logs, geochemical data, DFIT and PVT on two wells, and a proppant log on one well. There are conventional microseismic (MS) data on two wells in addition to FO-based MS data. The completion design, which varied in stage design, proppant, and fluid loading along and between the wells, is covered in detail in Zakhour et al., 2021. The child horizontal wells are spaced at ~700 ft with about 250 ft in vertical variation. See Fig D 2 for a schematic of the wells.

Looking at the project area from the top view, we can separate the project area into a North sector and a South sector. The South sector includes the parent wells where depletion or parent-child effects come into play, and the North sector, which has the vertical well (B5PH) and the slant core well (B6S), will have no depletion effects. See Fig D 2 for a delineation of the North and South sectors.

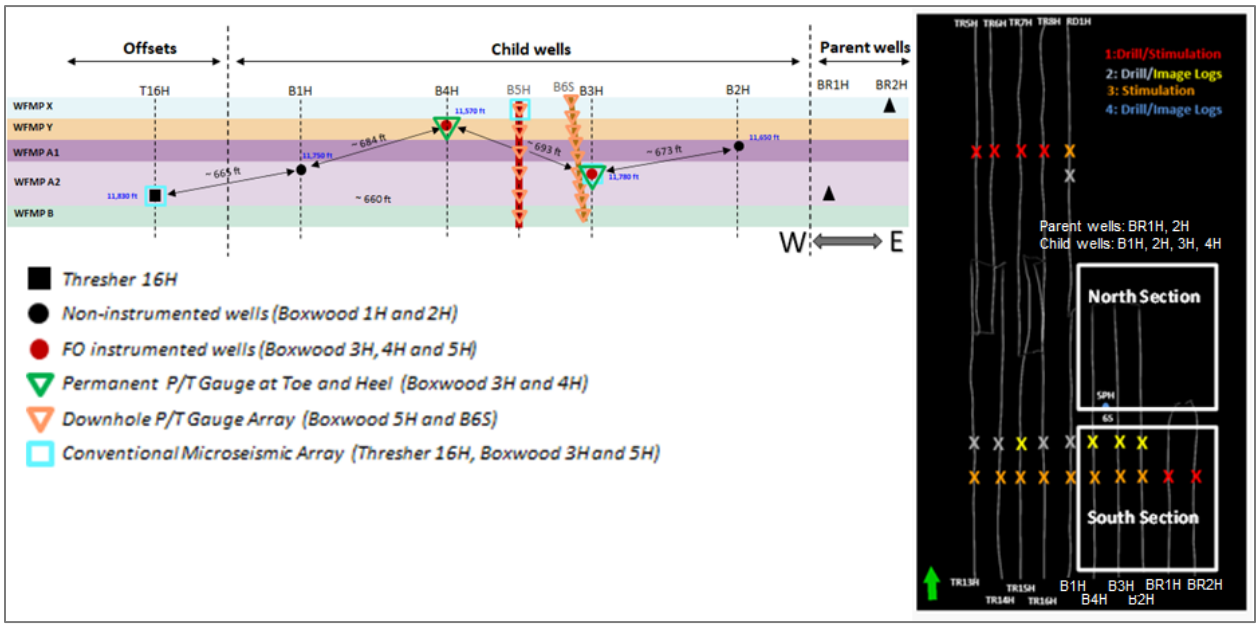

Fig D 2—Left: Schematic of the HFTS-2 wells (gun barrel view); Right: Delineation of the North and South sectors (plan view)

HFTS-2 Dataset

Microseismic Data

A full description of the microseismic acquisition and processing is provided in Howell, 2021. The objective of the microseismic acquisition is to estimate SRV and integrate observations with

other diagnostic techniques to understand well and reservoir interactions better. The primary observations include:

- Eastward growth of events during the BX1H and BX2H stimulations toward the BR1H and BR2H due to reactivation in overlapping stages (Fig D 3)
- Limited horizontal growth of seismicity for the BX1H and eastward growth for the BX2H stages north of the BR1H and BR2H overlap (Fig D 4)
- Additional horizontal asymmetry for the BX2H and BX4H due to sequential ordering of completions
- Majority of seismicity is vertically constrained from top of Wolfcamp to Wolfcamp-B.

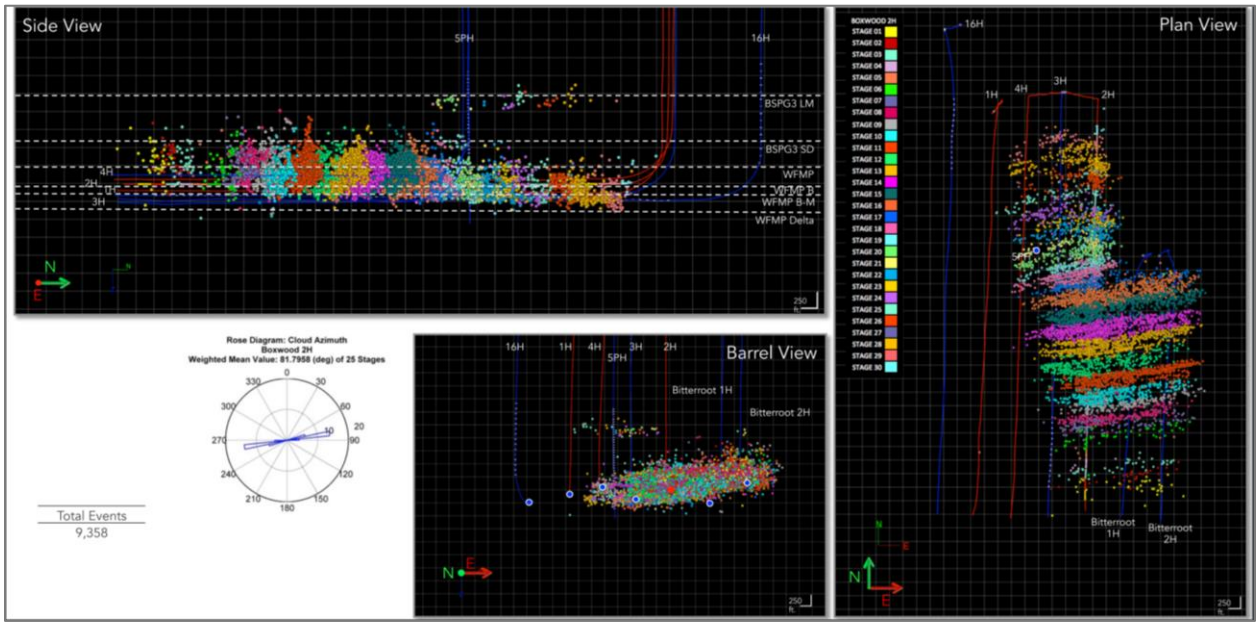

Fig D 3—Microseismic display of high-quality events from the BX2H completion. The gun-barrel and plan views demonstrate the eastward growth in the area overlapping the Bitterroot wells.

Fig D 4 shows a split comparison of the stages of BX1H affected by depletion and the stages without any depletion effects. Most of the microseismic events (failures) are within the lowest

effective stress zone (violet zone), and the non-depleted stages show a more confined event distribution.

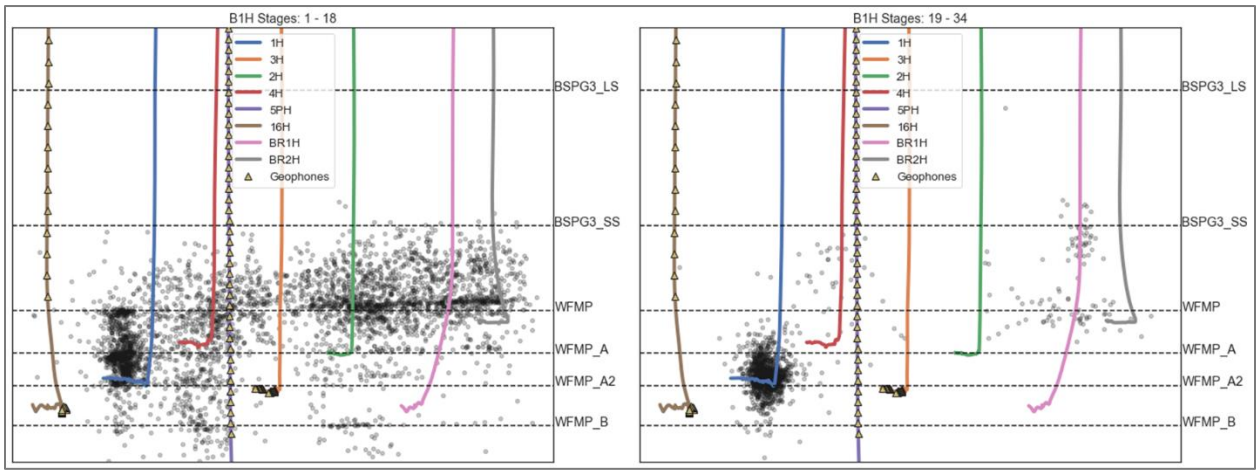

Fig D 4—Split comparison of microseismic events for stages in the depleted (Left) and non-depleted (Right) zones.

The DAS microseismic was not used for SRV estimates because events were mapped using a single plane solution, which does not yield accurate 3D locations. However, the seismic deformation was compared to the aseismic deformation recorded by the low-frequency DAS. As seen in Fig D 5, the dynamic vertical growth of the microseismic lags compared to the strain response on the low-frequency DAS, which demonstrates that the hydraulic fracture front is generally aseismic.

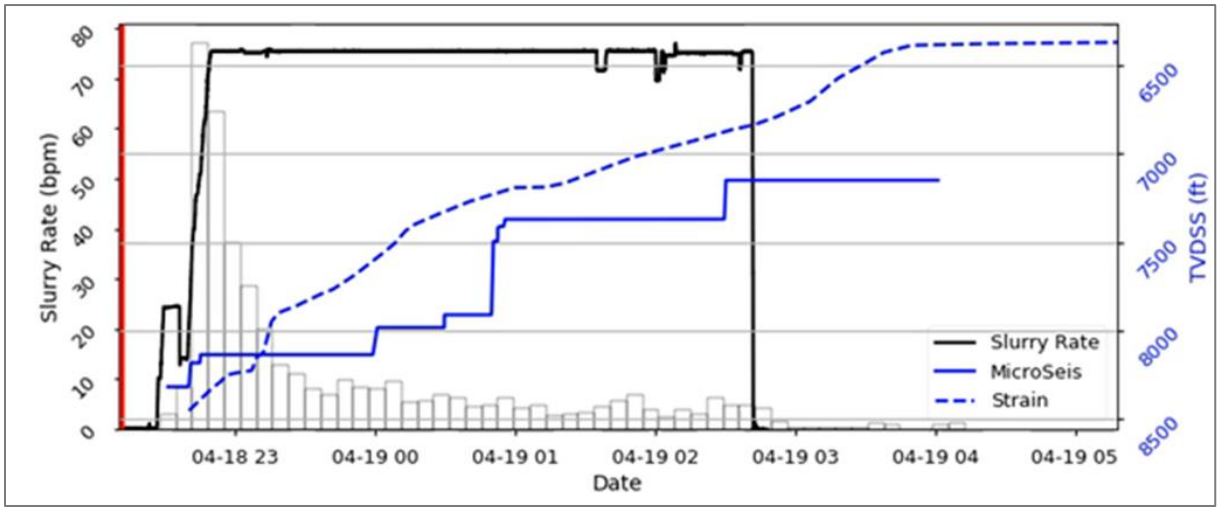

Fig D 5—Dynamic upward growth of the microseismic (solid blue) vs. strain signal recorded by the low-frequency DAS (dashed blue). The microseismic lags the strain response.

Pre- and Post-Stimulation Logs and Core Data

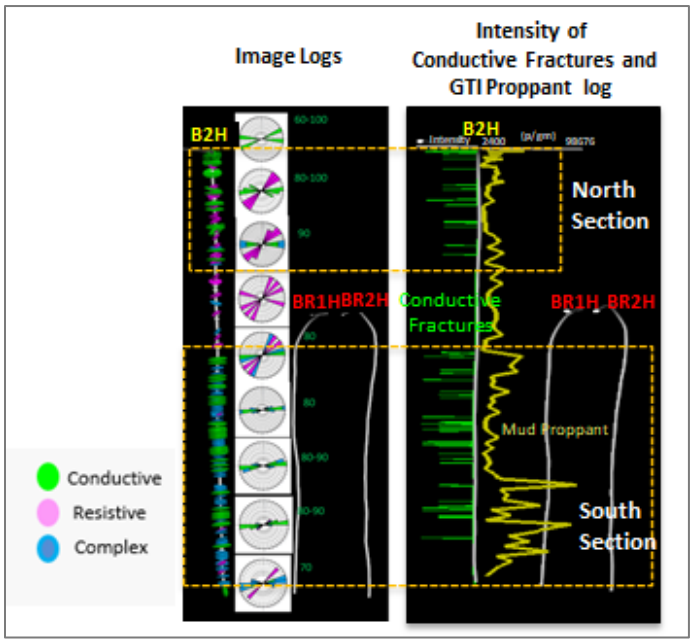

Fig D 6—Image and GTI proprietary proppant logs in the North and South sectors

The highlights of the stimulation logs and core interpretation as related to the integration with other datasets are covered in this section; the details are covered in Bessa et al., 2021. The SRV core obtained from the slant well (B6S) showed that the hydraulic fracture was planar and the orientation for Shmax was around 80°, which was confirmed by microseismic data, fiber optic data, and a regional sonic azimuthal anisotropy study. The image logs on BX2H, which were obtained before stimulation of the child wells but after the parent wells' stimulation, also show two distinct fracture sets: NE-SW oriented resistive fractures, and hydraulic-induced conductive fractures oriented around 80°. The intensity of conductive fractures along the lateral length of BX2H showed an interesting trend separating the North and the South sectors. The South sector, affected by the parent wells' stimulation, saw a higher intensity of conductive fractures,

as shown in Fig D 6. This observation was corroborated by the GTI proprietary proppant analysis, which measured the count of proppant in the mud log samples along the lateral length.

Fiber Optic Data

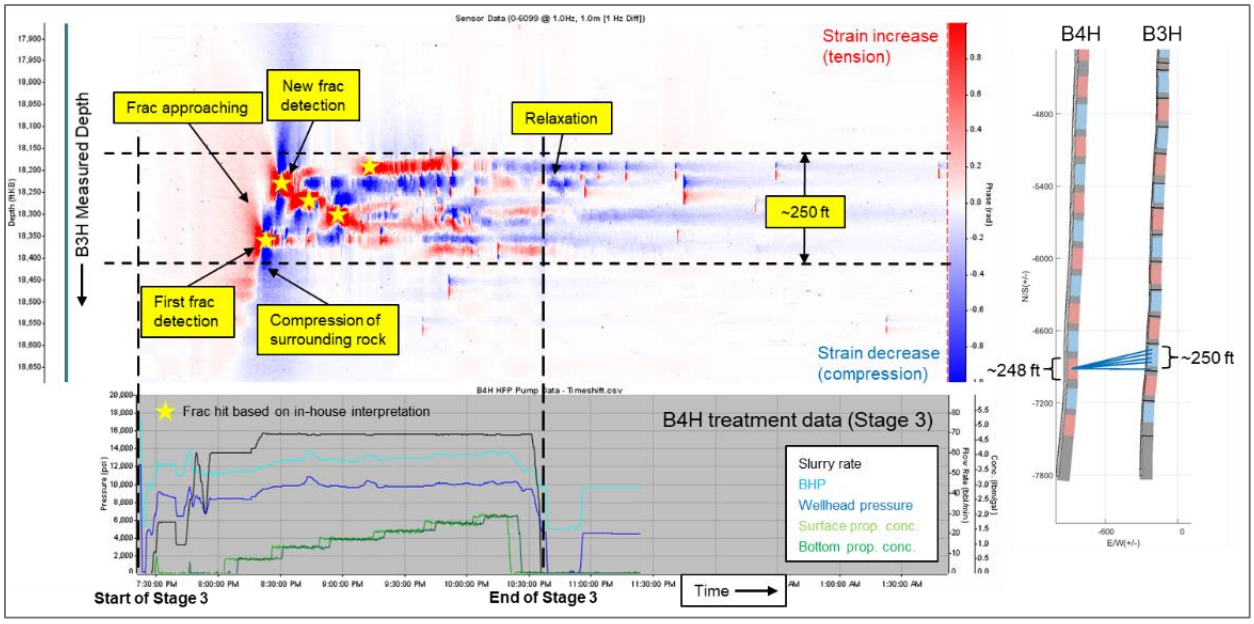

Fig D 7—Far-field cross-well strain data acquired on BX3H during the treatment of Stage 3 (6×24) on BX4H

In the HFTS-2 project area, fiber optic cable was permanently installed in two horizontal child wells (BX3H, BX4H) and one vertical well (B5PH). This unique three-well design enables spatial and temporal HF propagation and production depletion monitoring. There are two kinds of data obtained from this fiber: near-wellbore survey and far-field survey. The near-wellbore survey measures the response from the activity in the fiber wells, whereas the far-field survey measures the response from the activity in the offset wells. In the near-wellbore survey, Distributed Acoustic Sensing (DAS) and Distributed Temperature Sensing (DTS) data were acquired during stimulation of the two horizontal fiber wells. These data were used to quantify pumped fluid/proppant allocation among the clusters and evaluate stimulation efficiency for different completion designs. During the production phase, Distributed Strain Sensing (DSS) (Jin et al. 2021) data were acquired in the near-wellbore region, which allowed us to gain insights on time-dependent fracture property changes. The integrated analysis and interpretation of the near-wellbore survey data are covered in detail in Zakhour et al., 2021.

Through the far-field survey, cross-well strain rate data were obtained by the low-frequency DAS technique from all three fiber wells and integrated with other diagnostics to achieve a better understanding of spatial and temporal characteristics of hydraulic fracture propagation (Molenaar and Cox, 2013; Jin and Roy, 2017; Ugueto et al., 2019). Fig D 7 shows a typical example of cross-well strain acquired on the BX3H well during the treatment of Stage 3 on BX4H consisting of 6 clusters, 24 perforation holes, and 32-ft perforation cluster spacing. With the start of the stage injection, the emerging cone-shaped red strain rate signals indicate the propagation of hydraulic fractures from BX4H to BX3H, and 5 frac hits were indicated by yellow stars, where there is significant tensile deformation while the surrounding rocks are being

compressed simultaneously. Fig D 7 also clearly shows that the lateral coverage (248 ft) of frac hits on BX3H is almost the same as the stimulated stage length (250 ft) on BX4H. This observation is common to all treatment stages on the BX1H, BX2H, and BX4H wells, which indicates planar fracture propagation in the formation. As stated in the previous section, the Shmax orientation is suggested to be around 80° through integrated data analysis from multiple diagnostics (i.e., FO, MS, image logs, and SRV core).

Fig D 8 shows the frac hits detected on the BX3H and BX4H wells during the treatment of BX1H and BX2H. The blue bars represent the cluster number of each treatment stage, while the orange and green bars represent the number of detected frac hits from vendor and in-house interpretations. For the BX1H well, which was the first well stimulated in the pad, BX4H detected more frac hits than did the BX3H well due to its proximity to BX1H. During the treatment of BX2H, more frac hits were also detected on BX4H than on the BX3H well, although BX3H is closer to BX2H horizontally. This observation can be explained by the shorter vertical distance between BX2H and BX4H, which also implies the upward growth trend of the hydraulic fractures. The relatively small number of detected frac hits on BX3H for Stages 1–17 on the BX2H well indicates a clear eastward growth preference for the BX2H stages that overlap with the two parent wells due to the production depletion effect.

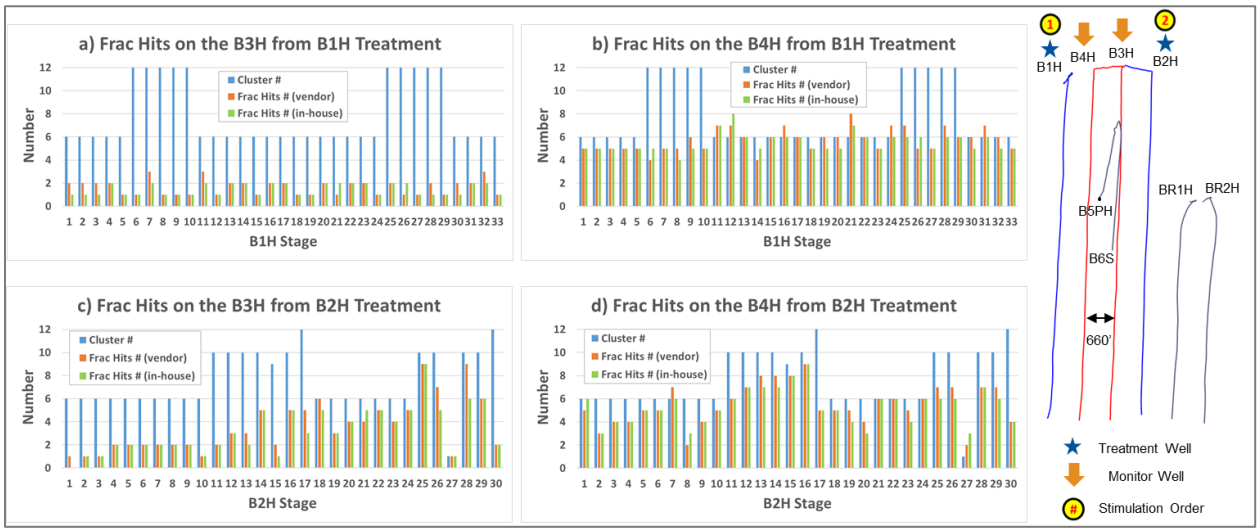

Fig D 8—Frac hits on the BX3H and BX4H wells during the treatment of BX1H and BX2H.

During the treatment of the child wells (BX1H-BX4H), far-field cross-well strain data were also acquired in the vertical fiber well, B5PH, which offered a great opportunity to gain better understanding of vertical propagation and height of hydraulic fractures. Fig D 9 shows the strongest cross-well strain data acquired on the B5PH during the treatment of two stages on the BX1H and BX4H wells. FO is very sensitive to small strain changes, and for that reason the strongest strain signals on B5PH could cover from 2nd Bone Spring to Wolfcamp-B, and the total height of strain signals is as large as ~2,000 ft. However, the strain signals in the black-circled areas (from 3rd Bone Spring Sand to Wolfcamp-A2) almost immediately faded away as the pump shut off in the treatment well, whereas the strain signals in the shallower formations

continued to extend upward. This observation indicates more mechanically induced strains from the 3rd Bone Spring Sand to Wolfcamp-A2, as they show a stronger correlation with hydraulic fracturing operations and actual fractures created.

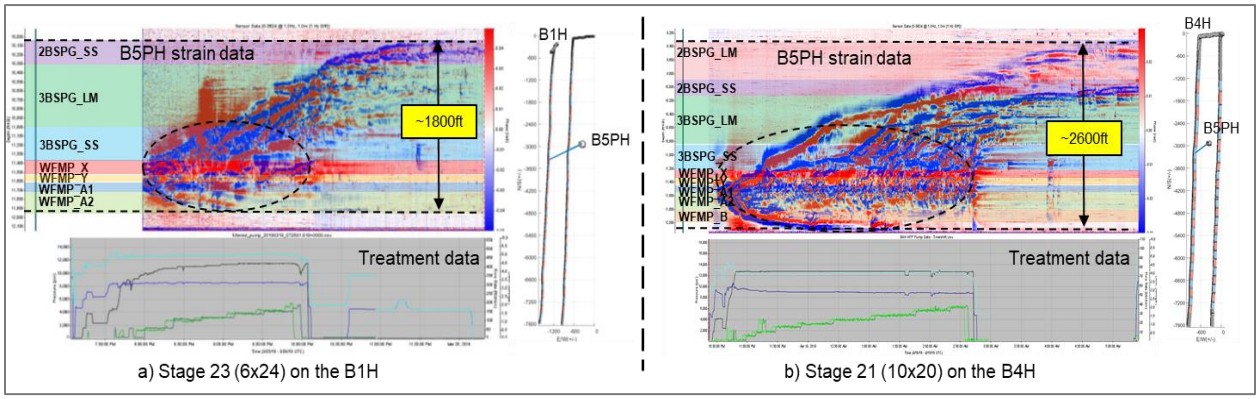

Fig D 9—Strong far-field cross-well strain data acquired on B5PH during the treatment of Stage 23 (6×24) on the BX1H well (a) and Stage 21 (10×20) on the BX4H well (b)

FO-based MS monitoring was conducted in the HFTS-2 project, and the results were compared with conventional MS data. Some of the key insights from the FO interpretation include: fluid/proppant allocation and evaluation of stimulation efficiency for different completion designs, observation of planar fracture propagation based on the far-field survey, and determination that the vertical propagation of hydraulic fractures from FO strain data should be an upper limit on fracture height and a data point for Shmax orientation. Only the highlights of the FO setup and far-field survey data interpretation are covered in this paper, but the insights on stimulation efficiency and completion designs comparison from analysis of near-wellbore survey data are covered in Zakhour et al., 2021.

Bottomhole Gauges

The pressures from bottomhole gauges were an important part of the HFTS-2dataset, quantifying the impact of frac hits and depletion. As many as 8 gauges on the vertical well (B5PH) and 12 gauges on the slant well (B6S) were installed spanning the formations from 3rd Bone Spring Sand to Wolfcamp-B. Each of child wells also had a bottomhole gauge. See Fig D 10 for a pictorial representation of the gauges in relation to the child wells. The pressure data were analyzed during the stimulation of the child wells as well as during the production period.

During Stimulation:

The slant well was drilled after the stimulation of the child wells, so the vertical well gauges (8) along with the child well gauges were analyzed during the stimulation. As an example, the pressure changes and pressure derivatives of the shallowest gauge are shown in Fig D 10a during the stimulation of Stage 23 of well BX1H. The pressure derivative shows a strong inflection during the stimulation event. Analyzing all the gauges, we observe that the frac hit severity increases as we go to the shallowest gauge, indicating the preferential upward direction of fracture propagation (Fig D 10b). Some of the other conclusions from the data are that all the child wells had frac hits on the gauges, the frac hits are perfectly aligned with the Shmax

direction, and the existing gauge coverage isn't sufficient for fracture height estimation, as we see a response even in the shallowest gauge.

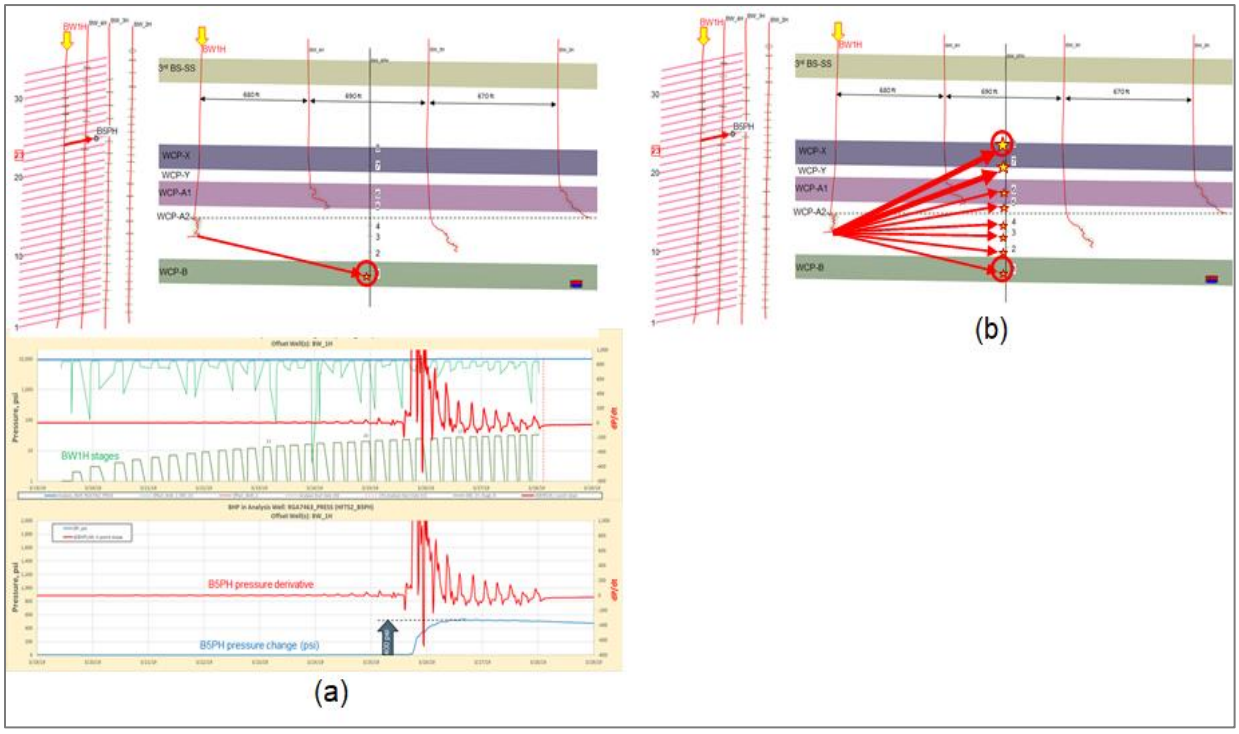

Fig D 10—a) Pressure change (blue curve) and pressure derivative (red curve) in bottommost panel showing the impact of stimulation of Stage 23 in well BX1H on shallowest gauge in B5PH; b) Severity of frac hits decreases with depth in the vertical well gauges.

During Production:

The pressure drops seen in the gauges in vertical well B5PH show the depletion in each of the benches except Wolfcamp-B (Fig D 11), which is confirmed by other diagnostics that show that the fractures don't grow downward. Fig D 12shows that bottomhole pressures measured at the same time at similar depths in the vertical well (B5PH) and slant well (B6S) were similar, lending confidence to the measurements.

Well Interference Test Data

Two-well interference tests were conducted in the HFTS-2 area. In Feb. 2020, the first FO-based well interference and production logging test was designed and executed based on a proprietary procedure developed by ConocoPhillips (Jin et al., 2019). This test was conducted to identify flow connections between BX4H and the offset well, and to estimate the production log from the FO data for BX4H. After a long, stable production period and an 18-hour shut-in period, all involved wells in this test were cycled shut-in or open for shorter intervals of a few hours. Through analysis of the DAS data acquired on BX4H, no identifiable well interference between BX4H and the offset wells was observed, but the shut-in and open intervals (hours)

were too short to record interpretable pressure gauge responses for analyzing communications between the child wells and the vertical or slant well. (See Fig D 13)

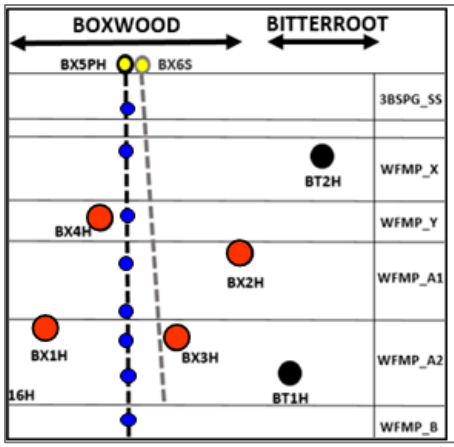

B5PH Gauge	Bench	6-month ΔBHP
1	BS3 (Shallowest)	-790 psi
2	WC-X	-763 psi
3	WC-Y	-632 psi
4	WC-A1	-470 psi
5	WC-A1	0 psi
6	WC-A2	-307psi
7	WC-A2	-307 psi
8	WC-B (Deepest)	0 psi

Fig D 11—B5PH gauges pressure drop showing depletion in each bench

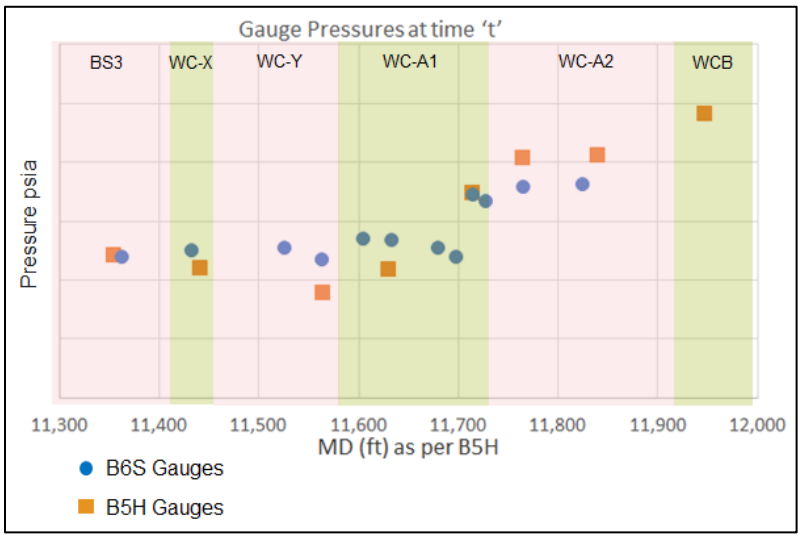

Fig D 12—Bottomhole pressures in the vertical and slant well gauges

The second test in Sept. 2020 was a dedicated pressure interference test with longer shut-in and open time intervals (3-6 days) on the two child wells, BX3H and BX4H. The longer durations allowed enough time for pressure signals to reach the offset wells and offered a better chance to confirm the well communications after 7 months of production. Fig D 14 shows that the pressure response from shutting in and opening the BX3H and BX4H wells were picked up by four gauges in vertical well B5PH and 8 gauges in the slant well B6S. These signals enabled estimation of the SRV drainage height, which was 420 ft above the landing depth (Fig D 14). The pressure signals at the gauges were weaker than the signals during the stimulation event. The drainage height estimated was compared with the other diagnostics during stimulation, but the pressure interference dataset differed from the diagnostics because the gauge signals (pressure depletion and derivatives) were a function of the overall drainage at that point in time and not

the stimulation event. However, the drainage heights were in line with the estimations from completions and reservoir modeling, microseismic, and FO data.

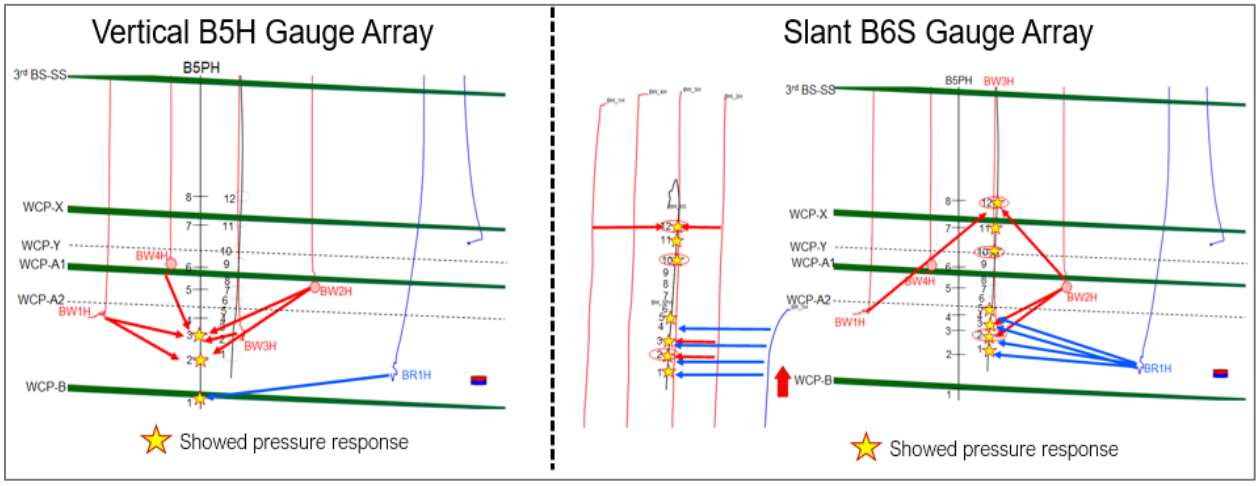

Fig D 13—Pressure gauge responses during the FO-based interference test in Feb. 2020

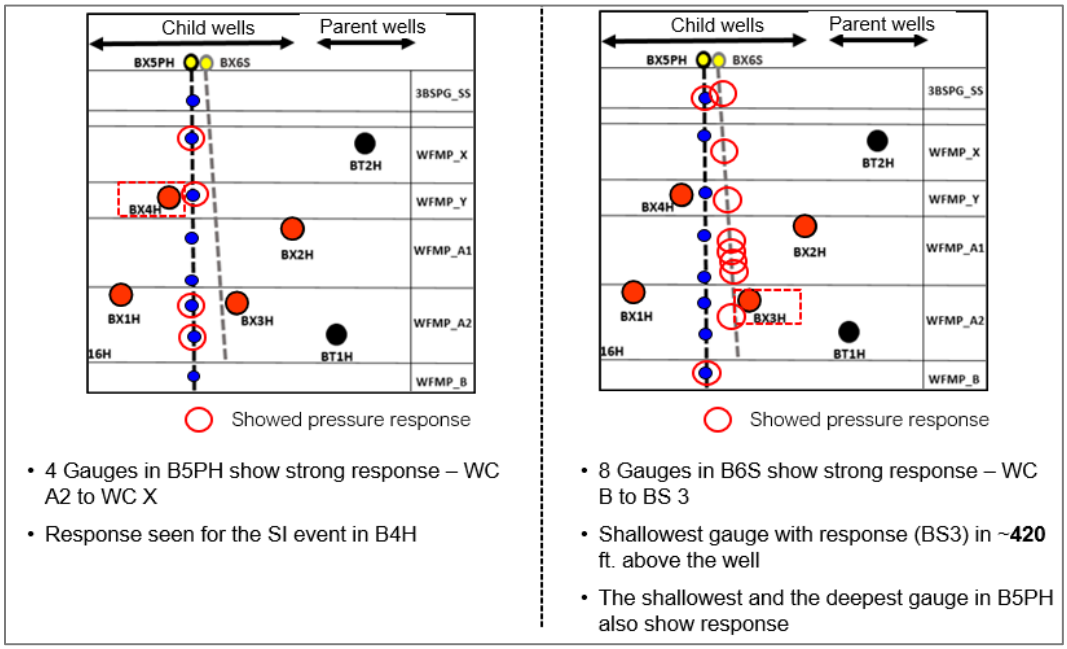

Fig D 14—Pressure signal at the gauges during the dedicated Well Interference Test

During the two interference tests, Distributed Strain Sensing (DSS) data were acquired on BX4H and showed encouraging potential for analyzing time-dependent fracture property changes in

the near-wellbore region. The detailed interpretation and comparison with pumped fluid/proppant distribution among the clusters are covered in Zakhour et al., 2021.

Subsurface Models

Completions

All the child wells (BX1H–BX4H) were completed sequentially in a single well completion format. The completion designs were varied using Design of Experiments (DoE), which is discussed in detail in Zakhour et al., 2021. The extensive dataset of DFIT, falloff instantaneous shut-in pressure (ISIP), microseismic, image logs, and pressure interference were all available, so the completion modeling workflow had to be catered to include the essential elements. Modeling the impact of depletion from parent wells was critical to arriving at an accurate fracture geometry and characteristics in line with those obtained from diagnostics, which were only available for the child wells, not the parent wells. The first step of the workflow involved calibrating the non-depleted section of the child wells (North sector) to create an equivalent model for the parent wells. This intermediate step to create an updated stress map (pore pressure and Shmin) of the area enabled an accurate simulation of the subsequent child wells. These simulated child-well fractures were then calibrated with the extensive diagnostics dataset. Due to the absence of zipper frac completion, intra-well stress shadowing was sufficient to improve the calibration process.

Simulation Modeling

Two approaches were employed for simulation modeling. The first was a traditional approach in which the model uses outputs from the completion models statistically along with in-house scripts for asymmetric fracture geometries and all the diagnostics data (FO, PIT, MS, BHPs) to match history. The second was a comprehensive geomechanics and flow simulation loop approach that couples and iterates between the geomechanics/completions models (GOHFER) and the dynamic simulation models (tNav) to incorporate the geomechanical stress shadowing. This approach takes more time to set up and run, but it provides an accurate understanding of the parent-child effects and helps optimize the stimulation design. The comprehensive modeling workflow for HFTS-2 is highlighted in the completions modeling section above.

Results and Discussion

Areal Coverage of Hydraulic Fractures

During Stimulation:

The comprehensive diagnostics dataset acquired during this project enabled the estimation of the hydraulic fracture dimensions. Fig D 15 shows the areal coverage or length estimation of hydraulic fractures in four child wells from the various diagnostics and simulation results. The diagnostic-based (MS and FO) estimations for hydraulic fracture lengths (eastward and westward) are highlighted by the blue boxes, and the modeling-based results (fracture modeling from GOHFER and history-matched simulation) are highlighted by the red boxes. The results in

Fig D 15 are presented for the North sector (no depletion effects) and the South sector (strong parent-child effects), respectively.

Because BX2H is the closest child well to the two parent wells in the east, the fracture length results from diagnostics and simulations in the South sector show a significant eastward growth preference for the stages that overlap with the parent wells due to the strong depletion effect. This also aligns well with the identified hydraulic fractures of the parent wells from the interpretations of image log and proppant log data acquired on the BX2H well prior to stimulation (Fig D 6). This eastward growth trend of hydraulic fractures was not observed for the stages of BX2H in the North sector. This critical observation is common to the BX1H, BX3H, and BX4H wells, which indicates the necessity of handling the North sector and South sector individually in the modeling efforts.

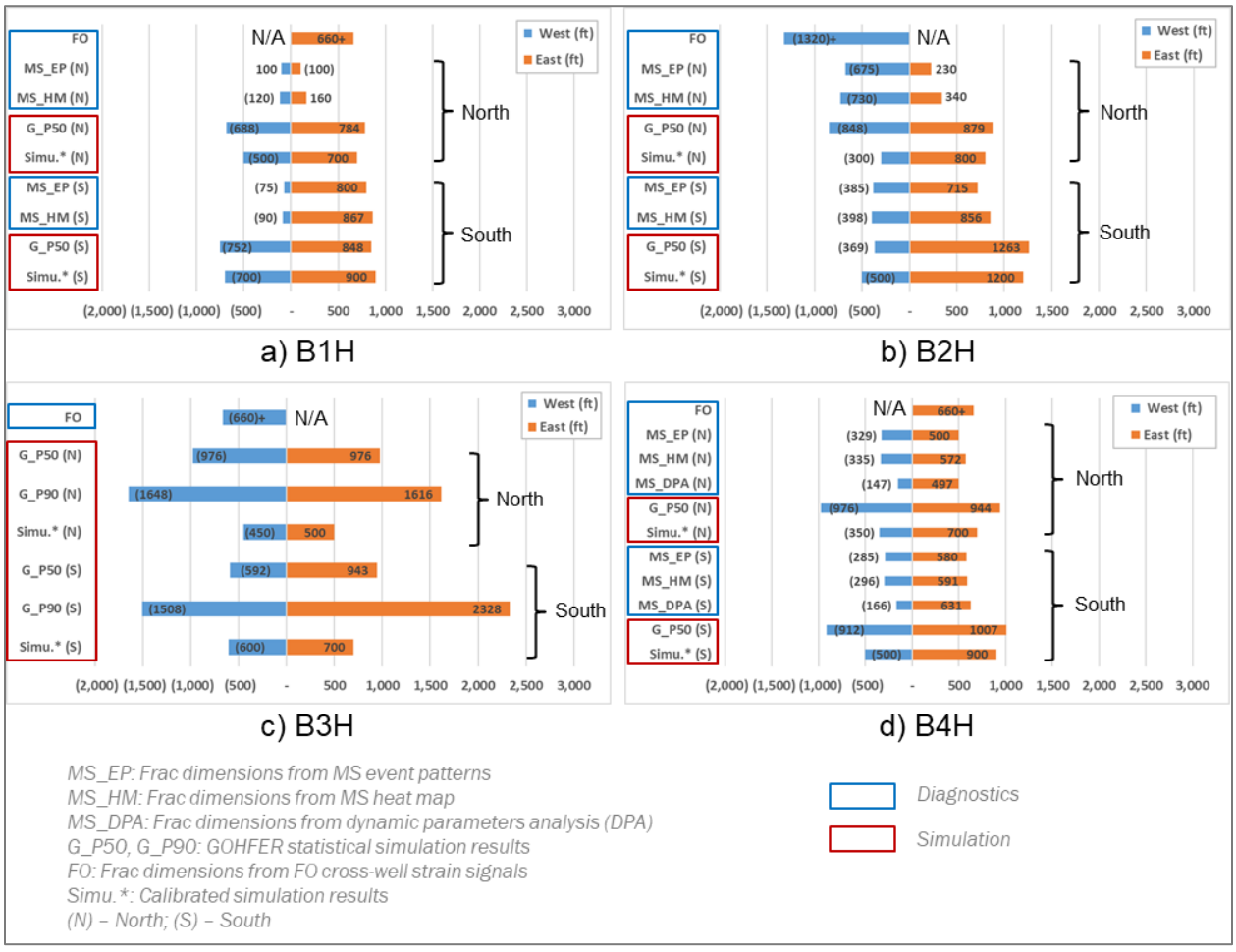

Fig D 15—Areal coverage of hydraulic fractures in child wells from various diagnostics and simulation results

During Production:

Through comprehensive analysis of the acquired FO data along with pressure gauge responses, the two well interference tests did not show areal connections between child wells, but a few of the vertical and slant well pressure gauges picked up a clear signal response from the "shut-in"

and "open" well events. The intensity of the pressure signal at the vertical and slant well gauges during production starts and stops appears to be weaker than that during the well stimulation phase.

The main implication of an asymmetric fracture from parent well influence will be on well spacing. The child wells need to be planned properly from a well placement and fracture sequencing perspective to maximize the new SRV formed by the fracturing process. If diagnostics are not available, sensitivities on fracture geometry asymmetry need to be considered.

Vertical Coverage of Hydraulic Fractures

During Stimulation:

Fig D 16 shows the vertical coverage or height estimation of hydraulic fractures in the four child wells from various diagnostics and simulation results. All the child wells showed frac hits on the vertical well (B5PH), both from the pressure gauge responses (Fig D 10) and far-field cross-well strain data. In terms of gauge response, the strongest effect was seen on the shallowest gauge located in the base of the 3rd Bone Spring formation, and the magnitude of the response decreased with depth towards the Wolfcamp-B formation. This observation indicates that the hydraulic fractures tend to grow upward during stimulation, which is in good agreement with larger upward fracture height estimations from the various diagnostics. For both the North and

South sectors, the microseismic-based fracture height estimations match well with the values from pressure gauge data and statistical GOHFER simulation results.

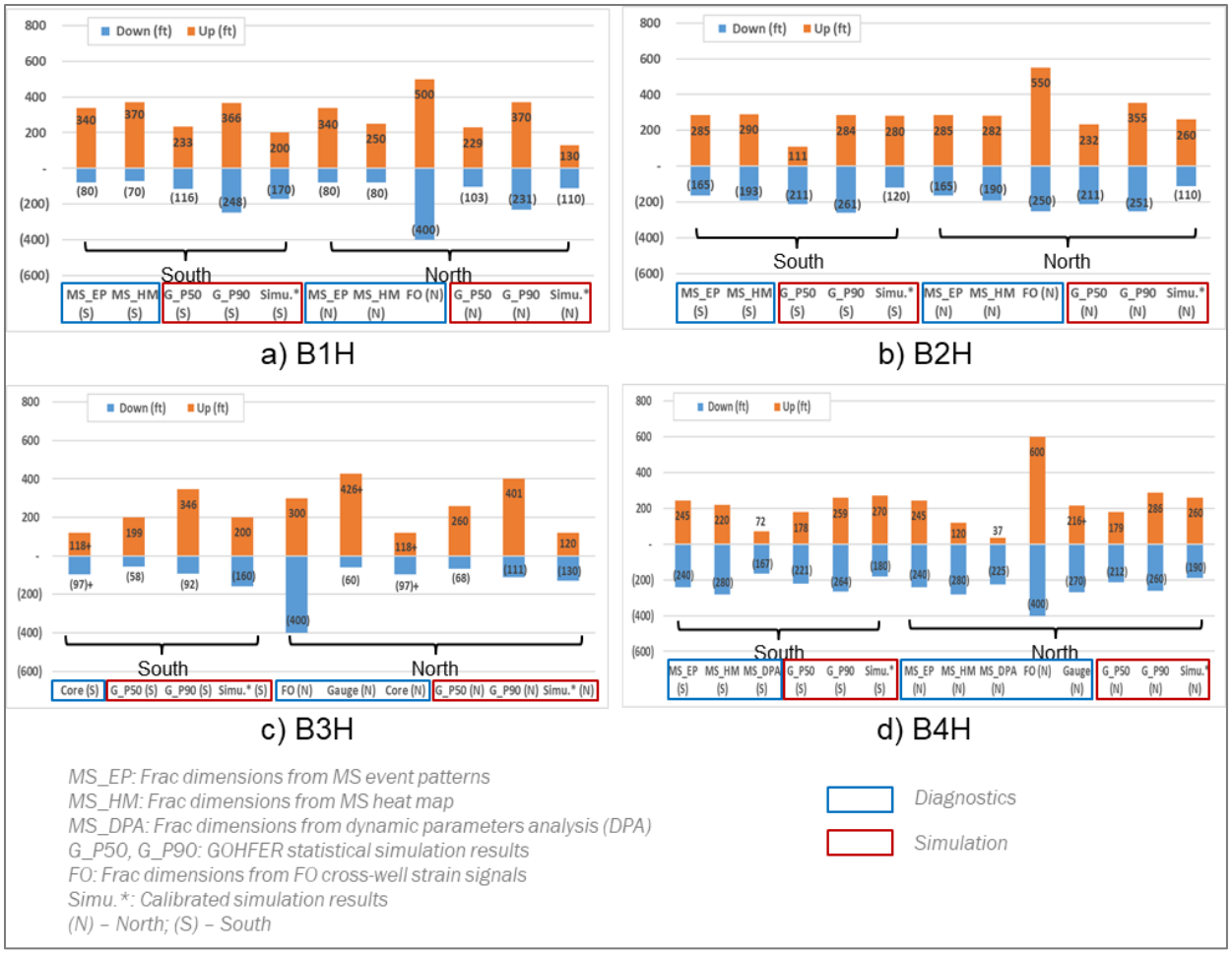

Fig D 16—Vertical coverage of hydraulic fractures in child wells from various diagnostics and simulation results

In comparing different diagnostics, the fracture height estimations based on FO data always appear to be the upper bounds, which is due to the high sensitivity of FO to small strain changes that are not detectable by other diagnostics. Fig D 17 shows the integration of cross-well strain data on the B5PH well during the treatment of Stage 21 on BX4H with MS events distribution and pressure depletion profiles (at 1-, 2-, and 3-months of production) from 8 gauges on the B5PH well. The three panels share the same vertical depth axis. The stronger, mechanically induced strain signals in deeper formations are better correlated with MS events distribution (blue curve in the middle panel) for BX4H and the fracture height implication from pressure gauge data. A couple of points to note on the gauge data: 1) The height inference is based on

production depletion and not stimulation, and 2) There are no gauges shallower than the 3rd Bone Spring, limiting the height inference to those benches.

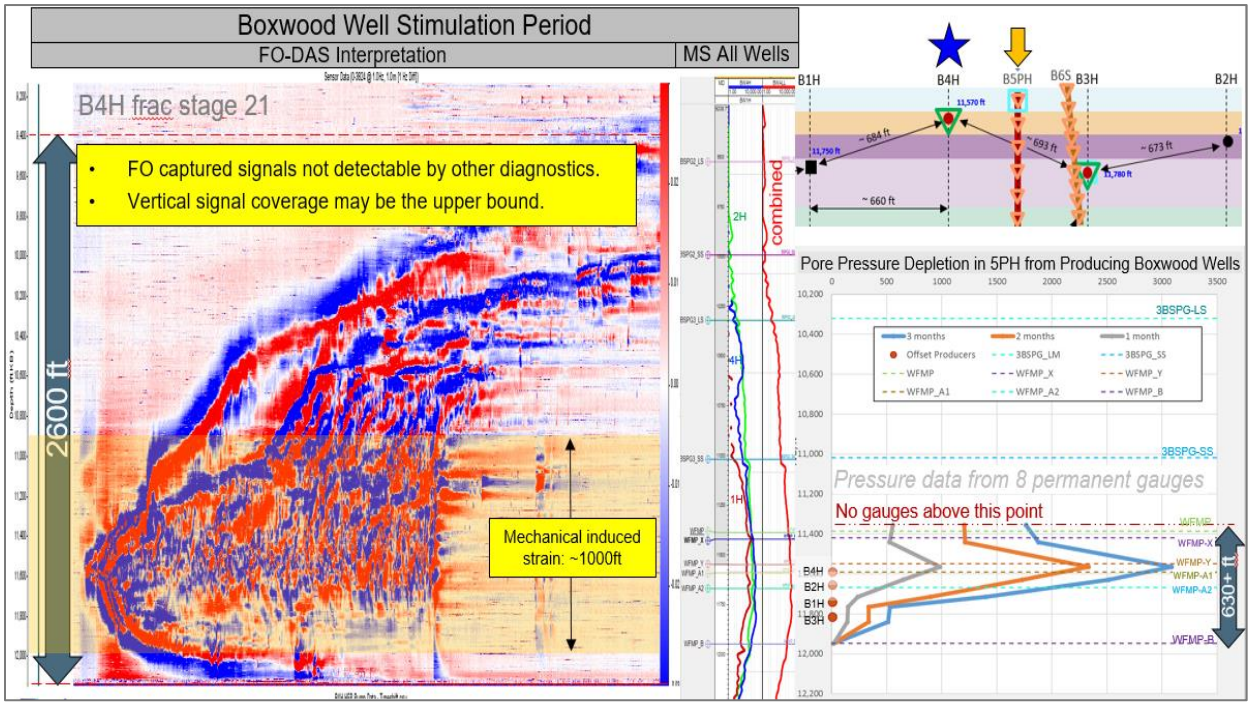

Fig D 17—Integration of the FO vertical coverage data with microseismic and pressure gauge data

During Production:

A large pressure drawdown was observed all the way from the shallowest gauge in 3rd Bone Spring to the deeper gauges in Wolfcamp-A2 (Fig D 11). Since there were no gauges installed on B5PH and B6S above the bottom of the 3rd Bone Spring formation, it was difficult to obtain pressure depletion information for shallower benches through conventional diagnostics. The FO along the wellbore of B5PH provides an alternative method to measure strain change as the proxy of vertical production depletion profile for all the wells. Fig D 18 shows the strain change profiles acquired on the B5PH during the FO sensing test in Sept. 2020, when all the Boxwood wells were in a steady flow status before BX3H and BX4H were shut in. The strain measurement baseline in this test is very close to time stamp #1, as shown in Fig D 18a, and therefore there is almost no strain change in all benches at time stamp #1 (Fig D 18b). For time stamp #2 at the end of a steady flow period when there was about 45 psi BHP drawdown on BX4H, Fig D 18c clearly shows strain depletion from the top of 3rd Bone Spring Sand to the middle of Wolfcamp-A2, whereas no strain depletion is evident in 3rd Bone Spring Lime and Wolfcamp-B. Since DSS is very sensitive to small rock deformation induced by pore pressure depletion, the strain change

results during the steady flow period may provide a proxy of vertical production depletion profile from 3rd Bone Spring Sand to middle of Wolfcamp-A2 for all wells.

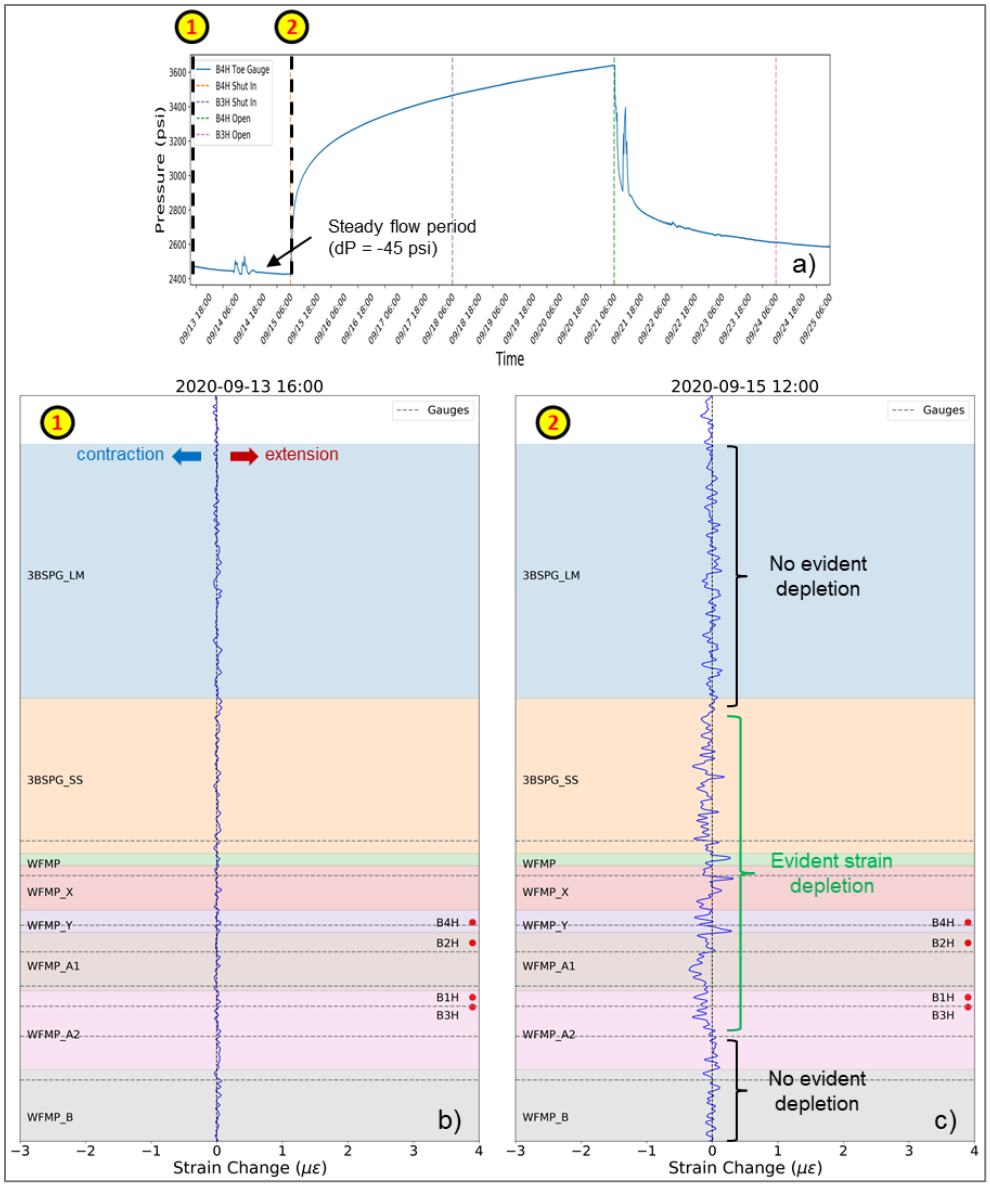

Fig D 18—Strain change profiles during the steady flow period in the Sept. 2020 test. a) BX4H BHP change. b) Strain change profile at time stamp #1. c) Strain change profile at time stamp #2. Vertical dashed line at 0 indicates no strain change, and horizontal dash lines i and horizontal dash lines indicate locations of 8 P/T gauges on the B5PH. Red dots represent landing depth of four child wells.

Parent-Child Effects

The child well image logs serve as a good indicator for parent well HF tracking. The post-stimulation MS events have an eastward bias, in line with pre-stimulation image logs for stages that overlap parent wells (Fig D 4, Fig D 6). Fig D 19 shows that during the child well stimulation (BX2H), tubing head pressures from the parent wells BR1H (blue curve) and BR2H (green curve)

show strong frac hits. Even for the second offset child well (BX3H), which is 1,000–1,300 ft away from the parent wells, stimulation showed weak frac hits at the parent wells. In addition to the above diagnostics, calibrated subsurface models also showed a difference in geometries for stages affected by the depletion of parent wells.

The main implication of depletion (seen vertically) will be on co-development of multiple benches in a single section. Frac hits during stimulation of child wells show a pressure response, but a much stronger indication of effective drainage across all the formations of interest is the depletion seen during production. This depletion has strong implications on how these multiple formations can be co-developed.

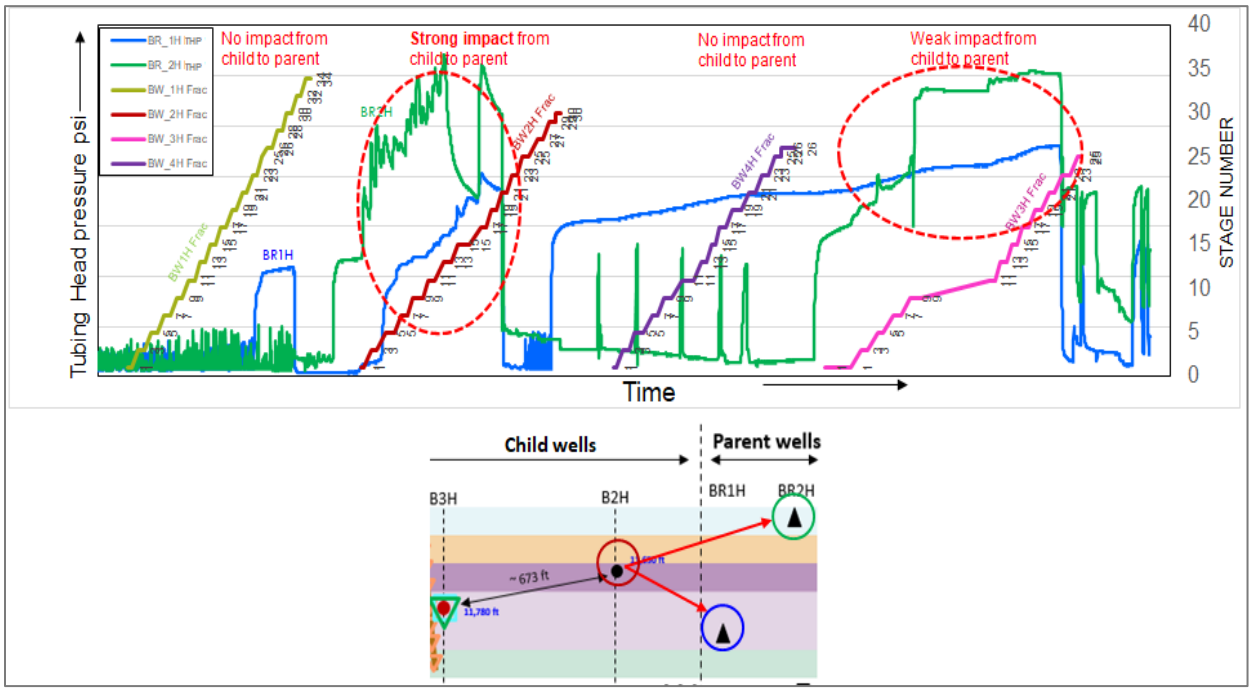

Fig D 19—Top: Impact of child well stimulation (BX1H-BX4H) on the THP in parent wells (BR1H and BR2H); Bottom: Schematic showing the placement of the wells.

Conclusions

The comprehensive dataset acquired in HFTS-2 presents a unique opportunity to compare independent techniques to arrive at HF metrics (i.e., stimulation height and half-length) and quantify parent-child effects.

Areal Coverage: Conventional MS (and FO MS) were used to compute fracture half lengths, which were compared with diagnostics (FO strain, gauge, image logs), observations, and calibrated subsurface models. A post-production interference test did not show offset well communication, indicating that the pressure signals at the gauges were weaker than the signals during the stimulation event.

Vertical Coverage: Vertical coverage during stimulation was monitored using a vertical monitoring well. The stronger mechanical strain signals showed good correlation with MS event

intensities, geomechanical properties, and gauge inferences. Vertical depletion was estimated based on vertical/slant well gauges, and strain depletion tests showed that the fiber-based height estimation was an upper bound on fracture height.

Parent-child effects: Diagnostics and calibrated subsurface models show asymmetry in child well fracture geometries for stages that overlap parent wells. Child well image logs serve as a good indicator for parent well HF tracking. Child well MS events had an eastward bias, in line with pre-stimulation image logs and confirmed by parent well frac hits.

References

Bessa, F., Jerath, K., Ginn, C., et al. 2021. Subsurface Characterization of Hydraulic Fracture Test Site-2 (HFTS-2) Delaware Basin. Paper presented at the SPE/AAPG/SEG Unconventional Resources Technology Conference, Houston, Texas.

Howell, B. 2021. Microseismic at HFTS-2: A story of three stimulated wells. Paper presented at the SPE/AAPG/SEG Unconventional Resources Technology Conference, Houston, Texas, USA.

Jin, G., & Roy, B., 2017. Hydraulic-fracture geometry characterization using low-frequency DAS signal. *The Leading Edge*, **36**(12): 975-980.

Jin, G., Friehauf, K., Roy, B., et al. 2019. Fiber Optic Sensing-Based Production Logging Methods for Low-Rate Oil Producers. Paper presented at the SPE/AAPG/SEG Unconventional Resources Technology Conference, Denver, Colorado. https://doi.org/10.15530/urtec-2019-943.

Jin, G., Ugueto, G., Wojtaszek, M., et al. 2021. Novel Near-Wellbore Fracture Diagnosis for Unconventional Wells Using High-Resolution Distributed Strain Sensing during Production. *SPE J*. https://doi.org/10.2118/205394-PA.

Maity, D. 2021. A Systematic Interpretation of Subsurface Proppant Concentration from Drilling Mud Returns: Case Study from Hydraulic Fracturing Test Site (HFTS-2) in Delaware Basin. Paper presented at the SPE/AAPG/SEG Unconventional Resources Technology Conference, Houston, Texas.

Molenaar, M. M., & Cox, B. E. 2013. Field Cases of Hydraulic Fracture Stimulation Diagnostics Using Fiber Optic Distributed Acoustic Sensing (DAS) Measurements and Analyses. Paper presented at the SPE Unconventional Gas Conference and Exhibition, Muscat, Oman. https://doi.org/10.2118/164030-MS.

Ugueto, G. A., Todea, F., Daredia, T., et al. 2019. Can You Feel the Strain? DAS Strain Fronts for Fracture Geometry in the BC Montney, Groundbirch. Paper presented at the SPE Annual Technical Conference and Exhibition, Calgary, Alberta, Canada. https://doi.org/10.2118/195943-MS.

Zakhour, N., Jones, M., Zhao, Y., et al. 2021. HFTS-2 Completions Design and State-of-the-Art Diagnostics Results. Paper presented at the SPE/AAPG/SEG Unconventional Resources Technology Conference, Houston, Texas.

Appendix E: Analysis of Completion Design Impact on Cluster Efficiency and Pressure-Based Well Communication in HFTS-2 Delaware Basin

Authors: ***Andrea Vissotski, Amit Singh, Peggy Rijken, Richard Reverol***

Summary

The Hydraulic Fracturing Test Site 2 (HFTS-2) is a joint industry project in the Delaware basin to advance hydraulic fracturing understanding and improve productivity in shale reservoirs. The project integrates multi-disciplinary approaches to evaluate different completion designs, well spacing, inter-well communication, and stimulated rock volume, among other factors. This paper focused on two major areas related to hydraulic fracture performance. First, an analysis of different completion designs on cluster efficiency based on near well Distributed Acoustic Sensing (DAS). Second, an evaluation of well and completion designs on inter-well fracture driven interactions (FDIs) based on downhole pressure monitoring.

Fluid/sand distribution and cluster efficiency analyses were based on near wellbore DAS data collected from two adjacent horizontal wells completed in two different landing zones in the Wolfcamp formation. These wells had different completion designs aiming to evaluate the effect of normal vs. extended stage lengths, perforation hole tapering and limited entry. Standard deviation from ideal fluid/sand distribution and waterfall plots were used to evaluate cluster efficiency for each design and stage.

Inter-well FDIs analysis was conducted among the horizontal wells and a vertical monitor well. One horizontal well served as the monitor well while the other horizontal well was being treated. The vertical well was instrumented with downhole pressure and temperature gauges to aid monitoring fracture height growth. The pressure response during and after fracturing was characterized based on maximum pressure increase value and slope. Pressure response vs. FDIs trigger factors such distance, cluster efficiency and stage fluid volume were also analyzed.

Based on the different completion and perforation designs tested, DAS analysis suggests that limited entry design worked best. Extreme limited entry showed the potential of high perforation erosion and reduced cluster efficiency. The limited entry and tapered perforation design demonstrated potential to improve the cluster efficiency for extended stage lengths.

Pressure monitoring across formation units proved to be critical to understand fracture interactions and fracture vertical growth. Pressure communication across different formation units during hydraulic fracturing operation indicate fractures grew upwards during Wolfcamp wells fracturing. However, this pressure communication dissipated over time. High intensity FDIs were recorded when the frac stages were closer to the pressure gauge location in the monitor wells. Some of these stages that produced high intensity FDIs also had high fluid volume per cluster and low cluster efficiency.

The multi-disciplinary and high-quality data collected from HFTS-2 helped to further understand why completion approaches such as limited entry and tapered perforation design are successful in improving cluster efficiency. The DAS data combined with downhole high-resolution pressure

measurements also helped to quantify the effect of lower cluster efficiency data on the incidence and intensity of FDIs.

Introduction

Horizontal well drilling and multi-stage hydraulic fracturing are technology enablers to economically produce hydrocarbons from unconventional reservoirs as they can expose more reservoir area needed in ultra-low permeability reservoirs. There are several key components that need to be properly designed and optimized to efficiently produce unconventional reservoirs. These components span the development cycle and include well landing (drilling & reservoir description); hydraulic fracture placement, fracturing fluid and proppant selection, conductivity, fracture driven interactions or FDIs (completion/fracturing design); and stress evolution with depletion (production and development management) (Singh et al., 2020).

Within hydraulic fracture placement, there are important design considerations such as pump rate, clusters per stage, cluster spacing, number of perforation holes, perforation location, diameter, and orientation. The goal is to maximize the exposure from the well to the reservoir by directing fluid and proppant to all clusters so that multiple hydraulic fractures can be created per stage. The term 'cluster efficiency' is often used to quantify the number of clusters being treated compared to the goal of treating all clusters. Previous studies with fiber optic diagnostics used near-well Distributed Acoustic Sensing (DAS) to quantify cluster efficiency. These studies have shown fluid heel-ward biased and only 60% of clusters receiving proppant and fluid (Holley and Kalia, 2015; Ugueto et al., 2016; Somanchi et al., 2017). This situation is likely caused by stress shadowing from previous fracture stage that created stress variability across the new clusters (Rousell and Sharma, 2011), variable perforation hole diameter due to non-centralized perforation guns (Cramer et al.,2019), perforation location (Wehunt et al., 2020), in-situ stress heterogeneity along the lateral wellbore and higher momentum in proppant which causes proppant toe-biased distribution at high pump rate (Liu, X et al., 2021). Current perforation design changes to counteract low cluster efficiency are outlined below (Singh et al., 2020).

- Variable Shot Cluster (VSC) or 'tapered perforation', uses variable friction to overcome stress shadow and heel-ward bias.
- Limited entry perforation uses smaller number of perforation holes to create higher perforation friction to divert fluid to other clusters
- Equal perforation hole diameter created with advanced perforation charges.

An additional step being taken by the industry to reduce completion costs is to increase the stage length and add more clusters along. These stages are often referred to as Extended Stage Length (ESL) and can reach high cluster efficiency when combined with VSC, limited entry and equal perforation hole diameter (Singh et al. 2020).

Another key component of completion/fracturing design is to account for Fracture Driven Interactions (FDIs) or 'frac-hits'. FDIs are the influence of new hydraulic fractures on nearby fractures. FDIs can occur in the same well (intra-well or stress shadowing) and between adjacent wells (inter-well). Current industry focus is on inter-well FDIs as they can affect the productivity of new and existing wells (Miller et al., 2016, King et al., 2017, Whitfiled et al., 2018, Garza et al.

2019, Jacobs, 2019). There are several factors that can contribute to FDIs. Frequent evidence shows that controllable factors such depletion, reduced well spacing and low cluster efficiency can contribute to FDIs (Cao et al.,2017, Hao et al, 2017, Vidma et al. 2018, Wang et al., 2019, Bommer et al., 2020, Dashti and Liang, 2020). Fewer studies also show evidence of controllable contributing factors such larger volume per cluster, fast ramp up in brittle formations and viscous fracturing fluids (King et al., 2008, Gil et al., 2011, Mack et al., 2017). The list of uncontrollable factors that can create FDIs includes natural fractures, regional faults, large horizontal stress anisotropy, weak vertical stress contrast and in-situ stress (Daniels et al., 2007, King et al, 2008, Wang et al., 2019).

FDIs can be directly measured by changes in pressure in a monitor well(s) due to fracturing activity in a nearby well. There are multiple ways to set up a monitoring well for FDIs surveillance: fully completed lateral monitoring, a single isolated and completed stage, wellbore with one or more externally mounted bottom hole gauges and uncompleted/unperforated wellbore also known as Sealed Wellbore Pressure Monitoring (SWPM). Detailed information can be found in Haustveit et al., 2020. Fully completed laterals are arguably the most common surveillance although signals can be dampened due to the large hydraulic fracture surface exposed to the incoming FDIs. In contrast, isolated stage and external gauge monitoring usually produce clearer signals, they can detect incoming FDIs earlier than the other set ups and the pressure magnitude change is larger. It is important to highlight that pressure magnitude changes in the monitoring well are relative to the position of the gauge and the location of the frac stage being treated. SWPM is a rising surveillance technology that can be more sensitive than a full completed lateral and still be cost effective. Other complementary surveillance technologies for FDIs include, microseismic, fiber optics (DAS, DTS and Low Frequency DAS – LF-DAS), chemical tracers and production monitoring.

HFTS-2 provided a unique surveillance program to evaluate hydraulic fracture performance. Near well DAS was used to analyze the impact of different completion on cluster efficiency of two wells, while isolated downhole pressure monitoring was used to analyze FDIs.

Overview on surveillance and completion designs used in HFTS-2

The Hydraulic Fracturing Test Site 2 (HFTS-2) is a joint industry project in the Delaware basin to advance hydraulic fracturing understanding and improve productivity in shale reservoirs. The project targeted several layers of the Wolfcamp formation with eight horizontal wells and one vertical well used for surveillance. Adjacent to the test site, two horizontal wells have been produced for couple of years prior to the fracturing of the test site wells. A gun barrel view schematic of the tests site is shown in Fig E 1.

Wells 1 (through) 4 were spaced horizontally by approximately 660 ft and stimulated sequentially in 2019 (order shown in yellow circles in Fig E 3). The number of stages and the ratio of total amount of sand (100-mesh) and fluid (slickwater) is also shown in Fig E 3 for all wells including Wells 13,14,15 and 16 which were zipper fractured. Well 5 corresponds to the monitoring vertical well instrumented with permanent fiber optic cable and eight permanent pressure and temperature (P/T) gauges across, above and below the target layers. Well 5 LF-DAS and pressure measurements were used to evaluate vertical pressure communication and FDIs

from the nearby wells. This paper focuses on Wells 1, 2, 3 and 4 as they had additional instrumentation and were closer to Well 5 as shown in Fig E 3.

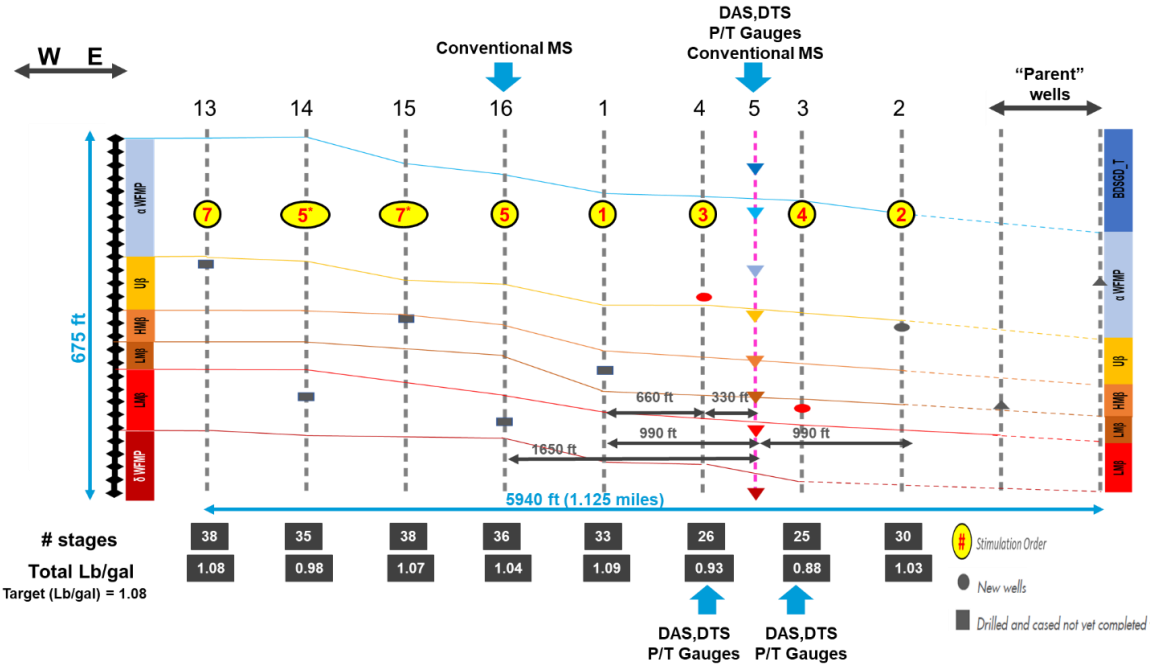

Fig E 1—Gun barrel schematic of test site showing relative position of wells across Wolfcamp formation. Colored triangles denote the depth external downhole P/T gauges in Well 5. Well 3 and 4 had isolated bottom hole P/T gauges in the toe and heel sections as wells as permanent fiber optics.

Well 3 and Well 4 had permanent fiber optics acquiring near well DAS which served for the evaluation of cluster efficiency of different stage designs. Fig E 2 shows the design variations made to the base case. These variations included smaller number of perforations ranging from Aggressive Limited Entry (ALE), Aggressive Limited Entry with Tapered perforation (ALE T) to Extreme Limited Entry (ELE). Also, larger number of clusters and extended stage length (ESL) with tapered perforations were applied in the heel stages. Both wells had same casing size, perforation hole diameter and cluster spacing.

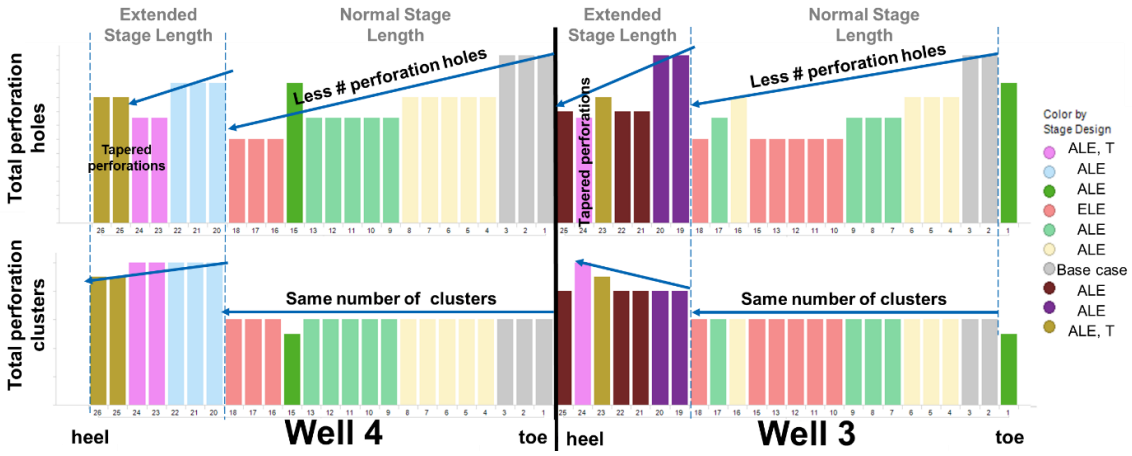

Fig E 2—Stage completion designs schematic for Well 3 and Well 4 showing variation of perforation holes and number of clusters for Aggressive Limited Entry (ALE), Extreme Limited Entry (ELE) and Tapered Perforations (T) used in Extended Stage Length (ESL). ELE used least amount of perforation holes.

After fracturing, Well 4 had its toe and heel downhole P/T gauges isolated. These stages were used to monitor possible FDIs towards Well 4 during fracturing of Well 3 as depicted in Fig E 3. Well 2 is located towards the East and was fractured ahead of Well 4 and 3. The reservoir between these wells has not been depleted, however the two parent wells are located East past Well 2.

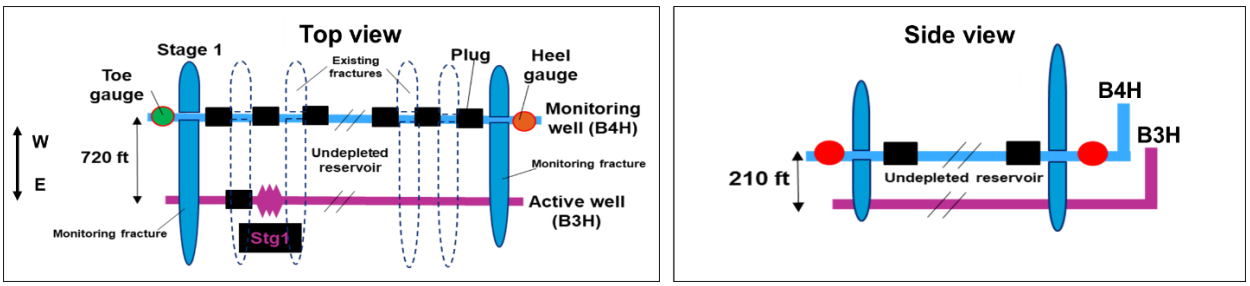

Fig E 3—Location schematic of isolated downhole P/T gauges in Well 4 during fracturing of Well 3. The fractures created in stage 1 of Well 4 were used to monitor FDIs from Well 3. These wells were spaced horizontally by 660 ft and vertically offset by 220 ft. Reservoir is nondepleted between these wells however some level of depletion is expected towards the East.

Data Analysis and Results

Impact of design parameters on cluster efficiency

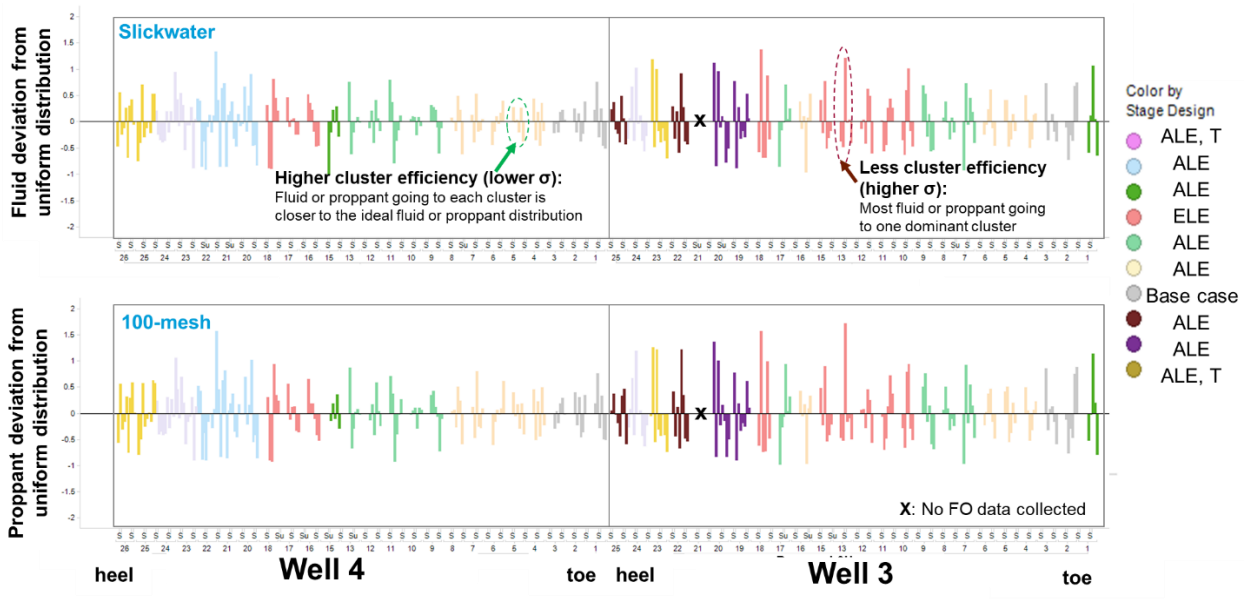

Fig E 4—Slickwater and sand distribution deviation from uniform distribution (σ = 0) calculated from near wellbore DAS on a stage basis for Wells 3 and 4. High σ or low cluster efficiency was more frequent in heel stages and in designs with smaller number of perforations per stage

The amount of slickwater and 100-mesh sand going to each cluster per stage was quantified using near well DAS and their deviation from the uniform distribution were calculated based on standard deviation (σ). Low σ means the fluid or proppant going to each cluster is closer to uniform distribution, therefore the cluster efficiency is high. High σ means the fluid or proppant going to each cluster is going to one or few clusters, therefore the cluster efficiency is low. Slickwater and 100-mesh deviation from the uniform distribution (σ=0) for each stage design (Base Case, ALE, ELE, ALE T) is shown in Fig E 4. In overall, 100-mesh and slickwater had similar deviations which implies that no significant fluid or proppant bias occurred. Fig E 6 deviation plots also shows that higher σ was more frequent in heel stages and in designs with smaller number of perforations per stage. Therefore, potential factors affecting cluster efficiency such limited entry, stage length and tapered perforations were investigated with support of slurry distribution changes overtime during the stage treatment using DAS waterfall plots. Results of the evaluation of cluster efficiency by limited entry designs are shown in Fig E 5. The highest cluster efficiency (σ=0.37) and most repeatably was seen with the ALE design with same number of cluster and 25% fewer number of perforation holes compared to the base design. ELE, with the same number of clusters and 50% less perforation holes, had the lowest cluster efficiency and less repeatability.

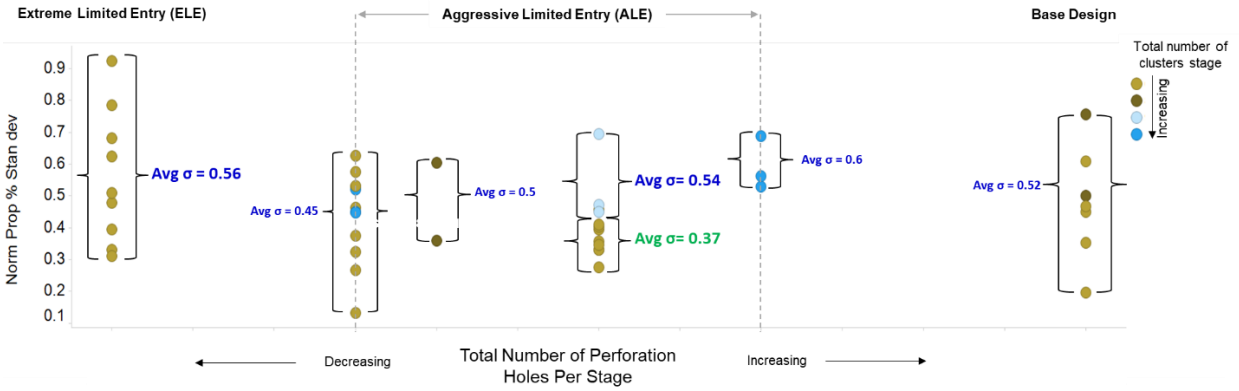

Fig E 5—Evaluation of limited entry on cluster efficiency (σ). Higher cluster efficiency and most repeatably was seen with the ALE designs.

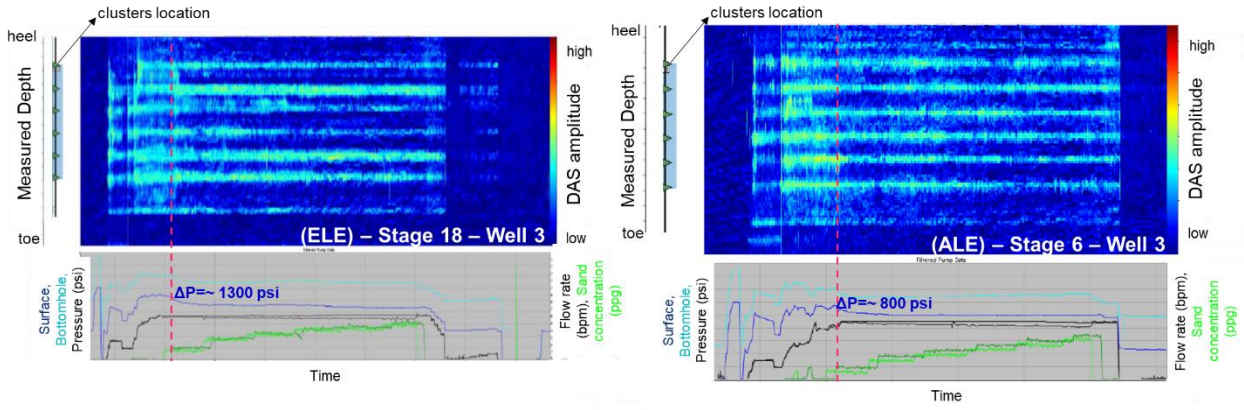

Fig E 6—DAS waterfall plots (top) and treatment plots (bottom) for ELE and ALE completion examples. Warm colors in the DAS waterfall plot denotes slurry entering the perforation clusters. Number of clusters taking slurry decreased over time as fracturing treatment progresses in Well 3, ELE design likely due to perforation erosion. Some leakage to the prior stage was captured with DAS.

Fig E 6 shows DAS waterfall plots examples comparing a stage toe ALE and mid-section stage ELE for Well 3. ELE (right plot) shows middle clusters received less slurry after sand arrived at the perforations, as suggested by the well head pressure (WHP) decrease of approximately 1300 psi. Lower WHP drop occurred in ALE likely linked to less perforation erosion. This aid to continued slurry flow to all clusters which and delivered higher cluster efficiency than in ELE as shown in Fig E 6.

Results of the evaluation of cluster efficiency by stage length and tapered perforations are presented in Fig E 7. For same number of perforation holes per stage, higher cluster efficiency was obtained with base case or Normal Stage Length (NSL) compared to ESL. Tapered perforations aid to improve cluster efficiency in ESL compared to ESL without tapered perforations.

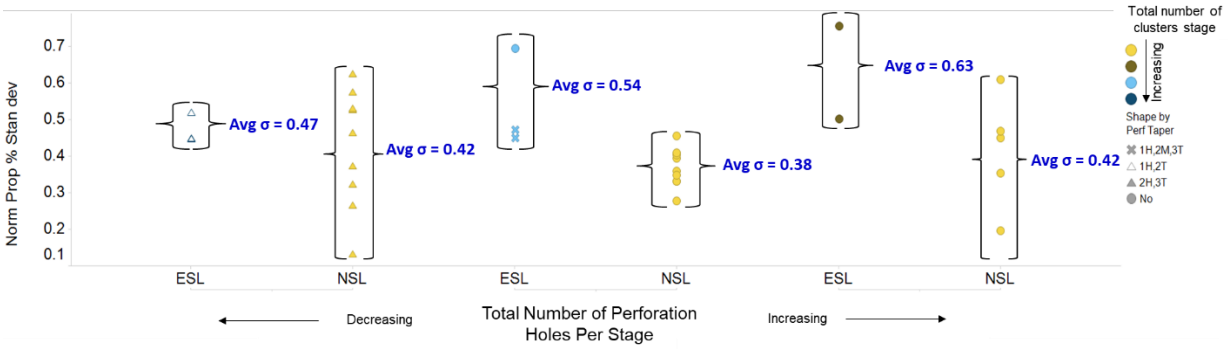

Fig E 7—Evaluation of stage length and tapered perforations on cluster efficiency standard deviation (σ). Completion designs in Normal Stage Length (NSL) helped to deliver higher cluster efficiency compared to those used in Extended Stage Length (ESL). However, tapered perforations aid to improve cluster efficiency in ESL.

Impact of well location and completion design on Fracture Driven Interactions (FDIs)

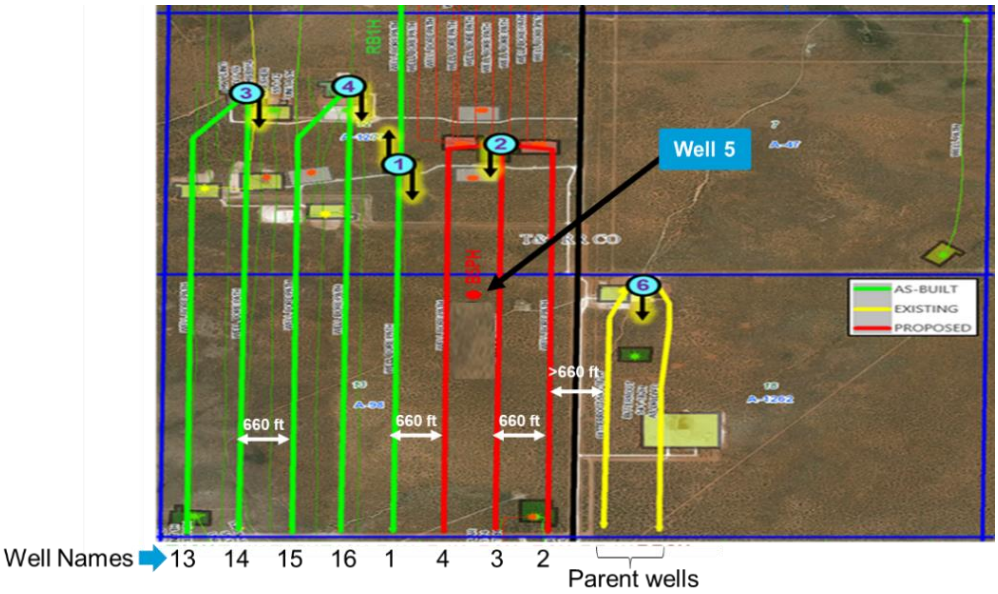

Fig E 8—Wells layout – top view showing Well 5 location in test site and relative position to horizontal wells

Vertical Well 5 has seven P/T gauges installed across the target formation Wolfcamp and one P/T gauge installed in the formation above (Third Bone Springs) covering approximately 625 ft TVD as shown in Fig E 1. Well 5 is also located close to the mid sections of Wells 1 thru 4 which allowed to cover a larger area of analysis (Fig E 8). In addition to pressure measurements, LF-DAS plots were used to complement the FDIs analysis towards Well 5 from adjacent wells.

Well 4 was used to monitor Well 3 during fracturing with isolated external P/T gauges. Previously created fractures in Stage 1 of Well 4 transmitted the pressure influence coming from Well 3 from stage 1 thru 9 to the toe gauge. Later stages measurements were not used for analysis as signal deteriorated or became noisy. Similarly, the heel gauge captured clearer signal

from Well 3 starting in stage 17 thru the last stage 25. Stages analyzed for FDIs from Well 3 to Well 4 are circled in Fig E 9.

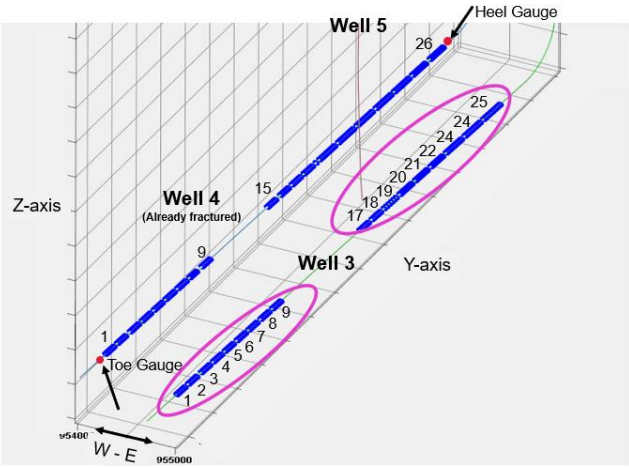

Fig E 9—Wells layout – 3D view of Well 4 and Well 3. Blue cylinders indicate the frac stages locations; red circles indicate the P/T gauges in Well 4. Circled stages created clear pressure signal in Well 4.

FDIs and fracture height based on monitoring vertical Well 5 – downhole external P/T gauges

Four distinctive pressure zones were measured by the gauges prior to the fracture jobs in the test site as shown in Fig E 10. The upper gauge in the Third Bone Spring formation (BDSG) recorded the lowest pressure, followed by the α and β/δ Wolfcamp formations. The pressure zones re-arranged after the first frac job (Well 1 - β Wolfcamp). As Well 1 and other wells fracture jobs progressed, larger pressure changes occurred in the upper gauges presumably in the zones with lower reservoir pressure (BDSG and α-Wolfcamp). This suggests fractures grew up towards these zones, however, the pressure communication dissipated over time. Vertical pressure monitoring across the formation of interest and neighboring formation was key to understand fracture height growth. Detailed analysis per well is presented next. Further analysis is recommended to estimate the drainage reservoir volume (DRV) and contributing fracture height to production. This exercise can be valuable to adjust, if needed, the fluid/proppant intensity per cluster and landing zones depths for continued improvement of hydraulic fracture designs.

Well 1 is located 990 ft away from Well 5 in the horizontal direction (x-direction). Increasing pressure variation occurs as Well 1 frac stages were approaching Well 5 in the y-direction; less fluctuation occurs as the stages were pumped further away as shown in detailed for Well 1 in Fig E 11. For those stages where positive disturbance is detected (stages 20 thru 33), it is observed

that pressure declines after each stage is completed. Pressure continues declining in all pressure gauges at different rate after the frac job for Well 1 is finished as shown in Fig E 11.

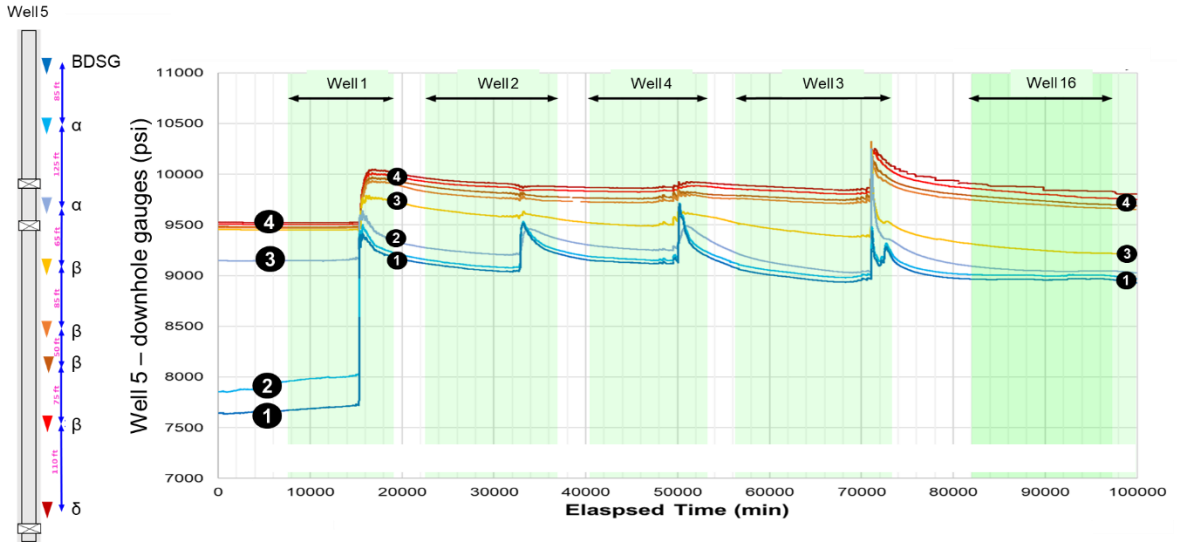

Fig E 10—Well 5 pressure measurements at different depths during fracturing jobs in test site. For wells further away from Well 5 (16,15,14 and 13) detailed pressure changes were not capture by gauges.

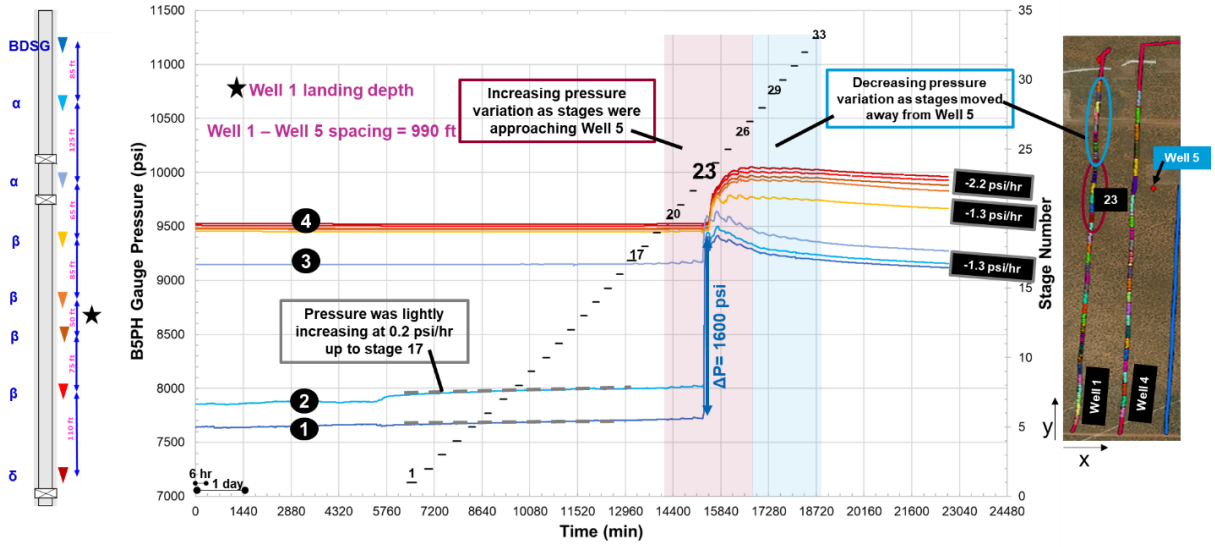

Fig E 11—Well 5 pressure measurements at different depths during the fracturing job of Well 1 communication from β-Wolfcamp to α-Wolfcamp and Third Bone Spring.

The highest-pressure changes (up to 1600 psi in BDSG) occurred during fracturing of stage 23 which is not the closest stage based on horizontal distance to Well 5. However, accounting for fracture azimuth and crosschecking with LF-DAS, stage 23 fractures likely reached the closest Well 5 as shown by increasing LF-DAS signal in that specific stage (Fig E 12). At this time, it is not possible to conclude that LF-DAS measured above the Well 5 gauges are an indication vertical

communication or fracture height. Further pilots with P/T gauges along shallower depths is encouraged to establish if pressure communication occurs during fracturing.

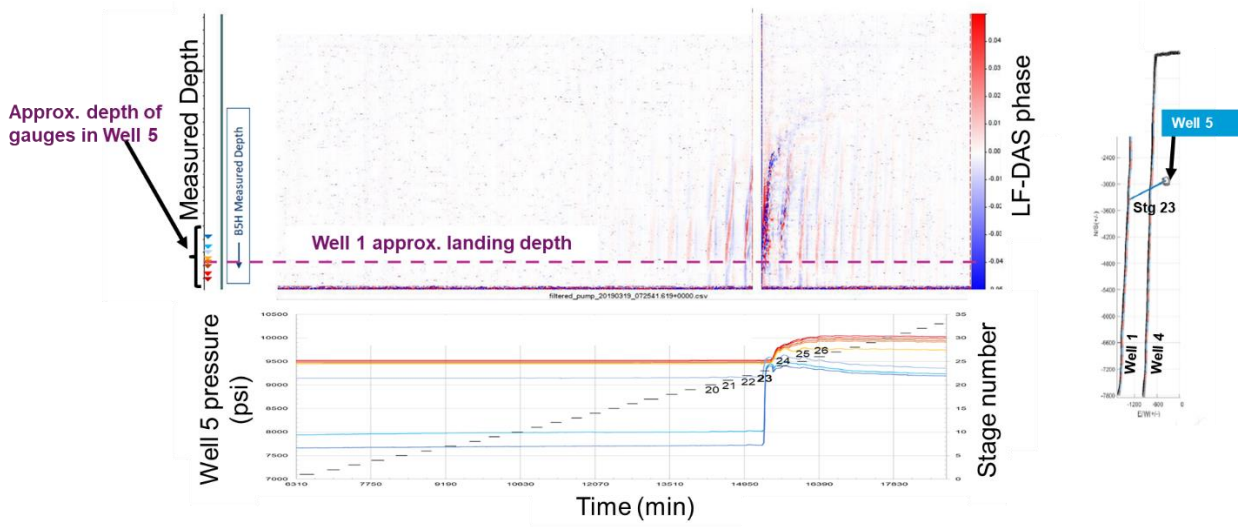

Fig E 12—Integration of Well 5 LF-DAS measurements (top plot) and pressure (bottom) during fracturing of Well 1. The LF-DAS plot shows the strain rate measured by the fiber optic cable sensing along vertical Well 5. Strain response (red and blue colors) in vertical wells provides information on the vertical growth of hydraulic fractures (Zhang et al, 2021). Pressure change measured by gauges shared similar trend with the LF- DAS strain rate.

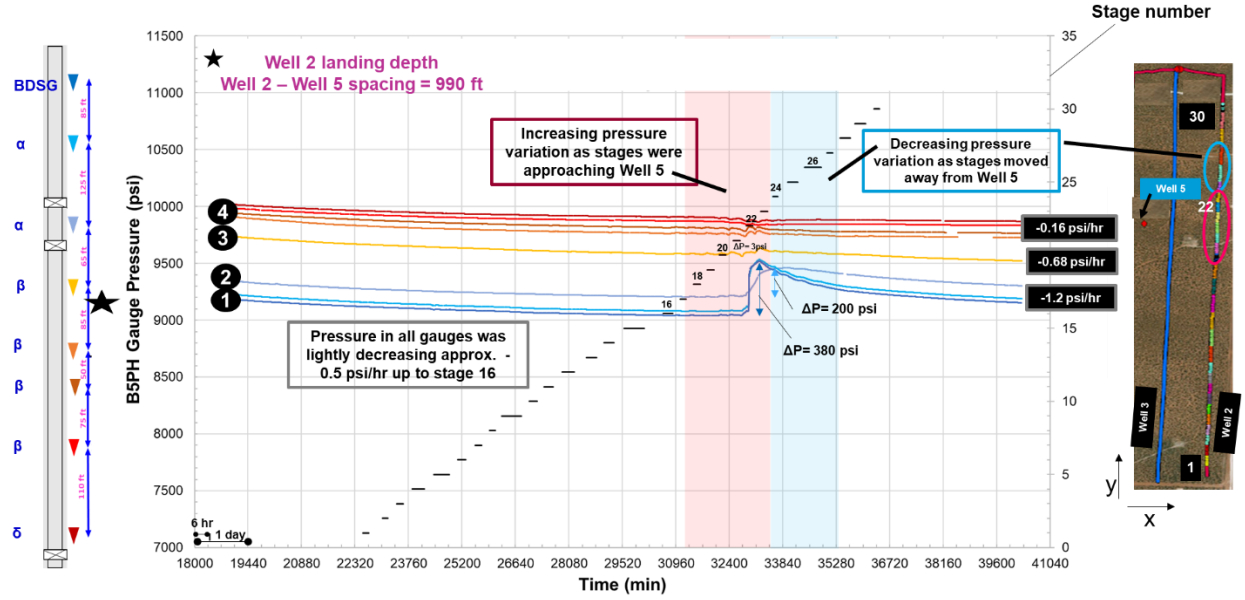

Fig E 13—Comparison Well 5 pressure response during Well 2. Well 2 (second shallowest) lands at similar depth of zone 2, however, zone 3 & 4 gauges registered higher pressure change. Communication from β-Wolfcamp to α-Wolfcamp and Third Bone Spring.

Similarly, to Well 1, pressure communication with Well 5 was analyzed for Well 2, 3 and 4 as shown in Fig E 13, Fig E 14 and Fig E 15 respectively. In general, pressure variation in Well 5 was

mainly function of proximity of the fracture stage to B5PH (y-direction). With exception of Well 2, the magnitude of the variation is also related to horizontal wells landing as those gauges in similar or above the landing depth registered the highest pressure increases during fracturing.

Well 2 was second in frac order, 990 ft away from Well 5 (x-direction) and landed right below the 'yellow gauge' (zone 3) in Fig E 13. Interestingly, Well 2 did not induce significant pressure change in this gauge, rather 200 to 380 psi pressure increase was registered from stage 22 in the upper gauges (blue gauges – zone 3 and 4). This may be due to overpressure at the top of the fracture as explained in Fisher and Warpinkski (2012). This phenomenon may take place in very tall fractures where smaller fracture width occurs at the origin of the fracture and larger fracture widths at the top. Further modeling studies of fracture geometry and volumetrics are recommended to corroborate this behavior.

Well 4 was the third in frac order, 660 ft away from Well 5 (x-direction) and landed right above the depth of the 'yellow gauge'. As fracture stages got closer to Well 5 in the y-direction, the pressure in the 'blue gauges' in zone 4 increased, maximum pressure change was around 500 psi during stage 22. Pressure response in Well 5 due to Well 2 is shown in Fig E 14.

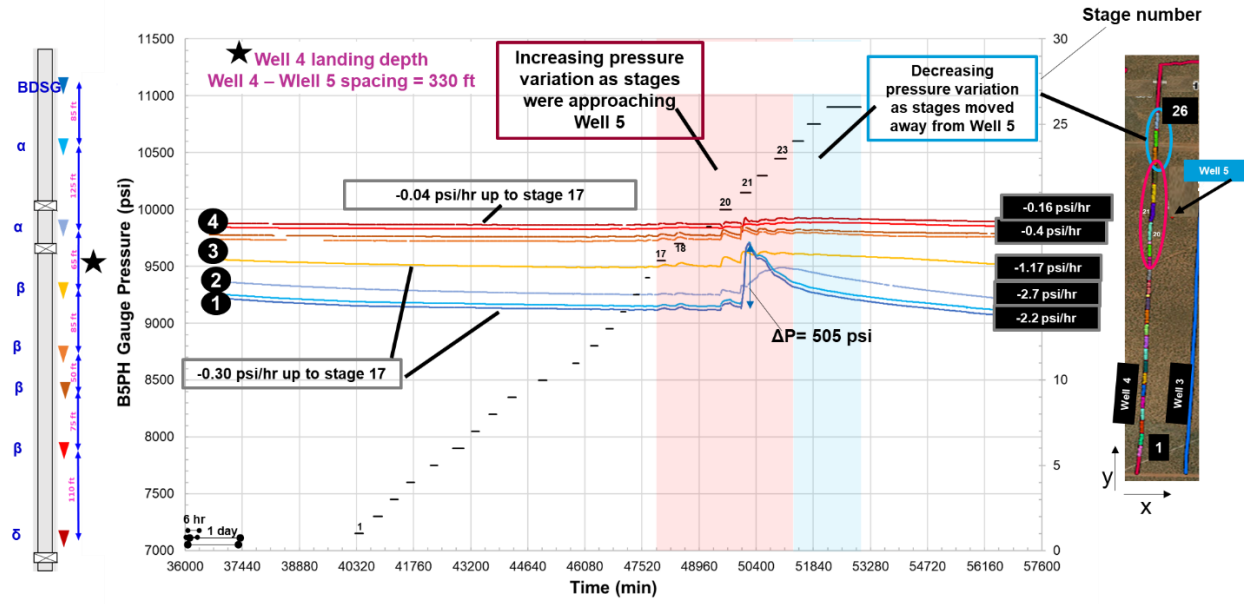

Fig E 14—Comparison Well 5 pressure response during Well 4. Well 4 (shallowest well) was landed above the 'yellow gauge' depth. The gauges in zone 1 & 2 measured higher pressure increase (~505 psi) than in Well 2 (deeper well).

The deepest well, Well 3, was fractured last and spaced 660 ft away from Well 5 (x-direction). Landed between the 'orange' and 'red' gauges, Well 3 created high pressure increase all pressure zones, particularly high in zones 2 and 3 which are closer to Well 3 landing zone. Less notable pressure increase was measured in zone 1 likely due to larger vertical separation. Interestingly, a second spike in pressure was measured past the closest stage (stage 21) to Well 5. As shown in Fig E 15, Well 5 pressure decline was arrested starting at stage 24 Hydraulic

connection of later stages to earlier ones may explain this situation, however its origin remains unclear due to absence of LF- DAS response (Fig E 16).

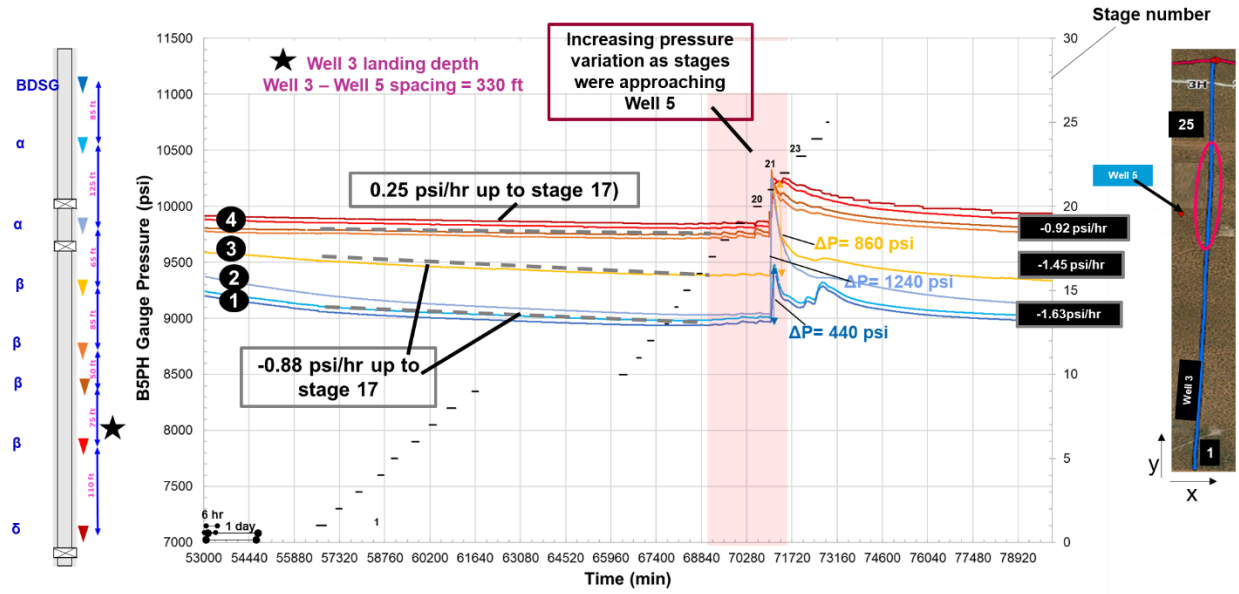

Fig E 15—Comparison Well 5 pressure response during Well 3 fracturing. Well 3 was the deepest well of the test site and landed above 'red gauge' (zone 4)

Fig E 16 shows LF-DAS plots and downhole pressure for Well 2,4 and 3. LF-DAS strain reacted comparably to pressure in Well 5, with increasing intensity as frac stages approached the monitor well in the y-direction. More detailed LF-DAS analysis of HFTS-2 wells is presented in Zhang et al., 2021.

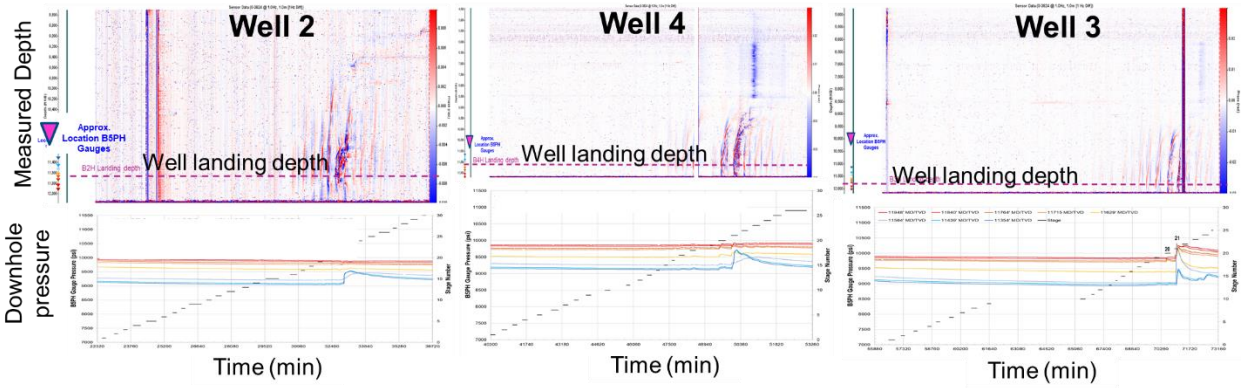

Fig E 16—Integration of Well 5 pressure and DAS strain measurements during fracturing of Well 2,4 and 3. Strain response (red and blue colors) in vertical wells provides information on the vertical growth of hydraulic fractures (Zhang et al, 2021). Similar to Well 1, the pressure change measured by gauges shared similar trend with the LF- DAS strain rate.

As it occurred with Well 1, LF-DAS signal recorded disturbance couple of thousand feet above the horizontal wells landing zones. P/T gauges measurements were limited to 700 feet above

the landing zones. Additional pressure monitoring is required to establish if actual pressure communication occurred at the shallow depths LF-DAS suggests.

FDIs based on isolated downhole P/T gauges in horizontal Well 4

As mentioned before, Well 4 was instrumented with downhole P/T gauges in the toe and heel sections of the well. After fracturing, these gauges were isolated so that the first and last stage of Well 4 can be used to monitor FDIs during Well 3 fracturing. Fig E 17 shows the pressure readings of Well 3 from toe and heel gauges (dark and light green respectively) while it is being fractured. The plot in the left shows Well 4 toe gauge (dark pink) while the heel gauge readings are shown in the right (light pink). Enclosed by the dashed boxes are those stages with consistent readings and therefore used in the analysis.

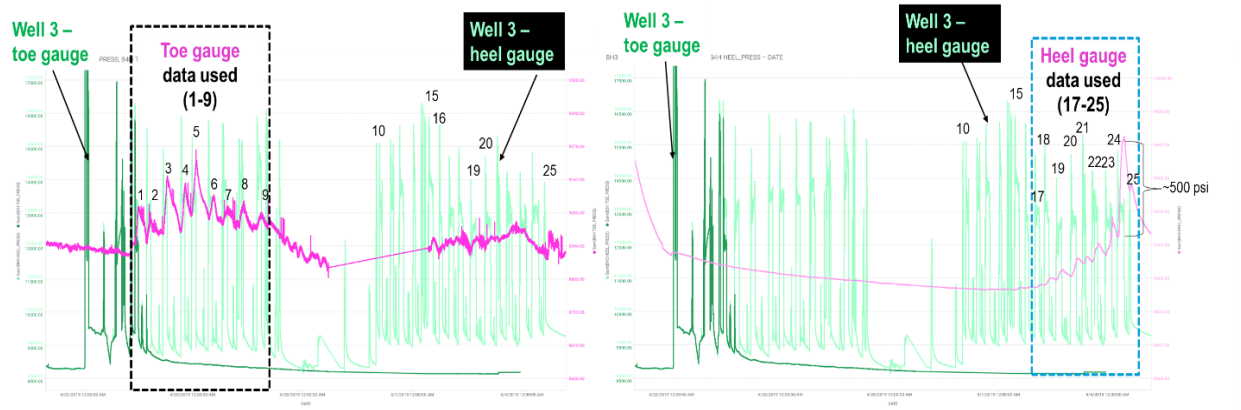

Fig E 17—Well 4 toe and heel pressure response (pink) to Well 3 fracturing (green). Enclosed by the dashed boxes are those stages with consistent readings and therefore used in the analysis.

Fig E 18—ΔP_{max} as function of distance between stages and gauge location (y-direction). With exception of Well 3 first toe stages, ΔP_{max} increases as the frac stage gets closer to the gauge location

The pressure change (ΔP_{max}) on Well 4 due to Well 3 frac stages was calculated and plotted along the distance between the stage and the Well 4's gauge location (Δ_y) as shown in Fig E 18. In general, ΔP_{max} increases as the frac stage gets closer to the gauge location. It appears though that the first toe Well 3 stages created smaller ΔP_{max} when compared to those Well 3 heel stages at the same Δ_y. Possible explanations such influence of parent wells depletion and cluster efficiency will be presented next.

Microseismic events showed Well 3-toe stages biased toward the East where the parent wells are located. In contrast, the mid and heel stages further away from the parent wells appear more contained as shown in Fig E 19. After years on production, parent wells can create a pressure sink that reduces the stress around the drained area. This depleted area can attract the fractures from the test site. This may explain why Well 4 located at the West of Well 3 did not see very large ΔP_{max} from the toe stages. More detailed microseismic analysis of Well 3 and other wells is presented in Tan, 2021.

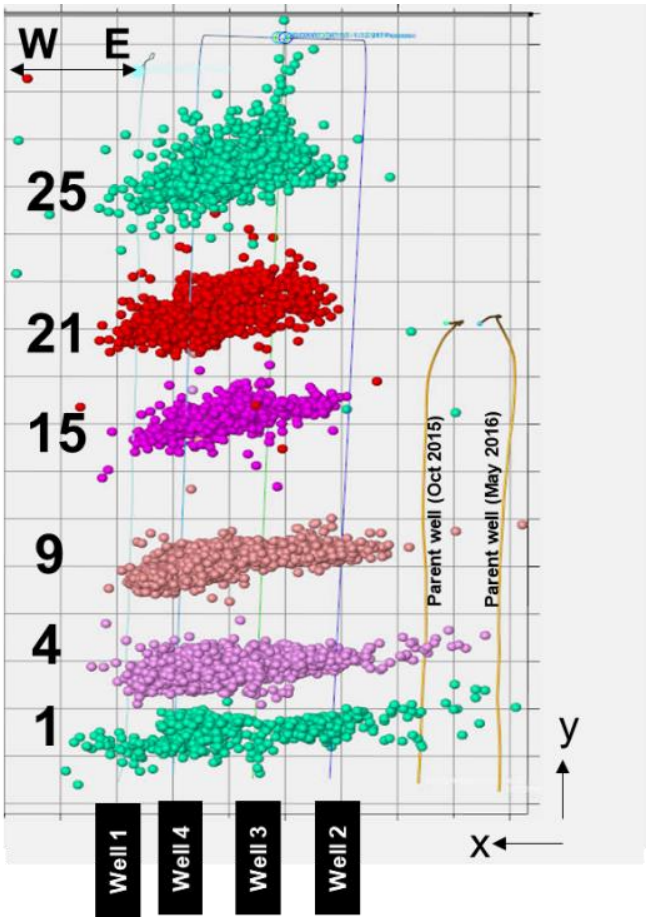

Fig E 19—Microseismic events showed Well 3-toe stages biased towards parent wells likely due to depletion.

Cluster efficiency is an additional factor that could had influenced ΔP_{max} in Well 4. For comparable stages (similar Δ_y), higher cluster efficiency - green circles - created lower ΔP_{max}. In Fig E 20, see highlighted stages of stages 4 & 5 vs. stage 24 or toe stage 6 vs stage 23. Both

parent wells depletion and cluster efficiency may had played a role in FDIs between Well 3 and 4.

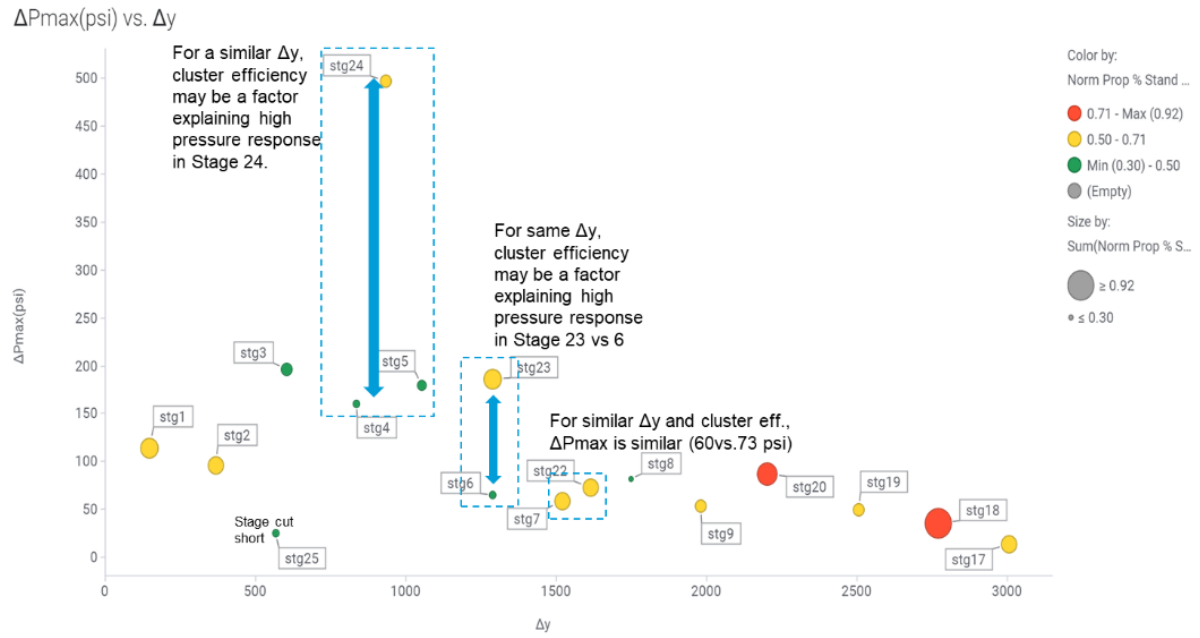

Fig E 20—ΔP_{max} vs. Δ_y and cluster efficiency. For very similar distance to the pressure gauges, data shows evidence for some stages that low cluster efficiency (yellow dots) created ΔP_{max} when compared to stages with high cluster efficiency.

Conclusions

Based on the different completion and perforation designs tested, DAS analysis suggests that limited entry design worked best. Extreme limited entry showed the potential of high perforation erosion and reduced cluster efficiency. The limited entry and tapered perforation design demonstrated ability to improve the cluster efficiency for extended stage lengths.

Pressure monitoring across formation units proved to be critical to understand fracture driven interactions and fracture vertical growth. Pressure communication across different formation units during hydraulic fracturing operation indicate fractures grew upwards during Wolfcamp wells fracturing. However, this pressure communication dissipated over time. Further analysis is recommended to estimate the drainage reservoir volume (DRV) and contributing fracture height to production. This exercise can be valuable to adjust, if needed, the fluid/proppant intensity per cluster and landing zones depths for continued improvement of hydraulic fracture designs.

High magnitude FDIs were recorded when the frac stages were closer to the pressure gauge location in the monitor Well 4, typical behavior of isolated monitor stages. Interestingly, the monitor stage (s) was able to capture FDIs further away from its location which suggests wider interconnection of fractures likely from Well 3 FDIs and fracture networks created by wells completed previously in the test site. Some of the stages that produced high magnitude FDIs

also low cluster efficiency but other factors such depletion from parent wells may have played a role.

The multi-disciplinary and high-quality data collected from HFTS-2 helped to further understand why completion practices such as limited entry and tapered perforation design are successful in improving cluster efficiency. The near wellbore DAS data combined with downhole high-resolution pressure measurements also helped to quantify the effect of lower cluster efficiency data on the incidence and intensity of FDIs.

References

Cao, R., Li, R., Girardi, A. et al. 2017. Well Interference and Optimum Well Spacing for Wolfcamp Development at Permian Basin. Paper presented at the SPE/AAPG/SEG Unconventional Resources Technology Conference, Austin, Texas. https://doi.org/10.15530/URTEC-2017-2691962

Cramer, D., Friehauf, K., Roberts, G. et. Al. 2019. Integrating DAS, Treatment Pressure Analysis and Video-Based Perforation Imaging to Evaluate Limited Entry Treatment Effectiveness. Paper presented at the SPE Hydraulic Fracturing Technology Conference and Exhibition, The Woodlands, Texas. https://doi.org/10.2118/179124-MS

Daniels, J. L., Waters, G. A., Le Calvez, J. H., et al. 2007. Contacting More of the Barnett Shale Through an Integration of Real-Time Microseismic Monitoring, Petrophysics and Hydraulic Fracturing Design. Paper presented at the SPE Annual Technical Conference and Exhibition, Anaheim, California. https://doi.org/10.2118/110562-MS

Dashti, G. and Liang, B. 2020. Depletion Effect Quantification and Mitigation of the Offset Wells. Paper presented at the SPE Annual Technical Conference and Exhibition, Virtual. https://doi.org/10.2118/201703-MS

Fisher, K. and Warpinski, N. 2012. Hydraulic-Fracture-Height Growth: Real Data. *SPE Production & Operations*, **27**: 8–19. https://doi.org/10.2118/145949-PA

Garza, M., Baumbach, J., Prosser, J. et al. 2019. An Eagle Ford Case Study: Improving an Infill Well Completion Through Refracturing of Offset Parent Wells. Paper presented at the SPE Hydraulic Fracturing Technology Conference and Exhibition, The Woodlands, Texas. https://doi.org/10.2118/194374-MS

Gil, I., Nagel, N., Sanchez-Nagel, M. et al. 2011. The Effect of Operational Parameters on Hydraulic Fracture Propagation in Naturally Fracture Reservoirs – Getting Control of the Fracture Optimization Process. Paper presented at the 45th US Rock Mechanics/ Geomechanics Symposium, San Francisco, California.

Hao, S., Zhou, D., Chawathe, A. et al. 2017. Understanding the frac-hits impact on a Midland basin tight-oil well production. Paper presented at the SPE/AAPG/SEG Unconventional Resources Technology Conference, Austin, Texas. https://doi.org/10.15530/URTEC-2017-2662893

Haustveit, K., Elliot, B., Haffener, J. et al. 2020. Monitoring the Pulse of a Well through Sealed Wellbore Pressure Monitoring, a Breakthrough Diagnostic with a Multi-Basin Case History. Paper presented at the SPE Hydraulic Fracturing Technology Conference and Exhibition, The Woodlands, Texas. https://doi.org/10.2118/199731-MS

Holley, E. H. and Kalia, N. 2015. Fiber-optic Monitoring: Stimulation Results from Unconventional Reservoirs. Paper presented at the SPE/AAPG/SEG Unconventional Resources Technology Conference, San Antonio, Texas. https://doi.org/10.15530/URTEC-2015-2151906

Jacobs, T. Oil Gas Producers Find Frac Hits in Shale Wells a Major Challenge. 2019. *Journal of Petroleum Technology*, **69**(04): 29–34. https://doi.org/10.2118/0417-0029-JPT

King, G. E., Haile, L., Shuss, J. A. et al. 2008. Increasing Fracture Path Complexity and Controlling Downward Fracture Growth in the Barnett Shale. Paper presented at the SPE Shale Gas Production Conference, Fort Worth, Texas. https://doi.org/10.2118/119896-MS

King, G. E., Rainbolt, M. F., Swanson, C. 2017. Frac Hit Induced Production Losses: Evaluating Root Causes, Damage Location, Possible Prevention Methods and Success of Remedial Treatments. Paper presented at the SPE Annual Technical Conference and Exhibition, San Antonio, Texas. https://doi.org/10.2118/187192-MS

Liu, X., Wang, J., Singh, A. et al. 2021. Achieving Perfect Fluid and Proppant Placement in Multi-Stage Fractured Horizontal Wells: A CFD Modeling Approach. Paper presented at the SPE

Hydraulic Fracturing Technology Conference and Exhibition, The Woodlands, Texas. https://doi.org/10.2118/204182-MS

Mack, M. G., Taylor, S. M., Rich, J. et al. 2017. Can Moment Tensor Inversion Aid Engineering Decisions? A Delaware Basing Case Study. Paper presented at the SPE/AAPG/SEG Unconventional Resources Technology Conference, Austin, Texas. https://doi.org/10.15530/URTEC-2017-2693686

Miller, G., Lindsay, G., Baihly, J. et al. 2016. Parent Wells Refracturing: Economic Safety Nets in an Uneconomic Market. Paper presented at the SPE Low Perm Symposium, Denver, Colorado. https://doi.org/10.2118/180200-MS

Roussel, N. P., and Sharma, M. M. 2011.Optimizing Fracture Spacing and Sequencing in Horizontal-Well Fracturing. *SPE Production & Operations*, **26**(02): 173–184. https://doi.org/10.2118/127986-PA

Singh, A., Liu, X., Wang, S. et al. 2020. Integrated Economic Solutions to Maximize Productivity and EUR in UCR Multistage Hydraulic Fractured Wells. Paper presented at the International Petroleum Technology Conference, Dhahran, Kingdom of Saudi Arabia. https://doi.org/10.2523/IPTC-20192-MS .

Somanchi, K., Brewer, J. and Reynolds, A. 2017. Extreme Limited Entry Design Improves Distribution Efficiency in Plug-n-Perf Completions: Insights from Fiber-Optic Diagnostics. Paper presented at the SPE Hydraulic Fracturing Technology Conference and Exhibition, The Woodlands, Texas. https://doi.org/10.2118/184834-MS

Tan, Y., Wang, J., Rijken, P., et al. 2021. Mechanism Microseismic Generation During Hydraulic Fracturing – with Evidence From HFTS 2 Observations. Paper presented at the Unconventional Resources Technology Conference, Houston, Texas.

Ugueto C., G. A., Huckabee, P. T., Molenaar, M. M. et al. 2016. Perforation Cluster Efficiency of Cemented Plug and Perf Limited Entry Completions; Insights from Fiber Optics Diagnostics. Paper presented at the SPE Hydraulic Fracturing Technology Conference, The Woodlands, Texas. https://doi.org/10.2118/179124-MS

Vidma, K., Abivin, P., Dunaeva, A. et al. 2018.Far-field Diversion Technology to Prevent Frac-Hits in Tightly Spaced Horizontal Wells. Paper presented at the SPE Annual Technical Conference and Exhibition, Dallas, Texas. https://doi.org/10.2118/191722-MS

Wang, S., Tan, Y., Sangnimnuan, A. et al. 2019. Learnings from the Hydraulic Fracturing Test Site (HFTS) #1, Midland Basin, West Texas – A Geomechanics Perspective. Paper presented at the SPE/AAPG/SEG Unconventional Resources Technology Conference, Denver, Colorado. https://doi.org/10.15530/urtec-2019-1570

Wehunt, C. D., Naik, S. J., and Singh, A. 2020. More Bang for the Buck – Optimized Perforating Design for Unconventional Reservoirs. Paper presented at the SPE Hydraulic Fracturing Technology Conference and Exhibition, The Woodlands, Texas. https://doi.org/10.2118/199730-MS

Whitfield, T., Watkins, H., Dickinson, L. J. 2018. Pre-Loads Successful Mitigation of Damaging Frac Hits in the Eagle Ford. Paper presented at the SPE Annual Technical Conference and Exhibition, Dallas, Texas. https://doi.org/10.2118/191712-MS

Zhang, Z., DiSienna, J., Bevc, D., et al. 2021. Hydraulic fracture characterization by integrating multidisciplinary data from the Hydraulic Fracturing Test Site 2 (HFTS-2). Paper presented in the Unconventional Resources Technology Conference, Houston, Texas.

Appendix F: Hydraulic fracture characterization by integrating multidisciplinary data from the Hydraulic Fracturing Test Site 2 (HFTS-2)

Authors: ***Zhishuai Zhang, James DiSiena, Dimitri Bevc, Ivan Lim Chen Ning, Yunhui Tan, Laura Swafford, Mike Craven, Kelly Hughes, Andrea Vissotski***

Summary

Various technologies have traditionally been used to monitor and describe hydraulic fractures from different perspectives. This work demonstrates the value of data integration for hydraulic fracture characterization when multiple data resources are available. The Hydraulic Fracturing Test Site 2 (HFTS-2) is a hydraulic fracturing research project in the Delaware Basin with multiple surveillance techniques including fiber optics sensing, microseismic, pressure/temperature gauges, etc. We integrated the multidisciplinary data from the HFTS-2 to characterize hydraulic fractures. The integrated data revealed interesting fracture propagation features including layering, vertical propagation affected by pore pressure gradient, and different microseismic activities due to difference in-situ conditions. These findings can be insightful for understanding hydraulic fracture propagation. The comparison among multiple surveillance data also helps us to evaluate the roles of various surveillance technologies and provides us experience to make informative decisions depending on different monitoring objectives.

Introduction

Successful hydraulic stimulation is essential for unconventional resource development. However, the characterization of hydraulic fractures is extremely challenging. Multiple surveillance technologies, such as microseismic (Maxwell, 2014; Grechka & Heigl, 2017), fiber optics (Jin & Roy, 2017), pressure (Spicer & Coenen, 2018), and temperature (Sierra, et al., 2008), have been developed to monitor fracture growth with varying degrees of success. As a widely used hydraulic fracturing surveillance technology, traditional microseismic monitoring uses surface, shallow buried, or down hole geophones to detect and record small earthquakes associated with hydraulic stimulation (Maxwell, 2014). The extent and occurrence of microseismic events are used to characterize the growth of hydraulic fractures. The microseismic source parameters provide information on the fracture mechanism and stress states around hydraulic fractures. However, the challenges are the not-well-understood mechanism of microseismic occurrence and the potentially location uncertainties of microseismic events (Zhang, Rector, & Nava, 2017).

Fiber optics strain sensing have been used for hydraulic fracturing monitoring from different perspectives. Distributed Acoustic Sensing (DAS) can be used for microseismic data acquisition (Karrenbach, et al., 2017). It provides wide spatial coverage and high spatial sampling rate with adequate signal-to-noise ratio. This facilitates the identification various seismic phases, which can be used to improve microseismic event location and fracture characterization (Lellouch, Meadows, Nemeth, & Biondi, 2020). However, DAS measures the strain only along the axial direction. This makes the microseismic event location using DAS signal from a single well ambiguous and moment tensor inversion very challenging. In addition to seismic monitoring, Jin and Roy (2017) showed that the low-frequency content of DAS signal provides information on the strain or strain rate induced by hydraulic fractures. This strain responses of hydraulic fractures can also be measured with the Distributed Strain Sensing (DSS). In the case of

deploying along a horizontal monitoring well, the strain response provides information on the opening, closing, fracture hit, and stress shadowing effect related to hydraulic fractures (Zhang, et al., 2020; Liu, et al., 2020; Tan, et al., 2021). In the case of deploying along a vertical monitoring well, this data provides information on the vertical growth of hydraulic fractures. The limitation of this technology is that the strain responses of hydraulic fractures is a near field effect which decays as $1/distance^2$. Thus, the DSS or low-frequency DAS data are insensitive to fracture behaviors further away from the monitoring well. Various other technologies have been used to characterize hydraulic fractures such as DTS (Li, et al., 2020), noise intensity logging (Molenaar, Hill, Webster, Fidan, & Birch, 2012), pressure (Kampfer & Dawson, 2016), tracer (Wood, Leonard, Senters, Squires, & Perry, 2018), geochemistry (Liu, Michael, Johansen, Brown, & Allwardt, 2017), time-lapse Vertical Seismic Profiling (VSP) (Byerley, Monk, Aaron, & Yates, 2018), etc. Data from these surveillances present fracture growth from certain perspectives but are typically interpreted separately or with limited integration. To maximize the value of data from various sources, we need to integrate these data to form a complete picture of hydraulic fractures. In addition, data integration allows us to compare and mutually validate different surveillance technologies, thus, provides insight into the pros and cons of these technologies. Hydraulic Fracturing Test Site 2 (HFTS-2) provides excellent resources to carry out this data integration study (Ciezobka, 2018). We constructed a project that includes low-frequency DAS, noise intensity logging, microseismic, pressure, temperature, stimulation, and petrophysics data to characterize hydraulic fractures. The work of integrating data from different service providers is non-trivial but extremely beneficial. It allows us to compare various surveillance data within the same spatial and temporal coordinate system. With the integrated dataset, we were able to identify a few interesting fracture growth behaviors, which are difficult to be noticed with any individual dataset.

HFTS-2 project and surveillance overview

The HFTS-2 is a hydraulic fracturing research project in the Delaware Basin part of the Permian Basin (Ciezobka, 2018). The aim of the HFTS-2 is to improve recovery, mitigate environmental impact, and lower cost by advancing the hydraulic fracturing technology. The test site includes eight new producing wells that penetrate five intervals of the Wolfcamp 2 Formation and a vertical pilot well, which is cored and logged. Fig F 1 shows a portion of the involved wells and the area studied by this paper. In addition to five (B1H, B2H, B3H, B4H, and T16H) of the eight stimulation wells, Fig F 1 also shows BR1H and BR2H, which are two parent wells that were previously produced. The horizontal spacing and vertical spacing of adjacent wells are approximately 200 m (660 ft) and 60 m (200 ft) respectively.

In this study, we focus on the stimulation of B1H, B2H, and B4H, which are sequentially stimulated and comprehensively monitored with surveillance technologies such as fiber optic sensing, microseismic, pressure and temperature gauges (Fig F 1). DAS and DTS are deployed along B3H, B4H, and B5PH for acoustic and temperature measurement. Cross-well low-frequency DAS data along all three wells are processed for B1H and B2H stimulation. In the case of B4H stimulation, noise intensity log was acquired from B4H and cross-well low-frequency DAS data were processed for fibers along B3H and B5PH. The microseismic activities are monitored with DAS as well as the five geophone arrays in T16H, B3H, and B5PH. Eight

pressure/temperature (P/T) gauges deployed along the B5PH to stride the targeted stimulation zones.

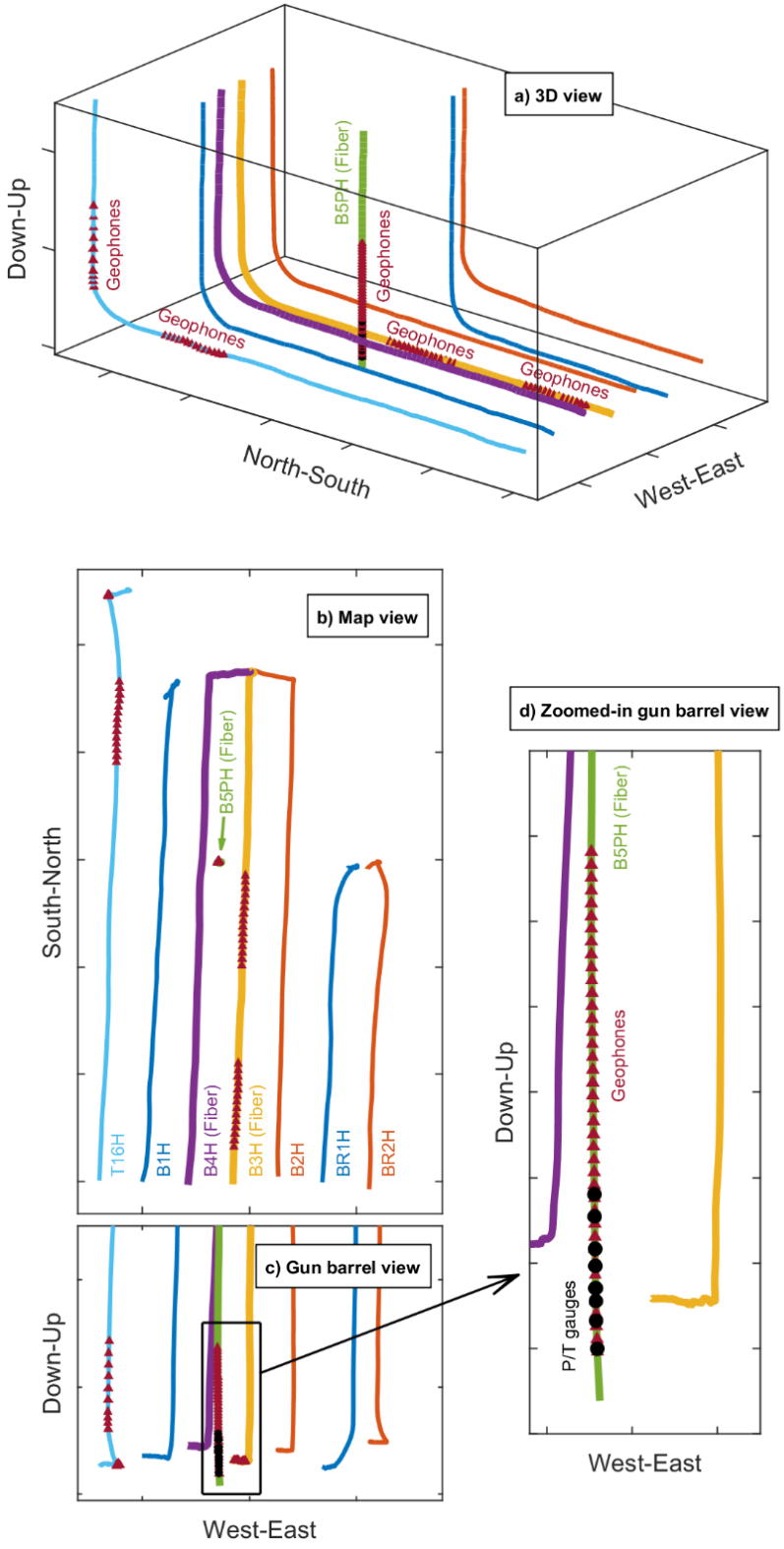

Fig F 1—The studied wells and area of this work (A portion of the HFTS-2 project) involves B1H, B2H, and B4H as stimulation wells. The BR1H and BR2H are previously produced parent wells. B3H, B4H, and B5PH are equipped with fiber optic sensors. Five geophone arrays and the fiber optic sensing were used for microseismic surveillance. Eight P/T gauges were deployed in the B5PH vertical well to monitor the stimulation zone.

Data integration

Data from different service providers usually have different coordinate systems, scales, time and space references. This makes it difficult to compare data from different service providers with each other. To make effective comparison and analysis, we construct a project which incorporates all available information in the same reference system. Eight representative stimulation stages are shown by Fig F 2 to Fig F 9 in stimulation time order for convenient comparison and analysis. Information integrated in this study include low-frequency DAS data, noise intensity logs, microseismic data, pressure and temperature acquired by gauges in B5PH, well logs, and stimulation information. The caption of Fig F 2 describes in detail how the integrated information is presented.

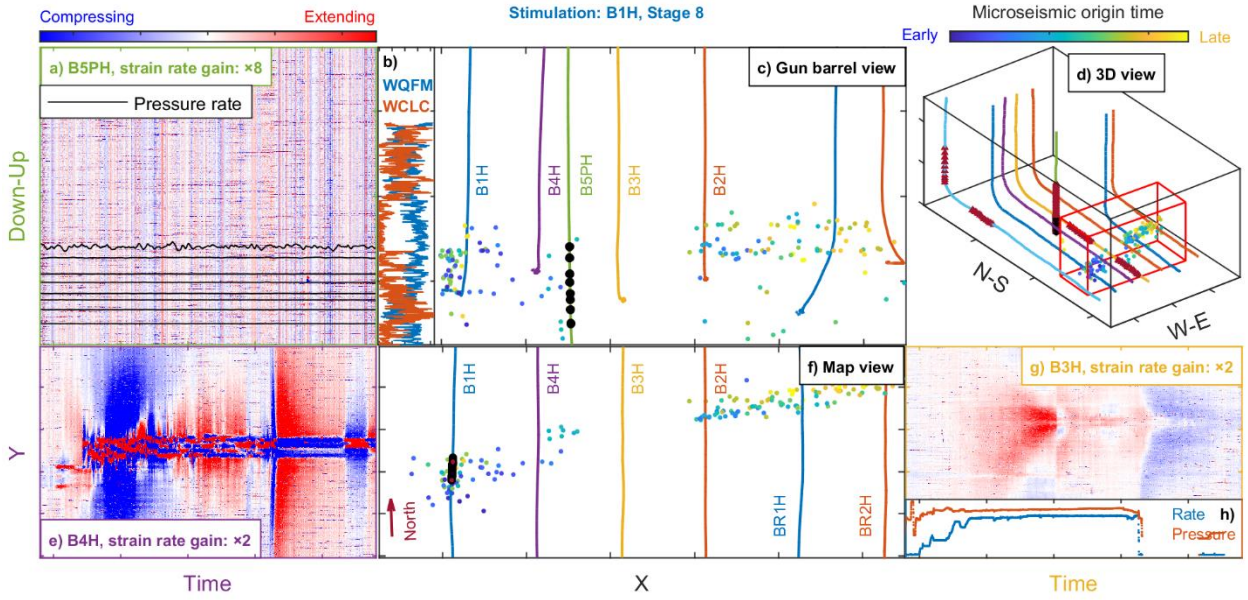

Fig F 2—The data integration result of Stage 8 of B1H stimulation. d) is a 3D view of the whole project. The gun barrel view and map view of the red box region in d) is shown by c) and f) respectively. Black circles in c) represent the P/T gauge locations. The red circles in f) show the locations of perforation shots. Dots in c), d), and f) represent microseismic events color coded with their origin times. a), e), and g) show the strain rate measured by the fiber optics sensing along B5PH, B4H, and B3H. The black lines on a) shows the pressure change rate measured by the eight gauges in B5PH. b) shows the dry weight of quartz-feldspar-mica (WQFM) and dry weight of calcite (WCLC) according to litho-scanner along the B5PH and h) shows the stimulation information. Time and space in different subfigures are all aligned with each other with the only exception of the 3D view d). This stage is a typical example of the early stages of B1H stimulation, during which some microseismic events have been quickly attracted by the region previously depleted by the BR1H and BR2H production. The strain rate pattern in g) is an example of the hydraulic fracture bypassing the monitoring fiber from above or below without intersection (Zhang, et al., 2020).

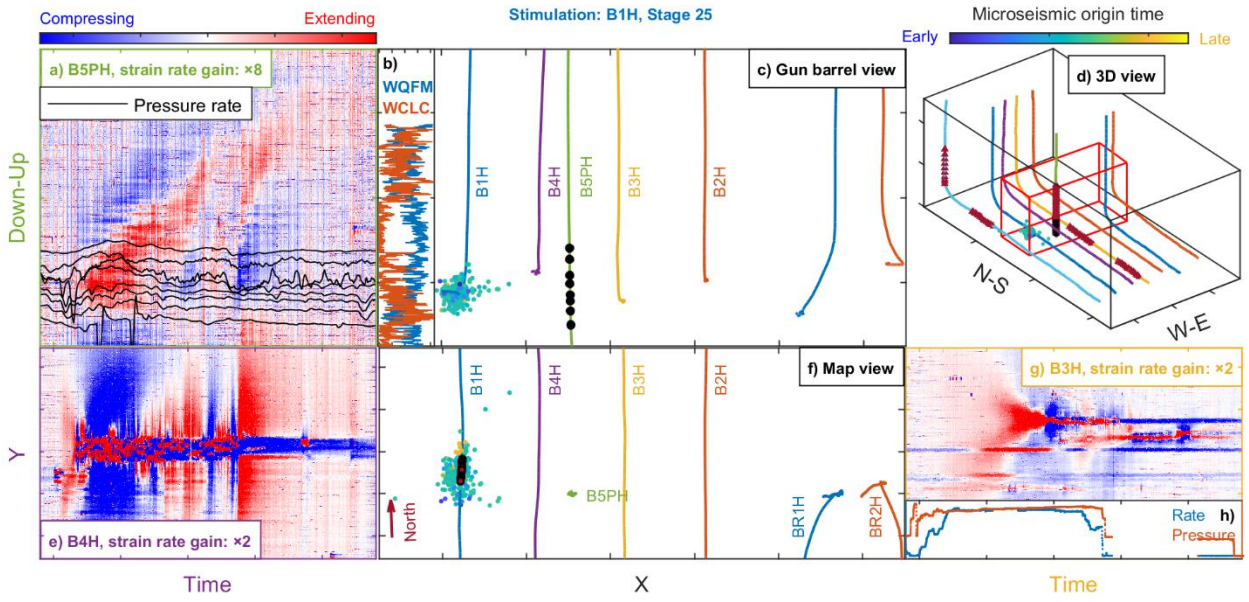

Fig F 3—This is a later stage of B1H stimulation. a: the pressure change rate measured by the P/T gauges shares similar trend with the low-frequency DAS measured strain rate. This observation also applies to Fig F 4a, Fig F 5a, and Fig F 9a. The upward growth of the hydraulic fracture is more significant than its downward growth. This is also shown by Fig F 4a, Fig F 8a, and Fig F 9a.

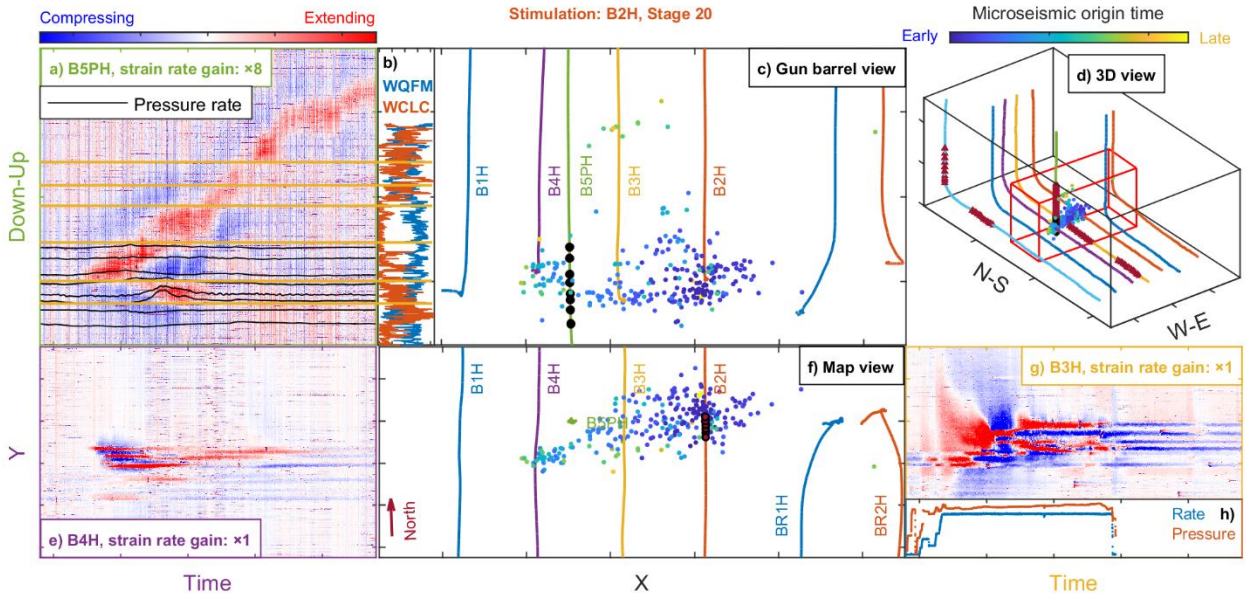

Fig F 4—This is an early stage of B2H stimulation. a: similar with Fig F 3a, the pressure change rate measured by the P/T gauges shares similar trend with the low-frequency DAS measured strain rate, and the upward growth of the hydraulic fracture is more significant than its downward growth. The effect of layering was annotated by yellow lines on a). The

vertical span of the low-frequency DAS strain along the B5PH is taller than that of Fig F 3a, and shorter than that of Fig F 9a.

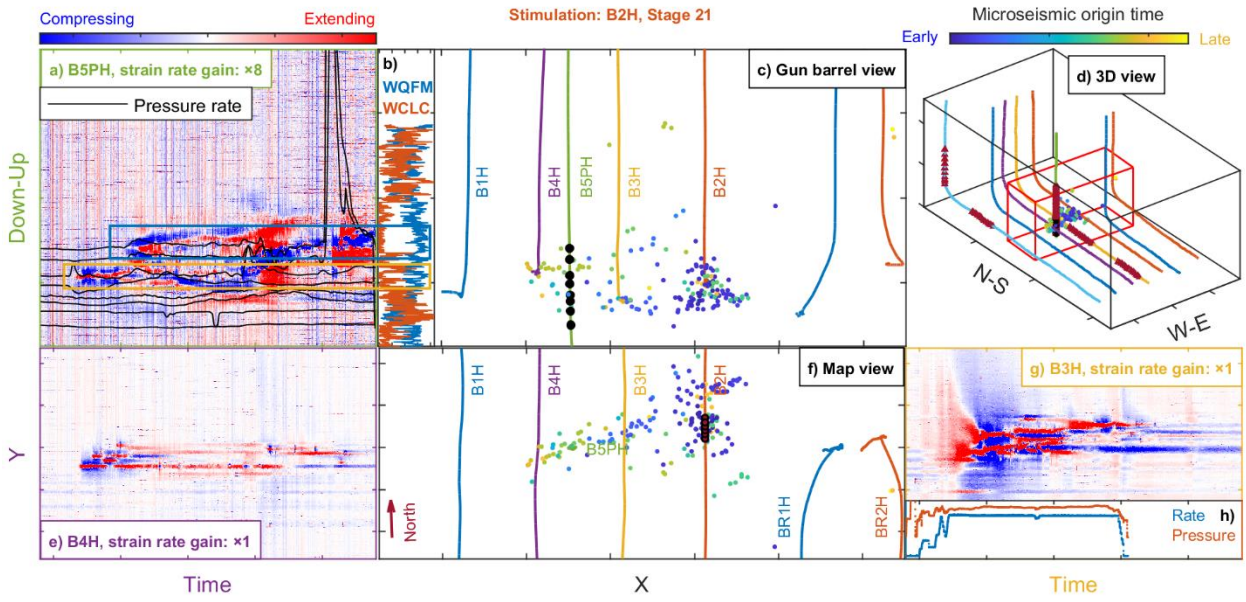

Fig F 5—Stage 21 of B2H stimulation. a: similar with Fig F 3a, the pressure change rate measured by the P/T gauges shares similar trend with the low-frequency DAS measured strain rate with the except of a high peak pressure measurement after pumping stop. This may indicate a direct fluid communication with the vertical monitoring well due to leakoff. Fiber optics strain data shows the effect of both layered fractures (the yellow rectangle) in a vertically heterogeneous well log interval and elliptic shaped fracture (the blue rectangle) in a relatively homogenous layer well log interval.

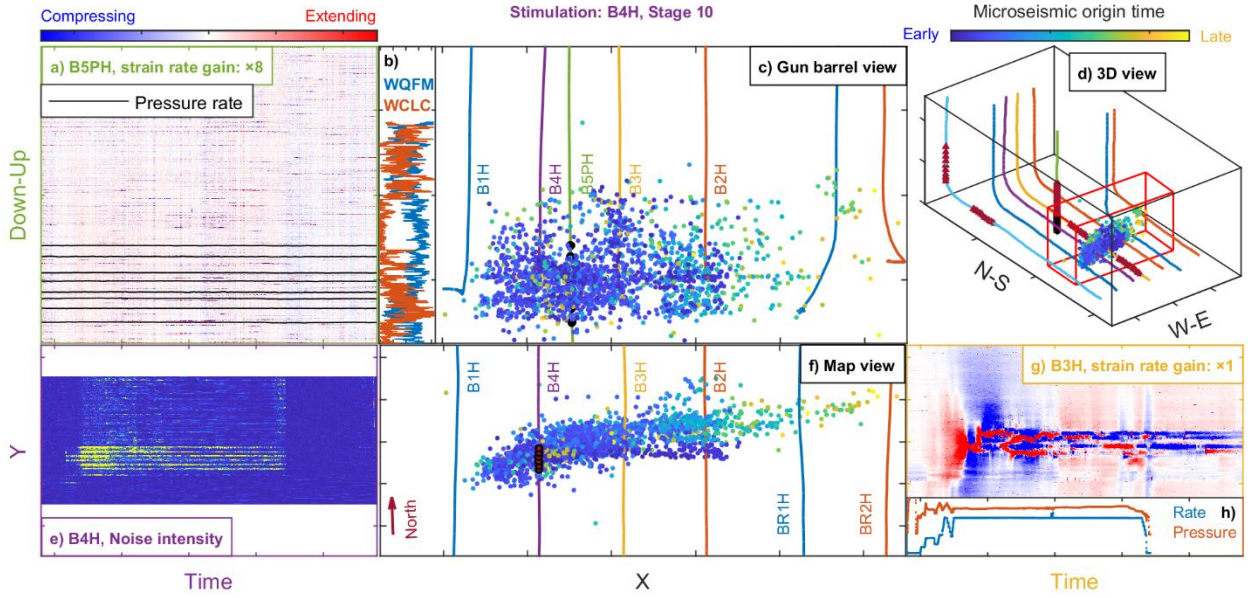

Fig F 6—Stage 10 of B4H stimulation as an early stage of B4H stimulation. The data shown by each subplot is the same with that explained by the caption of Fig F 2 except that e) is showing noise intensity log instead of strain rate measured by the fiber optics sensing along B4H.

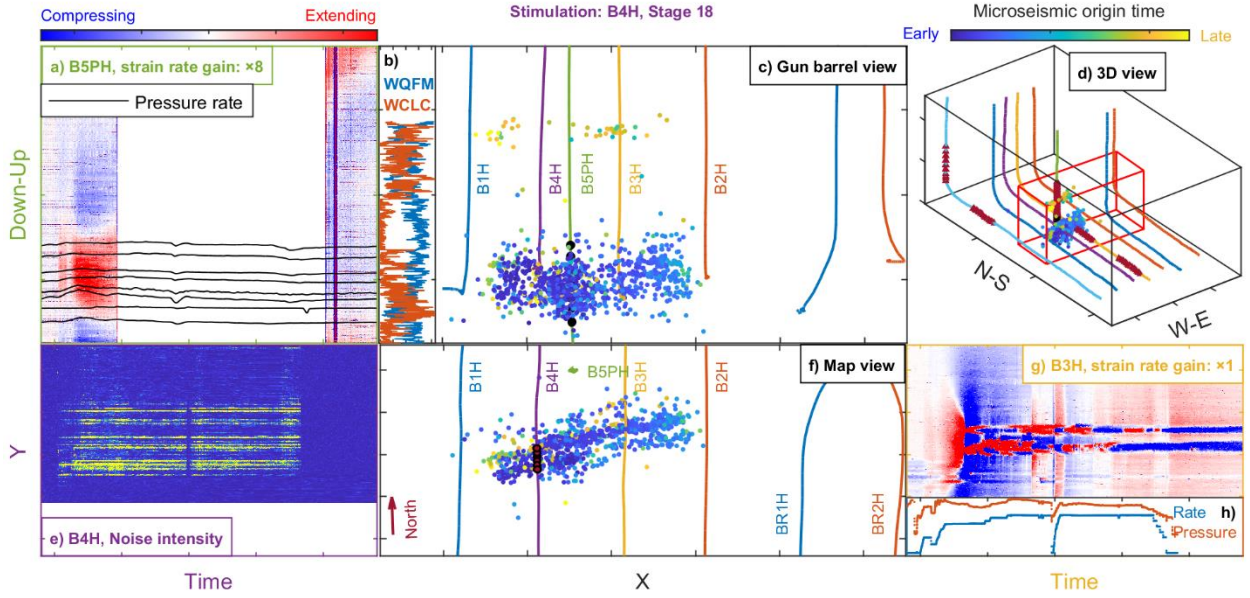

Fig F 7—This is Stage 18 of B14H stimulation. Both microseismic (f) and low-frequency DAS data (g) show the signatures of two fracture planes/clusters. However, the noise intensity log in e) shows activities towards the heel side of the stimulation zone. We have observed several cases with similar inconsistency such as Fig F 8e. f) and g) show an example of double fracture planes/clusters.

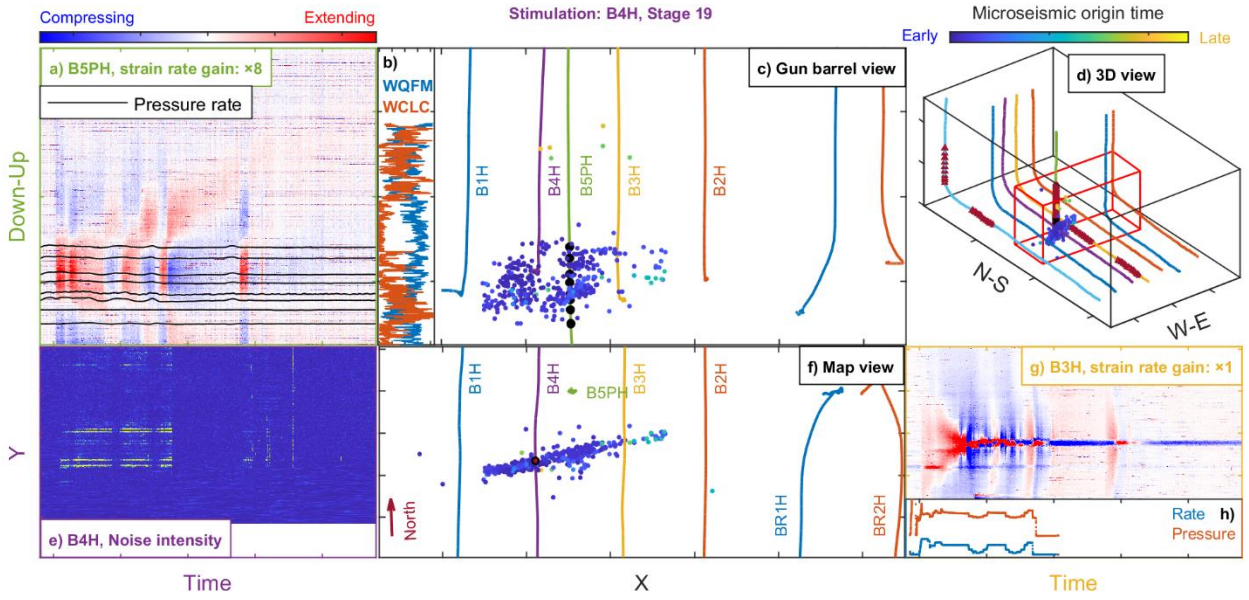

Fig F 8—According to microseismic data in f) and low-frequency DAS data in g), a single hydraulic fracture plane/cluster was stimulated due to single perforation cluster design. Similar with Fig F 7, the noise intensity log in e) shows high intensity noises towards the heel side of the perforation shot locations, which may be noise with unknow source. f) and g) show an example of single fracture plane/cluster.

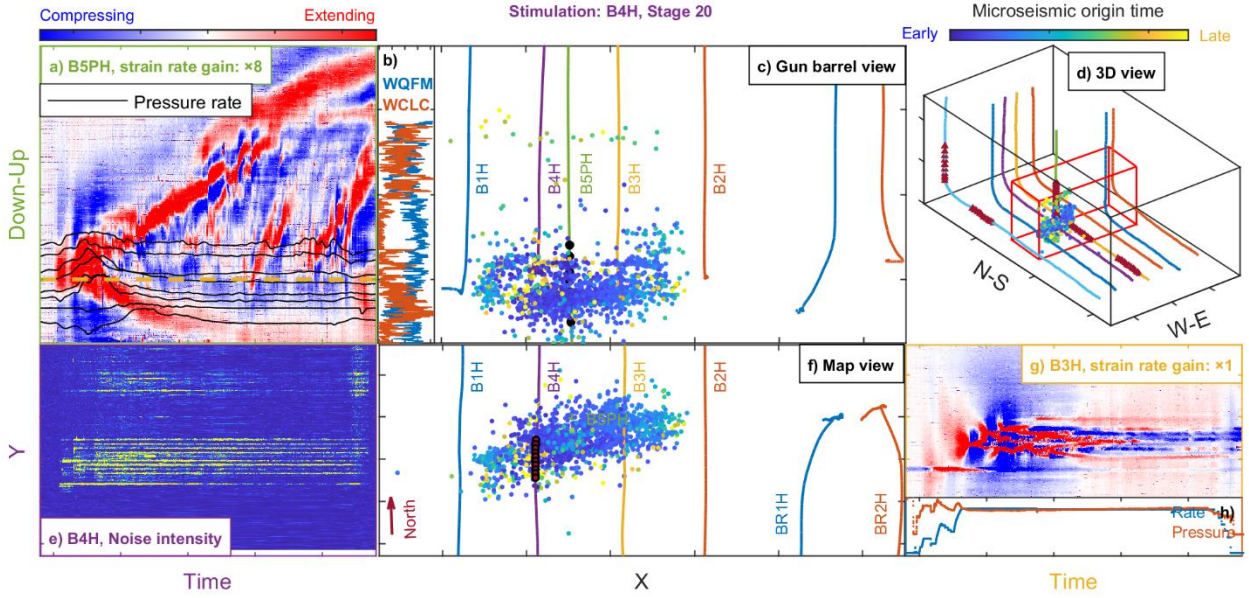

Fig F 9—This is Sage 20 of B4H stimulation. a): similar with Fig F 3a, the pressure change rate measured by the P/T gauges shares similar trend with the low-frequency DAS measured strain rate, and the upward growth of the hydraulic fracture is more significant than its downward growth. The upward growth of hydraulic fractures is more significant above the depth marked by the yellow dashed line than the downward growth below this line. This significant

asymmetric upward and downward growth of hydraulic fractures may be due to asymmetric pore pressure gradient as explained by Fig F 11.

Integrated data analysis and interpretation

Comparison between low-frequency DAS and P/T measurement from downhole gauges

We started by comparing the low-frequency DAS data along the B5PH vertical monitoring well and the P/T data, which is from the downhole gauges in the same well. In general, the pressure change rate shares similar trend with the strain rate (Fig F 3a, Fig F 4a, Fig F 5a, and Fig F 9a). This reveals the effectiveness of both monitoring technologies. The discrepancy may be due to the fact that they measure closely related but different parameters (vertical strain rate versus pore pressure rate) and the presence of noise.

A detailed comparison of three stages of B2H stimulation is shown in Fig F 10. The pressure rate shows similar trend with the strain rate except at the upper two gauges after Stage 21 stimulation (orange rectangle in Fig F 10b). The pressure and temperature measured by these two downhole gauges increased significantly (blue rectangle in Fig F 10a) when this discrepancy between pressure change rate and strain rate occurred. This may be due to a direct fluid communication to the P/T gauges due to fluid leak-off after Stage 21 stimulation, which induced fractures nearest to the vertical B5PH observation well (Fig F 5). The fiber optics strain measurement is insensitive to the pore pressure change while the P/T gauges measure the pore pressure. The difference in their measured parameters results in their discrepancy when there is a direct fluid communication. In summary, the fiber optic strain and pressure data can mutually

validate each other. Each of them has its own advantage and disadvantage. By combining these two data, we can maximize the information obtained from these measurements.

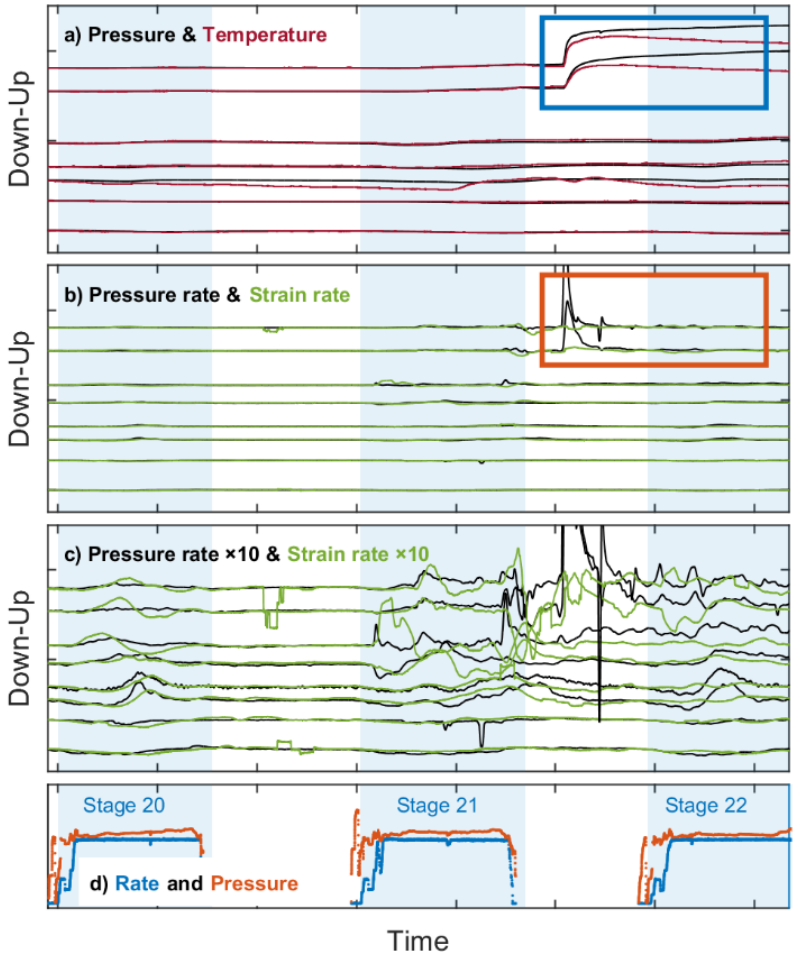

Fig F 10—P/T gauges measurement in comparison with the low-frequency DAS measured strain rate (green lines) at the corresponding gauge locations during the Stage 20 to 22 of the B2H stimulation. a) shows pressure (black lines) and temperature (red lines) measured by the P/T gauges. b) is the pressure change rate (black lines) according to the P/T gauges in comparison with the strain rate (green lines) from low-frequency DAS measurement. c) is the same with b) but the pressure rate and strain rate data are gained by ten times to reveal detailed variation. d) is the stimulation information. The pressure rate shows similar trend with the strain rate except at the upper two gauges after Stage 21 stimulation as shown by the orange rectangle in b). This large discrepancy corresponds to a sudden increase in temperature as marked by the blue rectangle in a). This may be a result of direct fluid communication to the P/T gauges due to fluid leak-off.

Vertical propagation behavior of hydraulic fractures

The data provides information on the vertical growth of hydraulic fractures are mainly the fiber optics strain data from the vertical B5PH well and the microseismic locations.

Upward growth

According to the fiber optics strain data shown by Fig F 3a, Fig F 4, and Fig F 9a, the upward growth of the low-frequency DAS signal is more significant than the downward growth. However, the microseismic data are mainly concentrated around the stimulation depth, except a

small number of shallow events in Fig F 4, Fig F 5, and Fig F 7 to Fig F 9. Given that the amplitude of strain (near-field term in seismology) decays as $1/distance^2$ from its source, the observed signal represents an upward fluid propagation or fracture propagation. This may indict an aseismic zone between the upper portion of the strain signal and the stimulation zone.

To understand the cause of the significant upward propagating low-frequency DAS signal and shallow microseismic events, we show the one-day average pressure prior to the stimulation measured by the P/T gauges in the vertical B5PH well in Fig F 11. The pressure gradient is much larger (pressure decreases faster when going upward) than the hydrostatic pressure gradient above the depth marked by the yellow dashed line in Fig F 9a, and Fig F 11. This low-pressure shallow zone may cause the fractures to grow more rapidly upward than downward.

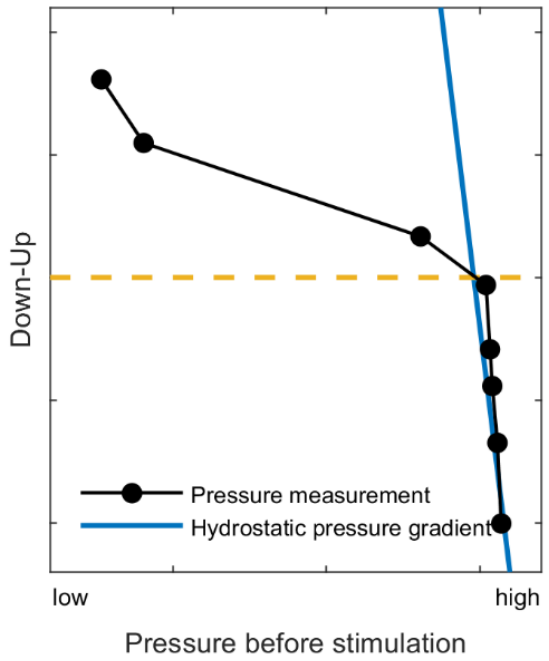

Fig F 11—One-day average pressure measured by P/T gauges before stimulation. Above the yellow dashed line, the pore pressure gradient is larger (significant lower pressure when going up) than the hydrostatic pressure gradient. This may be the reason of the significant asymmetric upward and downward growth of hydraulic fractures. This yellow dashed line corresponds to the depth marked by the yellow dashed line in Fig F 9a.

Effect of layering

From the low-frequency DAS data along the vertical B5PH monitoring well, we can see signatures of different fracture shapes such as layered fractures and elliptical shaped fractures. Fig F 5a is an example where both layered (yellow rectangle) and elliptical shaped (blue rectangle) fractures can be observed from the low-frequency DAS data. Zhang et al. (2020) carried out a numerical simulation which confirmed the variance in shapes of these fractures. By comparing the low-frequency DAS data with well log information (Fig F 5) from the same well, we can see the elliptical shaped fracture corresponds to an interval where the well log is vertically homogeneous while the layered fracture corresponds to an interval where the well log

shows significant vertical variation. This consistency between the layering of fractures is also revealed on a larger scale by Fig F 4a, and Fig F 4b as annotated by the yellow lines.

Vertical enlargement and increased microseismic activities during restimulation

We compared the low-frequency DAS data and microseismic data during stimulation of B1H, B2H, and B4H, which are three consecutive stimulated wells. From the low-frequency DAS data (Fig F 3a, Fig F 4a, and Fig F 9) along the vertical B5PH well, we can observe increased fracture height during restimulation. In the meantime, there are gradually more microseismic activities associated with the later stimulated wells. This phenomenon is consistent with the majority of the stages of these three stimulation wells (Fig F 12). While the mechanism of this vertical fracture enlargement and increased microseismic activities need further investigation, the observation may readily assist in understanding the role of microseismic technology in hydraulic fracturing monitoring and stimulation design.

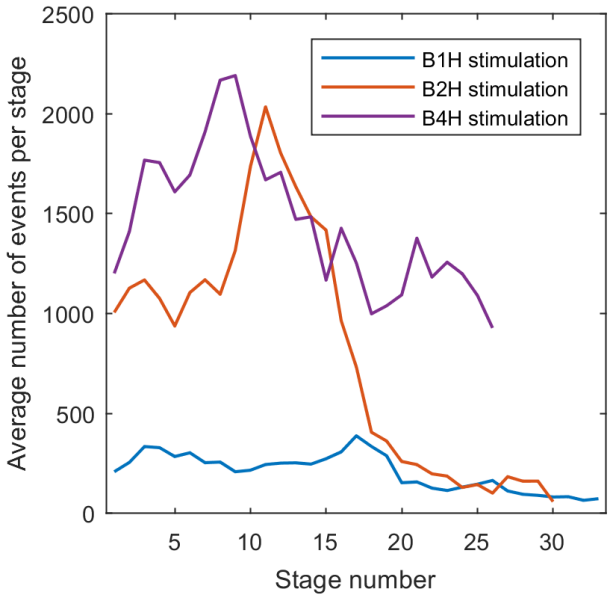

Fig F 12—Number of microseismic events per stage (slightly smoothed by averaging nearby stages to facilitate visualization) for the three studied stimulation wells. For the early stages (stage 1 to stage 17), the microseismic activities are affected by the previously depleted BR1H and BR2H wells since there are a significant decrease in the number of microseismic events when going from early stages (affected by BR1H and BR2H) to later stages (unaffected by BR1H and BR2H) for all three stimulation wells. The number of microseismic events increases as the formation was restimulated for both early stages and later stages.

Number of fracture planes/clusters

To evaluate the resolution of microseismic data on distinguishing fracture planes or fracture clusters, we may compare the microseismic locations in the map views on Fig F 8f, Fig F 7f, and Fig F 9f, which are from the same stimulation well and at comparable distances to the monitoring geophone arrays. Thus, it is reasonable to assume that they have similar signal to noise ratios and location uncertainties. Fig F 8 shows an example of surveillance result from a single perforation cluster stimulation design. Both the microseismic data (Fig F 8f) and the low-

frequency DAS data along an offset well (Fig F 8g) shows features of single hydraulic fracture plane/cluster. Similarly, the microseismic data (Fig F 7f) and low-frequency DAS data (Fig F 7f) for an adjacent stimulation stage show the feature of two hydraulic fracture planes/clusters. As a comparison, we cannot clearly tell the number of hydraulic fracture planes/clusters from the other adjacent stimulation stage as shown by Fig F 8, which may have multiple hydraulic fracture planes. The accuracy and precision of a microseismic survey dependent on factors such as acquisition geometry, reliability of velocity model, S/N, and processing strategies. Its resolution on defining fracture planes/clusters may vary from survey to survey. However, this comparison sheds light on the location precision of microseismic data by providing a field example. In this typical case, microseismic data can distinguish among single, double, and multiple hydraulic fracture planes/clusters.

Discussion

The HFTS-2 project provides a comprehensive data set for data integration study. In a typical hydraulic fracturing work or pilot, even though only a limited type of data is acquired, efforts should still be taken to integrate available data for interpretation. For instance, the fiber optics strain data from a vertical monitoring well should be compared with the well log information from the same well to understand the vertical growth of the hydraulic fractures. The microseismic data should be compared with the low-frequency DAS data since they can usually be obtained from different frequency content of the same DAS data.

Though some interpretations made in this work remain to be further verified, the values of data integration for fracture characterization and surveillance technology comparison are obvious. This work provides a prototype of data integration for hydraulic fracturing surveillance. Additional integration and interpretation can be carried out to include further information on geology, production, stimulation design, etc.

In addition to qualitative interpretation, data integration can be also valuable for calibrating numerical modeling results. One example is that the result of any hydraulic fracturing simulation should be consistent with all available data such as low-frequency DAS data and pressure gauge data. These data can also be integrated to constrain any related models instead of being used separately. The mindset of data integration should also be applied to the surveillance of any other subsurface activities.

Conclusions

We integrated microseismic, low-frequency DAS, noise intensity logging, pressure, temperature, and petrophysics data from the HFTS-2 project to characterize hydraulic fractures. Data integration significantly increases knowledge about hydraulic fractures without requiring more information. It also helps to mutually validate different surveillances technologies.

The integration of multidisciplinary data from HFTS-2 requires an interdisciplinary collaboration among scientists and engineers with various knowledge domains. The integration results and its

interpretation provide a comprehensive understanding of hydraulic fractures that can be beneficial to geophysicists, geomechanicists, petroleum engineers, and geologists.

References

Byerley, G., Monk, D., Aaron, P., et al. 2018. Time-lapse seismic monitoring of individual hydraulic frac stages using a downhole DAS array. *The Leading Edge*, **37**(11): 802-810.

Ciezobka, J., 2018. Hydraulic Fracturing Test Site 2 (HFTS2). [Online] https://www.netl.doe.gov/sites/default/files/netl-file/J-Ciezobka-HFTS2.pdf.

Grechka, V. & Heigl, W. M. 2017. Microseismic monitoring. Society of Exploration Geophysicists.

Jin, G. & Roy, B. 2017. Hydraulic-fracture geometry characterization using low-frequency DAS signal. *The Leading Edge*, **36**(12): 975-980. https://doi.org/10.1190/tle36120975.1

Kampfer, G. & Dawson, M. 2016. A novel approach to mapping hydraulic fractures using poromechanic principles. Paper presented at the 50th U.S. Rock Mechanics/Geomechanics Symposium, Houston, Texas.

Karrenbach, M. et al. 2017. DAS Microseismic Monitoring and Integration With Strain Measurements in Hydraulic Fracture Profiling. Paper presented at the SPE/AAPG/SEG Unconventional Resources Technology Conference, Austin, Texas. https://doi.org/10.15530/URTEC-2017-2670716

Lellouch, A., Meadows, M., Nemeth, T., et al. 2020. Fracture properties estimation using distributed acoustic sensing recording of guided waves in unconventional reservoirs. Geophysics, 85(5): M85-M95. https://doi.org/10.1190/geo2019-0793.1

Liu, F. et al. 2017. Time-lapse geochemistry (TLG) application in unconventional reservoir development. Paper presented at the SPE/AAPG/SEG Unconventional Resources Technology Conference, Austin, Texas. https://doi.org/10.15530/URTEC-2017-2670186

Liu, Y. et al. 2020. Rock Deformation and Strain-Rate Characterization during Hydraulic Fracturing Treatments: Insights for Interpretation of Low-Frequency Distributed Acoustic-Sensing Signals. *SPE Journal*, **25**(05): 2251-2264. https://doi.org/10.2118/202482-PA

Li, X. et al., 2020. Distributed acoustic and temperature sensing applications for hydraulic fracture diagnostics. Paper presented at the SPE Hydraulic Fracturing Technology Conference and Exhibition, The Woodlands, Texas. https://doi.org/10.2118/199759-MS

Maxwell, S., 2014. Microseismic Imaging of Hydraulic Fracturing. Society of Exploration Geophysicists.

Molenaar, M. et al., 2012. First downhole application of distributed acoustic sensing for hydraulic-fracturing monitoring and diagnostics. *SPE Drilling & Completion*, **27**(01): 32-38. https://doi.org/10.2118/140561-PA

Sierra, J. R. et al., 2008. DTS Monitoring of Hydraulic Fracturing: Experiences and Lessons Learned. Paper presented at the SPE Annual Technical Conference and Exhibition, Denver, Colorado. https://doi.org/10.2118/116182-MS

Spicer, S. & Coenen, E., 2018. Estimation of Fracture Geometries From Poroelastic Pressure Responses in Offset Wells. Paper presented at the SPE/AAPG/SEG Unconventional Resources Technology Conference, Houston, Texas. https://doi.org/10.15530/URTEC-2018-2886118

Tan, Y. et al., 2021. Geomechanical Template for Distributed Acoustic Sensing Strain Patterns during Hydraulic Fracturing. *SPE Journal*, **26**(02): 627-638. https://doi.org/10.2118/201627-PA

Wood, T. et al., 2018. Interwell Communication Study of UWC and MWC Wells in the HFTS. Paper presented at the SPE/AAPG/SEG Unconventional Resources Technology Conference, Houston. https://doi.org/10.15530/URTEC-2018-2902960

Zhang, Z. et al., 2020. Modeling of fiber-optic strain responses to hydraulic fracturing. *Geophysics*, **85**(6): A45-A50. https://doi.org/10.1190/geo2020-0083.1

Zhang, Z., Rector, J. W. & Nava, M. J., 2017. Simultaneous inversion of multiple microseismic data for event locations and velocity model with Bayesian inference. *Geophysics*, **82**(3): KS27-KS39. https://doi.org/10.1190/geo2016-0158.1

Appendix G: Observations and Modeling of Fiber-Optics Strain on Hydraulic Fracture Height Growth in HFTS-2

Authors: ***Jiehao Wang, Yunhui Tan, Peggy Rijken, Xinghui Liu, Amit Singh, Yan Li***

Summary

Understanding fracture height growth can be of great significance to optimizing field development and improving recovery. The Hydraulic Fracturing Test Site 2 (HFTS-2) has provided a unique opportunity and an advanced dataset to allow us to observe and understand fracture geometries rigorously. Low-frequency distributed acoustic sensing (DAS) data from a vertical well in HFTS-2 showed three key observations: (i) excessive upward height growth (>1000 ft) with an average growth rate of ~8-10 ft/min and limited downward growth of the hydraulic fractures during pumping, (ii) considerable additional upward fracture height growth (~300 ft) after well shut in, and (iii) very complex low-frequency DAS strain rate patterns for a small fiber-to-stage offset. Advanced geomechanical modeling was performed to simulate the hydraulic fracture propagation and the resulting strain responses in the vertical direction. The modeling results demonstrated asymmetric upward and downward fracture height growths as observed in HFTS-2 with a similar upward height growth rate. Simulated waterfall plots of vertical strain rate showed distinct patterns for different fiber-to-fracture distances. The upgrowing fracture top tip can be clearly identified by the interfaces between compressing and extending zones. It was also found that the complex strain rate patterns observed in HFTS-2 for small fiber-stage offsets were not caused by the mechanical layering but possibly result from the simultaneous propagation of multiple hydraulic fractures at different rates. The simulation results improved the understating of the HFTS-2 low-frequency DAS data and the simulated strain rate patterns could also serve as templates for fracture height interpretation from low-frequency DAS data in future.

Introduction

While hydraulic fracturing is critical to unlock the potential of unconventional reservoirs and has been carried out for many decades, challenges still remain in understanding fracture propagation and estimating final geometry in the subsurface. With increased horizontal lateral length and decreased cluster spacing design, these challenges have become greater. Understanding how a fracture propagates and knowing the final fracture extent is crucial for optimizing completion design and well spacing to improve ultimate recovery. Furthermore, fracture height growth has been long recognized as difficult to measure and estimate due to its dependency on numerous factors such as stress and stress barriers, mechanical stratigraphy, weak interfaces / bedding planes, etc.

The Hydraulic Fracturing Test Site 2 (HFTS-2) is a large collaborative field-based research experiment performed in the Delaware Basin, West Texas. Similar to HFTS-1 (Ciezobka et al., 2018; Wang et al., 2019), its main objective is to improve the understating of the hydraulic fracturing process through utilization of advanced diagnostics and collection of through-fracture

cores to provide undisputable evidence and attributes of the created hydraulic fractures (Ciezobka and Reeves, 2020).

The HFTS-2 provides a unique opportunity to understand fracture height growth, via an advanced surveillance program including microseismic, pressure gauge, and low-frequency distributed acoustic sensing (DAS) strain monitoring. Among the surveillance data, low-frequency DAS provided the most interesting/surprising observations in terms of geometric information of hydraulic fractures, including both length and height propagation.

Recent progress in distributed fiber optics sensing has made monitoring of strain responses during hydraulic fracturing possible (Ugueto et al., 2019). The strain along fiber orientation in neighboring wells can be revealed by performing low pass filtering of DAS signals. Particularly, in horizontal cross well fibers, multiple studies have identified the "heart-shape" tensile zone in front of a hydraulic fracture tip and "compressional zones" next to the hydraulic fracture walls (Jin et al. 2017; Liu et al. 2020 a; Zhang et al. 2020; Tan et al. 2021). Because the tensile heart-shape zone is ahead of the hydraulic fracture itself, it is possible to forecast the arrival of hydraulic fracture before the fluid reaches the monitoring well. Hence it has been proposed to use this information to monitor "frac-hits" (Liu et al. 2020 b). The fiber-optics strain data was also found to be useful for calibrating inputs of fracture modeling by matching fracture geometry, propagation rate, frac hit orientation, and the number of frac hits (Shahri et al., 2021).

In the vertical direction, however, less progress has been made using low-frequency DAS strain data. The main reason is that the vertical fiber can only monitor the few stages close to the well where the fiber is installed. The strain signal becomes weaker quickly as distance increases (Tan et al., 2021). Since very few studies are available in literature (Tan et al., 2021; Zhang et al., 2020), the responses of the vertical strain to the propagation of hydraulic fractures are not very well understood. However, the vertical fiber is a powerful diagnostic tool to monitor fracture height growth, which is hardly achieved by the horizontal fiber. Extensive vertical fiber-optics strain data was collected from HFTS-2 for this purpose. Thus, it is important to appropriately understand and interpret the vertical strain data corresponding to the hydraulic fracture height growth.

In this study, we provided geomechanical interpretations for the vertical fiber-optics strain data obtained in HFTS-2 through a forward numerical modeling. The low-frequency DAS-observed strain data was first introduced along with a few key observations. Then, the modeling methodology was briefly described, followed by a numerical model setup. Finally, the modeling results were present to interpretate the field observations.

Data/Observations

The HFTS-2 site consists of a vertical pilot hole and eight horizontal wells targeting the Wolfcamp A formation, as shown in Fig G 1. Permanent fiber optic sensing cables were deployed in the vertical pilot hole (B5PH) and two of the horizontal wells (B4H and B3H). B5PH, B3H, and T16H were installed with conventional microseismic arrays. Pressure/temperature (P/T) gauges were also deployed along the B5PH. The pad was stimulated in the order of B1H, B2H, and B4H

using plug and perf techniques, during which comprehensive diagnostic data was collected. This study was focused on the low-frequency DAS signals monitored during the stimulation of B1H.

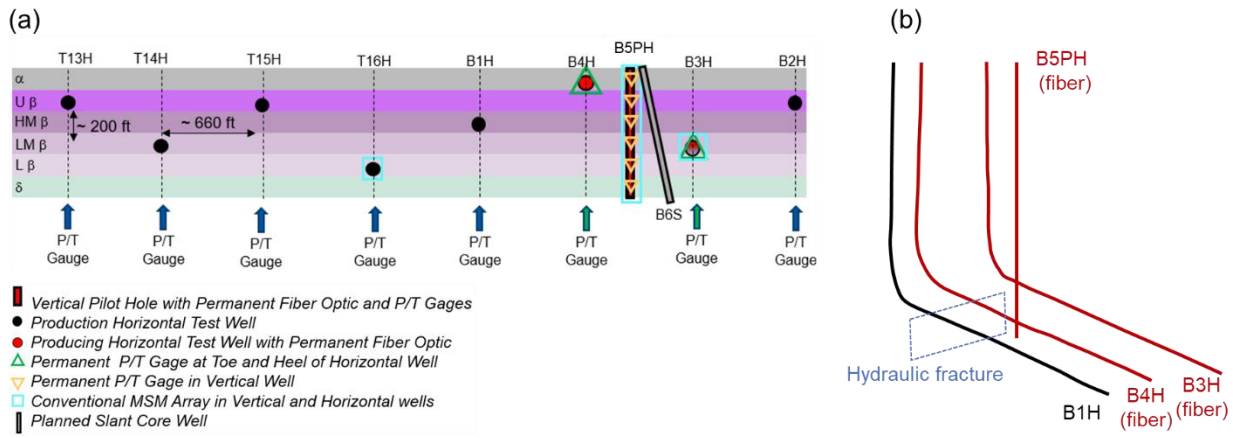

Fig G 1—(a) Gun barrel view of wells and diagnostic instrumentations of HFTS-2; (b) 3D view of the B1H, B4H, B3H, and B5PH. Treatment of B1H is the focus of this study.

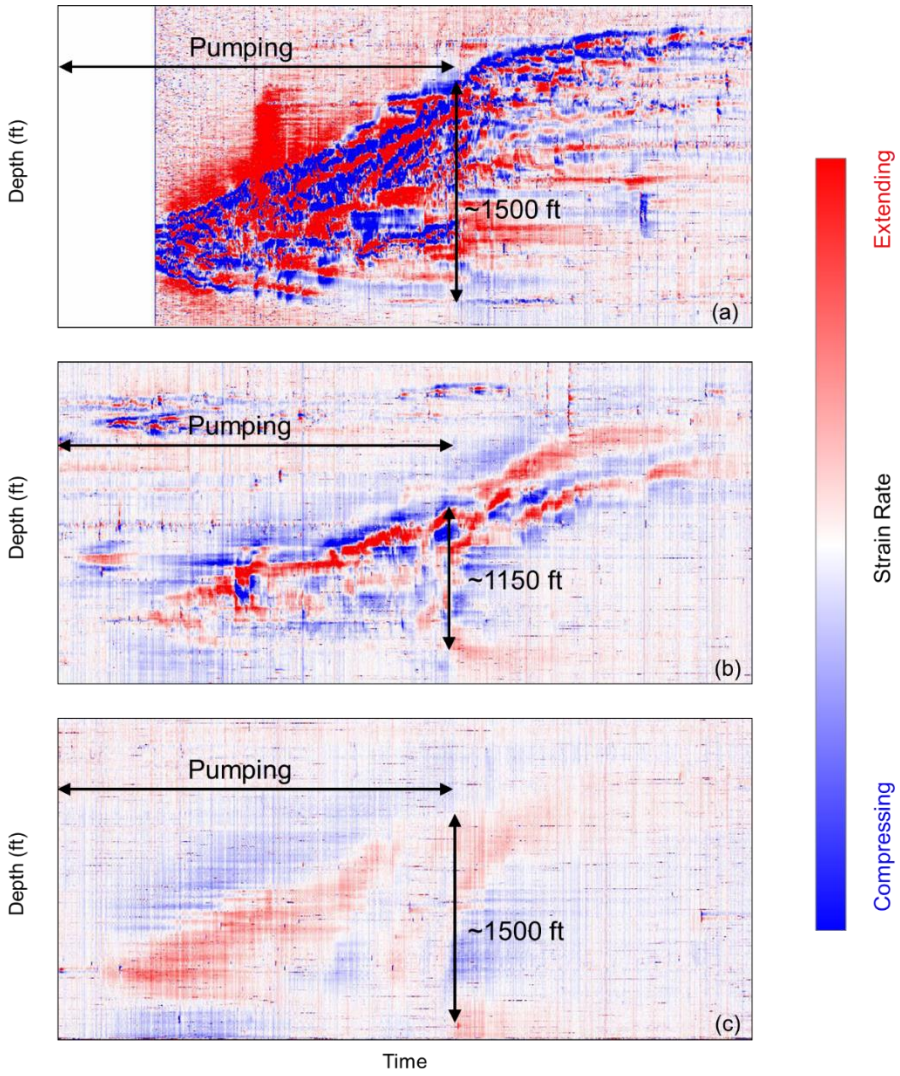

Fig G 2—LF DAS-observed strain rate patterns from vertical pilot hole (B5PH) in HFTS-2 during stimulation of B1H:: (a) is the closest stage, probably passing through B5PH; (b) is a farther stage which is about 200 ft from B5PH; and (c) is the farthest to the monitor well, approximately 400 ft away. The pumping durations are approximately 180 min.

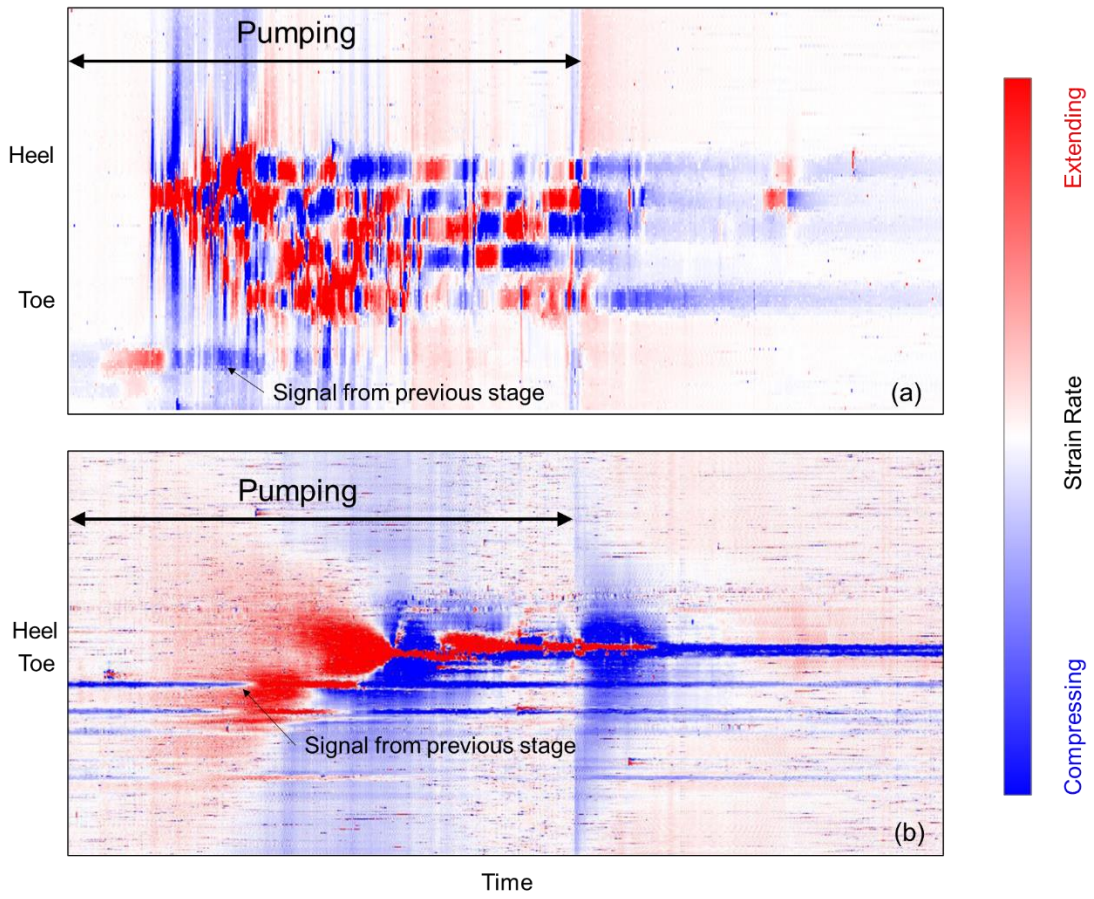

Fig G 3—Low-frequency DAS-observed strain rate patterns from (a) B4H and (b) B3H. This is the same fracturing stage as the one shown in Fig G 2(a). B4H and B3H are approximately 660 ft and 1320 ft away from the treatment well B1H. The pumping durations is approximately 180 min.

Fig G 2 shows the strain rate patterns measured by the low-frequency DAS (B5PH) during the stimulations of three stages in B1H. The stage in Fig G 2(a) is the closest to the fiber optics and the hydraulic fractures probably passed B5PH from its both sides, while these in Fig G 2(b) and (c) are about one and two stages away, respectively. Approximately five fractures were created out of six clusters in each stage, as evidenced by the strain rate pattern from the horizontal fiber optics in B4H (see Fig G 3(a)). Only two fractures out of these five reached B3H at the end of the treatment, as shown by Fig G 3(b). There are three key observations about the fracture height growth emerging from the DAS-observed strain rate data:

1. Excessive hydraulic fracture height growth during pumping. The height of hydraulic fracture can be interpreted from the strain rate patterns (details will be introduced in the modeling results section), and it was observed that the fracture height was generally ~1000-1500 ft when pumping was completed. The upward growth of the hydraulic fractures was more significant than the downward growth. This behavior is also

supported by the observed microseismic events (Tan et al., 2021) and a comprehensive integrated data analysis (Zhang et al., 2021).

2. Considerable upward fracture height growth after well shut in. Continued fracture height growth was found after pumping stopped which ultimately increased the total fracture height to ~1300-1800 ft.
3. Very complex strain rate patterns for a small fiber-to-stage offset. The characteristic of the strain rate pattern varied as a function of distance between the fiber and the stage. A very complex pattern with many alternating red and blue strips sloping upwards was observed for the closest stage. These strips gradually disappeared as the stage moving farther away from the fiber, which makes the strain rate pattern to be cleaner and simpler.

Methodology

We use the Chevron proprietary 3D fully coupled finite element simulator, capable of modeling dynamic fracture propagation, to investigate the key observations mentioned above. The simulator combines hydraulic fracture growth, multiphase porous flow, heat convection and conduction, and poroelastic deformation in a single application, in an implicit fully coupled formulation. However, the modeling in this study is limited to isothermal and single-phase flow conditions.

The simulator allows multiple hydraulic fractures in a single simulation, but all propagating fractures are currently restricted to being along the sides, top, or bottom of a single 3D grid. The geomechanical and porous flow modeling for the reservoir is performed in the 3D grid, while 2D grids are set up for the hydraulic fractures whose paths are pre-defined along specific boundaries. The 3D reservoir grid and 2D fracture grids communicate through both geomechanical and fluid flow parameters. The geomechanical and porous flow solutions of the reservoir regulate the fracture modeling through the calculations of fracture widths, fracture propagation criteria, and leakoff rates, while the solved fluid pressures within the fractures controls reservoir modeling by providing normal traction and pore pressure boundary conditions. The governing equations of this hydraulic fracturing model are briefly introduced below, while additional details (such as the numerical implementation and validation) are available at Dean and Schmidt (2009).

Reservoir-Flow Model

The mass conservation equation for porous flow in reservoir is written as

$$\frac{\partial}{\partial t}(\rho\varphi) + \nabla \cdot (\rho \boldsymbol{v}) = 0$$

Eq. G 1

where φ is the porosity, ρ is the fluid density, and $\boldsymbol{v}$ is the fluid velocity vector defined by Darcy's law as

$$\boldsymbol{v} = -\frac{k}{\mu}(\nabla p - \rho g \nabla h)$$

Eq. G 2

where k is the permeability, μ is the fluid dynamic viscosity, p is the fluid pressure, g is the gravitational constant, and h is the vertical depth.

Geomechanical Model

The strain-displacement relation of the rock is expressed as

$$\varepsilon_{ij} = \frac{1}{2}\left(u_{i,j} + u_{j,i}\right)$$

Eq. G 3

where ε_{ij} is the strain (expansion corresponds to positive strains in this paper), and u_i and u_j are the displacement in the i-direction and j-direction, respectively, and the subscripted comma followed by an index indicates partial differentiation with respect to each coordinate. The equilibrium equation is defined as

$$\sigma_{ij,j} + f_i = 0$$

Eq. G 4

where σ_{ij} is the total stress and f_i is the body force in the i-direction. According to poroelastic theory, the constitutive relation for the deformed rock is written as

$$\sigma_{ij} = \sigma_{ij}^0 + \frac{E}{1+\nu}\left(\varepsilon_{ij} + \frac{E}{1-2\nu}\varepsilon_{kk}\delta_{ij}\right) - \alpha(p - p^0)\delta_{ij}$$

Eq. G 5

where σ_{ij}^0 is the in-situ stress, p^0 is the initial pore pressure, E is the elastic modulus, ν is the Poisson's ratio, α is a Biot's constant, and δ_{ij} is the Kronecker delta.

The relationship between the porosity, the strains, and the pore pressure is defined as

$$\varphi = \varphi_0 + \alpha\varepsilon_{ii} + \frac{1}{M}(p - p_0)$$

Eq. G 6

where φ_0 is the initial porosity, M^{-1} is a second Biot's constant.

Fracture Model

The volumetric flow rate per unit length within the fracture is defined by Poiseuille's law as

$$\vec{Q} = -\frac{w^3}{12\mu}(\nabla p - \rho g \nabla h)$$

Eq. G 7

where w is the fracture width calculated by the reservoir geomechanical model. The conservation of mass in the fracture is written as

$$\frac{\partial}{\partial t}(\rho w) = -\nabla(\rho Q) + q_w - q_L$$

Eq. G 8

where q_w represents well injection into the fracture, and q_L accounts for the leakoff from the fracture into the reservoir which is calculated by the fluid flow model in the reservoir.

The fracture propagation is modeled by releasing the nodes at the fracture tip, which are previously constrained by zero displacement, when a fracture-opening criterion is satisfied. For a linear-elastic, plane-strain condition, the width of a mode I fracture near the tip can be expressed in terms of the stress-intensity factor, K_I, as

$$w(\Delta a) = \frac{4(1-\nu^2)}{E} K_I \sqrt{\frac{2\Delta a}{\pi}}$$

Eq. G 9

where Δa is the distance from the fracture tip in the direction normal to the leading edge of the fracture. A node at the fracture tip will be released when the fracture width at a neighboring node exceeds

$$w_{neighbor} \geq \frac{4(1-\nu^2)}{E} K_{IC} \sqrt{\frac{2\Delta a_{neighbor}}{\pi}}$$

Eq. G 10

where K_{IC} is the toughness of the rock and $\Delta a_{neighbor}$ is the distance from a neighboring node to the node at the fracture tip.

Model setup and result extraction (dense time domain output)

The problem considered is the propagation of one wing of a planar hydraulic fracture from a horizontal well, as shown by Fig G 4. The reservoir was set to be a cuboid with a length (X) of 2500 ft and a width (Y) of 555 ft, and its depth spans from 9500 ft to 12000 ft. The horizontal well was landed at a depth of 11625 ft along Y axis and perforated at the location of Y = 0. This pre-defines the fracture path to be along one side of the 3D reservoir grid, i.e., the boundary of Y = 0. Multiple vertical wells with fibers were set along a vertical plane parallel with and at 237.5 ft away from the treatment horizontal well (i.e., X = 237.5 ft), and their distances from the fracture range from 0 to 555 ft to examine the strain and strain rate fields at different locations.

Table G 1—Reservoir properties used in simulations

Reservoir Property	Value
Porosity, φ (-)	0.08
Permeability, k (mD)	0.0005
Biot's constant, α (-)	0.5
Toughness, (psi*in$^{1/2}$)	1000

Sonic logging interpretation provides the mechanical properties and in-situ stresses for the reservoir modeled in this section. The interpreted Young's modulus, E, Poisson's ratio, $\boldsymbol{\nu}$, and minimum horizontal stress, S_{hmin}, were assigned to the model (see Fig G 5(a), (b), and (c)). A modified S_{hmin} profile was also employed to allow the model results to better match observed

fracture height growth rate. This will be discussed in detail in the next section. The other properties of the reservoir were assumed to be homogenous as listed in Table G 1.

Initially, the boundary conditions of the 3D reservoir grid included a constant traction of 9988 psi applied on the top with roller boundaries along all the other sides, and all the boundaries were set as no-flux. During fracture propagation and shut-in, the boundary conditions of the fracture wall (the nodes satisfying the fracture-opening criterion on the boundary of Y = 0) were switched to traction- and pressure-controlled determined by the fluid pressure within the fracture. The fracturing fluid was injected to the fracture through the cells connected with the perforation cluster of the horizontal well. The total pumping duration was 180 min followed by a shut-in stage of 120 min. The vertical strain within the reservoir along the plane of X = 237.5 ft was recorded in every timestep, which allows the calculation of vertical strain rate in a dense time domain at any arbitrary fiber location along that plane.

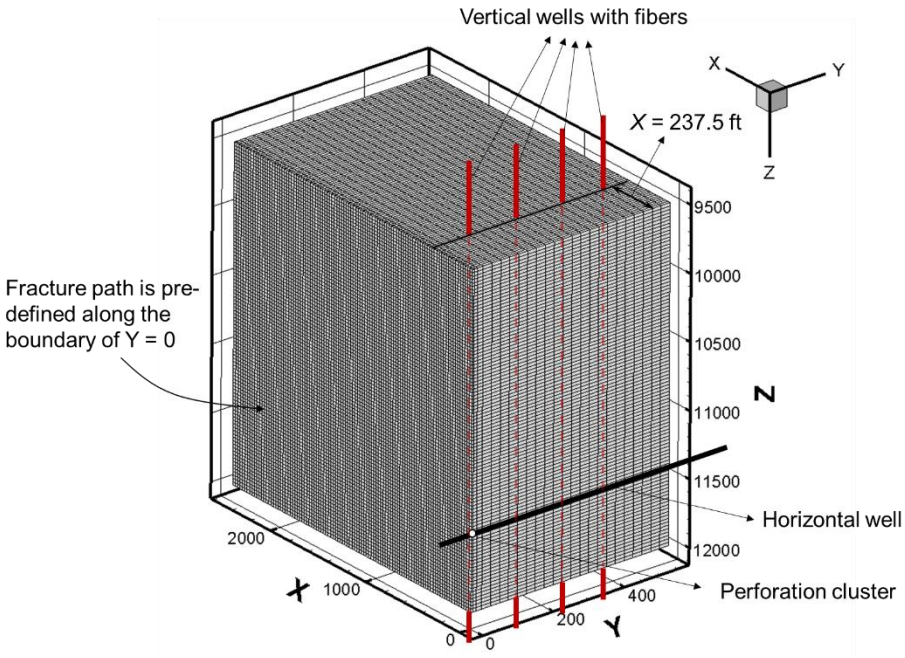

Fig G 4—Hydraulic fracturing model geometry. The propagation of one wing of a planar fracture from a horizontal well is considered. The fracture path is pre-defined along the boundary of Y = 0. Multiple vertical wells with fibers were installed along the plane of X = 237.5 ft to monitor the strain/strain rate responses.

Discussion of results

In this section, we present the simulated height growth of a single hydraulic fracture and the resulting strain/strain rate fields at various locations within the reservoir. Mechanisms causing the complex DAS-observed strain rate patterns in HFTS-2 are then investigated based on simulation results.

Hydraulic fracture height growth

The original S_{hmin} obtained from well log interpretation was first used to perform a hydraulic fracturing simulation. However, the fracture height in this case was constrained by high stress

contrast in layers around the depth of 11200-11300 ft, and the height growth rate is only ~3-4 ft/min (see Fig G 6) which is much smaller than the observed values from the vertical fiber in HFTS-2. Considering many uncertainties and limitations involved in the interpretation of acoustic logging data, a modified S_{hmin} profile was generated by averaging the measured S_{hmin} and 0.7 times the vertical stress with a few thin layers with high stress contrast and gradient removed, as shown by Fig G 5(c). It was then used in the hydraulic fracturing modeling instead of the original S_{hmin}. The modeling results show that a fracture height growth rate of ~8-10 ft/min was achieved with this modified S_{hmin} profile and the fracture height reached ~1400 ft after pumping stops, which is similar to the field observations. Although there are uncertainties in the modified stress accurately representing the field, it is evident that the excessive hydraulic fracture height growth is achievable if the stress contrast between layers is limited.

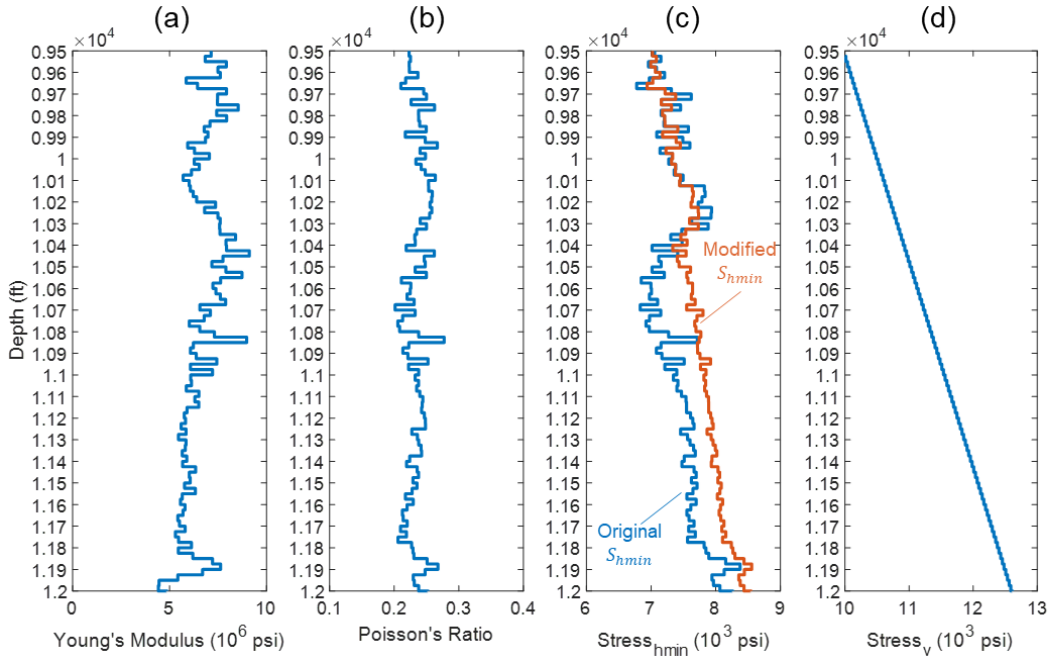

Fig G 5—Reservoir mechanical properties and in-situ stresses used in the simulations. (a) Young's modulus, (b) Poisson's ratio, and the original minimum horizontal stress in (c) are interpreted from the acoustic logging data. A modified minimum horizontal stress is also employed in the simulation. (d) The vertical stress is obtained by assuming a constant gradient. The horizontal well was landed at the depth of 11625 ft in the model.

The evolution of the fracture geometry for the case with modified S_{hmin} is shown in Fig G 7. The fracture initiated from the wellbore and kept growing laterally and upwards. Its downwards propagation is limited by the high stress zone below the wellbore. It should be noted that the simulated fracture length is smaller compared with the observations in HFTS-2. This may attribute to a single fracture model in this study, which assumes uniform treatment placed into each cluster and excludes the stress shadow interference among multiple propagating fractures. However, this difference in fracture length is inconsequential for this study as the focus is the strain/strain rate responses monitored by the vertical fibers. The red dashed line in Fig G 7

indicates the plane along which the vertical fibers were located, and it was passed by the fracture tip at a time around 50 min.

Continued fracture height growth after shut-in was not achieved in the simulations as the numerical algorithm used in the simulator always iterates for an equilibrium solution at each timestep which prohibits continued node-opening without additional fluid supply. Studies on post-injection growth of a hydraulic fracture receive less attention compared to the injection stage, but can be found in Garagash (2006), Chuprakov et al., (2017), Wang et al. (2018), etc.

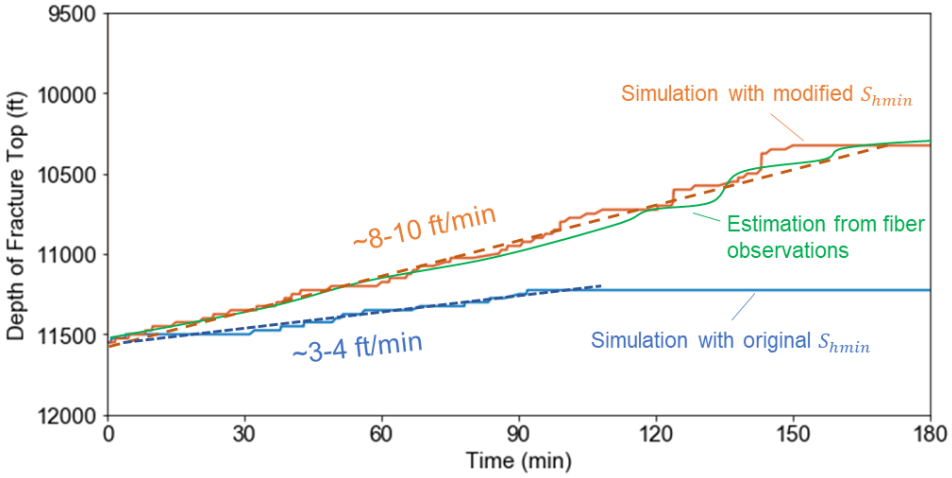

Fig G 6—Depth of the top of the hydraulic fracture as a function of time for two simulation cases with different minimum horizontal stress profiles. The blue line results from the original S_{hmin} interpreted from downhole measurements, while the orange line results from the modified S_{hmin} profile. The green line represents an estimation from fiber observations.

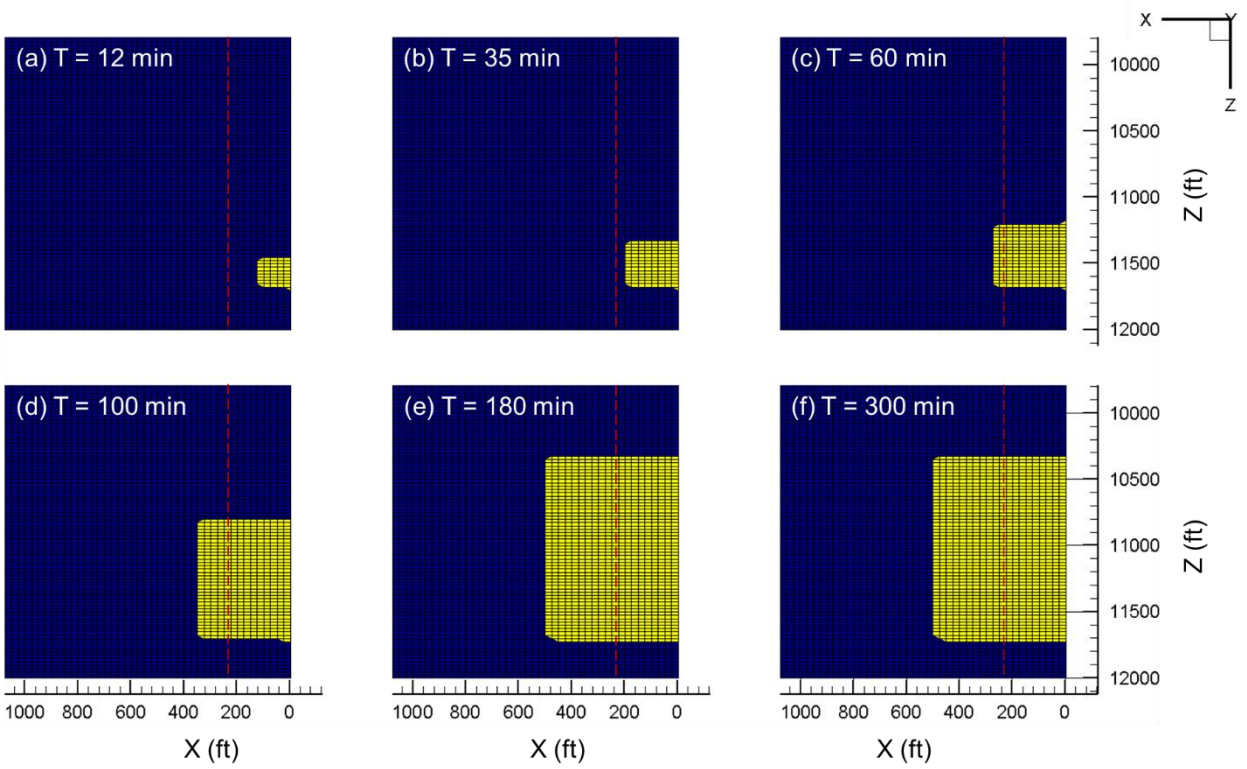

Fig G 7—Geometry of simulated hydraulic fracture (one wing) at different time instants. Pumping stops at 180 min and the well is shut in afterwards. The red dashed lines represent the plane along which the vertical fibers locate.

Responses of strain and strain rate to hydraulic fractures

Before looking at the temporal evolution of strain/strain rate along a vertical fiber, it is beneficial to explore the spatial distribution of the vertical strain along the vertical plane perpendicular to the fracture. Fig G 8 illustrates this spatial distribution along the plane of X = 237.5 ft at different times for the case with modified S_{hmin}. Since the fracture front tip reached this plane at T = ~50 min, Fig G 8(a) and (b) show the scenario with a propagating fracture towards this plane, while the other four subfigures are for the situation where the fracture intersected with the plane. It is worth noting that the vertical strain field shows a marked response to the propagating fracture even at a very early time (T = 12 min) when the fracture front tip is still ~115 ft away, and this response became stronger as the fracture continued approaching to this plane. It is apparent from Fig G 8(a) and (b) that there is a compression zone with an elliptical shape in front of the fracture. Three extension zones are observed above, below, and on the side of this compression zone radiating outwards into the reservoir. These three extension zones are separated by two additional compression zones. The overall characteristic of this vertical strain distribution still maintains similar after the fracture crossing this plane. However, strong strain concentrations occurred around the fracture tips in both extension and compression zones, as shown by Fig G 8(c)-(f) and highlighted in Fig G 8(d) for an example. At T = 180 min, the compression zone

around the fracture was penetrated by the extension zone on the side at the depth of ~10800-11100 ft, which is possibly due to a few local layers with high modulus and high Poisson's ratio.

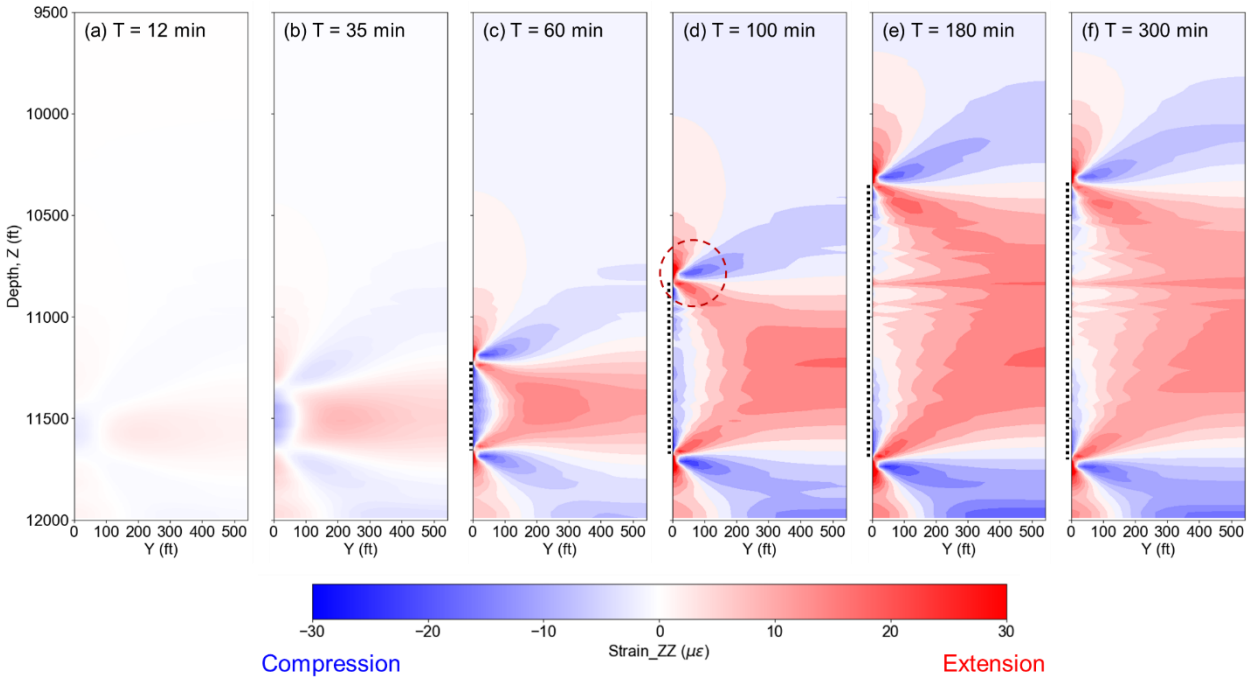

Fig G 8—Distribution of vertical strain along the plane with vertical fibers (X = 237.5 ft) at six different time instants. The fracture tip reached this plane at T = ~50 min. The black dashed line represents the fracture height. As an example, the red dashed circle highlights a strain-concentrated region (with both extension and compression) around the fracture tip.

Fig G 9 shows the temporal evolution of strain and strain rate fields (waterfall plots) by vertical fibers at various distances from the fracture along the plane of X = 237.5 ft. The black dashed lines represent the outlines of fractures. The strain fields highlight the fracture body across the

entire height. They show compression when the fiber is close to the fracture (Fig G 9(a)) and gradually change to extension as the fiber moves farther away (Fig G 9(c), (e), and (g)).

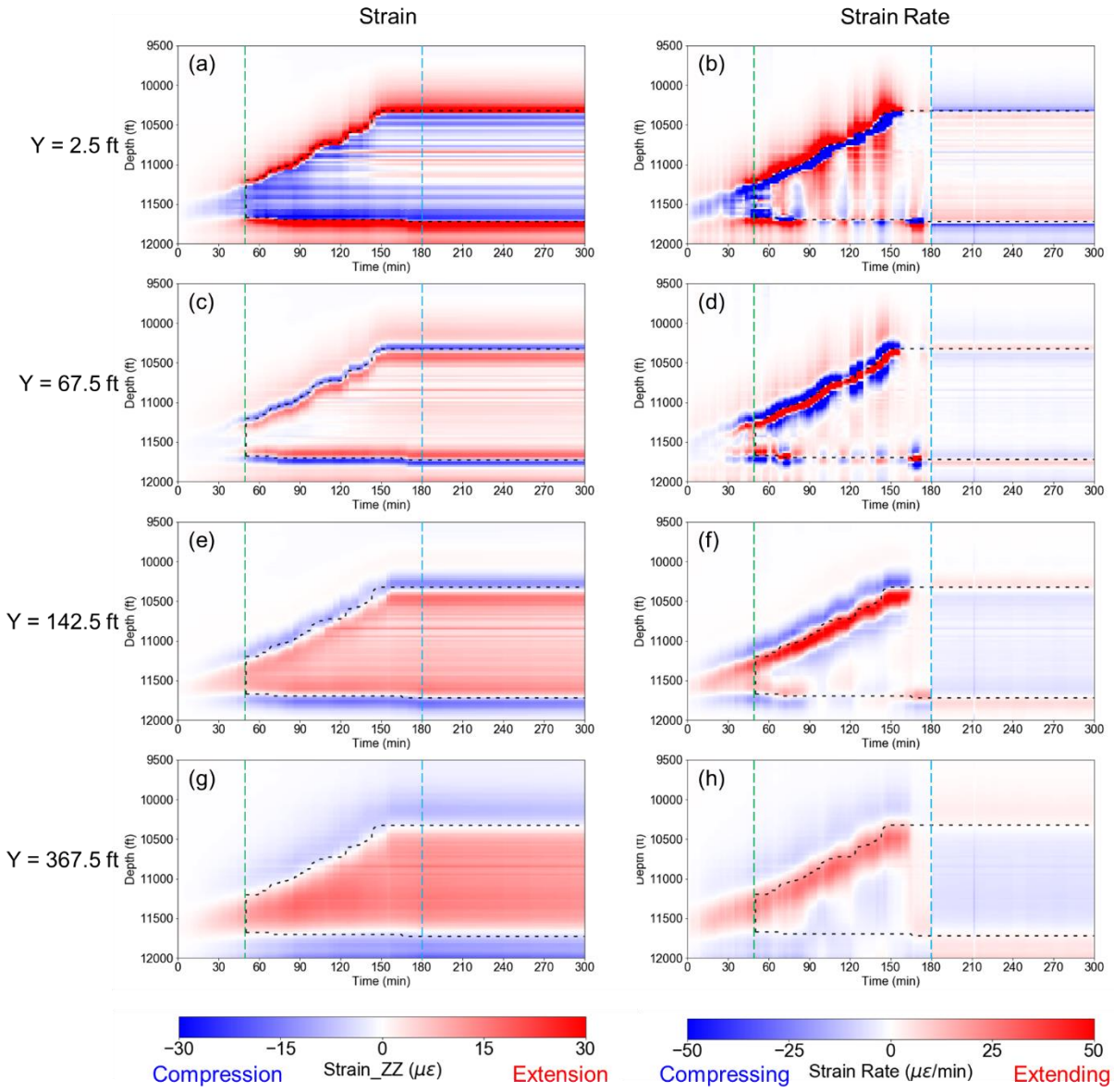

Fig G 9—Modeled DAS strain and strain rate responses by vertical fibers with various offsets from the fracture. The offsets are labeled on the left of each row. The fibers were set at the plane of X = 237.5 ft. The green dashed lines represent the times when the fracture front tip reached this plane. The blue dashed lines represent the times of well shut in. Note that the strain rate after shut in was magnified 300 times to increase the visibility. The black dashed lines represent the outlines of fractures.

Strain concentrations are apparent around the top and bottom tips of the fracture for a relatively small fracture-fiber offset (Fig G 9 (a) and (c)), as illustrated by the red dashed circle in Fig G 8. Unlike the strain field data, the strain rate patterns can better capture the fracture tips due to the significant strain variations around them during fracture propagation. Two strips, one red and one blue, were observed extending upwards when the fiber was very close to the fracture (Y = 2.5 ft, as shown by Fig G 9(b)), and the interface between them tracked the depth

of the fracture top. This pattern was changed to one red strip sandwiched by two blue strips when the fracture-fiber offset was increased to Y = 67.5 ft (Fig G 9(d)), and again, the top interface was almost overlapped with the fracture boundary. As the fiber moved farther away, these blue and red strips were gradually widened and smeared, and a big red zone was formed below the upward-growing fracture top tip at Y = 367.5 ft (Fig G 9(h)). The top edge of this red zone can be used as an approximation for the location of the fracture top tip.

The regions in vicinity of the fracture bottom tip were relatively quiet in terms of the strain rate response, due to the limited downward propagation of the fracture. Similar quiet zones were also found around the fracture top tip when a plateau of upward propagation was reach around T = 160 min. The strain rate responses of the fracture body were relatively faded, and relaxations of the bottom part of the fracture were observed due to the slight reduction of the fracture width, as illustrated in Fig G 10.

The green dashed lines in Fig G 9 represent the times when the fracture front tip passed the fibers. It is interesting that the strain rate field detected the approaching fracture at a very early time, even though the fracture front tip was still hundreds of feet away. This effect should be taken into consideration when the field DAS-observed strain rate data is interpreted, since the fracture-arrival time might be later than a strain rate pattern shows. The blue dashed lines indicate the times when pumping stops (T = 180 min). The strain rate fields experienced polarity flips because the fracture changed from dilation to deflation due to the cease of fluid supply and continued leakoff. It should be noted that the original strain rate after pumping stops was too small to be visualized due to the extremely small leakoff rate, and thus, it was manually magnified 300 times in Fig G 9 for a better visualization. The simulated strain rate patterns illustrated in this section could serve as templates for the interpretation of fracture height based on the low-frequency DAS data in the future.

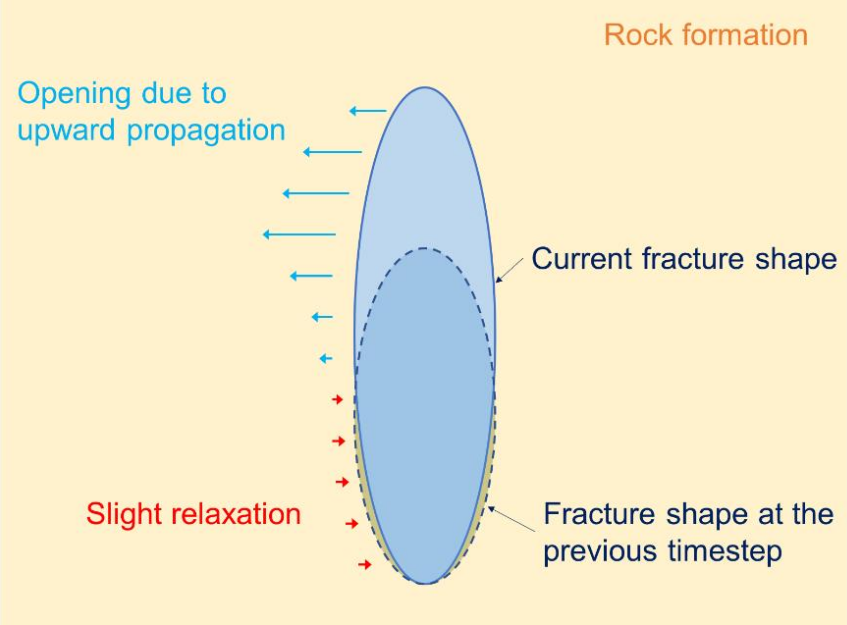

Fig G 10—Schematic of fracture width change due to upward propagation. The solid and dashed ovals represent the fracture cross-sectional shapes at the previous and current timesteps, respectively. The blue and red arrows illustrate the changes in fracture width along the fracture height between the two timesteps. Note that an extremely large fracture height growth (not-to-scale) was plotted here for a better visualization.

Complex strain rate patterns for small fiber-stage offsets

The DAS strain rate responses observed from HFTS-2 show complex patterns with alternating red and blue strips when the fractured stage is close to the monitor vertical fiber (see Fig G 2(a)). Initially, we hypothesized that these complex patterns were caused by the variation of rock mechanical properties in different layers. Since the strain rate patterns obtained from the simulations in the previous subsection are relatively clean without strips in fracture body regions (Fig G 9(b) and (d)), we performed two more cases with increased contrasts in mechanical properties between layers. One of them is with alternating Poisson's ratios of 0.28 and 0.2 in layers and a homogenous Young's modulus of 6.5×10^6 psi, as shown by Fig G 11(a) and (b). Fig G 11(c) and (d) illustrate the strain rate patterns captured by vertical fibers at small and large distances from the fracture, respectively. The strain rate pattern did show strips across the entire fracture body. But most of these strips are along horizontal direction in the waterfall plot and are aligned with the layers. Similar observations were found with alternating Young's moduli of 9×10^6 psi and 4×10^6 psi in layers and homogenous Poisson's ratio of 0.24 (Fig G 12). The strain rate patterns resulting from high contrasts in mechanical properties are different from the DAS-observed patterns, where the strips are not necessarily aligned with layers. Therefore, the complex DAS-observed strain rate patterns should not be attributed to the mechanical layering.

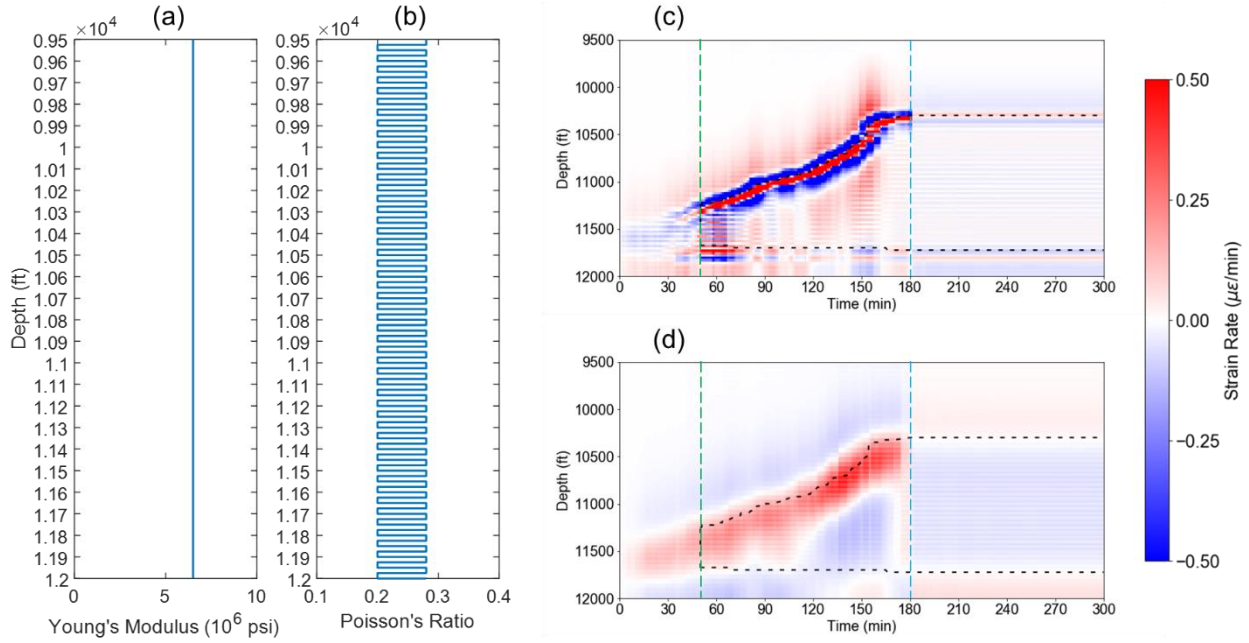

Fig G 11—Hydraulic fracturing simulation with (a) a homogenous Young's modulus and (b) alternating Poisson's ratios in layers. (c) and (d) are the modeled strain rate patterns monitored by vertical fibers at ~40 ft and ~400 ft away, respectively.

After rejecting the hypothesis about mechanical layering, we propose that the complex DAS-observed strain rate patterns might result from the effect of multiple fractures. Since the simulator is incapable of modeling propagation of multiple fractures, we proposed a method to approximate the strain rate patterns for multiple fractures within a stage based on superposition of simulation with single fractures. It is assumed that five equally spaced fractures were created in a stage and propagated in parallel without interacting with each other. Two different scenarios are considered here: (i) all the fractures took the same amount of fluid and arrived at the fiber at the same time (Fig G 13(a)); and (ii) the heel clusters took more fluid than the toe clusters and the fractures passed the fiber with time offsets (Fig G 13(b)). The second scenario better represents the reality than the first one since the heel clusters generally experience less stress shadow from the previous stages. This is supported by strain rate pattern monitored by a horizontal fiber as shown in Fig G 3. A vertical fiber was installed with an offset from the stage center. The strain rate patterns monitored by this fiber is calculated by superposing the strain rate response resulting from individual fracture.

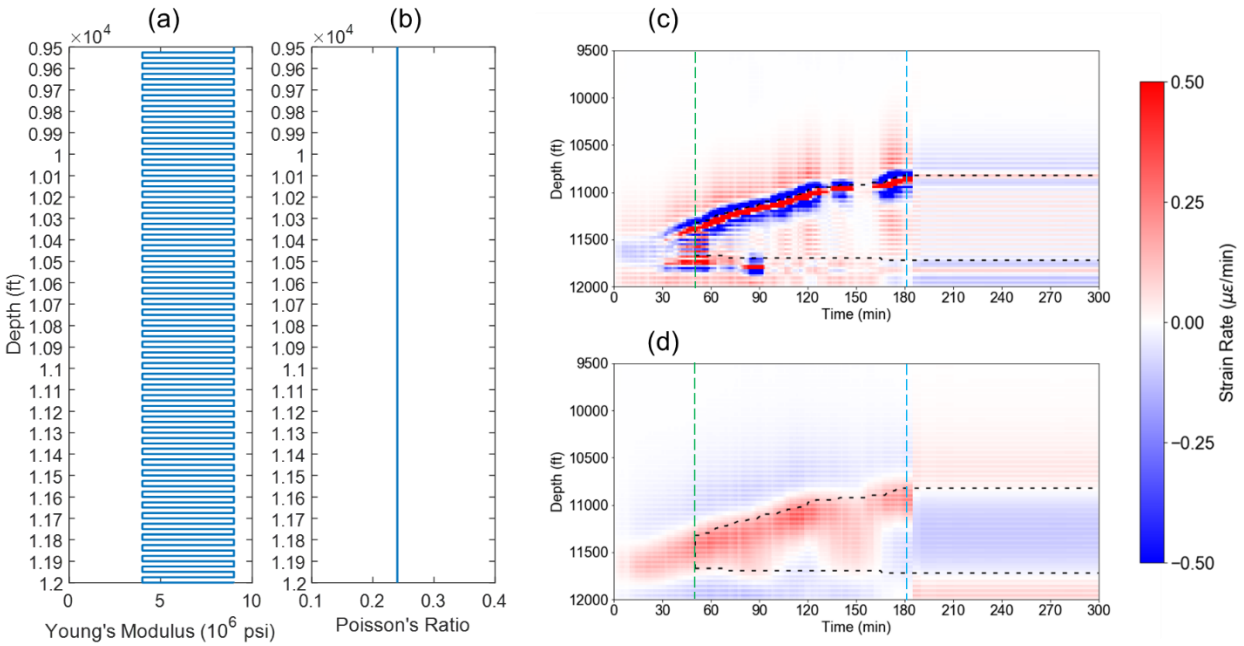

Fig G 12—Hydraulic fracturing simulation with (a) alternating Young's moduli in layers and (b) a homogenous Poisson's ratio. (c) and (d) are modeled strain rate patterns monitored by vertical fibers at ~40 ft and ~400 ft away, respectively.

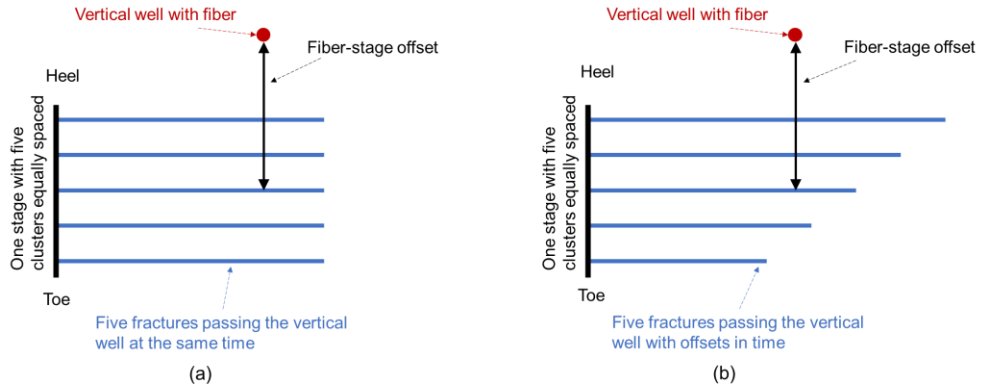

Fig G 13—Map view of five equally spaced fractures within a stage passing a vertical fiber (a) at the same time and (b) with time offsets. Strain rate patterns monitored by the fiber can be obtained by superposing the strain rate resulting from each individual fracture.

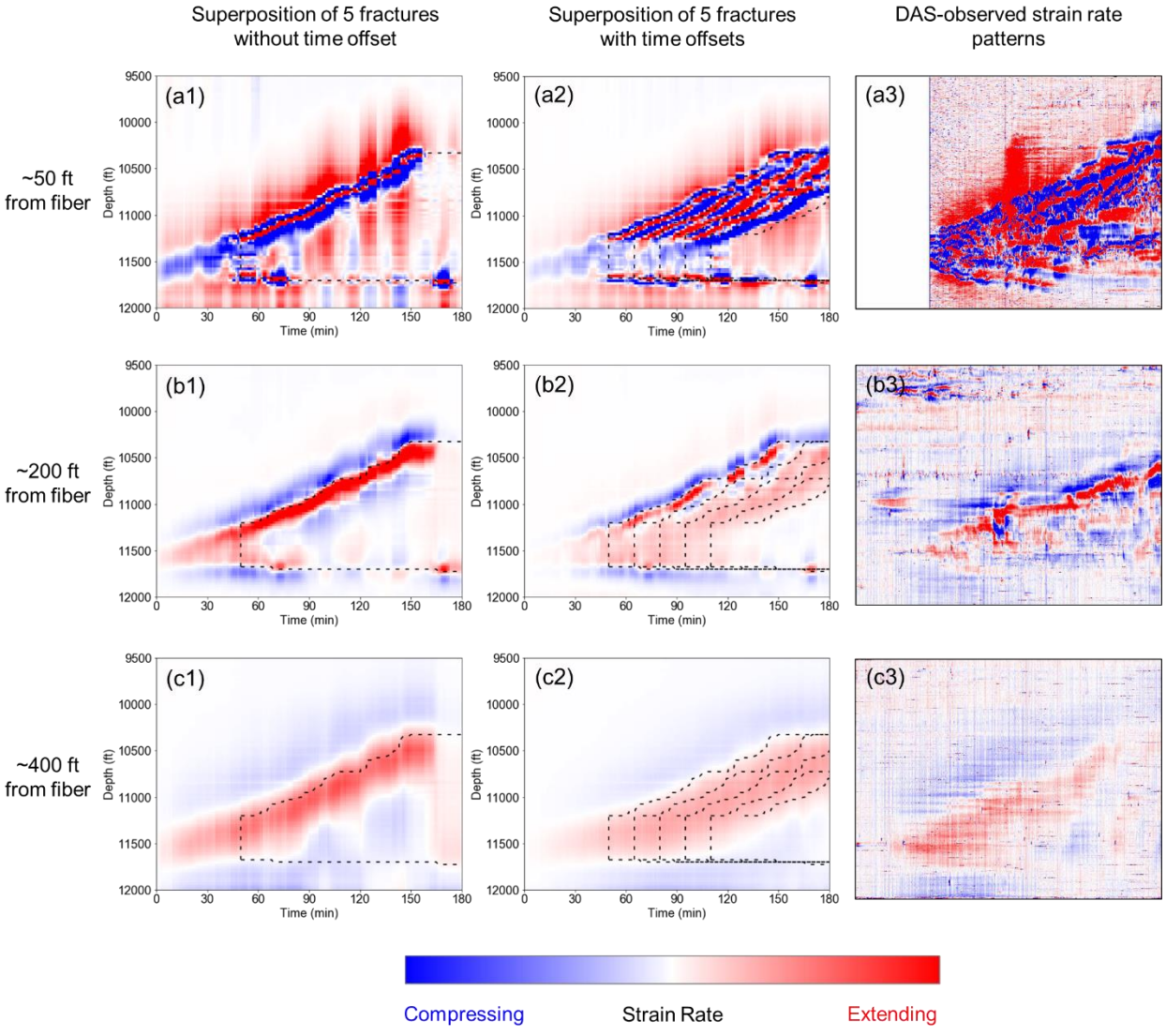

Fig G 14—(a1, b1, c1, a2, b2, and c2) Modeled and (a3, b3, and c3) observed DAS strain rate responses to multiple fractures within a stage. They are monitored by vertical fibers with different offsets from the stage center, and the offset values are labeled on the left of each row. (a1), (b1), and (c1) are for the scenario with all fractures passing the fiber at the same time, while (a2), (b2), and (c2) are for the scenario with fractures passing the fiber with time offsets. The black dashed lines represent the outlines of fractures.

Fig G 14 shows the modeled DAS strain rate patterns for both the two above-mentioned scenarios with different fiber-stage offsets. The strain rate responses to multiple fractures are very similar to those to a single fracture if all the fractures pass the fiber at the same time, as can be seen from Fig G 14(a1), (b1), and (c1). If the fractures propagated at different velocities and passed the fiber sequentially with time offsets, the strain pattern becomes quite complex for the stage closest to the fiber (fiber-stage offset of ~50 ft), as shown by Fig G 14(a2). Several alternating red and blue inclined strips were observed from the waterfall plot which is very similar to the DAS-observed strain rate pattern in HFTS-2 (Fig G 14(a3)). This suggests that the multiple fracture effect is the plausible mechanism of the complex strain rate patterns observed for the small fiber-stage offsets. These strips track the boundaries of each individual fracture, which makes it possible to approximate the number of the main hydraulic fractures in this stage and the height of each fracture. However, there is still a "clean" region in this strain rate pattern around the bottom part of the fractures. This suggests that (i) the hydraulic fractures created are more complicated because of bifurcation, swarming, interaction with natural fractures, bedding slip, etc. (Gale et al., 2018); and (ii) height growth rate of each individual fracture within a stage is different due to stress shadow effect. When the stage is farther away from the fiber, these red and blue strips become blurred (fiber-stage offset of ~200 ft as shown by Fig G 14(b2)) and then disappeared (fiber-stage offset of ~200 ft as shown by Fig G 14(b3)). This is also consistent with the DAS-observed strain rate patterns (Fig G 14(b3) and (c3)). Admittedly, the superposition method used here is a first-order approximation which has oversimplified the problem, however, in view of the modeling difficulties, this analysis is adequate to bring some fundamental and delicate insights into the strain rate responses of a vertical fiber to the propagation of multiple fractures.

Conclusions

The HFTS-2 provides a unique opportunity to infer the hydraulic fracture geometries through a comprehensive dataset obtained by a leading-edge surveillance program. In this study, the low-frequency DAS strain data monitored in a vertical pilot hole, combined with an advanced geomechanical modeling, was used to understand hydraulic fracture height growth in HFTS-2.

Excessive hydraulic fracture height growth (~1000-1500 ft) was observed during pumping with the upward growth much more significant than the downward growth. The average height growth rate was approximately 8-10 ft/min. Similar height growth was achieved in the numerical modeling. Considerable upward height growth (~300 ft) after shut-in was observed from the low-frequency DAS strain data, but the numerical simulations were not able to show this behavior due to numerical algorithm limitation.

Simulated strain rate patterns resulting from a single fracture displayed different characteristics for different fracture-fiber offsets. The upward growing fracture top tip was identifiable by the interfaces between extending and compressing zones. The HFTS-2 low-frequency DAS strain data showed a complex strain rate patterns when the stage is very close to the monitoring

vertical fiber. It was demonstrated by the simulation results that a plausible cause of this phenomenon was the simultaneous propagation of multiple fracture at different rates. The simulated strain rate patterns could be utilized as templates for fracture height interpretation from low-frequency DAS data in future.

References

Chuprakov, D. A., Izimov, R. M., & Spesivtsev, P. E., 2017. Continued hydraulic fracture growth after well shut-in. Paper presented at 51st US Rock Mechanics/Geomechanics Symposium. American Rock Mechanics Association.

Ciezobka, J., Courtier, J., & Wicker, J., 2018. Hydraulic fracturing test site (HFTS)–project overview and summary of results. Paper presented at Unconventional Resources Technology Conference, Houston, Texas. https://doi.org/10.15530/urtec-2018-2902355

Ciezobka, J. & Reeves, S. 2020. Overview of Hydraulic Fracturing Test Sites (HFTS) in the Permian Basin and Summary of Selected Results (HFTS-I in Midland and HFTS-II in Delaware). Paper presented in Latin America Unconventional Resources Technology Conference, Virtual. https://doi.org/10.15530/urtec-2020-1544

Gale, J. F., Elliott, S. J. & Laubach, S. E., 2018. Hydraulic fractures in core from stimulated reservoirs: core fracture description of HFTS slant core, Midland Basin, West Texas. Paper presented in Unconventional Resources Technology Conference, Houston, Texas.

Garagash, D. I., 2006. Plane-strain propagation of a fluid-driven fracture during injection and shut-in: Asymptotics of large toughness. *Engineering fracture mechanics*, **73**(4), 456-481. https://doi.org/10.1016/j.engfracmech.2005.07.012

Jin, G. and Roy, B., 2017. Hydraulic-fracture geometry characterization using low-frequency DAS signal. *The Leading Edge*, **36**(12), 975-980. https://doi.org/10.1190/tle36120975.1

Liu, Y., Wu, K., Jin, G., et al. 2020a. Rock Deformation and Strain-Rate Characterization during Hydraulic Fracturing Treatments: Insights for Interpretation of Low-Frequency Distributed Acoustic-Sensing Signals. *SPE J*, **25**(05): 2251-2264. https://doi.org/10.2118/202482-PA

Liu, Y., Wu, K., Jin, G., et al. 2020b. Fracture-Hit Detection Using LF-DAS Signals Measured during Multifracture Propagation in Unconventional Reservoirs *SPE Res Eval & Eng*, **24**(03): 523–535. https://doi.org/10.2118/204457-PA

Shahri, M., Tucker, A., Rice, C., et al. 2021. High Fidelity Fibre-Optic Observations and Resultant Fracture Modeling in Support of Planarity. Paper presented at the SPE Hydraulic Fracturing Technology Conference and Exhibition, Virtual. https://doi.org/10.2118/204172-MS

Tan, Y., Wang, J., Rijken, P., et al. 2021, Mechanism of Microseismic Generation During Hydraulic Fracturing – With Evidence From HFTS 2 Observations, Paper presented at Unconventional Resources Technology Conference, Houston, Texas. https://doi.org/10.15530/urtec-2021-5296.

Tan, Y., Wang, S., Rijken, M., et al. 2021. Geomechanical Template for Distributed Acoustic Sensing Strain Patterns during Hydraulic Fracturing. *SPE Journal*, **26**(02): 627-638. https://doi.org/10.2118/201627-PA

Ugueto, G. A., Todea, F., Daredia, T., et al. 2019. Can You Feel the Strain? DAS Strain Fronts for Fracture Geometry in the BC Montney, Groundbirch. Paper presented at the SPE Annual Technical Conference and Exhibition, Calgary, Alberta, Canada. https://doi.org/10.2118/195943-MS.

Wang, J., Elsworth, D. & Denison, M.K., 2018. Hydraulic fracturing with leakoff in a pressure-sensitive dual porosity medium. *International Journal of Rock Mechanics and Mining Sciences*, **107**: 55-68. https://doi.org/10.1016/j.ijrmms.2018.04.042

Wang, S., Tan, Y., Sangnimnuan, A., et al. 2019. Learnings from the Hydraulic Fracturing Test Site (HFTS)# 1, Midland Basin, West Texas—A Geomechanics Perspective. Paper presented at Unconventional Resources Technology Conference, Houston, Texas. https://doi.org/10.15530/urtec-2019-1570.

Zhang, Z., Fang, Z., Stefani, J., et al. 2020. Modeling of fiber-optic strain responses to hydraulic fracturing. *Geophysics*, **85**(6): A45-A50. https://doi.org/10.1190/geo2020-0083.1

Zhang, Z., DiSiena, J., Bevc, D., et al. 2021, Hydraulic fracture characterization by integrating multidisciplinary data from the Hydraulic Fracturing Test Site 2 (HFTS-2). Paper presented at Unconventional Resources Technology Conference, Houston, Texas. https://doi.org/10.15530/urtec-2021-5039.

Appendix H: Inference of Induced Fracture Geometries Using Fiber-Optic Distributed Strain Sensing in Hydraulic Fracture Test Site 2

Authors: ***Stephen Bourne, Kees Hindriks, Alexei A. Savitski, Gustavo A. Ugueto, Magdalena Wojtaszek***

Summary

Fiber-optic Distributed Strain Sensor observations in a vertical well allow rapid inference of the time evolution of nearby hydraulic fracture heights and their vertical aperture distributions during stimulation and depressurization. We describe a computationally efficient deconvolutional model based on an elastostatic kernel for fracture opening within an isotropic, homogeneous, linear elastic medium. An application of this model to observations from the Hydraulic Fracture Test Site 2 reveals that ultimate fracture heights are typically greater than those indicated by microseismic monitoring, and some hydraulic fractures continue their upward growth for several hours after high-pressure injections ceased.

Introduction

Ensuring the containment of hydraulically induced fractures below suitable geological seals is critical to maintaining the subsurface integrity of conventional or unconventional hydrocarbon production, CO_2 storage or geothermal extraction processes. Where hydraulic fractures are engineered, such as to enable or enhance unconventional hydrocarbon production, then ensuring the vertical fracture extents remain within the target zone helps to lower costs and improve production. This all requires suitable monitoring methods to verify fracture containment and, if necessary, to provide reliable alerts that enable timely and effective deployment of control measures. Distributed Strain Sensors deployed within a nearby vertical well may offer a suitable monitoring capability if reliable information about vertical fracture extents can be extracted from the observed strain fields in a timely fashion.

Fiber-optic Distributed Temperature Sensor (DTS), and Distributed Acoustic Sensor (DAS) signals are routinely used to monitor hydraulic fracture stimulations (Molenaar, Fidan, and Hill 2012) and their associated microseismic emissions (Karrenbach et al. 2019), but knowledge about vertical fracture extents remained limited. More recently, fiber-optic Distributed Stain Sensors (DSS), sometimes known as Low-Frequency Distributed Acoustic Sensors (LF-DAS), began to measure the strain field induced by hydraulic fracturing (Jin and Roy 2017). This led to the rapid growth of DSS field observations and their qualitative interpretation to infer hydraulic fracture geometries (Ichikawa et al. 2019; Ugueto et al. 2019; Richter et al. 2020; Wu et al. 2020; Jin et al. 2021). To aid these interpretations, geomechanical models compute the

expected DSS fiber-strains induced by a given geometry of hydraulic fracturing using 3D finite-element (Sherman et al. 2019; Tan et al. 2020) and 3D boundary-element (Liu et al. 2020; Zhang et al. 2020) methods.

Building on these models, there are some quantitative analyses of horizontal-fiber strain rates observations to estimate fracture-fiber intersection times (Jin et al. 2019), and fracture width time series (Liu et al. 2021; Liu, Jin, and Wu 2021; Liu et al. 2021b). Fracture widths at the fracture-fiber intersection are estimated using a least-squares inversion, where the matrix of

influence coefficients between finite fracture sources and the DSS fiber-strains are computed as the integral of point source elastostatic solutions over each source element according to the boundary element method. As the fiber is orthogonal to the fracture plane, this geometry is predominately sensitive to the time-evolution of fracture apertures close to the fracture-fiber intersection and offers limited sensitivity to the either the vertical or horizontal distribution of fracture apertures further away from the fiber.

This boundary element method is applicable to a wide range of fracture-fiber geometries but may be computationally slow. For some geometries, solutions may be obtained using faster Fourier transform methods (Segall 2010). A vertical fiber offset from a vertical deep fracture is one such suitable geometry and will also be sensitive to the distribution of fracture apertures along the vertical line formed by the projection of the fiber on to the fracture surface. This combination of computational efficiency and vertical resolution of the fracture geometry should offer advantages for fracture containment monitoring.

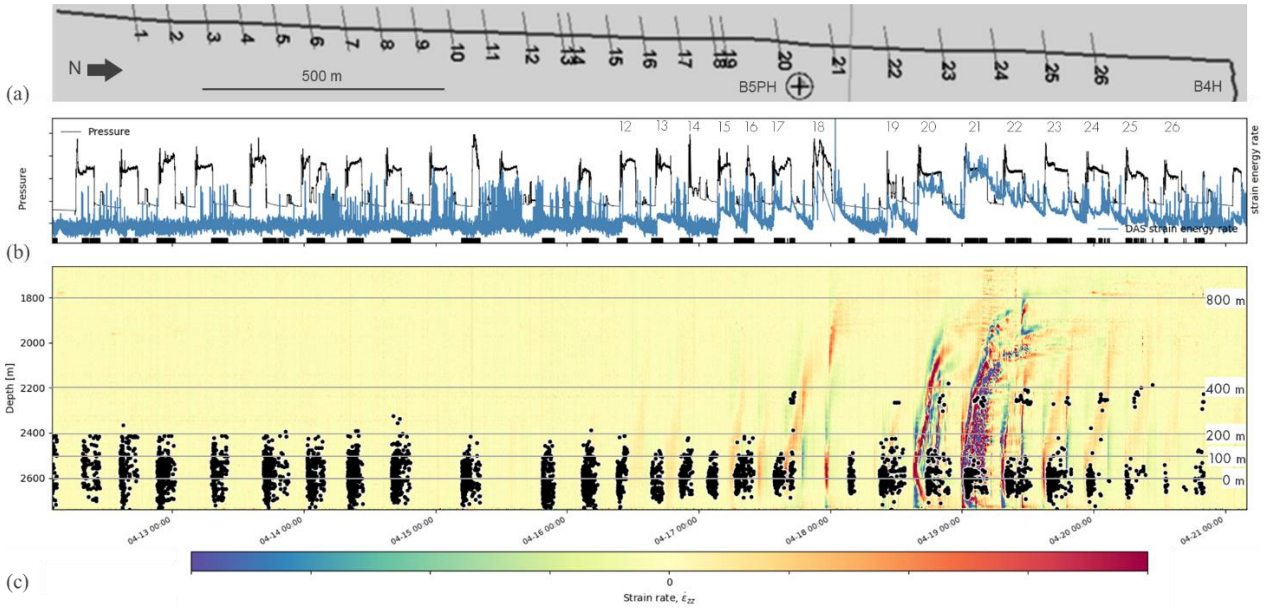

Fig H 1— (a) Map locations of the vertical observation well B5PH instrumented with fiber-optic distributed strain sensing, and the horizontal B4H well path with its hydraulic fracture stimulation stages 1-26. Tick marks denote the fracture orientations for each stage. Well B5PH is located within 100 m of well B4H and within 150 m of the closest stimulation stage (20). (b) Time series of well head pressures (black curve), fiber strain energy rates (blue curve), and microseismic events (black ticks) during hydraulic fracture stimulations of horizontal well B4H with stages 12—26 labelled. (c) The associated time series of vertical fiber strain rates, $\dot{\varepsilon}_{zz}(t,z)$, recorded in observation well B5PH and microseismic event depths (black dots). Grey lines denote heights above the perforations.

The Hydraulic Fracture Test Site 2 in the Permian Delaware Basin, West Texas provides an opportunity to evaluate the capabilities of fiber-optic Distributed Strain Sensors for fracture containment monitoring. Of interest is the horizontal production well, BH4, drilled within the Wolfcamp shale formation and, subsequently, stimulated by hydraulic fracturing. To monitor these hydraulic fracture stimulations, a vertical well, B5PH, is located within 100m of B4H and instrumented with a fiber-optic Distributed Strain Sensor (Fig H 1). A microseismic monitoring

system comprising of five down-hole geophone arrays provides comprehensive coverage along the length of B4H.

Theoretical aspects

Hydraulic fracturing induces a strain tensor field, $\varepsilon_{ij}(t,\mathbf{x})$, that varies with time, t, and location, $\mathbf{x}$, within the surrounding medium that encodes information about evolving fracture aperture field, $a(t,\mathbf{x}_f)$ over the fracture surface locations, $\mathbf{x}_f$. Fiber-optic Distributed Strain Sensors sample one component of this strain tensor field, $\varepsilon_w(t,\mathbf{x})$, along the fiber path locations, $\mathbf{x}$. This information allows inference of fracture aperture field for the region of the fracture closest to the fiber. The strain fields induced by displacement discontinuities distributed over dislocation surfaces within an isotropic homogeneous linear elastic half-space may be obtained using superposition of the point source solution for an opening-mode dislocation (Mindlin 1936; Okada 1992),

$$\varepsilon_{ij}(t,\mathbf{x}) = \int_S a(t,\mathbf{x}_f)\mathcal{L}_{ij}(\mathbf{x}_f,\mathbf{x})d\mathbf{x}_f$$

Eq. H 1

where kernel, $\mathcal{L}$, is the elastostatic strain field at $\mathbf{x}$ due to a unit, point source, a is the opening-mode dislocation at $\mathbf{x}_f$ on fracture surface, S. For a homogeneous half-space and deep fractures where the vertical extent of the fracture is small compared to its depth below the free surface, the elastostatic kernel is stationary, such that $\mathcal{L}(\mathbf{x}_f,\mathbf{x}) = \mathcal{L}(\mathbf{x}_f - \mathbf{x})$, which permits obtaining solutions as a convolution using Fast Fourier Transforms,

$$\varepsilon_{ij}(t,\mathbf{x}) = a(t,\mathbf{x}_f) * \mathcal{L}_{ij}(\mathbf{x}_f - \mathbf{x})$$

Eq. H 2

where $*$ denotes the convolution operator. The strain rate field, $\dot{\varepsilon}_{ij}(t,\mathbf{x})$, then follows as the temporal derivative, $\partial_t\varepsilon_{ij}(t,\mathbf{x})$, that may also be obtained by convolution of the fracture aperture field with a time-dependent elastostatic kernel, such that

$$\dot{\varepsilon}_{ij}(t,\mathbf{x}) = a(t_f,\mathbf{x}_f) * \dot{\mathcal{L}}_{ij}(t_f - t, \mathbf{x}_f - \mathbf{x})$$

Eq. H 3

where t and t_f denote time coordinates for the elastic medium and the fracture apertures, respectively. We then choose to describe the temporal covariance, $\mathrm{K}_{aa}(\Delta t)$, of the fracture aperture field with the stationary exponential quadratic kernel function,

$$\mathrm{K}_{aa}(\Delta t) = e^{-\Delta t^2/2\sigma^2}$$

Eq. H 4

and σ is the characteristic correlation time scale selected to represent the time-sampling. In the limit of instantaneous elastic equilibrium, the temporal covariance between fracture apertures and the elastostatic strain rates of the medium is

$$\mathrm{K}_{a\dot{\varepsilon}}(\Delta t) = \partial_t \mathrm{K}_{aa}(\Delta t) = -\frac{\Delta t}{\sigma^2} e^{-\Delta t^2/2\sigma^2}$$

Eq. H 5

With this result, the strain rate kernel takes the form:

$$\dot{\mathcal{L}}_{\mathrm{ij}}(\Delta t, \Delta \mathbf{x}) = \mathrm{K}_{a\dot{\varepsilon}}(\Delta t)\, \mathcal{L}_{\mathrm{ij}}(\Delta \mathbf{x})$$

Eq. H 6

Fiber-optic Distributed Strain Sensors observe the along-fiber strain, ε_{w}, component of the strain tensor field which depends on the fiber orientation, such that

$$\varepsilon_{\mathrm{w}} = \varepsilon_{\mathrm{ij}} n_i n_j$$

Eq. H 7

and n_i is the unit fiber path vector. In this notation, there is summation over the repeated i and j indices that range over the set of spatial coordinates $\{\mathrm{x}, \mathrm{y}, \mathrm{z}\}$. This allows the elastostatic tensor kernels, $\mathcal{L}_{\mathrm{ij}}$ and $\dot{\mathcal{L}}_{\mathrm{ij}}$, to be contracted to the along-fiber kernels, $\mathcal{L}_{\mathrm{w}}$ and $\dot{\mathcal{L}}_{\mathrm{w}}$, as

$$\mathcal{L}_{\mathrm{w}} = \mathcal{L}_{\mathrm{ij}} n_i n_j$$

Eq. H 8

$$\dot{\mathcal{L}}_{\mathrm{w}} = \dot{\mathcal{L}}_{\mathrm{ij}} n_i n_j$$

Eq. H 9

The convolutional model for Distributed Strain Sensor, ε_{w} or $\dot{\varepsilon}_{\mathrm{w}}$, due to the proximal fracture aperture field, a, may then be written as:

$$\varepsilon_{\mathrm{w}}(\mathrm{t}, \mathbf{x}) \;=\; a(t, \mathbf{x}_f) * \mathcal{L}_w(\mathbf{x}_f - \mathbf{x})$$

Eq. H 10

$$\dot{\varepsilon}_{\mathrm{w}}(\mathrm{t}, \mathbf{x}) \;=\; a(t, \mathbf{x}_f) * \dot{\mathcal{L}}_w(\mathbf{x}_f - \mathbf{x})$$

Eq. H 11

Likewise, the deconvolutional model for the inferred fracture aperture field, $\tilde{a}$, given the along fiber strain or strain rate fields is:

$$\tilde{a}(t, \mathbf{x}_f) \;=\; \varepsilon_{\mathrm{w}}(\mathrm{t}, \mathbf{x}) * \mathcal{L}_w^{-1}(\mathbf{x}_f - \mathbf{x})$$

Eq. H 12

$$\tilde{a}(t, \mathbf{x}_f) \;=\; \dot{\varepsilon}_{\mathrm{w}}(\mathrm{t}, \mathbf{x}) * \dot{\mathcal{L}}_w^{-1}(t_f - t, \mathbf{x}_f - \mathbf{x})$$

Eq. H 13

Convolutional models of vertical planar fractures observed by offset vertical fibers indicate $\mathcal{L}_w$ is essentially a smoothed second derivative operator on the vertical aperture distribution, $a(t, z)$, for the closest part of the fracture to the fiber,

$$\varepsilon_{\mathrm{w}} = a \;* \mathcal{L}_w \approx \partial_{zz} \bar{a},$$

Eq. H 14

where $\bar{a}$ is a smoothed representation of the aperture field, a, and the smoothing length-scale is the fracture-fiber distance. This means the observed fiber strains, ε_{w}, are an excellent fracture aperture edge detector. As the largest aperture edges are typically associated with the fracture tip line, vertical fiber strains highlight the depth location of the upper fracture tip, and the lower

fracture tip if the fiber extends to that depth. Likewise, for a vertically propagating fracture, the observed fiber strain rates, $\dot{\varepsilon}_w$, highlight movement of the upper and lower fracture tips.

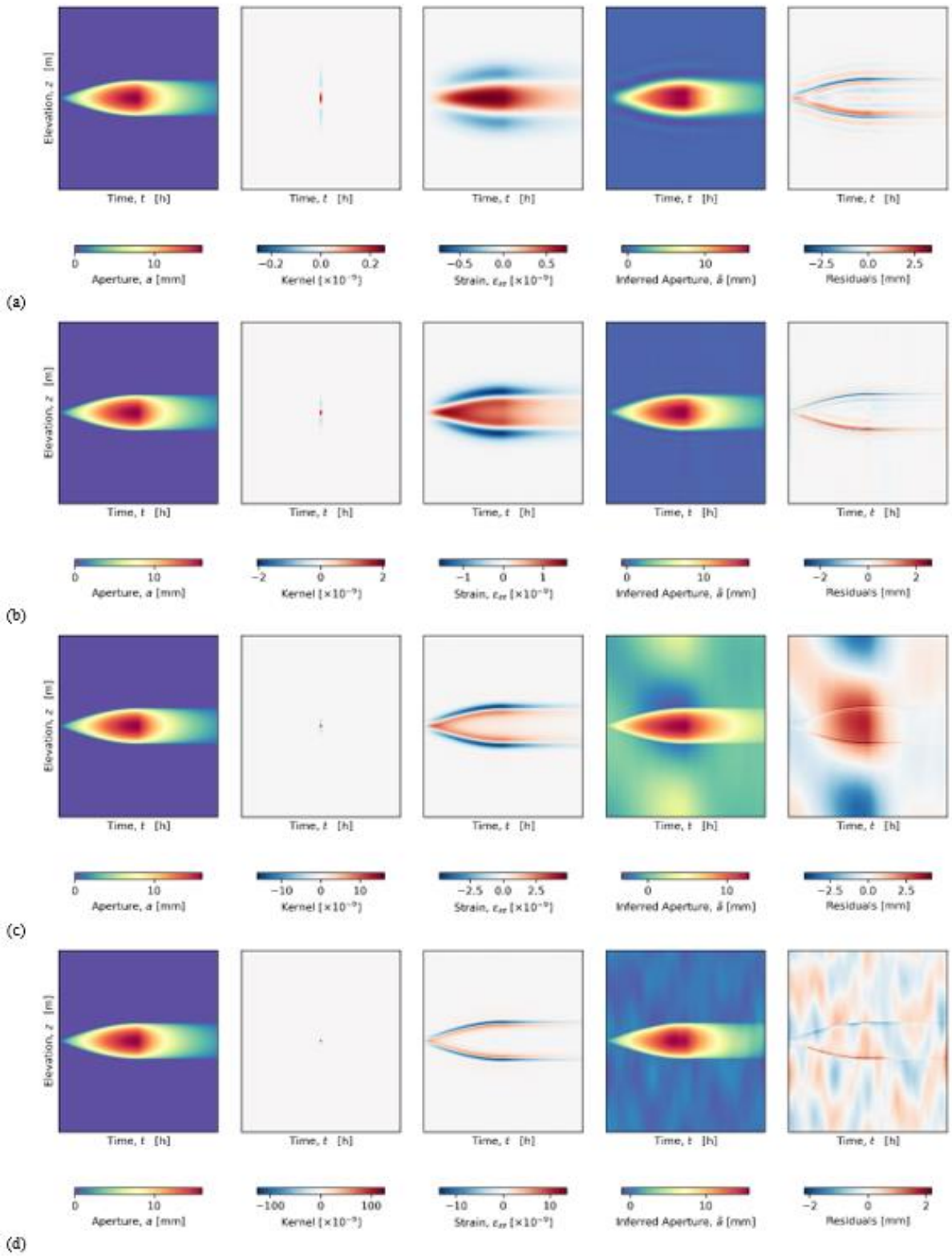

Fig H 2—Inference of fracture apertures, $\tilde{a}(t,z)$, by deconvolution of simulated vertical strain observations, $\varepsilon_{zz}(t,z)$, with 1% random uncorrelated noise, and offset from the vertical fracture plane by (a) $h/2$, (b) $h/4$, (c) $h/8$, and (d) $h/16$ where h is the ultimate height extent of the simulated fracture stimulation.

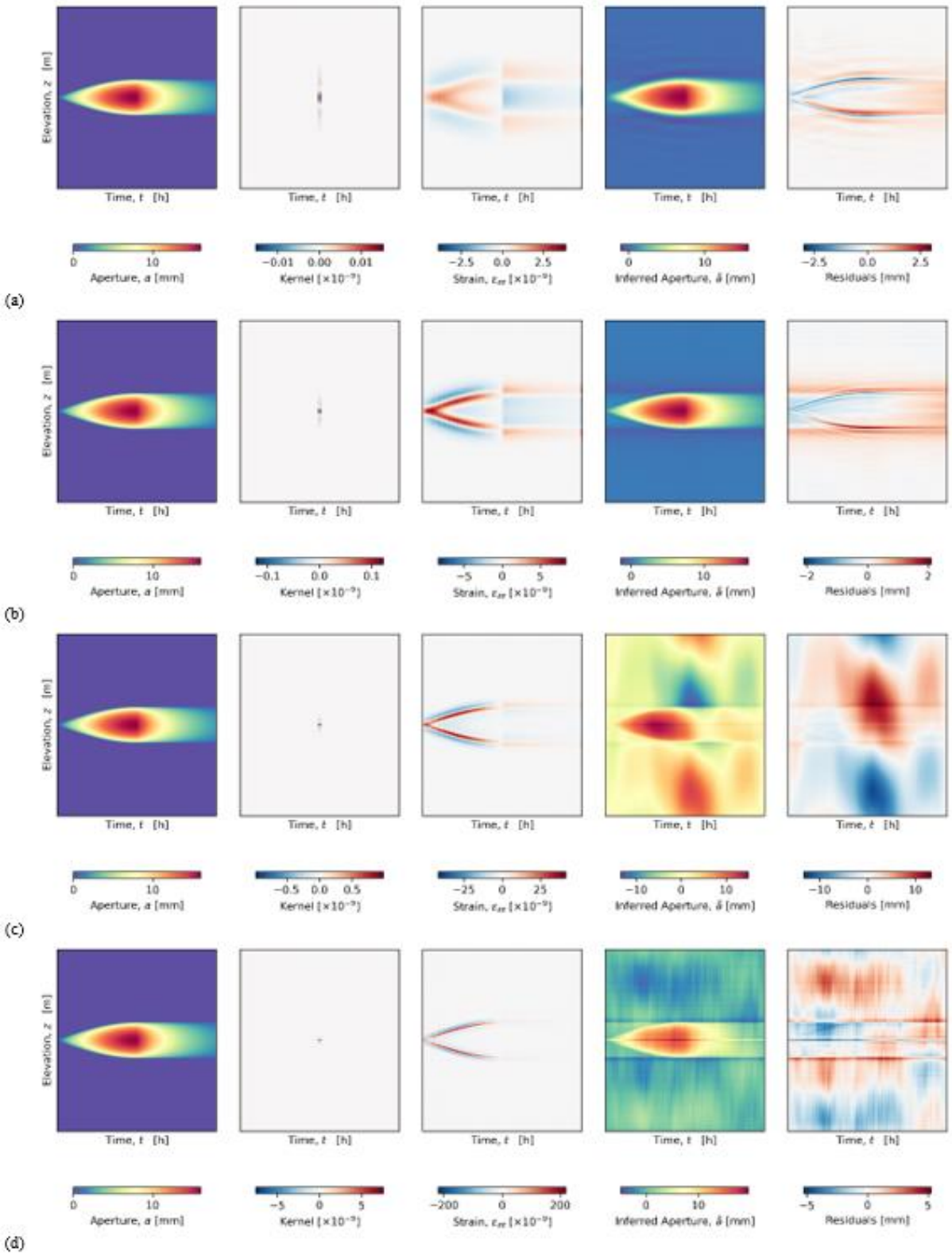

Fig H 3—As Fig H 2, except for this time for the simulation and deconvolution of fiber strain rates, $\dot{\varepsilon}_{zz}(t,z)$.

Results from Synthetic Fiber Strain Data

Fig H 2 shows the results obtained by sequential application of the convolutional and deconvolutional fiber strain models to a synthetic aperture field of a propagating vertical planar fracture. This synthetic fracture has an elliptical shape with an elliptical aperture distribution consistent with a homogeneous internal fracture driving stress. During the synthetic fracture stimulation phase, the fracture propagates at prescribed rates with a fixed horizontal-to-vertical aspect ratio, α, and remains centered on the perforation location, $\mathbf{x}_p$. During the synthetic depressurization phase, the fracture geometry remains fixed, and the fracture apertures reduce in proportion to the depressurization that is taken to follow an exponential decline.

The vertical fiber path is located at distance d_s from the horizontal stimulation well and distance d_f from the fracture plane. As we assume the ultimate fracture height above the perforation, h, remains small relative to the perforation depth below the free surface, $h \ll z_p$, solutions only depend on this geometry via the ratios d_s/h and d_f/h. As we are interested in solutions for a vertical observation well located close to the horizontal stimulation well, we select $d_s/h \ll 1$ such that the solution is not sensitive to d_s/h. Now the models only depend on the fracture-fiber distance relative to the ultimate fracture height, d_f/h and the rows of Fig H 2 show results obtained for $d_f/h = \{1/2, 1/4, 1/8, 1/16\}$, and $\alpha = 3$. Results for $\alpha > 3$ are essential indistinguishable from $\alpha = 3$ as the vertical fiber strains are primarily sensitive to the fracture apertures over a vertical band that is within a horizontal distance d_f of the perforation.

The first column of Fig H 2, shows the time-depth evolution of the synthetic fracture aperture field, $a(t,z)$, which remains as before. The second column shows the elastostatic kernel, $\mathcal{L}_w$, that defines the physical covariance between the fracture apertures and the along-fiber strains, ε_w. Notice that the vertical extent of these kernel scales with the fiber-fracture distance. The kernel shape is characterized by a vertical elongation strain (red) centered at the same depth as the fracture point source, flanked by contractional strains (blue) just above and below the point source.

The third column shows the time-depth variation of the along-fiber strains in response to the opening and growth of the synthetic fracture according to the convolutional model with the addition of 1% uncorrelated, random noise. The near-field response (Fig H 2d) sharply highlights the upper and lower fracture tips as they propagate away from the perforation depth during the stimulation phase. The fracture tip precisely corresponds to the zero-crossing of the strain doublet where elongational strains (red) localize just behind the fracture tip and contractional strains (blue) localize just ahead of the opening fracture tip. This means:

- The upper fracture tip appears as a *negative-over-positive* (blue-over-red) strain doublet, and
- The lower fracture tip appears as a *positive-over-negative* (red-over-blue) strain doublet.

Mathematically, this behavior reflects superposition of point sources located at and behind the fracture tip. For the upper tip, the contractional strains contributed below each point source are cancelled by the elongational strain centered on the neighboring point source below. Physically,

this behavior reflects fracture-normal elongation of the medium beyond the fracture tip coupled by the Poisson effect to contraction in the orthogonal directions, including the fiber direction. For stress-balance, opposing strains arise behind the fracture tip.

The far-field response (Fig H 2a) offers less vertical resolution as the kernel length-scale becomes comparable to the distance between the upper and lower fracture tips. This means the *negative-over-positive* strain doublet from the upper tip overlaps and reinforces the *positive-over-negative* strain doublet from the lower tip creating a *negative-over-positive-over-negative* strain triplet. If zero-crossings within this strain triplet are used to identify the fracture tips this will over-estimate the vertical fracture extent with the true upper fracture tip located slightly below the upper zero-crossing and the true lower fracture tip located slightly above the lower zero-crossing.

During the depressurization phase the synthetic fracture extent remains fixed whilst the elliptically distributed fracture apertures decline. The along-fiber strains reflect this process as the depth of strain doublets and triplets remain fixed whilst their amplitudes decline in proportion to the declining fracture apertures. Any residual fiber strains will indicate residual fracture apertures.

The third and fourth columns of Fig H 2 show the inferred aperture distribution, $\tilde{a}$, and the residuals relative to the true synthetic field, $a - \tilde{a}$. In these synthetic examples the deconvolution model accurately recovers the upper and lower fracture tip depths through time and the intervening aperture distribution. Vertical resolution limits are imposed by the elastostatic kernel size and the imposed random uncorrelated noise. This limits the precision of fracture tip identification, to no better than the kernel resolution which depends on fracture-fiber distance.

In the far-field (Fig H 2a) resolution is most-limited by the kernel scale, and deconvolution results contain typical-observed ringing artifacts associated sharp discontinuities. In these cases, inferred apertures outside the true fracture extent oscillate about zero with diminishing amplitude away from the true fracture tips. In the near-field (Fig H 2d) resolution is most-limited by the imposed uncorrelated random noise which appears in the inferred aperture with vertical and temporal correlation scales are proportional to the $\mathcal{L}_w$ kernel correlation scales.

Results from Synthetic Fiber Strain Rate Data

Table H 1—Summary of strain rate doublets associated with the upper and lower fracture tips during fracture opening and closing. The transition from fracture opening to closing causes these strain rate doublets to flip polarity.

	Fracture opening	Fracture closing
Upper fracture tip	negative-over-positive	positive-over-negative
Lower fracture tip	positive-over-negative	negative-over-positive

Fig H 3 shows equivalent results to Fig H 2 except for fiber strain rates. The strain rate fields show the same doublet features that help to identify the upper and lower fracture tips. The

principal difference is the polarity flip of these strain rate doublets as the fracture switches from opening to closing (Table H 1).

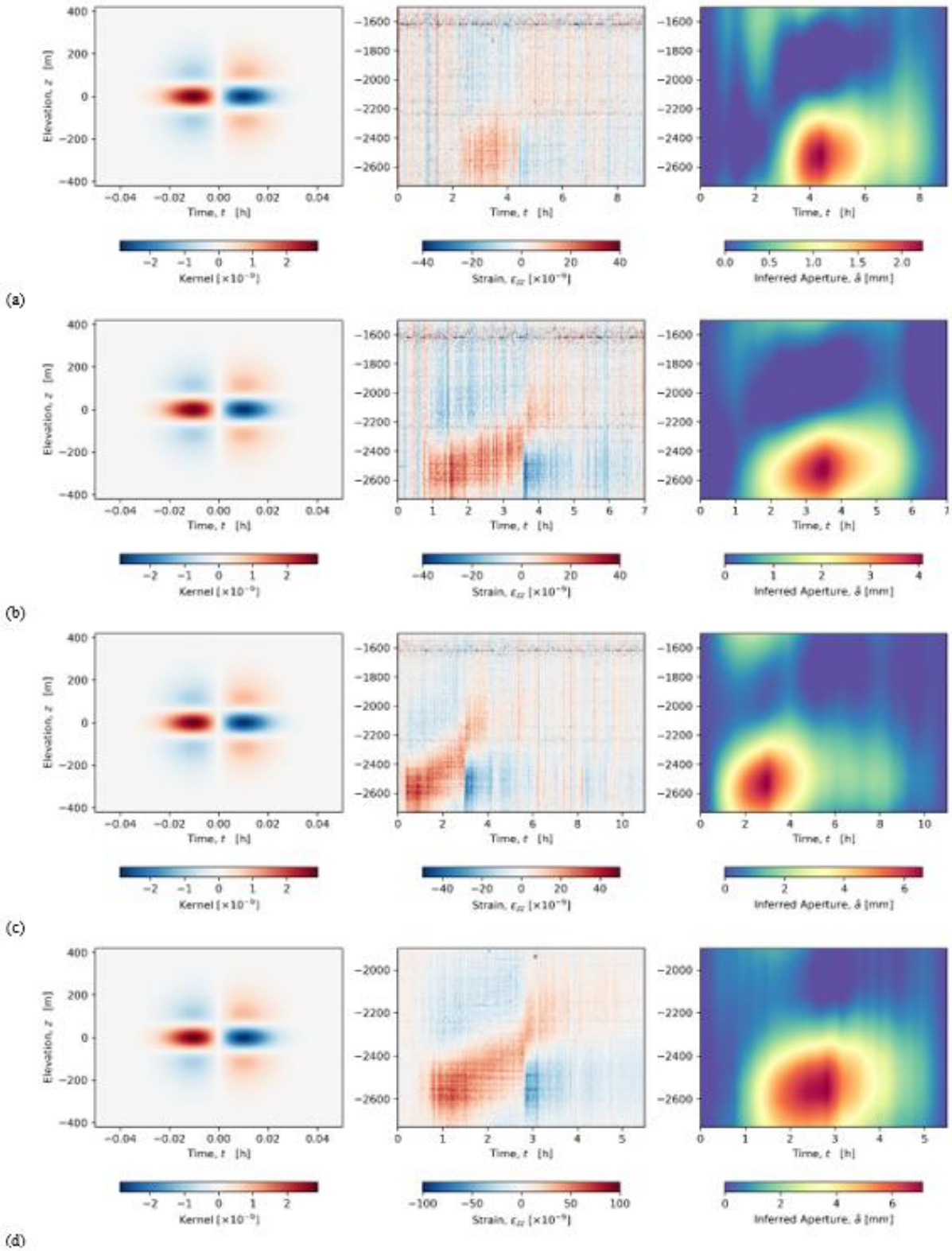

Fig H 4—Inference of fracture apertures, $\tilde{a}(t,z)$, by deconvolution of vertical fiber strain rate observations, $\dot{\varepsilon}_{zz}(t,z)$, in well B5PH during stimulation of well B4H in stages (a) 12, (b) 13, (c) 14, and (d) 15.

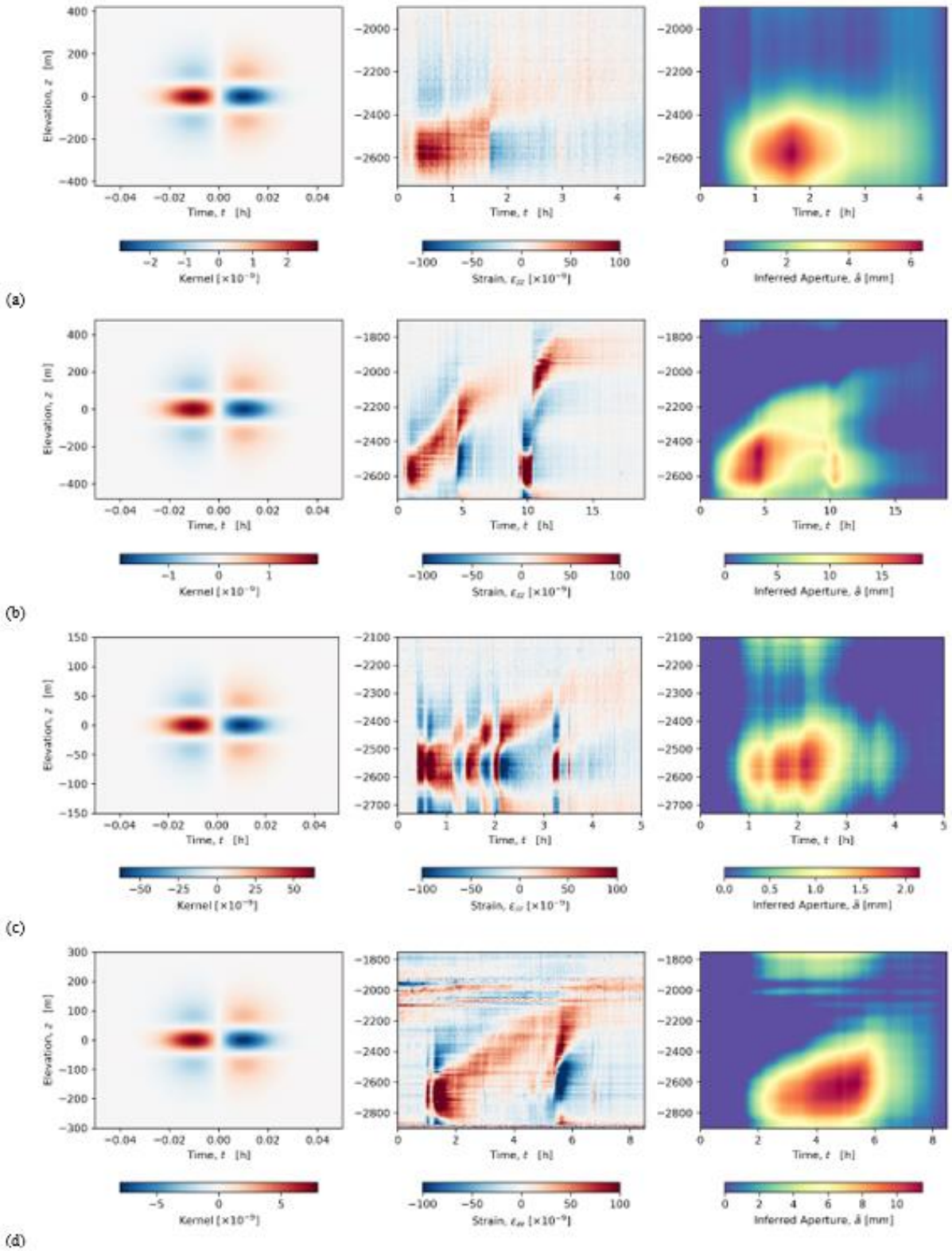

Fig H 5—Inference of fracture apertures, $\tilde{a}(t,z)$, by deconvolution of vertical fiber strain rate observations, $\dot{\varepsilon}_{zz}(t,z)$, in well B5PH during stimulation of well B4H in stages (a) 16, (b) 17 – 18, (c) 19, and (d) 23.

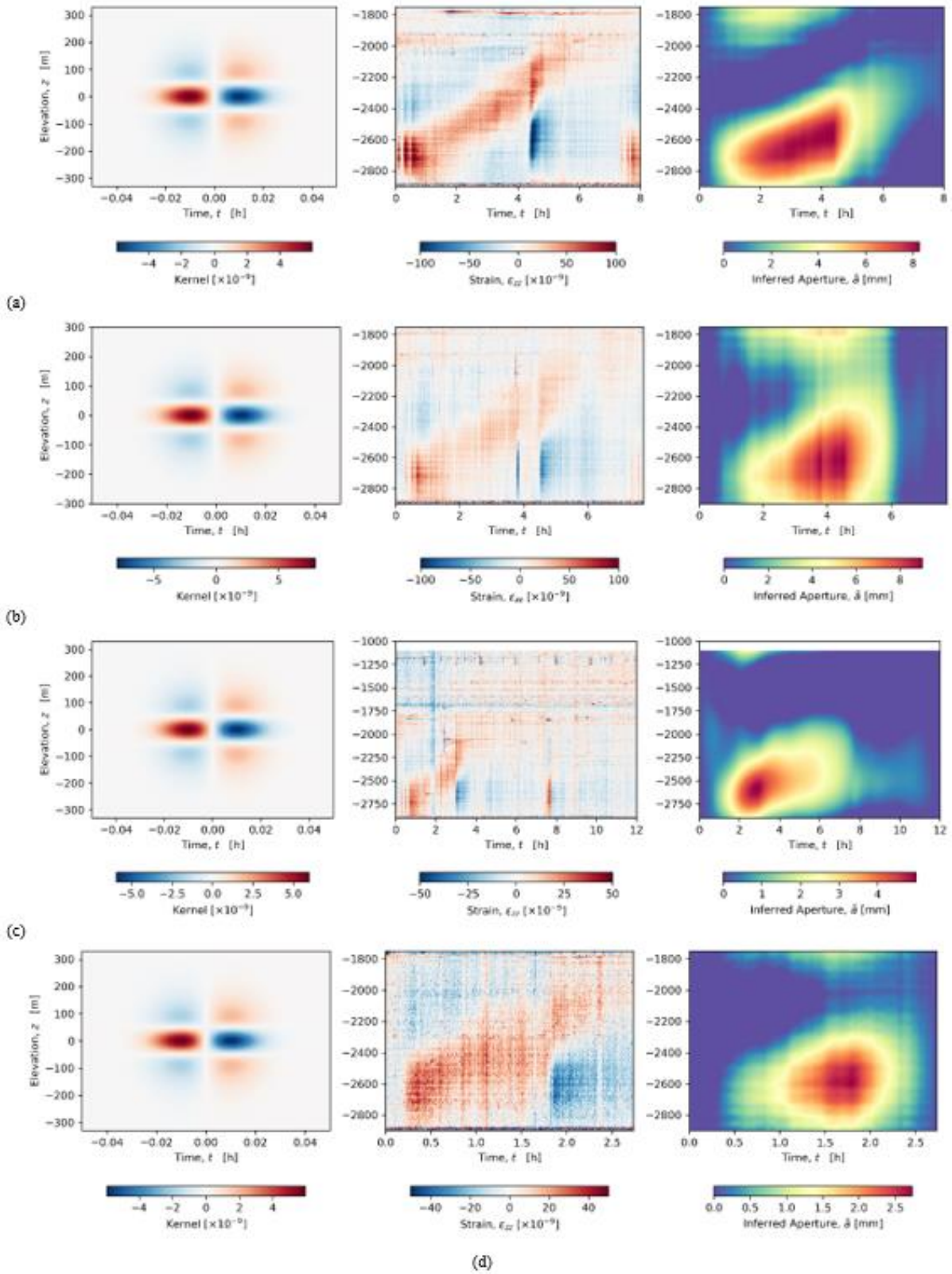

Fig H 6—Inference of fracture apertures, $\tilde{a}(t,z)$, by deconvolution of vertical fiber strain rate observations, $\dot{\varepsilon}_{zz}(t,z)$, in well B5PH during stimulation of well B4H in stages (a) 24, (b) 25, (c) 26a, and (d) 26b.

Deconvolution of fiber strain rates accurately recovers the true aperture distribution in both the far-field (Fig H 3a) and the near-field (Fig H 3d). As before, far-field results are limited by kernel resolution and the associated ringing effects associated with the under-resolved fracture tips. Likewise, near-field results are limited by strain rate noise that is projected by deconvolution into the inferred aperture field with correlations imposed by the kernel. If the correlation scales of this projected noise happen to be comparable to the correlation scales of the true aperture field, then the inferred apertures may contain some artifacts that are difficult to identify (Fig H 3c). These deconvolution results also show indications of image wrapping, especially over the time coordinate which we attribute to periodic boundary conditions in the Fast Fourier Transforms used to compute the convolutional and deconvolutional models. This shows up as late-time true apertures appearing as faint contributions to the early-time inferred apertures such as faint indications of the ultimate fracture height appearing throughout the time series. These artifacts may be diminished by padding the strain rates with zeros to move these boundary effects well beyond the region of interest.

Results from HFTS2 Fiber Strain Rate Data

Fig H 4, Fig H 5, and Fig H 6 show the observed vertical fiber strain rates, $\dot{\varepsilon}_{zz}$, within well B5PH and the inferred time-depth distribution of fracture apertures, $\tilde{a}$, according to the deconvolutional model for stimulation stages 12—19 and 23—26 within the horizontal well B4H. Each stimulation stage involves injection via multiple adjacent perforations designed to propagate multiple parallel vertical hydraulic fractures. If the spacing between these perforations is much smaller than their distances to B5PH, then the deconvolution model yields the total fracture aperture summed over all fractures using a single kernel corresponding to the mean fracture-fiber distance. This is the case for all stages except the very closest stages to B5PH (20—22) where no single kernel represents all the fractures. These cases would require sequential deconvolution using multiple kernels to represent the multiple distinct fractures. As such we exclude stages 20—22 from this analysis of single deconvolutions.

Inspection of the observed strain rates fields allows ready identification of negative-over-positive (blue-over-red) strain rate doublets that indicate the upper fracture tip during fracture opening and vertical growth followed by a polarity reversal that indicates the onset of fracture closure. The inferred aperture fields appear broadly like our synthetic aperture fields (Fig H 2) with upward propagation of the upper fracture tip accompanied by an increasing maximum aperture during the stimulation phase followed by a static upper fracture tip and a declining maximum aperture during the depressurization phase. In all these cases residual fracture apertures after depressurization appear to be small or undetectable relative to the maximum inferred apertures attained during the stimulation phases.

Stage 17—18 (Fig H 5b) and stage 24 (Fig H 6a) all show evidence of unexpected upward fracture propagation during the depressurization phase. During the stimulation phase of stage 24, the upper fracture tip propagates 400m upwards (from an elevation of -2600m to -2200m) at a constant rate over 4 hours (Fig H 6a, 0.5—4.5 h). This is followed by rapid closure of the fracture around the perforation depth over the next 2 hours (Fig H 6a, 4.5—6.5 h) leaving no detectable residual aperture at this depth. However, over the same period (4.5—6.5 h), the upper fracture tip continues to propagate an additional 200m upwards at the essentially the

same rate as before (from an elevation of -2200m to -2000m). During this time the inferred fracture apertures below the upward propagating upper tip appear to decline. At t = 8h, the only detectable residual apertures are 400—600m above the perforation depth.

Stage 17—18 likewise shows a 400m upward propagation of the upper fracture tip at a steady rate during stimulation (0.5—5h) accompanied by increasing fracture apertures around the perforation depth. During depressurization, fracture apertures decline rapidly around the perforation elevation (-2600m) to about 25% of their previous maximum value at t = 10h. Just 200m above the perforations, the fracture also closes but at about half the rate to about 50% of the previous maximum value at t = 10h. Over this same period, the upper fracture tip continues to propagate upwards, albeit at a slower rate than before, to climb an additional 150m over 5 hours (from an elevation of -2200m to -2050m). Subsequent re-pressurization (t = 9.5—10.5h) partially reopens the fracture around the perforation depth but only up to the level of the largest residual apertures remaining after the previous depressurization (-2400m). In contrast, the 200m interval above this (-2400 to -2200m) shows no evidence of fracture opening during this re-pressurization period. However, further above this (-2200 to -2000m) the upper tip of residual fracture apertures resumes upward propagation climbing an additional 50m (-2050 to -2000m) during the second depressurization phase (t = 9.5—12h) whilst the fracture recloses around the perforations.

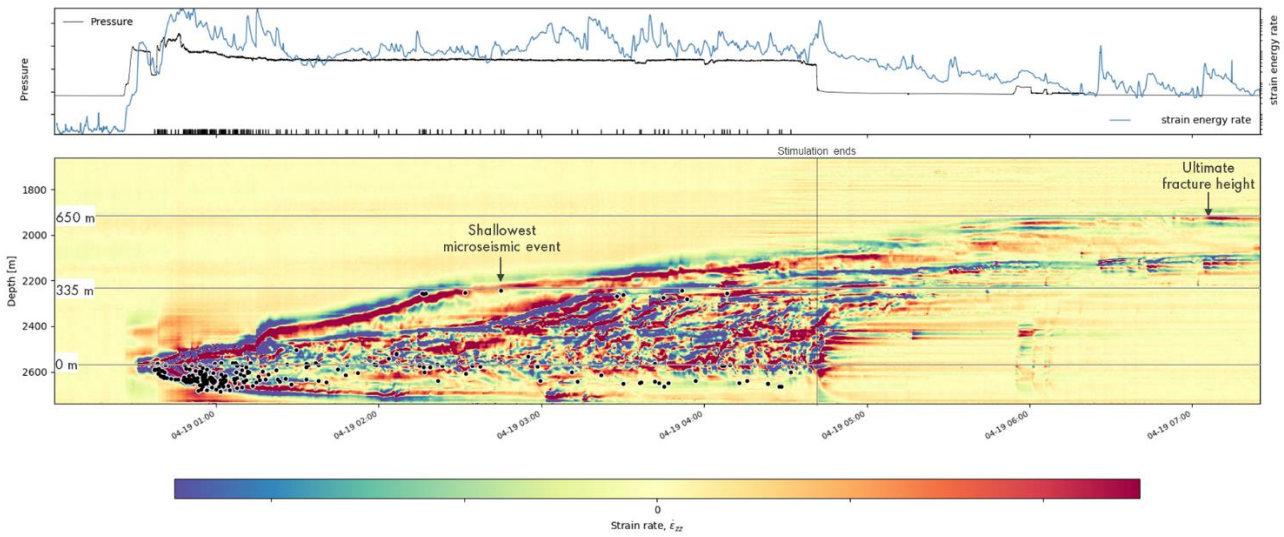

Fig H 7—Stage 21 hydraulic fracture stimulation of well B4H. (a) time series of well head pressures (black curve), fiber strain energy rates (blue curve) and microseismic event times (black ticks). (b) Time-depth distribution of fiber strain rates in vertical observation well B5PH, and microseismic events (black dots). Grey lines denote heights above the perforations.

In almost all cases the perforation depths where hydraulic fracture may initiate are close to the lowest usable fiber depth. This means the fiber strain rates are largely insensitive to the lower fracture tip. Stage 19 (Fig H 5c) does however show an example of a downward propagating lower fracture tip. In some cases, the lower fracture aperture distribution appears to wrap around into the upper part of the images. Similar effects were also seen in the synthetic data

where non-zero values happen to exist close to the edges of the image and are associated with periodic boundary conditions on the Fast Fourier Transform. Correlated noise is seen in the fiber strain rate data as transient noise events along the entire fiber (vertical bands) and persistent noisy or quiet channels at some locations along the fiber (horizontal bands). Depending on their strength and clustering, some of these bands project into the inferred fracture aperture field appearing again as vertical and horizontal bands.

Discussion

Upward propagation of the upper tip of an opening fracture induces a characteristic strain rate doublet feature at the same depth on any nearby vertical fiber-optic distributed strain sensor. Deconvolution of such strain rate data indicates the vertical aperture profiles during fracture stimulations and closures indicating the maximum vertical extents and the residual aperture distributions. However, the time-depth path of the upper fracture tip is readily identifiable directly on the fiber strain rate data, without requiring deconvolution or any other processing step, as it is closely associated with the zero-crossing of the fiber strain doublet as it moves steadily with time.

The shallowest microseismic event is often taken to indicate vertical hydraulic fracture extent through time. Localized shear stress induced close the tip line of an opening fracture is capable of inducing seismogenic shear failures detectable by microseismic monitoring arrays with locatable hypocenters at the microseismic source point. For this method to be mostly reliable, most fracture tips must induce shear failure, and most of these shear failures must be seismogenic, and most of these microseismic events must be located accurately. Should any of these assumptions prove unreliable then the apparent height of a hydraulic fracture based on the shallowest microseismic event will also be unreliable. Moreover, should the fracture propagate up through formations resilient to shear failure or prone to aseismic shear failure then the shallowest microseismic event will systematically under-estimate the true vertical fracture extent.

Fig H 1c compares the time-depth distribution of vertical fiber strain rates and microseismic events. The shallowest microseismic events associated with each stage of hydraulic fracturing are typically 200m above the perforations and sometimes 400m. In contrast, the fiber strain doublets associated with the upper fracture tip, where visible, always extend significantly above the shallowest microseismic event, sometimes reaching 800m above the perforations.

Fig H 7 shows stage 21 in greater detail. Fractures initiate at the perforation depth with some downward growth of the lower fracture tip and greater upward growth of the upper tip. In between the image is much more complex, which we attribute to multiple interacting parallel fractures that may inhibit or promote each other's growth. Focusing on the upper strain rate doublet of the tallest fracture above the perforations, we observed most microseismic events originate around the perforations depth, but the shallowest microseismic events occur 335m above the perforations and with origin times similar to the time the upper tip of the tallest fracture passes this depth. However, the growth of this tallest fracture tip up to this height or above this height induces no other microseismic events. Fiber strains indicate the ultimate height of this tallest fracture is 650m above the perforations which is almost twice the height indicated by the shallowest microseismic event. Evidently most of the upwards propagation of

this fracture tip was either aseismic or induced microseismic events with too little energy to be detected and located.

At the end of the high-pressure fracture stimulation period, the tallest fracture is 500m above the perforations. As soon as the injection pressure reduces, fiber strain rates indicate fracture closure around the perforation depth. However, the strain rate doublet associated with the upper tip of the tallest fracture continues its path upwards (Tan et al. 2020) at the same rate and with the same polarity consistent with fracture opening. Unlike the high-pressure stimulation period, the continuity of this shallowest strain rate doublet is occasionally interrupted. We suspect this might indicate different fractures trading places as the tallest fracture. Regardless, the tallest fracture appears to grow an additional 150m upwards over 2 hours after the end of high-pressure injection. This seems to require sufficient closure of the fracture around the perforations to limit vertical pressure communication within the fracture such that fluids pressure within the upper part of the fracture remain above the fracture pressure at these depths for at least 2 hours.

Conclusions

The convolutional model provides a rapid method for simulating the time-depth distribution of fiber strains or strain rates induced by any given time evolution of deep hydraulic fracture geometries. Likewise, the deconvolutional model provides a rapid method for inferring the time-depth distribution of hydraulic fracture apertures given fiber-optic Distributed Strain Sensor observations along a nearby vertical observation well.

Application of these models to HFTS2 data indicate the shallowest reported microseismic depth during fracture stimulation is not a reliable indicator for the ultimate fracture height due to the possibility of non-seismogenic fracture growth within some formations. Vertical fracture aperture profiles inferred using fiber optic Distributed Strain Sensors that sample the fracture-induced strain field indicate fracture heights sometimes extend significantly above the shallowest microseismic event depth. Upward fracture growth may also continue during fluid pressure relaxation despite fracture closure around the perforation interval.

References

Ichikawa, M., et al. 2019. Case Study of Hydraulic Fracture Monitoring Using Multiwell Integrated Analysis Based on Low-Frequency DAS Data. *Learning Edge*, **39**(11): 794-800. https://doi.org/10.1190/tle39110794.1

Jin, G., et al. 2021. Novel Near-Wellbore Fracture Diagnosis for Unconventional Wells Using High-Resolution Distributed Strain Sensing during Production. *SPE Journal*, **26**(05): 1–10. https://doi.org/10.2118/205394-PA.

Jin, G, Kevin, M., Baishali, R., et al. 2019. Machine Learning-Based Fracture-Hit Detection Algorithm Using LFDAS Signal. *Leading Edge*, **38**(7): 520–24.

Jin, G., & Baishali, R. 2017. Hydraulic-Fracture Geometry Characterization Using Low-Frequency Das Signal. *Leading Edge*, **36**(12): 975–80.

Karrenbach, M., et al. 2019. Fiber-Optic Distributed Acoustic Sensing of Microseismicity, Strain and Temperature during Hydraulic Fracturing. *Geophysics*, **84**(1): D11–D23.

Liu, Y., Ge, J., & Kan, W. 2021. Quantitative Hydraulic-Fracture Geometry Characterization with LF-DAS Strain Data: Numerical Analysis and Field Applications. Paper presented at the SPE Hydraulic Fracturing Technology Conference and Exhibition, Virtual.

Liu, Y., Ge J., Kan W., et al. 2021a. Hydraulic-Fracture-Width Inversion Using Low-Frequency Distributed-Acoustic-Sensing Strain Data—Part I: Algorithm and Sensitivity Analysis. *SPE Journal*, **26**(01): 359–371. https://doi.org/10.2118/204225-PA

Liu, Y., Ge J., Kan W., et al. 2021b. Hydraulic-Fracture-Width Inversion Using Low-Frequency Distributed-Acoustic-Sensing Strain Data Part II: Extension for Multifracture and Field Application. *SPE Journal*, **26**(05): 2703-2715. https://doi.org/10.2118/205379-PA

Liu, Y., Kan, W., Ge, J., et al. 2020. Rock Deformation and Strain-Rate Characterization during Hydraulic Fracturing Treatments: Insights for Interpretation of Low-Frequency Distributed Acoustic-Sensing Signals. *SPE Journal*, **25**(5): 2251–2264.

Mindlin, R. D. 1936. Force at a Point in the Interior of a Semi-Infinite Solid. *Physics*, **7**: 195–202.

Molenaar, M. M., Erkan, F., & David, J. H. 2012. Real-Time Downhole Monitoring Of Hydraulic Fracturing Treatments Using Fibre Optic Distributed Temperature and Acoustic Sensing. Paper presented in SPE/EAGE European Unconventional Resources Conference and Exhibition, Vienna, Austria. https://doi.org/10.2118/152981-MS.

Okada, Y. 1992. Internal Deformation Due to Shear and Tensile Faults in a Half-Space. *Bulletin of the Seismological Society of America*, **82**: 1018–1040.

Richter, P., et al. 2020. High-Resolution Distributed Acoustic Sensor Using Engineered Fiber for Hydraulic Fracture Monitoring and Optimization in Unconventional Completions. Paper presented in SEG International Exposition and Annual Meeting. https://doi.org/10.1190/segam2019-3215860.1

Segall, P. 2010. Earthquake and Volcano Deformation Earthquake and Volcano Deformation. Princeton University Press.

Sherman, C., Robert, M., Joseph M., et al. 2019. Geomechanical Modeling of Distributed Fiber-Optic Sensor Measurements. *Interpretation*, **7**(1): SA21-SA27.

Tan, Y., et al. 2020. Geomechanical Template for DAS Fiber Strain Patterns during Hydraulic Fracturing. Paper presented in Society of Petroleum Engineers Annual Technical Conference & Exhibition. https://doi.org/10.2118/201627-MS

Ugueto, G. A., Todea, F., Daredia, T., et al. 2019. Can You Feel the Strain? DAS Strain Fronts for Fracture Geometry in the BC Montney, Groundbirch. Paper presented at the SPE Annual Technical Conference and Exhibition, Calgary, Alberta, Canada. https://doi.org/10.2118/195943-MS.

Wu, Y., P. Richter, R. Hull, & M. Farhadiroushan. 2020. Hydraulic Frac-Hit Corridor (FHC) Monitoring and Analysis with High-Resolution Distributed Acoustic Sensing (DAS) and Far-Field Strain (FFS) Measurements. *First Break*, **38**(6): 65–70.

Zhang, Z., Fang, Z., Stefani, J., et al. 2020. Modeling of fiber-optic strain responses to hydraulic fracturing. *Geophysics*, **85**(6): A45-A50. https://doi.org/10.1190/geo2020-0083.1

END OF REPORT